

PRINCIPLES OF HELIOPHYSICS:
a textbook on the universal processes
behind planetary habitability

by

Karel Schrijver, Fran Bagenal, Tim Bastian, Jürg Beer, Mario Bisi,
Tom Bogdan, Steve Bougher, David Boteler, Dave Brain, Guy Brasseur,
Don Brownlee, Paul Charbonneau, Ofer Cohen, Uli Christensen,
Tom Crowley, Debrah Fischer, Terry Forbes, Tim Fuller-Rowell,
Marina Galand, Joe Giacalone, George Gloeckler, Jack Gosling,
Janet Green, Nick Gross, Steve Guetersloh, Viggo Hansteen, Lee Hartmann,
Mihaly Horanyi, Hugh Hudson, Norbert Jakowski, Randy Jokipii,
Margaret Kivelson, Dietmar Krauss-Varban, Norbert Krupp,
Judith Lean, Jeff Linsky, Dana Longcope, Daniel Marsh, Mark Miesch,
Mark Moldwin, Luke Moore, Sten Odenwald, Merav Opher, Rachel Osten,
Matthias Rempel, Hauke Schmidt, George Siscoe, Dave Siskind,
Chuck Smith, Stan Solomon, Tom Stallard, Sabine Stanley, Jan Sojka,
Kent Tobiska, Frank Toffoletto, Alan Tribble, Vytenis Vasyliunas,
Richard Walterscheid, Ji Wang, Brian Wood, Tom Woods, and Neal Zapp

Principles of heliophysics, V 2.1

Copyright ©2024 The authors

ISBN-13: 9798847272711 (paperback)

ISBN-13: 9798353812982 (hardcover)

<https://arxiv.org/abs/1910.14022>

Cover design for the Amazon/KDP version by Karel Schrijver

Printed in the United States of America

Contents

Preface (do read it!)	vii
1 Stars, planetary systems, and the local cosmos	1
1.1 Preparing for the future	1
1.2 Considering planetary habitability	2
1.3 Heliophysics: unification, coupling, exploration	3
1.4 The language of heliophysics	7
1.5 A timeline of exploration of planetary systems	10
2 Neutrals, ions, and photons	13
2.1 Conditions in the local cosmos	13
2.2 Gravitationally stratified atmospheres and stellar winds	16
2.3 Photons, collisions, ionization, and differentiation	25
2.4 On collisions and currents, and on neutrals and pickup ions	31
2.5 Sources of plasma	38
3 MHD, field lines, and reconnection	39
3.1 Introduction	39
3.2 (Magneto-)Hydrodynamics	44
3.2.1 MHD equations, individual terms, and special cases	46
3.2.2 The induction equation	49
3.3 Waves in magnetized plasmas	52
3.4 MHD, magnetic field lines and reconnection	54
3.5 A few notes about conditions	61
3.5.1 Solar atmosphere <i>vs.</i> terrestrial magnetosphere	61
3.5.2 Heliosphere	62
4 Dynamos of Sun-like stars and Earth-like planets	63
4.1 Dynamo settings	63
4.1.1 Earth and other terrestrial planets	67
4.1.2 The Sun and other stars	69
4.2 Dynamo principles	69
4.3 Essentials of fluid motions in dynamos	72

4.4	Insights from approximate stellar dynamo models	75
4.5	Mean-field dynamo models	77
4.6	Dynamos in other stars	88
4.7	Dynamos in terrestrial planets	90
5	Flows, shocks, obstacles, and currents	95
5.1	Introductory overview	95
5.2	Low-velocity interactions versus shocks	98
5.3	Elementals of shocks and other discontinuities	100
5.4	The magnetized solar wind and the Parker spiral	105
5.5	Flow-based interactions in heliophysics	107
5.5.1	Solar-wind stream interactions	107
5.5.2	A non-conducting body without atmosphere	112
5.5.3	Flow around a conducting body	114
5.5.4	Plasma flow around a permanently magnetized body	116
5.5.5	A closed magnetosphere	116
5.5.6	The open magnetosphere	118
5.5.7	Solar wind-magnetosphere-ionosphere interaction	122
5.5.8	A large-scale flow impinging on a fast outflow	127
6	Magnetic (in-)stability and energy pathways	129
6.1	Introduction	129
6.1.1	Introducing solar flares and coronal mass ejections	131
6.1.2	Introducing geospace (sub-)storms	132
6.2	Terrestrial magnetospheric disturbances	135
6.2.1	Energy pathways and reservoirs	135
6.2.2	What leads to explosive energy releases?	137
6.2.3	Terrestrial magnetospheric substorms	140
6.2.4	Terrestrial magnetic storms	141
6.3	Models of solar impulsive events	142
6.3.1	The magnetic reservoir	142
6.3.2	Two-dimensional force-free models	143
6.3.3	Three-dimensional force-free models	146
6.3.4	Formation of the pre-eruption field	148
6.3.5	Observed signatures of flares and CMEs	150
6.4	Magnetic instabilities and reconnection	154
7	Torques and tides	159
7.1	Introduction	159
7.2	Magnetic torques	161
7.2.1	Stellar winds and magnetic braking	161
7.2.2	Planetary magnetospheric torque	162
7.2.3	Magneto-rotational coupling	165
7.2.4	Disk winds	166

7.3	Gravitational tides	168
7.3.1	Spin-orbit interactions	168
7.3.2	Orbital interaction	171
7.4	Planetary atmospheric tides	172
8	Particle orbits, transport, and acceleration	175
8.1	Introduction	175
8.2	Single particle motion	177
8.3	Phase space density and Liouville's theorem	181
8.4	The collisionless Boltzmann equation	182
8.5	Particle scattering and transport	185
8.5.1	Solar energetic particles	188
8.5.2	Galactic cosmic rays	190
8.6	Particle acceleration in shocks	193
8.7	Relativistic particles in planetary radiation belts	201
8.7.1	Electron acceleration mechanisms	201
8.7.2	Proton acceleration in the radiation belt	205
8.7.3	Radiation belt losses at Earth	205
9	Convection, heating, conduction, and radiation	207
9.1	Convective and radiative energy transport	207
9.2	Heating and cooling of the solar outer atmosphere	211
9.3	Magnetic activity and atmospheric radiation	214
10	Evolution of stars, activity, and astrospheres	217
10.1	Evolution of stars	217
10.2	Stellar activity and its evolution	221
10.2.1	Overall activity level	221
10.2.2	Flares	223
10.2.3	Rotation rates	225
10.2.4	Stellar infancy: birth to the zero-age main sequence	227
10.2.5	Stellar teenage years: ZAMS - 1 Gyr	227
10.2.6	Stellar adulthood: 1-5 Gyr	228
10.3	Evolution of astrospheres	229
10.3.1	Effects of a variable ISM on heliospheric structure	229
10.3.2	Long-term evolution of stellar winds	232
10.3.3	Astrospheric field patterns in time	236
11	Formation of stars and planets	239
11.1	Introduction	239
11.2	(Exo-)Planets and (exo-)planetary systems	241
11.2.1	Exoplanet formation	243
11.2.2	Exoplanet migration	245
11.2.3	Exoplanet geology	246

11.2.4 Exoplanets and binary star systems	247
11.3 Formation and early evolution of stars and disks	247
11.3.1 Observations of star-forming processes	247
11.3.2 Properties of young stars	251
11.3.3 The rotation rate of very young stars	253
11.3.4 Protoplanetary disks and gravity	255
11.3.5 Dust-disk evolution	257
11.3.6 Disk evaporation	259
12 Irradiance, atmospheres, and habitability	263
12.1 Evolving planetary habitability	263
12.1.1 Earth's formative phase	264
12.1.2 The habitable zone	265
12.1.3 Oxygen, methane, and carbon dioxide over time	267
12.1.4 Water over time	268
12.2 Atmospheres and climates of Venus, Earth, and Mars	269
12.3 Irradiance, orbits, spin, and climate	271
12.3.1 Atmospheric effects and albedo	271
12.3.2 Orbital changes	278
12.4 Planetary atmospheres, geological activity, and stellar winds	280
12.4.1 On time scales beyond millions of years	280
12.4.2 On time scales of up to several millennia	286
13 Upper atmospheres and magnetospheres	289
13.1 Upper-atmospheric chemistry and insolation	289
13.2 Maintaining ionospheres	293
13.2.1 Ionization	293
13.2.2 Recombination	294
13.2.3 Venus and Mars	297
13.3 Setting geospace climate	298
13.3.1 Geospace climate response to solar photon irradiation	298
13.3.2 Geospace climate at earlier terrestrial ages	303
13.3.3 Geospace climate and Earth's magnetic field	305
13.3.4 Geospace climate dependence on the solar wind	308
14 Cosmic rays and magnetic fields over time	311
14.1 Introduction	311
14.2 Long-term energetic-particle exposure of Earth	312
14.2.1 Generation of cosmogenic radionuclides	312
14.2.2 Transport and deposition of cosmogenic radionuclides	315
14.3 Radionuclides as proxies of magnetic variability	317
14.3.1 Geomagnetic field	318
14.3.2 Solar variability	319
14.3.3 Very-long time scale variability in cosmic-ray exposure	320

14.4 Exposure to supernovae	321
15 Applied heliophysics, <i>mutatis mutandis</i>	323
15.1 Activities to take you beyond the present-day solar system	325
Activities	
16 Activities	327
Chapter 1. Stars, planetary systems, and the local cosmos	327
Chapter 2. Neutrals, ions, and photons	328
Chapter 3. MHD, field lines, and reconnection	332
Chapter 4. Dynamos of Sun-like stars and Earth-like planets	334
Chapter 5. Flows, shocks, obstacles, and currents	339
Chapter 6. Magnetic (in-)stability and energy pathways	342
Chapter 7. Torques and tides	344
Chapter 8. Particle orbits, transport, and acceleration	345
Chapter 9. Convection, heating, conduction, and radiation	346
Chapter 10. Evolution of stars, activity, and asterospheres	349
Chapter 11. Formation of stars and planets	351
Chapter 12. Irradiance, atmospheres, and habitability	354
Chapter 13. Upper atmospheres and magnetospheres	356
Chapter 14. Cosmic rays and magnetic fields over time	358
Chapter 15. Applied heliophysics, <i>mutatis mutandis</i>	360
17 Solutions and supplemental text for selected activities	363
17.1 Activity 13: Solar wind travel time	363
17.2 Activity 15: Parker solar wind; basics	363
17.3 Activity 16: Mean free paths and MHD	365
17.4 Activity 21: Penetration depth of energetic particles	367
17.5 Activity 22: Collisions and conductivities	367
17.6 Activity 28: cgs to SI	368
17.7 Activity 35: Plasma β in the Parker solar wind	368
17.8 Activity 37: Thin flux tube and hydrostatic equilibrium	369
17.9 Activity 51: Mean-field induction equation	370
17.10 Activity 53: Babcock-Leighton surface flux dispersal	370
17.11 Activity 64: Solar surface to heliosphere: PFSS	371
17.12 Activity 66: Solar wind behind a non-conducting body	373
17.13 Activity 69: Temperature at the wind stagnation point	374
17.14 Activity 70: Magnetopause distances	375
17.15 Activity 85: Coronal loop cooling time scales	375
17.16 Activity 92: Magnetic braking of the Sun	376
17.17 Activity 94: Tidal breakup	377
17.18 Activity 105: Drift velocity	377
17.19 Activity 107: SEP paths and scattering	377

17.20Activity 112: Setting the scale of granulation	378
17.21Activity 113: Acoustic cutoff	379
17.22Activity 115: Optical depth and field strength	380
17.23Activity 121: Properties of coronal loops	380
17.24Activity 126: Least-massive post-main-sequence star	381
17.25Activity 138: Earth masses in the Sun-forming cloud	381
17.26Activity 140: The Jeans Mass	382
17.27Activity 174: Molecular diffusion coefficients	382
17.28Activity 186: Earth's magnetopause distance over time	382
17.29Activity 189: ^{10}Be production on a hypothetical Mars	383
17.30Activity 193: Exposure to supernovae	383
17.31Activity 200: Reaching Earth's climate from scratch	383

Appendices

Version history	385
List of Figures	390
List of Tables	391
Bibliography	401
Subject index	403
Physical constants, plasma quantities, and vector identities	411

Preface (do read it!)

Heliophysics is the system science of the physical connections between the Sun and the solar system. As the physics of the local cosmos, it embraces space weather and planetary habitability. The wider view of comparative heliophysics forms a template for conditions in exoplanetary systems and provides a view over time of the aging Sun and its magnetic activity, of the heliosphere in different settings of the interstellar medium and subject to stellar impacts, of the space physics over evolving planetary dynamos, and of the long-term influence on planetary atmospheres by stellar radiation and wind.

Based on a series of NASA-funded Summer Schools for early-career researchers, this

Heliophysics

helio-, pref., on the Sun and environs, from the Greek helios.

physics, n., the science of matter and energy and their interactions.

Heliophysics is the

- *comprehensive new term for the science of the Sun - Solar System Connection.*
- *exploration, discovery, and understanding of our space environment.*
- *system science that unites all of the linked phenomena in the region of the cosmos influenced by a star like our Sun.*

Heliophysics concentrates on the Sun and its effects on Earth, the other planets of the solar system, and the changing conditions in space. Heliophysics studies the magnetosphere, ionosphere, thermosphere, mesosphere, and upper atmosphere of the Earth and other planets. Heliophysics combines the science of the Sun, corona, heliosphere and geospace. Heliophysics encompasses cosmic rays and particle acceleration, space weather and radiation, dust and magnetic reconnection, solar activity and stellar cycles, aeronomy and space plasmas, magnetic fields and global change, and the interactions of the solar system with our galaxy.

From NASA's "Heliophysics. The New Science of the Sun - Solar System Connection: Recommended Roadmap for Science and Technology 2005 - 2035."

Table 1: *Heliophysics: definition.*

Table 2: Chapters and their authors in the *Heliophysics* book series sorted by theme (continued on the next page), not showing introductory chapters.

Universal and fundamental processes, diagnostics, and methods	
I.2. Introduction to heliophysics	<i>T. Bogdan</i>
I.3. Creation and destruction of magnetic field	<i>M. Rempel</i>
I.4. Magnetic field topology	<i>D. Longcope</i>
I.5. Magnetic reconnection	<i>T. Forbes</i>
I.6. Structures of the magnetic field	<i>M. Moldwin et al.</i>
II.3 In-situ detection of energetic particles	<i>G. Gloeckler</i>
II.4 Radiative signatures of energetic particles	<i>T. Bastian</i>
II.7 Shocks in heliophysics	<i>M. Opher</i>
II.8 Particle acceleration in shocks	<i>D. Krauss-Varban</i>
II.9 Energetic particle transport	<i>J. Giacalone</i>
II.11 Energization of trapped particles	<i>J. Green</i>
IV.11 Dusty plasmas	<i>M. Horányi</i>
IV.12 Energetic-particle environments in the solar system	<i>N. Krupp</i>
IV.13 Heliophysics with radio scintillation and occultation	<i>M. Bisi</i>
Stars, their planetary systems, planetary habitability, and climates	
III.3 Formation and early evol. of stars and proto-planetary disks	<i>L. Hartmann</i>
III.4 Planetary habitability on astronomical time scales	<i>D. Brownlee</i>
III.11 Astrophysical influences on planetary climate systems	<i>J. Beer</i>
III.12 Assessing the Sun-climate relationship in paleoclimate records ...	<i>T. Crowley</i>
III.14 Long-term evolution of the geospace climate	<i>J. Sojka</i>
III.15 Waves and transport processes in atmosph. and oceans	<i>R. Walterscheid</i>
IV.5 Characteristics of planetary systems	<i>D. Fischer & J. Wang</i>
IV.7 Climates of terrestrial planets	<i>D. Brain</i>
The Sun, its dynamo and its magnetic activity; past, present and future	
I.8. The solar atmosphere	<i>V. Hansteen</i>
II.5 Observations of solar and stellar eruptions, flares, and jets	<i>H. Hudson</i>
II.6 Models of coronal mass ejections and flares	<i>T. Forbes</i>
III.2 Long-term evolution of magnetic activity of Sun-like stars	<i>C. Schrijver</i>
III.5 Solar internal flows and dynamo action	<i>M. Miesch</i>
III.6 Modeling solar and stellar dynamos	<i>P. Charbonneau</i>
III.10 Solar irradiance: measurements and models	<i>J. Lean & T. Woods</i>
IV.2 Solar explosive activity throughout the evol. of the solar system	<i>R. Osten</i>

textbook is intended for students in physical sciences in later years of their university training and for beginning graduate students in fields of solar, stellar, (exo-)planetary, and planetary-system sciences. The lecturers at the Summer Schools developed a series of five volumes on Heliophysics ([four published in printed form](#) by Cambridge University Press, and one online at the Heliophysics Summer School [website](#)) contain in total 1919 pages of text and figures, in 56 topical chapters (see Table 2): Vol. I:

Table 2: (Continued from the previous page) Chapters and their authors in the *Heliophysics* book series sorted by theme, not showing introductory chapters.

Astro-/heliospheres, interstellar environment, and galactic cosmic rays	
I.7. Turbulence in space plasmas	<i>C. Smith</i>
I.9. Stellar winds and magnetic fields	<i>V. Hansteen</i>
III.8 The structure and evolution of the 3D solar wind	<i>J. Gosling</i>
III.9 The heliosphere and cosmic rays	<i>J. Jokipii</i>
IV.3 Astrospheres, stellar winds, and the interst. medium	<i>B. Wood & J. Linsky</i>
IV.4 Effects of stellar eruptions throughout astrospheres	<i>O. Cohen</i>
Dynamos and environments of planets, moons, asteroids, and comets	
I.10. Fundamentals of planetary magnetospheres	<i>V. Vasyliūnas</i>
I.11. Solar-wind magnetosphere coupling	<i>F. Toffoletto & G. Siscoe</i>
I.13. Comparative planetary environments	<i>F. Bagenal</i>
II.10 Energy conversion in planetary magnetospheres	<i>V. Vasyliūnas</i>
III.7 Planetary fields and dynamos	<i>U. Christensen</i>
IV.6 Planetary dynamos: updates and new frontiers.....	<i>S. Stanley</i>
IV.10 Moons, asteroids, and comets interact. with their surround.	<i>M. Kivelson</i>
Planetary upper atmospheres	
I.12. On the ionosphere and chromosphere	<i>T. Fuller-Rowell & C. Schrijver</i>
II.12 Flares, CMEs, and atmospheric responses	<i>T. Fuller-Rowell & S. Solomon</i>
III.13 Ionospheres of the terrestrial planets	<i>S. Solomon</i>
III.16 Solar variability, climate, and atmosph. photochemistry ...	<i>G. Brasseur et al.</i>
IV.8 Upper atmospheres of the giant planets	<i>L. Moore et al.</i>
IV.9 Aeronomy of terrestrial upper atmospheres	<i>D. Siskind & S. Bougher</i>
Technological and societal impacts of space weather phenomena	
II.2 Introduction to space storms and radiation	<i>S. Odenwald</i>
II.13 Energetic particles and manned spaceflight	<i>S. Guetersloh & N. Zapp</i>
II.14 Energetic particles and technology	<i>A. Tribble</i>
V.2 Space weather: impacts, mitigation, forecasting	<i>S. Odenwald</i>
V.3 Commercial space weather in response to societal needs	<i>W. Tobiska</i>
V.4 The impact of space weather on the electric power grid	<i>D. Boteler</i>
V.5 Radio waves for communication and ionospheric probing	<i>N. Jakowski</i>

Schrijver and Siscoe (2011); Vol. II: Schrijver and Siscoe (2012b); Vol. III: Schrijver and Siscoe (2012a); Vol. IV: Schrijver *et al.* (2016); and Vol. V: Schrijver and Siscoe (2015). The present volume presents a selection of these texts, while adding new text as connecting or summarizing material, with an overall text length that is about one-fifth of the original textbooks.

The topics in this volume are organized to emphasize universal processes from a perspective that draws attention to what provides Earth (and similar (exo-)planets) with a relatively stable setting in which life as we know it can thrive. This text aims to serve as a textbook-style volume for which the original Heliophysics books are the

extended ‘readers’ with much more detail, and domain-specific topical chapters. Note that references from the original texts were omitted here (see the original volumes for those); references for new texts can be found in the Bibliography, where also source references to figures are provided as needed.

This volume is intended for students in physical sciences in later years of their university training and for beginning graduate students in fields of solar, stellar, (exo-)planetary, and planetary-system sciences. This contrasts with the intended audiences for the Heliophysics volumes which included the community of mid-to-advanced graduate students, the cohort of early postdoctoral researchers, and those professional researchers looking for review-like introductions into fields of heliophysics adjacent to their own. In targeting the audience of advanced undergraduate and beginning graduate students, many of the deeply technical details discussed in the original volumes were omitted, introductions were broadened, and the emphasis was placed on processes rather than on details of equations, states, or numerical experiments.

Throughout this work the original text from the Heliophysics volumes is directly quoted, following a volume and chapter reference, where between double quotation marks, but with equations, units (here cgs-Gaussian throughout with a few exceptions [1]), and symbols modified where needed for homogeneity throughout this work, with edits (and some corrections) shown between brackets, with many parenthetical notes removed, and with citations of the professional literature left out (and those to other sections in the books modified as appropriate).

The source texts in the series of Heliophysics books are referenced in the margins as # [roman]:#[arabic].#[arabic]. For example, Vol. I, Section 9 in Chapter 2 would be referred to as “I:2.9” in the margin or in captions. The original sources of all of the figures can be found in the figure captions of the Heliophysics books, but for many here a reference to the original publication is included for figures not made by the Heliophysics authors but whose original authors have given permission to have their artwork used in this volume. A few figures were replaced by color versions or by alternative figures.

Activities for the reader

New here compared to the printed volumes is the inclusion of 200 ‘activities’ (starting in version 1.3; see the chapter on ‘Version history’ for a description of changes) in the form of problems, exercises, explorations, literature readings, and ‘what if’ challenges. Many contain additional information complementing the main text, so I suggest you read them as you go along, if not on first reading, then at least on review. {⓪} [2] Some were developed by the teachers for the Heliophysics Summer School but

¹ A good resource for unit conversions (and many other things related to plasma physics) is the online [NRL plasma formulary](#).

² Exercises are flagged as {A#} or {⓪A#}, also in the margin, with continuous numbering throughout (**this numbering is Version dependent!**). Activities can be found in Ch. 16. For a selection of of these Activities, solutions and/or supplemental reading are provided in Ch. 17 – these selected Activities are marked ⓪ in the margin and in the compilation in Ch. 16.

'Space weather' is the term used to describe an ensemble of changing conditions in the vicinity of Earth and, by extension, any other body in a planetary system, typically occurring on time scales up to a few days. Often, the term is implicitly taken to refer also to the conditions from the solar dynamo outward to the furthest reaches of the heliosphere that are involved in space weather around Earth. Much of what is described in this volume therefore concerns space weather: heliophysics contains the science of space weather. However, where the science of space weather focuses on phenomena that can impact society through short-term variability, this text takes the long view by putting the spotlight on evolutionary changes in the states of star-planet systems. As such, this text does describe the foundational processes of space weather, but is not concerned with the impacts of space weather on technological infrastructure, does not address the challenges of forecasting space weather, and skips coupling mechanisms such as ground-induced currents (GICs) associated with geomagnetic disturbances and ground-level enhancements (GLEs) of energetic particles. This choice of focus is motivated by my desire to introduce the reader to the science of heliophysics from the perspective of habitability on time scales on which stellar and planetary atmospheres change, and indeed up to time scales on which stars and their planets evolve, and to do that in a relatively compact form. As you go through this text, you should realize that many of the processes described here have consequences for society, ranging from system design choices to potentially substantial failures in one or more of the infrastructures that we have come to rely on, including continuous and reliable electric power, positional information, and means of communication. Interruptions in quality or availability of any of these can have substantial consequences that may be costly or life-threatening on scales that may involve single individuals or populations of millions. Descriptions of the impacts of space weather can be found in the Heliophysics books in Chapters II:2, II:13, II:14, H-V:2, H-V:3, H-V:4, and H-V:5; another resource is a 'roadmap' document (Schrijver *et al.*, 2015) that reviews the state of our knowledge of space weather and its technological and societal impacts, and what is needed to advance our abilities to forecast space weather.

Table 3: Heliophysics and space weather

most are newly created specifically for this volume. They are meant to let the reader look up a definition, to introduce a moment of reflection on an equation or figure, to see connections to similarities elsewhere, to get a feel for the magnitude of things or the relative importance of processes, or to consider what would happen under conditions other than those encountered in our Solar System; they are not meant to particularly exercise mathematical skills. There are five classes of activities as indicated at their start: "Look up" to familiarize you with processes, numbers, and definitions, "Consider" to make you think about processes, "Show" for applications of equations or numerical estimates, "Background" for further information, and "Advanced/Group" for larger activities to explore beyond the textbook and/or to undertake with a group of students in a class. At the end of the book, in Activity 200, the reader is asked to reflect back

on all the processes that are involved in the habitability of Earth and, by analogy, of exoplanets elsewhere in the Universe.

Terminology

As you go through this volume, you will encounter words that have somewhat different meanings in different communities. For example, 'convection' is often used in the magnetospheric community to describe movement that in astrophysics would be referred to as 'advection', while 'convection' in that discipline is reserved for overturning plasma motions involved in the transport of thermal energy. Another example is that of the word 'dynamo' which in astrophysics and planetary sciences is used to describe the ensemble of processes maintaining a magnetic field against decay, often with an alternating temporal character. In ionospheric physics, it is often used for processes where differential motions of (neutral plus ionized) gas and magnetic field exchange energy through work.

You will also note that terms may describe locations or something in a location, or a property of what is in that location. For example, 'ionosphere' may sound like a location descriptor but actually refers to only the ionized medium in an atmosphere (with 'thermosphere' used for the overlapping neutral environment). The term 'chromosphere', which describes a stellar environment in some respects not dissimilar to an ionosphere-thermosphere, encompasses both the ionized and neutral components; it is often used as an indicator of a volume above a stellar surface in a certain thermal range, but is defined formally (as you will see later) by the properties of the radiative transfer of the medium.

Finally, there are words like 'late-type star' that have nothing to do with a temporal attribute, but which survived an older era where the nature of stars was not yet understood and where cooler was erroneously interpreted as older.

I hope that all terms are properly defined where first used. Here, I want to raise your awareness that as you talk to colleagues in other disciplines they may not only be puzzled by processes that you study, but that communication may be hampered by misinterpretation of the terms that you use: language can be a very precise tool, but only if the user is aware of how the listener/reader may interpret the words that are being used.

Online resources associated with the Summer School

- If you are looking at a paperback or hardcover version of this book from Amazon/KDP then look for a free e-version at <https://arxiv.org/abs/1910.14022> which uses hyperrefs for easy navigation. It also has many figures in color, as does the hardcover edition, that are shown in gray-scale in the paperback.
- The Summer School's home is at <https://heliophysics.ucar.edu>.
- Many of the Heliophysics lectures can be found [on YouTube](#) by searching for 'Heliophysics Summer School'.

A few notes on other resources

The [figures](#) published in the Heliophysics book series are available on-line at the [website](https://heliophysics.ucar.edu) of the Heliophysics Summer School (<https://heliophysics.ucar.edu>), where you can also find labs (with instruction manuals) and many recorded lectures sorted by theme (in part hosted on youtube).

There is a subject index in this volume but note that the online version of this book can be searched with the tools of web browsers and pdf viewers to provide an effective and entirely comprehensive alternative way to find topics.

This volume focuses on processes, not on their measurements. For an introduction to some of the aspects of remote and *in-situ* sensing within the Heliophysics series I refer to the following chapters that focus on that aspect in particular: Chs. II:3, II:4, IV:5, and IV:13.

You can find a [list](#) of English-language textbooks, popular texts, topical monographs and book series, related to the science of space weather and published since 1990 in [Knipp and Cade \(2020\)](#).

Explore [NASA's Scientific Visualization Studio](https://svs.gsfc.nasa.gov) at <https://svs.gsfc.nasa.gov> for a variety of images and movies — real and simulated.

Navigating the pdf version at arXiv:2001.01093

References to sections, figures, tables, and equations in this book are shown in red, pointers to the bibliography are shown in green, and references to web pages are shown in blue. Clicking on any of these jumps to that location or web page. How you get back to reading where you left off depends on how you are viewing this file and on what type of device. For example, this [web site](#) shows a list of keyboard shortcuts to move around the pdf version of this book with Acrobat Reader. Using that on a Mac, you can return to the page you came from by pressing [command + left-arrow] after clicking on a link to a figure, section, or activity. When using Mac OS Preview, look under the 'Go' menu for navigation shortcuts (where you will see that the equivalent of the above is [command + left bracket]).

Corrections and updates

This version of the textbook is subject to corrections and updates. I welcome input from students, teachers, and colleagues: if you see a typo or an explanation that you think is in error, or if you believe a serious update is in order, please [email me](mailto:heliophysicsnutshell@gmail.com): heliophysicsnutshell@gmail.com! Be as specific as you can about where the text is that you think should be changed, what to change it to, and why it needs such a change. Your input will help improve this text for all users.

Acknowledgements

I thank all the Heliophysics authors and other teachers in the Heliophysics Summer School for the skill with which they taught me as one of the participants in the School as well as for their patience with me as one of the editors of the book series. This

volume was supported by the Johannes Geiss Fellowship of the International Space Science Institute. I am indebted to Jürg Beer, Paul Charbonneau, Terry Forbes, Marina Galand, Dana Longcope, Sten Odenwald, and Matthias Rempel for their insightful comments on an earlier version of the manuscript, and to Nick Gross for working through most of the Activities, noting errors, adding tasks, and developing new Activities. Special thanks go to Tom Bogdan who worked through the entire draft volume.

Karel Schrijver, March 27, 2024
karelschrijver.com

“A physical understanding is a completely unmathematical, imprecise, and inexact thing, but absolutely necessary for a physicist.”, R.P. Feynman, in *The Feynman Lectures on Physics, Vol. II*.

Chapter 1

Stars, planetary systems, and the local cosmos

Chapter topics:

- The rationale for this book
- Heliophysics: the system science of the physical connections between the Sun and the solar system
- Magnetohydrodynamics as the basic language of heliophysics
- Basic glossary for heliophysics
- A timeline of exploration of (exo-)planetary systems

1.1 Preparing for the future

By the time you reach the end of this book, you will have the basic set of tools of scientific imagination involved in understanding what couples stars and planets. What you will learn is universal, literally: it does not matter which stars and planets we speak of: whether of those few nearby or of the many distant ones. Nor does it matter whether they are those few that we are long familiar with or the many that we know about, so far, only in a statistical sense. It does not matter either whether your particular interests lie within the Solar System or beyond it: the same principles apply in our local cosmos as in the most distant planetary system we shall ever have access to.

But looking forward to your science-based career, whether as a researcher or as a teacher, as a journalist or as a politician, you need to be familiar with what is known. That is particularly true in order to discover something new. And to appreciate the value of a discovery, you need to know how to apply what you know to what is not (yet) known. You will need to imagine things no one has ever seen, but not arbitrarily: science demands that you come up with what appears most probable, not merely with things that are possible. Richard Feynman (in *The meaning of it all*) said it this way: 'It is surprising that people do not believe that there is imagination in science. It is a very interesting kind of imagination, unlike that of the artist. The great difficulty is in

trying to imagine something that you have never seen, that is consistent in every detail with what has already been seen, and that is different from what has been thought of.’

The pace at which exoplanets are being discovered is simply amazing. What we can learn from them, and from our Solar System, offers so many opportunities to learn yet more. I realize that going through the first nine chapters will be hard, because they have to build your foundation, because they cover so many different branches of science, and because they look at things so different from everyday life. But these first nine chapters look for commonalities, for ‘universal processes’ that help create in your mind a virtual laboratory: in the astronomy we cannot turn dials to explore things under different conditions, but we can compare environments and look for what they have in common and for what sets them apart.

The final six chapters require prior digestion of the first nine. These final six invite you to imagine, scientifically, Earth in the distant past and future, Earth-like planets in a variety of orbits around Sun-like stars, and the space environments and climates of tropospheres of exo-worlds. Future discoveries have their beginnings in lessons from the past:

1.2 Considering planetary habitability

Planetary systems are, statistically speaking, about as common as stars. We have learned a lot about stars over the century that followed the realization that they are huge nuclear fusion reactors and that most, like the Sun, function also as giant dynamos. In contrast, firm evidence that planetary systems are common companions to stars was only obtained within the past two decades. It is therefore no surprise that much still needs to be learned about how planets form, how planetary systems evolve, and what the conditions are near planetary surfaces (if indeed a solid or liquid surface exists). The combination of exoplanetary science and the study of the local cosmos is enlightening us as much about the history and future of our Solar System as about the growing number of planetary systems that have been observed in some detail. Whether life exists anywhere beyond Earth remains to be established, but scientists are making rapid headway in knowing about the conditions that life on Earth has been subjected to since its genesis and also the conditions that any life on any other planet would be subjected to depending on the properties of their central star and companion planets.

Heliophysics deals with all of the aspects of ‘living with a star’ on time scales from fractions of a second to billions of years. The series of Heliophysics books offers an introduction to a large cross section of that vast scientific field. In the present volume, we focus on the universal processes that tie together the branches of heliophysics with particular emphasis on those processes that are relevant to what one might describe as ‘planetary habitability’. With life having been found on only a single astrophysical body we do not have a particularly well-considered concept of what ‘planetary habitability’ might mean, of course. But we have an intuitive feel for it: a long-lived planet orbiting a long-lived star, with a fairly substantial planetary atmosphere that is neither too hot nor too cool to allow chemistry to be complex (and, in many minds, restricting that to chemistry that involves liquid water), shielded well enough (but not necessarily

perfectly) from energetic radiation (both electromagnetic and particulate) by that atmosphere and by a planetary magnetic field. The star's irradiance onto a 'habitable planet' should not vary too much, comet and asteroid impacts should be limited, atmospheric erosion slow, . . . If that sounds like we are describing the Sun-Earth system then that is no surprise: we know it has made the Earth habitable to a diversity of life that is on one hand astoundingly diverse and on the other – at the molecular level – remarkably homogeneous.

As the number of known exoplanetary systems is bound to keep growing rapidly, and as our instrumentation and methods are bringing exoplanetary atmospheric science within our grasp, it is clear that our understanding of the Solar System and its central star provide crucial guidance to the study of 'planetary habitability' and – some day rather soon, one should anticipate – the study of extraterrestrial life. That expectation has guided the selection of topics covered in this volume.

^[3] “If we gaze upon the uncountable array of stars strewn across the vault of the heavens, one may know that the remarkable things one will come to know about heliophysics in the pages that follow are presently unfolding around those very stars and planetary systems that give light to the night sky. Heliophysics is truly a universal science.” I:2.9

1.3 Heliophysics: unification, coupling, exploration

“Walk along an island beach on a clear, breezy, cloudless night, or stand on the spine of a barren mountain ridge after sunset, and behold the firmament of stars {A1} glittering against the coal-black sky above. They fill the sky with their timeless, brilliant flickering [(mostly caused by the terrestrial atmosphere)]. With binoculars or even a small telescope one finds that even the lacy dark matrix between the vast sea of stars is populated with still more stars that are simply too faint to be seen with the naked eye. Within the Milky Way galaxy, that stretches from horizon to horizon, the density of stars against the background sky is even greater. I:3.1

Each twinkling point of light is a star not too unlike our own Sun. The Sun is an ordinary star that features so prominently in our lives and on the pages of [the Heliophysics book series, as in this volume,] because of its proximity. The next closest star, α Centauri (which is a triple system in which Proxima Centauri is currently the closest to Earth), is almost a million times farther away (at 4.22 light years), and the others are farther still. We may now say with some confidence that many of the stars are surrounded by planets of various sizes. {A2} Some of these orbital companions are so immense that they are stars in their own right: double-star systems are quite common. {A3}

With the same measure of confidence we may assert that most of these stars possess magnetic fields; that these magnetic fields create hot outer atmospheres, or coronae, that drive magnetized winds from their stars; and that these variable plasma winds {A3}

³ Throughout this work the original text from the Heliophysics volumes is directly quoted (with edits between brackets) with references shown in the margin like this: #[roman]:#[arabic].#[arabic]. So, for example, Vol. I, Section 9 in Chapter 2 would be referred to as I:2.9.

Table 1.1: Basic glossary for domains and phenomena in heliophysics (continued on the next page).

- *active region*: a bipolar area of relatively strong magnetic flux, mostly consisting of magnetic *plage* (underlying the chromospheric *plage*) and, by definition, containing one or more *sunspots* at some point in its evolution (*cf.* Fig. 4.4). Collectively they form two active-region belts located on opposite hemisphere.
- *ast(e)rosphere*: equivalent of a heliosphere around another star (Sect. 10.3)
- *aurora*: A visual phenomenon associated with geomagnetic activity visible mainly in the high-latitude night sky, resulting from collisions between atmospheric gases and precipitating charged particles (mostly electrons) guided by the geomagnetic field from the magnetotail.
- *chromosphere*: domain above the Sun’s visible ‘surface’, with temperatures around 10,000–20,000K (see Table 2.3)
- *corona*: the hottest domain of the Sun’s atmosphere, at ≥ 1 MK (Table 2.3)
- *coronal hole*: formally a coronal region that is dark in X-rays and EUV; generally identified with a region where the Sun’s magnetic field is ‘open’, *i.e.*, reaches into the heliosphere (*e.g.*, Sect. 2.2)
- *coronal loop*: a high-temperature atmosphere within the Sun’s corona, constrained to the volume of a magnetic ‘flux tube’ (*e.g.*, Sect. 3.4)
- *coronal mass ejection*: impulsive expulsion of magnetized material from a star into an astrosphere (*e.g.*, Fig. 5.1, Sect. 3.1)
- *current sheet*: defined in Table 3.1
- *exosphere*: outermost domain of an atmosphere in which collisions are rare and ballistic trajectories dominate for constituent particles (*e.g.*, Sect. 2.3)
- *facula* and *bright point*: a small flux tube in near-photospheric layers viewed towards the solar limb or disk center, respectively (*e.g.*, Sect. 9.1)
- *flare*: impulsive conversion of magnetic energy in a stellar atmosphere into thermal and non-thermal particles and bulk plasma motion, and appearing as a brightening over much of the stellar spectrum, although not significantly in total stellar brightness except for the most energetic events (*e.g.*, Sect. 3.1)
- *filament/prominence*: A volume of gas at chromospheric temperatures suspended within the corona by magnetic forces, seen as dark ribbons threaded over the solar disk. A filament beyond the edge of the solar disk seen in emission against the dark sky is called a prominence
- *flux tube/rope*: defined in Table 3.1

blow past the orbiting planets, distorting their individual magnetospheres, and push outward against the surrounding interstellar medium. Where the ram pressure of the stellar wind becomes comparable to the surrounding pressure (gas, magnetic, and cosmic ray) of the interstellar medium, a bow shock forms. This serves to mark the farthest extent of the mechanical impact of the star on its surrounding environment: a sphere of influence, so to speak. ^[4] {A4}

⁴ See Tables 1.1 and 1.2 for definitions of the most common descriptors used for domains in, or phenomena related to, heliophysics. For a more extensive glossary of terms used in this volume, see, for example

Table 1.2: *Basic glossary for domains and phenomena in heliophysics (continued from preceding page).*

- *(super-)granulation:* granulation is the pattern of convective cells visible in the solar photosphere with a typical scale length of 1 Mm (see Fig. 9.1); supergranulation is a much larger cellular pattern with a scale length of 20–30 Mm that manifests primarily in velocity maps and in its ordering of the magnetic network (see Fig. 4.4)
- *geomagnetic (sub-)storm:* Storm: A worldwide disturbance of the Earth’s magnetic field, distinct from regular diurnal variations. Substorm: A geomagnetic perturbation lasting 1 to 2 hours, which tends to occur during local post-midnight nighttime. The magnitude of the substorm is largest in the auroral zone. (*e.g.*, Sects. 6.2 and 6.1.2)
- *heliosphere:* the extended region where the solar wind dominates over the interstellar medium (*e.g.*, Fig. 5.1)
- *ionosphere:* the ionized component of a planetary atmosphere, largely overlapping with the thermosphere (*e.g.*, Sect. 2.3)
- *magnetosphere:* a magnetic environment, generally of a planet, in which the intrinsic or induced magnetic field of the central body dominates over external fields or flows (*e.g.*, Fig. 5.1)
- *mesosphere:* layer between stratosphere and thermosphere (Sect. 2.2)
- *photosphere:* ‘surface’ of a star, at the rapid transition from opaque to transparent
- *stratosphere:* at Earth, the domain between troposphere and mesosphere where temperature rises with height and convection is rare (*e.g.*, Sect. 2.2)
- *solar (or sunspot or activity) cycle:* quasi-cyclic variation in the number of sunspots seen on the solar surface when averaged over time scales of months (*e.g.*, Fig. 4.5)
- *(spectral, total) solar irradiance:* solar input into a planetary atmospheric system in the form of photons (*e.g.*, Sect. 2.2)
- *sunspot:* a ‘flux tube’ in the near-surface layers, with suppressed internal convection, and large enough that lateral influx of radiation cannot prevent the interior from cooling relative to the surrounding photosphere and thereby appearing relatively dark (*e.g.*, Sect. 4.1.2)
- *thermosphere:* outer layers of a planetary atmosphere in which the temperature increases with height (*e.g.*, Sect. 2.2), specifically the neutral particles
- *(solar) transition region:* a domain between chromosphere and corona with a very strong temperature gradient dominated by conduction (see Sect. 9.2)
- *troposphere:* the lower layers of a planetary atmosphere (*e.g.*, Sect. 2.2)

Our Sun has and does all of these things, and we refer to the sphere of influence carved out by the solar wind as our heliosphere. It is not really spherical and it varies in extent with solar activity. But in broad terms we may safely think of it as extending about 100 times further from the Sun than the Earth’s orbit. We have yet to agree on the name for such spheres of influence around the other stars (for which astrospheres has been proposed), but there can be little doubt that such environments are as commonplace as the many points of light we see strewn across the sky on a dark

<https://hesperia.gsfc.nasa.gov/sfttheory/glossary.htm>; for a glossary of terms related to space weather, see <https://www.swpc.noaa.gov/content/space-weather-glossary>.

and cloudless night.”

“Heliophysics encompasses the study of the various physical processes that take place within the sphere of influence of the Sun (*i.e.*, the heliosphere), and by analogy, those environments surrounding most other typical stars. But heliophysics also defines a specific method of study. This method embraces a holistic connected-system approach. It emphasizes a comparative context in which to understand a process by the many facets it presents in its various incarnations throughout the heliosphere. Taken together, each diverse facet serves to fill out a complete and physically satisfying picture of a given process or phenomenon.

The physical processes and phenomena that we will encounter in [this volume] are themselves especially diverse. They include the rapid and efficient energization of thermal particles to suprathreshold energies, the generation and annihilation of magnetic field, stellar variability and activity cycles, space weather, turbulent transport of energy and momentum, [the coupling between ionized and neutral atmospheres, and atmospheric chemistry,] to name just a few. Heliophysics fills a critical need to establish a unified science that connects these seemingly unrelated concepts in a manner that emphasizes complementarity over individuality, function over form, and generality over specificity.

Along with unification, coupling provides the second principal pillar upon which heliophysics rests. The heliosphere is a collection of coupled systems. It is fortunate that many of the linkages essentially operate only in one direction. That is to say, system A impacts system B, but B has little influence on A. Under these circumstances it is expedient to treat system A independent of the behavior of system B. This provides a certain economy of effort and scale, and it often reduces the (apparent!) complexity of a problem. For example, complex geomagnetic activity has no impact on solar flares, and the solar wind does not influence the Sun’s cyclic variability.

Linkages, especially when several are present and working at cross purposes, can lead to confusion and spirited debate over what is a root cause and what is simply a resulting effect. The cause and effect relationship between solar flares and coronal mass ejections is a good case in point. Consider, for example, what the purported cause and effect relationship might be between a sore throat and a fever. Because a sore throat often starts before a fever develops one might be tempted to assign the effect to the fever and take the sore throat to be the cause. Fortunately, medical research informs us that both are effects and the root cause is the influenza virus. Heliophysics is needed to play this very same role in sorting out the appropriate relationships (or lack thereof) between any variety of physical effects that often occur contemporaneously throughout the heliosphere.

Solar variability does influence our climate here on Earth. This fact is certainly not negotiable in a purely scientific context and is arguably one of the most important linkages between the Sun and the Earth. Satellites have confirmed that the solar irradiance is variable on time scales from minutes to decades. The fluctuations are greatest on the shortest time scales. Day-to-day irradiance changes are on the order of a percent versus tenths of a percent over a solar cycle. The magnitude and sense of

irradiance trends over centuries and millennia are currently difficult to determine with any measure of certainty. Slow but steady progress on this question is being made through the studies of paleoclimate records. Over much longer time scales, stellar evolution theory provides assurances that significant changes in solar irradiance have taken, and will take, place with dramatic impacts on our climate and way of life.

What is debatable, however, is precisely what the direct relationship is between solar variability and climate change over any particular time scale, or epoch, of interest. For example, various opinions have been advanced that span the entire gamut from wholly inconsequential to complete solar responsibility for the gradual warming of the planet that has been observed since the middle of the 20th Century. Yet, it may not even make sense to speak of direct relationships between drivers and the behavior of systems which are as nonlocal, nonlinear and plagued by various hystereses as is our climate here on Earth.

The third and final pillar upon which heliophysics rests is the exploration of Earth's neighborhood in space. As a space-faring civilization we have visited all the planets, [several asteroids and] comets and numerous planetary satellites. We have ventured to the boundaries of the heliosphere and have flown through various parts of our magnetosphere. We have a spacecraft [that passed] the Pluto/Charon system [and after that flew by Kuiper-belt object 486958 Arrokoth, provisionally known as 2014 MU₆₉ and nicknamed Ultima Thule]. Heliophysics enables our exploration to be successful and at the same time gains in knowledge and understanding from our exploration initiatives.

In summary, heliophysics is the systems-mediated study of the physical processes that take place within the Sun's sphere of influence. It is based upon the three pillars of unification of physical processes and phenomena, coupling of distinct physical systems, and the exploration of our neighborhood in space. And it is broadly applicable to the environments around most ordinary stars."

1.4 The language of heliophysics

"The language of heliophysics is mathematics. And the body of literature from ¹³ which heliophysics draws its substance and in turn records its accomplishments is the physics of magnetized plasmas. With only a rudimentary knowledge of a language, a literature is incomprehensible, except, perhaps in translation. And even in translation so much of the original meaning and the nuance the author wished to convey are inevitably lost, or worse, misinterpreted by even the most conscientious translator.

The most precise, and intellectually demanding, literary prose of heliophysics assigns a phase-space distribution function to each individual species of particle. By a species one may simply mean free electrons, protons, or oxygen molecules, or even photons. In some applications it might be necessary to distinguish between oxygen molecules in different excited (vibrational, rotational and electronic) states, or between iron atoms at different stages of ionization, or between different senses of photon polarization. In any case, the evolution of each distribution function is obtained by setting the total time derivative equal to the net production/loss of an individual species by various

collisional or radiative processes. Such evolution equations are commonly referred to as Boltzmann, or Vlasov equations. When there is no net gain or loss, then Liouville's Theorem asserts that the vanishing of the total time derivative of the distribution function conserves the phase space density for each species [(see Sect. 8.4)].

In specifying the total time derivative it is necessary to determine the forces acting upon a given particle species. For uncharged particles, gravitational attraction is the only important consideration. Accordingly, to the system of equations for the individual distribution functions one must add Poisson's equation in order to specify the gravitational field based on the mass distribution provided by those particles with mass. Charged particles are also subject to electromagnetic interactions. Thus we must also include Maxwell's equations to deduce the electric and magnetic fields based on the distribution of charges and currents provided by the charged particle species.

{A5}

{A5}

In principle, this suffices to provide a complete description of the grammar and syntax of heliophysics at a very elegant, learned and precise level. In practice the task of following through with this program (a) is prohibitively difficult with or without the assistance of the computer, (b) is subject to the problem that the initial conditions are not known with any degree of certainty, (c) is complicated by the fact that many of the collisional and radiative transition probabilities are not even approximately known, and (d) requires that certain conditions be fulfilled so that electromagnetic interactions can be separated into large-scale fields and small-scale collisions. Finally, this comprehensive description usually provides far more information than is usually necessary for comparing with observations or understanding the predictions of a theory over specified temporal and spatial scales.

At the opposite extreme from the scholarly literary prose is the common vernacular. For heliophysics, if high literary prose centers on Poisson, Maxwell, Boltzmann and Vlasov, then the vernacular is single-fluid, ideal, magnetohydrodynamics, or MHD for short (see Ch. 3). MHD is a continuum fluid description that does not distinguish between particle species, averages (in some sense) over particle collisions, ignores radiative effects altogether, and is based on velocity moments of the underlying distribution functions. It retains Poisson without modification, but takes certain liberties with Maxwell. Boltzmann and Vlasov drop out of the picture entirely.

MHD can be rigorously derived from Poisson/Maxwell/Boltzmann/Vlasov under various conditions that are not altogether unreasonable for very many heliophysical applications. Usually this involves following the behavior of a physical process or phenomenon over course-grained spatial and temporal scales. In other words, it is a useful, and indeed often very accurate, description of the 'big picture'. Because of its relative simplicity, ideal MHD provides a useful context in which to interpret and understand the behavior of magnetized plasmas at a basic and often extremely intuitive level. On the other hand, ideal MHD is often applied to processes or phenomena to which it does not actually apply. Generally speaking, if collisional and radiative relaxation times are short compared to the coarse-grained time scale of interest then ideal MHD is likely to be a reasonable option. But 'gotchas' are always present.

The successful derivation of the MHD equations requires a closure prescription, which may be regarded as a consequence of the familiar, 'no free lunch' maxim. Closure entails specifying a tractable procedure to determine the pressure tensor (second-order velocity moment) in terms of the fluid density (zeroth-order velocity moment), the bulk fluid velocity (first-order velocity moment), and the magnetic field. The so-called polytropic approximation — in which the pressure is a scalar proportional to the particle number density raised to a specified power — is the simplest option. A power law index of unity corresponds to an isothermal process (constant temperature). A power law index equal to the ratio of specific heats describes an isentropic (constant specific entropy) process that also manages to conserve energy. More complicated options are possible and are often tailored to accommodate specific situations. A successful and accurate closure scheme is inevitably based on some additional *a priori* knowledge of the behavior of the particle trajectories, or the general nature of the particle distribution functions.

In contrast to the Poisson-Maxwell-Boltzmann-Vlasov description, ideal MHD is a system of nine partial differential equations for nine dependent variables [(shown in Table 3.3 and discussed in Ch. 3)]: the gravitational potential, the fluid density and pressure, the fluid velocity (3 components) and the magnetic field (3 components). These equations are (a) the Poisson equation to describe gravity, (b) the continuity equation expressing the conservation of mass, (c) the closure relation to specify the pressure tensor, (d) the equation for the conservation of momentum, or the force-balance equation (3 components), and (e) the magnetic induction equation (3 components).

Of course, between ideal MHD and the Poisson-Maxwell-Boltzmann-Vlasov description lies a vast real estate filled with a plethora of compromise or hybrid descriptions. The number of such schemes is limited only by the imagination and ingenuity of the investigators. Multi-fluid treatments allow for individual densities, velocities and pressures associated with different particle species or groupings of particle species, but retain a single gravitational potential and magnetic field applicable to every fluid. This formulation is useful when the time scales of interest are short compared to characteristic inter-species collisional relaxation times, but long compared to the analogous intra-species times.

Another intermediate scheme employs high-order moment closures. These schemes are necessary when the species distribution functions deviate significantly from the fully-relaxed Maxwellian. Often this situation occurs when significant spatial gradients are imposed on the system. Additional partial differential equations are then used to describe the time-evolution of the components of the pressure tensor. The closure is postponed to the next higher level of the heat flux tensor (third-order velocity moment), or in extreme circumstances to even higher-order moments.

Hybrid schemes treat some species as fluids and retain a Boltzmann-Vlasov – or kinetic – description for others. Indeed even a single species of particle may be partitioned in such a fashion that some of the particles are treated kinetically (generally the high energy suprathermal tail of the distribution function) while the remainder are described as a fluid (the thermal core of the distribution). Such schemes are

particularly useful in describing the energization of charged particles; [we see this in action in Ch. 8].

In summary, there is a bewildering array of schemes that are presently invoked to describe the behavior of magnetized plasmas in the heliosphere. They encompass an extremely wide range of complexity. Each is specifically tailored to a given physical process and phenomenon. They are not simply interchangeable, but have their own individual strengths and weaknesses. One should always choose the simplest description that will suffice for understanding the problem in hand. Use all the information and knowledge you have at your disposal about the nature and behavior of a physical system in selecting a scheme. If the heliophysics concepts can be adequately framed in the common vernacular, then eschew the sophisticated flowery prose unless nothing less will do.”

1.5 A timeline of exploration of planetary systems

NASA’s Heliophysics Division within the Science Mission Directorate was previously known as the Sun-Earth Connections Division. That earlier name reflected that much of its research focused on how solar activity impacts our home planet. As probes explored ever more of the solar system, researchers realized that learning about the science of terrestrial space weather and of the evolution of Earth’s climate system was boosted by the incorporation of discoveries from around the solar system; the name change of the Division reflected the shift to a broader perspective that was already taking place in the research community. As exoplanets were found to be more common than stars, the application of the science of heliophysics to the exploration and understanding of processes in exoplanetary systems, and in particular to exoplanetary habitability, presents a natural development of the discipline. The multi-disciplinary science arena that looks into star-planet couplings has accelerated rapidly alongside astronomical exploration.

In 1969, half a century ago, astronauts first landed on Earth’s sole moon. The first successful robotic landers touched down on the much more distant Venus and Mars in 1970 and 1976, respectively, and in the same decade spacecraft flybys provided the first, fleeting close-ups of Jupiter and Saturn. It was not until two decades later, however, that missions that explicitly targeted these giant planets revealed how fundamentally distinct these worlds are from our own.

The Galileo satellite started exploring the Jupiter system in late 1995, swinging by moon after moon. The Cassini-Huygens mission reached Saturn in 2004, exploring the giant planet, its rings and satellites, and even sending a lander onto Titan, the only moon in the solar system with a substantial atmosphere. These spacecraft uncovered a fascinating diversity of environments on dozens of moons: many are cold worlds enrobed in miles-thick ice; some with volcanoes spewing molten rock but others whose volcanoes somehow gush liquid water or nitrogen; and then there is Titan with its seas of liquid methane and ethane. Their pictures are as stunning and diverse as the scientific discoveries enabled by these spacecraft. The far reaches of the Solar System continue to offer surprises: dwarf planets Haumea and Makemake, objects in

the distant Kuiper belt, were not discovered until 2004 and 2005, respectively.

As the close-up exploration of the largest planets in the solar system got underway, a revolution was about to befall astronomers looking much further out. It started in 1995 with the announcement of the first exoplanet, now known as 51 Pegasi b, orbiting a star like our own Sun. There are now well over 5,000 exoplanets on the books^[5] (almost half of which were found with NASA's *Kepler* satellite), but the number expected to exist is vastly larger: by carefully quantifying what our available methods can and cannot observe, scientists estimate that there are over a hundred billion planetary systems in our Milky Way galaxy alone, with perhaps of order ten billion planets with some similarity to Earth.

Apart from its very existence, 51 Pegasi b had another surprise in store: at 150 Earth masses and orbiting its star almost 20 times closer than Earth does the Sun, this "hot Jupiter" should not have existed by theories of the time. These and many subsequent observations have changed our ideas on how planetary systems form and evolve: we now realize that orbits can change so that planets may be discovered well away from where they formed; planets can engage in gravitational fights that can cause losers to be ejected as lone 'nomads' into interstellar space; planets exist that have two stars to cast twin shadows on their surfaces; ... Many planets orbit their stars at distances where water, if there is any, may exist in liquid form on their surface for billions of years, as on Earth where it enabled the development of life.

These discoveries have intensified the astronomers' hunt for extraterrestrial life in which also solar-system scientists participate. Organic molecules cause the haze in the icy-cold atmosphere of Saturn's Titan and are vented in cryo-volcanic plumes rising from the ice-locked deep ocean of nearby Enceladus. There are many sizable moons and dwarf planets in the solar system that are rich in water, although much of it is frozen solid. The combination of liquids and organics in many places around our solar system fuels theories of life and plans for space missions designed to look for it near to home.

But exoplanet astronomers have the advantage of the vast number of systems. Their challenge is that even the largest telescopes can image exoplanets no better than as an unresolved blur the size of the instrumental point spread function, if indeed they can separate the reflected light from the exoplanets from the light of the stars that they orbit. In fact, most of what we learn about exoplanets comes from analyzing how their star's light is modified in brightness or color by the exoplanets, either by adding some reflected starlight or by taking away some light should they move in front of their star during their orbit. Careful study of these effects as observed with the most powerful telescopes can reveal which gases contribute to the changes. This is receiving a big boost from NASA's James Webb Space Telescope that started operations in 2022 and more from future telescopes. So much was discovered in the most recent few decades; what will the next several decades bring?

⁵ See <https://exoplanetarchive.ipac.caltech.edu> and <http://exoplanet.eu>.

Chapter 2

Neutrals, ions, and photons

Chapter topics:

- Conditions in the local cosmos
- Gravitational stratification
- Cycle-driven variability of the solar spectral irradiance
- Penetration depth of sunlight and its impact on the terrestrial atmosphere

Key concepts:

- Pressure scale height and differential stratification by atomic/molecular mass
- The role of electron heat conduction in powering the solar wind
- Collisional mean-free path
- Optical depth

2.1 Conditions in the local cosmos

The local cosmos discussed in this book exhibits an enormous diversity of conditions. Figure 2.1 is one perspective of this in its comparison of number densities and temperatures: densities range over more than 28 orders of magnitude (more than the contrast between solid rock and the 'vacuum' of low-Earth orbit) and temperatures over 5 orders of magnitude. The magnetic field, another crucial parameter that is explored starting in Ch. 3, provides another dimension and adds its own physical processes. All together, these physical parameters cover a wide range of states that include solids, liquids, gases, and ionized and magnetized particle ensembles called plasmas.

Matter in most of the domain of heliophysics is electrically conducting, being generally at least partially or even fully ionized as will be abundantly clear from the chapters in this volume. Ionization can be a consequence of high-speed collisions between particles in a hot medium and/or of high energies in the thermal radiation associated with high temperatures. A hot medium can result from the transport and conversion of different forms of energy where a balance of thermal sources and sinks may only be reached at high temperatures. Examples of such settings are the interior and the atmospheric domains of the Sun. In these environments, internal collisional

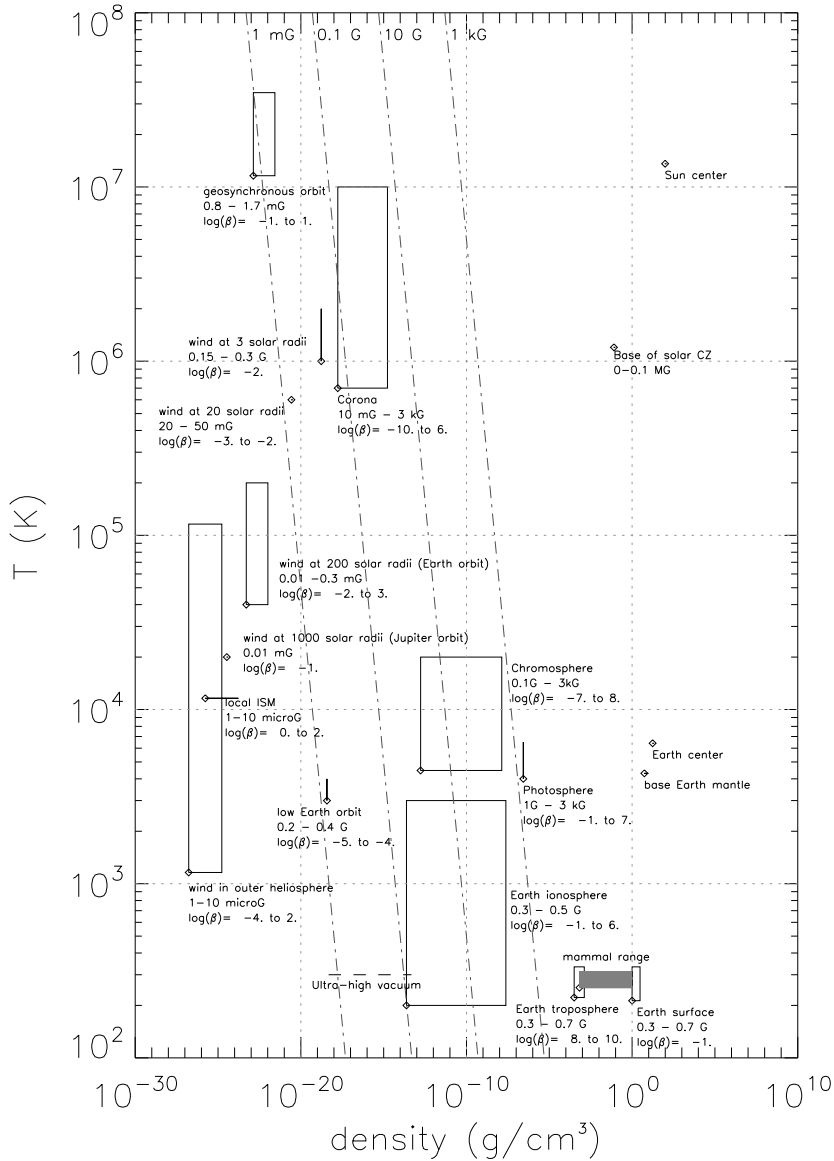


Figure 2.1: Temperature versus mass density for a variety of conditions within the local cosmos. Some typical ranges are indicated, and labeled with magnetic field strengths (in Gauss) found in that domain, followed by estimated ranges of the plasma β , i.e., the ratio of energy density in plasma over that in the magnetic field (Eq. 3.24), in this scaling for a fully ionized hydrogen-dominated plasma. [Dash-dotted lines show where the plasma β equals unity for the field strengths shown near the top of the diagram, making the same assumptions about the plasma. Fig. I:1.1]

Table 2.1: *Present characteristics and climates of the terrestrial planets. [Modified after Table III:7.1, with added surface gravity, escape velocity, and escape energies E_{esc} for protons and atomic oxygen.]*

	Venus	Earth	Mars
Radius	6050 km	6400 km	3400 km
Orbital radius	0.72 AU*	1 AU	1.52 AU
Rotation period	243 days	24 hours	24.6 hours
Surface gravity	8.9 m/s ²	9.8 m/s ²	3.7 m/s ²
Escape velocity	10 km/s	11 km/s	5 km/s
E_{esc} for H ⁺ , O	0.5, 9 eV	0.6, 10 eV	0.1, 2 eV
Surface temp.	740 K	288 K	210 K
Surface pressure	92 bar	1 bar	7 mbar
Composition	96% CO ₂ 3.5% N ₂	78% N ₂ 21% O ₂	95% CO ₂ 2.7% N ₂
H ₂ O content	20 ppm	10,000 ppm	210 ppm
Precipitation	None at surface	Rain, frost, snow	Frost
Circulation	1 cell/hemisph.; quiet at surface but very active aloft	3 cells/hemisphere; local and regional storms	1 cell/hemisphere or patchy circulation; global dust storms
Maximum surface wind	~3 m/s	>100 m/s	~ 30 m/s
Seasons	None	Comparable northern and southern seasons	Southern summer more extreme

* An AU, or Astronomical Unit, is the average distance between Sun and Earth.

ionization and recombination, as well as excitation and de-excitation processes dominate in balancing ionization and recombination rates. Alternatively, ionization can be the result of impacts of externally-generated high-energy particles (such as solar energetic particles or particles accelerated in a planetary magnetosphere) or be caused by irradiation by solar photons of sufficiently high energy (typically X-ray and [extreme] ultraviolet) such as occurs in planetary ionospheres and cometary tails. {A6}

Much of what is described in this volume deals with the physics of magnetized plasmas, and much of that physics is approximated by a description known as magnetohydrodynamics, or MHD, as introduced in Ch. 3. In the present chapter, however, we first look at the more familiar situation of neutral gases, also because many of the phenomena discussed in this volume occur in the layers of planetary atmospheres for which the concept of hydrodynamics – in which magnetic field is ignored – gives us a good starting point. Later in this chapter, we focus on where ionization becomes important. For now disregarding the effects of magnetic fields, the limits of pure ('non-magneto-') hydrodynamics are reached in the high tenuous layers of planetary atmospheres where collisions are infrequent and other processes enter into our discussion, such as chemical differentiation subject to gravity or even outflows from the body in question. {A6}

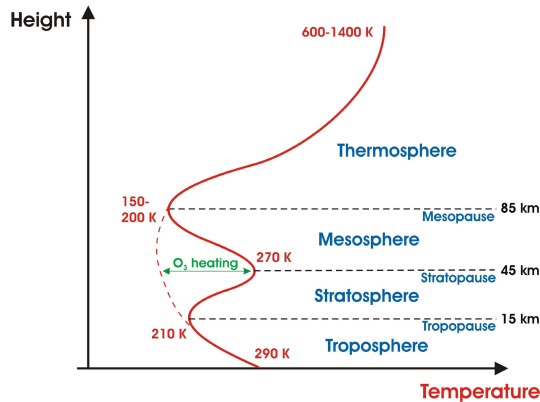


Figure 2.2: Average vertical temperature profile through Earth’s atmosphere. The general shape of the temperature profile is reasonably consistent to the point where it can be used to define the four main neutral atmosphere ‘layers’, from the troposphere to the thermosphere. The temperature of the uppermost layer, the thermosphere, increases steeply with altitude due to absorption of solar extreme ultraviolet (EUV) and far-ultraviolet (FUV) radiation. The thermosphere and upper mesosphere are partially ionized by the same EUV radiation, which varies by a factor of three over the solar cycle, and by auroral particle precipitation. [The effect of absorption by ozone is specifically highlighted. Fig. I:12.1] For a color version of this figure, see *arXiv:2001.01093*.

A great variety of phenomena in the local cosmos have their foundation in the electrical conductivity of the media within which they occur. This may be in the generation and maintenance of magnetic field deep inside the Sun and in most of the planets, in the many phenomena driven by the interaction of the magnetized flow of the solar wind with Solar-System bodies, or even in the processes in the ionized domains of atmospheres of many of these bodies. In most situations discussed in this volume, that conductivity has its origin not in the metallic behavior of the medium as it does deep inside Earth but rather in the ionization of matter: whereas in metals ions are relatively immobile and share some of their electrons, in a plasma both the ions and the electrons are entirely unbound on microscopic scales. This chapter introduces electrical conductivity in a magnetized medium, here looking at plasma with a low degree of ionization; fully ionized plasmas are discussed in Ch. 3.

2.2 Gravitationally stratified atmospheres and stellar winds

Among the planetary atmospheres in the Solar System, those of Venus and Mars are most similar to those of Earth. The abundances of their primary constituents – mostly CO_2 and N_2 , and, on Earth, N_2 and O_2 – are compared in Table 2.1. Note that the order of the most abundant components as well as the absolute base pressures differ markedly.

A sketch of the Earth’s atmospheric vertical thermal structure is shown in Fig. 2.2. The temperature gradually drops from the surface – where the bulk of the conversion of solar irradiance into heat occurs – through the troposphere due to adiabatic expansion.

Table 2.2: *Extent and important species for upper atmospheric regions of the terrestrial planets. [Table IV:7.3; added planetary radii R_p (km). More detailed information is provided in the text and figures of Ch. 13.]*

	Venus	Earth	Mars
	$R_{p,\text{♀}} = 6052$	$R_{p,\text{♁}} = 6378$	$R_{p,\text{♂}} = 3396$
Thermosphere	~120-250 km	~85-500 km	~80-200 km
	CO ₂ , CO, O, N ₂	O ₂ , He, N ₂	CO ₂ , N ₂ , CO
Ionosphere	~150-300 km	~75-1,000 km	~80-450 km
	O ₂ ⁺ , O ⁺ , H ⁺	NO ⁺ , O ⁺ , H ⁺	O ₂ ⁺ , O ⁺ , H ⁺
Exosphere	~250-8,000 km	~500-10,000 km	~200-30,000 km
	H	H, (He, CO ₂ , O)	H, (O)

At greater altitudes the absorption of short-wavelength sunlight by tenuous gas that is less efficient in cooling through radiation leads to increased temperatures in the stratosphere (mainly by photons between about 2,000 Å and 3,000 Å) and in the thermosphere (for wavelengths mostly short-ward of 2,000 Å). Energy leaves the Earth's atmospheric domains mainly by infrared radiation from the lower regions, which also leads to a decrease in temperature above the stratosphere by radiation from the mesosphere. The densities in the thermosphere are so low, and the dominant chemical constituents such inefficient radiators, that downward thermal conduction exceeds radiative losses above about 100 km (see Ch. IV:9). Table 2.2 compares the properties of the upper atmospheres of the three terrestrial planets (with significant atmospheres), *i.e.*, the thermospheres, the ionized constituents referred to as the ionospheres that largely overlap with the thermospheres, and the exospheres beyond that; the reasons for the apparent chemical mismatch between the neutral molecular and the ionized components are discussed in Ch. 13. ^[6]

For the Sun's atmosphere, there is a comparable pattern of temperature with height: moving upward, the temperature drops throughout the lower atmosphere (the 'photosphere' from which the bulk of the solar irradiance is emitted; also referred to as the 'solar surface' by astronomers, despite the fact that the Sun is entirely gaseous throughout), but then increases again in the chromosphere (extending a few thousand km above the photosphere) and then shoots up to form an extended, hot corona. Some of the physical properties of these domains (along with a rough definition of the terms) are summarized in Table 2.3. The reasons behind this similarity in pattern are partly the same, partly completely different. A similarity is that energy is most efficiently radiated from the low, dense atmospheric layers, and poorly from high, tenuous layers where conductive redistribution plays an important role. But the heat input differentiates the two: the solar chromosphere and corona are not heated by absorption of photons from the solar surface (which is thermodynamically impossible because the atmospheric temperature is higher than the surface temperature) but by

⁶ This volume focuses on terrestrial planets; we refer to Ch. IV:8 for an introduction to the upper atmospheres of the giant planets.

Table 2.3: Basic parameters for, and definitions of, domains in the solar atmosphere. Note that all regions of the solar atmosphere are very inhomogeneous and that these values are only meant to give a rough idea of their magnitudes. [Table I:8.1, here converted to cgs-Gaussian units, and with solar properties added. n_e and n_H are the densities of electron and neutral hydrogen; the plasma β is defined in Eq. (3.24)]

Region	n [cm^{-3}]	n_e/n_H	T [K]	B [Gauss]	β
Photosphere ¹	10^{17}	10^{-4}	$6 \cdot 10^3$	1 – 1500	> 10
Chromosphere ²	10^{13}	10^{-3}	$2 \cdot 10^4 - 10^4$	10 – 100	10 – 0.1
Transition region ³	10^9	1	$10^4 - 10^6$	1 – 10	10^{-2}
Corona ⁴	10^8	1	10^6	1 – 10	$10^{-2} - 1$
Sun: radius $R_\odot = 7 \cdot 10^5$ km; surface gravity $g_\odot = 274 \text{ m/s}^2$; bolometric luminosity $L_{\text{bol}} = 4 \cdot 10^{33}$ erg/s; effective temperature $T_{\text{eff}} = 5772$ K, defined such that $L_{\text{bol}} \equiv \sigma T_{\text{eff}}^4 4\pi R_\odot^2$					

Definitions: ¹ the photosphere is the layer from which the bulk of the electromagnetic radiation leaves the Sun (this layer has an optical thickness $\tau_\nu \lesssim 1$ in the near-UV, visible, and near-IR spectral continua, but it is optically thick in all but the weakest spectral lines); ² the chromosphere is optically thin in the near-UV, visible, and near-IR continua, but optically thick in strong spectral lines - it is often associated with temperatures around 10,000 – 20,000 K; ³ the transition region is a thermal domain between chromosphere and corona in which thermal conduction leads to a steep temperature gradient; ⁴ the corona is optically very thin over the entire electromagnetic spectrum except at radio wavelengths and in a few spectral lines - the term is often used to describe the solar outer atmosphere out to a few solar radii with temperatures exceeding ~ 1 MK.

dissipation of electrical currents and a variety of waves running through the plasma (both generated by the convective flows below the solar surface, and coupled into the outer atmosphere via the Sun’s magnetic field; see Sect. 9.3). The amount of energy converted in the solar outer atmosphere from chromosphere to corona and solar wind is a function of the instantaneous magnetic activity. This activity exhibits an 11-year quasi-cyclic pattern that is often referred to as ‘the sunspot cycle’ because it was discovered from multi-decade records of sunspot counts.

The Sun’s radiative input into the Earth’s atmosphere (known as the spectral irradiance, $S(\lambda)$) exhibits a significant variability depending on solar magnetic activity (Figure 2.3). The overall emission from the solar photosphere varies little with magnetic activity, that from the warm chromosphere mildly, and that from the hot corona strongly.

{A7} As a result, the relative variability in $S(\lambda)$ through the solar cycle increases markedly short-ward of about 3,000 Å: $(S_{\text{max}} - S_{\text{min}})/S_{\text{min}}$ climbs from below one part in 1,000 long-ward of 3,000 Å to near unity short-ward of 1,000 Å. The absorption of the most variable segment of the spectral irradiance in Earth’s atmosphere occurs primarily above about 50 – 100 km (Fig. 2.4), causing the high atmosphere to evolve strongly in temperature and density in response to the solar sunspot cycle (see Fig. 2.6),

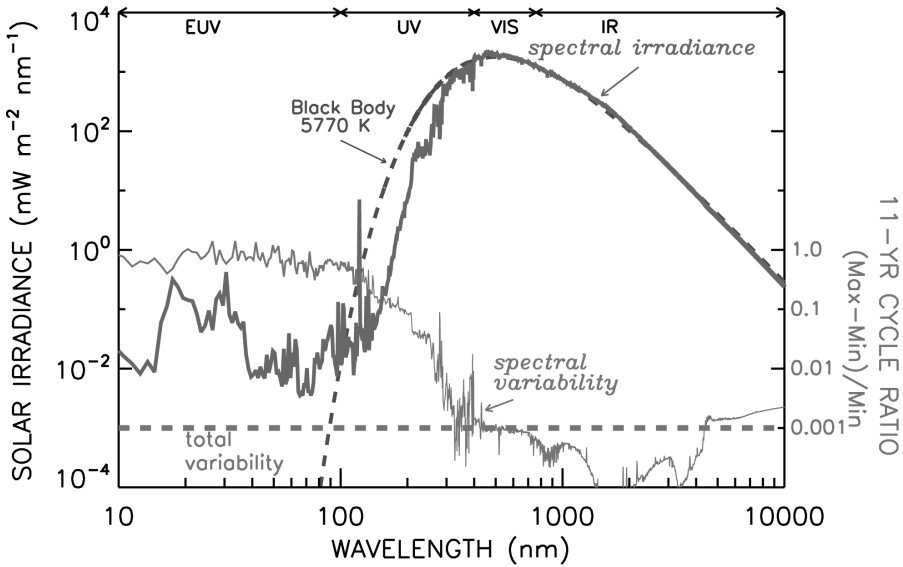


Figure 2.3: Comparison of the solar spectrum and the black body spectrum for radiation at 5770 K (the approximate temperature of the Sun's visible surface). Also shown is an estimate of the variability of the solar spectrum during the 11-y solar cycle, inferred from measurements (at wavelength below 4000 Å) and models (at longer wavelengths) and, for reference (dashed line), the solar cycle 0.1% change in the total solar irradiance. [Fig. III:10.1]

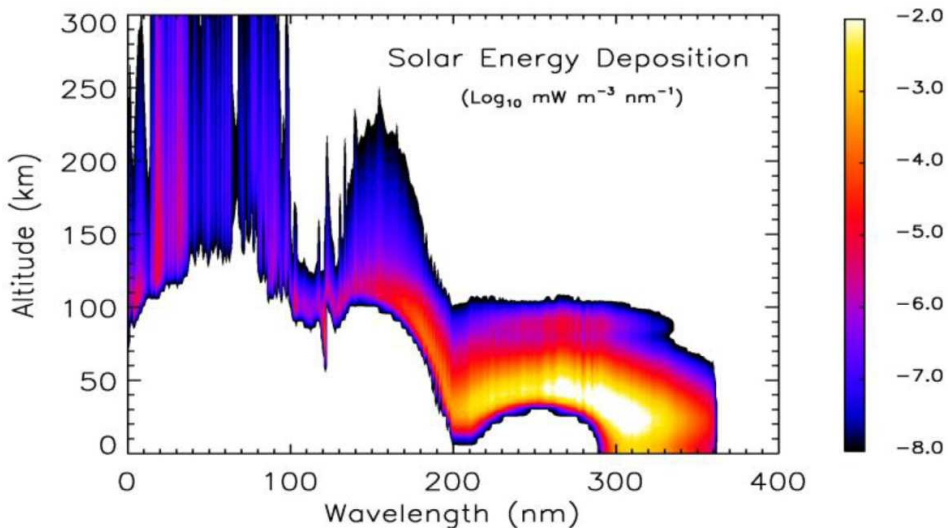


Figure 2.4: [Altitude of penetration of the solar radiation as a function of wavelength [from X-rays through 3600 Å]. The color range shows the amount of energy deposited in the different layers of the atmosphere for the different parts of the solar spectrum (on a logarithmic scale, in units of $\text{mW}/\text{m}^3/\text{nm}$ [or $10^{-3} \text{ erg}/\text{s}/\text{cm}^3/\text{Å}$]). [Fig. III:13.3] For a color version of this figure, see [arXiv:2001.01093](https://arxiv.org/abs/2001.01093).

further modulated as Earth goes through its weakly elliptical orbit around the Sun and its rotation about a tilted axis, and with variable contributions from geomagnetic activity (see Chs. 12 and 13).

Wavelengths short-ward of about 2400 Å and about 1250 Å can dissociate O₂ and N₂, respectively, and short-ward of about 900 Å can ionize, *e.g.*, O atoms. Consequently, the atomic and ionic components in the Earth’s atmosphere do not show up significantly below around 100 km in altitude because all ionizing and dissociating wavelengths have been absorbed by that depth into the atmosphere (see Ch. 13); above that altitude, the abundances of the ionic and atomic components all reflect solar, orbital, and diurnal cycles.

The density stratification in much of the lower atmosphere of the terrestrial planets (defined as below about 100 km for Earth) can be understood to first order by looking at the behavior of a stationary gas subject only to gravity. “The frequent collisions of molecules in a gas close to thermal equilibrium enable the Maxwellian [velocity distribution (with corresponding exponential energy distribution)] of the individual particles to be characterized by the basic fluid properties of pressure, p , temperature, T , number density, n , and mass density, ρ , that are related by the perfect gas law:

$$p = nkT = (\rho/m)kT = \rho\mathcal{R}T/\mu, \quad (2.1)$$

where k [$(1.4 \times 10^{-16}$ erg/K)] and \mathcal{R} [$(8.31 \times 10^7$ erg/K/mol)] are the Boltzmann and universal gas constants, respectively, and m is the mean molecular mass [while μ the mean molecular mass in atomic units]. The fluid concept of pressure in the atmosphere represents the weight of the column of gas above.

The neutral gas under the influence of the planet’s gravitational force gives rise to the concept of hydrostatic balance, which states that the change in pressure with height, dp , is closely balanced by the weight of the fluid, $nmgdh$ (where m is the mean molecular mass in [grams] and h is the height), under the action of the planet’s gravitational acceleration, g . The concept is expressed mathematically as:

$$\frac{dp}{dh} = -\rho g = -p/H_p. \quad (2.2)$$

This basic equation describes the exponential decrease in gas density with altitude, and results in the concept of the pressure scale height,

$$H_p = kT/mg, \quad (2.3)$$

which represents the [height difference] through which the gas pressure [in an isothermal atmosphere] will decrease by a factor of $e = \exp(1)$. Earth’s upper atmosphere extends for about a dozen scale heights above 100 km altitude, with scale heights changing from about 5 km to 50 km with increasing altitude, as the temperature increases from about 180 K to over 1000 K (see Fig. 2.2).

[The] quasi-equilibrium implied by hydrostatic balance does not exclude the possibility of vertical winds. The assumption simply demands that the rate of [flow] is such that the atmosphere adjusts at a comparable rate. The term quasi-hydrostatic

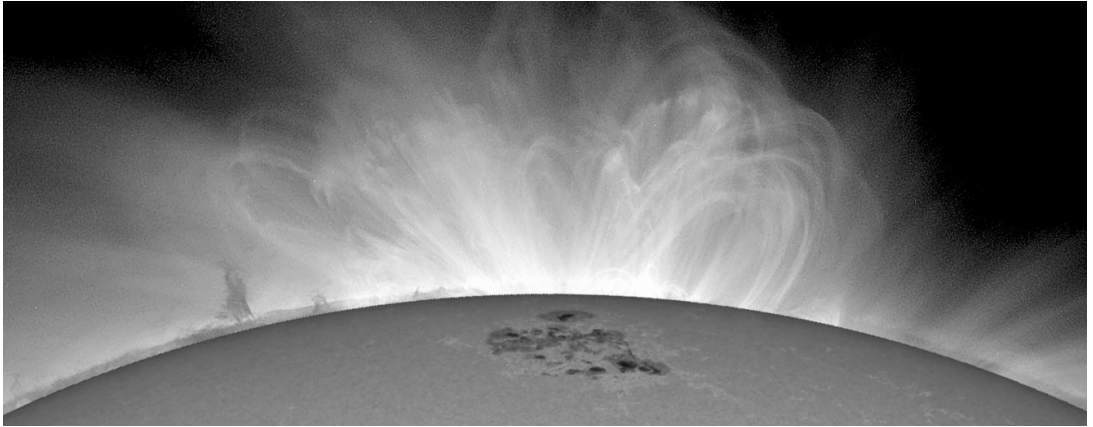


Figure 2.5: Composite image of solar coronal loops over an active region (observed in the SDO/AIA 193 Å channel, most sensitive to coronal temperatures around 1.5 MK). The foreground image that masks the on-disk corona is an SDO/HMI intensity image showing a large sunspot group approaching the limb from which most of the coronal loops in this composite image emanate. The dark band between the solar limb in visible light and the overlying corona is the chromosphere which is itself EUV-dark and opaque to coronal emissions, thus blocking the EUV emission from the corona behind it, showing up partially masked by foreground coronal emission. The images were taken on 2022/09/04 around 20 UT, and were rotated by 115° counterclockwise from solar north.

balance is the more correct expression in the case of accommodating vertical winds in the system. [...] Vertical winds in Earth’s upper atmosphere of the order of 100 m/s can be accommodated within the quasi-hydrostatic assumption.” {A11} {A12}

The quasi-hydrostatic description applies not only to planetary atmospheres but is also used for the interior of the gas giants, for the interior and lower-atmosphere of the Sun, and – as we shall see later – even inside magnetic ‘containers’ in the solar atmosphere that are known as flux tubes (see Table 3.1 for a definition), one incarnation of which are ‘coronal loops’ – which is the general term describing the emitting structures seen in EUV and X-ray images of the Sun’s hot outer atmosphere. Table 2.3 summarizes characteristic physical parameters for the domains within the solar atmosphere from the solar ‘surface’ (photosphere) up into the corona (see also Fig. 2.5 for an example image showing coronal loops above a sunspot region). These numbers should be seen as characteristic values only: all these domains span a few orders of magnitude in density and all are very dynamic at any given location, while moreover the solar magnetic field plays a key role in them as it structures multitudes of adjacent distinct atmospheres along magnetic field bundles (Sect. 3.4). The solar corona is visible at X-ray and EUV wavelengths up to several hundred thousand kilometers. The coronal plasma is mostly contained in magnetic structures relatively low down, but increasingly with height the gas pressure forces the magnetic field to ‘open’ into the heliosphere. The plasma on ‘open field’ streams out to form the solar wind, resulting in a low-density and consequently dark lower coronal region known as

Table 2.4: Basic parameters of the fast and slow solar wind [near Earth; modified after Table I:9.1. Notes: (1) subscripts 'e', 'p', and 'i' are used to denote electrons, protons, and other ions, respectively; (2) 'FIP' stands for 'first ionization potential'; 'low-FIP' is a group of elements with first-ionization potentials below 10 eV.]

Property (1 AU)	Slow wind	Fast wind
Speed	430 ± 100 km/s	700 – 900 km/s
Ion density	$\simeq 10$ cm ⁻³	$\simeq 3$ cm ⁻³
Flux	$(3.5 \pm 2.5) \times 10^8$ cm ⁻² s ⁻¹	$(2 \pm 0.5) \times 10^8$ cm ⁻² s ⁻¹
Magnetic field	60 ± 30 μ G	60 ± 30 μ G
Temperatures	$T_p = (4 \pm 2) \times 10^4$ K $T_e = (1.3 \pm 0.5) \times 10^5$ K $> T_p$	$T_p = (2.4 \pm 0.6) \times 10^5$ K $T_e = (1 \pm 0.2) \times 10^5$ K $< T_p$
Anisotropies	T_p isotropic	$T_{p\perp} > T_{p\parallel}$
Structure	filamentary, highly variable	uniform, slow changes
Composition	He/H $\simeq 1 - 30\%$ low-FIP enhanced	He/H $\simeq 5\%$ near-photospheric
Minor species	n_i/n_p variable $T_i \simeq T_p$ $v_i \simeq v_p$	n_i/n_p constant $T_i \simeq (m_i/m_p)T_p$ $v_i \simeq v_p + v_A$
Associated with	streamers, transiently open field	coronal holes

a 'coronal hole'.

The quasi-hydrostatic description even forms a useful, albeit very crude, approximation for that part of extended atmosphere of the Sun that is the inner-heliospheric domain of the solar wind: whereas there is in fact an outflow, this 'vertical wind' leaves the stratification nearly hydrostatic for many solar radii above the solar surface, as we shall see shortly.

Table 2.4 summarizes a few characteristics of the solar wind near Earth orbit. Outside of dynamic coronal mass ejections (Ch. 6), the solar wind is predominantly in one of two states, referred to as the 'fast wind' and the 'slow wind'. These states originate from distinct environments on the Sun, and because the Sun rotates underneath the radially outflowing wind, slow and fast streams unavoidably interact – see Sect. 5.5.1. For what follows here, we focus on domains where only one of these types of wind prevail for several days, which is the time it takes to flow from Sun to Earth (the geometry of the magnetic field that it carries is discussed in Sect. 5.4). {A13}

The medium of the heliosphere is fundamentally distinct from that of the lower 100 km of the terrestrial atmosphere: the solar wind is primarily made up of hydrogen with a lesser amount of helium, is hot and therefore almost fully ionized, and is threaded by a magnetic field. The dynamics of the solar wind and the ways in which it interacts with planetary magnetospheres is modulated by that magnetic field but, as first noted by Parker (1958), the basic stratification and flow of the solar wind can be understood

from its high temperature: because it is hot and ionized, the electrons in the solar wind are very efficient at conducting heat, and that is all it takes to understand how it can lead unavoidably to a fast wind that can escape solar gravity. It is not simply an 'evaporation' off the Sun; after all, even at some millions of degrees, "the sound speed c_s — essentially the mean ion speed — is much smaller than the [escape speed v_{esc} which can be derived by equating a particle's kinetic energy with its gravitational potential energy at the surface:

$$v_{\text{esc}} = \sqrt{2GM/r}. \quad (2.4)$$

For the solar corona, the sound and escape speeds are]

$$c_s \approx \sqrt{kT/m} \approx 100 \text{ km/s} \ll v_{\text{esc}} = \sqrt{2GM_{\odot}/R_{\odot}} = 618 \text{ km/s}, \quad (2.5)$$

where k is Boltzmann's constant, T the coronal temperature, m the mean particle mass, G the universal gravitational constant, and M_{\odot} and R_{\odot} the solar mass and radius, respectively.

Mass and momentum balance radially away from the Sun [in an assumed uniform, strictly radial flow] at heliocentric distance r can be written

$$\frac{d}{dr}(\rho v 4\pi r^2) = 0 \quad (2.6)$$

$$\rho v \frac{dv}{dr} = -\frac{dp}{dr} - \rho \frac{GM_{\odot}}{r^2}, \quad (2.7)$$

with ρ the mass density, v the flow speed. Then $p = 2nkT$ is the gas pressure in an electron–proton plasma with n representing the electron or proton number density, and $\rho = mn$ where m is the mean particle mass which is given by $m \approx m_p/2$ for an electron–proton plasma. {A14}

[The] consequence of the thermal conduction in a million degree corona is to extend the corona; *i.e.*, the temperature falls off slowly with distance from the Sun. Thus, in a hypothetical *static* atmosphere, we find a pressure at infinity given by {A14}

$$\frac{dp}{dr} = -nm \frac{GM_{\odot}}{r^2}, \quad (2.8)$$

$$p(r) = p_0 \exp \left[-\frac{mGM_{\odot}}{2k} \int_{R_{\odot}}^r \frac{dr}{r^2 T(r)} \right]. \quad (2.9)$$

Thus, if the temperature falls less rapidly than $1/r$, we find that $\lim_{r \rightarrow \infty} p(r) > 0$, we expect a non-vanishing pressure at infinity when the corona is extended. In particular, we find that for reasonable temperatures and densities n_0 , T_0 at the 'coronal base' this pressure is much larger than any conceivable interstellar pressure.

[The observed slow decrease of temperature with distance from the Sun, caused by the efficient thermal conduction that is mostly carried by electrons, implies that the solar wind must expand supersonically into interstellar space. For a spherically symmetric, single-fluid, isothermal outflow,] the equations of mass and momentum conservation (Eqs. 2.6, 2.7) can be rewritten to give {A15}

$$\frac{1}{v} \frac{dv}{dr} \left\{ v^2 - \frac{2kT}{m_p} \right\} = \left\{ \frac{4kT}{m_p r} - \frac{GM_\odot}{r^2} \right\} \quad (2.10)$$

[The solar wind starts slow, but is supersonic further out in the heliosphere; such a] transonic wind passes through a critical point at

$$r_c = \frac{m_p GM_\odot}{4kT} \quad \text{where} \quad v_c = \sqrt{\frac{2kT}{m_p}} \quad (2.11)$$

[(note the dependence on stellar mass). {A16} {A17} Formally, the equations allow such a flow] to match *any* pressure as $r \rightarrow \infty$ [although in reality the reach of the flow is limited by the existence of an interstellar medium (Sec. 5.5.8)].

Let us examine this transonic wind solution in somewhat greater detail. If we integrate the force balance, Eq. (2.7), from the coronal base to the critical point r_c we find a density ρ_c at the critical point given by

$$\rho_c = \rho(r_c) = \rho_0 \exp \left\{ -\frac{m_p GM_\odot}{2kT R_\odot} + \frac{3}{2} \right\}. \quad (2.12)$$

Note that this density is almost exactly the same as if there had been *no* solar wind flow: *The subsonic corona in the solar wind is essentially stratified as a **static** atmosphere.*

We can also find the resultant mass flux for the wind by examining the density and the velocity at the critical point:

$$(nv)_r = n_c v_c \frac{r_c^2}{r^2} \propto \rho_0 T^{-3/2} \exp \left[-\frac{C}{T} \right] \quad (2.13)$$

where ρ_0 is the density at the coronal base [and C a constant]. *The mass flux is proportional to the density at the coronal base and depends exponentially on the coronal temperature.*” The actual solar wind is not only driven by thermal conduction from the coronal environment (which supplies energy for the work of driving the wind against gravity), but also by magnetic waves, known as Alfvén waves, whose fluctuations act as an additional pressure term, and whose dissipation aids in heating far above the solar surface, all of which is particularly important for the fast wind streams; more on that in Sect. I:9.5. Another note on more detail is found in Sect. I:9.6, which begins to explain why for a more realistic solar wind description that also allows for helium, the exponential dependence of the solar mass loss on temperature is much weakened into a power-law dependence of temperature.

Note that it is not only the efficient thermal conduction per se that leads to a significant solar wind, but also the high temperature and low particle mass, and that that is the reason for the contrast with Earth’s atmosphere. In Eq. (2.2) gravity is approximated by a constant, leading to a formal solution for the pressure stratification of the terrestrial atmosphere that tends to zero exponentially even for an isothermal atmosphere; this is not a bad approximation for an atmosphere in which the pressure scale height (at most some 50 km) is well below 1% of the planet’s radius, so gravity

changes little even over many scale heights above the surface. But in the hot corona, the pressure scale height for the hydrogen-dominated gas at ≈ 2 MK is about $0.15R_\odot$, so gravity diminishes noticeably in the first few pressure scale heights, hence its distance dependence needs to be reflected in Eq. (2.7). The relatively weaker gravity (and the correspondingly reduced escape energy) at large heights leads to a transonic wind at coronal temperatures.

On a side note (to which we return in Ch. 11), the same equation Eq. (2.7) also informs us about an accelerating inflow (for which $vdv/dr > 0$ as both $v < 0$ and $dv/dr < 0$) enabling the formation of stars and planetary systems: gravity can win out over a pressure difference on very large scales in the Galaxy on which stars form, because now gravity in fact is built up by the infalling matter itself so that M_\odot needs to be replaced to read

$$\rho v \frac{dv}{dr} = -\frac{dp}{dr} - \rho \frac{G}{r^2} \int_0^r \rho 4\pi r^2 dr. \quad (2.14)$$

“To make a star of a given mass M from a gas with temperature T , gravity must overcome the pressure support. [One way to estimate the required properties of a cloud involved in the initiation of star formation is to look at Eq. (2.14) and see when conditions cannot remain in a stationary balance, *i.e.*, when $v = 0$ cannot be maintained. That occurs when] the radius R of the protostellar cloud exceeds the critical radius]

$$R_c(M, T) \gtrsim \frac{GM}{c_s^2} = \frac{GM\mu m_p}{kT}, \quad (2.15)$$

where c_s is the sound speed and m_p is the mass of the hydrogen atom. Taking a mean molecular weight $\mu = 2.3$, appropriate for molecular hydrogen plus helium, and a typical cold molecular cloud temperature of $T = 10$ K, Eq. (2.15) implies that a solar mass star must collapse from a cloud of radius $R \sim 2 \times 10^4$ astronomical units (*[i.e.*, Sun-Earth distances; shorthand] AU).”

You will see the logic used in these examples applied throughout this book, and indeed astrophysics in general: approximations in functional forms, simplifications about geometries, and order of magnitude estimates are used throughout to aid in the basic understanding what is going on. With these tools, analytical and – far more commonly – numerical solutions become interpretable in terms of the basic, common processes. How much can be simplified to show the basics, however, depends on the environment: heliophysics, as is physics in general, is about simplifying as much as is allowed, but no more.

2.3 Photons, collisions, ionization, and differentiation

In our everyday lives we can get away with taking it for granted that the atmosphere around us is the same no matter where we are. Moreover, we may take it to be true that this atmosphere is a mixture of mostly N_2 and O_2 . And that this atmosphere is a very poor electrical conductor and that its winds are unaffected by the planetary magnetic field. As it turns out, none of these properties that we take for granted apply outside

of the domain where we live: the chemical mixture depends on height in planetary atmospheres and is affected by the variable spectral irradiance from the Sun's outer atmosphere, ions and thus electrical conductivity are important in most of the local cosmos, and magnetic fields influence flows and vice versa almost everywhere in space. In this section, we focus on the processes that make the atmospheric composition dependent on location, primarily altitude. In the next section, Section 2.4, we start looking at the role of ions in electrical conductivity and flows, although the role of magnetic fields in that is the focus of Ch. 3.

The scale height for different atmospheric constituents depends on the molecular or atomic mass, and is thus in principle different for different chemicals. But as long as the mixing by winds and (turbulent) convection is fast enough compared to the time scale by which the chemical separation can occur by diffusive settling, the atmospheric composition will remain uniform, and all major species will share the same scale height. When collisions become relatively infrequent above the homopause (at about 100 km for Earth), and diffusive settling exceeds mixing by flows, separation of chemicals by molecular mass occurs; see Ch. 13. The rate of separation depends on the diffusion coefficients, which themselves depend on chemical species and density, and on the chemical reactions that couple species (and, in the ionosphere, also through ion-neutral interactions), relative to turbulent mixing efficiency; see the discussion in Ch. IV:9.

Still higher in the atmosphere, where collision frequencies become so low that the mean free path approaches or exceeds the formal pressure scale height, the description of the medium as an ideal gas fails. That environment, where particles essentially move ballistically over long distances subject only to gravity (still disregarding any effects of electric and magnetic fields), is known as the exosphere. The exospheric base height can be estimated by looking at collision frequencies.

The characteristic frequency at which a particle in a non-magnetized plasma or a non-ionized gas of identical particles, all characterized by a temperature T and at particle density n , collides with other such particles is given by

$$\nu = \sigma_{cc} v_{\text{rel}} n = \sigma_{cc} \left(\frac{kT}{m} \right)^{1/2} n, \quad (2.16)$$

where σ_{cc} is the mutual collision cross section and v_{rel} is the velocity of one particle relative to another. In computing the mean free path, the velocity cancels out, leaving only the density as a variable:

$$\lambda_{\text{mfp}} = \frac{v_{\text{rel}}}{\nu} = \frac{1}{\sigma_{cc} n}. \quad (2.17)$$

By way of example, let us look at neutral atoms with a collisional cross section of order, say, $3 \times 10^{-16} \text{ cm}^2$ (as for hydrogen atoms). For these, a density of $3 \times 10^8 \text{ cm}^{-3}$ (reached at roughly 500 km in Earth's atmosphere, depending on solar activity) would correspond to $\lambda_{\text{mfp}} \approx 100 \text{ km}$. This order-of-magnitude estimate shows that this density in the Earth's atmosphere roughly forms the point at which a vertically moving atom could jump over a scale height, or essentially through the bulk of overlying matter,

so where the assumption that we can work with the medium as a gas of electrically neutral particles fails; this is about the point where the Earth's atmosphere transitions into an exosphere where neutral atoms move essentially ballistically.

On the Sun, in contrast, the neutral hydrogen population could still be described by hydrodynamics at that density because of the much larger scales involved, if matter were largely neutral there; however, that density is reached only in the corona where high temperatures cause hydrogen and helium to be fully ionized (see Table 2.3), and collisions occur via long-range electromagnetic forces between charged particles (see Table 3.4 for mean-free path estimates in an ionized medium, which, with Eq. (2.17), shows the larger effective collision cross section for Coulomb collisions). Lower down in the solar atmosphere where neutrals do dominate, the mean free path lengths are significantly smaller: the plasma throughout the Sun up to the inner corona behaves like a gas in which (often turbulent) flows counter gravitational separation. There are fractionation effects deep inside the Sun where mixing by flows is negligible on solar evolutionary time scales. Chemical differentiation is also seen in the atmosphere in the minority species, specifically determined by the energy required for first ionization of the atom (see Fig. I:9.2); this differentiation, not by diffusive settling but likely related to MHD waves and by EUV and X-ray irradiation of the chromosphere from the higher atmosphere, is still inadequately understood and not further discussed here.

Below the Earth's exosphere and above the mesosphere, in a domain ranging from roughly 110 km to around 500 km in altitude, *i.e.*, throughout much of the bulk of the thermosphere, lies a domain where collisions are frequent enough that the gas approximation is largely valid but not frequent enough to maintain uniform mixing of the chemicals that make up the terrestrial atmosphere up to that height: the atmosphere up to heights of about 110 km “is known as the homosphere and is constantly being mixed by turbulent wave eddies. It is only at altitudes above about 110 km that turbulent mixing gives way to molecular mixing processes, where each species begins to be distributed vertically under its own pressure scale height or hydrostatic balance, see Eq. (2.2). A heavy species, such as carbon dioxide, will decrease in concentration with height more rapidly than a lighter species, such as atomic oxygen (see Fig. 2.6). Each species, i , will have its own characteristic scale height H_{pi} , where $H_{pi} = kT/m_i g$, which is the vertical distance a species will decrease in partial pressure and number density by a [factor of e]. The upper atmosphere differs from the lower atmosphere in this respect such that the mean mass of the fluid will change with altitude, as well as other gas parameters such as the specific heat, c_p . [...]

The vertical distribution of species also has a global seasonal/latitudinal structure from large scale [...] inter-hemispheric circulation from summer to winter. Closure of this circulation drives an upwelling of material across surfaces of constant pressure in the summer hemisphere and a downwelling in the winter hemisphere. The upwelling causes the heavier molecular rich gas, which had diffusively separated at lower altitudes, to be transported upwards to increase the mean molecular mass in summer. In winter the downwelling reduces the mean mass.”

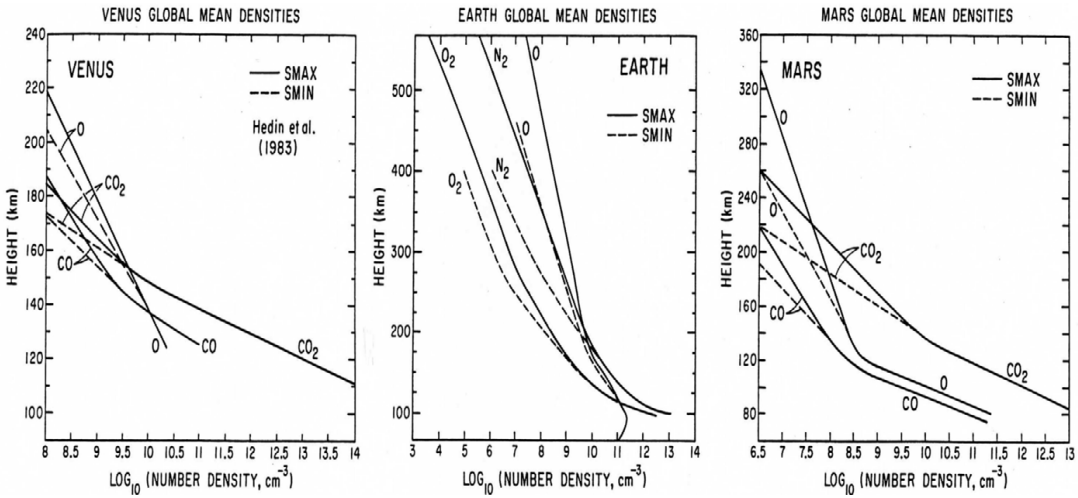


Figure 2.6: Comparison of the global mean vertical profiles of the major species in the neutral upper atmospheres of a) Venus, b) Earth, and c) Mars for low and high solar activity. *SMIN* and *SMAX* indicate solar minimum and maximum conditions. Note that the turbopause heights (where turbulent mixing and diffusive separation are comparable) are 135, 110, and 125 km for Venus, Earth, and Mars, respectively. [Note: the International Space Station orbits at an altitude of ~ 400 km. Figs. I:12.2, IV:9.1; source: Bougher and Roble (1991).]

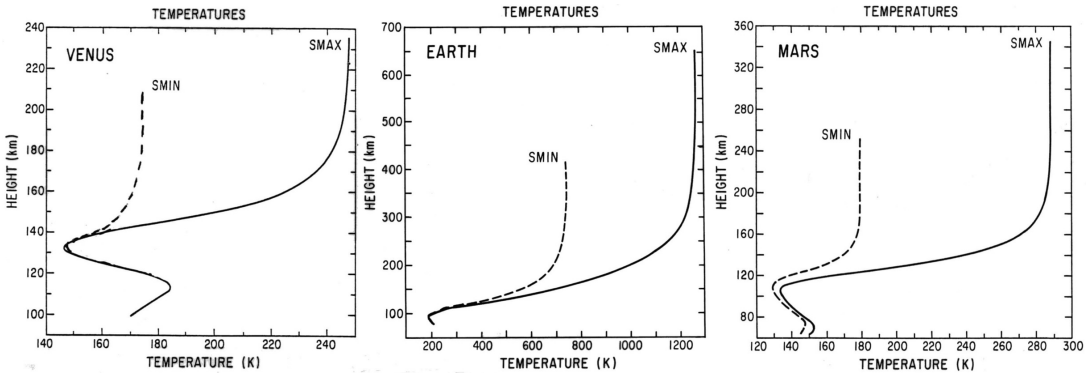


Figure 2.7: Three planet global mean temperature profiles for solar minimum (*SMIN*) and maximum (*SMAX*) conditions. [Note the differences in horizontal and vertical scales. Fig. IV:9.3; source: Bougher and Roble (1991).]

The seasonal changes in insolation and the resulting circulations subject to Coriolis forces on the rotating planet are modulated by the effects of space weather. These effects include the X-ray and (E)UV part of the solar spectral irradiation, dissipation of electrical currents, and energetic particles precipitating from the magnetosphere. All of these (and others discussed in Chs. 5, 6 and 14) lead to heating, ionization, and dissociation of the high atmosphere. “Early investigation of the terrestrial ionosphere through its effect on radio waves resulted in description by means of layers, principally the *D*, *E*, and *F* layers, the latter subdivided into *F*₁ and *F*₂ [(sketched in Fig. 2.8)]. This terminology continues to influence our current concept of the nature of energy

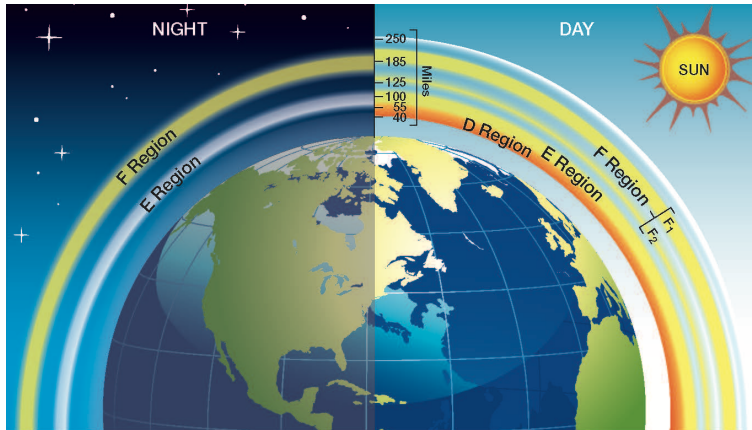


Figure 2.8: Sketch (not to scale) of the 'regions' in the terrestrial ionosphere. Source: NASA/SVS. For a color version of this figure, see [arXiv:2001.01093](https://arxiv.org/abs/2001.01093).

deposition in atmospheres, although the misleading term 'layer' has given way to 'region'. The term 'layer' arose from the observation of systematic variation in the height at which the critical frequency of reflection occurs in ionospheric radio sounding; this method cannot detect ionization above the peak of a region, which explains the appearance of layers. Radar and spacecraft measurements now give a more complete picture of peaks and valleys and reveal the complex morphology of the ionosphere. [...] An overview of the altitude dependence and variability of Earth's ionosphere is given in Figure 2.9, showing the diurnal and solar-cycle changes and the locations of the named regions."

"An additional historical artifact in terminology is the word ionosphere itself. Because the atmospheric ionization was discovered before the neutral thermosphere in which it is contained, anything above the stratosphere is often referred to as the ionosphere, resulting in a common misconception that this region of the atmosphere is mostly ionized. In fact, it is mostly neutral, ranging from less than a part in a million ionized during the day at 100 km altitude to about 1% ionized at the exobase (~600 km, depending on solar activity; compare Fig. 2.12). Even at 1000 km, there is only of the order of 10% ionization. At several thousand km, where ions (mostly protons) finally become dominant, the region is defined as the plasmasphere. [...] In the bulk of the terrestrial ionosphere] O^+ is the most important ion, particularly in the extensive F_2 region above ~200 km. The F_1 region from ~150 to ~200 km appears as a mere plateau in the profile, but is distinguished by a transition to molecular ions, particularly NO^+ . The low levels of N_2^+ , given the dominance of N_2 at these altitudes, is noteworthy. {A18} The E region from ~100 to ~150 km exhibits a small peak, dominated by O_2^+ and NO^+ ."

"Much of the external sources of heating, ionization, and dissociation of a planetary atmosphere comes from the absorption of photons or particles impinging on the neutral atmosphere. The physics defining the altitude profile of the three processes is the same. For example, the rate of ionization, q [($cm^{-3} s^{-1}$)], by solar radiation intensity, $I(h)$

III-13.1

{A18} I-12.4.1

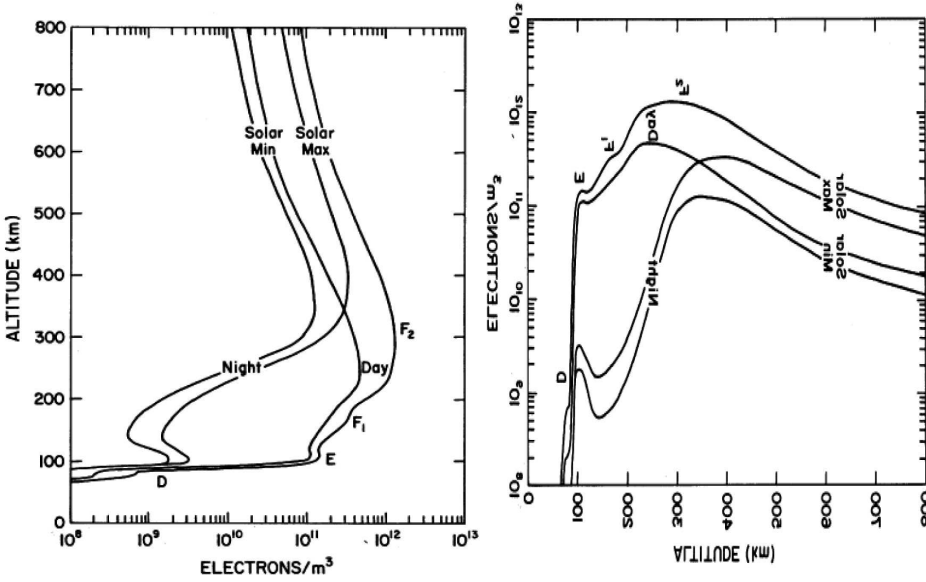


Figure 2.9: [left:] Overview of the altitude distribution of Earth's ionosphere for daytime and nighttime conditions, at high and low solar activity. [Fig. III:13.1] [right: One of multiple different conventions between planetary scientists and astrophysicists is that the height coordinate is usually displayed vertically for planetary scientists and horizontally for stellar scientists. This flipped and rotated version of the figure conveys the difference in appearance.]

[($\text{erg cm}^{-2} \text{s}^{-1}$)], at some height in the atmosphere of number density, $n(h)$, can be expressed as a product of four terms:

$$q = \sigma_a I(h) n(h) \eta_i, \quad (2.18)$$

where σ_a [(cm^2) is the atomic] absorption cross section [for a wavelength interval matching that of I ,] and η_i [(erg^{-1})] is the ionizing efficiency; η_i could equally be the heating or dissociation efficiency. The intensity of the radiation gradually decreases along the path through the atmosphere starting from an initial intensity of $I(h = \infty)$. The altitude deposition profile depends on the absorption coefficient and on the atmospheric number density, which varies exponentially with height. Clearly the product of the intensity of the radiation, I , that decreases as the source penetrates the atmosphere, and on the atmospheric number density, $n(h)$, that increases with increasing depth into the atmosphere, must reach a maximum at some altitude or, more correctly, at some pressure level [(except, of course, for visible wavelengths for which the atmosphere is largely transparent, in which case the surface absorption and reflection need to be taken into account)]. The level of penetration is referred to as the optical depth, τ , which is expressed mathematically as

$$\tau = \sigma_a n(h) \frac{H_p(h)}{\cos(\chi)}, \quad (2.19)$$

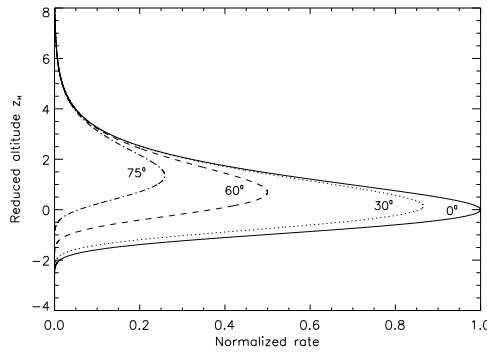


Figure 2.10: The vertical profile of the classical Chapman profile appropriate for heating, ionization, or dissociation in a stratified hydrostatic atmosphere irradiated from above, relative to a reference height, shown for different slant angles χ . [Fig. I:12.4]

where the product of the number density $n(h)$ at height h with the scale height $H_p(h)$ at that level represents the integrated content of a column of gas above that point, and χ is the angle from the zenith at which the radiation penetrates a planar atmosphere. [The above expression is valid as long as the curvature of the atmosphere can be neglected, so for angles $\chi \lesssim 75^\circ$.] {A19}

The profile of the rate of heating, ionization, or dissociation from these processes takes the form of the classical Chapman profile, as depicted in Fig. 2.10, and is given mathematically by {A19}

$$q(h) = I_\infty \exp \left[-\sigma_a n(h) \frac{H_p(h)}{\cos(\chi)} \right] \eta_i \sigma_a n(h). \quad (2.20)$$

{A20} The peak of the profile is at unit optical depth, which depends on the mass of atmosphere above traversed by the energetic photon or particle. This corresponds to a fixed pressure level for a given angle of incidence. The depth of penetration into the atmosphere of a photon or particle in pressure coordinates therefore does not change with the gas temperature or the degree of thermal expansion. Even with the changing heating over the solar cycle or during a [magnetospheric] storm that might cause a thermal expansion of the atmospheric gas, that same radiation will still penetrate and produce heating or ionization at the same pressure level. The altitude associated with that pressure and the local number density would, of course, be different since they depend explicitly on gas temperature.” {A21}

2.4 On collisions and currents, and on neutrals and pickup ions {A21}

The terrestrial upper atmosphere is coupled to the Earth’s magnetic field through the ionized component of the atmosphere (referred to as the ionosphere) that is in turn collisionally coupled to the neutral molecular and atomic medium within which

it is embedded. The dynamics of these couplings in the overall system of solar wind, magnetosphere, and ionosphere are discussed mostly in later Chs. 5, 6, and 13. Here, we look at the consequence of the ionized medium threaded by a dynamic magnetic field and embedded in moving neutral gas: electrical currents. In the terrestrial atmosphere, the effects depend sensitively on the magnetic latitude because of the orientation of the magnetic field: at high latitudes, where the field is predominantly vertical, the connection with the magnetosphere dominates and the dissipated power can lead to substantial heating. At mid and low latitudes, where the field is mostly horizontal, internal processes dominate that provide less dissipative power than at higher magnetic latitudes, but that do contribute to transport of plasma.

A moving electrical charge subject to a magnetic field experiences a Lorentz force perpendicular to its velocity and to the magnetic field, in a direction that depends on the sign of the charge. Also allowing for an electrical field to be present, the total force equals:

$$\mathbf{F}_L = m \frac{d\mathbf{v}}{dt} = q\mathbf{E} + \frac{q}{c} \mathbf{v} \times \mathbf{B}. \quad (2.21)$$

In case $\mathbf{E} = \mathbf{0}$ and in the absence of collisions, electrons and ions thus would spiral about the magnetic field line in opposite directions [(much more on that in Sect. 8.2)]. Their gyration radii and frequencies are very different because of their difference in mass and thermal velocity (see Table 18.2). Where the gyration radii are well below the gradients in the magnetic field, these opposite circular motions do not lead to a net current in the absence of collisions. However, when field gradients are substantial within the gyration radii of the particles (most readily for the ions, in particular the more energetic ones) the particles drift perpendicular to the field in directions opposite for opposite charges, thus leading to a current; one important heliophysical setting in which this occurs is in the Earth's inner magnetosphere, where the gradient drift of primarily the energetic ions leads to the 'ring current' (see Sect. 8.2).

In the variety of settings in heliophysics, collisions may occur among the electron and ion populations (see Ch. 3 for that), or with neutral particles (the focus here). In ionospheres, the neutral particles are atoms and molecules of a body's atmosphere. In, say, the environments of comets, planetary rings, or in the outer heliospheric solar wind the neutral particles, in contrast, may be either dust particles, escaping atmospheric gas, or inflowing neutral interstellar atoms.

Let us start with a collision in which no charge-transfer occurs in a setting where the charged particle senses both a magnetic and electric field. In each such collision of an electron or ion with a neutral particle, the gyro-motion of the electron or ion involved is modified. Because of the opposite charges of the electron and ion populations, they attempt to gyrate about the magnetic field in opposite directions as they are accelerated by the electric field; consequently, they exhibit a net drift perpendicular to the magnetic field with ions and electrons moving in the same direction and at the same rate. There is no net current (see the left-hand side of Fig. 2.11), but if

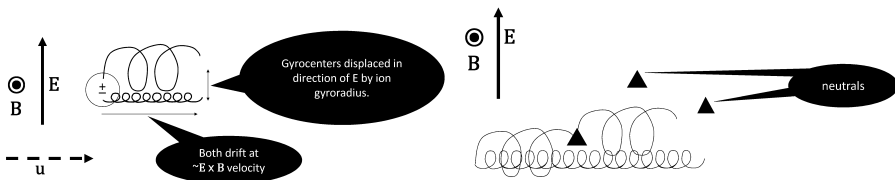


Figure 2.11: Schematic of interactions of plasma with neutrals. Left: Initial motion of pickup ions and electrons. The gray circle represents a neutral composed of a positively charged ion and a negatively charged electron. The directions of plasma flow velocity, \mathbf{u} , of the magnetic field, \mathbf{B} , and of the electric field, \mathbf{E} , are indicated. In the image, following dissociation, the ion path starts upward and the electron path starts downward. Although initial motion is along \mathbf{E} for the ion, the Lorentz force causes the path to twist, resulting in motion around \mathbf{B} at the ion cyclotron period, leading to a net drift at a velocity of $\mathbf{E} \times \mathbf{B}/B^2$. The electron initially moves in the $-\mathbf{E}$ direction. Its motion also rotates around \mathbf{B} , but at the electron cyclotron frequency. The net effect is a transient current in the direction of \mathbf{E} . Right: Schematic of the effect of collisions with neutrals for a case with the collision frequency of order the ion cyclotron frequency. Triangles represent neutrals. The effect of collisions is to slow the motion in the $\mathbf{E} \times \mathbf{B}$ direction of the ions but not of the electrons [(which have other collision and gyrofrequencies)] and to displace the ions in the direction of \mathbf{E} . A net current arises, with one component along $-\mathbf{E} \times \mathbf{B}$ (a Hall current) and one component along \mathbf{E} (a Pedersen current). [Fig. IV:10.3]

there are collisions roughly at the same frequency as the gyrofrequency (different for particles of different masses), the situation changes fundamentally: collisions interrupt the gyromotion, and this results in a net separation of the charges. A graphic example, discussed in more detail below, is given in Fig. 2.11(right).

If collisions are very infrequent, or to be precise if the electrons or ions can gyrate about the magnetic field many times between collisions, the electrical conductivity across the magnetic field is very low. If collisions are very frequent for both ions and electrons, hardly any charge separation can occur between collisions, and the electrical conductivity perpendicular to the magnetic field is also very low. Peak perpendicular conductivity depends on the direction relative to the electric field and is reached depending on the ratios of collision and gyro-frequencies, as shown below.

Collisions between the populations of charged and neutral particles in the presence of a magnetic field while allowing for bulk flows is described through multiple equations. One of these captures the transfer of momentum that affects the force balance (touched upon towards the end of this section) almost entirely by looking at ions because they carry the bulk of the mass. Another accommodates electrical currents that arise from the differential behavior of the ions and electrons subject to the magnetic field. A third describes the energy transfer through the collisional effects formulated as Ohmic dissipation in the energy balance.

How collision frequencies influence currents in the ionosphere/thermosphere, where the neutral component is the most common, can be approximated as follows (collisions between charged particles are ignored here because collisions with the abundant neutrals

are far more common in the bulk of the terrestrial ionosphere). “If we take the magnetic field to be aligned with the z axis, then the generalized Ohm’s law [(the derivation of which is shown for a fully ionized plasma in Ch. 3)], $\mathbf{j} = \boldsymbol{\Sigma}_e \cdot \mathbf{E}_0$ (where \mathbf{E}_0 is the total electric field: $\mathbf{E}_0 = \mathbf{E} + \frac{1}{c}\mathbf{v} \times \mathbf{B}$), contains the conductivity tensor

$$\boldsymbol{\Sigma}_e = \begin{pmatrix} \sigma_P & \sigma_H & 0 \\ -\sigma_H & \sigma_P & 0 \\ 0 & 0 & \sigma_{\parallel} \end{pmatrix}, \quad (2.22)$$

where the Pedersen ($\perp \mathbf{B}, \parallel \mathbf{E}_{\perp}$), Hall ($\perp \mathbf{B}, \perp \mathbf{E}_{\perp}$), and parallel ($\parallel \mathbf{B}$) conductivities are given [by:

$$\sigma_P = \frac{n_e e c}{B} \left(\left[\frac{M_e}{1 + M_e^2} \right] + \left(\frac{e}{q_i} \right) \left[\frac{M_i}{1 + M_i^2} \right] \right); \quad (2.23)$$

$$\sigma_H = \frac{n_e e c}{B} \left(\left[\frac{M_e^2}{1 + M_e^2} \right] - \left(\frac{e}{q_i} \right) \left[\frac{M_i^2}{1 + M_i^2} \right] \right); \quad (2.24)$$

$$\sigma_{\parallel} = \frac{n_e e c}{B} \left(M_e + \left(\frac{e}{q_i} \right) M_i \right) \quad (2.25)$$

(where the equations from Sect. I:12.6 were rewritten to the above by using the expression for $\omega_{e,i}$ below). For characteristic values of these conductivities in the terrestrial ionosphere, see Figure I:12.5. Here, $M_{e,i} = \omega_{e,i}/\nu_{e,i}$ are the electron and ion magnetizations, with $\omega_{e,i} = |q_{e,i}|B/m_{e,i}c$ the electron and ion (with charge q_i) gyro-frequencies around the field of strength B , $m_{e,i}$ are the electron and ion masses, ν_{en} and ν_{in} the electron-neutral and ion-neutral collision frequencies.] The effect of the collisions is to rotate the net current from the direction of \mathbf{E} at high altitudes towards the negative $\mathbf{E} \times \mathbf{B}$ direction at low altitudes. In the terrestrial ionosphere, the] current and dissipation reach a peak at the altitude where the Pedersen and Hall conductivities are equal, around 125 km. For high-frequency currents, like those that may occur in the solar chromosphere, the dissipation may increase markedly (see Sect. I:12.8). Note that σ_P is generally dominated by the ion term.” {A22}

The collisional coupling between ions and neutrals causes momentum exchange (through the drag force that works to reduce the velocity difference between these two populations) and energy dissipation (in the form of Joule heating). “The electrodynamic properties can be conveniently separated into a high [magnetic] latitude region, where the current flow in the ionosphere is connected to the magnetospheric current system, and a mid and low latitude region, where the majority of the current flow and polarization electric fields are controlled internally by the thermosphere-ionosphere conductivity and dynamics.” “In the ionosphere, currents flowing perpendicular to the magnetic field are produced by electric fields and neutral winds. Although collisions between ions and the neutral gas are relatively infrequent [in Earth’s upper atmosphere] above ~ 160 km, they are sufficient to accelerate the neutral component, *i.e.*, the thermosphere, at high latitudes to many hundreds of m/s over periods of tens of minutes or more [to speeds well in excess of those associated with solar heating]. [...]

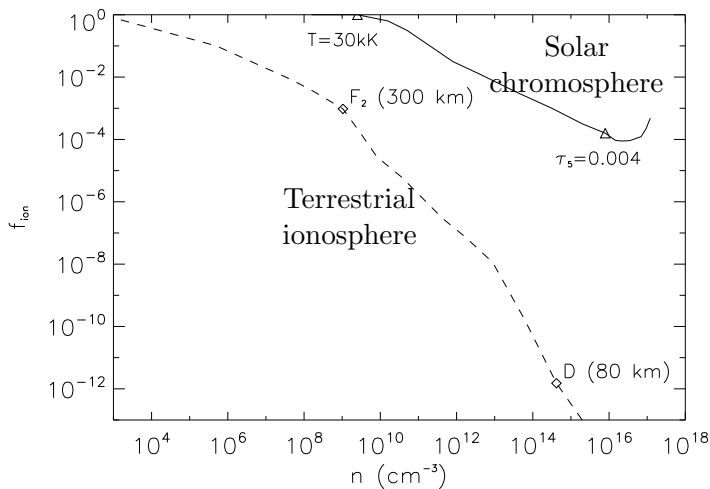


Figure 2.12: Comparison of densities, n (cm^{-3}), and ionization fractions, f_{ion} , for a characteristic dayside ionosphere (dashed) and mean chromosphere (solid). The diamonds mark the mean values for the ionospheric D and F_2 regions, centered on about 80 km and 300 km, respectively. The triangles denote the base of the chromosphere (defined here as at a continuum optical depth of $\tau_5 = 0.004$) and the top of the chromosphere (where the temperature exceeds 30 000 K). [Fig. I:12.13]

At low altitude, ~ 100 km, the ions are forced to move with the neutral gas, whether stationary or moving. The large-scale wind system at this altitude is driven by the tidal and planetary waves propagating from the lower-atmospheric terrestrial weather system, and the mass of the atmosphere is such that ion drag has little or no impact on the neutral dynamics. The altitude range between 100 and 160 km altitude is the narrow altitude range that is responsible for most of the dissipation of electromagnetic energy from the magnetosphere. The neutral dynamics and conductivity in this boundary region between space and atmospheric plasma are critical.” “At mid and low [magnetic] latitudes the electric fields [in Earth’s ionosphere] arise largely from internal dynamo processes driven by the conversion of neutral wind kinetic energy to electromagnetic energy, and are typically an order of magnitude smaller (a few mV/m) than high-latitude fields. The energy involved is also much smaller. The importance of the small electric fields at low latitudes is no longer the Joule heating and momentum dissipation, but rather their role in the redistribution of plasma.” Some of these effects are touched upon generically in Sect. 5.5.7, with a more comprehensive discussion for Earth’s ionosphere in Sect. I:12.6.

In much of the discussion of magnetized plasma in the Sun’s interior and atmosphere in subsequent chapters, the Hall and Pedersen conductivities are often assumed to be negligible. A similar approximation is often seen in the study of the heliosphere and

planetary magnetospheres. The Sun’s chromosphere, however, is an environment with a strong neutral population and with collision frequencies not so high that Pedersen and Hall conductivities are effectively ignorably small. The chromosphere is located immediately above the photosphere (which itself has a thickness of roughly a single scale height of about 100 km), and extends over a height range of some 2,500 km, spanning roughly a dozen pressure scale heights in a highly dynamic setting that is strongly patterned by the magnetic field, before the transition region is reached in which the temperature rapidly rises to coronal values.

“The Earth’s ionosphere has a range of degrees of ionization, starting from the essentially neutral troposphere below, reaching an ionization fraction of about 10^{-4} – 10^{-3} around 200 km in height, and exceeding a few percent by 1 000 km. In the case of the chromosphere, the ionization fraction starts at about 10^{-4} around photospheric heights, drops through 10^{-5} through the classical ‘temperature minimum’ around 500 km in height, and then increases through a few percent around 1 500 km in height, continuing to near-complete ionization in the solar corona. Figure 2.12 compares the densities and ionization fractions for mean states characteristic of the ionosphere and chromosphere. Note that the neutral densities in the D–F₂ ionospheric region are comparable to those in the chromosphere, but the ion densities are at least 1 000 times lower at any given neutral density, resulting in a much weaker ion-neutral coupling in the ionosphere than in the chromosphere.

Let us look back at Eqs. (2.23)-(2.25) and assess their meaning for both chromosphere and ionosphere. In the limit of a weak magnetic field or a high collision frequency, the ion and electron magnetizations $M_{e,i} = \omega_{e,i}/\nu_{e,i} \rightarrow 0$, $\sigma_P \rightarrow \sigma_{\parallel}$, $\sigma_H \rightarrow 0$; hence, currents are more readily aligned with the *electric* field, as expected. As the collision frequencies with the neutral population decrease, the above expressions would have current and *magnetic* field aligned (as both $\sigma_{P,H} \rightarrow 0$) [...]

In the chromosphere of a solar [sunspot] region, $M_e(500 < h < 2000 \text{ km}) = \mathcal{O}(100)$, decreasing rapidly towards the photosphere to $M_e(h = 0) = \mathcal{O}(0.01)$ at the solar surface. Some studies find the proton magnetization to remain below unity throughout the chromosphere, up to the transition into the corona (these findings depend on the atmospheric domain, of course, and on the models used [...]). Consequently, the bulk of the active-region chromosphere has an anisotropic conductivity of at least a factor of 10 difference between the field-aligned and transverse components. Conduction in the corona is almost exclusively field aligned (and thus essentially free of Lorentz forces), while photospheric conduction is nearly isotropic. [...]

Now, let us look at different environments, and illustrate not only currents but also the effects of momentum transfer. “At comets and in the vicinity of moons, such as Io and Enceladus, that are significant sources of neutral gas, various processes that convert neutral atoms or molecules into ions are important to consider. Neutrals can be ionized by photons (photoionization) or by collisions with other particles, typically electrons (impact ionization). An additional process that affects the interaction region is charge exchange in which a neutral gives up a charge to an ion. The original ion, now neutral, carries off its incident momentum while the original neutral becomes an

ion at rest in the frame of the neutral gas.

The ions introduced into the plasma by ionization of neutrals modify the bulk properties of the plasma. Consider a situation in which the neutrals are at rest relative to [a location] towards which the plasma flows at (bulk) velocity \mathbf{u} . Photoionization and impact ionization add mass to the plasma whereas charge exchange between the ionized or neutral form of the same element does not change the mass density. All three processes slow the bulk flow because the new ions must be accelerated so that their average motion matches that of the bulk plasma and the process extracts momentum from the incident plasma. These processes also change the thermal energy of the plasma and may modify the plasma composition. The complex effects associated with pickup can significantly modify the interaction region surrounding a moon or a comet.

The relation between pickup and currents is shown schematically in Fig. 2.11a. The newly ionized ion senses the electric field of the flowing plasma and begins to move in the direction of this electric field. The electron that has separated from the ion is initially accelerated in the opposite direction. After one gyroperiod, the average separation of the gyrocenters of the two charges is close to one ion gyroradius

$$r_{\text{gi}} = m_{\text{ion}} v_{\text{ion}} c / qB \quad (2.26)$$

where m_{ion} is the ion mass, v_{ion} is its thermal velocity, and q is its charge (see Sect. 8.2 for details on single-particle motions). {A24} The result of the separation of charges is to produce a transient current density in the direction of the electric field. If the pickup is occurring at a rate \dot{n} , where \dot{n} is the number of ionizations per unit volume and time, then the pickup current [density] is {A24}

$$\dot{j}_{\text{pickup}} = q \dot{n} r_{\text{gi}}. \quad (2.27)$$

Because pickup current flows across the background field, a cloud of pickup ions acts much like a solid conducting obstacle in the flow and imposes the same types of perturbations, *i.e.*, it slows and diverts the incident flow” in a way outlined in Ch. 5.

In this volume, we do not go into the behavior of dusty plasmas. The interested reader is referred to Ch. IV:11, which introduces the subject as follows: “The study of dusty plasmas bridges a number of traditionally separate subjects, for example, celestial mechanics, mechanics of granular materials, and plasma physics. Dust particles, typically micron and submicron sized solid objects, immersed in plasmas and UV radiation collect electrostatic charges and respond to electromagnetic forces in addition to all the other forces acting on uncharged grains. Simultaneously, dust can alter its plasma environment by acting as a possible sink and/or source of electrons and ions. Dust particles in plasmas are unusual charge carriers. They are many orders of magnitude heavier than any other plasma particles, and they can have many orders of magnitude larger (negative or positive) time-dependent charges. Dust particles can communicate non-electromagnetic effects, including gravity, neutral gas and plasma drag, and radiation pressure to the plasma electrons and ions. Their presence can influence the collective plasma behavior by altering the traditional plasma wave modes and by triggering new types of waves and instabilities. Dusty plasmas represent the

most general form of space, laboratory, and industrial plasmas. Interplanetary space, comets, planetary rings, asteroids, the Moon, and aerosols in the atmosphere, are all examples where electrons, ions, and dust particles coexist.” {A25}

[A25]

2.5 Sources of plasma

There are many sources of plasma around the heliosphere: all it takes is some neutral medium subjected to sufficient energy to ionize particles. The bulk source medium can be the largely neutral gas in the Sun’s surface layers, but dissipation of (magnetic) waves and currents, as well as the acceleration of particles in electric fields result in heating and ionization of the Sun’s outer atmosphere. The larger planets have neutral atmospheres of which the top layers are ionized by solar radiation and by suprathermal particle precipitation. Moons may be large enough to have their own atmosphere (as is the case for Titan at Saturn), while others may still have some matter around their surfaces because these are subjected to sputtering by the solar wind or, for moons within planetary magnetospheres, by magnetospheric particles, or matter may be supplied by geysers (as on Enceladus at Saturn) or volcanoes (as on Io at Jupiter) that contribute molecules (including SO_2 , SO , S_2 , H_2S , ...) as well as atoms. Comets have a coma of gas that sublimates off the nucleus, along with dust. And dusty material is around in the rings of all the giant planets. Whereas the magnetized and ionized components of the interstellar medium cannot penetrate each other (as discussed in Chs. 3 and 5), neutral interstellar-medium particles can make it deep into the heliosphere, following free-fall trajectories in the collisionless environment until they are subjected to a charge-exchange collision with solar-wind ions.

Chapter 3

MHD, field lines, and reconnection

Chapter topics:

- The fundamental difference between gravity and magnetism
- MHD as a low-order description of single-fluid plasma dynamics
- Alfvén, fast-mode, and slow-mode waves
- Processes and scales of reconnection

Key concepts:

- General, force-free, and potential magnetic fields
- Magnetic pressure and tension
- Magnetic structures: current sheets and flux tubes
- Reconnection: failure of ideal MHD and of frozen-in field lines

3.1 Introduction

“Absent the magnetic field, neither solar activity nor magnetic storms – the solar and terrestrial sources of [variable conditions referred to as space weather ^[7] – would exist. . . .] Although in principle fossil magnetic fields could have remained from the creation of the Solar System, this appears not to be the case. Witness the 22-year magnetic cycle of the Sun and the reversals of the Earth’s magnetic field. On shorter time scales, the magnetic topography of the solar surface changes so rapidly that it must be monitored constantly as input for space weather forecasts. {A26}

[The contrast between magnetic variability and gravitational persistence has its origin in the sources of the two fields: the magnetic field, \mathbf{B} , has its origin in a variable source, namely the relative motion of differently charged particles, while the gravitational field, \mathbf{g} , springs forth from a conserved (positive definite) source.] The {A26}

⁷For introductions to the impacts of space weather on society and its technological infrastructure we refer to Chs. II:2, II:12, and H-V:1-5.

conserved source of the gravitational field is mass, as can be seen in the [non-relativistic] field equations that apply to the gravitational field:

$$\nabla \cdot \mathbf{g} = -4\pi G\rho, \quad \nabla \times \mathbf{g} = \mathbf{0}, \quad (3.1)$$

where G is the gravitational constant and ρ is the mass density. Thus, gravity is determined by the amount of mass present and its distribution. Because mass is conserved and the gravitational force causes matter to collapse into systems in which the gravitational force is almost perfectly balanced by thermal pressure or inertial forces, gravitationally organized matter tends to be stable over eons [...] In contrast, the pertinent field equations for the magnetic field are

$$\nabla \cdot \mathbf{B} = 0, \quad \nabla \times \mathbf{B} = \frac{4\pi}{c} \mathbf{j} \quad (3.2)$$

[(the second expression holds if all velocities involved are well below light speed).] The source term for the magnetic field in these equations is electrical current, \mathbf{j} , which, unlike mass, is not a conserved quantity [(although $\nabla \cdot \mathbf{j} = 0$) and which can point in any direction]. Thus we see that \mathbf{B} is a product of dynamo or other magnetohydrodynamic (MHD) processes that generate current in real time. The crucial distinction is that unlike the gravitational field, which is in effect a byproduct of a conserved, definite quantity of mass and so is inherently persistent, the magnetic field is generated by a variety of plasma motions in the Sun, in the solar wind, and in planetary magnetospheres on time scales shorter than what would be needed to reach an equilibrated state. Hence, the local cosmos is constantly adjusting and attempting to relax, but it never gets to such a quasi-stationary state. The consequence of this is what we call weather, including [...] space weather.”

“There is an important difference regarding the types of volumes that the gravitational and magnetic tension forces organize. The gravitational field has no shielding currents ($\nabla \times \mathbf{g} = \mathbf{0}$) [because its source is the positive-definite mass density ($\nabla \cdot \mathbf{g} = -4\pi G\rho$); consequently, gravity] has no discontinuities because that would require an infinite mass density. Hence, the gravitational field is relatively homogeneous; it varies smoothly and continuously in space. On the other hand, [owing to the fact that electrical charges can be of either sign, a magnetic field can contain] shielding currents ($\nabla \times \mathbf{B} = \frac{4\pi}{c} \mathbf{j}$) which spontaneously form discontinuities,” that are commonly referred to as current sheets [(see Table 3.1 for a definition)] despite the fact that their geometry is generally quite complex in the local cosmos. The combination of the distinct behaviors of gravitational and magnetic forces yields a rich diversity of phenomena in the local cosmos and beyond that emerge from the ‘universal processes’ captured in the MHD description of magnetized plasma.

Among the universal concepts in heliophysics one pair stands out in particular, namely that of *magnetic lines of force* – or commonly *magnetic field lines* – and of their *reconnection*. {A27} Field lines are abstractions; they are 1-dimensional virtual devices that are used to outline the geometry of magnetic structures in the local cosmos, in a way in which the tangent of the field line anywhere along it has the

Table 3.1: *Structures in the magnetic field.*

Current sheet: *Examples on large scales: heliospheric current sheet; magnetospheric current sheet.* E.g., Fig. 5.4. [I:6.2] “Our focus here is mainly on current sheets in the form of tangential discontinuities or rotational discontinuities that evolve into tangential-like discontinuities. Tangential discontinuities are non-propagating surfaces across which no magnetic flux passes as the magnetic field changes direction or strength or both, while total (magnetic plus thermal) pressure is continuous. [...] current sheets (tangential discontinuities) inevitably form in naturally occurring turbulent plasmas; [...] they form in the corona through the expansion of magnetic flux tubes that poke out of the photosphere [and] expand until at some altitude they press against each other forming a beehive pattern of flux tubes separated by current sheets [unless and until the currents dissipate and the field becomes potential]. [...] Interplanetary space is a honeycomb of outwardly advecting current sheets. [...] In the magnetospheric case, the solar wind snags magnetic field lines from the planet’s two poles on the sunward side and stretches them anti-sunward to form the characteristic two-lobe magnetospheric tail across which the magnetosphere’s analog of the heliospheric current sheet separates the two lobes.”

Flux tube, flux rope: *Examples: compact sunspots, pores, ‘bright points’; as an entity, they are bounded by a current sheet.* E.g., Fig. 9.3(top) and 9.1. [I:6.4] “A flux tube is the volume enclosed by a set of field lines that intersect a simple closed curve. The frozen-in flux condition of ideal MHD describes a parcel of plasma threaded by magnetic field lines as a conserved entity whose motion can be followed.” In the solar photosphere, flux tubes may emerge as preformed entities, or may form from by ‘convective collapse’. A flux rope is a flux tube twisted about itself (and thus carrying an internal net current); many magnetic configurations emerge into the solar photosphere as flux ropes; many form in the corona by the dynamics of the reconnecting field; coronal mass ejections inject ropes into the heliosphere (there known as ‘magnetic clouds’) while others form by reconnection across current sheets; at magnetopauses, flux ropes (‘flux transfer events’) form by reconnection; and flux ropes (‘plasmoids’) form by reconnection across the magnetospheric current sheet.

Cell: *Examples: planetary magnetosphere; heliosphere.* E.g., Fig. 5.1. [I:6.7] “Magnetic fields tied to gravitating bodies will expand to fill all space unless prevented from doing so. [...] the magnetic field’s expansionist ambition is checked by some other magnetic field-bearing plasma expanding from somewhere else. Each magnetic field is therefore encased within a definable volume, which we refer to as a cell. In the Sun’s case, the cell is the heliosphere. In the other cases mentioned, the cells are planetary magnetospheres. [...] The cellular structure] is like a Russian nesting doll in which one cell is encased within another. [...] within the heliosphere, the scale sizes of the objects already mentioned cover seven orders of magnitude”

same direction as the field there while the local field line density is equivalent to the magnetic field strength.

In a vacuum, magnetic field lines have no intrinsic temporal continuity. For example, consider the field between and surrounding magnets or electrical wires at time t_0 and again at time t_1 after having moved the magnets or wires into new positions. The lines of force used to visualize the field at times t_0 and t_1 are completely independent, the result only of the magnetic fields at the two instances in combination with two sets of points, one for t_0 and one for t_1 , selected by a researcher from which to compute the lines of force. In a plasma, however, field lines can be thought of as structures

whose continuity in time derives from the ionized matter that is contained in the flux bundle or tube that is centered on the field line. In our thinking, we should map these ‘lines of force’ to their 3-dimensional equivalent, the ‘flux tube’: as long as the ions and electrons once contained never move out of the flux tube, the field line has some temporal continuity. Whenever matter does migrate out of the flux tube, the attribute of continuity for the field line fails. However, if the locations where this occurs are compact compared to the field line’s length, one can think of field lines – that can never end in the divergence-free magnetic field except close onto other field lines – as being cut and connected onto another field line. Where that happens, the concept of ‘magnetic reconnection’ is then introduced to salvage that of the ‘field line’ as something that has an identity over time, at least while matter remains constrained to within the flux tube.

Field lines and their reconnection are but two of the concepts related to a variety of processes that occur in ionized gases (‘plasmas’) that are threaded by magnetic field. We come across such processes in the vastly different environments of the solar interior and of the far reaches of the heliosphere, and in the depths of planets as well as in the most tenuous parts of their outer atmospheres. Temperatures and densities (and, as we shall discuss later in this chapter, magnetic field strengths) differ by many orders of magnitude; a summary of some of the conditions encountered in the local cosmos that surrounds us is visually represented in Figure 2.1.

In everyday life we tend to ignore the Earth’s magnetic field, but we can do so only because of the low temperatures in which we live (which renders most material, except metals, non-conducting) combined with the high densities; together, as we shall see in more detail later in this chapter, these conditions make the forces exerted by the terrestrial magnetic field utterly negligible in our day-to-day affairs, except where we take special care to uncover them, such as in magnetic compasses. Conditions are markedly different, however, in the layers underneath the atmosphere of the Sun, throughout the extended solar atmosphere, and in the outermost reaches of atmospheres of all bodies in the Solar System: there, magnetism is effectively coupled to matter while the inertia of that matter is in much of the domain significantly lower in comparison to magnetic forces than in our daily settings. There, the magnetic field is an important player that adds a significant force to compete with pressure, gravity, and inertia. It provides a medium for a variety of waves (which this text merely touches upon), and changes the transport of thermal energy and energetic particles. Add to that the fact that the magnetic field is evolving on a range of spatio-temporal scales, and you have a source of continual change in conditions throughout the local cosmos.

The mathematical formulation of what happens in a magnetized plasma is often simplified through an ensemble approximation that is equivalent to the hydrodynamics used in the description of gases, but here including the magnetic field in what is called magnetohydrodynamics, or MHD for short. MHD is a description of the multitude of constituent particles in the local cosmos that relies on statistical averaging carried out by the medium itself, namely through interactions that lead to essentially Maxwellian velocity distributions, often assumed to be isotropic (but in some formulations distinct

*Table 3.2: MHD approximation and the concept of 'closure'.***Philosophy of magnetohydrodynamics:**

The fundamental assumption underlying the MHD equations as shown in Table 3.3, and the principal criterion to judge the applicability of that MHD approximation under given circumstances, is that the medium can be suitably described as a continuum. This presents us with a statistical criterion: MHD can be applied beyond a fiducial length, say L , such that there are sufficient particles in a volume L^3 such that statistical means – like density, mean velocity, pressure and so forth – have small variances or fluctuations about them. Within that volume, collisions (or wave-particle interactions) result in average properties of the medium that transform the need to describe each particle separately in its interaction with all others into an enormously truncated set of descriptions of statistical averages. This truncation is known as 'closure': the continuum description requires a closure relation at some level that relates an unknown high-order moment of the full particle distribution function, such as pressure, to lower-order moments (see Sect. 8.4 for more on that). An equation of state, as in Eq. (3.8), is predicated on there being ample collisions to isotropize the random motions and achieve a thermodynamic equilibrium, with its characteristic Maxwellian velocity distribution (or more than one if a multi-fluid description is used). The MHD equations as in Table. 3.3 describe a 5-moment continuum closure scheme using mass density, temperature, pressure, energy density, and velocity. As collisions become less frequent one is required to enforce closure at higher levels, examples of which lead to, *e.g.*, Eqs. (3.11) and (3.27). More generally dielectric and magnetization properties of the material enter in the definitions of D and H . Therefore, if by some other means (*e.g.*, by observation) you know how to close the moments (like in Sect. 2.2 for the solar wind by using the observationally motivated approximation that the temperature is constant throughout the heliosphere and the pressure is an isotropic scalar) then you can use the continuum fluid description to answer some questions even about a medium where collisions are a rare thing.

for directions along and perpendicular to the magnetic field) and for velocity equilibrium between electrons and ions. To this, a few other assumptions are made about local conditions: processes described by MHD assume that ion and electron interactions as well as their gyrations about the field occur on scales that are small compared to the gradients in the magnetic field while at the same time large compared to a distance (known as the Debye length) over which electrical charges can exist unshielded by other particles, with velocities well below relativistic, and only allowing for wave-like phenomena that are slow enough that electrical neutrality is achieved well within any time scale of interest and that are slow compared to the plasma frequency and electron/ion gyro-frequencies. However, interactions between particles should be infrequent enough that the medium should allow the electron and ion populations to move differentially with relative ease, *i.e.*, conditions should allow the medium to conduct electrical currents rather effectively.

MHD treats the ionized medium as a fluid by working with ensemble properties. In hydrodynamics this is generally allowed because of a high frequency of molecular collisions relative to the time scales of the processes on macroscopic scales. In many environments in heliophysics, however, collisions can be so rare that distances between collisions can be comparable to the scale of the system under consideration, while the solar wind is entirely collisionless beyond a few dozen radii from the Sun . . . and yet MHD has been shown to be a useful approximation. The key factor in making MHD useful is that the medium should not be able to maintain a significant electric field in its own reference frame. Even if collisions are rare in such a medium, long-range flights of the particles are impeded: the gyration of particles about the magnetic field reduces the scale of flight perpendicular to the field, while wave-particle interactions have a similar effect along the field. Consequently, the movement of individual charged particles in a plasma is coupled to the collective of its environment, resulting in a fluid-like behavior even if collisions are rare.

However, where binary interactions are important in the MHD description, the anisotropy imposed by the magnetic field does affect what approximations can be made. Most importantly, these effects are seen on gas pressure and viscosity. In a collisional plasma, these terms are generally essentially isotropic and thus described by scalars. But in a collisionless plasma, pressure and viscosity are anisotropic, and thus are approximated by tensors. In this volume, we generally use a scalar for pressure, and capture anisotropy in conductivity in Hall and Pedersen terms (see below and Ch. 2).

3.2 (Magneto-)Hydrodynamics

The equations of magnetohydrodynamics, or MHD, are based on the assumption that the plasma can be described as a continuum; see Table 3.2 for a very concise description of what that entails. The approximations used here lead to six equations that describe magnetized plasma subject to gravity, as shown in Table 3.3 (note that processes involving radiative transfer are largely omitted from this volume). {A28}

Five of these are essentially equations of hydrodynamics, namely continuity, momentum, energy, gravity, and the equation of state (EOS), with two important modifications: the magnetic, or Lorentz, force $(1/c)\mathbf{j} \times \mathbf{B}$ (6) is added in the momentum description, and there are additional terms (10) in the energy equation. We return to these terms and equations below, and discuss the additional equation, namely the induction equation Eq. (3.3), which couples the magnetic field to macroscopic flows and microscopic collisions, in some detail in Section 3.2.2. {A29}

In order to assess the validity of the assumption made to derive the MHD equations for the vastly different conditions with which heliophysics concerns itself we can look at a variety of dimensional and dimensionless numbers. Table 18.2 lists frequently used length and time scales, as well as some commonly used ratios, some of which have been given a name. Some of these are pertinent to microscopic, particle-level conditions and some are pertinent to macroscopic, system-level conditions. We introduce them here only briefly – most will be looked at explicitly later on – in order to give you an

Table 3.3: *Equations of magnetohydrodynamics for a fully-ionized plasma, ignoring radiative energy transport and radiation pressure, to be complemented by initial and boundary conditions to specify the solution.*

Single-fluid non-relativistic magnetohydrodynamics (MHD):

$$\text{Induction} \quad \frac{\partial \mathbf{B}}{\partial t} = \nabla \times (\mathbf{v} \times \mathbf{B}) - \nabla \times (\eta \nabla \times \mathbf{B}) \quad (3.3)$$

$$\text{Continuity} \quad \frac{\partial \rho}{\partial t} + (\mathbf{v} \cdot \nabla) \rho = -\rho \nabla \cdot \mathbf{v} + (S - L) \quad (3.4)$$

$$\begin{aligned} \text{Momentum} \quad \rho \frac{\partial \mathbf{v}}{\partial t} + \rho (\mathbf{v} \cdot \nabla) \mathbf{v} = & + \rho \mathbf{g} - \nabla p + \frac{1}{4\pi} (\nabla \times \mathbf{B}) \times \mathbf{B} \\ & + \nabla \cdot \boldsymbol{\tau} - \mathbf{v} (S - L) + (\mathbf{S}_p - \mathbf{L}_p) \end{aligned} \quad (3.5)$$

$$\text{Internal energy} \quad \rho \frac{\partial e}{\partial t} + \rho (\mathbf{v} \cdot \nabla) e = -p \nabla \cdot \mathbf{v} + \nabla \cdot (\kappa \nabla T) + (Q_\nu + Q_\eta) \quad (3.6)$$

$$\text{Gravity} \quad \nabla \cdot \mathbf{g} = \nabla^2 \Phi = -4\pi G \rho \quad (3.7)$$

$$\text{EOS} \quad p = (\gamma - 1) \rho e \quad (3.8)$$

Complemented by initial and boundary conditions

Online resources:

Plasma physics: [online NRL Plasma Formulary](#)

Vector calculus: [Wikipedia page](#)

Introduction to MHD [‘Essential magnetohydrodynamics for astrophysics’](#)
([Spruit, 2013](#))

Symbols: \mathbf{B} magnetic field; \mathbf{v} fluid velocity; $e = C_V T$ specific internal energy (e.g., energy per unit mass; $\frac{3}{2}kT/\mu$ for an ideal gas with μ the average mass per particle); p gas pressure; ρ mass density; Φ the gravitational potential and G Newton’s gravitational constant; \mathbf{g} gravity, $\tau_{ik} = 2\rho\nu (\Lambda_{ik} - \frac{1}{3}\delta_{ik}\nabla \cdot \mathbf{v})$ the viscous stress tensor with the deformation tensor $\Lambda_{ik} = \frac{1}{2} (\frac{\partial v_i}{\partial x_k} + \frac{\partial v_k}{\partial x_i})$; Q_ν viscous heating; and $Q_\eta = \eta |\mathbf{j}|^2 = \eta (c/4\pi)^2 |\nabla \times \mathbf{B}|^2$ the resistive (Ohmic) dissipation; ν , η_e and κ represent the viscosity, magnetic diffusivity, and the thermal conductivity tensor (which is highly anisotropic, with heat most effectively conducted by electrons moving along the magnetic field); $\gamma = C_p/C_V$ is the adiabatic index, the ratio of specific heats for constant pressure and constant volume. In an ideal, mono-atomic gas with 3 degrees of freedom $\gamma = 5/3$. S , L , \mathbf{S}_p and \mathbf{L}_p are source and loss terms for mass and momentum by introduction or loss of ions from a non-ionized reservoir.

impression of which types of processes or relative scales are important. For example, we can look at the length scale on which ions gyrate around the local magnetic field relative to the gradients in the field to assess whether the ions sense the magnetic field

in an ensemble sense such as required of a fluid or whether higher-order descriptions are needed. Or one can ask whether length scales involved are large enough that the plasma can be viewed as not having significant charge separation; the length scale on which electrostatic potential of any particle is effectively shielded by the surrounding plasma is known as the Debye length. Or one can look at the ratio of the average time between collisions and the time needed to complete one gyration around the magnetic field in order to assess whether the magnetic field can effectively be followed by the charged particles and whether the Hall current needs to be considered.

3.2.1 MHD equations, individual terms, and special cases

First, let us briefly review what the MHD equations express, the role of the individual terms, and some special cases:

- \mathbf{v} , p : The velocity \mathbf{v} reflects the mass-weighted bulk velocity (the first-order moment of the velocity distribution) of the electron-ion plasma. For a fully-ionized hydrogen plasma this equals $(m_i \mathbf{v}_i + m_e \mathbf{v}_e)/(m_i + m_e)$, which can be taken as the velocity of the center of mass of the ion-electron pairs that comprise the 'particles' of a 'single-fluid plasma.' The pressure p is the sum of the pressures of the electron and ion populations.

- Eq. (3.3): The induction equation (a combination of Faraday's law with Ohm's law, see Sect. 3.2.2) states that any local change in the magnetic field is associated with a 'curl', or 'circulation', in the component of plasma flows working perpendicular to the magnetic field and/or to the slippage of plasma relative to the magnetic field through finite diffusivity. Note that this form of the induction equation is linear in \mathbf{B} so that if $\mathbf{B}(t = 0) = \mathbf{0}$ then no field can arise at a later time. Sect. 3.2.2 touches on the fact that some terms were ignored to arrive at this form, some of which can act as a source term for magnetic field; this is not further discussed in this volume as the clouds out of which stars and planetary systems form initially are threaded by a galactic seed field from the outset (interested readers could look for 'battery effects', including the 'Biermann battery').

- Eq. (3.4): Continuity requires that the local plasma density changes only because of flow through a volume and by compression or dilation in doing so, unless there are sources or sinks within the volume.

- Eq. (3.5): The momentum (or force) equation (Newton's second law in volumetric form) summarizes how the plasma velocity is affected, as in hydrodynamics, by gravity, pressure gradients, and viscosity, but here also by the Lorentz force associated with currents flowing across the magnetic field.

- Eq. (3.6): The local energy density (here shown in a per-mass formulation of the first law of thermodynamics) is affected by flows, including compression or dilation, thermal conduction, and by viscous and resistive heating.

- Eq. (3.7): As mass is a positive definite quantity, it can only strengthen gravity, which can be represented by the gradient of a potential.
- Eq. (3.8): The equation of state couples pressure, density, and internal energy.
- Eqs. (3.3, 3.5): The induction and momentum equations are derived from the (mass-weighted) difference (see Sect. 3.2.2) and the sum of the equations of motions for the electrons and for the ions, each of which includes a term for their collisional coupling.
- ①: In case the term ② is negligible, Eq. (3.3) describes what is known as ‘ideal MHD’. In this case (see Sect. 3.4) the plasma and magnetic field must move with each other for velocity components perpendicular to the magnetic field, whereas plasma movement along the field is not affected by that field. In this condition, the field is said to be ‘frozen in’ the plasma. In such a state, the lines of force (‘field lines’) are advected with the flow while unable to break their connectivity between any plasma elements along their length; in non-ideal, or resistive, MHD such connections can be broken through a process known as ‘reconnection’. The concepts of field lines and reconnection are described in Section 3.4. {A30}
- ②: This term quantifies the effects of resistivity on the magnetic field by the dissipation and diffusion of the electrical current $\mathbf{j} = \frac{c}{4\pi} \nabla \times \mathbf{B}$. If the magnetic diffusivity η is constant throughout the medium, then term ② can be rewritten as $\eta \nabla \times (\nabla \times \mathbf{B}) = -\eta \nabla^2 \mathbf{B}$ (because $\nabla \cdot \mathbf{B} = \mathbf{0}$), which shows that it causes the magnetic field to decay diffusively; in the absence of ①, such as in a stationary plasma, this makes Eq. (3.3) a diffusion equation for decaying magnetic field. {A30}
- ③: For an incompressible fluid, ρ is constant as material flows throughout the volume under study, which consequently means that $\nabla \cdot \mathbf{v} = \mathbf{0}$, *i.e.*, that the velocity field is divergence free, and – unless there are terms like ④ to consider – Eq. (3.4) vanishes from the set. That also removes term ⑧ from Eq. (3.6), so that the energy density of the medium can only change by thermal conduction ⑨ and by viscous and resistive dissipation ⑩ (disregarding here, as we do throughout this chapter, the effects of radiation). {A31}
- ⑤: As formulated here, the isotropic part of the pressure tensor is expressed as a scalar, while the other terms are captured in the stress tensor. If only this scalar term is carried, then particle microscopic velocity distributions are taken to be isotropic. {A31}
- ⑥: Term ⑥ measures the interaction of the Lorentz force and the plasma flow. The vector product $(\nabla \times \mathbf{B}) \times \mathbf{B}$ can be reformulated (see Eq. 3.23) into the sum of a pressure-like term (that works to expand unless countered) and a

term that is equivalent to a tension (which works to straighten unless countered), showing that the magnetic field in a plasma behaves as if it were both like a gas and like a flexing rod or taut string. There is a special class of magnetic fields in which currents run parallel to the magnetic field; in that case $(\nabla \times \mathbf{B}) \times \mathbf{B} = \mathbf{0}$, *i.e.*, there is no Lorentz force, and these are consequently referred to as ‘force-free fields’, of which the potential field is a special (and lowest-energy) state. As the field is parallel to the current, there is a scalar field α such that $\nabla \times \mathbf{B} = \alpha \mathbf{B}$. If α is a uniform constant, this field is called ‘linear force free’ (which is mathematically easier to work with, but does not develop in general astrophysical settings); if not, the corresponding field is a ‘non-linear force-free’ field (to which we return in Sect. 6.3).

- (9): As for term (2) with uniform magnetic diffusivity η , here a uniform thermal conductivity κ would allow rewriting of term (9) to be proportional to $\nabla^2 T$, quantifying diffusion of thermal energy.
- (a), (b), (c): These terms reflect source and loss terms for mass and momentum density per unit volume through, *e.g.*, (de-)ionization of neutrals (including charge exchange) that are important, for example, where comets add gas and dust or around geysers on low-gravity moons (Sec. 2.4), or to the inflow of neutral matter into the solar wind from outside the heliosphere.

A few special cases:

- $\mathbf{B} = \mathbf{0}$: A field-free state (or a non-conducting, and thus current-free, gas in which the field does not apply force to the gas; see also under ‘Potential’ below) transforms Eqs. (3.3)–(3.8) into regular hydrodynamic equations.
- $\mathbf{v} = \mathbf{0}$: A static plasma is described by Eqs. (3.3)–(3.8) without terms (1), (3), (7), (8), and Q_ν in (10). Moreover, with no flows, no change can occur that involves bulk flows, so that, for example, the left-hand side of the momentum Eq. (3.5) has to equal $\mathbf{0}$. This yields an equation for magnetohydrostatic balance in which gravity, pressure gradient, and Lorentz force sum to zero.
- $\frac{\partial}{\partial t} = \mathbf{0}$: Stationary situation in which none of the variables can change. In particular, $\frac{\partial \mathbf{v}}{\partial t} = \mathbf{0}$ is a situation with stationary flows, which can be maintained only for limited times.
- Potential: In the case of a potential field, there are no currents in the system, *i.e.*, $\nabla \times \mathbf{B} = \mathbf{0}$. Consequently, term (6) vanishes because there is no Lorentz force. Term (2) also vanishes, leaving only term (1) in the righthand side of induction Eq. (3.3) (equivalent to the infinitely conducting case of ideal MHD with frozen-in field, or in which the field is maintained from outside of a current-free volume). To see to full consequence of this state, however, we need to realize that $\nabla \times \mathbf{B} = \mathbf{0}$ means that there is a magnetic potential Φ_m such that $\mathbf{B} = -\nabla \Phi_m$ from $\nabla^2 \Phi_m = 0$. Such a Laplace equation, once the boundary

condition is specified, has a unique solution. And for a current-free system with fixed boundary conditions that, in turn, means that \mathbf{B} cannot change in time, such that term (1) then implies that there is a scalar field Ψ such that $\mathbf{v} \times \mathbf{B} = \nabla\Psi$, of which one particular case has $\mathbf{v} \parallel \mathbf{B}$.

- Force free: See at (6) above in this listing.

3.2.2 The induction equation

“The induction equation, Eq. (3.3), arises from Ohm’s law combined with the non-relativistic approximation of the Maxwell equations. In its most general form Ohm’s law is a relation between electric current, electric field, magnetic field, plasma motions and electron pressure gradients. Ohm’s law is derived from an equation of motion for electrons in which the interaction with ions (defining the bulk motion of the plasma with velocity \mathbf{v} [because the ions, here taken to be dominated by singly-ionized species, by far outweigh the electrons]) is described through a collisional drag term related to the differential motion:

$$n_e m_e \frac{d\mathbf{v}_e}{dt} = -n_e e(\mathbf{E} + \frac{1}{c}\mathbf{v}_e \times \mathbf{B}) - \nabla p_e + n_e m_e \frac{\mathbf{v} - \mathbf{v}_e}{\tau_{ei}}. \quad (3.9)$$

Here \mathbf{v}_e denotes the electron velocity, τ_{ei} the collision time between electrons and ions, e the electron charge, m_e the electron mass, n_e the electron density, and p_e the electron pressure” (omitting gravity). \mathbf{E} and \mathbf{B} are the electric and magnetic vector fields.

By noting that the differential velocity between ions and electrons is proportional to the current,

$$\mathbf{j} = n_e e(\mathbf{v} - \mathbf{v}_e) \quad (3.10)$$

we can reformulate Eq. (3.9), when combined with the analogous version for the ions, to yield a formulation of Ohm’s law (here ignoring electron inertia and assuming pressure to be a scalar, *i.e.*, isotropic; compare with Section 3.4):

$$\mathbf{j} = \frac{\tau_{ei} n_e e^2}{m_e} (\mathbf{E} + \frac{1}{c}\mathbf{v} \times \mathbf{B}) - \frac{\tau_{ei} e}{m_e c} \mathbf{j} \times \mathbf{B} + \frac{\tau_{ei} e}{m_e} \nabla p_e. \quad (3.11)$$

{A32} Note that when the electric field expressed through the electron pressure gradient is ignored, this equation can be rewritten to an equivalent Ohm’s law discussed for the ionosphere in Ch. 2 that has a conductivity tensor with components as in Eqs. (2.23)-(2.25), from which terms with M_i disappear for the fully-ionized plasma because there are only ion-electron collisions, and in which the electron magnetization subject to collisions with neutrals, M_e , is replaced by $M_{ei} = eB/(mc\nu_{ei})$ for $\nu_{ei} = 1/\tau_{ei}$. In other words, the Hall term in Eq. (3.11) takes care of the anisotropic part of the conductivity in the fully ionized plasma. The Pedersen current, directed along \mathbf{E} is part of the first term on the right-hand side. {A33}

Specifically, “the second term on the right-hand side describes the Hall current, which becomes important if the collision time is longer than the electron gyration time, *i.e.*, when $\tau_{ei}\omega_L > 1$, where $\omega_L = eB/m_e$ denotes the Larmor {A33} I:3.2

(or [electron] gyro-)frequency. The Hall term leads to anisotropic plasma conductivity with respect to the magnetic field direction and is typically important in low-density plasmas in which τ_{ei} can be very large”. In many settings in heliophysics, the last two terms in Eq. (3.11) are ignored “(unless high-frequency plasma oscillations are considered), leading to the simplified Ohm’s law

$$\mathbf{j} = \sigma_e(\mathbf{E} + \frac{1}{c}\mathbf{v} \times \mathbf{B}) \quad (3.12)$$

with the plasma conductivity

$$\sigma_e = \frac{\tau_{ei}n_e e^2}{m_e}. \quad (3.13)$$

Using Ampère’s law, $\nabla \times \mathbf{B} = \frac{4\pi}{c}\mathbf{j}$, yields for the electric field in the laboratory frame

$$\mathbf{E} = -\frac{1}{c}\mathbf{v} \times \mathbf{B} + \frac{c}{4\pi\sigma_e}\nabla \times \mathbf{B} \quad (3.14)$$

leading to the induction equation through one of the Maxwell equations:

$$\frac{\partial \mathbf{B}}{\partial t} = -c\nabla \times \mathbf{E} = \nabla \times (\mathbf{v} \times \mathbf{B} - \eta \nabla \times \mathbf{B}) \quad (3.15)$$

with the magnetic diffusivity

$$\eta = \frac{c^2}{4\pi\sigma_e}. \quad (3.16)$$

In MHD, the equations are typically expressed in terms of the magnetic field \mathbf{B} and flows \mathbf{v} , with electric fields and currents eliminated from the system. This is done primarily out of mathematical convenience, since formulating the problem in terms of currents leads to intractable equations involving integrals of the currents over the entire volume under study.”

Whether a formulation in terms of the magnetic field or electrical currents is more convenient also depends on the inhomogeneity and anisotropy of the conductivity. The most extreme example is electrical engineering where cables give full control over the current, and thus a current-based description is clearly the method of choice. A formulation in terms of currents can be easier to work with also when currents can only flow along the field or are restricted to relatively thin layers with high conductivity, such as is the case in the ionosphere. In most MHD problems with highly conducting fluids, however, there is no *a priori* control over where currents flow, so that dealing with the magnetic field is typically the better choice. Because of this, solar and heliospheric physicists generally use arguments primarily based on the magnetic field; in space physics, however, and in particular in ionospheric physics, currents are often discussed.

Of interest to the induction equation Eq. (3.3) is the relative importance of the advection and diffusion-like terms on the right-hand side. One way to assess that is to reformulate it into characteristic scales and a frequently occurring dimensionless number: “Let L_t be a typical length-scale and v_t a characteristic velocity of the problem. Expressing the time in units of L_t/v_t and the spatial derivatives in the

induction equation Eq. (3.3) in units of L_t leads to the dimensionless form of the induction equation

$$\frac{\partial \mathbf{B}}{\partial t} = \nabla \times \left(\mathbf{v} \times \mathbf{B} - \frac{1}{\mathcal{R}_m} \nabla \times \mathbf{B} \right) \quad (3.17)$$

with the magnetic Reynolds number

$$\mathcal{R}_m \equiv \frac{v_t L_t}{\eta}. \quad (3.18)$$

The limit $\mathcal{R}_m \ll 1$ is referred to as diffusion dominated regime, in which the (dimensional) induction equation reduces to a diffusion equation of the form

$$\frac{\partial \mathbf{B}}{\partial t} = \eta \nabla^2 \mathbf{B}. \quad (3.19)$$

Here we made the additional simplifying assumption of a constant magnetic diffusivity η . Assuming that the magnetic field has a typical length scale L_t , we can estimate [its decay time scale:]

$$\tau_d \sim \frac{L_t^2}{\eta}. \quad (3.20)$$

The limit $\mathcal{R}_m \gg 1$ is referred to as the advection-dominated regime, in which the induction equation reduces to the equation of ideal MHD (except for possible boundary layers where diffusivity could be still important)

$$\frac{\partial \mathbf{B}}{\partial t} = \nabla \times (\mathbf{v} \times \mathbf{B}). \quad (3.21)$$

Expanding the expression of the right-hand side of this ideal induction equation leads to

$$\frac{\partial \mathbf{B}}{\partial t} = -(\mathbf{v} \cdot \nabla) \mathbf{B} + (\mathbf{B} \cdot \nabla) \mathbf{v} - \mathbf{B} (\nabla \cdot \mathbf{v}). \quad (3.22)$$

While the first term on the right-hand side describes the advection of magnetic field, the last two terms describe the amplification by shear (second term) and compression (third term)."

Of interest to the momentum equation Eq (3.5) is that a vector identity allows us to reformulate the Lorentz force "to equal:

$$\frac{1}{4\pi} (\nabla \times \mathbf{B}) \times \mathbf{B} = -\nabla \frac{B^2}{8\pi} + \frac{1}{4\pi} (\mathbf{B} \cdot \nabla) \mathbf{B}, \quad (3.23)$$

which shows that the Lorentz force is a sum of an isotropic pressure-like force and a tension force related to the curvature of the field" (note that both of these are insensitive to a reversal of the direction of the magnetic field). Because the pressure and tension terms, as does therefore the full Lorentz force, scale as $\mathcal{O}(B_t^2/L_t)$ (where the subscript 't' denotes a typical value of the quantity) they can be compared in magnitude to the pressure gradient force $\mathcal{O}(p_t/L_t)$; the ratio of magnetic and gas pressure terms in Eq. (3.5) yields an often-used dimensionless number in heliophysics, the plasma β : {A34} {A35}

$$\beta \equiv \frac{8\pi p}{B^2}. \quad (3.24)$$

I:3.2

{A34} {A35}

3.3 Waves in magnetized plasmas

Before we proceed with a discussion of field lines and reconnection, we look into an important aspect of a magnetized plasma, namely how it carries waves. Waves are important, among other things, in communicating information about changes in the field's structure or in boundary conditions or the effects of obstacles embedded in flows, while moreover they transport energy. “The waves that carry information through a magnetized plasma differ from the sound waves of a neutral gas, partly because of the anisotropy imposed on the fluid by a magnetic field and partly because the waves must be capable of carrying currents that modify the properties of both matter and magnetic field. The properties of such waves can be derived from the MHD [equations] by analyzing the evolution of small perturbations.

Consider a uniform plasma with constant pressure and density (p and ρ) whose center of mass is at rest ($\mathbf{v} = 0$). Assume that a constant background field (\mathbf{B}) is present and that neither sources nor losses need be considered. Small departures from this background state are taken to vary with space (\mathbf{x}) and time (t) as $e^{i(\mathbf{k}\cdot\mathbf{x}-\omega t)}$. Here, \mathbf{k} is the wave vector and ω is the angular frequency of the wave. Perturbations occur in density $d\rho$, velocity $d\mathbf{v}$, pressure dp , current \mathbf{j} , and field \mathbf{b} . Terms linear in small quantities in Eqs. (3.4) and 3.5) satisfy

$$-\omega d\rho + \rho \mathbf{k} \cdot d\mathbf{v} = 0 \quad (3.25)$$

$$-\omega \rho d\mathbf{v} = -\mathbf{k} dp + \frac{1}{4\pi} \mathbf{b}(\mathbf{k} \cdot \mathbf{B}) - \frac{1}{4\pi} \mathbf{k}(\mathbf{b} \cdot \mathbf{B}). \quad (3.26)$$

[If we assume an isentropic (*i.e.*, adiabatic and reversible) process, then Eq. 3.8 becomes $p\rho^{-5/3} = \text{constant}$, so that] the pressure perturbation in terms of the density perturbation is

$$dp/p = \gamma d\rho/\rho \quad (3.27)$$

and [the ideal induction equation Eq. (3.3 (with $\eta \equiv 0$))]

$$\omega \mathbf{b} = d\mathbf{v}(\mathbf{k} \cdot \mathbf{B}) - \mathbf{B}(\mathbf{k} \cdot d\mathbf{v}). \quad (3.28)$$

The solutions to Eqs. (3.25) to (3.28) are the roots of the equation

$$(\omega^2 - v_A^2 k^2 \cos^2 \theta)[\omega^4 - \omega^2 k^2 (c_s^2 + v_A^2) + k^4 v_A^2 c_s^2 \cos^2 \theta] = 0, \quad (3.29)$$

where θ is the angle between \mathbf{k} and \mathbf{B} , and the Alfvén speed (v_A) and the sound speed (c_s) have been introduced. These quantities characterize the speed of propagation of waves in a magnetized plasma and are defined by

$$v_A^2 = B^2/4\pi\rho, \quad (3.30)$$

$$c_s^2 = \gamma p/\rho. \quad (3.31)$$

The sound speed has the form familiar for a neutral gas. The Alfvén speed is a second natural wave speed characteristic of a magnetized plasma. Just as [one can work with

the dimensionless] sonic Mach number as the ratio of the flow speed to the sound speed, it is useful to define a dimensionless Mach number, the Alfvénic Mach number

$$M_A = v/v_A, \quad (3.32)$$

related to the Alfvén speed.

As mentioned [at Eq. (3.23)], the quantity $B^2/8\pi$ is the pressure exerted by the magnetic field, so both of the basic wave speeds are proportional to the square root of a pressure divided by a density. [... When $\beta = 8\pi p/B^2 \ll 1$,] magnetic effects dominate the effects of the thermal plasma, but in a high- β plasma, the plasma effects dominate.

Equation (3.29) is of sixth order in ω/k with three pairs of roots. One pair results from setting the first factor in Eq. (3.29) to zero; the resulting dispersion relation is

$$(\omega^2 - v_A^2 k^2 \cos^2 \theta) = 0. \quad (3.33)$$

This solution describes waves referred to as Alfvén waves. For this dispersion relation to apply, the magnetic perturbation must be perpendicular to both \mathbf{B} and \mathbf{k} (see Fig. IV:10.1a). This orientation implies that to first order in small quantities, the Alfvén wave does not change the field magnitude [$(\mathbf{B} + \mathbf{b})^2 = B^2 + 2(\mathbf{B} \cdot \mathbf{b})^2 + b^2 \approx B^2$]. The wave phase speed is $v_{\text{ph}} = \omega/k$ and $v_{\text{ph}} = \pm v_A \cos \theta$. [Wave packets] carry information at the group velocity, $\mathbf{v}_g = \nabla_{\mathbf{k}} \omega$, where the subscript on the gradient indicates that the derivatives are taken in \mathbf{k} space; the solution is $v_g = \pm \hat{\mathbf{B}} v_A$ where $\hat{\mathbf{B}}$ is a unit vector along the background field. The remarkable property of these waves is that they carry information only along the background field, and they bend the field without changing its magnitude. These properties are of considerable importance in interpreting the interaction of a flowing plasma with the solid bodies of the Solar System [(discussed in Ch. 5)].

Eq. (3.29) has two more pairs of roots, the zeroes of the fourth order polynomial in square brackets in Eq. (3.29), *i.e.*, the solutions

$$v_{\text{ph}}^2 = \omega^2/k^2 = \frac{1}{2} \left(c_s^2 + v_A^2 \pm [(c_s^2 + v_A^2)^2 - 4v_A^2 c_s^2 \cos^2 \theta]^{1/2} \right). \quad (3.34)$$

The solutions (two pairs, one positive and one negative, of roots) correspond to what are unimaginatively referred to as fast-mode (or magnetosonic) and slow-mode waves. The wave perturbations of both modes may have magnetic perturbations along and across \mathbf{B} (see Fig. IV:10.1b). Perturbations along \mathbf{B} change the field magnitude and the thermal pressure. The fast mode changes of thermal and magnetic pressure are in phase with each other; this implies that the total pressure fluctuates. The slow mode changes of thermal and magnetic pressure are in antiphase, and the total pressure fluctuations are very small. For waves propagating along the background field ($\cos \theta = \pm 1$), the solutions to Eq. (3.34) are c_s^2 and v_A^2 , with the larger of the two applying to the fast mode. For waves propagating at right angles to the background field ($\cos \theta = 0$), the [solutions] are $c_s^2 + v_A^2$ and 0, indicating that only fast-mode waves propagate across the field.”

{A36}

3.4 MHD, magnetic field lines and reconnection

“One of the most idiosyncratic aspects of space physics is the central role assigned to magnetic field lines. Particularly in studies of the Sun, the heliosphere and the magnetosphere, magnetic field lines are treated as full-fledged physical objects with their own dynamics. The electrical current, when needed, is derived *from* the magnetic field lines. These practices appear at odds to the basic approach, followed in elementary electrodynamics, of deriving the magnetic field *from* a current distribution and treating magnetic field lines at best as fictitious curiosities. However, physical laws such as Ampère’s law (without displacement current [because velocities are assumed to be well below relativistic]),

$$\nabla \times \mathbf{B} = \frac{4\pi}{c} \mathbf{j}, \quad (3.35)$$

do not attribute a causative nature to either side of the equality; they simply state the equality of two quantities. So either approach to satisfying Eq. (3.35), beginning with either \mathbf{j} or \mathbf{B} , is a valid one.

[The central role of \mathbf{B} in space physics has been furthered tremendously by the introduction of the concept of the field line.] A magnetic field line, sometimes called a line of force, is a space-curve $\mathbf{r}(\ell)$ which is everywhere tangent to the local magnetic field vector, $\mathbf{B}(\mathbf{x})$. This description can be cast as the differential equation

$$\frac{d\mathbf{r}}{d\ell} = \frac{\mathbf{B}[\mathbf{r}(\ell)]}{|\mathbf{B}[\mathbf{r}(\ell)]|}, \quad (3.36)$$

whose solution, starting from some initial point $\mathbf{r}(0)$, is a magnetic field line. [...] A field line is a curve, and therefore has zero volume. A *flux tube* may be constructed by bundling together a group of field lines. The net flux, Φ , of the tube is the integral $\int \mathbf{B} \cdot d\mathbf{a}$ over any surface pierced by the entire tube. Because $\nabla \cdot \mathbf{B} = 0$, the tube must have the same flux at every cross section.

The only way, in general, to find a field line is to integrate the differential Eq. (3.36).

A solution to the field line equation, Eq. (3.36), can in principle be found for a magnetic field at any instant. What is not immediately evident is why such a curve should be physically significant, even if one concedes that the magnetic field itself is significant. There is, in fact, no single reason that field lines will be significant under general circumstances — this is why students are often warned not to attribute undue importance to them. There are, however, numerous circumstances arising in space physics whereby a magnetic field line can achieve a degree of [utility]. The following is a brief list of the most common, applicable to a wide variety of plasma regimes from general 1, to the fluid regime 2, to MHD 3, to ideal MHD 4.

1. *General: single particle motion.* Subject to no other forces than a relatively stationary magnetic field, [the guiding center of a charged particle will remain tied to a single field line while the particle gyrates about that] according to its mass and charge [(discussed in detail in Sect. 8.2)]. Drifts will displace the particle’s guiding center by several gyro-radii after it has traversed a length

comparable to the field's curvature radius or gradient scale. Global scales of space plasmas are typically much, much greater than the gyro-radii of their electrons, and to a lesser extent of their heavier ions (the Earth's geomagnetic ring current is a counterexample to this[; see Activity 24]). Waves in the field may scatter particles (important in, *e.g.*, the Earth's radiation belts, [and for solar and galactic cosmic rays propagating through the heliosphere, see Ch. 8]), but this too is generally unimportant. Field lines therefore serve as excellent approximations of the electron orbits. [...]

2. *Fluid regime: thermal conductivity and solar coronal loops:* In a diffuse, high-temperature plasma, thermal energy is conducted principally by electrons. When electrons are strongly magnetized (*i.e.*, the cyclotron frequency is much greater than the collision frequency) their orbits will follow field lines over long distances between collisions at which point they scatter a perpendicular distance no greater than a single gyro-radius. The huge disparity between parallel and perpendicular scattering distances makes thermal conductivity highly anisotropic. Consequently, heat is conducted parallel to the magnetic field far more readily than perpendicular to the field.

Due to this anisotropic conductivity, heat deposited somewhere in a plasma is rapidly and efficiently conducted to all points on the same field line, at least while collision frequencies remain relatively low. [In the coronal setting, for example, the] plasma β is also generally low, so plasma flows are mechanically confined by the field. This means that a bundle of field lines will behave as a one-dimensional autonomous atmosphere, at least as long as reconnection is relatively unimportant. [...]

3. *MHD: Alfvén wave propagation:* Low-frequency waves in a magnetized plasma [(see Section 3.3)] comprise three branches: slow magnetosonic, fast magnetosonic and shear Alfvén waves. The group velocity of the shear Alfvén wave is exactly parallel to the local magnetic field. In the limit of very short wavelengths, any small localized disturbance will therefore propagate along a path following a magnetic field line. This means that a given field line will 'learn' of perturbations anywhere along itself at the Alfvén speed. In this sense the magnetic field line has a dynamical integrity similar to that of a piece of string. Indeed, it is common to derive the Alfvén speed intuitively using the analogy to a string under tension. [...]
4. *Ideal MHD: frozen-in field lines:* [...] At its simplest, the frozen-in-field-line theorem states that if two fluid elements lie on a common field line at one time, then they lie on a common field line at all times past and future. This follows directly from the ideal induction equation, ([Eq. (3.3) with $\eta \equiv 0$]), and from the fact that fluid elements move at the same velocity \mathbf{v} that appears in it."

The mathematics of ideal MHD is such “that differentiation along a field line is interchangeable with differentiation along a flow trajectory. From this it follows

that a field line linking two fluid elements can be traced either before or after following the flow of those elements. That is a restatement of the [frozen-in-field-line] theorem introduced above. One can thereafter imagine 'labeling' all the fluid elements along a given field line and then following those fluid elements as they move at their own velocities, \mathbf{v} . These material elements, which are manifestly real, will trace out a single field line at all times, so that [the field line is a useful concept in thinking about plasma motions. Wherever $\eta \neq 0$ in Eq. (3.3) field lines lose their nature as coherent entities; more on this below where we discuss reconnection.]”

Field lines and flux tubes have taken on a remarkable degree of utility in the thinking of many working in the various branches of heliophysics. “The motion of plasma along the magnetic field does not stress the field and incurs no dynamic back-reaction on the plasma through the action of the Lorentz force. Magnetic field lines therefore serve as conduits for moving energy, mass, momentum and energetic particles from point to point in the heliosphere. Heliophysics accordingly focuses on the magnetic connectivity of the Earth to the Sun, of the magnetotail to the polar caps, of the Io plasma torus to the Jovian magnetic field, and so forth. Magnetic field lines are truly the interstate highway system, the Autobahn network, the autostrada web of the heliosphere.” {ⓐA37}

Field lines as true, persistent entities have their greatest utility in ideal (non-resistive) MHD. But ideal MHD, in which field lines always connect the same parcels of plasma, fails when magnetic diffusivity becomes important in the MHD approximation, or when the basic assumptions of MHD itself fail on the smallest time or length scales. Then field is no longer 'frozen in' wherever that happens, and the very concept of continuity of field lines in space and time loses validity. Failure of the field-line concept as it is discussed above is captured by the term 'reconnection.' This term, widely used, turns out to be very loosely defined. “It can be used to refer to the changing connectivity in a vacuum potential field as much as to the decoupling of particle motions from the background magnetic field by any number of concepts, ranging from inertia to wave-particle interactions, or from resistivity to infinitesimal current sheets. It is thus as much a culturally accepted term for something that we really do not understand, as a descriptor of a well-understood consequence: we can say that reconnection occurs whenever the approximation of frozen-in flux fails.”

Non-ideal MHD sees reconnection as a consequence of resistivity. “To determine a realistic resistivity for a collisionless plasma requires consideration of the generalized Ohm's law. For a fully ionized plasma it can be written as

$$\mathbf{E} = -\frac{1}{c}\mathbf{v} \times \mathbf{B} + \frac{\mathbf{j}}{\sigma_e} + \frac{m_e}{ne^2} \left[\frac{\partial \mathbf{j}}{\partial t} + \nabla \cdot (\mathbf{v}\mathbf{j} + \mathbf{j}\mathbf{v}) \right] + \frac{\mathbf{j} \times \mathbf{B}}{nec} - \frac{\nabla \cdot \mathbf{p}_e}{ne}, \quad (3.37)$$

where $\mathbf{v}\mathbf{j}$ and $\mathbf{j}\mathbf{v}$ are dyadic tensors [(with components $v_n j_m$ and $v_m j_n$)] and \mathbf{p}_e is the electron stress tensor. Term i on the right-hand side of this equation is the convective electric field, while the term ii is the field associated with Ohmic dissipation caused by

electron-ion collisions. The conductivity, σ_e , is the inverse of the electrical resistivity, η . The next group of terms (iii) describes the effects of electron inertia [(which is ignored in Eq. (3.11) as another approximation of Ohm's law, while the latter describes also simplifies pressure by assuming it to be isotropic). The next term, (iv),] is the Hall effect. Ion inertia is negligible because the large mass of the ions means that they do not contribute significantly to a change in the current density. Finally, the term (v) includes the electron gyro-viscosity, which is considered by many to be important at [any point where the magnetic field vanishes, *i.e.*, at a] magnetic null. For a partially ionized plasma, collisions between charged particles and neutrals lead to additional terms associated with ambipolar diffusion.

Although all of the terms on the right-hand side of the generalized Ohm's law, other than the first, allow field lines to slip through the plasma, they do not all produce dissipation. For example, the inertial terms in (iii) do not cause the entropy of the plasma to increase. Thus, even though one may speak of inertial effects as creating an effective resistivity, this resistivity does not necessarily lead to dissipation.

Which terms are important in a particular situation depends not only upon the plasma parameters, but also upon the length and time scales for variations of these parameters. For magnetic reconnection, we normally want to know which non-ideal terms are likely to be significant within the current sheet where the frozen-flux condition is violated. Because each non-ideal (*i.e.*, diffusion) term in the generalized Ohm's law contains either a spatial or temporal gradient, we can estimate the significance of any particular term by computing the gradient scale-length, L_t , required to make the term as large as the value of the convective electric field, $\frac{1}{c}\mathbf{v} \times \mathbf{B}$, outside the diffusion region.

Consider, for example, the three inertial components of term (iii). If we assume that $\nabla \approx 1/L_t$, $|\mathbf{j}| \approx (c/4\pi)B_t/L_t$ and $\partial/\partial t \approx v_t/L_t$, say, where L_t is a typical length-scale and v_t a typical velocity, then these three components of (iii) will be of the same order as the convective electric field if

$$\frac{cm_e}{4\pi ne^2} \frac{v_t B_t}{L_t^2} \approx \frac{V_t B_t}{c}. \quad (3.38)$$

In other words, in order for the inertial terms to be important in a current sheet, its thickness ℓ_{inertia} should be

$$\ell_{\text{inertia}} \approx \left(\frac{c^2 m_e}{4\pi n e^2} \right)^{1/2} \approx \lambda_e, \quad (3.39)$$

where

$$\lambda_e = \frac{c}{\omega_{pe}} = \left(\frac{c^2 m_e}{4\pi n e^2} \right)^{1/2} = 5.3 \times 10^5 n^{-1/2} \quad (3.40)$$

is the electron-inertial length or skin-depth [(which characterizes the depth in a plasma into which electromagnetic radiation can penetrate)], c is the speed of light and

$$\omega_{pe} = (4\pi n e^2 / m_e)^{1/2} = 5.6 \cdot 10^4 n_e^{1/2} \quad (3.41)$$

is the electron plasma frequency.

Similarly, for the Hall term (iv)

$$\frac{B_t^2}{4\pi n e L_t} \approx \frac{V_t B_t}{c} \quad (3.42)$$

or

$$\ell_{\text{Hall}} \approx \frac{c}{M_A} \left(\frac{\mu m_p}{4\pi n e^2} \right)^{1/2} \approx \frac{\lambda_i}{M_A}, \quad (3.43)$$

where

$$\lambda_i = \frac{c}{\omega_{pi}} = \left(\frac{\mu c^2 m_p}{4\pi n e^2} \right)^{1/2} = 2.3 \times 10^7 \left(\frac{\mu}{n} \right)^{1/2} \quad (3.44)$$

is the ion-inertial length or skin-depth [(below which ions decouple from electrons, and the magnetic field may no longer be frozen into the plasma overall but instead into the electron fluid), and $\mu = m_i/m_p$]. The Alfvén Mach number equals [$M_A = V_t/v_A$,] and $\omega_{pi} = (4\pi n e^2/m_i)^{1/2}$ the ion plasma frequency, and v_A the Alfvén speed [(see Eq. 3.30 and Table 18.2)].

For the electron-stress term (v) we can write

$$\frac{n k T_t}{n e L_t} \approx \frac{V_t B_t}{c} \quad (3.45)$$

if we assume $|\mathbf{p}_e| \approx n k T_e$ and $T_e \approx T_i \approx T$. Solving for L_t leads to

$$\ell_{\text{stress}} \approx \frac{\beta^{1/2}}{M_A} r_{\text{gi}}, \quad (3.46)$$

where [the plasma β is given by Eq. (3.24) and the ion-gyro radius for the average thermal velocity (v_{Ti}) equals $r_{\text{gi}} = (k T m_i)^{1/2} c / e B$; see also Table 18.2.]

Finally, for the collision term (ii), \mathbf{j}/σ_e ,

$$\frac{c B_t}{4\pi \sigma_e L_t} \approx \frac{M_A v_A B_t}{c}. \quad (3.47)$$

[where σ_e^{-1} is] also the magnetic diffusivity, η . Using Spitzer's formula for the collisional resistivity, η , of a plasma (see) we obtain

$$\eta = \frac{(k m_e T_e)^{1/2}}{n e^2 \lambda_{\text{mfp}}}, \quad (3.48)$$

where

$$\lambda_{\text{mfp}} = \frac{3}{4\pi^{1/2}} \frac{(k T_e)^2}{n e^4 \ln \Lambda} = 1.1 \times 10^5 \frac{T_e^2}{n \ln \Lambda} \quad (3.49)$$

is the mean-free path for electron-ion collisions. Combining these expressions with those for the electron and ion inertial lengths we obtain [an estimate for the length scale below which effects of collisions become important to field diffusion:]

$$\ell_{\text{collisions}} \approx \frac{\beta^{1/2}}{M_A} \frac{\lambda_e \lambda_i}{\lambda_{\text{mfp}}}. \quad (3.50)$$

Table 3.4: Comparison of order-of-magnitude plasma parameters in different environments (cgs-Gaussian units – i.e., length scales in cm, n in cm^{-3} , T in K, B in Gauss, electric fields in statV cm^{-1}). [Modified after I:5, merging two tables in SI units]

Parameter	Laboratory experiment ¹	Terrestrial magnetosphere ²	Solar corona ³	Solar interior ⁴
region scale L_s	10	10^9	10^{10}	10^9
density n_t	10^{14}	10^{-1}	10^9	10^{23}
temperature T_t	10^5	10^7	10^6	10^6
field strength B_t	10^3	10^{-4}	10^2	10^5
Debye length λ_D	10^{-4}	10^5	10^{-1}	10^{-8}
ion gyro radius r_{gi}	10^{-1}	10^7	10	10^{-2}
ion inertial length λ_i	1	10^8	10^3	10^{-4}
Coulomb logarithm $\ln(\Lambda)$	11	33	19	3
coll. mean-free path λ_{mfp} ⁵	1	10^{18}	10^6	10^{-7}
$\ell_{\text{inertia}}(\lambda_e)$	10^{-2}	10^6	10	10^{-6}
$\ell_{\text{Hall}}(\lambda_i)$	1	10^8	10^3	10^{-4}
ℓ_{stress}	10^{-1}	10^7	10^{-1}	1
$\ell_{\text{collision}}$	10^{-2}	10^{-5}	10^{-5}	10^{-1}
plasma β	10^{-2}	10^{-1}	10^{-4}	10^4
Lundquist no. $L_u(\approx \mathcal{R}_m)$	10^3	10^{14}	10^{14}	10^{10}
Dreicer field E_D	10^{-1}	10^{-17}	10^{-6}	10^7
$E_A(= v_A B/c)$	1	10^{-6}	10^1	1
$E_{\text{SP}}(= E_A/\sqrt{\mathcal{R}_m})$	10^{-2}	10^{-13}	10^{-7}	10^{-6}

¹ The Magnetic Reconnection eXperiment (MRX) at Princeton Plasma Physics Laboratory;

² plasma sheet; ³ above a solar active region; ⁴ at the base of the solar convection envelope [at a depth of about 200,000 km around which many consider primary dynamo mechanisms to operate; ⁵ note that this is a purely collisional mean-free path, ignoring other couplings that may occur through the magnetic field].

Note that the length-scale, $\ell_{\text{collision}}$, of the spatial variations required to achieve significant field-line diffusion is inversely proportional to the mean-free path, λ_{mfp} . As λ_{mfp} increases, the diffusion caused by collisions becomes less effective, and increasingly sharper gradients are required to maintain the size of the dissipation term, \mathbf{j}/σ_e .

[Table 3.4 lists] various plasma parameters along with the characteristic scale-lengths for four different regions where reconnection is thought to occur. The parameter L_s is the global (system-level) scale-size of the region, and the fundamental quantities from which all other parameters are derived are the density n , temperature T , and magnetic field B . For convenience, we assume that the Alfvén Mach number M_A is unity and that the electron and ion temperatures are roughly equal. The most extreme plasma environments listed in Table 3.4 occur in the magnetosphere, which is completely

collisionless, and in the solar interior which is highly collisional.

In addition to the parameters discussed above, Table 3.4 also lists the value of the *Debye length* [whose expression is shown in Table 18.2.] The number of particles within a Debye sphere (*i.e.*, $4\pi n\lambda_D^3/3$) must be larger than unity in order for the generalized Ohm's law to hold. Otherwise, the collective behavior which characterizes a plasma breaks down. The number of particles in a Debye sphere for the environments shown in Table 3.4 ranges from 10^{14} for the magnetosphere to only about four for the solar interior at the base of the convection zone. Also shown in the table is the Lundquist number, L_u , which is the same as the magnetic Reynolds number, \mathcal{R}_m [introduced in Eq. (3.18)], when the flow and Alfvén speeds are the same. For a collisional plasma the Lundquist number based on L_s can be expressed as

$$L_u = \frac{v_A}{v_d} = \frac{L_s v_A}{\eta} = 2. \times 10^8 \frac{L_s T_e^{3/2} B_t}{(\mu n)^{1/2} \ln(\Lambda)} \quad (3.51)$$

[...] In the expression on the right, η has been replaced by Spitzer's formula for the electrical resistivity of collisional plasma.

The characteristic scale-lengths in Table 3.4 provide an indication of which terms in the generalized Ohm's law of Eq. (3.37) are likely to be important for reconnecting current sheets. As with MHD shocks and turbulence, the large-scale dynamics of the flow cause the current sheet to thin until it reaches a length-scale where field-line diffusion is effective. Thus, in principle, the term with the largest characteristic length-scale in Table 3.4 is the one that will be most important. Because the Hall term has the largest length in every environment except the solar interior, one might conclude that it is generally the most important. However, this conclusion does not take into consideration the fact that the Hall term tends to zero in the region of a magnetic null point or sheet. The Hall term on its own does not contribute directly to reconnection, since it freezes the magnetic field to the electron flow. [...] An excessively small scale does indicate that any process associated with that term is unlikely to be important. Therefore, on this basis, we can conclude that collisional diffusion is not important in the terrestrial magnetosphere or the solar corona, and that the electron-inertial terms and the Hall term are not important in the solar interior. [...] On the other hand, if a term is not associated with an obviously 'excessively small' scale, it is difficult to know whether a particular term is really as important as suggested by its relative length scale; evaluating such cases] requires a complete analysis of the kinetic dynamics, which is a rather formidable task.

Although the collision length-scale, $\ell_{\text{collision}}$, is equally small in both the magnetosphere and the corona, the general importance of collisions for these two regions is quite different. In the magnetosphere the collision-mean-free path, λ_{mfp} , is nine orders of magnitude larger than the global scale-size, L_s , but in the corona it is four orders of magnitude smaller than the global scale. Thus, we can be confident that collisional transport theory applies to large-scale structures in the corona even though it is not applicable within thin current sheets or dissipation layers. By contrast, in the magnetosphere, collisions are so few that collisional transport theory does not apply at

any scale.

Another important issue concerning the applicability of collisional theory is the strength of the electric field in a frame moving with the plasma. If this field exceeds the *Dreicer electric field* defined by

$$E_D = \frac{e \ln(\Lambda)}{\lambda_D^2} = \frac{4\pi e^3}{k} \frac{\ln(\Lambda) n}{T_e} = 10^{-11} \frac{n \ln(\Lambda)}{T_e}, \quad (3.52)$$

runaway acceleration of electrons will occur. The most likely location for the production of runaway electrons in a reconnection process is in a thin current sheet that forms at the null point. This field could be as large as the convective electric field based on the Alfvén speed, that is

$$E_A = \frac{1}{c} v_A B_t = 7.2 \frac{B_t^2}{(\mu n)^{1/2}}, \quad (3.53)$$

or as low as the Sweet-Parker electric field

$$E_{SP} = \frac{E_A}{\mathcal{R}_m^{1/2}}, \quad (3.54)$$

where \mathcal{R}_m is the magnetic Reynolds number based on the inflow Alfvén speed (*i.e.*, the inflow Lundquist number). As shown in Table 3.4, the Dreicer field in the magnetosphere is much smaller than E_A or E_{SP} , so runaway electrons will always be generated by reconnection there. On the other hand, in the solar interior the Dreicer field is so large that runaway electrons never occur. In the intermediate regimes of the laboratory and the solar corona, the Dreicer field lies between E_A and E_{SP} , so perhaps runaway electrons are only produced when very fast reconnection occurs.

Even in completely collisionless environments like the Earth’s magnetosphere, it is still sometimes possible to express the relation between electric field and current density in terms of an anomalous resistivity. For example, [...] the electron inertial terms (iii) in the generalized Ohm’s law of Eq. (3.37) lead to an anomalous resistivity

$$\frac{1}{\sigma_e^*} = \frac{\pi B_\perp}{2ne}, \quad (3.55)$$

where B_\perp is the field normal to the current sheet. This resistivity is derived solely from a consideration of the particle orbits, and in the magnetotail current sheet it may be larger than any anomalous resistivity due to wave-particle interactions. A typical example of the latter is the anomalous resistivity due to ion-acoustic waves”.

For some discussion of reconnection in two and three dimensions in the Heliophysics books, see I:5.3 and I:5.4. More on the effects of reconnection follows in Chs. 6 and 8.

3.5 A few notes about conditions

3.5.1 Solar atmosphere *vs.* terrestrial magnetosphere

The scale lengths estimated for the importance of terms in Ohm’s law in Table 3.4 are very much smaller than the scale of the corona itself and even compared to any

active region, but importantly also very much smaller than the angular resolution achievable by imaging instruments (currently about 1 arcsec or ~ 700 km for space-based EUV imagers). Consequently, the scale on which reconnection occurs in the corona is not observed, while the effects of such reconnection become apparent in the magnetic geometry and plasma atmospheres on scales well above the reconnection itself.

In contrast, in the terrestrial magnetosphere all but the length scale, $\ell_{\text{collision}}$, on which collisional effects could contribute significantly as a term in the generalized Ohm's law are large enough that spacecraft can scan reconnection regions as they fly through, while constellations of spacecraft can probe reconnection in multiple dimensions.

Another significant distinction is that in the terrestrial magnetosphere the ion-gyro radius (particularly for relatively heavy and energetic particles) is not small compared to the scale on which these particles probe the magnetic field. This is an important cause behind what is known as the ring current (see Sect. 8.2) that is largely carried precisely by such particles. For solar conditions, in contrast, such effects of particle gyration are not directly evident on any observable scale.

3.5.2 Heliosphere

“Adopting typical solar wind values near Earth of $n_t = 5$ particles/cm³ for density, $v_t = 400$ km/s solar wind speed and $B_t = 50 \mu\text{G}$ magnetic field strength (values consistent with Table 2.4) we can evaluate the expected energy density of the solar wind, which can be broken down into three components: flow, magnetic and thermal. [...] The flow energy density is estimated to be

$$e_{v,\odot} \equiv \left(\frac{1}{2} \rho v^2 \right)_{\text{sw}} \approx \frac{1}{2} m_p n v_{\text{sw}}^2 \approx 7 \times 10^{-9} \left(\frac{n(\text{cm}^{-3})}{5} \right) \left(\frac{v(\text{km/s})}{400} \right)^2 \text{ erg/cm}^3. \quad (3.56)$$

The energy density of the solar wind's magnetic field is

$$e_{B,\odot} \equiv \left\langle \frac{B^2}{8\pi} \right\rangle \approx 1. \times 10^{-10} \left(\frac{B(\mu\text{G})}{50} \right)^2 \approx 0.015 e_{v,\odot} \text{ erg/cm}^3, \quad (3.57)$$

while the thermal energy density using values from Table 2.4] is

$$\begin{aligned} e_{T,\odot} &\equiv \left\langle \frac{3}{2} n k (T_e + T_i) \right\rangle \approx 2.5 \times 10^{-10} \left(\frac{n(\text{cm}^{-3})}{6} \right) \left(\frac{T_e(K)}{1.2 \times 10^5} + \frac{T_i(K)}{1.4 \times 10^5} \right) \\ &\approx 0.03 e_{v,\odot} \text{ erg/cm}^3 \end{aligned} \quad (3.58)$$

where $T_{i,e}$ are the solar wind ion and electron temperatures. Taking the [values from Table 2.4], the above [These] estimates show that the bulk of the energy in the solar wind at Earth is in the flow:” $e_{v,\odot} \sim 30 e_{B,\odot} \sim 70 e_{T,\odot}$ {A38}

{111}

{A38}

Chapter 4

Dynamos of Sun-like stars and Earth-like planets

Chapter topics:

- Basic stellar structure (colors, masses, radii), and (cyclic) magnetism
- Basic structure of the terrestrial planets and the contrast of the rotation/convection time scales (in the Reynolds number) with stars
- Principle of dynamos: the conversion of mechanical energy into electromagnetic energy through induction
- Energy sources and fluid flows that enable stellar and planetary dynamos

Key concepts:

- Rotation (through Coriolis forces) introduces a source term for magnetic field in the induction equation
- The mean-field dynamo approximation relies on a separation of scales not strictly supported by the convective spectrum
- Back reaction of the magnetic field on the flow limits dynamo strengths
- An 'interface dynamo' relies on storage of field below the convective envelope, and a 'flux-transport dynamo' involves global meridional circulation

4.1 Dynamo settings

Stellar and planetary dynamos thrive wherever sufficiently vigorous flows of a conducting medium transport substantial thermal energy in an adequately spinning body. The energy transported has to come from a reservoir that may date back to the formation of the body (in planets or very young stars) or may have its origin in nuclear fusion (in stars) or in solidification – the latter often accompanied by chemical separation – or nuclear fission (in terrestrial planets). The flows that transport the energy may be dominated by Coriolis forces (in planets where flows are slow compared to spin rates) or by stratification (including chemical gradients in planets, while in stars pressure gradients of the compressible medium limit how far matter can efficiently

rise before overturning). The amount of energy transported is regulated by the source in the deep interior as well as by the sink at the top of the dynamo region. In Sun-like stars that sink is the stellar surface, and the properties of radiative transfer through these surface layers are important in determining the internal structure of the entire star as it balances the energy produced by nuclear fusion with its luminosity. In a planet like Earth, the energy transport in the dynamo region of the core is determined to a large extent by the convective motions in the enveloping mantle that transport heat to where it is ultimately lost through the surface.

“The formal difference between the type of dynamos that we are interested in here and the self-excited dynamos in power plants is the homogeneous distribution of conductivity (that would lead to a short-circuit situation) that does not put any constraints on electric currents (electric wires could be considered as special cases of a highly inhomogeneous conductivity distribution). For this reason these dynamos are also called homogeneous fluid dynamos.”

In stars, “[t]hermonuclear fusion in their cores converts matter into thermal energy and electromagnetic radiation which, in the Sun, is transported outward via the diffusion of photons. In the solar envelope, the plasma becomes more opaque as the temperature drops, which inhibits radiative diffusion and steepens the temperature gradient relative to the adiabatic temperature gradient. The stratification soon becomes superadiabatic [(i.e., has a temperature gradient steeper than for adiabatic conditions in which no energy enters or leaves a volume of gas)] and thermal convection [gradually] takes over as the primary mechanism for transporting energy to the solar photosphere where it is radiated into space. {A39} [All stars with a mass of somewhat above that of the Sun or less than that have such a convective envelope during their ‘main-sequence’ (equilibrated hydrogen-fusing) phase (see Figs. 4.1 and 4.2); the least massive stars are fully convective. All of these stars power a dynamo during the longest-lived mature phase, and all stars do during their initial birth phases and in the last phases of their lives, both of which are short compared to the mature phase (Ch. 10). Stars cool enough to have a convective envelope reaching into their surface layers are known as ‘cool stars’.^[8] {A40}

The solar convection zone occupies approximately the outer 30% of the Sun by radius. It is here where [a small fraction of the] internal energy of the plasma is converted to kinetic energy and then [a small fraction of that] to magnetic energy, aided by radiation and gravity. Radiative heating [of the bottom of the] convection

⁸ Astronomers characterize the properties of stars based on their spectrum. The overall shape gives an indication of the surface temperature, while details of spectral lines (generally in absorption, but some in emission) provide finer detail used in classification schemes. One such scheme frequently used is that of ‘spectral type’ in the Morgan-Keenan (MK) scheme: only after the classes were introduced was a monotonic mapping to temperature established, going from hot to cooler: *O*, *B*, *A*, *F*, *G*, *K*, *M*, *L*, and *T* (with the last two fairly recent additions for very cool, very faint stars, with *T* reaching the domain of ‘brown dwarfs’). The letter is followed by a subclass from 0 to 9, and commonly an indicator of ‘luminosity class’: a roman numeral indicative of the size of the star: I, II, III, IV, and V for supergiants, bright giants, giants, subgiants, and main-sequence or dwarf stars. The term ‘main sequence’ refers to a band in brightness-color diagrams, such as Fig. 4.2, within which stars spend most of their lives, as long as they are steadily fusing hydrogen into helium.

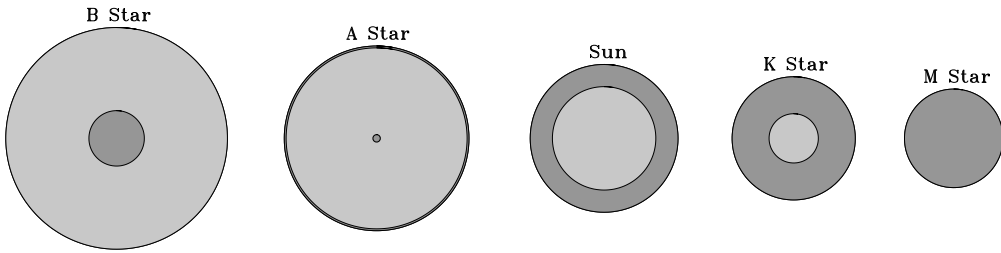
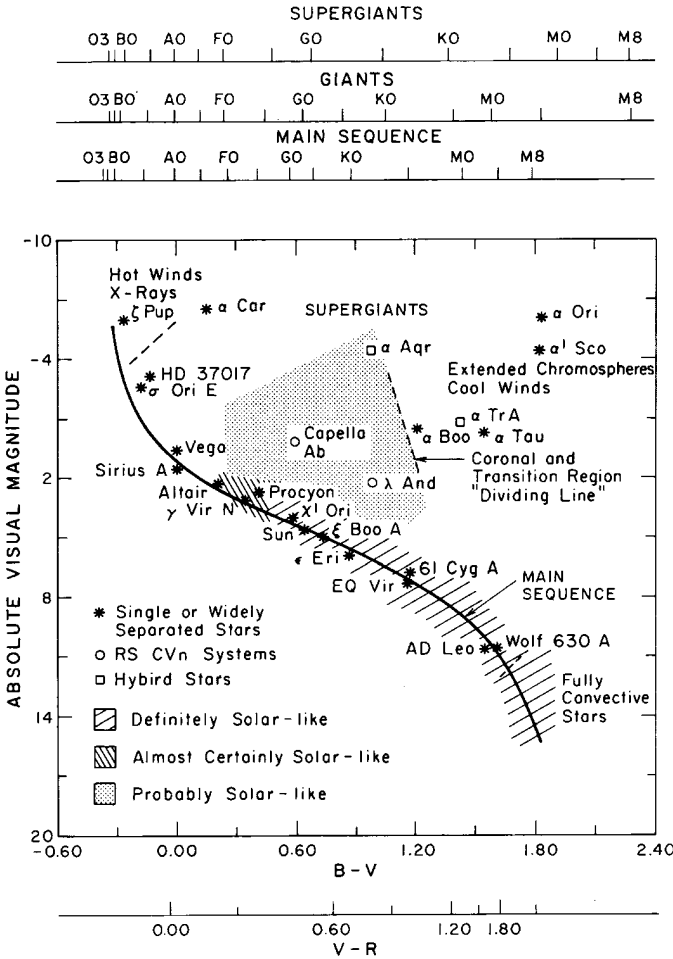


Figure 4.1: Schematic representation of the radiative (light grey) and convective (dark grey) internal structure of main-sequence stars. The thickness of the outer convection zone for the A-star is here greatly exaggerated; drawn to scale it would be thinner than the black circle delineating the stellar surface on this drawing. Relative stellar sizes are also not to scale: a B0 V star has a radius of $\sim 7.5 R_{\odot}$, and an M0 V star has a radius of $\sim 0.6 R_{\odot}$, i.e., 12 times smaller. [Fig. III:2.10]

zone and radiative cooling in the photosphere maintain a superadiabatic temperature gradient that sustains convective motions by means of buoyancy. In a rotating star, convection transports momentum as well as energy, establishing shearing flows and global circulations. These mean flows work together with turbulent convection to amplify and organize magnetic fields through hydromagnetic dynamo action, giving rise to the rich display of magnetic activity so striking in modern solar observations.”

The Sun’s large scale magnetic field exhibits a quasi-periodic modulation on a roughly 11-year basis during which the level of magnetic activity waxes and wanes as a pattern of activity migrates from mid to low latitudes, then to pick up again at higher latitudes, with some temporal overlap in the early and late phases of these cycles. For stars like the Sun, the mean level of activity as expressed by the surface-averaged absolute magnetic flux density ranges over more than three orders of magnitude, depending on the stellar rotation rate, age, and internal structure (more on that in Sect. 9.3; see also III:2). “[T]he *existence* of solar and stellar magnetic fields is in itself not really surprising; any large-scale fossil field present at the time of stellar formation would still be there today at almost its initial strength, because the Ohmic dissipation timescale is extremely large for most astrophysical objects [(Eq. 3.20)]. The challenge is instead to reproduce the various observed spatiotemporal patterns [...], most notably the cyclic polarity reversals on decadal timescales.”

As to planetary dynamos, “[s]pace missions revealed that most planets in the Solar System have internal magnetic fields (see Ch. I:13), but there are exceptions (Venus, Mars). Some planets seem to have had a field that is now extinguished (*e.g.*, Mars). In many cases with an active dynamo the axial dipole dominates the field at the planetary surface, but Uranus and Neptune are exceptions. Saturn is special because its field is extremely symmetric with respect to the planet’s rotation axis. The field strengths at the planetary surfaces differ by a factor of 1000 between Mercury and Jupiter [(*cf.* Table 5.3)]. A full understanding of this diversity in the morphology and strength



For main-sequence stars

Sp. type	M/M_{\odot}	T_{eff}	BC
A0	3,2	9600	-0.25
F0	1.7	7300	0.02
G0	1.1	5900	-0.07
K0	0.78	5000	-0.19
K5	0.69	4400	-0.62
M0	0.60	3900	-1.17

Absolute bolometric magnitude $M_{\text{bol},*}$ (a logarithm of the brightness of a star normalized to a standard distance), absolute visual magnitude M_V and stellar luminosity L_* expressed in solar units (L_{\odot}) are related through:

$$L_*/L_{\odot} = 10^{0.4(M_{\text{bol},\odot} - M_{\text{bol},*})},$$

while $M_{\text{bol}} = M_V + BC$, where BC is the 'bolometric correction' that corrects the brightness of the star in the V ('visual' filter) bandpass to the bolometric brightness.

Figure 4.2: A Hertzsprung-Russell diagram showing stars with substantial magnetic activity in shaded or hatched domains, which are distinguished in groups of solar-likeness as indicated in the legend. The main sequence where stars spend most of their lifetime fusing hydrogen into helium in their cores is indicated by a solid curve; well above that lies the domain of the supergiant stars, with the giant star domain in between. Also indicated is the region where massive winds occur and where hot coronal plasma appears to be absent. Some frequently studied stars (both magnetically active and nonactive) are identified by name. The axes above the main panel show the spectral types (see footnote 8) for supergiant, giant, and main-sequence stars for the corresponding spectral color index $B - V$ or corresponding $V - R$ index. [Fig. III:2.8, with an added information panel on the right; figure source: Linsky (1985).]

of planetary magnetic fields is still lacking, but a number of promising ideas have been suggested and backed up by dynamo simulations. Some of the differences can be explained by a systematic dependence of the dynamo behavior on parameters such as rotation rate or energy flux, whereas others seem to require qualitative differences in the structure and dynamics of the planetary dynamos.”

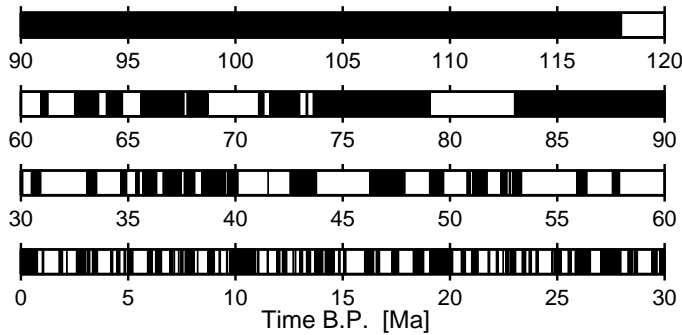


Figure 4.3: *Polarity of the geomagnetic field for the past 120 million years, with time running backward from left to right in each row (before present - B.P., i.e., 1950 - in units of millions of years). Dark regions indicate times when the dipole polarity was the same as today, in white regions it has been opposite. [Fig. III:7.4]*

“Earth serves as the prototype for the terrestrial planets. [...] There is a core with radius $R_{\text{core}} \approx 0.55R_{\text{planet}}$, [the outer part of which is liquid]. The small inner core, with a radius $0.35R_{\text{core}}$, is [solid]. The core appears to consist predominantly of iron. [...]

The total internal heat flow at the Earth’s surface is $4.6 \cdot 10^{20}$ erg/s (although a large number, it is only 0.03% of the total power coming into the Earth’s atmosphere by insolation). Roughly one half of it is balanced by the heat generated by the decay of uranium, thorium and the potassium isotope ^{40}K inside the Earth. The remainder of the heat flow is due to the cooling of the Earth. The loss of gravitational potential energy associated with the contraction of the Earth contributes a modest amount, but is much less important than it is in young stars or in gas planets. How much of the Earth’s heat flow comes from the core is rather uncertain. Recent estimates that are based on different lines of evidence mostly fall into the range $(0.5 - 1.5) \cdot 10^{20}$ erg/s, although values as low as $(0.3 - 0.4) \cdot 10^{20}$ erg/s have also been discussed. Most of the radioactive elements reside in the silicate crust and mantle. Some amount of potassium may be present in the core, but the majority of the core heat must be due to cooling. It is important to note that the heat loss from the core is regulated by the slow solid-state convection in the mantle. The core, which convects vigorously in comparison to the mantle and which is thermally well-mixed, delivers as much heat as the mantle is able to carry away.”

4.1.1 Earth and other terrestrial planets

Solar System bodies that have a present-day active dynamo include Mercury and Earth among the terrestrial planets, the jovian moon Ganymede, and all the giant planets; see Table 5.3 for their global properties.

“The surface magnetic field of the Earth has a strength of about 0.5 G with mainly dipolar character. [The dipole axis is tilted by a variable amount over time with respect to the axis of rotation, such that the magnetic north pole has wandered from as far

south as about 70 degrees in geographic latitude to within a few degrees from the geographic north pole over the past two centuries]. From studies of rock magnetism (when rocks cool below the Curie point they preserve the magnetic field that was present in them at that time) it is known that the Earth had a magnetic field over the past 3.5×10^9 years and that the strength and orientation of the field varied significantly on time scales of 10^3 to 10^4 years. A given polarity typically dominates for about 200 000 years with quick reversals on a time scale of a few thousand years in between [(see Fig. 4.3)]. While the orientation of the axis of the dipole changes significantly with time, the dipole moment is aligned with the axis of rotation when averaged over $\sim 10^4$ years.”

In contrast to the case of cool stars, “[r]adiative heat transfer is not an issue in planetary cores, but liquid metal is a good thermal conductor. The heat flux that can be transported by conduction along an adiabatic temperature gradient, $(dT/dr)_{\text{ad}} = T/H_T$, is sometimes called the ‘adiabatic heat flow’ (T is absolute temperature, $H_T = c_p/(\zeta g)$ is the temperature scale height with c_p the heat capacity, ζ the thermal expansivity and g the local gravitational acceleration). In terrestrial planets, the adiabatic heat flow can be a large fraction of the actual heat flow, or it may exceed the actual heat flow, in which case at least the top layers of the core would be thermally stable. Near the top of Earth’s core approximately $(0.3 - 0.4) 10^{20}$ erg/s can be conducted along the adiabat, *i.e.*, close to the minimum estimates for the entire core heat flow. But even if all the heat flux near the core-mantle boundary were carried by conduction, a convective dynamo can exist thanks to the inner core. At the inner core boundary, the adiabatic temperature profile of the convecting outer core crosses the melting point of iron. The latter increases with pressure more steeply than the adiabatic gradient, which is the reason why the Earth’s core freezes from the center rather than from above. As the core cools, the inner core grows with time by freezing iron onto its outer boundary. This has two important implications for driving the dynamo. The latent heat that is released upon solidification is an effective heat source, which contributes to the heat budget approximately the same amount as the bulk cooling of the core. [...] A second, perhaps more important effect is that the light elements in the outer core are preferentially rejected when iron freezes onto the inner core. Hence, they become concentrated in the residual fluid near the inner core boundary. This layering is gravitationally unstable because of the reduced density, which leads to compositional convection that homogenizes the light elements in the bulk of the fluid core. Compositional convection contributes as much as, or more than, thermal convection to the driving of the geodynamo in recent geological times.

Most predictions for the inner core growth rate imply that the inner core did not exist for most of the history of the Earth. Rather, it would have nucleated between 0.5 and 2 billion years ago. In the absence of an inner core, only thermal convection by secular cooling of the fluid core (and perhaps radioactive heating) can drive a dynamo, which is less efficient than the present-day setting. A change in the geomagnetic field properties might be expected upon the nucleation of the inner core, but no clear indication for such an event has been found in the paleomagnetic record.”

“No direct evidence on the existence or non-existence of a solid inner core is available for any planet other than Earth. But the possible absence of an inner core could explain why Venus and Mars do not have an active dynamo. On Earth, mantle convection reaches the surface in the form of plate tectonics, which is a fairly efficient mode of removing heat from the interior. None of the other terrestrial planets have plate tectonics. In their cases, mantle convection is confined to the region below the lithosphere, a rigid lid of some 100 – 300 km thickness through which heat must be transported by conduction. Without plate tectonics, the heat flow is expected to be significantly lower not only at the surface, but also at the top of the core, where it is very probably subadiabatic. If no inner core exists to provide latent heat, it is then subadiabatic throughout the core. Furthermore, compositional convection is also unavailable to drive a dynamo. The slower cooling of the planetary interior in the absence of plate tectonics concurs with the idea that an inner core has not (yet) nucleated in the cases of Mars and Venus. Early in the planets’ history the cooling rate was probably much higher and the associated core heat flow large enough for thermal convection. The demise of the dynamo must have occurred when the declining heat flow dropped below the conductive threshold.”

For discussion of dynamos in non-terrestrial planets, see Ch. III:7.

4.1.2 The Sun and other stars

“The Sun shows magnetic field on all observable scales [(Fig. 4.4)] with a significant range in field strength, from individual sunspots with magnetic field strengths of 2 500 to 3 000 G to the average field strength of the global field of only a few Gauss.

The most prominent feature of solar magnetism is the 11-year sunspot cycle (if one considers the field reversals the full period is 22 years), which is reflected in the changing number of sunspots appearing on the surface of the Sun. In the beginning of a cycle spots appear at latitudes of about 35°, while close to the end they appear almost at the equator. This property is commonly summarized in the so-called solar butterfly diagram [(Fig. 4.5)]. During the epoch of minimum, the large-scale field of the Sun is most dipolar; the reversal of the poles takes place during solar maximum. On a longer time scale the magnetic activity changes significantly in amplitude and is interrupted by epochs of 100 – 200 years in duration where sunspots are [infrequent or] completely absent [(such as during the Maunder Minimum, about 1645–1715). ...] Observations of the stellar luminosity or of chromospheric (UV/optical) and coronal (X-ray) emission show that a majority of solar-like stars are magnetically active and around a third to a half show cyclic activity with periods in the range from 3 to 30 years.”

{A42}

{A41}

4.2 Dynamo principles

“Dynamo action refers to the conversion of mechanical energy into electromagnetic energy through induction. In [stars and in planets alike], the mechanical energy is supplied by fluid motions in electrically conducting regions inside [these bodies] and the electromagnetic energy produces the observed [...] magnetic fields. A dynamo is referred to as *self-sustaining* if it does not require any external magnetic field

{A41} {A42} IV:6.1

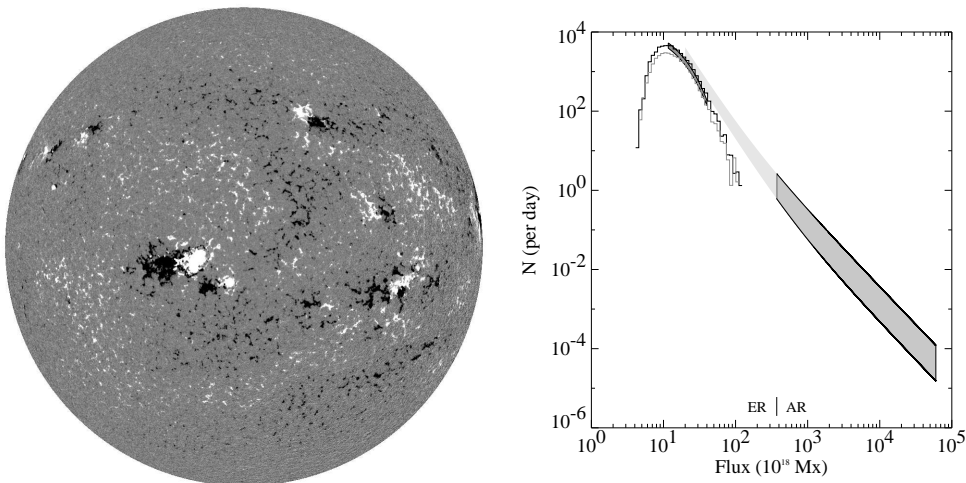


Figure 4.4: Left: *First solar magnetic map (magnetogram) of the current millennium, taken by SOHO’s MDI on 2001/01/01 00:03 UT. The magnetogram (with white/black for negative/positive line of sight polarity) shows a variety of active regions, embedded in patches of largely unipolar enhanced supergranular network, mixed-polarity quiet Sun regions, and low-flux polar caps (weak at this near-maximum phase of the cycle, and weakened further in the line-of-sight flux map because of projection effects on the near-vertical magnetic field).* Right: *Distribution function of emerging magnetic bipolar regions on the Sun, showing the emergence frequency per day per flux interval of 10^{18} Mx, estimated for the entire solar surface. The shaded region on the right envelopes the range of the active-region spectrum for solar cycle 22 (for half-year intervals around sunspot minimum and maximum). The histograms on the left are for the ephemeral regions; the shaded band shows where observations are least affected by spatial (lower cutoff) and temporal (upper cutoff) biases. The spectrum for regions below $\sim 10^{19}$ Mx has yet to be determined; the cutoff here is caused by the limited resolution of the SOHO/MDI magnetograph. [Fig. III:2.1]*

contributions for regeneration (except initially for a starting seed field).

The fundamental equation governing this induction process is known as the *Magnetic Induction Equation* [Eq. (3.3) in Table 3.3; its derivation and its limitations are described in Sect. 3.2.2. That equation is complemented by the requirement that the currents and the driving flows that are associated with the magnetic field are entirely contained within the body, and that the transition to outside the body for the field is smooth (compare I:3.3). ...]

By inspecting the two terms on the right-hand side of Eq. (3.3) we see that magnetic field can grow or decay in time through two processes. The first term (1) involves interactions of the velocity and magnetic fields through electromagnetic induction and acts as a source/sink term for field generation. The second term (2) represents diffusion due to Ohmic dissipation. To ensure magnetic field does not decay away in time, field must be generated as fast as or faster than its diffusion. A necessary

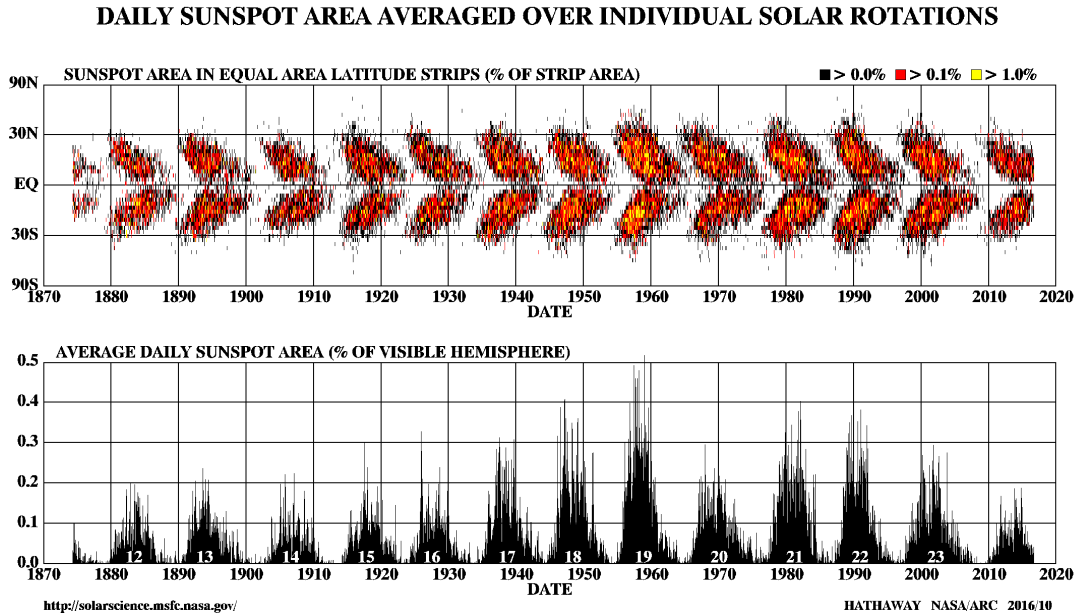


Figure 4.5: ‘Butterfly diagram’ showing (top) sunspot latitudes (also activity belts) and (bottom) total fractional area coverage as a function time. [updated with data through 2018] For a color version of this figure, see *arXiv:2001.01093*.

condition for self-sustained dynamo action is therefore that the induction term (1) be larger than the diffusion term (2) in Eq. (3.3). By using characteristic scales for the variables in the Magnetic Induction Equation (*i.e.*, B_t for the magnetic field scale, v_t for the velocity scale and L_t for a length scale) we derive a common measure of the ratio of field generation to field diffusion known as the *magnetic Reynolds Number*: $\mathcal{R}_m \equiv v_t L_t / \eta$, see Eq. (3.18).]

Upon first glance, it seems reasonable that the magnetic Reynolds number must be larger than unity for dynamo action to be possible. However, more rigorous theoretical analyses suggest that the lower bound for \mathcal{R}_m is instead closer to π^2 and planetary numerical dynamo simulations typically find \mathcal{R}_m must be larger than $\sim 20 - 50$ for self-sustained dynamo action to occur. These higher values are due to the complexities in the velocity field morphologies that cannot be captured in the simple estimate given in Eq. (3.18):” after all, it is a big leap from small-scale field generated on the scale of the flow (such as sketched in Fig. 4.6) to a large-scale field. In cool stars, \mathcal{R}_m typically far exceeds critical values for dynamo action because of the large scales and relatively fast flows involved (see Sect. III:5.3.2).

A perspective of what actually supplies the energy to power the dynamo is provided by integrating the induction equation Eq. (3.3) over the object’s volume to establish

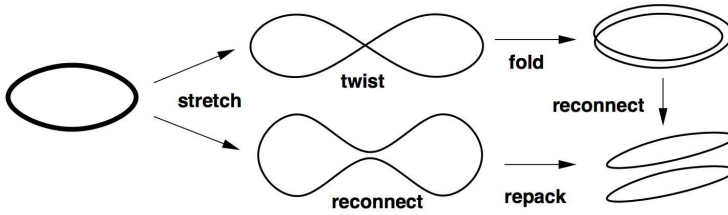


Figure 4.6: Illustration of two possible flux-rope dynamos. In both cases the field amplification takes place during the stretch operation. The twist-fold (top) and reconnect-repack (bottom) steps are required to remap the amplified flux-rope into the original volume element so that the process can be repeated. Magnetic diffusivity is essential to allow for the topology change required to close the cycle. Each cycle increases the field strength by a factor of 2. [Fig. H-1:3.3]

the total energy in the system:

$$\frac{d}{dt} \int_V \frac{B^2}{4\pi} dV = - \oint_{\partial V} \mathbf{S} \cdot \hat{\mathbf{n}} dS - \eta \int_V j^2 dV - \int_V \mathbf{v} \cdot (\mathbf{j} \times \mathbf{B}) dV. \quad (4.1)$$

The first term on the right is the Poynting flux $\mathbf{S} = (1/4\pi)\mathbf{B} \times (\mathbf{v} \times \mathbf{B})$, which is the energy via the electromagnetic field through a surface into or out of the system across the closed boundary surface ∂V (ignorable if the stellar wind does not take too much power away compared to the total). The second term is the dissipative loss (assuming here that η is uniform). The final term shows that the magnetic energy in the system can be maintained against the dissipative losses only if there are sufficient flows working against – *i.e.*, have an antiparallel component relative to – the Lorentz force $\mathbf{F} = (1/c)\mathbf{j} \times \mathbf{B}$. {A43}

4.3 Essentials of fluid motions in dynamos

In essence, to drive a large-scale stellar or planetary dynamo, the magnetic field must be subjected to a combination of flow components of a different nature that have their origin in convection and rotation. “Fig. 4.6 illustrates the basic ingredients required to amplify a closed magnetic field loop. After a full cycle, the magnetic field strength and the flux have doubled (two loops, each with the original magnetic flux) and the process can be repeated. This very simple illustration points out already a few fundamental properties of a dynamo process. To be able to remap the magnetic field configuration into the original volume element, three-dimensional motions are required. Amplification through stretching is possible in a strictly two-dimensional domain, but there is no way to move the resulting field to return to the right-hand side of the image. The two examples also point out the crucial role of diffusivity in changing the topology of the field. The ‘stretch-twist-fold’ mechanism (excluding diffusive steps) leads to loops of increased complexity, while the ‘stretch-reconnect-repack’ process explicitly involves magnetic diffusivity and ends up with two flux ropes [(see Table 3.1 for a definition)] of similar topology. A reconnection step at the end of the ‘stretch-twist-fold’

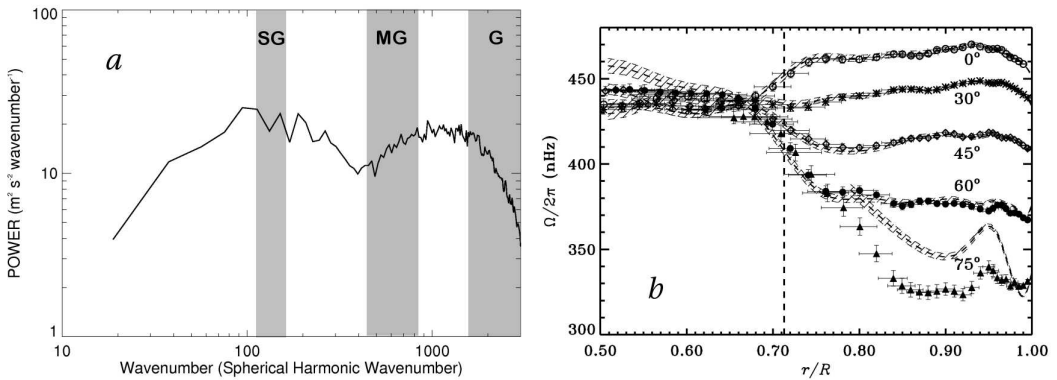


Figure 4.7: Panel a: Power spectrum of the convective velocity field in the solar photosphere obtained from Doppler measurements, plotted as a function of spherical harmonic degree ℓ . Mean flows and p -modes are filtered out. The falloff beyond $\ell \sim 1500$ reflects the resolution limit of the Michelson Doppler Imager (MDI) instrument onboard the SOHO spacecraft from which these data were obtained and is therefore artificial. Shaded areas indicate the approximate size ranges of supergranulation (SG), mesogranulation (MG) and granulation (G). Note that the expected supergranulation spectral peak at $\ell \sim 4400$, corresponding to $L \sim 1$ Mm, is not resolved. Panel b: The solar internal rotation profile inferred from helioseismic inversions. Angular velocity $\Omega/2\pi$ is shown as a function of fractional radius r/R_{\odot} for several latitudes as indicated. Symbols and dashed lines denote different inversion methods, known as subtractive optimally localized averages (SOLA) and regularized least squares (RLS) respectively. Vertical $1\text{-}\sigma$ error bars (SOLA) and bands (RLS) are indicated and horizontal bars reflect the resolution of the inversion kernels. The vertical dashed line indicates the base of the convection zone. [Fig. III:5.1; panel a is based on data from this source: Hathaway et al. (2000); source panel b: Thompson et al. (2003).]

process leads to a similar result. In the case of the 'stretch-twist-fold' dynamo the sign of the twist does not matter."

The driving flow of dynamos in stars and planets is energy-transporting convection. "Thermal convection is familiar to most of us from our daily experience; warm air rises and cooler air sinks. When a fluid is heated from below it overturns, provided the temperature gradient is large enough, which here means that it must not only be greater than the adiabatic temperature gradient (the Schwarzschild criterion) but it must also overcome stabilizing influences such as thermal and viscous diffusion, rotation, compositional gradients (the Ledoux criterion), and magnetic flux. An intuitive way to think about convection (and to derive the Schwarzschild and Ledoux criteria) is to consider a small isolated volume, or *parcel*, of fluid that will buoyantly rise like a hot air balloon if its density is less than that of its surroundings or sink like a stone if its density is greater (the parcel is assumed to be in pressure equilibrium with its surroundings so density and temperature are anticorrelated). [For a compressible medium, this is the conceptual framework behind mixing length theory which goes on to say that the parcel will lose its identity, dispersing into the background, after traveling a vertical distance of order a pressure scale height H_p . [...]

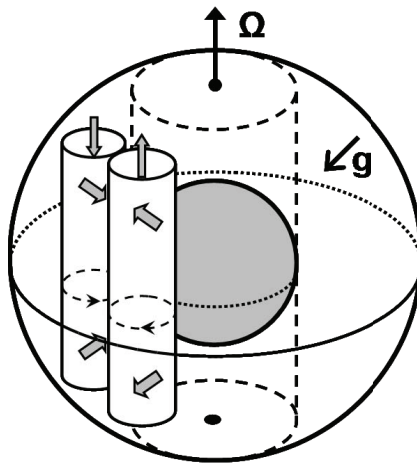


Figure 4.8: Columnar convection in a rotating spherical shell near onset. The inner core tangent cylinder is shown by broken lines. Under Earth’s core conditions the columns would be much thinner and very numerous. [Fig. III:7.6]

With this intuitive picture in mind, we may expect that the vertical scale of solar convection should vary tremendously from the deep convection zone where the stratification is relatively gentle ($H_p \sim 35$ Mm) to the solar surface layers where the density and pressure drop precipitously ($H_p \sim 36$ km) as [radiation escapes freely into space]. The associated drop in temperature near the surface triggers the recombination of hydrogen and other ions, which modifies the opacity, decreases the particle number density, and releases latent heat, altering the thermodynamics (in particular the equation of state and the specific heats) and contributing to the convective enthalpy transport. Add in radiative energy transfer and the result is what we call solar granulation; the continually shifting pattern (lifetime ~ 5 min) of small-scale convection cells (with a horizontal extent ~ 1 Mm) that blankets the solar surface and accounts for the dappled appearance of the solar photosphere (Fig. I:8.3).”

{A44}

Also the global-scale flows are important in the solar dynamo. The solar surface exhibits a differential rotation: the equator rotates faster than the poles, with a smooth latitudinal gradient between these. {A45} “Helioseismology now reveals that this monotonic decrease in angular velocity with increasing latitude persists throughout the convection zone, with an abrupt transition to nearly uniform rotation in the radiative interior (Fig. 4.7b). The transition region near the base of the convection zone is known as the solar tachocline [...]. There is also a less dramatic but no less significant *near-surface shear layer* in which the rotation rate systematically decreases by about 10-20 nHz from $r = 0.96R_\odot$ to the photosphere. This is most apparent at low latitudes but may also occur at higher latitudes. [...] {A46} {A47}

The striking difference in the rotation profile of the convective envelope and that of the radiative interior implicates convection as the primary source of the differential

{A44}

{A45}

III:5:2.3

{A46}

{A47}

rotation. Furthermore, it tells us that giant cells are large enough and slow enough to be influenced by the rotation of the star. The magnitude of nonlinear advection $[(\mathbf{v} \cdot \nabla \mathbf{v})]$ relative to the Coriolis force $[(\boldsymbol{\Omega} \times \mathbf{v})]$ is quantified by the [Rossby number:

$$N_R = \frac{v_t}{\Omega L_t}, \quad (4.2)$$

where v_t and L_t are characteristic velocity and length scale, respectively.] In the deep solar convection zone it is of order unity or less whereas it is much greater than unity in the solar surface layers. {A48} Coriolis-induced velocity correlations in the convection redistribute angular momentum via the Reynolds stress, generating a substantial rotational shear: $\Delta\Omega/\Omega \sim 30\%$ where $\Omega(r, \theta)$ is the angular velocity and $\Delta\Omega$ is the angular velocity difference between equator and pole. {A49} Furthermore, {A49} the nature of the redistribution is such that the angular velocity increases away from the rotation axis, $\partial\Omega/\partial d_\theta > 0$ where $d_\theta = r \sin(\theta)$ is [the distance to the axis of rotation]. This is in stark contrast to the behavior one would expect from isotropic turbulent diffusion (if $\Delta\Omega/\Omega \ll 1$) or from fluid parcels that tend to locally conserve their angular momentum as they move ($\partial\Omega/\partial d_\theta < 0$), [which would behave as sketched in Fig. 4.8]. Giant cells must be a global phenomenon distinct from supergranulation.”

These solar flow patterns are in striking contrast to what fluid motions in the planets are thought to look like: “the latter often tend to be quasi-two-dimensional. This is largely a consequence of rapid rotation. Planets are smaller than stars and generally spin faster (with the exception of compact remnants such as pulsars). In the fluid cores and mantles of terrestrial planets and the extended atmospheres of many gas giant planets, the convective time scales are much longer than the rotation period, implying very low Rossby numbers [...]. This gives rise to elongated, quasi-2D convective structures such that the flow is relatively invariant in the direction parallel to the rotation axis (Fig. 4.8). In the atmospheres and oceans of terrestrial planets, on the other hand, quasi-2D dynamics arises simply by virtue of the geometry; global-scale horizontal motions are confined to thin spherical shells.” III-5.5.4

4.4 Insights from approximate stellar dynamo models

Astrophysical dynamos have been studied for many decades, and whereas the fundamental ingredients may be known, there is no proper theory of dynamo action in stars and planets: there is no validated dynamo model that matches all stellar observations or that has been demonstrated to successfully forecast the Sun’s magnetism over multiple sunspot cycles, nor do planetary dynamo models successfully reproduce, for example, the quasi-irregular reversals in the terrestrial magnetic field. Nonetheless, dynamo concepts do guide our thinking as to the important ingredient processes as well as the possible internal structure and dynamics of both the magnetic field and the plasma/magma flows involved. The remainder of this chapter is an exploration of some of these to create a sense of how dynamos in stars and planets are thought to function.

“All solar and stellar dynamo models to be considered in this chapter operate within a sphere of electrically conducting fluid embedded in vacuum. We restrict ourselves III-6.1

here to axisymmetric mean-field-like models, in the sense that we will be setting and solving evolutionary equations for the large-scale magnetic field, and subsume the effects of small-scale fluid motions and magnetic fields into coefficients of these partial differential equations. Working in spherical polar coordinates (r, θ, ϕ) , we begin by writing:

$$\mathbf{v}(r, \theta) = \mathbf{v}_p(r, \theta) + d_\theta \Omega(r, \theta) \hat{\mathbf{e}}_\phi, \quad (4.3)$$

$$\mathbf{B}(r, \theta, t) = \nabla \times (\mathcal{A}(r, \theta, t) \hat{\mathbf{e}}_\phi) + \mathcal{B}(r, \theta, t) \hat{\mathbf{e}}_\phi, \quad (4.4)$$

where $d_\theta = r \sin(\theta)$, \mathbf{v}_p is a notational shortcut for the component of the large scale flow in meridional planes, and Ω is the angular velocity of rotation, which in the solar interior varies with both depth and latitude, and is now well-constrained by helioseismology. Note that in this prescription neither of these large-scale flow components is time dependent. This **kinematic approximation** is an assumption that is tolerably well-supported observationally. Substituting these expressions in the MHD induction equation in Eq. (3.3) allows separation into two coupled 2D partial differential equations for the scalar functions \mathcal{A} and \mathcal{B} defining respectively the poloidal and toroidal components of the magnetic field:

$$\frac{\partial \mathcal{A}}{\partial t} = \eta \left(\nabla^2 - \frac{1}{d_\theta^2} \right) \mathcal{A} - \frac{\mathbf{v}_p}{d_\theta} \cdot \nabla (d_\theta \mathcal{A}), \quad (4.5)$$

$$\begin{aligned} \frac{\partial \mathcal{B}}{\partial t} &= \eta \left(\nabla^2 - \frac{1}{d_\theta^2} \right) \mathcal{B} + \frac{1}{d_\theta} \frac{\partial (d_\theta \mathcal{B})}{\partial r} \frac{\partial \eta}{\partial r} - \\ & d_\theta \nabla \cdot \left(\frac{\mathcal{B}}{d_\theta} \mathbf{v}_p \right) + d_\theta (\nabla \times (\mathcal{A} \hat{\mathbf{e}}_\phi)) \cdot \nabla \Omega, \end{aligned} \quad (4.6)$$

where we retain the possibility that η varies with depth. The shearing term ($\propto \nabla \Omega$) on the right-hand side of Eq. (4.6) acts as a source of toroidal field. However, no such source term appears in Eq. (4.5). This is the essence of Cowling’s theorem which in fact guarantees that an axisymmetric flow of the general form given by Eq. (4.3) *cannot* act as a dynamo for an axisymmetric magnetic field as described by Eq. (4.4). The construction of solar and stellar dynamo models, therefore, hinges critically on the addition of an extraneous source term in Eq. (4.5). The physical origin of this source term is what fundamentally distinguishes the various classes of solar and stellar dynamo models described [below].

Shearing of the poloidal magnetic field into a strong toroidal component by differential rotation [(as illustrated in Fig. 4.9)] is an essential ingredient of all solar cycle models discussed below. The growing magnetic energy of the toroidal field is supplied by the kinetic energy of the rotational shearing motion, which makes for an attractive field amplification mechanism, because in the Sun and stars the available supply of rotational kinetic energy is immense (unless the dynamo were entirely confined to a very thin layer, for example the tachocline, [the shear layer just below the Sun’s convective envelope into which convection overshoots]). Moreover, a strong, axisymmetric and temporally quasi-steady internal differential rotation is likely responsible for the

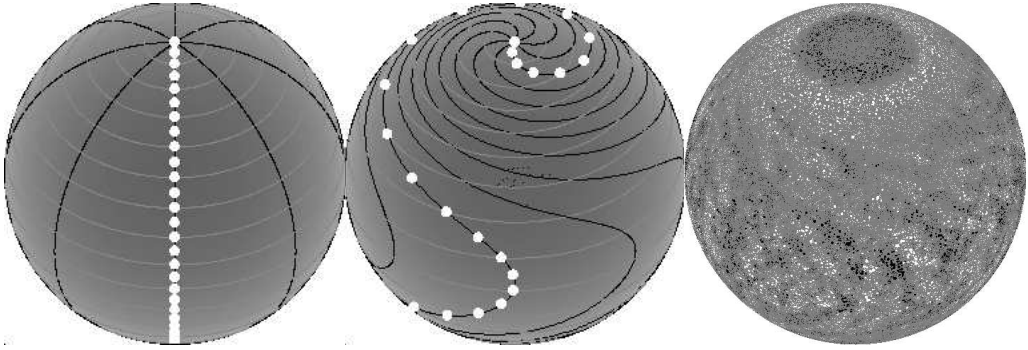


Figure 4.9: Left and center: Visualization of the effects of differential rotation and equator-to-pole meridional flow for Sun-like conditions: lines of equal longitude (with markers) are distorted into a spiral pattern. The center panel shows the distorted lines after 3 months. Right: Simulated magnetogram for a star like the Sun, [simulated with a flux-transport model with parameters as observed for the Sun,] but with an active-region emergence rate 30 times larger. The simulated star is shown from a latitude of 40° to better show the polar-cap field structure. [Fig. III:2.3]

observed high degree of axisymmetry observed in the Sun’s magnetic field on spatial scales comparable to its radius. This situation is very different from that encountered in planetary core dynamos, where differential rotation is believed to be much weaker, and energetics pose a much stronger constraint on dynamo action. Lacking the large-scale organization provided by differential rotation, planetary core dynamos also tend to produce non-axisymmetric large-scale fields. The one outstanding exception appears to be Saturn, and indeed in this case the high axisymmetry of the observed surface field may well reflect the symmetrizing action of differential rotation in the envelope overlying the metallic-hydrogen core. The important point remains that in the solar dynamo context, the assumption of an axisymmetric large-scale magnetic field is consistent with the observed and helioseismically-inferred axisymmetry and quasi-steadiness of internal differential rotation.”

4.5 Mean-field dynamo models

“Turbulence at a high magnetic Reynolds number \mathcal{R}_m [(Eq. 3.18)] is known to be quite effective at producing a lot of small-scale magnetic fields, where ‘small-scale’ is roughly $\mathcal{R}_m^{-1/2}$ times the length scale of the flow. In addition, under certain conditions, solar/stellar convective turbulence can also produce magnetic fields with a mean component building up on large spatial scales. These **mean-field dynamo models** remain arguably the most ‘popular’ descriptive models for dynamo action in the Sun and stars, but also in planetary metallic cores, stellar accretion disks, and even galactic disks.

Under the assumption that a good separation of scales exists between the large-scale

'laminar' magnetic field $\overline{\mathbf{B}}$ and the flow $\overline{\mathbf{v}}$, and the small-scale turbulent field \mathbf{B}' and flow \mathbf{v}' , it becomes possible to express the inductive and diffusive action of the turbulence on $\overline{\mathbf{B}}$ in terms of the statistical properties of the small-scale flow and field. {A50}

The corresponding theory of mean-field electrodynamics is discussed in detail in Ch. I:3. The turbulent flow introduces on the right-hand side of the induction equation Eq. (3.3) a term of the form $\nabla \times \overline{\mathcal{E}}$, where $\overline{\mathcal{E}}$ is a mean-electromotive force."

For a quick introduction to the origin of that term we can see what happens when "we decompose the magnetic field into a large-scale 'mean' field and the small-scale components through an averaging procedure. We assume in the following that the averaging procedure obeys the Reynolds rules: For any function f and g decomposed as $f = \overline{f} + f'$ and $g = \overline{g} + g'$, where the bar indicates the averaged and the prime the fluctuating quantity, we require that

$$\overline{\overline{f}} = \overline{f} \longrightarrow \overline{f'} = 0 \quad (4.7)$$

$$\overline{f + g} = \overline{f} + \overline{g} \quad (4.8)$$

$$\overline{f'g'} = \overline{f'g} \longrightarrow \overline{f'g} = 0 \quad (4.9)$$

$$\overline{\partial f / \partial x_i} = \partial \overline{f} / \partial x_i \quad (4.10)$$

$$\overline{\partial f / \partial t} = \partial \overline{f} / \partial t. \quad (4.11)$$

The averaging procedures that are of interest in the context of mean-field theory are the ensemble average (meaning a chaotic system is averaged over several representations of the chaotic system) and the longitudinal average, in which $\overline{\mathbf{B}}$ reflects the axisymmetric component of the large-scale magnetic field (multipole series with $m = 0$)." "In order to derive an equation for the time evolution of the mean field we apply the averaging procedure to the induction equation Eq. (3.3) which leads to

$$\frac{\partial \overline{\mathbf{B}}}{\partial t} = \nabla \times (\overline{\mathbf{v}' \times \mathbf{B}'} + \overline{\mathbf{v}} \times \overline{\mathbf{B}} - \eta \nabla \times \overline{\mathbf{B}}). \quad (4.12)$$

The new term which enters this equation compared to the original induction equation is the second order correlation electromotive force (EMF)

$$\overline{\mathcal{E}} \equiv \overline{\mathbf{v}' \times \mathbf{B}'}. \quad (4.13)$$

While the fluctuating velocity component \mathbf{v}' is assumed to be known (kinematic approach), \mathbf{B}' has to be computed from the induction equation. An equation for \mathbf{B}' can be derived by subtracting the mean-field induction equation Eq. (4.12) from the microscopic induction equation Eq. (3.3), which leads to

$$\frac{\partial \mathbf{B}'}{\partial t} = \nabla \times (\mathbf{v}' \times \overline{\mathbf{B}} + \overline{\mathbf{v}} \times \mathbf{B}' - \eta \nabla \times \mathbf{B}' + \mathbf{v}' \times \mathbf{B}' - \overline{\mathbf{v}' \times \mathbf{B}'}). \quad (4.14)$$

It is in general only possible to solve this equation by making strong assumptions, primarily because of the terms that are quadratic in the fluctuating quantities (closure problem)." For a more detailed description, see Sect. I:3.4.3. Here, we proceed with one

particular such assumption that leads to the conclusion that for “mildly inhomogeneous and near-isotropic turbulence, $\overline{\mathcal{E}}$ can be expressed in terms of the large-scale field $\overline{\mathbf{B}}$ as:

$$\overline{\mathcal{E}} = \alpha \overline{\mathbf{B}} - \beta \nabla \times \overline{\mathbf{B}}, \quad (4.15)$$

with

$$\alpha = -\frac{1}{3} \tau_{\text{corr}} \overline{\mathbf{v}' \cdot (\nabla \times \mathbf{v}')} \quad [\text{cm s}^{-1}], \quad \beta = \frac{1}{3} \tau_{\text{corr}} \overline{\mathbf{v}'^2} \quad [\text{cm}^2 \text{s}^{-1}], \quad (4.16)$$

where τ_{corr} is the correlation time for the turbulent flow. Note that the α -term is proportional to the (negative) kinetic helicity $[(\mathbf{v}' \cdot (\nabla \times \mathbf{v}'))]$ of the turbulence, which requires a break of reflectional symmetry. In stellar interiors and planetary metallic cores alike, this anisotropy is provided by the Coriolis force. Small-scale turbulence thus impacts the induction equation for the mean-field in two ways: it introduces a field-aligned electromotive force (the α -term), which acts as a source term and is called the ‘ α -effect’, and an enhanced ‘turbulent diffusion’ (the β -term), associated with the folding action of the turbulent flow. In principle, the α and β coefficients can be calculated from the lowest-order statistics of the turbulent flow. In practice, more often than not they are chosen *a priori*, although with care taken to embody in these choices what can be learned from mean-field theory. {A51}

Under mean-field dynamo theory, Eqs. (4.5)–(4.6) are now taken to apply to an axisymmetric large-scale mean magnetic field. With the inclusion of the mean-field α -effect and turbulent diffusivity, scaling all lengths in terms of the radius R of star or planet, and time in terms of the diffusion time {A51}

$$\tau_d = R^2 / \eta \quad (4.17)$$

based on the (turbulent) diffusivity in the convective envelope, these expressions become

$$\frac{\partial \mathcal{A}}{\partial t} = \eta \left(\nabla^2 - \frac{1}{d_\theta^2} \right) \mathcal{A} - \frac{\mathcal{R}_m}{d_\theta} \mathbf{v}_p \cdot \nabla (d_\theta \mathcal{A}) + C_\alpha \alpha \mathcal{B}, \quad (4.18)$$

$$\begin{aligned} \frac{\partial \mathcal{B}}{\partial t} = & \eta \left(\nabla^2 - \frac{1}{d_\theta^2} \right) \mathcal{B} + \frac{1}{d_\theta} \frac{\partial (d_\theta \mathcal{B})}{\partial r} \frac{\partial \eta}{\partial r} - \mathcal{R}_m d_\theta \nabla \cdot \left(\frac{\mathcal{B}}{d_\theta} \mathbf{v}_p \right) + \\ & C_\Omega d_\theta (\nabla \times (\mathcal{A} \hat{\mathbf{e}}_\phi)) \cdot (\nabla \Omega) + C_\alpha \hat{\mathbf{e}}_\phi \cdot \nabla \times [\mathcal{A} \nabla \times (\mathcal{A} \hat{\mathbf{e}}_\phi)]. \end{aligned} \quad (4.19)$$

We continue to use the symbol η for the total diffusivity, with the understanding that within the convective envelope this now includes the (dominant) contribution from the β -term of mean-field theory. Three non-dimensional numbers have materialized:

$$C_\alpha = \frac{\alpha_t R}{\eta}, \quad C_\Omega = \frac{\Omega_t R^2}{\eta}, \quad \mathcal{R}_m = \frac{u_t R}{\eta}, \quad (4.20)$$

with α_t , u_t , and Ω_t as reference values for the α -effect, meridional flow and envelope rotation, respectively. The quantities C_α and C_Ω are *dynamo numbers*, measuring the importance of inductive versus diffusive effects on the right-hand side of Eqs. (4.18)–(4.19). The magnetic Reynolds number \mathcal{R}_m here measures the relative importance of

advection versus diffusion in the transport of A and B in meridional planes. {A52}

Structurally, Eqs. (4.18)–(4.19) only differ from Eqs. (4.5)–(4.6) by the presence of two new source terms on the right-hand side, both associated with the α -effect. The appearance of this term in Eq. (4.18) is crucial for evading Cowling’s theorem.” {A52}

In what follows in this section, we first look at a simplified, linear mean-field dynamo model to illustrate the geometry and temporal evolution. Later, we look at non-linearities that lead to amplification and saturation of the field, and to the modulation of the magnetic cycles. First, the linear model: “In constructing mean-field dynamos for the Sun, it has been a common procedure to neglect meridional circulation, because it is a very weak flow. It is also customary to drop the α -effect term on the right-hand side of Eq. (4.19) on the grounds that with $R \simeq 7 \times 10^{10}$ cm, $\Omega_t \sim 10^{-6}$ rad s^{-1} , and $\alpha_t \sim 10^2$ cm s^{-1} , one finds $C_\alpha/C_\Omega \sim 10^{-3}$, independently of the assumed (and poorly constrained) value for η . Equations (4.18)–(4.19) then reduce to the so-called **$\alpha\Omega$ dynamo equations**. In the spirit of producing a model that is solar-like we use a fixed value $C_\Omega = 2.5 \times 10^4$, obtained by assuming [an equatorial angular velocity of] $\Omega_{\text{Eq}} \simeq 10^{-6}$ rad s^{-1} and $\eta = 50$ km 2 s^{-1} , which leads to a diffusion time $\tau_d = R^2/\eta \simeq 300$ yr.

For the total magnetic diffusivity, we use a steep but smooth variation of η from a high value (η_{CZ}) in the convection zone to a low value (η_{core}) in the underlying core [...]. A typical profile is shown in Fig. 4.10A (dash-dotted line). In practice, the core-to-envelope diffusivity ratio $\Delta\eta \equiv \eta_{\text{core}}/\eta_{\text{CZ}}$ is treated as a model parameter, with of course $\Delta\eta \ll 1$, because we associate η_{core} with the microscopic magnetic diffusivity, and η_{CZ} with the presumably much larger mean-field turbulent diffusivity. Taking at face values estimates from mean-field theory, one should have $\Delta\eta \sim 10^{-9}$ to 10^{-6} . The solutions discussed below have $\Delta\eta = 10^{-3}$ to 10^{-1} , which is still small enough to illustrate important effects of radial gradients in total magnetic diffusivity.

All solar dynamo models discussed in this chapter utilize the helioseismically-calibrated solar-like parametrization of solar differential rotation [...]. The corresponding angular velocity contour levels are plotted in Fig. 4.10B. Such a solar-like differential rotation profile is quite complex from the point of view of dynamo modelling, in that it is characterized by multiple partially overlapping shear regions: a rotational shear layer, straddling the core-envelope interface, known as the *tachocline*, with a strong positive radial shear in its equatorial regions and an even stronger negative radial shear in its polar regions, as well as a significant latitudinal shear throughout the convective envelope and extending partway into the tachocline; for a tachocline of half-thickness $w/R_\odot = 0.05$, the mid-latitude latitudinal shear at $r/R_\odot = 0.7$ is comparable in magnitude to the equatorial radial shear, and its potential contribution to toroidal field production cannot be casually dismissed.

For the dimensionless function $\alpha(r, \theta)$ we use an expression [...] that concentrates the α -effect in the bottom half of the envelope, and lets it vanish smoothly below, just as the net magnetic diffusivity does (see Fig. 4.10A). Various lines of argument point to an α -effect peaking in the bottom half of the convective envelope, because there the convective turnover time is commensurate with the solar rotation period, a

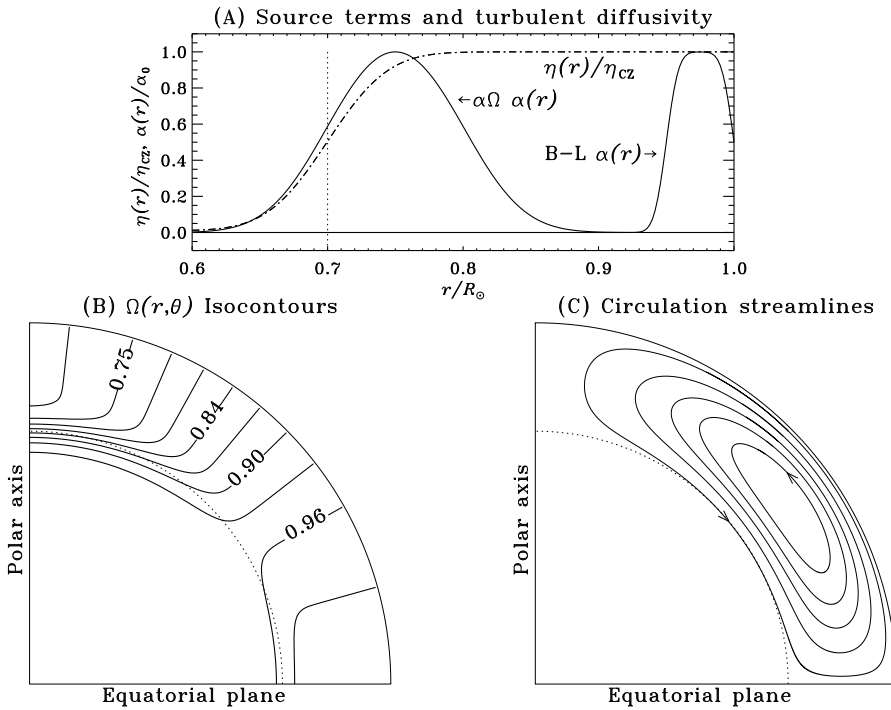


Figure 4.10: Various 'ingredients' for the dynamo models constructed in this chapter. Part (A) shows radial profiles of the total magnetic diffusivity η and poloidal source [terms: $\alpha(r)$ for the $\alpha\Omega$ dynamo and for the Babcock-Leighton (B-L) dynamo]. Part (B) shows contour levels of the rotation rate $\Omega(r, \theta)$ normalized to its surface equatorial value. The dotted line is the core-envelope interface at $r/R_\odot = 0.7$. Part (C) shows streamlines of meridional circulation, included in some of the dynamo models discussed below. [Helioseismic studies suggest that the meridional flow in the Sun is more complex than a single 'roll' of the flow, but that there may be (at least) two stacked on top of each other. A key point for a flux-transport dynamo is that the meridional flow at the base of the convective envelope is equatorward. Fig. III:6.1]

most favorable setup for the type of toroidal field twisting at the root of the α -effect (see Fig. I:3.5). [The choice made here for $\alpha(r, \theta)$ scales with latitude as $\cos \theta$, which] reflects the hemispheric dependence of the Coriolis force, which also suggests that the α -effect should be positive in the Northern hemisphere. The dimensionless number C_α , which measures the strength of the α -effect, is treated as a free parameter of the model. [...]

In such linear $\alpha\Omega$ models the onset of dynamo activity turns out to be controlled by the *product* of C_α and C_Ω :

$$D \equiv C_\alpha \times C_\Omega = \frac{\alpha_t \Omega_t R^3}{\eta_{CZ}^2}. \quad (4.21)$$

with positive growth rates materializing above a threshold value known as the *critical*

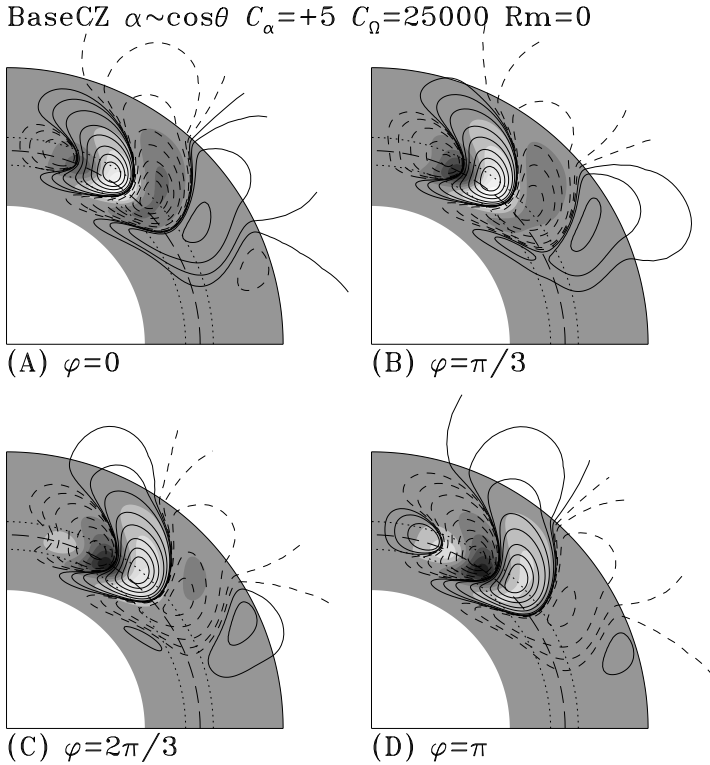


Figure 4.11: Four snapshots in meridional planes of our minimal linear $\alpha\Omega$ dynamo solution with defining parameters $C_\Omega = 25000$, $\Delta\eta = 0.1$, and $\eta_{CZ} = 50 \text{ km}^2/\text{s}$. With $C_\alpha = +5$, this is a mildly supercritical solution, with oscillation frequency $\omega \simeq 300 \tau_d^{-1}$ (see Eq. 4.17). The toroidal field is plotted as filled contours (gray to black for negative B , gray to white for positive B , normalized to the peak strength and with increments $\Delta B = 0.2$), on which poloidal field lines are superimposed (solid for clockwise-oriented field lines, dashed for counter-clockwise orientation). The long-dashed line is the core-envelope interface at $r/R_\odot = 0.7$. [Fig. III:6.2]

dynamo number. [...]

Figure 4.11 shows half a cycle of the dynamo solution, in the form of snapshots of the toroidal (gray scale) and poloidal eigenfunctions (field lines) in a meridional plane, with the symmetry axis defined by the stellar rotation oriented vertically. The four frames are separated by a phase interval $\varphi = \pi/3$, so that panel (D) is identical to panel (A) except for reversed magnetic polarities in both magnetic components [halfway through the cycle with period $P_{\text{cycle}} = 2\pi/\omega$]. Such linear eigensolutions leave the absolute magnitude of the magnetic field undetermined, but the relative magnitude of the poloidal to toroidal components is found to scale approximately as $|C_\alpha/C_\Omega|$.

The [model's magnetic field] is concentrated in the vicinity of the core-envelope interface, and has very little amplitude in the underlying, low-diffusivity radiative core. This is due to the oscillatory nature of the solution, which restricts penetration into

the core to a distance of the order of the electromagnetic skin depth $\ell_{\text{skin}} = \sqrt{2\eta_{\text{core}}/\omega}$. Having assumed $\eta_{\text{CZ}} = 50 \text{ km}^2\text{s}^{-1}$, with $\Delta\eta = 0.1$, a dimensionless dynamo frequency $\omega \simeq 300$ corresponds to $3 \times 10^{-8} \text{ s}^{-1}$, so that $\ell_{\text{skin}}/R \simeq 0.026$, quite small indeed.

Careful examination of Fig. 4.11(A)→(D) also reveals that the toroidal-poloidal flux systems present in the shear layer first show up at high latitudes, and then *migrate equatorward* to finally disappear at mid-latitudes in the course of the half-cycle. These *dynamo waves* travel in a direction given by $\alpha\nabla\Omega \times \hat{\mathbf{e}}_\phi$, *i.e.*, along contours of equal angular velocity, a result known as the *Parker-Yoshimura sign rule*. Here with a negative $\partial\Omega/\partial r$ in the high-latitude region of the tachocline, a positive α -effect results in an equatorward propagation of the dynamo wave, in qualitative agreement with the observed equatorward drift of the latitudes of sunspot emergences as the solar cycle unfolds (see Fig. 4.5).”

“Obviously, the exponential growth characterizing supercritical linear solutions must stop once the Lorentz force associated with the growing magnetic field becomes dynamically significant for the inductive flow. Because the solar surface and internal differential rotation show little variation with the phase of the solar cycle, it is usually assumed that magnetic back-reaction occurs at the level of the α -effect. In the mean-field spirit of *not* solving dynamical equations for the small-scales, it has become common practice to introduce an *ad hoc* algebraic nonlinear quenching of α directly on the mean-toroidal field B by writing:

$$\alpha \rightarrow \alpha(B) = \frac{\alpha_t}{1 + (B/B_{\text{eq}})^2} . \quad (4.22)$$

where $B_{\text{eq}} = (4\pi\rho u_t^2)^{1/2}$ is the equipartition field strength, of order 10^4 G at the base of the solar convective envelope. Needless to say, this simple **α -quenching** formula is an *extreme* oversimplification of the complex interaction between flow and field that is known to characterize MHD turbulence, but its wide usage in solar dynamo modeling makes it the nonlinearity of choice for the illustrative purpose of this [chapter: with this description, the only MHD equation that needs solving to experiment with dynamo action – as we do here – is the induction equation Eq. (3.3) that is now subjected to a parameterized coupling between the small-scale flow and field that may or may not be an appropriate approximation of reality. Note that α can, and in many models now is, time dependent, leading to what is called ‘dynamical α -quenching’.]

Introducing α -quenching in our model renders the $\alpha\Omega$ dynamo equations nonlinear, so that solutions are now obtained as initial-value problems starting from an arbitrary seed field of very low amplitude, in the sense that $B \ll B_{\text{eq}}$ everywhere in the domain. [...] At early times, $B \ll B_{\text{eq}}$ and the equations are effectively linear, leading to exponential growth [...]. Eventually, however, B becomes comparable to B_{eq} in the region where the α -effect operates, leading to a break in exponential growth, and eventual saturation.

The saturation energy level increases with increasing C_α , an intuitively satisfying behavior because solutions with larger C_α have a more vigorous poloidal source term. The cycle frequency for these solutions is very nearly independent of the dynamo

number, and is slightly *smaller* than the frequency of the linear critical mode (here by some 10 – 15%), a behavior that is typical of kinematic α -quenched mean-field dynamo models. Yet the overall form of the dynamo solutions very closely resembles that of the linear eigenfunctions plotted in Fig. 4.11.”

“The α -quenching expression in Eq. (4.22) implies that dynamo action saturates once the mean, dynamo-generated large-scale magnetic field reaches an energy density comparable to that of the driving small-scale turbulent fluid motions. However, various calculations and numerical simulations have indicated that long before the mean toroidal field B reaches this strength, the helical turbulence reaches equipartition with the *small-scale* turbulent component of the magnetic field. Such calculations also suggest that the ratio between the small-scale and mean magnetic components should itself scale as $\mathcal{R}_m^{1/2}$, where $\mathcal{R}_m = v_t L_t / \eta$ is a magnetic Reynolds number based on the turbulent speed but *microscopic* magnetic diffusivity. This then leads to the alternative quenching expression

$$\alpha \rightarrow \alpha(B) = \frac{\alpha_t}{1 + \mathcal{R}_m (B/B_{\text{eq}})^2} , \quad (4.23)$$

known in the literature as **strong α -quenching** or *catastrophic quenching* (see Ch. I:3 in Vol. I). Because $\mathcal{R}_m \sim 10^8$ in the solar convection zone, this leads to quenching of the α -effect for very low amplitudes of the mean magnetic field, of order 0.1 G. Even though significant field amplification is likely in the formation of a toroidal flux rope from the dynamo-generated magnetic field, we are now a very long way from the $10^4 - 10^5$ G demanded by simulations [needed for buoyantly rising flux ropes to survive emergence and to eventually lead to] sunspot formation.

[One] way out of this difficulty exists in the form of **interface dynamos**. The idea is beautifully simple: to produce and store the toroidal field away from where the α -effect is operating. [...] in a situation where a radial shear and α -effect are segregated on either side of a discontinuity in magnetic diffusivity taken to coincide with the core-envelope interface, the constant coefficient, cartesian form of the $\alpha\Omega$ dynamo equations support solutions in the form of traveling surface waves localized on the discontinuity in diffusivity. For supercritical dynamo waves, the ratio of peak toroidal field strength on either side of the discontinuity surface is found to scale as $(\eta_{\text{CZ}}/\eta_{\text{core}})^{-1/2}$. With the core diffusivity η_{core} equal to the microscopic value, and if the envelope diffusivity is of turbulent origin so that $\eta_{\text{CZ}} \sim L_t v_t$, then the toroidal field strength ratio scales as $\sim (v_t L_t / \eta_{\text{core}})^{1/2} \equiv \mathcal{R}_m^{1/2}$. This is precisely the factor needed to bypass strong α -quenching, at least as embodied in Eq. (4.23).”

So far, this discussion has ignored the large-scale flow system known as meridional circulation. Such a flow “is unavoidable in turbulent, compressible rotating convective shells. The $\sim 15 \text{ m s}^{-1}$ poleward flow observed at the surface has been detected helioseismically, down to $r/R_\odot \simeq 0.85$ without significant departure from the poleward direction, except locally and very close to the surface, in the vicinity of active region belts. Mass conservation requires an equatorward flow deeper down [(helioseismic measurements suggest that there may be two meridional overturning cells stacked

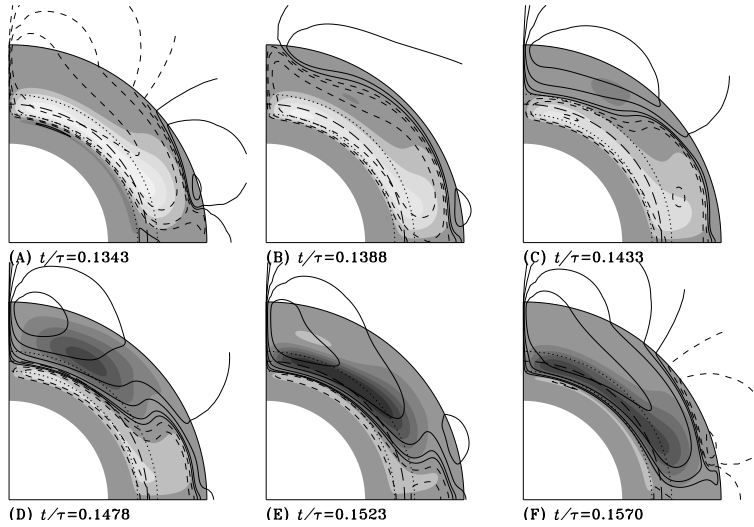


Figure 4.12: [Snapshots covering half a cycle of a Babcock-Leighton dynamo solution. The grey-scale coding of the toroidal field and poloidal field lines is as in Fig. 4.11.] This solution uses the same differential rotation, magnetic diffusivity and meridional circulation profile as for the advection-dominated $\alpha\Omega$ solution but now with the non-local surface source term as shown in Fig. 4.10(A) in the curve labeled 'B-L', with parameter values $C_\alpha = 5$, $C_\Omega = 5 \times 10^4$, $\Delta\eta = 0.003$, $\mathcal{R}_m = 840$. Note the strong amplification of the surface polar fields, and the latitudinal stretching of poloidal field lines by the meridional flow at the core-envelope interface. [Fig. III:6.6]

within the convective envelope, but confirmation is still pending of what is a challenging measurement close to the noise levels of helioseismology)].

Meridional circulation can bodily transport the dynamo-generated magnetic field (terms $\propto \mathbf{v}_p \cdot \nabla$ in Eqs. (4.5)–(4.6)). At low circulation speeds, the primary effect is a Doppler shift of the dynamo wave, leading to a small change in the cycle period and equatorward concentration of the activity belts. However, for a (presumably) solar-like equatorward return flow that is vigorous enough, it can overpower the Parker-Yoshimura propagation rule and produce equatorward propagation no matter what the sign of the α -effect is. The behavioral turnover from dynamo wave-like solutions sets in when the circulation speed in the dynamo region becomes comparable to the propagation speed of the dynamo wave. In this advection-dominated regime, the cycle period loses sensitivity to the assumed turbulent diffusivity value, and becomes determined primarily by the circulation's turnover time. Solar cycle models achieving equatorward migration of activity belts in this manner are often called **flux transport dynamos**. [...]

One interesting consequence [of meridional circulation] is that induction of the toroidal field is now effected primarily by the *latitudinal* shear within the tachocline, with the radial shear, although larger in magnitude, playing a lesser role because $B_r/B_\theta \ll 1$. The meridional flow also has a profound impact on the magnetic field evolution at $r = R$, as it concentrates the poloidal field in the polar regions. This leads

to a large amplification factor through magnetic flux conservation, so [these dynamo models] are typically characterized by very large polar field strengths, here some 20% of the toroidal field magnitude in the tachocline, even though we have here $C_\alpha/C_\Omega = 10^{-6}$. This concentrated poloidal field, when advected downwards to the polar regions of the tachocline, is responsible for the strong polar branch often seen in the time-latitude diagram of dynamo solutions including a rapid meridional flow. This difficulty can be alleviated, at least in part, by a number of relatively minor modifications to the model, such as the addition of a high- η subsurface layer, or displacement of the meridional flow cell towards lower latitudes, thus reducing the degree of polar convergence. [...]"

Yet another incarnation of solar cycle models is based on active region decay and dispersal. These go back to 1961 when Babcock “suggested that the polarity reversals of the high-latitude surface magnetic field are driven by the accumulation of magnetic fields released at low latitudes by the decay of bipolar magnetic regions. Figure 4.9 shows a numerical simulation illustrating this process, which leads to the buildup of a net poloidal hemispheric flux because the trailing member of the pair tends to be located at higher latitudes than the leading component, a pattern known as Joy’s rule, and therefore are subjected to less transequatorial dissipative flux cancellation than the leading members of the bipolar pair. Babcock went on to argue that in conjunction with shearing by differential rotation, this could explain the observed patterns of solar cycle polarity reversals. In subsequent years [he] turned this idea into a *bona fide* solar cycle model, known since as the **Babcock-Leighton model**. [...] The key point, from the dynamo perspective, is that the Babcock-Leighton mechanism taps into the (formerly) toroidal flux in the bipolar magnetic region to produce a poloidal magnetic component, and so can act as a source term on the right-hand side of Eq. (4.5). [...]

{A53} {A54}

To the degree that a positive dipole moment is being produced from a toroidal field that is positive in the N-hemisphere, this is operationally equivalent to a positive α -effect in mean-field theory. In both cases the Coriolis force is the agent imparting a twist on a magnetic field; with the α -effect this process occurs on the small spatial scales and operates on individual magnetic field lines. In contrast, the Babcock-Leighton mechanism operates on the large scales, the twist being imparted via the Coriolis force acting on the flow generated along the axis of a buoyantly rising magnetic flux tube that, upon emergence, gives rise to sunspot pairs. {A55}

Numerous dynamo models based on this mechanism of poloidal field regeneration have been constructed, based on the axisymmetric mean-field dynamo equations but with the α -effect replaced by a suitably designed source term on the right-hand side of Eq. (4.18). One important difference with the mean-field $\alpha\Omega$ models considered earlier is that the two source regions are now spatially segregated: production of the toroidal field takes place in or near the tachocline, as before, but now production of the poloidal field is restricted to the surface layers. A transport mechanism is then required to link the two source regions for a dynamo loop to operate. [... Most Babcock-Leighton models use the meridional circulation for this, which acts] as a form of conveyor belt, concentrating to high latitudes the surface magnetic fields released by the decay of

active regions, and dragging it down to the tachocline where shearing by differential rotation leads to the buildup of a new toroidal flux system, and thus to the onset of a new sunspot cycle. [...]

Figure 4.12 shows a series of meridional-plane snapshots of one such Babcock-Leighton dynamo solution, covering one sunspot cycle and starting approximately at sunspot maximum (based on magnetic energy as a proxy for sunspot number). Surface poloidal flux from the current cycle has begun to build up at low latitudes, and is rapidly swept to the pole, with polarity reversal of the polar field taking place shortly thereafter (panel B). As with the advection-dominated $\alpha\Omega$ solution discussed above, this solution is characterized by strong surface polar fields resulting from the poleward transport by the meridional flow of the poloidal component produced at lower latitudes, and the equatorward propagation of the toroidal field in the tachocline is also driven by the meridional flow. The turnover time of the meridional flow is here again the primary determinant of the cycle period. With $\eta = 30 \text{ km}^2 \text{ s}^{-1}$, this solution has a nicely solar-like half-period of 12.4 yr. All in all, this is once again a reasonable representation of the cyclic spatiotemporal evolution of the solar large-scale magnetic field.” {A56}

There are yet other non-linearities that can be considered in solar/stellar dynamo models. For example, in “the presence of stratification and rotation, a number of hydrodynamical (HD) and magnetohydrodynamical (MHD) instabilities associated with the presence of a strong toroidal field in the stably stratified, radiative portion of the tachocline can lead to the growth of disturbances with a net helicity, which under suitable circumstances can produce a toroidal electromotive force, and therefore act as a source of poloidal field. Different types of solar cycle models have been constructed in this manner. In nearly all cases the resulting dynamo models end up being described by something closely resembling the axisymmetric mean-field dynamo equations, the novel poloidal field regeneration mechanisms being once again subsumed in an α -effect-like source term appearing on the right-hand side of Eq. (4.18).” More on this in Sect. III:6.2.3. {A56}

The models discussed thus far all lead to a steadily repeating magnetic cycle, where appropriate after an initial growth phase. The Sun, however, displays a rather erratic modulation of its activity from one cycle to the next, “and certain aspects of the observed fluctuations may actually hold important clues as to the physical nature of the dynamo process.” Section III:6.3 discusses some of these processes, including those that could be responsible for long-term modulations of the solar cycle pattern (such as the Maunder Minimum): stochastic effects (with strong evidence from both models and observations for the importance of the scatter on tilt angles of active regions that reflect the influence of random convective flows during the rise of the flux to the surface), back reaction of the field on the flow patterns, and time delays through transport processes. Section III:6.3.5 discusses issues related to the forecasting of the solar cycle based on precursor signatures. {A57}

4.6 Dynamos in other stars

“Figure 4.1 illustrates, in schematic form, the internal structure of main-sequence stars, more specifically the presence or absence of convection zones. A *G*-star like the Sun has a thick outer convection zone, spanning the outer 30% in radius. As one moves to lower masses, the relative thickness of the convective envelope increases until, somewhere around spectral type *M5*, stars become fully convective [(see Fig. 4.2 for an HR diagram and indications of spectral types)]. Moving from the Sun to higher masses, the convective envelope becomes ever thinner, until somewhere around spectral type *A0* it essentially vanishes. However, at around the same spectral type hydrogen [fusion] switches from the proton-proton (or *p-p*) chain to the CNO cycle, for which nuclear reaction rates are much more sensitively dependent on temperature. Core energy release becomes strongly depth-dependent, leading to convectively unstable temperature gradients. The resulting small convective core grows in size as one moves up to larger masses. In an early *B*-star of solar metallicity, the convective core spans the inner 25% or so in radius of the star.

Main-sequence stars of the *O* and *B* [spectral type] combine vigorous core-convection and high rotation rates, which makes dynamo action more than likely. This expectation has been amply confirmed by 3D MHD numerical simulations of dynamo action in the convective cores of massive stars. [...] All these core dynamo models have one thing in common: the large [diffusivity contrast $\eta_{\text{core}}/\eta_{\text{envelope}}$ between the convective core and the stably stratified envelope] leads to a ‘trapping’ of the magnetic field in the lower part of the radiative envelope, a direct consequence of the difficulty experienced by an externally-imposed magnetic field to diffusively penetrate a good electrical conductor [(analogous to, but here the inverse of, the ‘skin depth’ issue that was discussed in Section 4.5 for a cooler star) ...] This long-recognized property of stellar core dynamos represents a rather formidable obstacle to be bypassed if the magnetic fields generated by dynamo action in convective cores are to become observable at the stellar surface [... In fact, in] a time-dependent situation where the core dynamo ‘turns on’ at or shortly before [a young star settles into a stable equilibrium represented by] the arrival on the zero-age main sequence, the time needed for the magnetic field to resistively diffuse to the surface can become larger than the star’s main-sequence lifetime, for masses in excess of about $5 M_{\odot}$.” (More on formation and evolution of stars in Ch. 10.)

“Stars with spectral types ranging from late-*B* to early-*F* ^[9] stand out as the least likely to support dynamo action, because they lack a convective region of substantial size. This squares well with various lines of observations; in particular, main-sequence *A*-stars are among the most ‘magnetically quiet’ stars in the HR diagram. A subset of late-*B* and *A* stars, namely the slowly-rotating, chemically peculiar *Ap/Bp* stars, do show strong magnetic fields, but even those show no sign of anything even mildly analogous to solar activity. The single pattern of temporal evolution noted is a decrease,

⁹ In stellar parlance, ‘late’ means ‘cooler’ and ‘early’ hotter. ‘late-*B*’ thus refers to *Bn*-type stars on the cooler side of the HR diagram, with digits *n* closer to 9 than to 0. ‘Late type stars’ is often used synonymously with ‘cool stars’, which refers to stars with convective envelopes immediately below their surface; see Fig. 4.2.

by factors of 2 to 3, in the overall strength of the surface field, most prominent in the early stages of main-sequence evolution. This seems compatible with the idea of diffusive decay of residual higher-degree eigenmodes, and slow decreases associated with flux conservation as the stars slowly expand in the course of their main-sequence evolution. For these reasons, the fossil field hypothesis remains the favored explanatory model for the magnetic field of Ap stars. It is also quite striking that the high field strength observed in Ap stars (a few times 10^4 G), in magnetized white dwarfs ($\sim 10^9$ G), and in the most intensely magnetized neutron stars ($\sim 10^{15}$ G) all amount to [a] total surface magnetic flux $\sim 10^{27}$ Mx, lending support to the idea that these high fields can be understood from simple flux-freezing arguments [along an evolutionary timeline for these objects] (see Ch. I:3). [...]”

“Until strong evidence to the contrary is brought to the fore, we are allowed to assume that late-type stars⁹ with a thick convective envelope overlying a radiative core host a solar-type dynamo. Observationally, a lot of what we know regarding dynamo activity in solar-type stars comes from the Mt. Wilson CaH+K survey[, a survey that focuses on a pair of strong resonance lines, which are known as the H and K lines, so named by Fraunhofer during early spectroscopic studies, and which were later found to be associated with singly ionized calcium; their signal reflects the chromospheric activity of a star.] Two important pieces of information can be extracted from these data, as constraints on dynamo models. The first is [that the overall level of CaH+K emission, which is taken as a measure of overall magnetic flux in the photosphere,] is found to increase with rotation up to 5 – 10 times the solar rotation rate, after which saturation sets in (see Ch. 10). The second is of course the cycle period, for [the minority of stars that exhibit a regular cycle.]”

The preponderance of strong magnetic field concentrated at high latitude in rapidly rotating solar-type stars (see Ch. 10) is also a potentially interesting discriminant. This can arise through channeling of buoyantly rising toroidal flux ropes along the polar axis [prior to surfacing], or efficient poleward transport of surface magnetic flux [after surfacing. ...]”^[10]

“With fully convective stars we encounter potential deviations from a solar-type dynamo mechanism; without a stably stratified tachocline and radiative core to store and amplify toroidal flux ropes, the Babcock-Leighton mechanism, the tachocline α -effect and the flux-tube α -effect all become problematic. Mean-field models based on the turbulent α -effect remain viable, but the dynamo behavior becomes dependent on the presence and strength of internal differential rotation, about which we really don’t know very much in stars other than the Sun. The full-sphere MHD simulations of an ‘M-star in a box’ are particularly interesting in this respect, as they indicate that fully convective stars do produce significant internal differential rotation and well-defined

¹⁰ As computers continue to grow more powerful, 3D MHD dynamo simulations are advancing towards generating cycling large-scale fields in modeled stellar convection zones. An entry point for that literature is provided, for example, in the by Charbonneau (2014). His contribution to [Living Reviews in Solar Physics](#) (Charbonneau, 2010) provides a description of advanced Babcock-Leighton type models that can now take observed magnetograms to provide forecasts of long-term trends of solar activity.

patterns of hemispheric kinetic helicity, both supporting the growth of a spatially well-organized large-scale magnetic component.

Moving to even cooler stars, as the luminosity drops and surface temperature falls below a few thousand K, the magnetic Reynolds number in the surface layers is expected to eventually fall back towards values approaching unity [because of the low degree of ionization at such temperatures]. Small-scale turbulent dynamo action may shut down, with magnetic activity then reflecting only the operation of a deep-seated, large-scale dynamo. Whether this transition is sharp or gradual, and whether it leads to well-defined observational signatures, remain open questions. There is certainly no *a priori* reason to presume that dynamo action should cease. Indeed, in some ways rapidly rotating very low-mass stars are getting closer to the physical parameter regime characterizing the geodynamo.”

4.7 Dynamos in terrestrial planets

“Planetary dynamos share with stellar dynamos that the basic physical concept for their description is that of convection-driven magnetohydrodynamic flow in a rotating spherical shell combined with the associated magnetic induction effects. [...]

Inside a shell of depth d with an electrical conductivity σ_e the fluid must move with a sufficiently large characteristic velocity v_t , so that the magnetic Reynolds number [in Eq. (3.18)] exceeds a critical value $\mathcal{R}_{m,crit}$ in order to have a self-sustained dynamo. The flow pattern must also be favorable for dynamo action, which requires a certain complexity. In particular helical (corkscrew-type) motion with a large-scale order in the distribution of right-handed and left-handed helices is suitable. The Coriolis force plays a significant part in the force balance of the fluid motion and influences the pattern of convection. With this the requirement for ‘flow complexity’ seems to be satisfied and self-sustained dynamo action is possible above $\mathcal{R}_{m,crit} \approx 40 - 50$.

At greater depth in the solar convection zone, the magnetic Reynolds number reaches values of order 10^9 for molecular values of the magnetic diffusivity. In the geodynamo \mathcal{R}_m is approximately 1000. This fairly moderate value allows for the direct numerical simulation of the magnetic field evolution without the need to use an ‘effective diffusivity’ or a parameterization of the induction process through a turbulent α -effect. [...]

The density in the Sun varies by many orders of magnitude and the convection region spans many density scale heights. The density changes associated with radial motion are thought to be important. Flow helicity [$(\mathbf{v} \cdot (\nabla \times \mathbf{v}))$] arises in the Sun because of the action of the Coriolis force on rising expanding and sinking contracting parcels of plasma. Strong magnetic flux tubes have their own dynamics, because the reduction of fluid pressure that compensates magnetic pressure reduced their density and makes them buoyant. In contrast, the dynamo region in Jupiter covers approximately one density scale height and much less in terrestrial planets. The two compressibility effects mentioned before probably do not play a significant role in planetary dynamos. Present geodynamo models usually neglect the small density variation and assume incompressible flow in the Boussinesq approximation (where

density differences are only taken into account for the calculation of buoyancy forces; see Activity 31).

Many models of the solar dynamo assume that most of magnetic field generation occurs at the tachocline, the shear layer between the radiative deep interior and the convection zone of the Sun. For planetary dynamo the process of magnetic field generation is thought to occur in the bulk of the convecting layer. [...] The relevant equation of motion for an incompressible fluid [in a corotating frame of reference] is

$$\rho \frac{\partial \mathbf{v}}{\partial t} + \rho(\mathbf{v} \cdot \nabla)\mathbf{v} + 2\rho\Omega \hat{\mathbf{e}}_z \times \mathbf{v} = \rho\zeta T g \hat{\mathbf{e}}_r - \nabla p' + \frac{1}{4\pi}(\nabla \times \mathbf{B}) \times \mathbf{B} + \rho\nu \nabla^2 \mathbf{v}, \quad (4.24)$$

where \mathbf{v} is velocity, Ω rotation rate, ρ density, p' non-hydrostatic pressure, ν kinematic viscosity, ζ thermal expansivity, g gravity, T temperature, \mathbf{B} magnetic field, r radius and z the direction parallel to the rotation axis. The terms in Eq. (4.24) describe, in order, the linear and non-linear parts of inertial forces, Coriolis force, buoyancy force, pressure gradient force, Lorentz force, and viscous force [(compare with Eq. (3.5))].

In the non-magnetic and rapidly rotating case, the primary force balance is between the pressure gradient force and the Coriolis force (geostrophic balance), similar as for large-scale weather systems in the Earth's atmosphere. [Assuming a stationary flow, and ignoring all other terms on the right of] Eq. (4.24) and taking the curl, we arrive at the Taylor-Proudman theorem, which predicts the flow to be two-dimensional with $\partial \mathbf{v} / \partial z = 0$. The only type of perfectly geostrophic flow in a sphere, *i.e.*, a flow that satisfies this condition, is the differential rotation of cylinders that are co-aligned with the rotation axis (geostrophic cylinders). Such a flow can neither transport heat in the radial direction, nor can it act as a dynamo. Convection requires motion away from and towards the rotation axis. This must violate the Taylor-Proudman theorem, because a column of fluid that is aligned with the z -direction will then stretch or shrink because it is bounded by the outer surface of the sphere. Hence the velocity cannot be independent from z . The necessity to violate the Taylor-Proudman theorem inhibits convection and requires that some other force, such as viscous friction, must enter the force balance. In order for viscosity to do so, the length scale of the flow must become small, at least in one direction. But the flow maintains a nearly geostrophic structure as far as possible. At the onset of convection it takes the form of columns aligned with the rotation axis (Fig. 4.8). They surround the inner core tangent cylinder like pins in a roller bearing. The tangent cylinder is parallel to the z -axis and touches the inner core at the equator. It separates the fluid core into dynamically distinct regions.

The primary circulation is around the axes of these columns. However, in addition there is a net flow along the column axes which diverges from the equatorial plane in anticyclonic vortices and converges towards the equatorial plane in columns with a cyclonic sense of rotation. The combination implies a coherently negative flow helicity in the northern hemisphere and positive helicity in the southern hemisphere, [which] can serve as an efficient dynamo of the α^2 -type.

When the motion becomes more vigorous at highly supercritical convection and when a strong magnetic field is generated, other forces such as inertia (advection of momentum) and the Lorentz force can affect the flow. However, one difference between

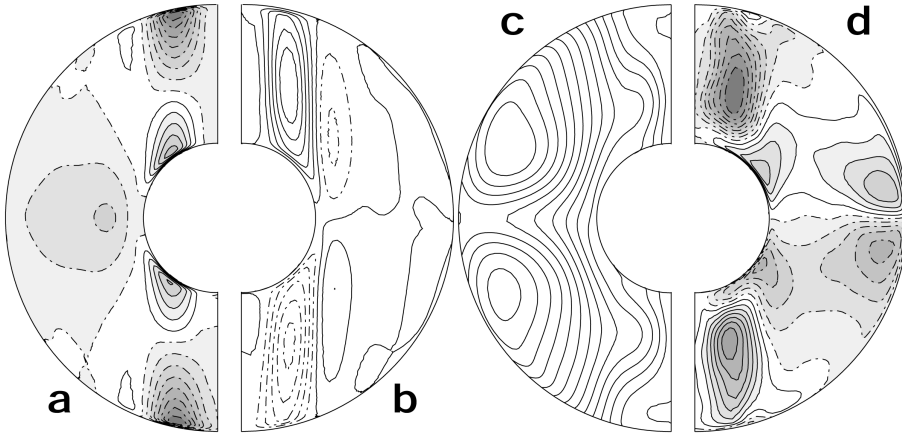


Figure 4.13: Time-averaged axisymmetric components of velocity and magnetic-field components for a planetary dynamo model with [Rayleigh number] $R_a^* = 0.225$, [Ekman number] $E = 3 \times 10^{-4}$, $P_r = 1$, [magnetic Prandtl number] $P_m = 3$, [Reynolds number] $R_m \approx 250$ and [Rossby number] $N_R \approx 0.1$. The grey-scale indicates absolute intensity. (a) Azimuthal velocity, broken lines are for retrograde flow, (b) streamlines of meridional velocity, full lines for clockwise circulation, (c) poloidal magnetic field lines, (d) azimuthal (toroidal) magnetic field, broken lines westward directed field. [Fig. III:7.8]

the solar dynamo and planetary dynamos is the different role of inertial forces versus the Coriolis force. Their ratio is measured by the Rossby number (Eq. 4.2). Deep in the solar convection zone $N_R \approx 1$ when the pressure scale height is taken for L_t . With typical estimates for the flow velocity in the Earth’s core (1 mm s^{-1}), the Rossby number is of order 10^{-6} when a global scale such as the core radius or shell thickness is used for L_t . Therefore, fluid motion in the geodynamo is often considered to be largely unaffected by inertial forces. The general force balance is believed to be that between Coriolis force, pressure gradient force, Lorentz forces and buoyancy forces. However, at small scales inertial forces may become important also in planetary dynamos and can potentially feed back on the large scale flow.

Like rotation, the presence of an imposed uniform magnetic field inhibits convection in an electrically conducting fluid. However, the combination of a magnetic field and rotation reduces the impeding influence that either effect has separately. This constructive interference is most efficient when the Coriolis force and the Lorentz force are in balance. [... Applied to dynamos, it is argued that when the Coriolis force exceeds the Lorentz force the field will strengthen, and when the Lorentz force exceeds the Coriolis force the convection will weaken. Hence, it is assumed that the field equilibrates when the forces match (referred to as a magnetostrophic balance). The field strength inside the geodynamo or in Jupiter’s dynamo seems to agree with that argument.] However, numerical dynamo simulations put some doubt on its validity.” More on that in Ch. III:6.

“The stretching of magnetic field lines by differential rotation in the case of the

solar dynamo, particularly at the tachocline, is thought to be of major importance for the generation of a toroidal magnetic field that is much stronger than the poloidal field. In most geodynamo models, in contrast, differential rotation does not contribute much to the total kinetic energy and the toroidal and poloidal magnetic field components have similar strength. As mentioned before, the flow is strongly organized by rotational forces and the vortices are elongated in the z -direction. Even at a highly supercritical Rayleigh number [(which measures the time scale of conductive relative to convective transport)] and in the presence of a strong magnetic field, the flow outside the inner core tangent cylinder is reminiscent of the helical convection columns found at onset. Inside the tangent cylinder, the flow pattern is different and often exhibits a rising plume near the polar axis (Fig. 4.13b). {A58} The plume is accompanied with a strong vortex motion (called a ‘thermal wind’) with a retrograde sense of rotation near the outer surface changing to prograde rotation at depth (Fig. 4.13a), because the Coriolis force acts on the associated converging flow near the inner core boundary and diverging flow near the outer boundary. {A58}

[...] There is general agreement that the axial dipole field is generated from the axisymmetric toroidal field by an α -effect associated with the helical flow in the convection columns outside the tangent cylinder. In mean-field theory as it is used in astrophysics, the α -effect is associated with unresolved turbulent eddies. In the geodynamo models a ‘macroscopic’ α -effect is observed.

The mechanism for generating the axisymmetric toroidal field is less clear and both an α -effect and differential rotation seem to play a role. Often two flux bundles in the azimuthal direction are found outside the tangent cylinder, with opposite polarity north and south of the equatorial plane (Fig. 4.13d). [T]hey are generated from the axisymmetric poloidal field by a similar macroscopic α -effect associated with the helical convection columns (α^2 -dynamo). Other authors show that the Ω -effect (the shearing of poloidal field by differential rotation) contributes strongly to the generation of axisymmetric toroidal field, even though the kinetic energy in the differential rotation is rather limited. While in weakly driven numerical dynamo models the regions inside the tangent cylinder, north and south of the inner core, are nearly quiescent, vigorous flow is found here in more strongly driven models. In these cases a strong axisymmetric toroidal field is found inside the tangent cylinder region, produced by the shearing of poloidal field lines in the polar vortex (Fig. 4.13a,c,d).” {A59}

Chapter 5

Flows, shocks, obstacles, and currents

Chapter topics:

- The behavior of sub- or super-Alfvénic plasma flows around (non-)conducting bodies and around bodies with an intrinsic magnetic field
- The formation, importance, and occurrence of shock waves
- The magnetized solar wind and its Parker spiral
- Interaction of the magnetized solar wind with a planetary magnetic field

Key concepts:

- Rankine-Hugoniot jump conditions for shock waves
- Stellar magnetic braking
- Open solar magnetic field into the heliosphere
- Planetary magnetospheres

5.1 Introductory overview

Much of what happens in the heliosphere originates in the interaction of an object or a plasma-filled volume with flows of magnetized plasma directed at it. The scales of the phenomena discussed here range from comets and asteroids up to the entire heliosphere where the solar wind couples to the interstellar medium. The interactions often involve shocks, such as in cases when a fast solar wind stream catches up with a significantly slower one, or where the solar wind envelops a magnetosphere. In other settings, they may involve smooth sub-Alfvénic adjustments in the flow, such as happens around many of the moons orbiting within the plasma-filled magnetospheres of the giant planets. The flow of magnetized plasma around a body may be affected by a magnetic field that it induces in that body's conducting deep interior or near-surface shell, or that induced field may add to an already present dynamo-generated field. The flow may pick up matter from an object's outer atmosphere through reconnection processes, or through ionization of neutral matter that enters it from outside, such

as happens when the solar wind engulfs a comet or because of interstellar-medium neutrals entering the heliosphere.

Despite this great variety of conditions, common patterns emerge. These are the focus of this chapter which reviews the effects of a plasma flow around objects from two different perspectives. One is to look into what happens to the external flow, the other is concerned with what happens to the atmosphere or magnetic field of the body that is cocooned by that flow. The first can be summarized by looking at what response is induced in the body by the magnetized external flow. Electrodynamics teaches us that the moving external magnetized plasma induces a current system in a conductor. In the extreme of a perfect conductor, that induced current corresponds to a magnetic field that counters the continuation of the external field inside the conductor so that there is no net field there. In the opposite extreme of a perfect insulator no field is induced and the external field permeates the body as in its surroundings. Intermediate conductivity induces an intermediate response.

Should the conductivity be limited to part of the body, the resulting field external to that body provides clues as to the location of the conducting medium and the magnitude of the conductivity. For example, a planetary system body with a relatively small conducting core that is enveloped by a non-conducting shell will have an induced field near that core that is comparable, but opposite, to the external field. The strength of that field (generally largely bipolar when a large-scale field flows by the object) decreases through the envelope towards the body's surface so that the external signature may be weak. If there is a conducting layer in a body that lies at or just above or below the surface (such as an electrolyte-laden ocean or a substantial ionosphere) the induced field can be strong if the conductance is high, leading to a net field outside the body that is markedly distinct from that of the incoming plasma. If the body has a substantial, sustained intrinsic magnetic field (*i.e.*, a dynamo in its interior, and thus a conducting volume somewhere in its interior) an induced field distorts the intrinsic field. For the incoming flow, the 'object' that it encounters is bounded by the permanent and/or induced field, and thus lies anywhere between the body's surface (or high in the atmosphere, if it has one) or where the magnetic field of that body is strong enough to withstand the momentum of the incoming flow of ionized, magnetized matter.

The consequence of the dynamo and induced field for the incoming flow is communicated by waves. If the incoming flow is relatively slow, specifically if it is sub-magnetosonic (see Sect. 3.3), the flow can be deflected well before approaching the 'object' and largely flow around it; how much flows around it depends on the magnetic field. If, in contrast, the flow comes in super-magnetosonically, the incoming flow is unaware of the object until forced to realize its presence, either (essentially) at the surface of the body or where its magnetic field is strong enough; there will be a shock that decelerates and deflects the flow. The interplay between the incoming field and the body's magnetic field through compression and reconnection drives magnetospheric and ionospheric processes, resulting in much of what we know as space weather, further modified by planetary rotation.

But 'obstacles' to flows in the local cosmos are not limited to planets, moons, and

other bodies. One example of another type of obstacle is the outflowing wind from a Sun-like star as it is encountered by the interstellar medium. Another is that of (relatively) fast wind streams and coronal mass ejections that catch up with slower wind plasma ahead of them; such pileups often include shocks, here with the potential of plasma becoming compressed in the collision zone rather than flowing around the 'obstacle' because the scales are such that there generally is no way 'around' the 'obstacles' within the characteristic time scale of the passage of such flows through a large part of the heliosphere.

Generally, when a flow interacts with another volume of magnetized plasma, the magnetic field is distorted in both volumes (if a field exists, which in heliophysics is commonly the case) and magnetic (Lorentz) forces play into the balance of forces, as expressed in the momentum equation Eq. (3.5). One can view this as a result of the pressure and tension forces ascribed to the magnetic field or, equivalently, to induced currents - the equations do not care about our perspective in this matter (see Ch. 3).

One key differentiating factor in how the flow and the enveloped volume interact is whether the magnetic fields in these two domains can connect or not. In the ideal-MHD approximation, in which effects of resistivity are ignored, the induction equation Eq. (3.3), through the frozen-in flux paradigm, leads to the conclusion that the two plasmas involved cannot interpenetrate: the flow moves around the impacted plasma as a wind that flows past a solid object. This can still lead to very complex dynamics, as diverse as for a wind flowing past a flag or around a supersonic jet-plane. If the magnetic field can reconnect, however, the plasmas can interact in entirely different ways, that include, for example, a variety of magnetospheric phenomena. The differentiator here is not solely the plasma resistivity but the effect of such resistivity within the interaction time scale of the flow passing by the enveloped volume as expressed by the magnetic Reynolds number (Eq. 3.18). The geometry of the interaction is also set by the Alfvén Mach number (Eq. 3.32).

In Sect. 11.3.2 we encounter another type of flow into a magnetosphere. In very young stars that are still surrounded by a gaseous disk, matter spirals gradually towards a still growing star. Close to the star, this accreting matter will diffuse into, and then be locked onto the magnetic field of the star. This allows the material to 'fall' through the stellar magnetosphere, while being channeled by the magnetic field, to end up near the surface of the star in what are known as 'accretion columns' (sketched in Fig. 11.7). But that is for later.

This chapter takes you through the following situations throughout the heliosphere:

{A60}

- Sects. 5.2, 5.3 and 5.4 are *introductions*: they discuss, respectively, **low-velocity interactions versus shocks**, the **elementals of shocks and discontinuities**, and the **magnetized solar wind and the Parker spiral** that forms as the wind flows out from the rotating Sun. Staying with the *solar wind*, Sect. 5.5.1 reviews **solar-wind stream interactions**.
- Next come discussions of *flows around bodies in the heliosphere*, beginning in Sect. 5.5.2 with a **non-conducting body without atmosphere**, then in

{A60}

Sect. 5.5.3 a **flow around a conducting body** without an intrinsic magnetic field.

- By Sect. 5.5.4 we reach *bodies with dynamos* and look at **plasma flow around a permanently magnetized body**, after which we can discuss *magnetospheres*: first, in Sect. 5.5.5 a **closed magnetosphere** which exists only in the world of ideal MHD, but then in Sect. 5.5.6 we introduce **the open magnetosphere** such as happens in the real world.
- Finally, we move on to what happens *within the magnetosphere of a planet or moon* as a consequence of the variable solar wind coupling to the body’s magnetic field: in Sect. 5.5.7 we talk about the overall system of **solar wind-magnetosphere-ionosphere interaction**, including the effects of rotation and advection.
- Finally, we return to the solar wind, looking at the outermost regions of the heliosphere, where the outflow meets the interstellar medium: Sect. 5.5.8 explores what happens when we have a **flow impinging on a fast outflow** but now on scales such that the flow can find a way around the outflowing plasma, in contrast to what happens in the case of wind streams interacting with comparable scales discussed in Sect. 5.5.1.

5.2 Low-velocity interactions versus shocks

In view of the great diversity in conditions encountered throughout the local cosmos “it may seem unlikely that general rules can describe the interaction regions. We are rescued from the need to treat each case as totally distinct by recognizing that physical theories often incorporate a small set of dimensionless parameters that control important aspects of a system, even if such properties as spatial scale, temperature, and flow velocity vary by many orders of magnitude. For a flowing plasma incident on an obstacle, the form of the interaction depends critically on how the flow speed is related to the speed of waves that transmit information about changes of plasma properties from one part of the system to another. An analogy to waves in neutral gases helps to clarify the concept. In the frame of an airplane in flight, the atmosphere flows onto the plane at some velocity, call it v . As the gas encounters the plane, pressure perturbations develop. Pressure perturbations launch sound waves that travel at the sound speed, c_s . If such waves can move away [in the forward direction] from the plane, they can divert the atmosphere upstream of the plane. But the waves are swept back toward the plane at the flow speed of the plasma. Only if $v < c_s$ is it possible for the waves to begin to divert the atmosphere well upstream of the plane. If $v > c_s$, as for a supersonic jet, the waves pile up in front of the plane, causing a shock to develop upstream. Only downstream of the shock is the flow diverted. Assuming that the plane is large compared with distances characteristic of atmospheric properties, the parameter that determines whether or not a shock will form is the (dimensionless) sonic Mach number of the surrounding atmosphere, v/c_s . [Shocks are described in Sect. 5.3.]

In a plasma, much as in a neutral gas, compressional perturbations develop when

Table 5.1: *Properties of the plasmas upstream of selected small bodies of the Solar System. [Listed are the Alfvén and magnetosonic Mach numbers and the plasma β (Eq. 3.24). Table IV:10.1].*

Obstacle	Ambient plasma	M_A	M_{ms}	β
Io, Europa, Ganymede	jovian magnetosph.	< 1	< 1	> 1
Asteroids	solar wind	> 1	> 1	~ 1
Comets	solar wind	> 1	> 1	~ 1
Moon	Earth's magnetosph. or solar wind	> 1 or < 1	> 1 or < 1	~ 1 or < 1

there is an obstacle in the flow. [...] Having identified [in Section 3.3] some of the waves that carry information through a magnetized plasma, we are now able to introduce the dimensionless parameters that help us understand aspects of flow and field perturbations. The magnetosonic Mach number (M_{ms}) is the ratio of the flow speed to the fast mode speed, taken as $(c_s^2 + v_A^2)^{1/2}$. M_{ms} reveals whether or not a shock is likely to form upstream in the flow. When $M_{ms} < 1$, compressional waves can travel upstream from the obstacle faster than the flowing plasma can sweep them back. These waves, moving upstream, can divert the incident flow around the obstacle, much as the bow wave of a ship diverts water to the sides, and no shock develops. However, as in the situation discussed in the context of supersonic flight, if $M_{ms} > 1$, compressional waves are unable to propagate upstream faster than they are swept back by the flow. They pile up to form a shock. Most bodies in the super-magnetosonic solar wind [...] create shocks standing somewhat upstream on their sunward sides. Downstream of the shock, plasma is heated, compressed, and diverted around the obstacle.

The Alfvén Mach number (M_A , [Eq. 3.32]) is the ratio of the speed with which the ambient plasma flows towards an obstacle divided by the Alfvén speed. We will see that this quantity controls the shape of the interaction region in planes containing the unperturbed plasma flow and the background magnetic field. The plasma beta (β , [see Eq. 3.24]) is the ratio of the thermal pressure to the magnetic pressure. This quantity enables us to understand how significantly the magnetic field structure can be modified by changes of the plasma pressure.

The plasma environment differs greatly among the small bodies of the Solar System. Some of the bodies are embedded in the solar wind, others in the plasma of a planetary magnetosphere, and some [...] move from one environment to another [(such as Earth's Moon, which spends part of each lunar orbit in Earth's magnetotail and the rest of the month in the solar wind)]. Table 5.1 lists some plasma properties relevant to the environment of selected bodies.”

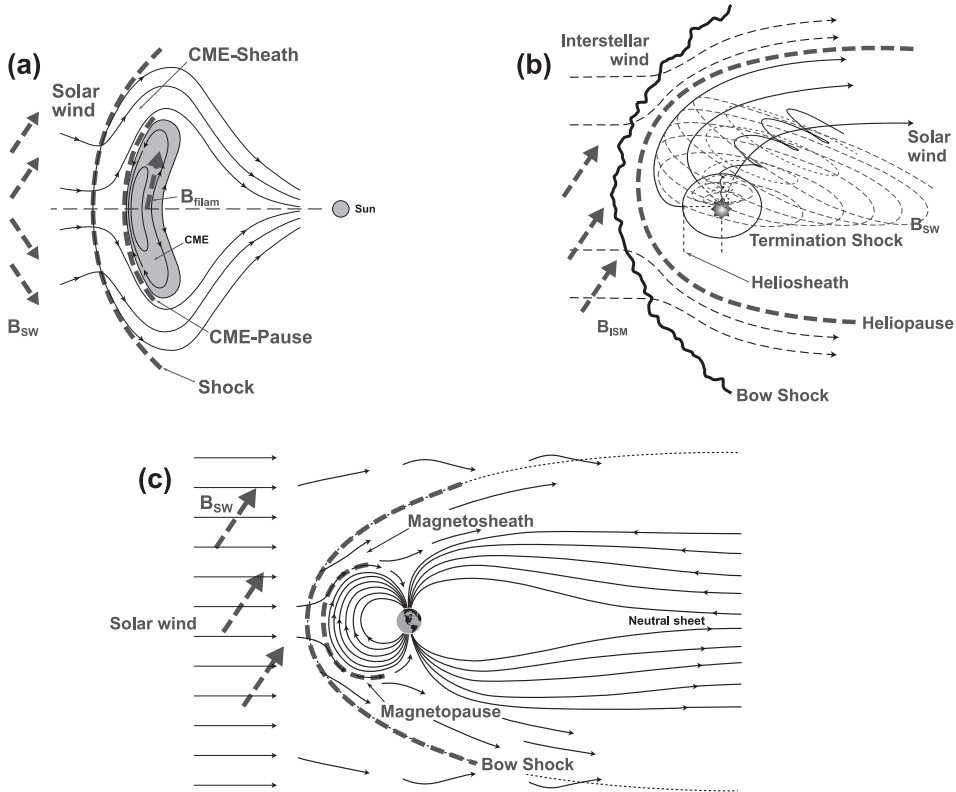


Figure 5.1: Schematic comparison of shocks around [coronal mass ejections (CMEs, magnetically-driven explosions from the solar atmosphere into the heliosphere)], the heliosphere, and the terrestrial magnetosphere [(all seen from around the equatorial plane)]. The figure shows some of the types of shocks and sheaths that exist in the heliosphere and their universal basic structures: (a) a CME [pushing its way super-Alfvénically into the solar wind]; (b) the outer heliosphere, and (c) Earth’s magnetosphere. The same basic structures appear: shocks where the solar wind becomes subsonic; the sheaths that separate the subsonic solar wind from the obstacle ahead; and the ‘pause’ where there is a pressure equilibrium between the subsonic solar wind and the obstacle’s environment. In the case of a CME these three structures are the shock, CME-sheath, CME-pause and the obstacle is the magnetic filament that drives the CME. In the case of the outer heliosphere the structures are the termination shock, heliosheath, and heliopause. The obstacle is the interstellar wind and the magnetic field it is carrying. If the interstellar wind is supersonic there is an additional shock, the bow shock. In the case of the Earth’s magnetosphere the structures are the shock, the magnetosheath, the magnetopause and the obstacle is the Earth’s dipolar magnetic field. [Fig. II:7.1]

5.3 Elementals of shocks and other discontinuities

Shocks that we discussed up to here develop when a flow speed exceeds the speed of waves that can serve as a warning to the flow that an obstacle lies ahead. Shocks can also form if non-linear effects in the propagation of a wave become important, such as when a wave runs into a medium in which strong gradients in density or

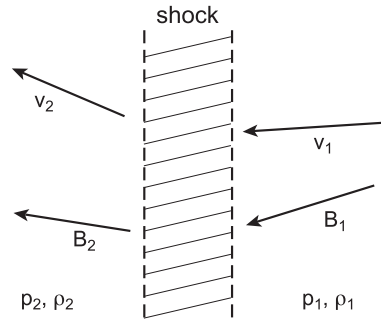


Figure 5.2: Diagram showing the region upstream (left) and downstream of a shock. [Fig. II:7.3]

temperature cause the wave amplitude to grow more rapidly than dissipation can limit that growth; examples of such shock waves are found in upward traveling pressure waves in atmospheres, including the Earth's and the Sun's, and also in very large and long-lived wind streams in the heliosphere.

“In the small-amplitude limit, the profile of a magnetohydrodynamic (MHD) wave does not change as it propagates, but even a small-amplitude wave will eventually distort due to *wave steepening*. The wave steepening happens when gradients of pressure, density and temperature become so large that dissipative processes (*e.g.*, viscosity, thermal conduction) are no longer negligible. In the steady state, a steady wave-shape – a *shock wave* – is formed in which the steepening effect of nonlinear advective terms balance the broadening effects of dissipation. The shock waves move at speeds larger than the ambient intrinsic speed, which for magnetized ionized matter in the heliosphere, is the magnetosonic speed. If the shock moves much faster than the magnetosonic wave, it is called a strong shock; if it moves just slightly faster, it is called a weak shock. The dissipation inside the shock front leads to a gradual conversion of the energy being carried by the wave into heat. In the heliospheric plasma, we have collisionless shocks in which the thermalization happens through wave-particle interactions. [...]

A propagating wave described by the ideal fluid equations leads to infinite gradients in a finite time. There is no solution for the ideal MHD equations. This is not surprising: ideal equations are valid when scales of variations are larger than the mean free path. The breakdown in ideal equations occurs in a very thin region, while the fluid equations are valid everywhere else. In this very thin region, it is difficult to describe the plasma in detail. The simple picture is a discontinuity dividing two roughly uniform fluids. An important aspect is that the simple picture of a discontinuity dividing two roughly uniform fluids is not usually applicable in a plasma. Shocks can involve turbulence for example. For this initial discussion, we make the simplifying assumption that there is a planar discontinuity of zero thickness that separates two uniform fluids, as depicted in Figure 5.2. We also assume that the shock is stationary [or, in other words, that we are in the co-moving frame of reference ...] The transition must be such as to conserve mass, magnetic flux, and energy. The MHD jump conditions are independent of the

physics of the shock itself and are known as the *Rankine-Hugoniot jump conditions*.”

“It is straightforward to obtain the Rankine-Hugoniot jump conditions from [Maxwell’s equations and] the MHD equations. Assuming steady state in the frame of reference of the shock, the equation for the conservation of mass [in Eq. (3.4) in the absence of sources and sinks,] gives

$$\rho_1 \mathbf{v}_1 \cdot \hat{\mathbf{e}}_\perp = \rho_2 \mathbf{v}_2 \cdot \hat{\mathbf{e}}_\perp, \quad (5.1)$$

[(where $\hat{\mathbf{e}}_\perp$ is a unit-length vector pointing in the direction normal to the shock)] or in a different notation

$$\{\rho \mathbf{v} \cdot \hat{\mathbf{e}}_\perp\} = 0, \quad (5.2)$$

where the symbol $\{\dots\}$ represents differences between the two sides of the discontinuity.

Conservation of momentum, [with Eq. (3.5) without sources, sinks, or viscosity,] yields

$$\left\{ \rho \mathbf{v} (\mathbf{v} \cdot \hat{\mathbf{e}}_\perp) + \left(p \hat{\mathbf{e}}_\perp + \frac{B^2}{8\pi} \hat{\mathbf{e}}_\perp - \frac{(\mathbf{B} \cdot \hat{\mathbf{e}}_\perp)}{4\pi} \mathbf{B} \right) \right\} = 0. \quad (5.3)$$

Conservation of energy, [...] results in

$$\left\{ \left(\frac{1}{2} \rho v^2 + \frac{\gamma p}{\gamma - 1} \right) (\mathbf{v} \cdot \hat{\mathbf{e}}_\perp) + \frac{c}{4\pi} (\mathbf{E} \times \mathbf{B}) \cdot \hat{\mathbf{e}}_\perp \right\} = 0. \quad (5.4)$$

[Note that $\mathbf{S} = (c/4\pi) \mathbf{E} \times \mathbf{B}$ is the Poynting flux, which measures the directional energy transfer in an electromagnetic field; compare with Eq. (4.1) where that is expressed for a plasma with infinite conductivity, as it is below in Eq. (5.10).]

Conservation of magnetic flux, [...] gives

$$\{\mathbf{B} \cdot \hat{\mathbf{e}}_\perp\} = 0. \quad (5.5)$$

The equation

$$\nabla \times \mathbf{E} = -\frac{1}{c} \frac{\partial \mathbf{B}}{\partial t} \quad (5.6)$$

[for a steady state] can be written as

$$\{\mathbf{E} \times \hat{\mathbf{e}}_\perp\} = \mathbf{0}. \quad (5.7)$$

Let us consider, now, the normal \perp and the tangential \parallel components relative to the shock’s surface so that the jump conditions can be written as:

$$\left\{ \rho v_\perp^2 + p + \frac{B_\parallel^2}{8\pi} \right\} = 0 \quad (5.8)$$

$$\left\{ \rho \mathbf{v}_\parallel v_\perp - \frac{\mathbf{B}_\parallel B_\perp}{4\pi} \right\} = 0 \quad (5.9)$$

$$\left\{ \left(\frac{1}{2} \rho v^2 + \frac{\gamma p}{\gamma - 1} + \frac{B^2}{4\pi} \right) v_\perp - (\mathbf{v} \cdot \mathbf{B}) \frac{B_\perp}{4\pi} \right\} = 0 \quad (5.10)$$

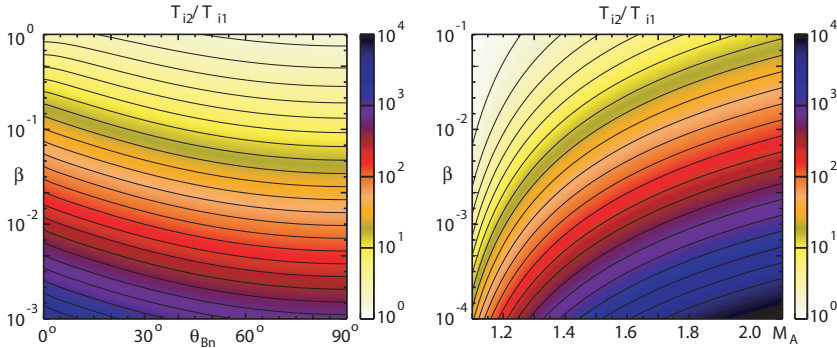


Figure 5.3: Iso-contours of shock heating, expressed as the ratio between downstream to upstream ion temperature T_{i2}/T_{i1} , as a function of shock-normal angle θ_{B_\perp} [(the angle between the shock normal and the upstream magnetic field)] (fixed $M_A = 2$) and Alfvén Mach number M_A (fixed $\theta_{B_\perp} = 45^\circ$) for low β plasmas. Derived from standard Rankine-Hugoniot conditions for fast shocks, assuming a specific heat ratio $\gamma = 5/3$. The graphs show that for a wide range of angles, there can be very substantial downstream heating at sufficiently low plasma β , as present in much of the solar corona. Such extreme heating may help form a seed population for further acceleration [into energetic particle populations that will be discussed in Ch. 8]. [Fig. II:8.1] For a color version of this figure, see arXiv:2001.01093.

$$\{B_\perp\} = 0 \quad (5.11)$$

$$\{\mathbf{v}_\perp \times \mathbf{B}_\parallel + \mathbf{v}_\parallel \times \mathbf{B}_\perp\} = \mathbf{0} . \quad (5.12)$$

Equations [(5.2) and] (5.8)–(5.12) are the Rankine-Hugoniot jump conditions that describe all types of shocks” and also allow for three types of discontinuities that are not shocks. An example of the heating associated with shocks is given in Fig. 5.3. ^[11]

“Discontinuities can be classified as either contact or rotational discontinuities. Contact discontinuities happen when there is no flow across the discontinuity, *i.e.*, $v_\perp = 0$, but $\{\rho\} \neq 0$. A classic example is the contact discontinuity of a mix of vinegar and olive oil. If $\{B_\perp\} \neq 0$ at a contact discontinuity then only the density changes across the discontinuity, which is rarely observed in plasmas. A tangential discontinuity occurs when $\{B_\perp\} = 0$, then $\{v_\parallel\} \neq 0$ and $\{B_\parallel\} \neq 0$ and $\{p + B^2/8\pi\} = 0$. This means that the fluid velocity and magnetic field in this case are parallel to the surface of the discontinuity but change in magnitude and direction, and that the sum of thermal and magnetic pressures is constant. [... Large heliophysical examples of tangential discontinuities with $\{B_\perp\} = 0$ are the heliospheric current sheet and the magnetospheric current sheet (illustrated in Fig. 5.4).]

¹¹ A note on terminology: a “parallel shock” propagates along the magnetic field, *i.e.*, has the vector $\hat{\mathbf{e}}_\perp$ normal to the shock front aligned along the magnetic field, or $\hat{\mathbf{e}}_\perp \parallel \mathbf{B}$. A “perpendicular shock” has $\hat{\mathbf{e}}_\perp \perp \mathbf{B}$.

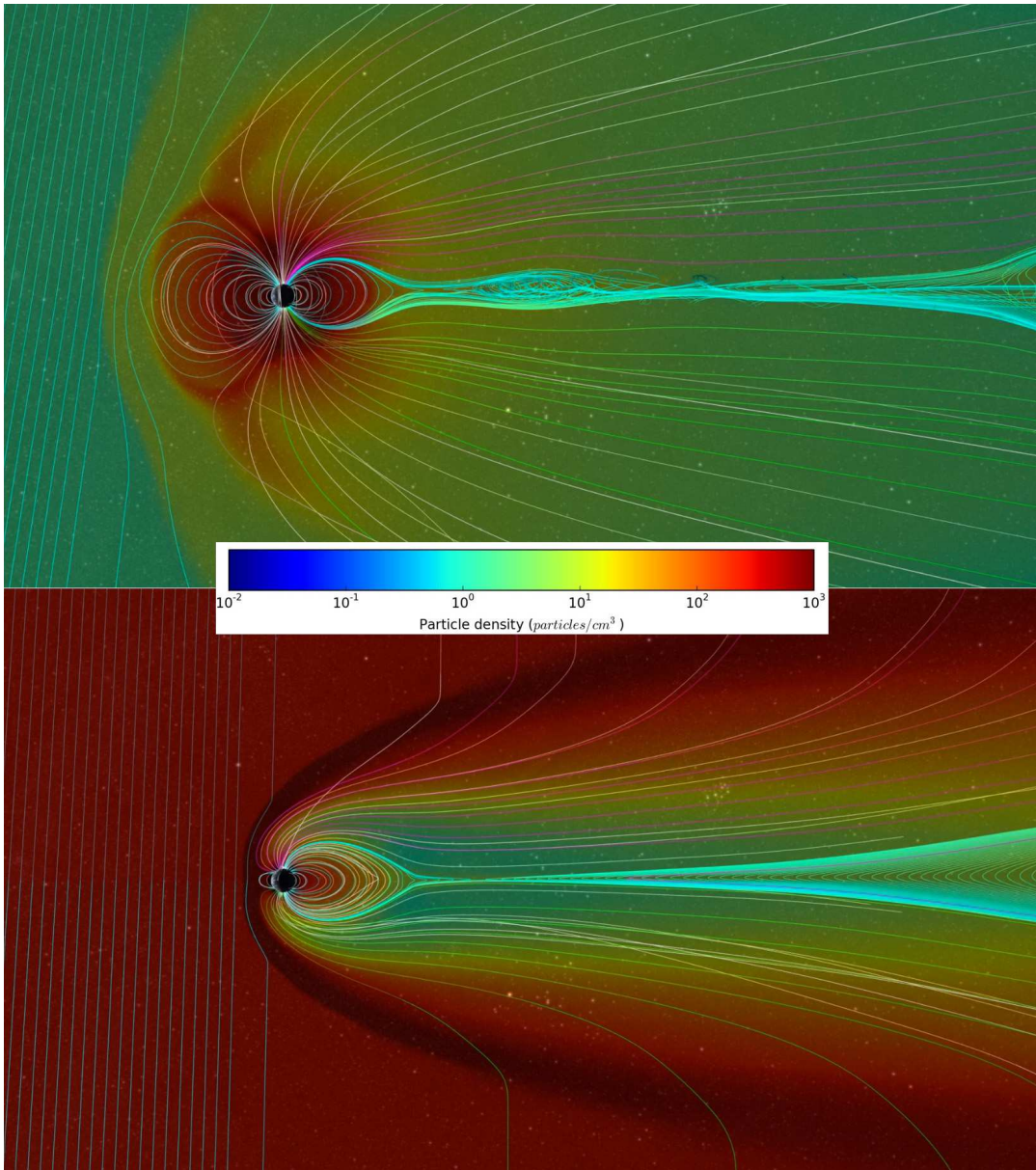


Figure 5.4: An MHD simulation of the Earth’s magnetic field subject to (top) a typical background solar wind and (bottom) about 3.5 h after subjecting that field to a coronal mass ejection similar to that thought to have hit the Earth after the Carrington-Hodgson solar flare of 1859. The current sheet, extending from the cusp in the field in the downwind direction, clearest in the bottom panel, is the interface between oppositely-directed magnetic fields. The color bar in the center shows how the particle density is encoded in color. Source: first and last frames of a [NASA animation \(https://svs.gsfc.nasa.gov/4189\)](https://svs.gsfc.nasa.gov/4189), based on the study by (Ngwira et al., 2014). See Fig. I:6.3 for a comparison of heliospheric and magnetospheric field configurations. For a color version of this figure, see arXiv:2001.01093.

A rotational discontinuity occurs when $\{v_\perp\} \neq 0$ and $\{\rho\} = 0$. From the jump conditions this implies that $\{v_\perp\} = 0$ and $\{p + B_\parallel^2/8\pi\} = 0$ so $\mathbf{v}_1 \cdot \hat{\mathbf{e}}_\perp = \mathbf{v}_2 \cdot \hat{\mathbf{e}}_\perp = v_\perp$ and $\rho_1 = \rho_2$. After some math, we find that $v_\perp^2 = B_\perp^2/4\pi\rho$, and that B_\parallel remains constant in magnitude but rotates in the plane of the discontinuity. [...]

The Rankine-Hugoniot jump conditions have 12 variables. Four upstream parameters are specified (ρ , v , B_\parallel , and B_\perp), so we have 7 equations for 8 unknowns. Therefore we need to specify one more quantity, namely the strength of the shock ρ_2/ρ_1 .”

Examples of tangential discontinuities are the heliopause and planetary magnetospheres when there is little reconnection (see Sect. 5.5.5). A rotational discontinuity occurs for example when reconnection at the magnetopause is relatively efficient (Sect. 5.5.6). Shocks occur upstream of where the solar wind meets planetary system objects (Sects. 5.5.2–5.5.6) as well as where it encounters the interstellar medium (Sect. 5.5.8), and also where fast wind streams plow into slower ones ahead as well as at the leading edge of relatively fast explosions called coronal mass ejections (Sect. 5.5.1).

5.4 The magnetized solar wind and the Parker spiral

Before we can discuss the interplay of the solar wind with objects throughout the heliosphere, we need to introduce two properties of the solar wind itself: the geometry of the magnetic field that it carries, and the consequence of wind gusts running at different velocities. First, the magnetic field:

”Let us briefly consider [a steady-state] outflow of ionized, magnetized gas from a *rotating* star with [a magnetic field that scales with distance from the star like a monopole, which is to say with a radially-flowing wind that stretches the field out from its effective base that lies, say, a few stellar radii above its actual surface ^{12]}] The salient aspects of such a flow are found even when only considering the equatorial plane and restricting attention to solutions where all variables are functions of r only. We make use of spherical coordinates r , ϕ , θ .

We find that the equation of mass conservation (for plasma mass density ρ moving at velocity \mathbf{v} and carrying a field \mathbf{B}) then can be written

$$\frac{1}{r^2} \frac{\partial}{\partial r} (\rho v_r r^2) = 0, \quad (5.13)$$

while the ϕ component of the momentum equation is given by

$$\rho \left(v_r \frac{\partial v_\phi}{\partial r} + v_\phi \frac{v_r}{r} \right) = \frac{1}{4\pi} \left(B_r \frac{\partial B_\phi}{\partial r} + B_\phi \frac{B_r}{r} \right) \quad (5.14)$$

or

$$\rho v_r \frac{1}{r} \frac{d}{dr} (r v_\phi) = \frac{1}{4\pi} B_r \frac{1}{r} \frac{d}{dr} (r B_\phi) \quad (5.15)$$

¹² This base is what is meant by the term ‘source surface’ introduced in Activity 64; within that surface, the field is approximated as corotating rigidly with the star.

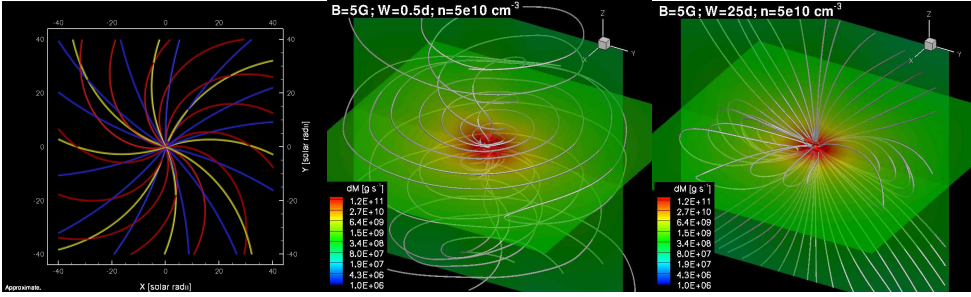


Figure 5.5: Left: Conceptual display of different stellar-wind magnetic field spirals for a Sun with a 4.6 day rotation period (red), a 10 day period (yellow), and a 26 day period (blue), as a function of distance in solar radii. Center/right: Results from numerical simulations for the stellar coronae of solar analogs with rotation period of 0.5 day (middle) and 25 days (right), [but assuming the same base field strengths and densities. Fig. IV:4.1; sources: left from Cohen *et al.* (2012) and center and right from Cohen and Drake (2014).] For a color version of this figure, see arXiv:2001.01093.

Mass conservation implies that $\rho v_r r^2$ is constant, while the divergence-free magnetic field requires that $B_r r^2$ is constant. Multiplying Eq. (5.15) with r^3 we see that

$$r v_\phi - \frac{B_r r^2}{\rho v_r r^2} \frac{1}{4\pi} r B_\phi = \text{constant} = L. \quad (5.16)$$

Under the assumptions above, the [ideal] induction equation is

$$\frac{1}{r} \frac{d}{dr} (r [v_r B_\phi - v_\phi B_r]) = 0. \quad (5.17)$$

For a star rotating with angular velocity Ω , radius R_s and with a [simplified monopolar] field so that $B_{\phi s} \approx 0$ [(with the index 's' meaning at the solar wind base or source surface)] we find that the induction equation implies

$$r (v_r B_\phi - v_\phi B_r) = \text{constant} \approx -R_s (R_s \Omega) B_{rs} = -\Omega r^2 B_r. \quad (5.18)$$

We can now solve Eq. (5.16) and Eq. (5.18) for v_ϕ and B_ϕ and using $M_A^2 = (v_r^2/v_A^2)$ with $v_A^2 = (B_r^2/4\pi\rho)$ we find

$$v_\phi = \Omega r \frac{M_A^2 (L/r^2 \Omega) - 1}{M_A^2 - 1}; \quad B_\phi = -\frac{B_r \Omega r}{v_r} \left(\frac{1 - (L/r^2 \Omega)}{M_A^2 - 1} \right) M_A^2. \quad (5.19)$$

Both expressions show that we must have $1 - (L/r^2 \Omega) = 0$ when $M_A^2 - 1 = 0$ [(formally, going to zero in such a way that their ratio remains finite)]. We define $r \equiv r_A$ where $M_A^2 = 1$. Thus, we must have $L = r_A^2 \Omega$. Notice [that v_r tends to a constant for large r , and thus $M_A^2 \propto \Omega r^2$ and as a result

$$\text{for large } r : v_\phi \approx \frac{\Omega r_A^2}{r} \rightarrow 0; \quad B_\phi \approx -\frac{B_r \Omega r}{v_r}, \quad (5.20)$$

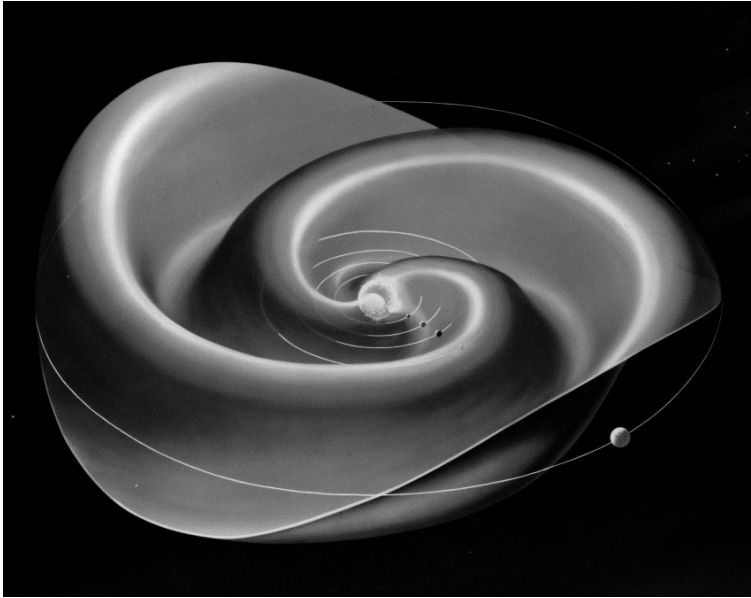


Figure 5.6: The heliospheric current sheet forms a warped, undulating structure extending from the top ridge of the helmet streamer belt [...] that sweeps by the planets as the Sun rotates once per 27 days (synodic period). The magnetic field changes direction across the current sheet. [image source: Wikipedia; see also Fig. I:9.3]

while

$$\text{close to the star : } v_\phi \approx \Omega r ; B_\phi \approx -\frac{B_r \Omega r}{v_A}. \quad (5.21)$$

In] other words, the magnetic field and stellar wind rotate like a solid body out to the critical point r_A where the radial flow speed is equal to the 'radial' Alfvén speed. Beyond this point the field is pulled along the wind into a spiral, the *Parker spiral*, as the flow becomes nearly radial far from the star". Figure 5.5 shows this spiral and also two MHD simulations of stellar winds (discussed in Sect. 10.3.3). Note that whereas B_r decreases as $\sim 1/r^2$, B_ϕ decreases as $\sim 1/r$. {A62} {A63}

5.5 Flow-based interactions in heliophysics

5.5.1 Solar-wind stream interactions

A 1D model of high-speed stream evolution

The solar wind stretches the high-coronal field nearly radially into the heliosphere, there to deform subject to solar rotation into the Parker spiral. The magnetic field in the solar wind has its roots in the two magnetic polarities on the solar surface. Although the solar surface field has myriad adjacent regions of either polarity, further from the Sun the low orders dominate, so that the heliospheric field often resembles that of a distorted bipolar pattern stretched out far beyond the planets. In this field the opposite polarities straddle a transition in field direction in a warped skirt around the

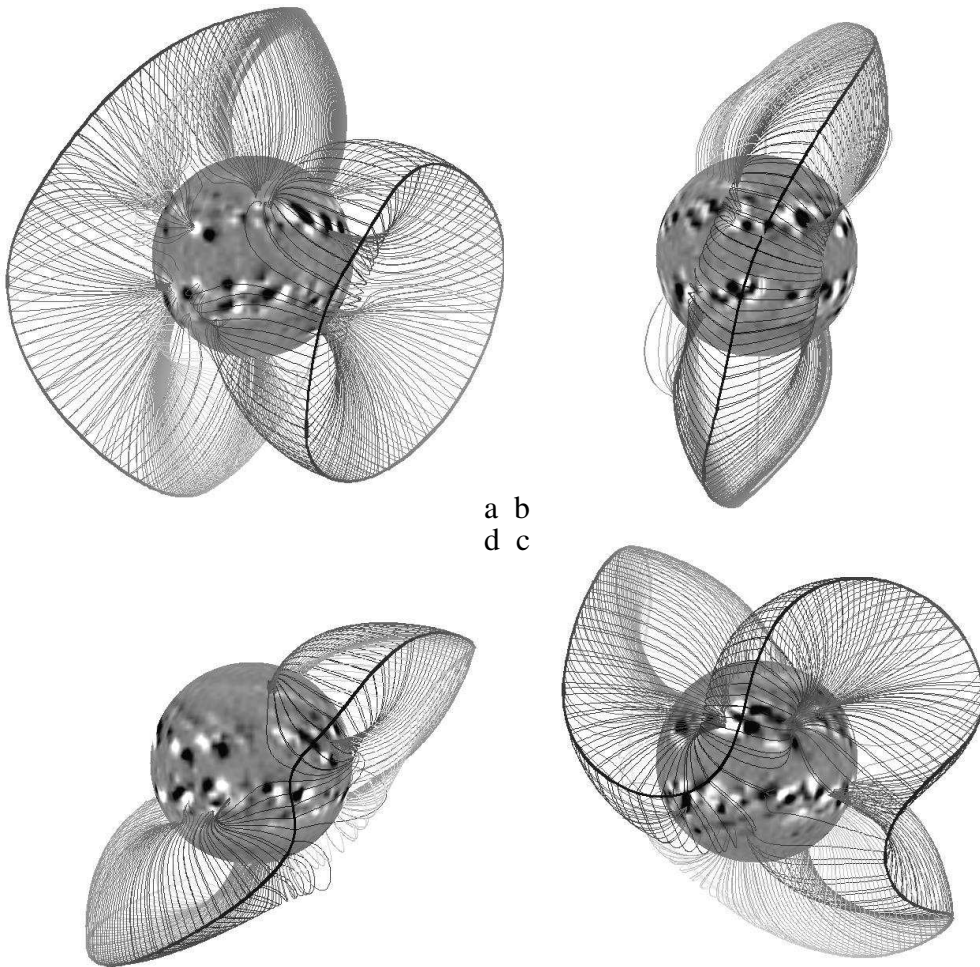


Figure 5.7: *The Sun's surface magnetic field is comprised of a multitude of dipolar regions of widely different fluxes, whose numbers wax and wane with the solar cycle. The large-scale coronal magnetic field, the foundation of the heliospheric field, expands from regions of partly open magnetic field that enclose the closed-field corona. This diagram shows the global topology of the Sun's field in a so-called potential-field source-surface (PFSS) approximation. In particular, it shows four realizations of the 'streamer belt' for a solar magnetic model; each belt separates opposite polarities of the field reaching into the heliosphere. Shown are four phases of the simulated magnetic cycle: clockwise from the top left, $t = 3.1, 3.6, 4.5, 6.0$ years into a sunspot cycle of 11. years. Each panel shows a magnetogram of the solar surface, the neutral line(s) at the source surface, and the highest closed field lines that reach up to the neutral line(s); the lines are colored so that the darkest colors are nearest to the 'observer.' The panels show, clockwise, an example of a near-quadrupolar situation; a strongly tilted dipolar case; a strongly warped current sheet; and another nearly dipolar case with less tilt relative to the solar equator. [Fig. I:8.1] For a short discussion how the 'streamer belts' in this figure map to 'helmet streamers' seen in coronagraph images and during eclipses, see Sect. 17.11.*

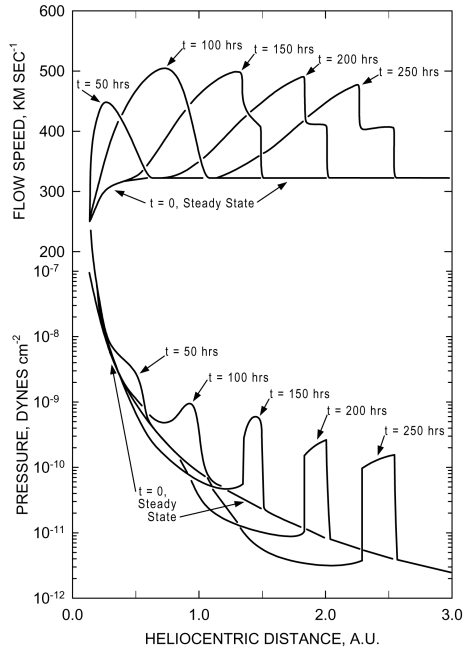


Figure 5.8: Snapshots of solar wind flow speed and pressure as functions of heliocentric distance at different times during the outward evolution of a high-speed stream as calculated using a simple 1D gas-dynamic code. After obtaining a steady-state solar wind expansion that produced a flow speed of 325 km/s far from the Sun, a high-speed stream was introduced into the calculation by linearly increasing and then decreasing the temperature (and thus also the pressure) by a factor of four at the inner boundary at 0.14 AU over an interval of 100 hrs. [Fig. III:8.4]

Sun, known as the heliospheric current sheet (sketched in its fundamental properties in Fig. 5.6; see Fig. 5.7 for a representation of an approximating (potential) field model at the foundation of that current sheet based on solar observations). {ⓂA64} Before going into this geometry, let us look into the simplified case of a 1-D radial outflow. {ⓂA64}

Different magnetic regions on the Sun lead to different speeds in the wind. [Outside of eruptive phases,] this typically manifests itself in so-called fast streams and slow streams (see Table 2.4 for their properties). Because the Sun rotates, the radially flowing fast and slow winds cannot avoid but to run into each other. “Because radially aligned parcels of plasma within a stream originate from different locations on the Sun, they are threaded by different magnetic field lines and thus cannot interpenetrate one another [without reconnection, and such reconnection proceeds relatively slowly in the solar wind compared to the characteristic time the wind takes to traverse much of the heliosphere]. Figure 5.8, which shows the result of a simple 1D gas-dynamic simulation, illustrates the basic reasons why high-speed streams evolve with increasing heliocentric distance. The rising portion of the high-speed stream steepens kinematically with

increasing heliocentric distance because gas (plasma) at the peak of the stream is traveling faster than the slower plasma ahead. As the speed profile steepens, material within the stream is rearranged; parcels of plasma on the rising-speed portion of the stream are compressed, causing an increase in pressure there, while parcels of plasma on the falling-speed portion of the stream are increasingly separated, producing a rarefaction.

It is common to refer to the compression on the leading edge of a high-speed stream as an interaction region. Being a region of high pressure, the interaction region expands into the plasma both ahead and behind at the fast mode speed (actually at the sound speed in the calculation shown in Figure 5.8). The leading edge of the interaction region is called a forward wave because it propagates in the direction of the solar wind flow; the trailing edge is called a reverse wave because it propagates sunward in the solar wind rest frame but is carried away from the Sun by the highly supersonic flow of the wind. Pressure gradients associated with these waves produce an acceleration of the slow wind ahead and a deceleration of the high-speed wind within the stream. The net result of the interaction is to limit the steepening of the stream and to transfer momentum and energy from the fast wind to the slow wind. [...]

As long as the amplitude of a high-speed stream is sufficiently small, it gradually dampens with increasing heliocentric distance in the manner just described. However, when the difference in speed between the slow wind ahead and the peak of the stream is more than about twice the fast mode (sound) speed the stream initially steepens faster than the forward and reverse pressure waves can expand into the surrounding plasma; thus in such cases the interaction region at first narrows with increasing heliocentric distance. The nonlinear rise in pressure associated with this squeezing eventually causes the forward and reverse waves bounding the interaction region to steepen into shocks. Because shocks (Sect. 5.3) propagate faster than the fast mode (sound) speed, the interaction region can expand once shock formation occurs. Observations reveal that relatively few stream interaction regions are bounded by shocks at 1 AU, but that most are near the equatorial plane at heliocentric distances beyond about 3 AU because the fast mode (sound) speed generally decreases with increasing distance from the Sun. At heliocentric distances beyond about 5 – 10 AU a large fraction of the mass and magnetic field flux in the solar wind at low heliographic latitudes is found within expanding compression regions bounded by shock waves on the rising portions of strongly damped high-speed streams. The basic structure of the solar wind near the solar equatorial plane in the distant heliosphere thus differs considerably from that observed near Earth. Stream amplitudes are severely reduced, and short-wavelength structure is damped out. The dominant structures at low latitudes (*i.e.*, within the band of variable wind ^[13]) in the outer heliosphere are expanding compression regions that interact and merge with one another to form what are commonly called global merged interaction regions, GMIRs.”

¹³ The solar wind originating from high latitudes is typically fast as long as there are polar cap fields, *i.e.*, in phases around solar minimum. The solar wind from mid-to-low latitudes is a mixture of fast and slow streams, particularly around solar maximum.

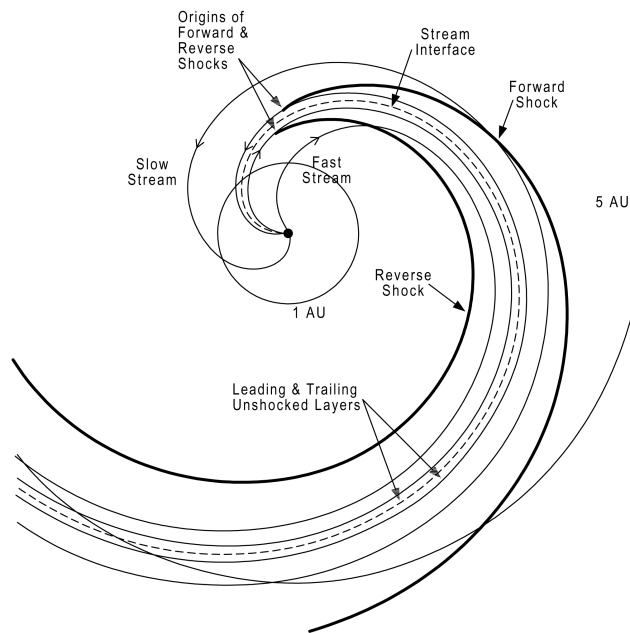


Figure 5.9: Idealized schematic illustrating the basic structure of a corotating interaction region in the solar equatorial plane. The dashed line threading the middle of the corotating interacting region (CIR) denotes the stream interface and the solid heavy lines indicate the forward and reverse shocks. Plasma immediately surrounding the stream interface is compressed, but not shocked. [Note that in this stationary model moving a radial cut through the Sun in the clock-wise direction is equivalent to going forward in time at any given angle. Fig. III:8.5; source: Crooker *et al.* (1999).]

Stream evolution in two and three dimensions

“Should the coronal expansion be time-independent but inhomogeneous in helio-centric latitude and longitude, stream evolution proceeds similarly at all longitudes, but the state of a stream’s evolution varies with longitude. Because of solar rotation, the interaction region on the leading edge of a high-speed stream is wound into a spiral that at any particular heliocentric distance is inclined to the radial direction at an angle intermediate to that of the magnetic field threading the slow and fast wind flows respectively, as illustrated in Figure 5.9. The entire pattern of interaction co-rotates with the Sun and the compression region is known as a corotating interaction region, CIR. It is important to note, however, that it is only the pattern that co-rotates with the Sun because each parcel of solar wind plasma moves radially outward in this simple picture, except within the interaction region itself where both radial and transverse deflections of the flow occur. Because a CIR is inclined relative to the radial direction the pressure gradients associated with the interaction region have both radial and azimuthal components. With increasing heliocentric distance the forward wave

propagates both anti-sunward and westward (in the direction of planetary motion about the Sun), whereas the reverse wave propagates both sunward (in the rest frame of the average solar wind) and eastward. As a result, the slow wind is accelerated outward and deflected westward within the interaction region and the fast wind is decelerated and deflected eastward there, thus accounting for the characteristic westward and then eastward flow deflections commonly associated with interaction regions on the leading edges of high-speed streams (see Figure III:8.3 and related discussion). One consequence of the transverse deflections is that they partially relieve the pressure build-up induced by stream steepening by allowing the plasma to slip aside. Thus solar wind streams steepen less rapidly than is predicted by the simple 1D simulation shown in Figure 5.8.”

“There is, of course, a three-dimensional aspect to stream evolution that becomes most apparent at heliocentric distances beyond about 3 – 4 AU and at latitudes away from the solar equatorial plane. [O]bservations have revealed (1) that the reverse shocks on the trailing edges of CIRs are observed both within the low-latitude band of solar wind variability and at latitudes $10^\circ - 20^\circ$ above that band, whereas the forward shocks on the leading edges of corotating interaction regions are generally confined to the low-latitude band itself; and (2) that in addition to the flow deflections already discussed, the slow wind is usually deflected in both solar hemispheres toward the opposite hemisphere at the forward shocks, whereas the fast wind is usually deflected poleward at the reverse shocks.” For more details, see Sect. III:8.5.

5.5.2 A non-conducting body without atmosphere

Next, we look at one of the simplest setups for a flow encountering a body: a non-conducting sphere moving relative to a low-density magnetized plasma. The non-conducting body has no intrinsic magnetic field, and no currents can be induced in it by the magnetized plasma through which it moves. For a low-density plasma, this means that no signal is sent upstream from that body that could modify the flow heading towards the body: the gas pressure is insignificant and the magnetic field is not affected by the non-conducting body, moving through it without generating reflected waves that might move upstream from the body. Consequently, the upstream plasma that is on a collision course with the body will, in essence, simply crash onto the body, while the plasma to the sides of that body continues to flow without noticing the object at all [(Fig. 5.10a)]. {A65} This is true regardless of whether the body is moving sub-Alfvénically or super-Alfvénically relative to the incoming plasma. Examples of rather non-conducting bodies in the Solar System are Earth’s Moon, Jupiter’s moon Callisto and Saturn’s moon Rhea (which are subjected to the sub-Alfvénical flow of the giant planets’ magnetospheric plasma throughout their orbits), and also many asteroids, particularly the S-type, or silicate-rich ‘rocky’ ones (note that MHD does not apply for asteroids small compared to gyro-radii of solar wind ions; among other things, this means there is no upstream shock, as that is a collective phenomenon).

In such situations, there will be a wake behind the body that is void of plasma immediately downstream of the body. This void has two primary effects. One is that

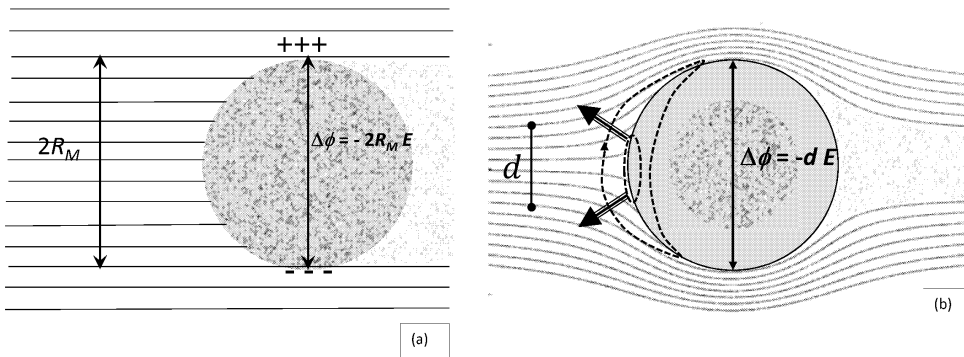


Figure 5.10: Schematics of plasma flow (shown by lines of flow) at velocity \mathbf{v} from the left onto (a) a non-conducting body and (b) a conducting body [with radius R_M]. In the plasma, \mathbf{B} is into the paper, \mathbf{E} is $-\mathbf{v}/c \times \mathbf{B}$ in both cases. Diagram (a) shows that a non-conducting body builds up surface charge that imposes a potential drop $\Delta\phi = -2R_M E$ across the diameter, producing an electric field that opposes the solar wind electric field. Diagram (b) shows the response of a conducting body that does not build up surface charge. Conducting paths allow current (shown schematically as a dashed line) to flow through the body and close in the incident flow. Heavy banded arrows identify the orientation of the resultant $\mathbf{j} \times \mathbf{B}$ force that diverts part of the incident flow. Because much of the incident flow has been diverted, the potential drop across the body is only $\Delta\phi = -d E$, where $d < R_M$ is the distance in the incident flow between the flow lines that just graze the body. The electric field that penetrates the body is a fraction of the upstream field determined by the fraction of the upstream flow that impacts the surface. In the wake region, gray in both diagrams, the plasma pressure is reduced and the magnetic pressure is increased relative to the upstream values. [Fig. IV:10.2]

the plasma pressure has dropped away, and consequently plasma will propagate into the void to refill it (at about the slow-mode speed), taking matter from an outward propagating domain behind a rarefaction front that moves out at essentially the fast-mode wave speed (somewhat anisotropically); this leads to a wake in density behind the body, forming a somewhat asymmetric conical V-shape, albeit with the wings ending on a terminator-like ring defined by where the incoming plasma is just tangent to the body's surface. The other effect is that because the contribution of the plasma to the total pressure falls away immediately behind the object, the field is somewhat strengthened (mainly by a motion perpendicular to the plane spanned by field and flow vectors) to regain total pressure balance, to adjust again further downstream as plasma refills the void. In the case of Earth's Moon in the solar wind, the void persists up to about a dozen lunar radii downstream. {A66}

Note that the Moon is not a perfect insulator, and in fact has something akin to a weak ionosphere because the incoming solar wind ionizes some of the surface dust, and the ongoing process of ionization of such 'pick-up particles' is associated with a current that can send a magnetic signal upstream; see Chs. IV:10&11. {A66}

5.5.3 Flow around a conducting body

When a conducting body moves through a magnetized plasma, the $-\mathbf{v}/c \times \mathbf{B}$ electric field associated with the relative motion induces a potential drop across the body. Because that body is conducting, a current flows to attempt to neutralize the charge buildup that would occur in the absence of such a current. That current closes through the incoming plasma in such a way that the associated Lorentz forces act to bend the plasma around the object (Fig. 5.10b), which, equivalently, sets up an induced magnetic field that, at infinite conductivity, would keep the external field entirely outside the conducting body. The conducting medium can be a metallic core (which in the case of the moons of the giant planets is generally too small to detect with significance) or a mantle ocean of water with dissolved electrolytes, *e.g.*, salts (which is seen on multiple moons of the giant planets, such as the Galilean moon Europa at Jupiter which is discussed in IV:10.5.2), a magma layer (as is inferred for another of the Galilean moons, Io) or an ionosphere in the upper layers of the body’s atmosphere (such as in the case of Venus discussed in Sect. 13.2.3).

Europa moves sub-Alfvénically within the jovian magnetosphere. Because its orbit is inclined by about 10° relative to Jupiter’s magnetic dipole moment, Europa senses a changing magnetic field throughout its orbit, so that not only a current system is induced by its motion, but that current system (and thus its associated perturbation magnetic field) evolves through the orbit. These changes (slightly modified by pickup ions playing their part) have revealed where the current flows, and thereby the existence of a conducting liquid underneath the non-conducting ice mantle.

The induced current system, or equivalently the induced magnetic field, sends out information about the obstacle into the plasma ahead. These waves, led by the magnetosonic fast-mode type, modify the upstream flow so that it can begin to deflect well ahead of the body. Part of the incoming flow may impact upon the surface if the conduction is not infinite. The rest of the flow is diverted around the body, leading to a narrower wake behind the body than in the case of an insulating body.

If the flow is coming in super-magnetosonically, however, no significant ‘warning signal’ can move upstream so that much of the flow will impact the body or flow very close to it, as it would in the case of large iron-rich asteroids (as has been argued, for example, for asteroid Ida, despite it being characterized as an S-type). But for many asteroids the scale is too small for MHD to apply, so the analogy with larger bodies fails in multiple respects.

Venus and Mars do not have active dynamos, but they do have conducting ionospheres. “The magnetic structure surrounding Mars and Venus is similar to that around magnetized objects because the interaction causes the magnetic field of the solar wind to drape around the planet. The draped field stretches out downstream (away from the Sun), forming a magnetotail (Fig. 5.11). The symmetry of the magnetic configuration within such a tail is governed by the orientation of the magnetic field in the incident solar wind, and that orientation changes with time. For example, if the interplanetary magnetic field (IMF) is oriented northward, the symmetry plane of the tail is in the east-west direction and the northern lobe field [has a component]

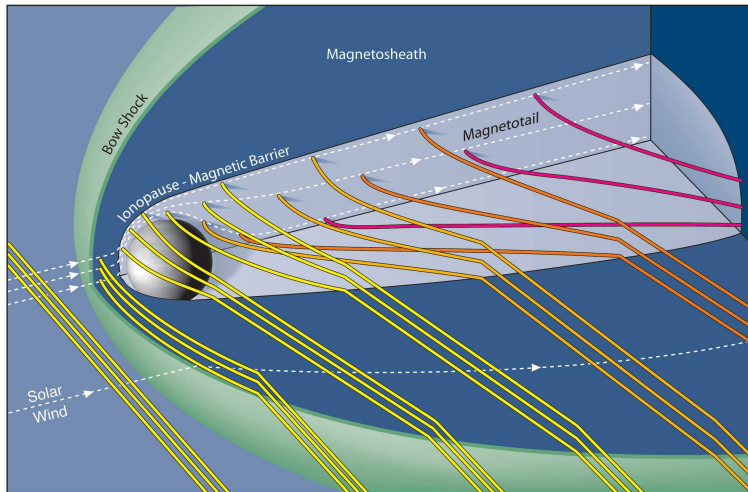


Figure 5.11: Sketch of the draping of tubes of solar magnetic flux around a conducting ionosphere such as that of Venus. The flux tubes are slowed down and sink into the wake to form a tail. [color version of Fig. I:13.12] For a color version of this figure, see *arXiv:2001.01093*.

away from the Sun while the southern lobe field [has a component] towards the Sun. A southward oriented IMF would reverse these polarities, and other orientations [(such as the east-west orientation in Fig. 5.11)] would produce corresponding rotations of the tail's plane of symmetry. {A67}

The solar wind brings in magnetic flux tubes that pile up at high altitudes at the dayside ionopause where, depending on the solar wind dynamic pressure [(ρv^2)], they may either remain for extended times, thus producing a magnetic barrier that diverts the incident solar wind, or may penetrate to low altitudes in localized bundles. Such localized bundles of magnetic flux are often highly twisted structures stretched out along the direction of the magnetic field. [These bundles] may be dragged deep into the atmosphere, possibly carrying away significant amounts of atmosphere. {A67}

While Mars' remarkably strong remanent magnetism ^[14] extends its influence > 1000 km from the surface, the overall interaction of the solar wind with Mars is more atmospheric than magnetospheric. Mars interacts with the solar wind principally through currents that link to the ionosphere, but there are portions of the surface over which local magnetic fields block the access of the solar wind to low altitudes. It has been suggested that 'mini-magnetospheres' extending up to 1000 km form above the regions of intense crustal magnetization in the southern hemisphere; these mini-magnetospheres protect portions of the atmosphere from direct interaction with the solar wind. [...]"

¹⁴'Remanent magnetism' is defined as the magnetic field that remains after the magnetizing field is removed.

5.5.4 Plasma flow around a permanently magnetized body

Ganymede, orbiting sub-magnetosonically in Jupiter’s magnetosphere, is the only moon with a substantial, large-scale internally maintained magnetic field. Of the planets, Earth and the giant planets all have magnetic fields sustained by dynamos, but in contrast to Ganymede and its surrounding plasma, they all move super-magnetosonically relative to the solar wind. In all of these cases, the bodies’ magnetic fields are the primary ‘obstacle’ to the plasma flowing around it. All deflect the plasma stream around them. In the ideal-MHD approximation, the field-carrying plasma should flow around the magnetic obstacle, with the distance out to which the body’s field can withstand the inflowing field dependent on the relative strength of the forces exerted (balancing magnetic fields and plasma inertial forces). In a realistic, non-ideal case, reconnection between the fields is important, which depends on the plasma parameters and on the relative directions of the two fields involved. In case the relative motion corresponds to a super-magnetosonic flow, a shock front develops; upstream of that, the inflowing plasma (generally the incoming solar wind) is, so to speak, unaware of the existence of the obstacle ahead, while the flow is deflected only after going through the shock, then moving around the obstacle at a reduced speed. This can still be faster than the Alfvén speed; see IV:10.4, which leads to a strong bending back of the wind flow around Earth into a bullet shape, in contrast to a V-shaped pattern for a sub-magnetosonic flow (*cf.* Fig. IV:10.4).

For those planets with a magnetic field of their own, *i.e.*, those with a dynamo, the solar wind leads to a shock-enveloped, asymmetrically-stretched magnetosphere. “In the most general context, we consider a *central object*: a distinct well-defined body held together (in most cases) by its gravity. It is immersed in a tenuous *external medium*, assumed to be sufficiently ionized so it behaves like a plasma. The *magnetosphere* is then the region of space around the central object within which the object’s magnetic field has a dominant influence on the dynamics of the local medium. An alternative and in some ways more precise view is to regard the magnetosphere as the region enclosed by its bounding surface, the *magnetopause*, the latter being defined as the discontinuity of the magnetic field where its direction changes: inside it is controlled by the magnetic field of the central object, while outside it is determined primarily by the magnetic field of the distant external medium. This definition is particularly useful for the magnetospheres of planets in the solar wind: the continual variability of the interplanetary magnetic field direction in contrast to the relative constancy of the planetary magnetic dipole allows in most cases an easy observational identification of the magnetopause.”

5.5.5 A closed magnetosphere

“The basic configuration of a prototypical planetary magnetosphere is sketched in Figure 5.12. Many of its characteristic structures can be understood on the basis of a simple model that takes into account only the two ingredients indispensable for the formation of a magnetosphere: the solar wind (mass density ρ_{sw} , bulk velocity \mathbf{v}_{sw}) and the planetary magnetic field (dipole moment $\mu_{\text{p}} = B_{\text{p}} R_{\text{p}}^3$, with B_{p} the surface magnetic field strength at the equator and R_{p} the radius of the planet). As a consequence of

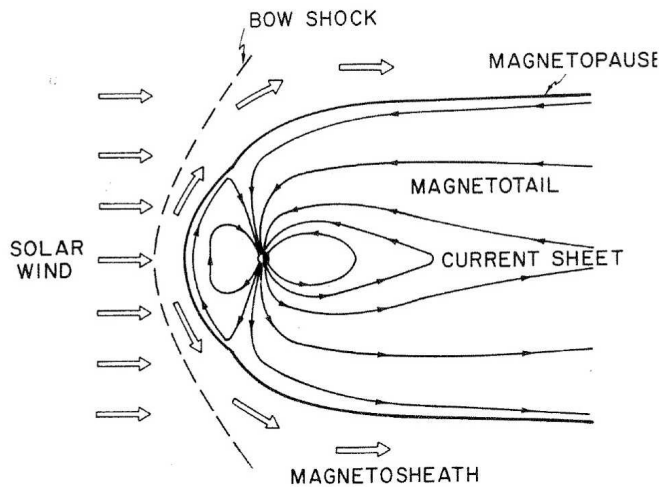


Figure 5.12: Schematic view of a magnetically closed magnetosphere, cut in the noon-midnight meridian plane. Open arrows: solar wind bulk flow. Solid lines within magnetosphere: magnetic field lines (direction appropriate for Earth). [Fig. I:10.1]

constraints imposed by the magnetohydrodynamic (MHD) approximation [...], the boundary surface between the solar wind and the planetary magnetic field — the magnetopause — is nearly impermeable both to plasma and to magnetic field, resulting in a clear separation between the two distinct regions of space: the magnetosphere itself, within which the magnetic field lines from the planet are confined and from which the solar wind plasma is excluded, and the exterior region beyond the magnetopause, to which the plasma that comes from the solar wind is confined. This simple *closed magnetosphere* is only a first-order approximation (in reality the magnetopause is not completely impermeable but allows, under certain conditions, some penetration of plasma and of magnetic field to produce the *open magnetosphere* described in Sect. 5.5.6); it does, however, describe fairly accurately the size and shape of the main structures.

The solar wind flow, initially directed away from the Sun, must be diverted around the magnetosphere, as indicated in Figure 5.12. Because the initial flow speed is supersonic and super-Alfvénic (faster than both the speed of sound and the Alfvén speed v_A), the solar wind is first slowed down, deflected, and heated at a detached *bow shock* standing upstream of the magnetopause (analogous to the sonic boom in supersonic aerodynamic flow past an obstacle). The region between the bow shock and the magnetopause, within which the plasma from the solar wind is flowing around the magnetosphere, gradually speeding up and cooling, is called the *magnetosheath* [...].

{A68}

The location of the magnetopause is determined primarily by the requirement of pressure balance: the total pressure (plasma plus magnetic) must have the same value on both sides of the discontinuity. In the simple closed magnetosphere considered here,

{A68}

the plasma pressure inside the magnetopause and the magnetic pressure outside are both neglected. The exterior pressure then scales as the linear momentum flux density in the undisturbed solar wind, $\rho_{\text{sw}} v_{\text{sw}}^2$ (often called the *dynamic pressure* [or *ram pressure*] of the solar wind), and is maximum in the sub-solar region, where the plasma near the magnetopause is almost stagnant. The interior pressure scales as the magnetic pressure of the dipole field, $(1/8\pi)(\mu_{\text{p}}/r^3)^2$ with μ_{p} the magnetic dipole moment of the planet, and thus varies strongly with distance from the planet. Equating the two gives an estimate for the distance R_{mp} of the sub-solar magnetopause:

$$R_{\text{mp}} = \frac{(\xi \mu_{\text{p}})^{1/3}}{(8\pi \rho_{\text{sw}} v_{\text{sw}}^2)^{1/6}} \quad (5.22)$$

where ξ is a numerical factor to correct for the added field from magnetopause currents ($\xi \simeq 2$ to first approximation). {@A69}

The distance given in Eq. (5.22) (with various choices of ξ) is often called the Chapman-Ferraro distance. [Here, we] consistently use the symbol R_{CF} for the distance defined by Eq. (5.22) with $\xi = 2$, *i.e.*, for the nominal distance of the sub-solar magnetopause predicted by pressure balance; [the symbol R_{mp} is reserved] for the *actual* distance of the sub-solar magnetopause in any particular context. Thus, $R_{\text{mp}} \simeq R_{\text{CF}}$ in the present case of a simple closed magnetosphere but not necessarily in the case of more general models. {@A70} {A71}

The pressure balance condition, combined with assumptions about the sources of the magnetic field within the magnetosphere, may be used to calculate not only the distance to the sub-solar point, but also the complete shape of the magnetopause surface (for discussion of such models at Earth, see Ch. I:11). Typically the magnetopause is roughly spherical on the dayside of the planet, facing into the solar wind flow (the effective center of the sphere being located behind the planet, very roughly at a distance $\sim 0.5 R_{\text{mp}}$), and is elongated in the anti-sunward direction. {@A70} {A71}

The magnetopause distance R_{mp} may be regarded as the characteristic scale for the size of a magnetosphere. Equal to R_{CF} in the case of negligible plasma pressure and no magnetic field sources other than the planetary dipole inside the magnetosphere, R_{mp} can be readily calculated from Eq. (5.22) given only a few basic parameters of the system. In the case that the plasma pressure or a non-dipolar field in the outer regions of the magnetosphere are not negligible, the qualitative effects on R_{mp} can still be estimated from pressure balance, as illustrated in Figure 5.13: (a) the actual distance R_{mp} is larger than the nominal distance R_{CF} (the value $\xi = 2$ instead of $\xi = 1$ is in fact a consequence of the non-dipolar field from the magnetopause currents), (b) a change of solar wind dynamic pressure produces a larger change of magnetopause distance — the magnetosphere is less ‘stiff’ if plasma pressure in the interior is significant.”

5.5.6 The open magnetosphere

“At the location of the planets, the interplanetary magnetic field is weak in the sense that the energy density of the magnetic field is very small in comparison to the kinetic energy density of solar wind bulk flow, or equivalently $v_{\text{A}}^2 \ll v_{\text{sw}}^2$ [(see Sect. 3.5.2)]. The flow of solar wind plasma past the magnetospheric obstacle deforms the magnetic

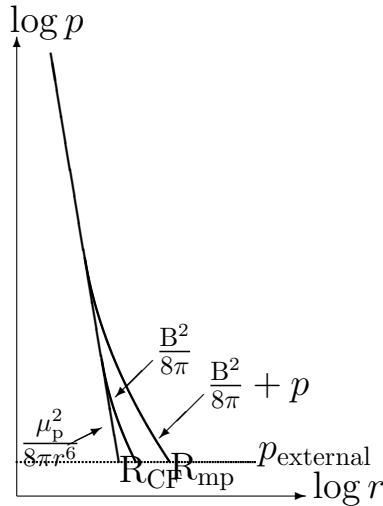


Figure 5.13: Variation of total pressure (magnetic plus plasma) with distance from the planet and its relation to the radial distance of the sub-solar magnetopause. Compared are the relationship in Eq. (5.22) to a schematic representation of a more realistic plasma-filled, non-dipolar planetary magnetic field. [Fig. I:10.2]

field lines within the magnetosheath and drapes them around the magnetopause, a process well modeled at Earth (*cf.* Sect. I:11.4). The magnetic field is amplified and may become dynamically no longer negligible as the magnetopause is approached, but the total pressure is in general not greatly modified, an increase of magnetic pressure often being offset by a decrease of plasma pressure. One might therefore anticipate that the effect of the interplanetary magnetic field on planetary magnetospheres should be minimal.

What is overlooked in the above discussion is the possibility that, through the process of *magnetic reconnection* [...], the magnetic field lines from the planet may become connected with those of the interplanetary magnetic field, to produce the magnetically *open magnetosphere*, sketched in Fig. 5.14 for the simplest case of the interplanetary magnetic field parallel to the planetary dipole moment [(and thus with antiparallel fields at their interface)]. The magnetopause is now no longer impermeable to the magnetic field, and as a consequence it no longer need be impermeable to plasma, either. {A72} {A73}

The modifications of the magnetospheric system implied by the open character of the magnetosphere are in some ways minor, in other ways very far-reaching. The location and shape of the dayside magnetopause is for the most part not greatly modified (in agreement with the expectations above). The component B_{\perp} of the magnetic field normal to the magnetopause is in general small compared to the magnitude of the field, $|B_{\perp}| \ll |B|$ (so much so that it is often difficult to establish by direct observation that $B_{\perp} \neq 0$, and much of the evidence for an open magnetosphere has been indirect). On {A72} {A73}

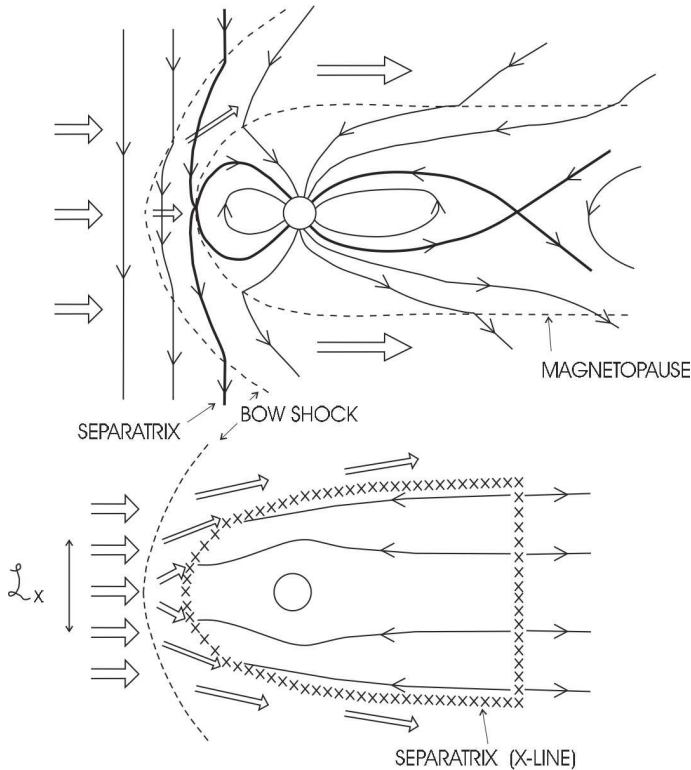


Figure 5.14: Schematic representation of a magnetically open magnetosphere. Top: cut in noon-midnight meridian plane; thick lines are magnetic field lines within the ‘separatrix surfaces’ that separate open from closed or open from interplanetary field lines; other conventions same as in Fig. 5.12. Bottom: cut in equatorial plane; a line of \times symbols represents intersection with the two branches of the separatrix; solid lines are streamlines of magnetospheric plasma flow, and \mathcal{L}_x represents the projection of the dayside magnetic reconnection region along streamlines into the solar wind. [Fig. I:10.3]

the other hand, the total amount of open magnetic flux Φ_M of one polarity can (at least at Earth) become comparable to the maximum amount that could reasonably be expected to be open (estimated as $\sim \mu_p/R_{mp}$, the dipole flux beyond the distance of the sub-solar magnetopause); despite $|B_\perp| \ll |B|$, this is possible if the effective length of the magnetotail is much larger than R_{mp} . [... That length is in large part determined by the efficiency of the reconnection process. This] depends greatly on the relative orientation of magnetic fields on the two sides of the magnetopause, one result of which is that the open character of the magnetosphere is most pronounced when the interplanetary magnetic field is parallel to the planetary dipole moment (*i.e.*, anti-parallel to the dipole magnetic field in the equatorial plane), $\mathbf{B}_{sw} \cdot \boldsymbol{\mu}_p > 0$. Because the direction of the interplanetary magnetic field is highly variable on all time scales, this can lead to pronounced time-varying changes of magnetospheric configuration as well as energy input and dissipation [...].”

Although diagrams of the terrestrial environment such as Fig. 5.14 generally include

Table 5.2: *Properties of the solar wind near the planets [after Table I:13.2]. Plasma β values assume a solar-wind temperature of 1.5 MK.*

Planet	Distance d_p (AU) ^a	Solar wind ion density (cm^{-3})	B_{IMF} (μG) ^c	$\approx \beta$	$\approx v_A$ (km/s)
Mercury	0.39	53	410	2	120
Venus	0.72	14	140	4	80
Earth	1	7 ^b	80	6	70
Mars	1.52	3	50	6	60
Jupiter	5.2	0.2	10	10	50
Saturn	9.5	0.07	6	10	50
Uranus	19	0.02	3	10	50
Neptune	30	0.006	2	10	50

^a $1 \text{ AU} = 1.5 \cdot 10^8 \text{ km}$; ^b The density of the solar wind fluctuates by about a factor of 5 about typical values of $n_{\text{sw}} \sim (7 \text{ cm}^{-3})/d_p^2$; ^c mean values.

Table 5.3: *[Intrinsic magnetic fields of Solar System bodies. After Table I:13.3, with planetary rotation periods P_p and planetary radii R_p].*

	Gany- mede	Mer- cury	Earth	Jupiter	Saturn	Uranus	Nep- tune
$B_{\text{dip,eq}}$ ^a	7.2 mG	3 mG	0.31 G	4.3 G	0.21 G	0.23 G	0.14 G
$B_{\text{max}}/B_{\text{min}}$ ^b	2	2	2.8	4.5	4.6	12	9
dipole tilt ^c	-4°	$\sim 10^\circ$	11.2°	-9.4°	-0.0°	-59°	-47°
dipole offset ^d	-	-	0.076	0.119	0.038	0.352	0.485
obliquity ^e	0°	0°	23.5°	3.1°	26.7°	97.9°	29.6°
$\delta\phi_{\text{sw}}$ ^f	90°	90°	$67\text{-}114^\circ$	$87\text{-}93^\circ$	$64\text{-}117^\circ$	$8\text{-}172^\circ$	$60\text{-}120^\circ$
P_p (h)	171	4223.	24	9.9	10.7	17.2	16.1
$R_p/R_{p,\oplus}$	0.41	0.38	1	11.2	9.4	4.0	3.9

^a Surface field at dipole equator. Values derived from modeling the magnetic field as an offset dipole; ^b ratio of maximum surface field to minimum, which equals to 2 for a centered dipole field (this ratio tends to increase with the planet's oblateness); ^c angle between the magnetic and rotation axes (positive values correspond to magnetic field directed north at the equator; the magnetic dip poles of the Earth's field are currently located at 86°N and 65°S latitudes and moving about 10° per century); ^d values (in planetary radii, R_p); ^e the inclination of a planet's spin equator to the ecliptic plane; ^f range of the angle between the radial direction from the Sun and the planet's rotation axis over an orbital period (in Ganymede's case, the angle is between the corotational flow and the moon's spin axis).

the bow shock, the processes discussed here are generic and apply equally when a magnetized plasma flows sub-Alfvénically around a magnetized body. One example is a numerical simulation of Ganymede orbiting within Jupiter's magnetosphere as shown

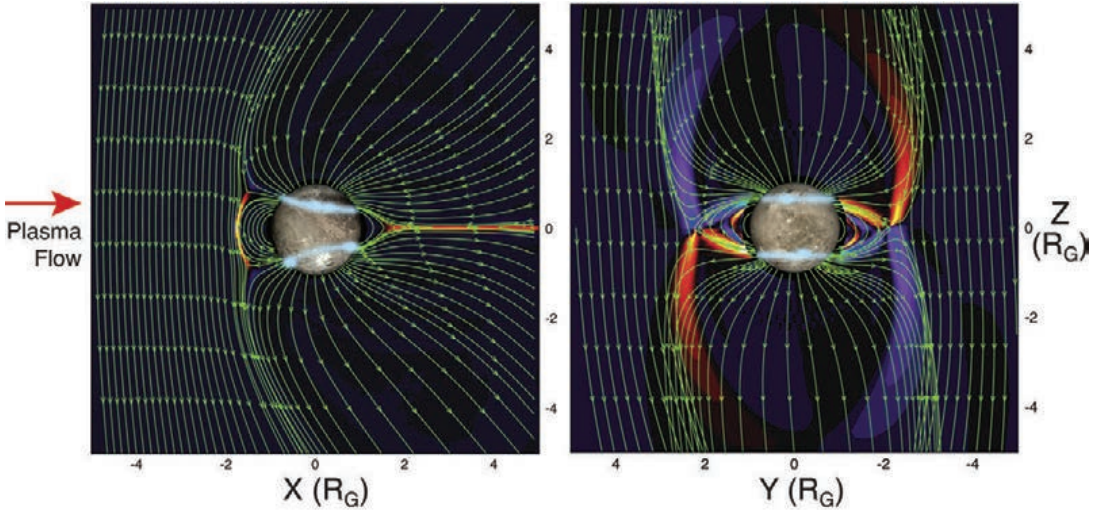


Figure 5.15: Numerical model of the magnetosphere of Ganymede with the satellite and the location of auroral emissions superimposed. [The shaded areas show the current density perpendicular to the plane; yellow-red out of the plane, purple-blue into the plane.] Left: view looking at the anti-Jupiter side of Ganymede. Right: View looking in the direction of the plasma flow at the upstream side (orbital trailing side) of Ganymede with Jupiter to the left. The shaded areas show the regions of currents parallel to the magnetic field; yellow-red anti-parallel, purple-blue parallel]. [Fig. I:13.11; source: Jia *et al.* (2008).] For a color version of this figure, see [arXiv:2001.01093](https://arxiv.org/abs/2001.01093).

in Fig. 5.15.

5.5.7 Solar wind-magnetosphere-ionosphere interaction

Fundamental principles

“A well-known consequence of the MHD approximation is a constraining relation between the plasma bulk flow and the magnetic field: plasma elements that are initially on a common field line remain on a common field line as they are carried by the bulk flow. Because magnetic field lines in the magnetosphere of a planet connect to the ionosphere of the planet, any discussion of plasma flow in the magnetosphere immediately involves questions of magnetosphere-ionosphere interaction. The field lines extend in fact into the interior of the planet, which in many cases is highly conducting electrically; hence it might seem that the magnetospheric flow should be constrained by the planet itself. This does not happen, however, because [...] most planets possess an electrically neutral (and effectively non-conducting) atmosphere, sandwiched between the ionosphere and the planetary interior. Although very thin in comparison to the radius of the planet, this layer suffices to break the MHD constraints and thus allows the plasma in the ionosphere and the magnetosphere to move without being necessarily attached to the planet; without such an insulating layer, much of the magnetospheric dynamics as we know it would not be possible.

While the plasma in the ionosphere can thus move relative to the planet, it remains

constrained to move more or less together with the plasma in the magnetosphere. The conventional formulation, however, describes the plasma flow rather differently in the two regions. The magnetosphere is treated, to first approximation at least, as an MHD medium, with the electric field \mathbf{E} related to the plasma bulk flow \mathbf{v} by the MHD approximation and with the electric current \mathbf{j} related to plasma pressure by stress balance. The ionosphere is treated, on the other hand, as a moving conductor (the conductivity results primarily from collisions between the ions and the neutral particles, planetary ionospheres being for the most part weakly ionized), with \mathbf{j} related by a conductivity tensor to $\mathbf{E} + \mathbf{v}_\perp \times \mathbf{B}/c$, where \mathbf{v}_\perp is the bulk velocity of the neutral medium. [... A few comments on this coupling:]

(1) As long as $v_A^2/c^2 \ll 1$ (*i.e.*, the inertia of the plasma is dominated by the rest mass of the plasma particles, not by the relativistic energy-equivalent mass of the magnetic field), \mathbf{v} produces \mathbf{E} but \mathbf{E} does not produce \mathbf{v} . The primary quantity physically is thus the plasma bulk flow, established by appropriate stresses. The electric field is the result of the flow, not the cause; its widespread use in calculations is primarily for mathematical convenience [...].

(2) The electric current in the ionosphere is not an Ohmic current in the physical sense, and its conventional expression by the 'ionospheric Ohm's law' [as discussed around Eq. (2.22)] has only a mathematical significance [...]. Physically, the current is determined by the requirement that the Lorentz force balance the collisional drag between the plasma and the neutral atmosphere when their bulk flow velocities differ. [...] The current in the ionosphere is thus governed by stress balance in the same way as the current in the magnetosphere [... while neglecting the time derivative term in the momentum equation.]

(3) Underlying the neglect of the time derivative (acceleration) terms in the momentum equations is the implicit assumption that any imbalance between the mechanical and the magnetic stresses (which, fundamentally, is what determines the acceleration of the plasma) produces a bulk flow that acts to reduce the imbalance, which then becomes negligible over a characteristic time scale (easily shown to be of the order of the Alfvén wave travel time across a typical spatial scale \mathcal{L} , *e.g.*, along a field line). The theory is thus applicable only to systems that are stable and evolve on time scales much longer than \mathcal{L}/v_A .

(4) For [phenomena well above the scale of plasma oscillations, so slow compared to $1/\omega_p$ and large compared to $\lambda_e \equiv c/\omega_p$,] (where ω_p is the electron plasma frequency and λ_e the electron inertial length, also known as collisionless skin depth)], \mathbf{j} adjusts itself to become equal to $(c/4\pi)\nabla \times \mathbf{B}$ and not the other way around; although \mathbf{B} is in principle determined from a given \mathbf{j} by Maxwell's equations (on a time scale of light travel time, $\sim \mathcal{L}/c$), in a large-scale plasma any $\mathbf{j} \neq (c/4\pi)\nabla \times \mathbf{B}$ is immediately (on a time scale $\sim 1/\omega_p$) changed by the action of the displacement-current electric field on the free electrons in the plasma. The current continuity condition $\nabla \cdot \mathbf{j} = 0$ is thus satisfied automatically; there is no physics in current closure — what is often discussed under that rubric is in reality the coupling of the Maxwell stresses along different portions of a field line."

Corotation

“Corotation with the planet is the simplest pattern of plasma flow in a planetary magnetosphere and one that plays a major role particularly in the magnetospheres of the giant planets. [...] If the planet possesses an insulating atmosphere, the rotation of the planet itself has no *direct* effect on plasma flow in the magnetosphere, as discussed in Sect. 5.5.7. What does affect plasma flow is the motion of the neutral upper atmosphere (thermosphere) at altitudes of the ionosphere (where the neutral and the ionized components coexist and interact). ‘Corotation with the planet’ is therefore not quite an accurate description. What really is meant is co-motion with the upper atmosphere, which in turn is then assumed to corotate with the planet, for reasons unrelated to the magnetic field: vertical transport of horizontal linear momentum from the planet to the neutral atmosphere (*e.g.*, by collisional or eddy viscosity and similar processes), together with an assumed small relative amplitude of neutral winds.

Any difference between the bulk flow of the neutral medium and the ionized component of the plasma in the ionosphere results in a collisional drag that must be balanced by the Lorentz force; without it, the drag force would soon bring the plasma to flow with the (much more massive) neutral medium. The Lorentz force in the ionosphere is coupled to a corresponding Lorentz force in the magnetosphere, which in turn must be balanced locally by an appropriate mechanical stress. The net result is that departure from corotation requires a mechanical stress in the magnetosphere to balance the plasma-neutral drag in the ionosphere; conversely, plasma will corotate if the stress in question is negligibly small. (It is fairly obvious that the direction of the stress must be more or less azimuthal, opposed to the direction of rotation.) Quantitatively, the requirements for corotation of magnetospheric plasma may be expressed by four conditions:

(1) Planet-atmosphere coupling: This is simply the assumption, discussed above, that the upper atmosphere effectively corotates with the planet.

(2) Plasma-neutral coupling in the ionosphere: the collisional drag of the neutral medium on the plasma must be sufficiently strong to ensure $\mathbf{v} \simeq \mathbf{v}_n$. The quantitative condition is derived in principle [from the momentum equation of the ionospheric plasma (horizontal components only; compare with Eq. (3.3) to see what is hiding in the ellipsis)

$$\frac{\partial \rho \mathbf{v}}{\partial t} + \dots = \mathbf{j} \times \mathbf{B}/c - \nu_{in} \rho (\mathbf{v} - \mathbf{v}_n) \quad (5.23)$$

with the left-hand side set to zero (where ν_{in} is the ion-neutral collision frequency),] but with one complication: what is relevant for the interaction with the magnetosphere is not the local current density \mathbf{j} but the current per unit length integrated over the extent of the ionosphere in altitude z , *i.e.*, the height-integrated current $\mathbf{I} \equiv \int \mathbf{j} dz$. A direct integration of Eq. (5.23) over height, however, is not simple because \mathbf{v} varies strongly with z (even when \mathbf{v}_n is independent of z , as usually assumed). The horizontal electric field, on the other hand, is essentially constant over the entire (relatively thin) height range of the ionosphere, from continuity of tangential components implied by Faraday’s law. It is thus convenient to first express \mathbf{j} by [the ionospheric Ohm’s law as

discussed around Eq. (2.22)] and then integrate over height to obtain

$$\mathbf{I}_\perp = (B/c) \left[\Sigma_P \hat{\mathbf{B}} \times (\mathbf{v}_0 - \mathbf{v}_n) - \Sigma_H (\mathbf{v}_0 - \mathbf{v}_n)_\perp \right] \quad (5.24)$$

where \mathbf{v}_0 is the plasma flow at the top side of the ionosphere, related to the [rest-frame electric field \mathbf{E} or the electric field \mathbf{E}^* in the frame moving with the neutral atmosphere] by

$$\mathbf{E}^* = -(\mathbf{v}_0 - \mathbf{v}_n) \times \mathbf{B}/c \quad \text{or equivalently} \quad \mathbf{E} = -\mathbf{v}_0 \times \mathbf{B}/c. \quad (5.25)$$

Σ_P and Σ_H are the height-integrated Pedersen and the Hall conductances, Σ_P being the more important one for magnetosphere-ionosphere interactions (Hall currents close within the ionosphere, to first approximation).

Obviously, to ensure $\mathbf{v}_0 \simeq \mathbf{v}_n$, the ionospheric conductance Σ_P must be sufficiently large in relation to the height-integrated current \mathbf{I} , which scales as the current per unit length in the magnetosphere and hence ultimately as the mechanical stresses in the magnetosphere. For a more precise criterion, one must consider a specific process. [...]

(3) MHD coupling from ionosphere to magnetosphere along magnetic field lines: conditions (1) and (2) ensure merely that the plasma corotates at the top side of the ionosphere, at the foot of a magnetic flux tube within the magnetosphere. For corotation to extend into the magnetosphere itself, the MHD constraining relation between the flow and the magnetic field must hold [(Eq. (3.5)...)]

(4) Stress balance to maintain centripetal acceleration in the magnetosphere: If conditions (1), (2), and (3) are satisfied, the plasma will be corotating at least as far as the components of \mathbf{v} perpendicular to \mathbf{B} are concerned, but the flow parallel to \mathbf{B} remains unconstrained. For the entire flow to be corotational, one further condition must be satisfied: there must exist a radial stress to balance the centripetal acceleration of the corotating plasma. In most cases, this stress is produced by the corotation itself, as the magnetic field lines are pulled out until their tension force becomes sufficiently strong to balance the centripetal acceleration.”

“The four conditions for corotation {A74} are all, in essence, local conditions at a given magnetic flux tube. Deviations from corotational flow when one or another of these conditions is no longer satisfied need not, therefore, be global but can be confined to limited regions. Typically, plasma flow in any particular magnetosphere may follow corotation in the inner regions, out to a critical radial distance in the equatorial plane, and then deviate significantly from corotation at larger distances. The critical distance depends on which of the four conditions is violated and by which process.” Section I:10.4.4 provides more discussion.

Magnetospheric convection

“Magnetospheric convection may be considered the other canonical pattern (besides corotation) of plasma flow in a planetary magnetosphere, one that plays an overwhelmingly important role in the magnetosphere of Earth. The basic concept is that the flow of solar wind plasma past the magnetosphere imparts some of its motion to plasma in the outermost regions of the magnetosphere, either directly by MHD coupling along open field lines or through an unspecified tangential drag near the magnetopause.

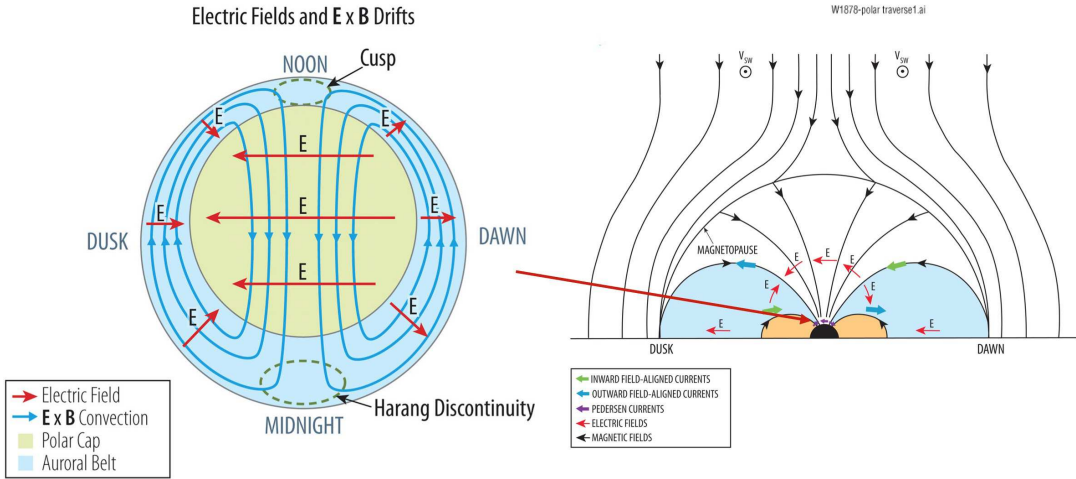


Figure 5.16: Schematic diagram of magnetospheric convection over the Earth’s north polar region (note the diagram extends in latitude only to the lower edge of the auroral belt). Left: streamlines of the plasma bulk flow and associated electric field (the Sun is towards the top). Right: Magnetic field and current systems for the northern hemisphere, for a southward interplanetary magnetic field, viewed from behind the Earth looking towards the Sun. [The red arrow indicates the small segment of this image shown on the right.] See Section I:10.4.3 for a detailed description and Sect. I:11.6 for corresponding MHD model results for the electric potential. For a schematic representation of magnetospheric convection throughout the magnetosphere, see Fig. I:13.4. [Source: NASA ;compare: Fig. I:10.5] For a color version of this figure, see arXiv:2001.01093.

By continuity of mass and magnetic flux transport, the flow then extends into the region of closed field lines or the interior of the magnetosphere, setting up a large-scale circulation pattern (which has some superficial resemblance to, but no real physical commonality with, what is called convection in ordinary fluid dynamics). Figure 5.16 illustrates the pattern, projected on the top-side ionosphere of the planet: shown on the left-hand side are the streamlines of the plasma bulk flow \mathbf{v} , which are also the equipotentials of the electric field according to Eq. (5.25). The lines of the electric field and the associated Pedersen currents are shown on the right-hand side [in red], along with a sketch of the implied Birkeland (*i.e.*, magnetic field-aligned) currents [in blue and green]. The yellow region is the polar cap, identified with the region of open field lines in the open magnetosphere; otherwise it represents the mapping (along field lines) of the boundary region where the solar wind motion is being imparted to magnetospheric plasma. The equatorial-plane counterpart of the flow outside the polar cap has been sketched in Fig. 5.14 (bottom).

A quantitative global measure of the strength of magnetospheric convection is the EMF (maximum line integral of the electric field) across the polar cap, \mathcal{E}_{PC} . Its physical meaning is that of the rate of magnetic flux transport (advection) through the polar cap. In an open magnetosphere, $c\mathcal{E}_{PC}$ equals the rate of reconnection of magnetic flux between the interplanetary and the planetary magnetic fields. Numerous empirical

studies at Earth have shown that for a southward interplanetary magnetic field (*i.e.*, [(at least partly) aligned with the Earth’s magnetic dipole, so that] $(\mathbf{B}_{\text{sw}} \cdot \hat{\boldsymbol{\mu}}_{\text{p}}) > 0$), \mathcal{E}_{PC} can be related to solar wind parameters roughly as

$$c\mathcal{E}_{\text{PC}} \simeq v_{\text{sw}} (\mathbf{B}_{\text{sw}} \cdot \hat{\boldsymbol{\mu}}_{\text{p}}) \mathcal{L}_{\times} \quad (5.26)$$

where \mathcal{L}_{\times} is a length that typically is a fraction (~ 0.2 to ~ 0.5) of the magnetopause radius R_{mp} . When comparing different magnetospheres, one often supposes that the ratio $\mathcal{L}_{\times}/R_{\text{mp}}$ is a more or less universal constant. Physically, \mathcal{L}_{\times} may be looked at as the length of the reconnection X-line on the magnetopause at which the magnetic field lines from the solar wind and from the planet first become interconnected, projected along the streamlines of the magnetosheath flow back into the undisturbed solar wind, as illustrated in Fig. 5.14.” {A75} {A76} {A77}

5.5.8 A large-scale flow impinging on a fast outflow {A75}

An example of colliding plasmas on the largest scale in heliophysics involves the interstellar medium into which the heliosphere is moving. Figure 5.1 “shows the prevailing picture of the global heliosphere. The structure is characterized by three flow discontinuities: the termination shock (TS), the heliopause (HP), and the bow shock (BS). The solar wind density and therefore its ram pressure falls off as r^{-2} , where r is the distance from the Sun. The wind speed is supersonic and super-Alfvénic, so when the ram pressure falls to the pressure of the ambient [interstellar medium (ISM)], the result is a shock, specifically the ellipsoidal TS in Fig. 5.1, where the flow is decelerated.” {A76} {A77} IV:33

If the ISM flow is super-Alfvénic, it also encounters a shock as it approaches the Sun, specifically the roughly hyperboloid shaped bow shock in Fig. 5.1, where the ISM flow is decelerated to subsonic speeds. However, the $v_{\text{ISM}} = 23 - 27 \text{ km s}^{-1}$ interstellar flow happens to yield an Alfvénic Mach number of $M_{\text{A}} \approx 1$, making the existence or nonexistence of a bow shock very much an open question. Much depends on the strength and orientation of the ISM magnetic field, B_{ISM} . The higher B_{ISM} is (and the more perpendicular to the ISM flow), the lower M_{A} should be, and less likely that there is a bow shock.

Even the seemingly small uncertainty in v_{ISM} is enough to make a difference. For many years the best assessments were believed to be the $v_{\text{ISM}} = 26.3 \pm 0.4 \text{ km s}^{-1}$ measurement of the ISM neutral He flowing through the Solar System by *Ulysses* and the $v_{\text{ISM}} = 25.7 \pm 0.5 \text{ km s}^{-1}$ measurement from ISM absorption lines. With these relatively high values, heliospheric modelers favored $M_{\text{A}} > 1$, implying the existence of a bow shock. However, later He flow measurements and a new analysis of ISM absorption line data have yielded lower velocities. Specifically, measurements of neutral He flow from *IBEX* suggest $v_{\text{ISM}} = 23.2 \pm 0.3 \text{ km s}^{-1}$, and $v_{\text{ISM}} = 23.84 \pm 0.90 \text{ km s}^{-1}$ from ISM absorption lines.

This has been enough for many to argue that $M_{\text{A}} < 1$ should be preferred, though [it has been argued] that including He⁺ density in the calculation of sound and Alfvén speeds instead of just assuming a pure proton plasma would still suggest $M_{\text{A}} > 1$ even if $v_{\text{ISM}} \approx 23 \text{ km s}^{-1}$. With M_{A} so close to 1, it is possible that the issue will not be

fully resolved until an interstellar probe mission of some sort is sent out to this region. However, with M_A so close to 1 it is also possible that secondary physical processes (*e.g.*, charge exchange interactions with neutral particles) make it fundamentally ambiguous whether any boundary that may exist out there should be called a true bow shock, or whether we should instead refer to it as a 'bow wave'.

Regardless of whether or not a bow shock exists, strong plasma interactions prevent the ISM plasma from mixing with the solar wind plasma. The roughly paraboloid heliopause in Fig. 5.1, lying between the termination shock and the bow shock (or wave) is the contact discontinuity separating the two plasma flows. Representing the boundary between solar wind and ISM plasma, the heliopause is generally considered the true boundary of the heliosphere.”

IV:3: “The basic structure in Fig. 5.1 is mostly defined by plasma interactions. The local ISM is partly neutral, but collisional mean free paths for neutrals are large compared to the size of the heliosphere, so their effects on heliospheric structure were long ignored. In essence, the assumption was that neutrals pass through the heliosphere unimpeded, feeling only the Sun’s gravity and photo-ionizing flux. However, in reality neutrals do participate in heliospheric interactions through charge exchange (CX). The CX interactions end up providing ways to remotely explore the heliosphere that would be impossible if the local ISM were fully ionized.

A CX interaction is a rather simple process by which an electron hops from a neutral atom to a neighboring ion (*e.g.*, $H^0 + H^+ \rightarrow H^+ + H^0$). Mean free paths for CX for most neutral ISM atoms are short enough that they do experience significant CX losses on their way through the heliosphere. The exceptions are the noble gases, which have low CX cross sections, explaining why neutral He flowing through the solar system is considered the best local probe of the undisturbed ISM flow.

Modeling neutrals in the heliosphere is very difficult because CX sends the neutrals wildly out of thermal and ionization equilibrium with the ambient plasma. Including neutrals in hydrodynamic models of the global heliosphere therefore requires either a fully kinetic treatment of the neutrals, or at least a sophisticated multi-fluid approach. The earliest models that could treat neutrals properly were from the 1990s. These models demonstrated that through CX, neutrals could have significant effects on heliospheric structure. The ISM protons are heated, compressed, deflected, and decelerated as they approach the heliopause, and thanks to CX [with the neutral component of that incoming ISM] the proton properties are at least partially imprinted on the neutral hydrogen as well, creating what has been called a 'hydrogen wall' of higher density [neutral hydrogen] around the heliosphere, in between the heliopause and the bow shock.” Section 10.3 (and Ch. IV:3) discusses stellar observations and inferences about astrospheres.

For us living deep inside the heliosphere, the consequences of the solar wind sculpting out a cavity in the interstellar medium are limited as no perturbations in the solar wind or its magnetic field can propagate against the super-Alfvénic wind. Nonetheless, the heliosphere that is shaped by this interplay does affect our exposure to cosmic rays that traverse it, see Ch. 14.

Chapter 6

Magnetic (in-)stability and energy pathways

Chapter topics:

- Magnetic instabilities in flares, CMEs, and magnetospheric (sub-)storms
- The appearance of solar flares across the electromagnetic spectrum
- Coronal and geomagnetic instabilities, chromospheric and ionospheric heating, charged particle precipitation, EM radiation, energetic neutrals
- Instability mechanisms (tearing mode, current-driven, interchange, and ballooning) that convert energy stored in a non-potential magnetic field

Key concepts:

- Solar flare ribbons and terrestrial aurorae
- Neupert effect
- Force-free field
- Reconnection

6.1 Introduction

Instabilities occur when mild perturbations to some energy reservoir provide access to an energy conversion pathway into a significantly reduced state of that reservoir. This can happen because the pathway itself develops (such as when a condition for fast reconnection is met), because the energy reservoir changes in content (as external sources insert energy), because the surrounding conditions change (for example, the direction of the solar wind magnetic field or the makeup of the solar magnetic landscape), or because a sufficiently large perturbation occurs (such as by variations in solar wind speed or the passage of a (shock) wave associated with another impulsive event). One analogy of a purely mechanical nature is the fall of a ball that is somehow nudged over the edge of a bowl; in that process, gravitational energy contained in the reservoir (the elevated ball in the bowl) is converted into the kinetic energy of the ball's fall, and ultimately into heat and waves (that themselves eventually dissipate into the

microscopic kinetic energy of heat) as the ball hits the floor. The magnetic field of volumes within the Sun’s atmosphere and of planetary magnetospheres can similarly destabilize: when deformed from a potential state, the added energy may be gradually dissipated thereby avoiding a (large-scale) instability or it may be stored for some time in a growing reservoir, then to be converted impulsively through a variety of pathways, eventually ending in kinetic or electromagnetic energy that is extracted from the magnetic field and the plasma that it holds. Tracking energy reservoirs and flows is often helpful in understanding processes.

The primary storage reservoir for what eventually develops into a solar impulsive event or a magnetospheric (sub-)storm is the distortion of the magnetic field away from a potential state. This elevated energy is often attributed in our thinking to electrical currents, but is stored throughout the distorted magnetic field. In quantitative terms, the maximum energy available for an impulsive event is the volume-integrated field energy in excess of the minimum level. The latter is often taken to be the potential field B_{pot} matching the observed surface field on the Sun or a reference dipole field B_{dip} for a planet, *i.e.*,

$$E_{B,\text{res}} = \frac{1}{8\pi} \int \left[B^2 - (B_{\text{pot,dip}})^2 \right] dV, \quad (6.1)$$

although that potential-field energy level may not practically be achievable (see discussions of helicity in solar conditions, or consider continued stressing of the geomagnetic field by a sustained solar wind). Note that this energy is an integral quantity: the local quantity $B^2 - (B_{\text{pot,dip}})^2$ measures the change in local energy density, but as the energy is contained in the field rather than in embedded electrical currents, regions with high values of $B^2 - (B_{\text{pot,dip}})^2$ do not necessarily correspond to locations of electrical current systems. {A78}

The observable signatures of magnetically-dominated instabilities in the solar atmosphere and in planetary magnetospheres have led to the development of a colorful and often unclear and ambiguous array of terms, generally introduced well before the processes themselves were understood and incorporated into an overall view. For example, present-day understanding ascribes the impulsive and decay phases of flares, coronal mass ejections (CMEs), and terrestrial magnetospheric (sub-)storms and their counterparts in other planetary magnetospheres to a loss of a quasi-equilibrium in, or a departure from, a quasi-steady evolution of the magnetic field that leads to a rapid increase in the rate of reconnection. The latter is associated, among other things, with the acceleration of populations of ions and electrons that lead to observable emissions in a wide range of wavelengths in the electromagnetic spectrum, among them the terrestrial auroral emissions and their solar counterpart, the flare ribbons. {A79}

Not {A80} {A81} only do these impulsive phenomena share many physical processes, they are also links in the chain of Sun-Earth connections: many of the more energetic solar field destabilizations are associated with both flares and CMEs (see Table 6.1), while CMEs that envelop a planet that has an intrinsic magnetic field often trigger (immediate or delayed) magnetospheric activity. {A81}

Table 6.1: *Solar flare classifications. [Listed are the GOES flare class, the corresponding flare-peak irradiance at the top of Earth’s atmosphere, the class and surface footprint based on chromospheric emission patterns, the fraction of such events associated with coronal mass ejections (CMEs), and the characteristic frequency of such events during the maximum and minimum of a typical solar cycle. Table II:5.1]*

GOES class	1-8Å peak (W/m^2) ($ker\text{g}/\text{cm}^2/\text{s}$)	H α class (percent)	H α Area (<i>millionths of hemisphere</i>)	CME fraction ^a	Events/year (<i>cycle max./min.</i>)
A	$>10^{-8}$	-	-	-	-
B	$>10^{-7}$	S	<200	-	-
C	$>10^{-6}$	1	>200	0.2	$>2000/300$
M	$>10^{-5}$	2	>500	0.5	300/20
X	$>10^{-4}$	3	>1200	0.9	10/one?
-	$>10^{-3}$	4	>1200	1.0	few?/none?

^a (approximate values)

6.1.1 Introducing solar flares and coronal mass ejections

“A solar flare is narrowly defined as a sudden atmospheric brightening, traditionally in chromospheric H α emission [(at 656 nm, associated with a 3 \rightarrow 2 level transition of hydrogen atoms, and thus the lowest-energy transition in the Balmer series)] but more practically now as a coronal soft X-ray source [(Fig. 6.1 summarizes the common names used for wavelength bands from radio to gamma rays)]. The physical processes resulting in a flare include restructurings of the magnetic field, non-thermal particle acceleration, and plasma flows. Flares have intimate relationships with other observable phenomena such as filament eruptions, jets, and coronal mass ejections [...]

The energy released in a solar flare is dominated by particle acceleration, both of electrons and ions. This means that the most direct observations are in the X-ray and γ -ray domains; note that non-thermal processes also usually dominate the emission signatures in the radio range (10^7 - 10^{12} Hz; meter–submillimeter wavelengths). Please refer to Ch. II:4 for a fuller discussion of the remote-sensing signatures. We will simply comment here that in general the hard X-ray spectrum ($h\nu \gtrsim 10$ keV [or wavelengths shortward of about 1 Å]) is dominated by electrons of this energy or greater, while the soft X-ray spectrum ($h\nu \lesssim 10$ keV) is dominated by the free-bound and bound-bound transitions of a thermal plasma with assumed Maxwellian distribution functions, and also usually assuming the electron and ion temperatures to be equal, *i.e.*, $T_e = T_i$. The free-bound process (radiative recombination) may also contribute to the hard X-ray spectrum under certain conditions.”

A common observed pattern, most frequently in eruptive flares associated with coronal mass ejections into the heliosphere, is that a volume of the corona over a magnetic polarity inversion line expands explosively (often involving a large-scale shock front) as the hard X-ray and γ -ray emission brightens impulsively, with two (or more)

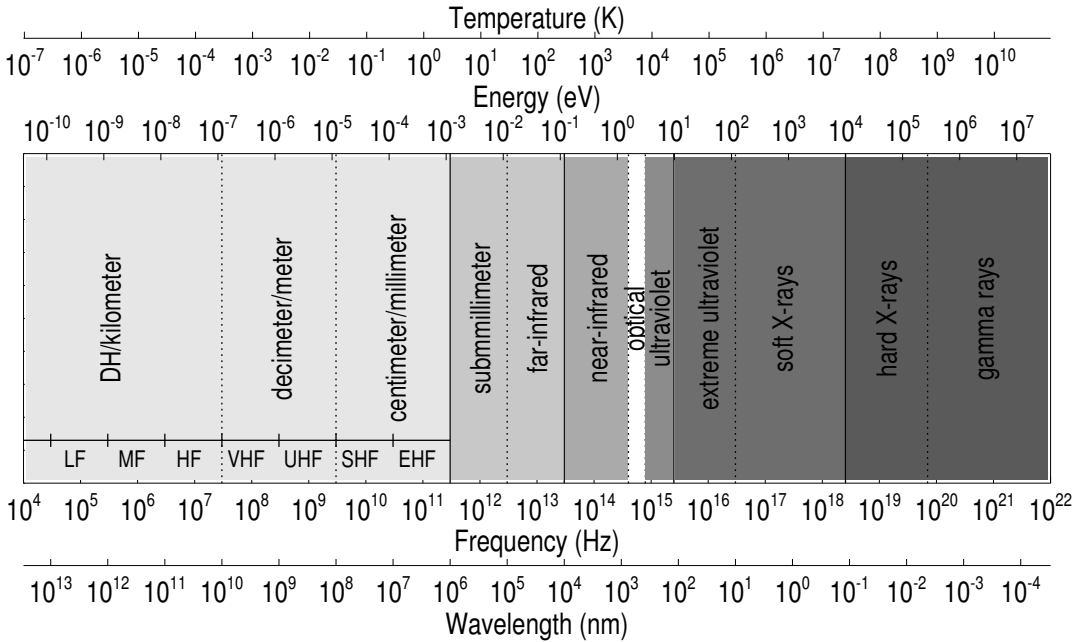


Figure 6.1: Overview of the electromagnetic spectrum with energy in electron volts and the equivalent temperature in Kelvin (top axes), frequency in Hertz, and wavelength in nanometers (bottom axes). Note that the AM band lies in the low- and medium-frequency (LF-MF) range and the FM band in the very-high frequency (VHF) range. [Fig. II:4.1]

ribbon-like brightenings at chromospheric and photospheric levels propagating away from the polarity inversion line, with a coronal mass ejection moving away while behind it the corona fills with heated plasma from the lower atmosphere, which then cools by radiation in the soft X-ray and EUV bands and by conduction into the lower, cooler atmosphere. See Fig. 6.2 for the characteristic evolution of a flare in wavelength space, and Fig. 6.3 for a sketch of the various emissions throughout the EM spectrum.

“The modern view of [solar flares] is via the soft X-ray monitoring by the GOES and other ‘operational’ spacecraft. We now routinely classify solar flares by their GOES classes: A, B, C, M, and X in decades, with the X class signifying $1\text{--}8\text{\AA}$ energy fluxes greater than 10^{-4} W/m^2 , on the order of 0.01% of the solar luminosity. Table 6.1 summarizes these and other properties, with very approximate correspondences between the [chromospheric] $H\alpha$ and GOES X-ray systems, and very approximate ranges for the number of flares that occur per year at maximum and minimum of the solar cycle.”

6.1.2 Introducing geospace (sub-)storms

In contrast to a flare or CME observed by imaging the electromagnetic radiation, a terrestrial magnetic storm is typically observed by sampling magnetic field changes at the Earth’s surface or tracked by monitoring energetic particles and their effects (such as in aurorae), with their root causes in elements of the Dungey cycle in the

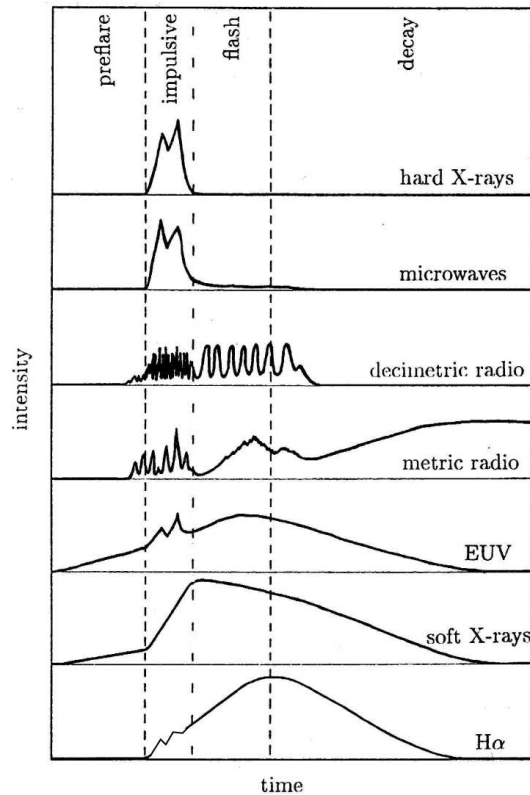


Figure 6.2: Schematic view of the evolution of solar flare emissions in different wavelengths, showing the intermingling of impulsive-phase and gradual-phase signatures across the spectrum. Note the wide variety of radio signatures. [In wide wavelength bands in the visible, the emission peaks in the impulsive phase of the flare. Fig. II:5.1; source: Benz (2002).]

geomagnetic tail. A terrestrial “magnetic storm is defined nowadays by the time variation of the geomagnetic Dst index, illustrated schematically in Fig. 6.4. The Dst index is a measure of a quasi-uniform magnetic disturbance field near the Earth, aligned with the dipole axis (northward [field] for $Dst > 0$), such as would be produced by a ring of electric current (westward [current] if $Dst < 0$) near the equatorial plane. A prolonged (hours to days) interval of negative Dst values constitutes a magnetic storm. The peak negative excursion is often taken as a measure of storm intensity: Dst -30 nT to -50 nT are weak storms, -50 nT to -100 nT moderate, and over -100 nT intense; storms over -300 nT occur at most a few times during a solar cycle (Earth’s dipole field at the equator is $\sim 31,000$ nT, [or 0.31 Gauss,] for comparison) [...]

[T]he field depression quantified by Dst is the result of plasma pressure that inflates the dipole field. The essential phenomenon of the magnetic storm is thus the addition of a large amount of plasma energy to the dipolar field region of the magnetosphere. Furthermore, it is now well established that this energy addition results from a particular condition in the solar wind: ‘a sufficiently intense and long-lasting interplanetary convection electric field’, meaning $-\mathbf{v} \times \mathbf{B}/c$, for the [interplanetary

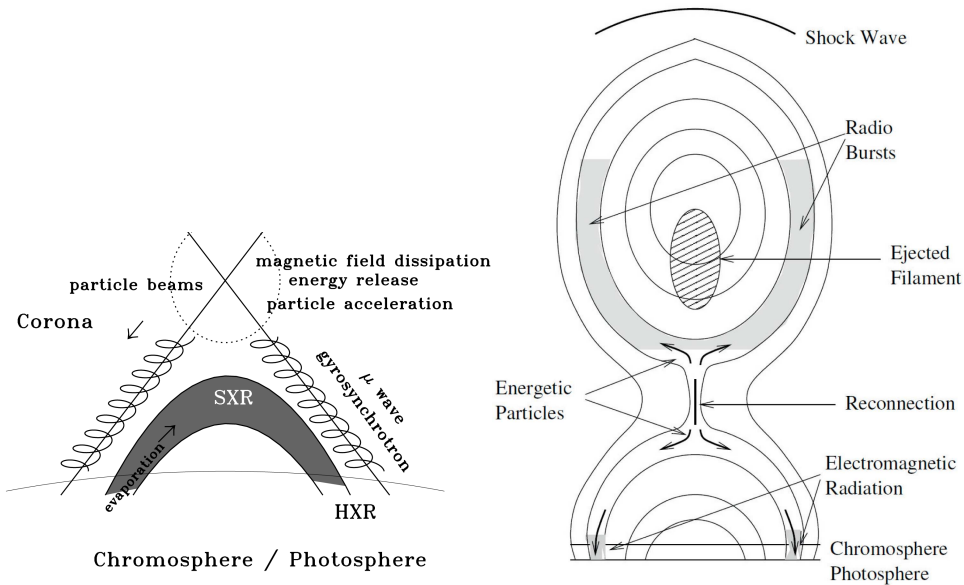


Figure 6.3: (left) Schematic arrangement in the outer atmosphere of the Sun or a comparable cool star indicating the flow of energy during a flare: a flare involves magnetic reconnection high in the atmosphere which accelerates particles, leading to motion along field lines upward away from or downward towards the visible surface. Resulting emissions include hard X-rays (HXR), soft X-rays (SXR), and microwave emission. [Fig. IV:2.1] (right) Concepts of particle acceleration and emissions in a solar [eruptive] event. [Fig. IV:12.6; source: (Kallenrode, 2003).]

magnetic field's (IMF's)] southward component.

In contrast to the magnetic storm, there is much less unanimity on what defines a magnetospheric substorm. Probably the most spectacular phenomenon, and the one most widely used as a unifying concept, is the auroral substorm, [... , which has a characteristic temporal development. Early to show up are] the auroral forms (light-emitting regions) during what is called the *expansion phase* of the substorm: beginning with an initial brightening at the lowest latitudes near midnight (*onset*), the aurora intensifies greatly, becomes very complex in spatial structure (*auroral breakup*) and expands, predominantly westward and poleward but also eastward, eventually subsiding in a *recovery phase*. This auroral development is accompanied by strong geomagnetic disturbances (commonly reaching ~ 1500 nT [or 0.015 G] and more), with a spatial distribution almost as complex as that of the aurora but describable roughly as equivalent to a current above the Earth (*auroral electrojet*) that is westward near and before midnight and eastward after midnight. [Essentially the same sequence occurs simultaneously in the two hemispheres,] at the (more or less) magnetically conjugate locations [...]”

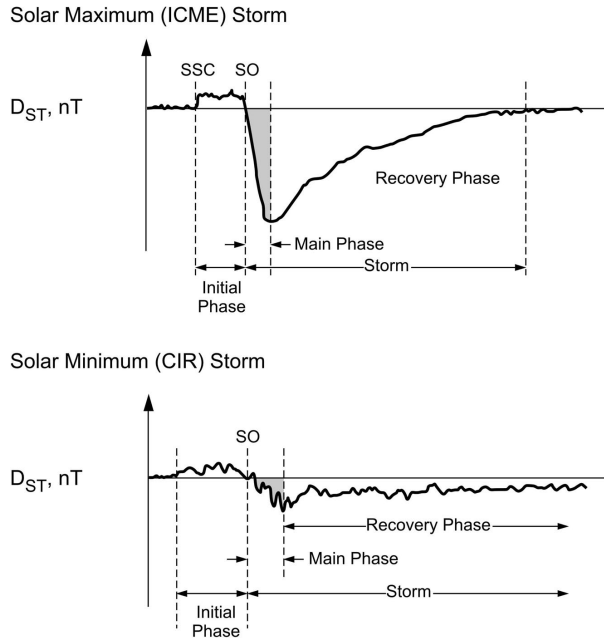


Figure 6.4: Schematic time history of geomagnetic field variation for two characteristic magnetic storms. Time range: several days. Vertical variation range: $\sim 100 - 200$ nT ($\sim 1 - 2$ mG). SSC: storm sudden commencement. SO: storm onset. The top panel shows the storm development in response to a characteristic interplanetary coronal mass ejection (ICME), and the bottom panel that for the passage of a corotating interaction region (CIR). [Fig. II:10.1; source: Tsurutani *et al.* (2006).]

6.2 Terrestrial magnetospheric disturbances

6.2.1 Energy pathways and reservoirs

“For the magnetosphere and the upper regions of the ionosphere [...] the solar wind is the only significant external source of energy available [because these regions are completely transparent to solar radiation ...] An interior source of energy available for a planetary magnetosphere is planetary rotation [...]

When considering the solar wind as the energy source, only the kinetic energy of plasma bulk flow is of importance; the thermal and magnetic energies of the solar wind can be neglected [...: they are relatively small to begin with (Sect. 3.5.2) while moreover] at the bow shock they are overwhelmed by additional thermal and magnetic energies extracted from the flow. Furthermore, to transfer magnetic energy across the magnetopause requires [...] a tangential component of the electric field which interacts with the magnetopause current to extract more mechanical energy from the plasma [...]. The interplanetary magnetic field does exert a dominant influence on energy conversion processes in a planetary magnetosphere, but primarily by control of magnetic reconnection processes and open field lines [...].”

“The following are among the principal loss and dissipation processes in planetary

magnetospheres, energy being lost primarily to the atmosphere in (1) and (2) and being removed outside the system (to 'infinity') in (3) and (4):

(1) **Collisional and Joule heating in the ionosphere.** If the bulk flow of plasma differs from the bulk flow of the neutral atmosphere (usually as a consequence of magnetospheric dynamics), there is energy dissipation given by $\mathbf{E}^* \cdot \mathbf{J}$, where \mathbf{E}^* is the electric field in the frame of reference of the neutral atmosphere. This is commonly referred to as 'ionospheric Joule heating'; [...] it is primarily frictional heating by collisions between plasma and neutral particles, Joule heating in the true physical sense ($\mathbf{E}' \cdot \mathbf{J}$, where \mathbf{E}' is the electric field in the frame of reference of the plasma) contributing only a small fraction of the total. The energy is removed from the magnetic field and converted (via kinetic energy of relative bulk flow as an intermediary) to heat (thermal energy), with the heating rate per unit volume partitioned approximately equally between plasma and neutrals.

(2) **Charged-particle precipitation.** Energetic charged particles that enter the atmosphere from above are usually said to be *precipitating*. They penetrate the atmosphere to a depth that increases with increasing energy, until their energy is lost, going partly into heating the atmosphere and partly into ionization or other interactions.

One source of precipitating particles is simple loss from the radiation belts or from the ring current and plasma sheet regions; {A82} the energy deposited in the atmosphere is taken from the mechanical (thermal) energy of the respective magnetospheric particle populations. In addition to these particles that precipitate merely because their velocity vectors are oriented in the appropriate direction, there are other sources of precipitating charged particles, in which the energy and the intensity of the particles have been enhanced by an acceleration process. In particular, the auroral phenomena that occur in nearly all of the planetary magnetospheres observed to date are generally interpreted as resulting from some special acceleration process that supplies the required intensities of precipitating charged particles. A widely accepted model, developed from extensive studies at Earth and applied to aurora at Jupiter and at Saturn, ascribes auroral acceleration to Birkeland (magnetic-field-aligned) electric currents accompanied by electric fields parallel to the magnetic field; the rate of energy supply to the precipitating particles is $E_{\parallel} J_{\parallel}$, hence the added energy is taken out of the magnetic field (in this model, an aurora occurs only when the Birkeland current is directed upward, corresponding to electron motion downward). Auroral acceleration has also been associated with intense Alfvénic turbulence (which contains fluctuating Birkeland currents) [...]

(3) **Emission of electromagnetic radiation.** A variety of processes in planetary magnetospheres produce electromagnetic radiations of various types: atomic and molecular line emissions (from the aurora and from magnetospheric interactions with plasma and neutral tori), radio waves (wideband and narrowband), a veritable zoo of plasma waves, and even X-rays (bremsstrahlung from precipitating electrons and, possibly, nuclear line emissions excited by very energetic precipitating particles). [...] As far as the energetics of planetary magnetospheres are concerned, however, the

amount of energy involved is negligibly small for most emissions, with only a few exceptions (UV radiation from the Io torus at Jupiter).

(4) **Energetic neutral particle escape.** Neutral particles that remain within a magnetosphere must be gravitationally bound to the planet; plasma particles within the magnetosphere, on the other hand, typically have speeds that exceed (often by a large factor) the gravitational escape speed — plasma is held within the magnetosphere by the magnetic field, not by gravity [...] Charge-exchange collisions between ions and neutrals, in which the outgoing neutral has the velocity of the incoming ion and vice versa, thus produce fast neutrals that escape from the system immediately, with their kinetic energy. This process represents a loss (generally by quite significant amounts) both of neutral particles and of energy from the magnetosphere.

(5) **Dissipation processes in the magnetosphere.** In regions of the magnetosphere with major departures from the MHD approximation (particularly where magnetic reconnection is occurring) dissipative processes such as Joule heating associated with effective resistivity may be significant. The primary effect is not energy loss but enhancement of conversion from magnetic to thermal energy.”

“The field approach to energy implies that energy may be regarded as *stored* in space [...] The primary reservoir of stored mechanical energy in a planetary magnetosphere is the thermal energy of its various plasma structures, especially the *plasma sheet* of the magnetotail or magnetodisk, the *ring current*, and the plasma and neutral *tori* associated with the planet’s moons; the kinetic energy of bulk flow of magnetospheric plasma also plays a role, particularly for plasma tori and in the case of rapid changes [...]

The primary reservoir of stored electromagnetic energy of importance for a planetary magnetosphere is the energy of the magnetic field [...] Because the energy of the planetary dipole field itself does not change (except on time scales of the secular variation, $\sim 10^2 - 10^3$ years for Earth) and thus has no effect on the energetics of the magnetosphere, a convenient measure of stored electromagnetic energy is the energy of the total magnetic field minus the (unchanging) energy of the dipole field, [reflected in Eq. 6.1].

The stored gravitational energy can be changed only by a net radial displacement of matter; any such effects in the magnetosphere are for the most part negligible in comparison to changes of mechanical or magnetic energy.”

6.2.2 What leads to explosive energy releases?

“The discussion so far has ignored time variations and has proceeded on the tacit assumptions that all the energy supply, conversion, and dissipations processes are more or less in balance. There is no general requirement for this to be the case, and in fact often it is not the case [...] The prototypical example is kinetic energy from the solar wind being converted into magnetic energy of the magnetotail at an increased rate due to enhanced dayside reconnection (in response to changed solar-wind conditions), but the rate of removal by conversion of magnetic energy into mechanical energy of magnetospheric plasma plus escape down the magnetotail not being equally enhanced (for reasons that need to be identified); in this case, the magnetic energy reservoir

II-10.3.4

II-10.5

increases with time and reaches a point at which (again, for reasons that need to be identified) the magnetic energy content can no longer be maintained but must be converted to other forms.”

First, let us look at topological changes involved in magnetospheric processes. “[M]agnetic flux transport and the increase of magnetic energy by stretching the field play an important role in supplying energy to the magnetosphere. Non-equilibrium configurations of the magnetotail that change the magnetic topology and allow different paths of flux transport are therefore of particular interest.

A simple sketch of a model widely invoked to interpret magnetospheric substorms at Earth is shown in Fig. 6.5, which displays a time sequence of magnetospheric configurations. Each panel shows the magnetic field line configuration in the noon-midnight meridian plane (left) as well as the configuration of magnetic singular X [lines (where field vectors of opposite directions cross; see, for example, Fig. 5.14)] and O lines [(around which field lines loop)] in the equatorial plane (right) and projected to the ionosphere (top); the equatorial projection, [...] is essential for describing the three-dimensional structure of the magnetic field. Panel 1 is the simplest topology of the open magnetosphere [(compare with Fig. 5.14)]. In panel 2, a small volume usually called a *plasmoid* appears deep within the closed-field-line region, bounded on the earthward side by a newly formed *near-Earth X-line* (NEXL) and threaded by magnetic field lines that encircle the attached O-line; ideally, the field lines are confined within the plasmoid and connect neither to the Earth nor to the solar wind (what the real topology is, however, is still uncertain). For the ideal topology, the plasmoid can be visualized in three dimensions as shaped roughly like a banana, oriented approximately dawn to dusk and tapering to zero thickness at both ends, with the X-line on its surface and the O-line running through the middle of its volume. The plasmoid grows (panel 3) by magnetic reconnection until it touches the separatrix of the open field lines (panel 4, *onset of lobe reconnection*); afterward (panel 5), the plasmoid is on interplanetary field lines and is carried away (presumably) by the solar wind.

A model of topological changes [internal to] a rotation-dominated magnetosphere [(such as Jupiter’s) differs] only in three respects: (1) the time sequence has been translated into an azimuthal-angle sequence, (2) field lines are stretched by the outflow of plasma from an internal magnetospheric source (planetary/magnetospheric wind) [...], (3) there are no counterparts to panels 4 and 5, since field lines connected to the solar wind are not considered. [...]

Next, let us look at the role of instabilities in causing rapid changes in topology. “Instabilities have attracted much attention as a possible way of inducing rapid change from equilibrium to non-equilibrium configurations – an alternative to straightforward evolution to non-equilibrium as the result of changing boundary conditions. [...]

(1) **Tearing-mode instabilities.** ‘Tearing mode’ is a generic term for instabilities that result in the reconnection of initially oppositely directed magnetic fields. They are obvious candidates for initiating topological changes of the magnetotail (in particular, those envisaged in Fig. 6.5).

(2) **Current-driven instabilities.** The concept that a sufficiently intense electric

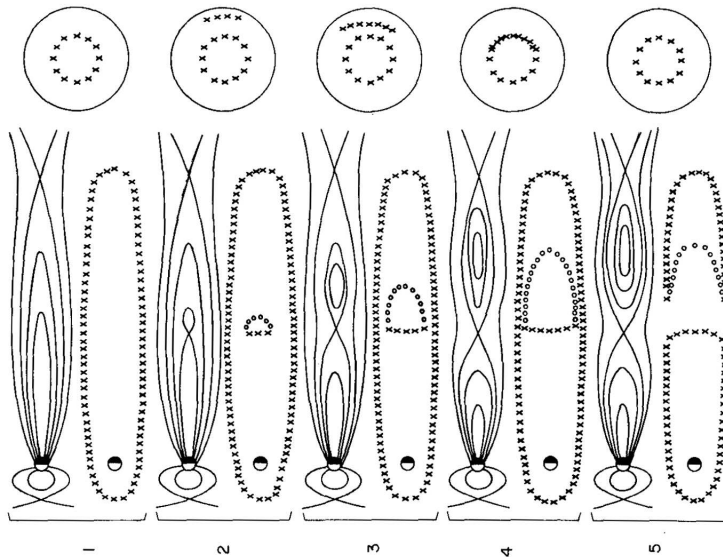


Figure 6.5: Possible changes of the magnetic field topology in the magnetotail of a solar-wind-dominated magnetosphere. The diagram is shown [with the Sun’s direction at the bottom] to facilitate comparisons with diagrams of filament eruptions [...]. Each panel in the sequence shows a side view of the magnetic field (left), the outline of the X lines [where field of opposite directions meet] seen from above the north pole (right), and a top-down view of the mapping of the reconnection region onto the Earth (top). [Compare this to the sketch of a solar eruption in Fig. 6.6; Fig. II:10.5; source: Vasylunas (1976).]

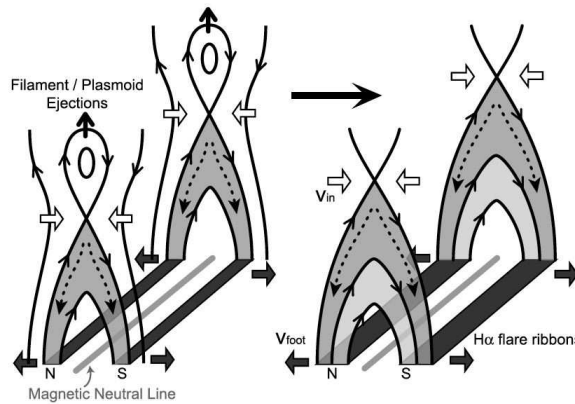


Figure 6.6: How the ribbon motion associated with solar flares sweeps out magnetic field during the reconnection process in the standard model. [Compare this solar eruption to the sketch of the magnetospheric substorm (righthand side of each panel) in Fig. 6.5; Fig. II:5.16; source: Asai et al. (2004).]

current may bring about its own breakdown, by creating conditions that impede current flow, was first suggested [...] as a model for solar flares. Under the name 'current disruption' it has been widely discussed as a model for substorm onset and expansion. Various instabilities that develop when the current density exceeds some threshold value have been proposed.

(3) **Interchange and ballooning instabilities.** Interchange instabilities which do not appreciably change the magnetic field are thought to be essential for plasma transport in rotation-dominated magnetospheres. Ballooning instabilities can be viewed roughly as interchange that does change the magnetic field. As a model for substorms, they have been invoked particularly at the transition between the dipole field and the magnetotail, in several variants.”

6.2.3 Terrestrial magnetospheric substorms

A substorm can be summarized as a two-stage process. “Stage 1 (growth phase): as a consequence of a southward interplanetary magnetic field, the configuration of the magnetosphere changes, its magnetic field becoming highly stretched (increased magnetic flux in the magnetotail, reduced flux in the nightside equatorial region). Stage 2 (expansion phase, initiated by the onset): the magnetic field changes to more nearly dipolar (increased flux on the nightside), and there is enhanced energy input and dissipation to the inner magnetosphere and the ionosphere/atmosphere; the process occurs on dynamical time scales (comparable to or shorter than wave travel times) and is accompanied (most probably) by changes of magnetic topology.

[In terms of energy flow paths: during stage 1, power input from the bulk flow kinetic energy of the solar wind is enhanced and is appreciably larger than the sum of power outputs due to heating, bulk motion, and plasma escape from the geomagnetic system. During stage 2, energy flow into mechanical energy of plasma and particularly plasma heating are enhanced; power flow through plasma and field escape and field reconfiguration presumably are enhanced in connection with topological changes]

The substorm growth phase is in essence the increase of open magnetic flux in the magnetosphere, which occurs for a two-fold reason. First, the flux addition rate at the dayside reconnection region increases as the solar wind transports more magnetic flux, of the sense opposite to the terrestrial dipole flux, toward the magnetosphere; the reasons for this are assumed to lie in the physics of magnetic reconnection. Second, the flux return rate at the nightside reconnection region does *not* increase to match the addition rate; the reasons for this are not at all well understood. [...] Within the magnetosphere, the net effect of the substorm growth phase is to remove magnetic flux from the nightside magnetosphere by flow toward the dayside reconnection region and to add magnetic flux to the magnetotail (enhanced stretching of magnetotail field lines).

The substorm expansion phase does return the magnetic flux, rapidly and spectacularly, from the magnetotail to the nightside magnetosphere (dipolarization of a previously stretched tail-like field); given that plasma in the magnetotail beyond a distance typically $\sim 15 - 20$ Earth radii is observed to flow away from Earth, the process must almost unavoidably proceed by topological changes of the type sketched

in Fig. 6.5. The energy input into plasma, energetic charged particles, and the aurora can be largely accounted for by adiabatic compression and Birkeland current effects. What remains highly controversial is how the process starts and why it is so sudden and catastrophic [...]

A further complication is the question of external versus internal influences. That the growth phase is initiated by changing solar wind conditions is the consensus view. The onset and expansion phase, on the other hand, are regarded by the majority as basically the result of internal dynamical processes, although subject to solar wind influences (*e.g.*, if the system is evolving toward instability, it may be pushed over the threshold by a change in the solar wind). A substantial minority, however, considers the substorm onset intrinsically as triggered by a solar wind change (typically toward a more northward interplanetary magnetic field)."

6.2.4 Terrestrial magnetic storms

"Our understanding of magnetic storms has been decisively influenced by a remarkable theoretical result, the Dessler-Parker-Skopke theorem, which relates the external magnetic field at the location of a dipole to properties of the plasma trapped in the field of the dipole. [T]he theorem states that $\mathbf{b}(0)$, the magnetic disturbance field of external origin at the location of a dipole of moment $\boldsymbol{\mu}_B$ [in an undisturbed state], satisfies

$$\boldsymbol{\mu}_B \cdot \mathbf{b}(0) = 2U_K \quad (6.2)$$

where U_K is the total kinetic energy content of plasma in the magnetosphere. What is remarkable is that the right-hand side does not depend on the spatial distribution, the partition between bulk-flow and thermal energy, or any properties of the energy spectrum. [...]

Although $\mathbf{b}(0)$ nominally is evaluated at the center of the Earth, it is also equal to the (vector) average of $\mathbf{b}(\mathbf{r})$ over the surface of the globe (by a theorem for solutions of Laplace's equation, satisfied within the globe by each Cartesian component). The Dst index is the average, over a low-latitude strip of the globe, of the disturbance field component aligned with the dipole; after some corrections (chiefly removing the contribution from induced earth currents), -Dst may be considered a reasonable proxy for the left-hand side of Eq. (6.2), as long as $\text{Dst} < 0$. The Dessler-Parker-Skopke theorem then provides a method of inferring the plasma energy content simply from the value of the Dst index. [...] Direct *in situ* observations have established that the greater part of the energy resides in what is called the ring current region.

Geomagnetic storms, particularly the intense ones, are characterized by unusually large amounts of energy stored as mechanical energy of plasma in the ring current region, in comparison to other storage regions. This implies that during the development of an intense storm the power [going from the magnetic reservoir to the ring-current plasma kinetic reservoir] is unusually large, on the average. Whether this enhanced conversion rate from magnetic energy into mechanical energy of ring current plasma [...] results from a different interaction process or simply from a different time sequence of solar wind parameters is an unresolved question. More specifically, can the energy for storms be supplied by a sequence of substorms (perhaps unusually frequent and/or

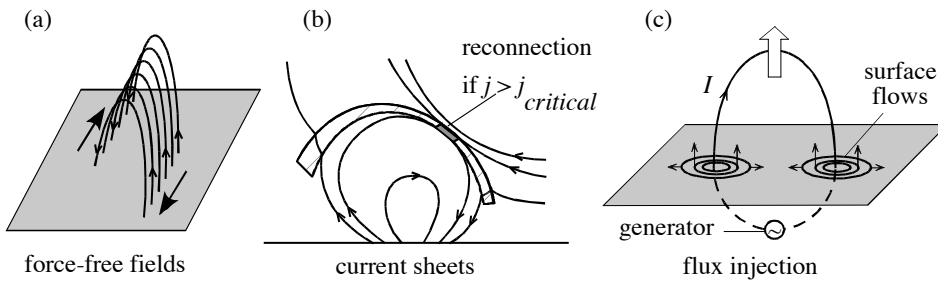


Figure 6.7: Schematic illustration of three different types of models that use magnetic energy to power a flare or CME. Panel (a): Magnetic energy is stored in the corona in the form of field-aligned currents that eventually become unstable. Panel (b): Magnetic energy is stored in the corona in the form of a thin current sheet that is suddenly dissipated when a micro-instability is triggered within the sheet. Panel (c): An example of a directly driven flare model. Here magnetic flux is suddenly injected from the convection zone into the corona at the onset of the flare or CME. Such a model produces a well-organized flow pattern during the impulsive phase (small arrows at surface in panel c). [Fig. II:6.8]

unusually intense), or is some other process required? A related question is that of *geoeffectiveness*: when interplanetary structures such as CME’s impinge on the Earth, under what conditions do they produce intense magnetic storms? (prolonged southward B_{sw} is one that is well established).” {A83}

6.3 Models of solar impulsive events

6.3.1 The magnetic reservoir

Storage models

“Although it is generally agreed that flares and CMEs derive their energy from the Sun’s magnetic field, exactly how the magnetic energy is extracted remains uncertain. One possibility is that a flare or CME occurs when a slowly evolving coronal magnetic field reaches a point where a stable equilibrium is no longer possible. The slow evolution of the corona is driven by the changes continually occurring in the photospheric field as a result of solar convection; [in phases before solar impulsive events, these processes build up the stored magnetic energy]. The equilibrium may disappear altogether or, alternatively, a stable equilibrium may simply become unstable. The continual emergence of new flux from the convection zone and the shuffling of the footpoints of closed coronal field lines increase the free magnetic energy in the corona. Eventually, these stresses may exceed a threshold beyond which a stable equilibrium cannot be maintained, and the field erupts. Models based on this principle are often referred to as *storage models*.

[...] Because the plasma in the photosphere is almost 10^9 times denser than the plasma in the corona, it is difficult for disturbances in the tenuous corona to have much effect on the photosphere and the deeper layers below it. Field lines mapping from the corona to the photosphere are thus said to be ‘inertially line-tied’ which means that

{A83}

II:6.2.1

the footpoints of coronal field lines are essentially stationary over the time scale of the eruption [...]

Unlike models of confined flares, models of CMEs must be able to explain not only the release of magnetic energy, but also how mass is ejected into interplanetary space. During a CME, magnetic field lines mapping from the ejected plasma to the photosphere are stretched outwards to form an extended, open field structure [...]” that resembles the sketches on the left of each of the panels in Fig. 6.5: plasmoids leaving the magnetosphere have been compared to filaments erupting as part of a CME.

Directly driven models

Some researchers “have proposed models that produce a sudden energy release in the corona by means of a surface or sub-surface current generator. In contrast to storage models, there is no build-up of magnetic energy in the corona prior to onset. Instead, there is a sudden injection of current or magnetic flux into the corona from below. As a rule, the models do not address the mechanism that leads to the sudden injection of current or flux. They simply posit that such an injection occurs, and then model the consequences of such an injection for the corona.” Section II:6.2.2 describes some of these models and their problems when compared to observations and physical conditions in the Sun; these are not further discussed here.

Pre-eruption current sheet models

“Because the magnetic energy in the corona is much larger than the thermal and gravitational energies, the magnetic force ($\mathbf{j} \times \mathbf{B}$) cannot, in general, be balanced by gravity or by a gas pressure gradient. Thus, as a rule, the coronal field will tend to be force-free, meaning that the current will flow along the direction of the magnetic field (*cf.* Fig. 6.7a). An exception to this rule occurs when a current sheet is present. In this case gas pressure within the sheet balances the strong magnetic field outside. If the current sheet is sufficiently thin, then the high temperature or density within the sheet may not be detectable. Thus the corona could still have the appearance of a plasma with a low gas to magnetic pressure ratio (*i.e.*, plasma $\beta \ll 1$). Figure 6.7b shows a flare model with such a current sheet, where a micro-instability within the sheet triggers an eruption.

Prior to onset, the current sheet grows as a consequence of the emergence of new magnetic flux into a pre-existing magnetic loop as shown in Fig. 6.7b. As the current sheet grows, it eventually reaches a point where a micro-instability is triggered because the current density exceeds some critical value. Once the micro-instability occurs, the electrical resistivity of the plasma in the sheet dramatically increases, and rapid reconnection ensues.”

6.3.2 Two-dimensional force-free models

“[M]any storage models use configurations that have currents flowing parallel to the magnetic field in the pre-eruption state. Thus, there is no [net] magnetic force anywhere in the configuration prior to eruption. To explain an eruption, such models need to show how a strong magnetic force can rapidly appear as a result of the slow evolution of the photospheric boundary conditions.

To illustrate the basic principles, we first consider a relatively simple flux-rope

model [...] for which the external field is] prescribed by

$$B_y + iB_x = \frac{2iA_0\lambda(h^2 + \lambda^2)\sqrt{(\zeta^2 + p^2)(\zeta^2 + q^2)}}{\pi(\zeta^2 - \lambda^2)(\zeta^2 + h^2)\sqrt{(\lambda^2 + p^2)(\lambda^2 + q^2)}}, \quad (6.3)$$

where $\zeta = x + iy$ and A_0 is the photospheric magnetic flux, or, equivalently, the magnetic vector potential at the origin. In this expression h is the height of the flux rope above the surface and p and q are the lower and upper tips of a vertical current sheet below the flux rope as shown in Fig. 6.8. The parameter λ is the half-distance between two photospheric field sources located at $\zeta = \pm\lambda$ on the surface [...]

Application of the frozen-flux condition at the surface of the flux rope determines the current in the rope. This condition keeps the magnetic flux between the flux rope and the surface constant in time. It also ensures that during an eruption there is no flow of energy into the corona if the normal component of the field at the base remains invariant. Consequently, the current in the flux rope is prescribed by

$$I = \frac{c\lambda A_0}{2\pi h} \frac{\sqrt{(h^2 - p^2)(h^2 - q^2)}}{\sqrt{(\lambda^2 + p^2)(\lambda^2 + q^2)}}. \quad (6.4)$$

This current decreases with time during an eruption as magnetic energy is converted into kinetic energy. This decrease becomes apparent only when the formula giving the dependence of q upon h and p is incorporated into the above expression [(for references, see Sect. II:6.2.4)].

The magnetic field configuration is shown in Fig. 6.8 for three different sets of parameters. The surface at $y = 0$ corresponds to the photosphere, and the boundary condition at this surface is

$$A(x, 0) = A_0 \mathcal{H}(\lambda - |x|), \quad (6.5)$$

where \mathcal{H} is the Heavyside step-function and A_0 is the value of A at the origin. This boundary condition corresponds to two sources of opposite polarity located at $x = \pm\lambda$.

[...] Depending on the choice of model parameters, there may be three equilibria, one equilibrium, or no equilibrium for a given set of parameters. In situations with three equilibria the magnetic energy of each equilibrium is different. For the isolated equilibrium shown in Fig. 6.8b the flux rope sits in an energy well as shown in Fig. 6.8e. If the flux rope is pushed downward toward the surface, compression of the magnetic field between the flux rope and the surface creates an upward force. If the flux rope is pulled upward away from the surface, magnetic tension from the overlying arcade creates a downward force. Line-tying^[15] plays a key role in creating the equilibrium because it prevents field lines from being pushed into, or pulled out of, the surface when the flux rope is perturbed.

An evolutionary sequence is created by assuming that the distance between the two sources at $\pm\lambda$ decreases at a rate that is much slower than the Alfvén time-scale in

¹⁵ Line-tying assumes that the surface footpoints of all magnetic field lines remain fixed at their initial positions during the eruption.

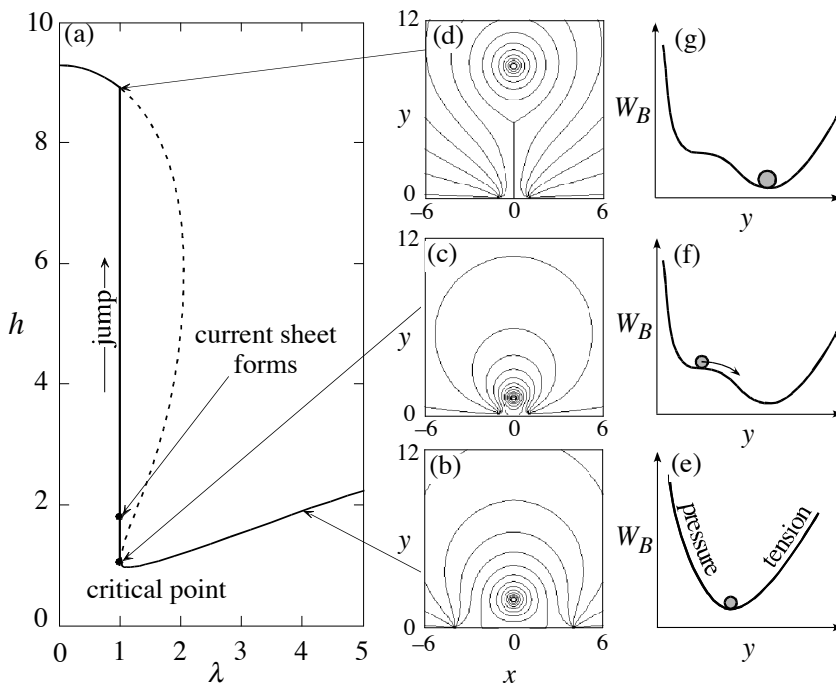


Figure 6.8: Ideal-MHD evolution of a two-dimensional arcade containing a magnetic flux rope [described by Eq. (6.3), with values p and q the height of the lower and upper tips of the of the current sheet below the flux rope.] Panel (a) shows the equilibrium curve for the flux rope height, h , in normalized units, as function of the source separation half-distance λ . Panels (b, c), and (d) show the magnetic field configuration at three different locations on the equilibrium curve, and panels (e, f) and (g) show the corresponding energy schematic for each configuration. The case shown is for a flux rope radius of 0.1 in normalized units. [Fig. II:6.9; source: Forbes and Priest (1995).]

the corona. A flux rope located on the lower portion of the equilibrium curves shown in Fig. 6.8a will erupt when the distance between the line sources becomes less than the height of the flux rope. When this location is reached, the unstable and stable equilibria coincide as shown in Fig. 6.8g. Once equilibrium is lost, the flux rope rapidly moves upwards. In the absence of reconnection ($p = 0$) the flux rope does not escape, but, instead, reaches a new equilibrium position with a vertical current sheet, as shown in Fig. 6.8d.

In the absence of any reconnection the amount of energy released by the loss of equilibrium is quite small, less than 5% [...] Thus, while the loss of equilibrium can account for the rapid onset of an eruption, it cannot, by itself, account for the large amount of energy released. For this, magnetic reconnection is needed. [...] For typical coronal conditions a very modest rate of reconnection is sufficient to allow escape. For reconnection rates corresponding to an inflow Alfvén Mach number, M_A , > 0.05 (at the midpoint of the current sheet sides) the flux rope can escape without any deceleration [...]"

MHD simulations are needed to analyze such an eruption with more realism, and also to understand the role of waves, including shocks that develop when the eruption speed exceeds the propagation speeds of any of the possible MHD waves. More on this in the Heliophysics books.

6.3.3 Three-dimensional force-free models

“It will probably come as no surprise that three-dimensional models are considerably more complex than two-dimensional ones. Three-dimensional field configurations are subject to a much greater number of instabilities. The helical ideal-MHD kink mode is an example of an inherently three-dimensional instability that does not exist in two dimensions. The dynamical evolution that occurs in three-dimensions is also more complicated. Fully nonlinear three-dimensional MHD turbulence can occur and magnetic reconnection exhibits new features that have no counterpart in two dimensions. Nevertheless, despite these additional complications, the underlying principles of the three-dimensional storage models remain the same.

[...] In order to show the relation of the relatively simple two-dimensional model of the previous section with these three-dimensional models, we take a reductionist approach. That is, we start with a very simple three-dimensional configuration and then sequentially add new features that increase its complexity. We start with the simple toroidal flux rope shown in Fig. 6.9. The antiparallel orientation of the current flowing on the opposite sides of the ring produces a repulsive force similar to the force between two parallel wires with antiparallel currents. For a small minor radius, a , this force, sometimes referred to as the hoop force, is approximately

$$F \propto \frac{I^2}{R} \ln(R/a), \quad (6.6)$$

where I is the flux-rope current, R is the major radius, and a is the minor radius of torus. The right-hand side of the above expression is the lowest order term of an expansion in the parameter a/R , so the expression is only valid for $a \ll R$ [...]

Just as for two-dimensional storage models, the three-dimensional models assume that the time scale of the eruption is so fast that any additional input of magnetic energy after the eruption starts, is completely negligible. Therefore, the flux associated with the flux rope current is conserved. In the limit that a/R tends to zero, the flux-rope current is roughly

$$I \approx \frac{I_0 R_0}{R \ln(R/a)}, \quad (6.7)$$

where I_0 and R_0 are initial values. If one considers the torus configuration as an initial state that subsequently evolves in response to the force, then R will increase to infinity, but as it does, so I will decrease to zero. In the process the magnetic energy associated with the flux rope’s initial current is converted into the kinetic energy of the expanding plasma ring.

To create an equilibrium one must add an additional magnetic field of the proper orientation and strength. In tokamak terminology such a field is called a strapping field. [...] Whereas it is possible to create a stable equilibrium by an appropriately

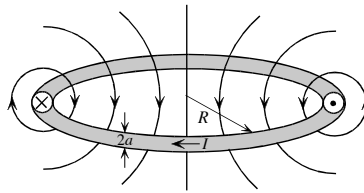


Figure 6.9: An isolated toroidal flux rope. The flux rope has a major radius, R , a minor radius, a , and carries a net toroidal current I . The antiparallel orientation of the current flowing on the opposite sides of the torus creates an outward force in the radial direction. [Fig. II:6.16]

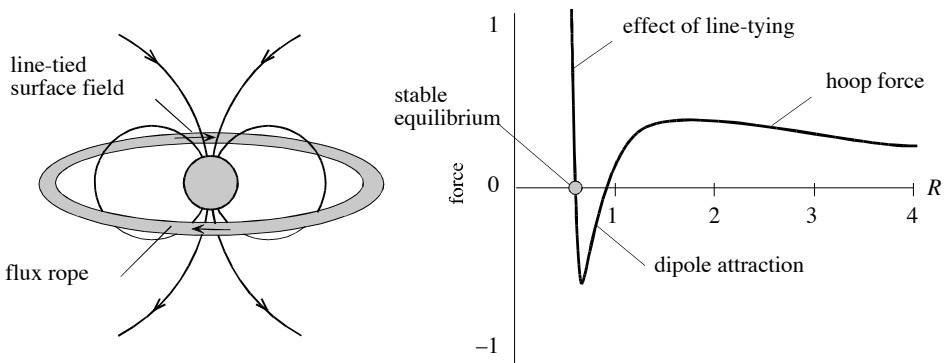


Figure 6.10: A stable toroidal equilibrium. (left) The addition of a line-tying surface representing the surface of the Sun creates the possibility of a stable equilibrium. Surface currents (which can be modeled using an image current) create an additional magnetic field component that gives rise to a second equilibrium position as shown on the right. The new equilibrium is stable because displacements away from it produce a restoring force. [Fig. II:6.18]

shaped] strapping field, an alternative possibility that is more appropriate for a storage model is to introduce a line-tying surface as shown in Fig. 6.10. The effect of line-tying can be modeled by introducing a fictitious image current below the surface. With the introduction of this additional current, a new equilibrium appears which, unlike the previous one, is stable. Stabilization is achieved because line-tying prevents field lines from being pushed into, or pulled out of, the surface [...]

Although we now have an eruptive model with some degree of three-dimensionality, it still has the drawback that the flux rope is not itself anchored to the solar surface. An analytical configuration that does have this property is shown in Fig. 6.11; [...] it consists of a toroidal flux rope that intersects the photospheric surface. The flux rope, with current I , is held in equilibrium by an overlying arcade (not shown in the figure) which is produced by subsurface magnetic charges $\pm q$ located along the centerline at a depth d below the photospheric surface at $z = 0$. Finally, there is a subsurface line current lying along the centerline. The strength of the current, I_0 , flowing in this

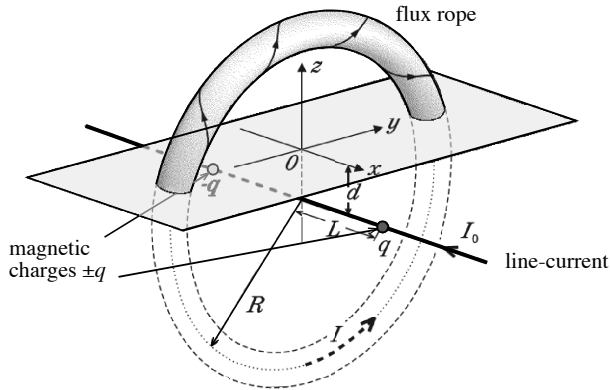


Figure 6.11: *The three-dimensional flux-rope model of Titov and Démoulin. The coronal magnetic field is produced by three different sources consisting of a flux rope current, a pair of magnetic charges, and a line current. The source regions located below the surface are fictitious constructs used to create the coronal field. The model does not prescribe the form of the subsurface field. [Fig. II:6.19; source: Titov and Démoulin (1999).]*

subsurface line controls the pitch of the coronal magnetic field. When I_0 is varied from small to large values, the configuration changes gradually from a highly twisted flux rope resembling a slinky to one that resembles a sheared arcade without a flux rope.

Although the magnetic field of [what is known as a Titov-Démoulin] configuration is still azimuthally symmetric about the centerline of the torus, the solar surface no longer shares this symmetry. Instead the surface is a flat plane that intersects the flux rope torus at some arbitrary position without influencing the field structure. Thus, any line-tied evolution of this configuration away from the initial state necessarily creates a highly asymmetrical configuration. An example of what such a configuration looks like is shown in Fig. 6.12. This figure shows two different views of an iso-current surface of the current density obtained from a simulation. This simulation starts with an unstable Titov and Démoulin configuration that is given a small perturbation. Within a few Alfvén scale times the configuration evolves into the kinked, omega-shaped flux rope shown in the figure. For this particular case, the initial instability is actually a helical kink instability rather than the torus instability discussed previously. However, it is possible to construct unstable Titov and Démoulin configurations that are unstable to the torus instability rather than the helical kink [...]"

6.3.4 Formation of the pre-eruption field

“An important issue that the above flux rope models do not address is the creation and growth of the magnetic stress that causes the field to erupt. It could be that most of the stress build-up occurs in the convection zone before the field emerges into the corona. Alternatively, it may be that the field emerges in a nearly unstressed, current-free state, and that the stress subsequently develops in response to the observed

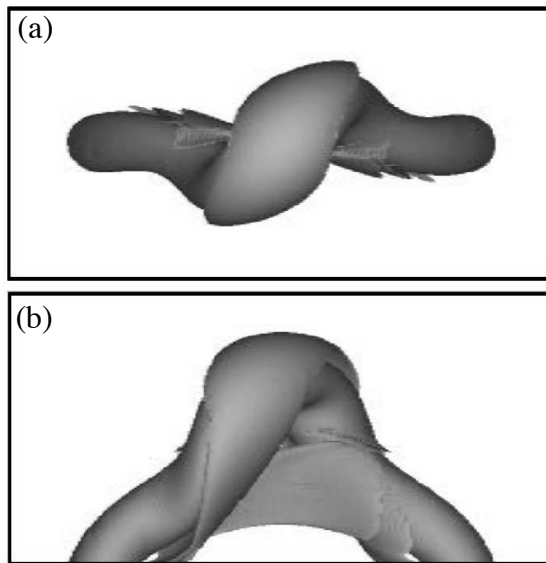


Figure 6.12: Top view (a) and side view (b) of constant current density surfaces from a simulation for an unstable Titov and Démoulin equilibrium. [Fig. II:6.20; source: Török *et al.* (2004).]

surface flows. In practice both possibilities are likely to occur at least at some level.

[Among the three-dimensional simulations that address this issue is one] called the *breakout model*. The evolution of this model is shown in Fig. 6.13. The initial state consists of a quadrupolar magnetic field that carries no current, so it contains no free-magnetic energy. Slowly shearing the central arcade around the equator gives rise to a set of stressed loops that push outward against the overlying arcade. As this happens, a curved, horizontal current sheet forms at high altitude at the pre-existing x-line. Eventually, the stresses build up to a level that causes an eruption. The nature of the mechanism that triggers the eruption has not yet been fully resolved, but it is likely that it consists of some kind of combination of both ideal and non-ideal processes.

[An alternative to this model is where a flux rope emerges into a pre-stressed field from below the photosphere.] Generally, the flux rope will tend to erupt once there are one or two turns in the portion of it that has emerged into the corona. However, if the flux rope emerges into a pre-existing arcade, the strength and orientation of this arcade also has a strong effect on whether an eruption occurs or not.

[...] One of the important issues that [various] studies address is the effect of mass loading on the emergence of a flux-rope into the low-density corona. Most of the CME models discussed in the previous section are based on the supposition that a flux rope exists in the corona prior to onset, but it is not obvious how such a structure could be formed. Formation of the flux rope within the convection zone followed by its buoyant rise into the corona immediately encounters the problem that mass cannot easily drain out of concave-upward portions of the magnetic field. Unless there is a way for the

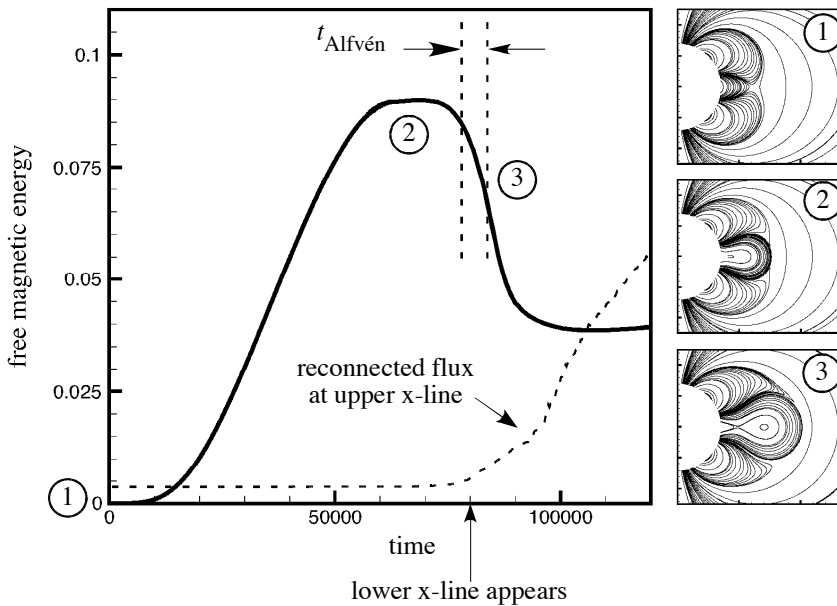


Figure 6.13: Numerical simulation of a storage model. The panel at left shows the free magnetic energy as a function time, while the three panels at right show contours of the magnetic flux surfaces at three different times. [Fig. II:6.21; source for inset panels: MacNeice *et al.* (2004).]

mass to drain out of the flux rope, the rope will remain half buried in the solar surface. One way around this difficulty is to suppose that the flux rope does not exist prior to the emergence of magnetic flux, but instead forms in the corona by a combination of converging flows and slow reconnection. Most dynamo models, however, predict that large-scale flux ropes will form near the base of the convection zone and then rise buoyantly to the solar surface to form an active region. Thus, this solution to the mass-loading problem involves both the destruction and reformation of the flux rope below and above the surface.”

6.3.5 Observed signatures of flares and CMEs

“The release of energy can either be ‘impulsive’, with time scales sometimes faster than 1 s, or ‘gradual.’ The impulsive and gradual signatures of a flare extend across the entire electromagnetic spectrum in a complicated way, as illustrated in Fig. 6.2. The terminology may not seem appropriate when one considers a slowly developing flare-like event, such as a quiet-Sun filament eruption; in such a case the ‘impulsive phase’ may take tens of minutes to evolve, and the hard X-ray emission may be below the detection level. Thus we don’t know how ‘impulsive’ the energy release really is in such an event, but in other respects it has the morphology of an ordinary active-region flare.”

“An individual flare can be divided into two main phases: impulsive and gradual. This generally refers to the timing of emissions relative to the processes thought to be

occurring in the flare. In the standard picture, the initial energy conversion caused by magnetic reconnection powers particle acceleration and possibly – depending on the energetics and on the magnetic configurations – a mass ejection. The downward-directed particles become trapped in loops and emit non-thermal incoherent radio emission ([compare Fig. 6.3]). Coherently emitting particles can be traveling either upwards out of the atmosphere or downwards into the atmosphere. Once the trapped particles precipitate from the magnetic trap, they deposit their energy in or just above the photosphere, producing thick-target non-thermal bremsstrahlung emission. This energy deposition results in the heating of the photospheric material to temperatures near 10^4 K, and emissions from FUV lines. All of this is associated with the impulsive phase of the flare. The flow of energy at this point proceeds back into the upper atmosphere, with line emission from the lower chromosphere. Thermal X-ray emission occurs as well. As the energy input into the system decreases, emissions of all flare components return to the pre-flare level.”

“We understand the impulsive and gradual phases to show the main energy [conversion out of the magnetic reservoir] and its aftermath (secondary effects), with the proviso that it is really not just that simple. The most prominent ‘aftermath’ is the action of coronal magnetic loops as an energy reservoir, with cooling time scales that can approach hours. This reservoir function is often described as the ‘Neupert effect’: the coronal manifestations of a flare tend to lag behind its chromospheric ones. This results from the finite time scale associated with the coronal density increase during the impulsive phase, via the process of ‘chromospheric evaporation.’ {A84} The decay time scale reflects its slower cooling and return to the lower atmosphere. The new material in the corona could be seen in the coronal emission lines, via free-free emission at radio wavelengths, or via free-free emission at soft X-ray wavelengths [...]

{A85}

“The Neupert Effect relationship [...] was formulated originally to describe the integral relationship between markers in a solar flare corresponding to the action of non-thermal particles, and the response from the atmosphere to the deposition of energy from these particles as it appears in coronal radiation. Written more generally,

$$L_{\text{gradual}}(t) \sim C_{\lambda\lambda'} \int_{t_0}^t L_{\text{impulsive}}(t') dt', \quad (6.8)$$

where $L_{\text{impulsive}}(t)$ is [evolving emission during the impulsive phase] which diagnoses the presence and action of particles accelerated in the explosive event (for stellar studies usually radio gyrosynchrotron, transition region FUV emission lines, or photospheric UV-optical continuum emissions), and $L_{\text{gradual}}(t)$ is the intensity corresponding to the gradual phase (usually coronal emission, but some chromospheric emission lines display the Neupert effect as well). The interpretation is that the gradual phase emission is responding to the buildup of energy that occurs as a result of the energy deposition being diagnosed by the impulsive phase emission. [... Note that] not all solar flares follow the standard flare scenario”: it appears to hold for some 80% of large flares, but overall for about half of all flares. The value of $C_{\lambda\lambda'}$ depends on the wavelength bands

II:3:2.2

{A84}

{A85} IV:2.1.2.1

[λ and λ'] used for both the impulsive and gradual phases.”

“The different atmospheric layers have a high degree of interconnectedness. Because a flare marks a transition between one quasi-stable configuration and another, the ordinary law of hydrostatic equilibrium dictates the run of pressure up through the atmosphere. A flare increases the gas pressure in the corona, at the expense of magnetic energy, and this can readily be detected at all levels). The hydrostatic scale height for pressure is given by $2k_{\text{B}}T_e/mg_{\odot}$, where k_{B} is the Boltzmann constant, T_e the temperature, m the mean molecular weight, and g_{\odot} the surface gravitational acceleration. For a flare temperature of 10^7 K, this scale height is a large fraction of the solar radius, much larger than the flare loop structures. Thus the vertical structure is isobaric in the upper chromospheric and coronal regions, and the chromosphere acts as a reservoir of mass to maintain this isobaric state as the flare loops cool, [lose pressure, and drain into the chromosphere] quasi-statically.”

“In the photospheric spectrum we see solar flares as brief flashes of white light and UV continuum. At present these sources are often not resolved either in space (Mm scales) or time (few sec scales). The bright emission regions are embedded in the ‘ribbon’ regions that become more prominent in the chromospheric and EUV coronal lines. In the coronal emissions one sees bright coronal loops developing slowly, with those from the highest temperatures appearing first and then cooling down through generally longer wavelengths, while at the same time shrinking in length. [...]

Solar flares are not luminous on the scale of the total solar irradiance (‘solar constant’), although they may produce a localized brightening seen against the bright photosphere. The powerful flare of November 4, 2003 was the first that could actually be detected in the total solar irradiance, by the radiometer on board the SORCE spacecraft. The signal, at roughly 5σ significance, amounted to about 300 ppm of the total signal, or 0.3 millimagnitudes in astronomical terms. There is a solar background noise level for such a measurement due to convection and oscillations; this amounts to some 50-100 ppm spread out over a bandwidth of a few mHz.

The localized brightening of a flare is much easier to see, of course, via an image even in white light. Carrington [was the first to see a solar flare. He described] his 1859 discovery as resembling the brilliance of Vega (α Lyrae), for example. [The photospheric brightening is a major fraction of a flare’s energy budget.] Soft X-ray emission, for example, contains only 5-10% as much luminosity. This gradual component [...] results from a thermal distribution (hot gas) for which the X-ray emission itself is a dominant cooling term. The non-thermal tail of the X-ray spectrum ($h\nu > 10$ keV), on the other hand, is due to bremsstrahlung from stopping particles. The bremsstrahlung mechanism is very inefficient, providing a fraction of order 10^{-5} of the energy losses. The rest of the energy winds up in longer-wavelength radiation, notably the visible/UV continuum.

We must also consider the bulk kinetic energy [involved in major solar impulsive events: CME kinetic energies can rival [total photon losses] in such cases. In rare cases a CME can occur in the absence of a major perturbation of the lower atmosphere. [...]] The partition of energy in a flare/CME event remains unclear physically and

hard to determine observationally.

The impulsive phase of a flare marks the period of intense energy release and strong non-thermal effects, including the launching of the CME. The traditional observational tools for the impulsive phase are hard X-ray emission and gyrosynchrotron emission at cm to mm radio wavelengths. The hard X-rays normally show two dominant footpoints embedded in ribbon regions of opposite magnetic polarity, but we do not presently understand why there are normally just two. The sources are compact and rapidly variable, and we associate them with the UV and white-light continuum emissions that also come from the footpoint regions. Other wavelengths show impulsive emission components as well as gradual ones. A clear impulsive-phase signature also appears even in the total irradiance, but rarely exceeds the background [variability: whereas the flare brightness commonly stands out against the local quiescent surface brightness, it stands out against among the overall variability of the entire disk only in the most energetic events) ...]

The hard X-ray spectrum above about 10 keV plays a central role in our understanding of the impulsive phase because the collisional energy losses of the bremsstrahlung-emitting electrons rival the total flare energy itself. This relationship can be established directly by inverting the hard X-ray spectrum, under model assumptions. The 'collisional thick target model' envisions a black-box accelerator of 10-100 keV electrons in the corona, with a directed beam penetrating to the chromosphere or even photosphere to excite UV and visible-light emission. This simple model has become less tenable as spatial resolution improves, since the WL/UV brightenings [observed with newer instruments] imply beams with extreme intensity [...]

'Gradual phase' refers to the thermal emission from the hot coronal material evaporated during the impulsive phase, plus the strong transition-region and chromospheric emissions driven by the cooling of these coronal loops. The loops connecting the roughly parallel ribbons form a semi-cylindrical *arcade* structure, divided into many unresolved loops. [...] The hot regions eventually cool to form the H α loop prominence system, whence thermal instability leads to the phenomenon of 'coronal rain'. The cooling also corresponds to shrinkage, as the gas pressure diminishes; shrinkage may also relate to the gradual release of energy as the coronal equilibrium returns to a stable configuration. This is the process termed 'dipolarization' in the geomagnetic community [...]"

"The expanding motions of flare ribbons provided one of the first clues to what we think of as the standard reconnection model of a flare [T]hese motions can be interpreted as an electric field. This is a motional or 'convective' electric field given by $\mathbf{E} = -\mathbf{v} \times \mathbf{B}/c$, and it is often taken as a measure of the reconnection rate. [T]he rate the ribbons sweep out the field should correspond in some sense to the rate at which energy is released during reconnection, and that at the same time the field guides the particle or heat flux responsible for the ribbon excitation."

"[T]he resemblance of terrestrial substorms to a two-ribbon solar flare, with ribbons of opposite magnetic polarity, has been repeatedly remarked upon" (compare Figs. 6.5

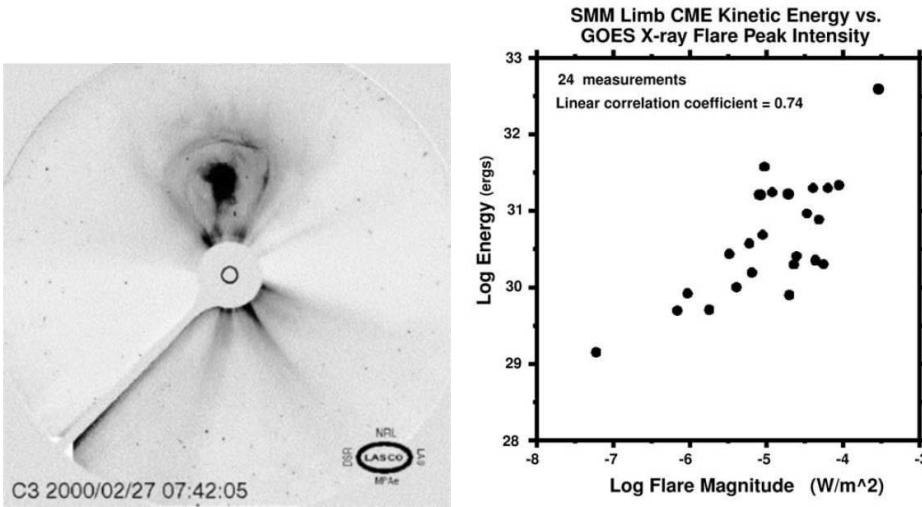


Figure 6.14: Left: Coronagraph observation of a CME that nicely shows the three-part structure: front, cavity, and (the bright core) filament (this is a file image taken from the LASCO database, presented in a reverse greyscale). Right: Correlation between inferred CME kinetic energy and peak GOES soft X-ray flux. [Fig. II:5.5; source: [Burkepile et al. \(2004\)](#).]

and 6.6). Note, however, that the process leading up to the event is entirely different: the unstable field configuration is built up by stressing and/or flux injection from below in the case of solar eruptions but driven via the wind-magnetosphere interaction from the outside in the case of terrestrial substorms.

“Major flare events almost invariably involve the ‘opening’ of the magnetic field as a CME; see Table 6.1 for the statistics [...] Observationally, [...] we often see a characteristic three-part structure: front, cavity, and filament (Fig. 6.14). This pattern makes it clear that the CME originated in a filament cavity near the surface of the Sun. A filament cavity consists of long, basically horizontal field, presumably more intense than its overlying ‘tie-down’ field that is more potential [...]

Modern images in coronal emissions such as soft X-rays allow a comparison of the coronal state before and after a CME event. Such comparisons revealed ‘dimming,’ readily interpreted as the evacuation of the mass of the corona by the CME eruption. The soft X-ray dimmings presumably correspond to the coronal depletions found via similar before/after comparisons of the visible corona.” {A86} {A87} {A88}

{A89} {A90}

6.4 Magnetic instabilities and reconnection

One of the mechanisms thought to be involved in the destabilization of magnetic configurations is reconnection. Fast reconnection is often accompanied by shocks, and both the motions in the reconnecting field and the shocks themselves contribute to energy conversion into a mixture of thermal and non-thermal populations. There is a

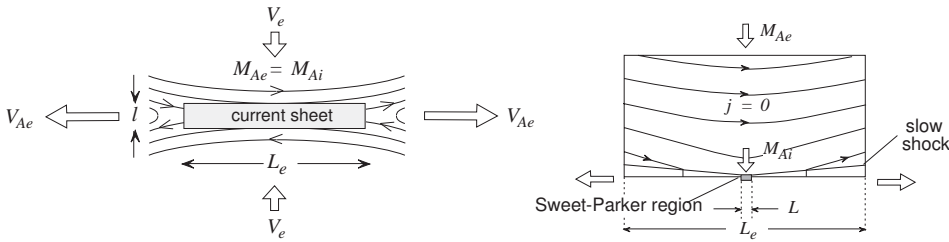


Figure 6.15: [(left)] *The Sweet-Parker field configuration. Plasma flows into the upper and lower sides of a current sheet of length L_e , but must exit through the narrow tips of the sheet of width l . Because the field is assumed to be uniform in the inflow region, the external Alfvén Mach number, $M_{Ae} = v_e/v_{Ae}$, at large distance is the same as the internal Alfvén Mach number, M_{Ai} , at the midpoint edge of the current sheet. [Fig. I:5.2] [(right)] *Petschek's field configuration. Here the length, L , of the Sweet-Parker current sheet is much shorter than the global scale length, L_e , and the magnetic field in the inflow is nonuniform. Two pairs of standing slow-mode shocks extend outwards from the central current sheet. Petschek's model assumes that the current density in the inflow region is zero and that there are no external sources of field at large distance. [Fig. I:5.3]**

vast literature on the topic, including how such processes contribute to instabilities in the solar corona and the magnetosphere. Here we touch only on the fundamentals, specifically the concepts involved in steady 2-dimensional reconnection; more comprehensive material (and references to further reading) moving towards the time-dependent and 3-dimensional real world is provided in I:5 and II:6.

Let us start with a highly simplified configuration, generally referred to as 'Sweet-Parker reconnection' of steady 2-dimensional reconnection in an incompressible plasma in a current sheet with [system-level] length scale L_e "as shown in [the left panel of] Fig. 6.15. Under these conditions [...] the speed of the plasma flowing into the current sheet is [approximately]

$$v_e = \left(\frac{v_{Ae} \eta}{L_e} \right)^{1/2} \quad (6.9)$$

where $v_{Ae} = B_e / \sqrt{4\pi\rho_e}$ is the Alfvén speed in the inflow region. The outflow speed of the plasma from the current sheet is the local Alfvén speed V_{Ae} .] The reconnection rate in two dimensions is measured by the electric field at the reconnection site. This electric field is perpendicular to the plane of Fig. 6.15, and it prescribes the rate at which magnetic flux is transported from one topological domain to another. In two-dimensional steady-state models this electric field is uniform in space. Therefore, the Alfvén Mach number, $M_{Ae} = v_e/v_{Ae}$, provides a quantitative measure of the reconnection rate, normalized by the characteristic electric field $v_{Ae}B_e$. [...]

In astrophysical and space plasmas [...] Sweet-Parker reconnection is usually too slow to account for phenomena such as geomagnetic substorms or solar flares. [A later model, known as 'Petschek reconnection', was developed to ensure much faster reconnection by encasing the] current sheet in an exterior field with global scale length L_e , [and by introducing] two pairs of standing slow-mode shocks radiating outwards

from the tip of the current sheet as shown in [the righthand panel of] Fig. 6.15. In Petschek’s solution most of the energy conversion comes from these shocks which accelerate and heat the plasma to form two hot outflow jets.

Petschek also assumed that the magnetic field in the inflow region was current free and that there were no sources of field at large distances. These assumptions, together with the trapezoidal shape of the inflow region created by the slow shocks, lead to a logarithmic decrease of the magnetic field as the inflowing plasma approaches the Sweet-Parker current sheet. This variation of the field leads in turn to Petschek’s formula for the maximum reconnection rate, namely

$$M_{\text{Ae[Max]}} = \pi / (8 \ln(L_e v_{\text{Ae}} / \eta)) \quad (6.10)$$

where [...] M_{Ae} is the Alfvén Mach number in the region far upstream of the current sheet as shown in Fig. 6.15. [...] The] Petschek reconnection rate is many orders of magnitude greater than the Sweet-Parker rate, and for most space and laboratory applications Petschek’s formula predicts that $M_{\text{Ae}} \approx 10^{-1}$ to 10^{-2} . [...]

It is not always appreciated that Petschek’s reconnection model is a particular solution of the MHD equations which applies only when [...] the flows into the reconnection region be set up spontaneously without external forcing [and] that there be no external source of field in the inflow region. In other words, the field must be just the field produced by the currents in the diffusion region and the slow shocks. In many applications of interest neither of these conditions is met.” “Even in circumstances where Petschek’s model would be expected to apply it apparently does not. [Numerical simulations suggest that it only does in case of a nonuniform, localized resistivity. This] does not contradict Petschek’s model because the model makes no explicit assumption about whether the resistivity is uniform or not. It is equally valid for both cases because it assumes only that the region where resistivity is important is localized. The numerical experiments carried out to date imply that the diffusion region can only be localized by enhancing the resistivity near the \times -line. Whether there might be other ways to localize the diffusion region (*e.g.*, a non-uniform viscosity) remains unknown.”

“An alternative approach to reconnection in current sheets was [developed by considering] what happens when a weak flow impinges on an \times -line in a strongly magnetized plasma as indicated in Fig. 6.16. The imposed flow creates a current sheet which achieves a steady-state when the rate of field line diffusion through the sheet matches the speed of the flow. [...]

For a steady-state MHD model the spatial variation of the field in the inflow region is the key quantity which [sets the] reconnection rate. [...] For any such model, the electric field is uniform and perpendicular to the plane of the field. Thus, outside the diffusion region $E_o = -v_y B_x / c$ where E_o is a constant, v_y is the inflow along the axis of symmetry (y axis in Fig. 6.16), and B_x is the corresponding field. Thus the inflow Alfvén Mach number, M_{Ae} , at large distances can be expressed as

$$M_{\text{Ae}} = M_{\text{Ai}} \left(\frac{B_i}{B_e} \right)^2 \quad (6.11)$$

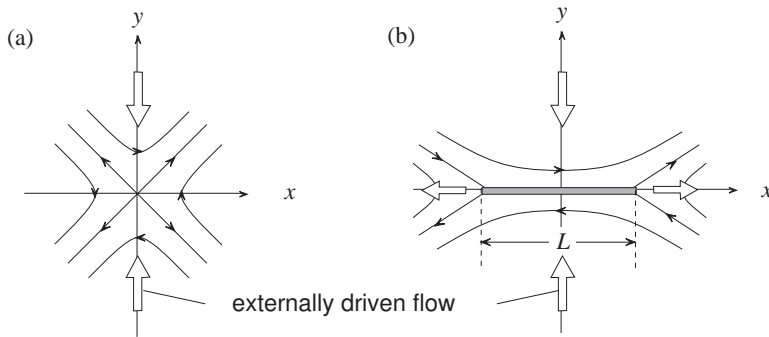


Figure 6.16: Syrovatskii's field configuration. Unlike Petschek's configuration, this one has external sources which produce an \times -type configuration even when local sources of current are absent. The application of external driving creates a current sheet whose length, L , depends on the temporal history of the driving and the rate at which reconnection operates. The fastest reconnection rate occurs when L is equal to the external scale length, L_e . [Fig. I:5.4]

where M_{Ai} is the Alfvén Mach number at the current sheet, B_i is the magnetic field at the edge of the current sheet, and B_e is the magnetic field at large distance.

In Syrovatskii's model the field along the inflow axis of symmetry is

$$B_x = B_i(1 + y^2/L^2)^{1/2} \quad (6.12)$$

where B_i is the field at the current sheet, y is the coordinate along the inflow axis, and L is the length of the current sheet. Combining (6.12) with (6.11) yields

$$M_{Ae} = M_{Ai}/(1 + L_e^2/L^2) \quad (6.13)$$

which has its maximum value when $L = L_e$. Thus the maximum reconnection rate in Syrovatskii's model scales [the same as] the Sweet-Parker model.

By comparison, the field in Petschek's model along this axis varies approximately as

$$B_x = B_i \frac{1 - (4/\pi)M_{Ae} \ln(L_e/y)}{1 - (4/\pi)M_{Ae} \ln(L_e/l)} \quad (6.14)$$

where l is the current sheet thickness. (This expression for the field is only a rough estimate since the actual variation in the region $y < L$ is more complex.) Evaluating this at $y = L_e$ and substituting the result into Eq. (6.11) gives

$$M_{Ai} = M_{Ae}/[1 - (4/\pi)M_{Ae} \ln(L_e/l)]^2 \quad (6.15)$$

The Sweet-Parker theory can be used to eliminate L_e/l , so as to obtain an expression for M_{Ae} [which] has a maximum value as given by equation (6.10). [...]"

Even a much longer summary than the above could not be conclusive: "There are many aspects of magnetic reconnection that have yet to be explored. Even well long studied topics such as steady-state two-dimensional reconnection are not fully understood. Many questions remain about how time-dependent reconnection works in

impulsively driven phenomena such as solar flares and geomagnetic substorms. For example, during the impulsive phase of eruptive solar flares the current sheet where reconnection occurs can grow at a rate that exceeds the Alfvén time scale of the system. This rapid growth means that no steady-state reconnection theory applies during the impulsive phase, and there are virtually no theories that predict how the reconnection rate scales with plasma resistivity in such a situation. [Another large challenge to our understanding of reconnection is that, despite] growing evidence that the reconnection process in both solar flares and the terrestrial magnetosphere may be turbulent, there are only few studies that address the issue of turbulent reconnection. The occurrence of plasma turbulence in a highly-structured environment poses a severe challenge to large scale numerical simulations, so progress in this area may be slow for sometime to come.”

Chapter 7

Torques and tides

Chapter topics:

- Angular-momentum loss through magnetized stellar winds
- Planetary magnetic fields as a cause of angular-momentum loss
- Angular-momentum transfer in planet-forming disks
- Tidal forces, covered-ocean formation on satellites, powering of dynamos

Key concepts:

- Gravitational tides and spin-orbit synchronization
- (Exo-)planetary atmospheric tides by solar/stellar irradiation
- Magnetic torques in stellar winds and accretion disks
- Alfvén surface

7.1 Introduction

Rotation and revolution are key properties for stars, planets, and indeed the entirety of planetary systems. For example, rotation is one of the essential ingredients of dynamo action in stars and planets, while climates are determined to a large extent by the Coriolis forces associated with planetary spin in combination with the overall duration of insolation on a planet's dayside, by the orbital eccentricity, and by the planetary obliquity, *i.e.*, the tilt of the planetary spin axis relative to the orbital plane. But spin rates evolve: stars slow their rotation because of their magnetic activity, while planetary rotation can change subject to tidal coupling with their moons, with their own atmospheres, and with their central stars. The latter, tidal synchronization of planetary spin and orbital motion, is likely common among exoplanets in the habitable zones of intrinsically faint M-type dwarf star because these exoplanets would have to have very tight orbits.

Also revolution is subject to change: planetary orbits need to be stable over long times to offer long-term habitability, but – as we discuss in Sects. 7.3.2 and 11.2 – orbits need to evolve for juvenile planets to grow efficiently and also, for instance, to transport water through a planetary system across the ice line from the cold outer reaches to the

habitable inner domain. ^[16] And if orbital dynamics (quantified in angular momentum) could not be efficiently transported through gas and dust, planetary systems and their central stars could not form as they are observed to do (see Sects 7.2.3, 7.2.4, and 11.3).

“Transport of angular momentum through the coupling of distant concentrations of mass occurs either through gravitational tides, by magnetic stresses, or by flows. Gravitational coupling has obviously played an important part in the spin-orbit synchronization of the Earth’s single moon. This coupling continues to be important as a stabilizer for the direction of the Earth’s spin axis, even as it causes the precession of that axis with associated climatic effects (Chs. III:11 and III:12). [This chapter reviews these processes, and more:] Tidal forces also act significantly on Jupiter’s moon Europa and Saturn’s moon Enceladus, in which it appears to result in liquid water in their interiors, which makes these moons interesting objects to study from an exo-biological perspective. Tidal spin-orbit coupling also leads to the formation of short-period, highly active binary stars (like the so-called RS CVn type systems). [...]

[This chapter also highlights a]ngular momentum transport via the magnetic field [which] is important in the coupling of proto-stars and young T Tauri stars to their surrounding disks and magnetized stellar winds. {A91} After the early formation phases of a planetary system, the loss of stellar angular momentum continues through a stellar wind, leading to magnetic braking of the stellar rotation and the concomitant gradual decrease in stellar activity with age. In tidally interacting binaries with one or more magnetically active components, the loss of spin angular momentum by a stellar wind drains the orbital angular momentum reservoir, eventually leading to the merger of the component stars, leaving an old but rapidly-spinning single star (like FK Comae). [The consequences of these couplings are discussed in Chs. 10 and 11.]

Angular momentum transport by flows inside astrophysical bodies is the cause of the near-rigid rotation with latitude and depth of the solar interior. But the models of the full convective envelopes of stars and giant planets need to advance significantly before we can use their results in, *e.g.*, magnetohydrodynamic dynamo models in which the non-rigid rotation and other large-scale circulations appear to be crucial.”

Even photons are involved in a form of tidal action: “Atmospheric tides are the response to periodic astronomical forcing. Atmospheric tides [on Earth] are forced primarily by the thermal heating due to the absorption of solar radiation by ozone and water vapor. These tides have periods which are the length of a mean solar day and its harmonics. [...]

This chapter briefly introduces each of these processes and the settings in which they are important, but the consequences of evolving orbital motions and spin rates are left for later chapters.

¹⁶ The temperature at which H₂O freezes into a solid in a proto-planetary disk is dependent on the partial pressure of the water vapor in the overall gas mixture, and is typically expected to lie in the range of 145 K to 170 K.

7.2 Magnetic torques

7.2.1 Stellar winds and magnetic braking

The solar wind discussed in Ch. 5 not only carries mass away from the Sun, but also angular momentum. “The conventional mechanism for stellar spin down is that stars lose angular momentum to the magnetized stellar wind in the concept called ‘magnetic braking’. In this process, the mass flux carried by the accelerating stellar wind conserves angular momentum as long as the wind speed is below the Alfvén speed, $v_A = B/\sqrt{4\pi\rho}$ (in cgs units of cm s^{-1}), where B is the local magnetic field strength, and ρ is the local mass density. Once the wind speed equals the Alfvén speed [(at the ‘Alfvén radius’; see Sect. 5.4) the wind is effectively decoupled] from the star. Another way to look at this process is to think of the magnetic field lines as rods [up to the Alfvén radius, beyond which the wind flows out essentially radially as if flung free from the star only at that radius (which in reality is a gradual process), dragging the magnetic field into a Parker spiral.] As a result, each field line applies a torque on the star and spins it down. This torque is proportional to the momentum of the wind at the Alfvén point, to the stellar rotation rate, and to the distance of the Alfvén point (the lever arm that applies the torque). The imaginary surface that contains all the Alfvén points is called the ‘Alfvén surface’ and the integral of the mass flux through this surface is the mass loss rate, \dot{M} , of the star to the stellar wind. For a spherically symmetric wind, and [a magnetic field that is close to uniformly distributed across the Alfvén surface,] we can calculate the total torque on the star and the total angular momentum loss rate, \dot{J} :

$$\dot{J} = -\Omega_* \dot{I}_{\text{shell}} = -\frac{2}{3} \Omega_* \dot{M} r_A^2, \quad (7.1)$$

where Ω_* is the stellar rotation rate, [\dot{I}_{shell} is the moment of inertia of a uniform shell of mass \dot{M} and radius r_A , and] r_A is the average distance to the Alfvén surface, and we assume constant moment of inertia [for the star (*i.e.*, we assume the time scale for angular momentum loss in this expression is short relative to the evolution of the internal structure of the star, which is appropriate for the long-lived ‘mature’ phase of the star, see Ch. 10). Note that Eq. (7.1) shows that the near co-rotation out to r_A^2 causes the solar wind to carry a factor of r_A^2/r_\odot^2 more angular momentum away from the star than is contained in the mass that is actually leaving the stellar surface.]

From Eq. (7.1) we see that the mass-loss rate is necessary to estimate the spin-down rate of a star. However, stellar winds of cool, Sun-like stars are very weak and cannot be directly observed (see Ch. 10), which makes it challenging to estimate \dot{J} as a necessary input for stellar evolution models [...]. Based on [measurements supported by modeling (described in Sect. 10.3.2) mass-loss rates in Sun-like stars] fall in the range between $10^{-15} - 10^{-11} M_\odot \text{ yr}^{-1}$ (the present-day solar mass-loss rate is $(2-3) \times 10^{-14} M_\odot \text{ yr}^{-1}$). However, stars can also lose mass via CMEs. In the case of the Sun, each CME carries some $10^{13} - 10^{17} \text{ g}$ into space, with an annual integrated mass-loss via CMEs of several percents of the ambient mass-loss. Therefore, CMEs on the Sun play very little role in the solar mass-loss. This role can become significant if the CME rate is higher by a factor of 10 or more. In this case, CMEs can even dominate the stellar mass-loss.”

But we know very little of CMEs of stars other than the Sun, or even of the Sun in its distant past, so this area is left for future exploration.

Let us make a few comparisons of energy budgets and time scales, using rough approximations only: The above-mentioned solar mass-loss rate can be combined with numbers in Table 2.4 to estimate the power needed to drive the flow of the solar wind (bulk kinetic energy), the Alfvén radius, and with that the rate at which rotational energy is drained from the Sun. Assuming for this estimate a constant mean wind velocity, a temperature of 1.5 MK for the high corona, an isotropic heliospheric magnetic field strength (approximating the field as radial), a total characteristic power associated with all forms of coronal radiative losses driven by solar magnetic activity of order $\approx 10^5$ erg/cm²/s (averaged over a solar cycle), and a moment of inertia of $I_{\odot} \approx 7 \times 10^{53}$ g cm² (see Ch. 10), one can conclude that (1) the solar wind kinetic energy flux is several times smaller than the coronal radiative losses, (2) the characteristic Alfvén radius is roughly 15 solar radii, and (3) the time scale for magnetic braking, *i.e.*, the ratio of angular momentum to loss rate of angular momentum for the present-day Sun is of order 10 Gyr. {ⓂA92}

In very rapidly spinning stars, the centrifugal forces that we have ignored for the solar wind, also need to be taken into account. An example where these dominate the process in the case of a cold wind is discussed in Sect. 7.2.4.

7.2.2 Planetary magnetospheric torque

We can make a similar comparison of energy budgets and time scales for the solar wind that delivers power to Earth’s magnetosphere and induces a torque on Earth’s rotation. First, let us look at the energy, then at the angular momentum. “The net rate of energy extraction (power) \mathcal{P}_{sw} from the solar wind flow is equal to the difference of the solar wind kinetic energy flux across two surfaces A perpendicular to the Sun-planet line, surface 1 ahead of the bow shock and surface 2 far downstream of the entire interaction,

$$\begin{aligned} \mathcal{P}_{\text{sw}} &= \frac{1}{2} \int_1 \rho v^3 dA - \frac{1}{2} \int_2 \rho v^3 dA \\ &= \frac{1}{2} \int \rho v (\bar{v}_1^2 - \bar{v}_2^2) dA \\ &\approx \dot{M}_{\text{ft}} \bar{v} \Delta v \end{aligned} \quad (7.2)$$

(subscripts ‘sw’ on ρ and v have been omitted, for simplicity), and the total force F is similarly equal to the difference of the linear momentum flux,

$$F_{\text{sw}} = \int_1 \rho v^2 dA - \int_2 \rho v^2 dA \approx \dot{M}_{\text{ft}} \Delta v, \quad (7.3)$$

where $\Delta v \equiv \bar{v}_1 - \bar{v}_2$ and $\bar{v} \equiv (\bar{v}_1 + \bar{v}_2)/2$ (bars indicate suitable averages) and

$$\dot{M}_{\text{ft}} = \int_1 \rho v dA \simeq \int_2 \rho v dA \quad (7.4)$$

is the amount of mass per unit time flowing through the region of interaction between the solar wind and the magnetosphere, to be distinguished from \dot{M}_{sw} , the mass input rate from the solar wind into the magnetosphere.^[17] Combining Eqs. (7.2) and (7.3) yields a relation between the power and the force (in the direction of solar wind flow),

{A93}

$$\mathcal{P}_{\text{sw}} = F_{\text{sw}} \bar{v}, \quad (7.5) \quad \text{{A93}}$$

which [has been used] to estimate the energy input into the terrestrial magnetosphere, under the assumption that the relevant force F_{sw} is the tangential (magnetotail) force acting primarily on the nightside, F_{MT} (see Sect. I:10.3.2)."

"While pressure from the external medium thus accounts for the formation and shape of the magnetosphere on the dayside of the planet, it cannot by itself explain the formation of the *magnetotail* on the night side. This structure, shown also in Figure 5.12, is a region of magnetic field lines pulled out into an elongated tail in the anti-sunward direction, with the magnetic field reversing direction between the two sides of a *current sheet* or *plasma sheet* in the equatorial region. To form this structure one needs an appropriate stress: a tension force pulling away from the planet. If we choose a closed volume bounded by a surface just outside the magnetopause plus a cross-section of the magnetotail (vertical cut at the right edge of Figure 5.12) and evaluate the force [...], the total tension force F_{MT} is given by the integral over the cross-section and the total pressure force F_{MP} by the integral over the magnetopause:

I:10.3.2

$$F_{\text{MT}} \simeq (B_t^2/8\pi) A_t \quad F_{\text{MP}} \simeq \rho_{\text{sw}} v_{\text{sw}}^2 A_t \quad (7.6)$$

where B_t is the mean magnetic field strength and A_t the cross-sectional area of the magnetotail (typically, A_t exceeds πR_{MP}^2 by a factor 3 to 4). Both F_{MP} and F_{MT} are directed away from the Sun and are exerted ultimately on the planet." "Note: if F [in Eq. (7.5)] is equated to the pressure force F_{MP} on the entire magnetopause, it can be shown that the associated \mathcal{P} does not go into the magnetosphere but represents the power expended in irreversible heating at the bow shock.

I:10.4.1

Calculating the power extracted from planetary rotation is somewhat simpler. The angular momentum of the rotating planet is $I_p \Omega_p$ and the kinetic energy of rotation is $\frac{1}{2} I_p \Omega_p^2$, where I_p is the moment of inertia and Ω_p the angular frequency of rotation [of the planet]. With \mathcal{T} the torque on the planet (component along the rotation axis),

$$\mathcal{P}_{\text{rot}} = \frac{d}{dt} \left(\frac{1}{2} I_p \Omega_p^2 \right) = \Omega_p \frac{d}{dt} (I_p \Omega_p) = \mathcal{T} \Omega_p, \quad (7.7)$$

a relation between the power and the torque, completely analogous to Eq. (7.5). [...]

¹⁷ Note that the final expressions in Eqs. (7.2) and (7.3) are approximations that assume that v_1 and v_2 are rather uniform across A . Whereas the upstream solar wind moving through 'surface 1' is generally quite uniform, this approximation is less tenable for the downstream flow through 'surface 2' which is placed in the geotail far downstream of Earth. This assumption thus limits the practical use of these expressions, although upper limits for \mathcal{P}_{sw} and F_{sw} are readily obtained by ignoring the downstream terms. Note also that magnetic and thermal contributions to solar wind energy and momentum flux in Eqs. (7.2) and (7.3) have been neglected as small in comparison to those of the bulk flow; see Sect. 3.5.2.

What happens to the linear momentum extracted from the solar wind flow is well understood: it is transferred to and exerts an added force on the massive planet. The angular momentum extracted from the rotation of the planet, on the other hand, can only be removed to ‘infinity,’ and identifying the mechanism by which it is transported away is indispensable for understanding the interaction. There are several possibilities:

(a) In magnetospheres with a significant interior source \dot{M} of plasma (from moons or planetary rings), angular momentum can be advected by the outward transport of mass [as long as the planet’s rotation period is below the orbital period of the plasma source]. For the simple example of plasma corotating rigidly out to a distance R_c and coasting freely beyond R_c , angular momentum is transported outward at the rate $\dot{M}R_c^2\Omega_p$, hence from Eq. (7.7) the extracted power is

$$\mathcal{P}_{\text{rot}} \simeq \dot{M} \Omega_p^2 R_c^2, \quad (7.8)$$

one half of which goes into the kinetic energy of bulk flow of the outflowing plasma (in this model), and the remainder is available for powering other magnetospheric processes (proposed for the magnetosphere of Jupiter).

(b) If the solar wind exerts a tangential force on the magnetosphere, it will also exert a torque whenever the distribution of the force is not symmetric about the plane containing the solar wind velocity and the planetary rotation axis. The torque may be estimated as $\mathcal{T} \sim R_{\text{MP}}\Delta F$, where R_{MP} is the distance to the dayside magnetopause and ΔF is the difference between the force on the dawn and on the dusk side; this gives the ratio of power from rotation to power from solar wind flow as

$$\mathcal{P}_{\text{rot}}/\mathcal{P}_{\text{sw}} \sim (\Delta F/F) (\Omega_p R_{\text{MP}}/v_{\text{sw}}). \quad (7.9)$$

In a slowly rotating magnetosphere such as Earth, $\Omega_p R_{\text{MP}}/v_{\text{sw}} \equiv \epsilon \ll 1$ and one also expects $\Delta F/F$ to scale as $\sim \epsilon$; hence the power extracted from rotation by the solar-wind torque is negligible.” “In principle, Ω_p decreases with time as the result of the torque, but in practice the rate of decrease is completely negligible. The time for the present magnetospheric torque to reduce appreciably the planet’s rate of rotation is several orders of magnitude longer than the [age of the Universe], both at Jupiter and at Earth; for the latter, this implies that the magnetospheric torque is much smaller than the lunar tidal torque.”

“(c) In a rapidly rotating open magnetosphere, on the other hand, magnetic field lines that extend from the planet into the solar wind may become twisted (by a process analogous to the formation of the Parker spiral in the solar wind), creating a Maxwell stress that transports angular momentum outward into the solar wind. This mechanism of extracting energy from planetary rotation was proposed for Jupiter (where it is now considered not important in comparison to mass outflow) and for Uranus.

(d) If the magnetic moment of the planet is tilted relative to the rotation axis, electromagnetic waves that carry away angular momentum may be generated by the rotation. This is generally believed to be the primary mechanism for energy loss from pulsars but is negligible for systems that are very small in comparison to c/Ω , the radius of the speed-of-light cylinder (which is the case for all planets in our Solar System and their magnetospheres).”

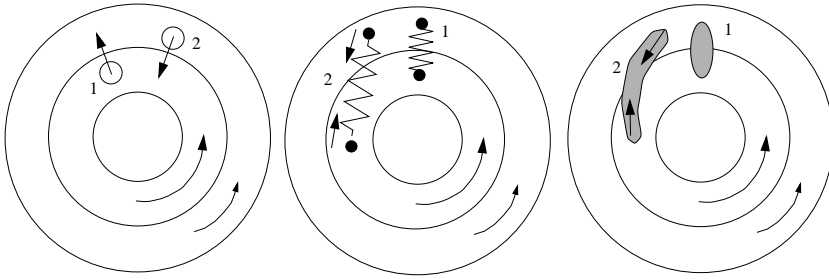


Figure 7.1: Schematic treatment of angular momentum transfer in a shearing disk with angular velocity decreasing outwards [as the orbiting material approximates Keplerian orbits]. An initially radial field is perturbed azimuthally (left panel); these azimuthal perturbations grow due to the shear in the disk (middle panel [going from time label '1' to time label '2']). In the case of gravitational instability (right panel), an excess of material gets sheared out by the differential rotation; the gravitational attraction on the sheared excess (spiral arm pattern) exerts a restoring force in the same sense as the magnetic case, again transferring angular momentum outward. [Fig. III:3.4; source: Hartmann (2009).]

7.2.3 Magneto-rotational coupling

As we saw in the case of the stellar wind, magnetic fields can support tension (Sect. 3.2.2) and thereby can essentially enforce co-rotation of gases at different distances from a star, at least out to where the field is strong compared to the inertial forces associated with the plasma. This not only holds for outflows such as stellar winds, but also in systems where matter is 'descending' onto the star, such as in very young proto-planetary systems where material has shaped itself into a disk spinning around an accreting star. More on that process in Ch. 11, but let us look at what a magnetic field that threads such a disk can do: a field can be an effective agent in transporting angular momentum outwards, thereby enabling the gas in the disk to spiral inwards and thus help form the star.

“As shown in the middle panel of Figure 7.1, if the magnetic field lines are thought of schematically as springs tying adjacent disk annuli together, then as differential rotation continually separates the regions 'tied' to the field (*e.g.*, evolution from ['1' to '2']), the 'springs' or field lines become stretched [and bent], and the resultant [tension] forces will work in the direction of spinning up the outer annulus while spinning down the inner annulus.

The magnetic fields shown in the top-down view of the middle panel of Figure 7.1 cannot be stretched indefinitely; at some point there will be reconnection and diffusion as the flow becomes turbulent. [In that case, an] initially vertical field is perturbed radially; these radial perturbations grow due to the shear in the disk; and eventually the field lines become so stretched that they pinch off and develop into full turbulence.

Although there is currently some controversy over the efficiency of this 'magneto-rotational instability', or MRI, it seems very likely that it provides a sufficiently effective

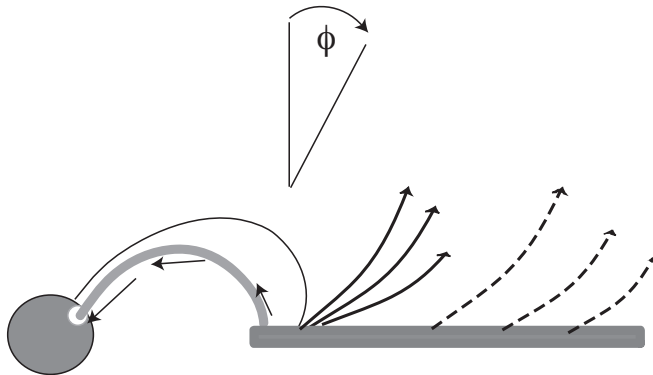


Figure 7.2: Schematic structure for a connected system of accretion disk, stellar wind, and stellar magnetosphere. Magnetic fields which, owing to a finite magnetic diffusivity, penetrate the disk inside the co-rotation radius (where the angular velocity of the rotating disk matches the angular velocity of the star) allow material to accrete (gray curve); fields penetrating the disk outside of corotation help provide a spindown torque (solid dark curve). In the \times -wind model, the wind arises from the disk just at corotation (curved solid arrows), while disk wind models involve mass loss from a wider range of disk radii (dashed arrows). Magnetic field lines pitched at angles $\Phi_e > 30^\circ$ allow for rapid, cold mass loss (see text). [Fig. III:3.7]

means of promoting accretion in astrophysical disks – provided, of course, that the magnetic field can couple effectively to the gas; there must be a sufficient population of ions and electrons to collide rapidly enough with neutral gas to make the MRI work. Protostellar disks are problematic in this regard: with much or most of their mass heavily shielded from ionizing radiation, and possessing temperatures far too low to effectively ionize even low-ionization potential metals like Na and K, it seems highly unlikely that the MRI can account for (at least low-mass) star formation on its own.” More on this in Ch. 11.

7.2.4 Disk winds

An alternative to transporting angular momentum outward through an accretion disk going against, and thereby enabling, matter to spiral inward is to remove angular momentum by a variant of a stellar wind, namely one that is cold and propelled by centrifugal forces. “The basic version of the cold, magnetically-driven wind takes advantage of the rapid disk rotation to fling material outward (and later collimate it). Near the disk it is assumed that the magnetic pressure is much larger than the gas pressure. In this limit, the magnetic fields are stiff at the launching region, *i.e.*, corotation of the inner wind is assured. In this case the energy (Bernoulli) constant of the motion [for a unit of mass] becomes

$$E = \frac{v_\phi^2}{2} + c_s^2 \ln \rho - \frac{1}{2} \Omega_o^2 r^2 - \frac{GM_*}{(r^2 + z^2)^{1/2}} = \frac{v_\phi^2}{2} + c_s^2 \ln \rho - \Phi_e, \quad (7.10)$$

where v_ϕ is the poloidal velocity, Ω_o is the (Keplerian) angular velocity of the disk in which the magnetic field is rooted, c_s is the (assumed isothermal) sound speed, and

Φ_e is an effective potential term including the effects of rotation and magnetic fields; [the terms in the central expression measure kinetic energy (first and third), change in internal energy in an isothermal process (second), and gravitational potential energy (fourth) at a distance r from the rotation axis of the disk, and height z above that disk]. The behavior of the flow depends upon the form of Φ_e , which in turn depends upon the geometry of the flow.

In the case of a perfectly vertical field, perpendicular to the disk, any material which flows outward must be propelled initially by gas pressure; the Keplerian rotation is of course insufficient by itself to drive outflow. The atmospheric structure is nearly hydrostatic until one reaches a radial distance such that

$$c_s^2 \sim \frac{GM_*}{(r^2 + z^2)^{1/2}}, \quad (7.11)$$

in analogy with a Parker thermal wind [(see Sect. 2.2 around Eq. 2.11)]. When the gas is cold, the flow 'starts' only at large radii; the flow interior to this must pass through many scale heights of density, resulting in negligible outflow.

In contrast, a field line tipped away from the rotation axis can effectively drive a cold flow, taking advantage of the $\frac{1}{2}\Omega_o^2 r^2$ term in Eq. (7.10). Neglecting thermal pressure,

$$E = \frac{1}{2}v_\phi^2 - \Phi_e, \quad (7.12)$$

where the 'effective' potential is

$$\Phi_e = -\frac{GM_*}{r_o} \left[\frac{1}{2} \frac{r^2}{r_o^2} + \frac{r_o}{(r^2 + z^2)^{1/2}} \right]. \quad (7.13)$$

Consider now a small displacement along the field line, with a coordinate given by s , and

$$ds^2 = dr^2 + dz^2. \quad (7.14)$$

At the base of the flow, the disk material is rotating at the local Keplerian velocity. This is an equilibrium state, because $d\Phi_e/ds = 0$ at $z = 0$. However, if $\partial^2\Phi_e/\partial s^2 < 0$, this equilibrium is *unstable*; any small perturbation along the field line will result in an increased (outward) poloidal velocity from Eq. (7.12). If θ is the angle between the field line and the disk plane, the critical stability criterion

$$\frac{\partial^2\Phi_e}{\partial s^2} = 0 \quad (r = r_o, z = 0) \quad (7.15)$$

requires $\tan^2\theta_c = 3$, or $\theta_c = 60^\circ$. Disk magnetic field lines which are tipped away from the rotation axis by an angle greater than 30° result in an unstable equilibrium, and rapid outflow will commence at the disk." This flow carries angular momentum away from the disk.

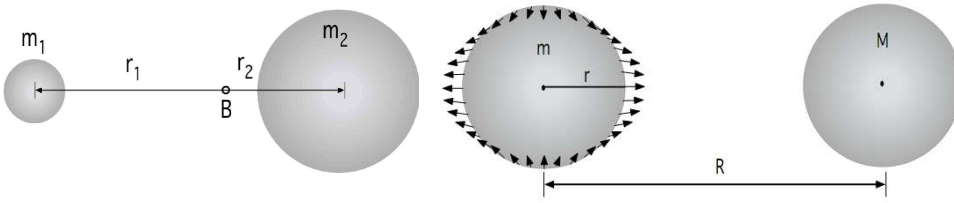


Figure 7.3: Left: Two bodies orbiting around the barycenter B. Right: Tidal acceleration induced by the body with mass M on the body with mass m with the distance R between their centers. [Fig. III:11.3]

7.3 Gravitational tides

7.3.1 Spin-orbit interactions

“A well known gravitational influence is the tidal force of Moon and Sun on Earth. [Similar tides occur in other planet-moon systems throughout the Solar System – and has led to spin-orbit synchronization for most of the major moons – and also in binary stars and in star-planet pairs with relatively tight orbits – more on that below.] To calculate the tidal acceleration, let us consider two masses M and m with the distance R between their centers as shown in Figure 7.3. According to Newton’s law of gravitation, the mass m feels the gravitational acceleration a :

$$g = -G \frac{M}{R^2} \tag{7.16}$$

However, each point of a body with mass m and radius r feels a different gravitational acceleration depending on the effective distance to mass M which ranges from $R - r$ to $R + r$. For the two extreme cases we find:

$$g = -G \frac{M}{(R \pm r)^2} = -G \frac{M}{R^2 (1 \pm r/R)^2}. \tag{7.17}$$

[In cases for which] r is much smaller than R this equation can be expanded into a Taylor series:

$$\frac{1}{(1 + x)^2} = 1 - 2x + 3x^2 - \dots, \tag{7.18}$$

$$g = -G \frac{M}{R^2} \pm G \frac{2M}{R^2} \frac{r}{R} \mp \dots \tag{7.19}$$

The tidal acceleration a_t is the difference between the effective and the gravitational acceleration :

$$a_t \approx \pm G \frac{2M}{R^2} \frac{r}{R}. \tag{7.20}$$

Note that a_t decreases with the third power of R . As a result of this the tidal accelerations are relatively small. On Earth the tidal acceleration is about $1.1 \times$

©A94

10^{-6} m s^{-2} due to the Moon and $0.5 \times 10^{-6} \text{ m s}^{-2}$ due to the Sun compared to the gravitational acceleration of about 10 m s^{-2} . This corresponds to an expected lunar tidal effect of about 70 cm. In reality, the average tide is about 30 cm because of a slight deformation of the Earth. In the case of the Sun, the tidal effects caused by the planets are very small; [t]he largest effects are due to Venus and Jupiter with a theoretical tide in the order of 1 mm.

As a result of the friction between the tide and the planet, the rotation [and revolution tend towards synchronizing]. In the case of Earth this [results in a slowing down of the spin rate by] about one second per year. Some 2.5 billion years ago the length of a day was only about 6 hours. Because the angular momentum must be conserved this leads to a corresponding increase in the distance between Moon and Earth (4 cm per year) as measured by laser technique. {A95} The tidal friction generates a power of $3 \times 10^{19} \text{ erg/s}$ which is mostly dissipated in the ocean. There are indications that this tidal power affects the global ocean circulation which plays a crucial role in the climate system by transporting energy from low to high latitudes. {A95} The tides act also in the atmosphere causing changes in pressure, temperature, and wave propagation.

There are climatic effects on Earth related to the lunar tides. The plane in which the moon moves is inclined to the ecliptic by about 5° . The points where the lunar orbit crosses the ecliptic are called nodes. As a result of the gravitational force of the Sun on the Moon the orbital spin axis of the Moon precesses, which leads to a continuous slight shift of the nodes. After 18.6 years the nodes are back to their original position. The inclination of the Moon's rotation axis has an effect on the amplitude of the tides. The amplitude of the lunar nodal tide is only about 5% of the daily diurnal tide but integrated in space and time it becomes significant. The 18.6 yr cycle and sometimes also its second subharmonic of 74 yr have been found in the arctic ocean temperature and sea ice extent and in drought records.

The dynamics of a multibody system such as the Solar System is largely determined by gravitation. The bodies orbit around the barycenter. In the case of a two-body system with a large body (Sun) and a small body (planet) the orbit is an ellipse with the large body in one of the focal points. {A96} In a multibody system (Solar System) the gravitational interaction between the bodies disturbs slightly their orbital parameters. For example the planets (mainly Jupiter and Saturn) change the eccentricity of the Earth's orbit with periodicities of about 100,000 and 400,000 years which has an effect on the amount of solar radiation received from the Sun" determined by the orbital eccentricity; more on that in Sect. 12.3.2 around Eq. (12.10). {A96}

The effects of the solar tides on the Earth's orbit are negligible, but that will not stay that way. Late in the life of the Sun, as it runs out of fuel (see Ch. 10), the Sun will swell up into what is known as a red giant. In fact, its "diameter increases by approximately two orders of magnitude. The physical expansion of giant stars results in the assimilation of many of the planets that may have formed in their formerly habitable zones [(defined as the distance from the star where liquid water can be present on a planet's surface)]. In the case of the Sun, current predictions indicate

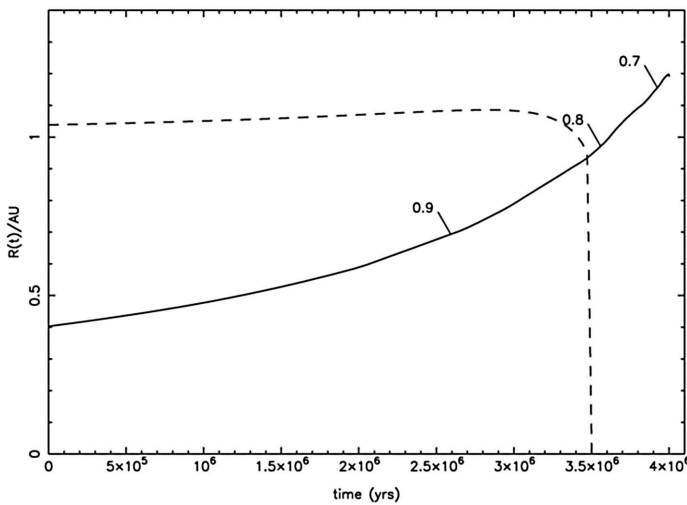


Figure 7.4: The diameter of the future red-giant Sun (solid; in AU; [the labels along the curve show the Sun’s mass at the time expressed in present-day solar masses]) and the size of Earth’s orbit (dashed) during the 4 million years leading up to the phase when the Sun reaches maximum brightness. Earth’s orbit expands slightly as the Sun loses mass but the Sun expands to the point where tidal drag causes Earth’s orbit to decay and intersect the Sun’s upper layers. These calculations predict that Earth will be destroyed in the Sun’s atmosphere 7.59 billion years from present. [Fig. III:4.6; source: Schröder and Connon Smith (2008).]

that the Sun will expand (Fig. 7.4) to nearly 1 AU, engulfing both Venus and Mercury. Because the Sun loses over 40% of its mass during [its phases as a red giant], Earth’s orbit will actually expand to conserve angular momentum. This seemingly places Earth just beyond the presently modeled maximum diameter of the Sun but detailed modeling indicates that Earth will be assimilated into the Sun because of tidal effects. Tidal forces raise a bulge in the Sun’s upper layers that follows Earth and provide a retarding force that causes Earth’s orbit to decay. {A97} Earth is totally vaporized by this process due to the power generated by its ~ 25 km/s entry into the Sun’s upper atmospheric layers. If Earth had formed 15% further from the Sun it would have escaped assimilation. Mars and all other planets are well beyond the effects of gas drag and tidal effects and are safe from total destruction although they are severely heated and rendered lifeless during the Sun’s red giant phase.”

This effect of orbital synchronization by gravitational tides occurs for all close-in planets, and has a particular consequence if we look at the evolution of the billions of planetary systems throughout the Galaxy. “In the far future, the Universe will look quite different than it does at present. All massive bright stars will have evolved and become invisible. Only the slowly evolving and faint M stars will persevere. After several tens of billions of years of Galactic evolution, questions about habitability will only concern the bodies that remain, these faint low mass red stars and planets that orbit them in thin habitable zones close to their surfaces[; ...] they are the most

numerous stars now in the Universe and [...] in the long term they will be the only stars in the Universe. Compared to the Sun these low mass stars offer new challenges to understanding habitability. Although faint, they have pronounced flare activity which generates both UV and energetic particle fluxes capable of harassing life. Due to their faintness, their habitable zones are so close to the stars that planets can be tidally locked with one side always facing out to space. This can cause thin atmospheres to freeze out on the dark side of planets although sufficiently thick atmospheres may be able to adequately distribute heat and prevent this calamity.”

Tides also have their consequences on the multitude of double stars: roughly one in two of the stars seen in the sky are pairs of stars orbiting their joint center of gravity. “The gravitational tides in binaries with periods of order a week or less (depending on stellar masses and radii) are so strong that the orbital and rotational periods of these stars are synchronized on time scales much less than the main-sequence life time. Because any cool-star components of such binaries lose angular momentum through their wind, they will tend to spin down, but the tidal coupling replenishes the lost rotational angular momentum from the reservoir of orbital angular momentum. This causes the orbital separation to shrink, the locked orbital and rotational periods to decrease, and – counterintuitively – the activity to increase with age until eventually the stars merge into a single, rapidly-rotating but old star (forming the class of FK Comae stars).” III:3.5

Another consequence of gravitational tides in the case of a tilted rotation axis relative to the orbital plane is precession. “The precession is a wobbling of the Earth’s axis of rotation which is caused by the tidal forces associated with the Moon and the Sun. Because the Earth is spinning, its shape deviates slightly from a sphere leading to an equatorial bulge. Tidal forces act on the bulge and force the axis to precess. The periods of [Earth’s] precession range from 19,000 to 24,000 years.” {A98} III:1.3

7.3.2 Orbital interaction {A99}

Differential gravitational forces are also thought to be of major importance in the formative phases of planetary systems, specifically acting between clumps of matter once these have condensed within the spinning accretion disk, and in even earlier phases when gravity may have led to unstable situations in which relatively dense areas may form by contraction and compression. “As shown in the right-most part of Figure 7.1, [such early gaseous concentrations will be] sheared due to the differential rotation. The gravitational attraction of one ‘end’ of the spiral arm pulls on the other; this has the effect of accelerating the outer material at the expense of decelerating the inner material – *i.e.*, transferring angular momentum outward. [One among several distinct mechanisms (see Ch. 11)], it appears that this mechanism [of gravitational instability (GI)] will prevent most of the mass from remaining in the disk, but instead will allow accretion toward the central object.” III:3.2

These same gravitational forces are likely to play a major role in enabling forming planets to grow into giants: growing planets set up wave-like density disturbances in large spirals, and the interaction of the growing planet with the matter in these spirals can cause all of the constituent parts to change their orbits, as long as the mass

in the disk is not too small compared to that in the growing planet. “For example, the combination of observations and numerical experiments suggests that gas giants accumulate up to a few hundred Earth masses of material – first the solids and then increasingly rapidly gases – within a matter of a few million years. This process is aided in its efficiency by the migration of growing planets within the young planetary system: planets are not bound to their initial orbits, but can migrate either inward or outward, subject to gravitational interactions, thus having access to a large volume of the primordial disk from which to collect material. Interestingly, it appears that it is the very collection process of matter onto the growing planet that causes mass redistributions within the disk so that their tidal effects can make planets migrate, particularly if other planets are forming elsewhere in the system, while the gravitational coupling between multiple young planets in eccentric orbits can scatter bodies around (both in distance from their central star and in orbital inclination).”

“The realization that exoplanets are mobile during the early stages of formation has led to many studies of dynamical interactions. The details of migration and the parking mechanisms that [can lead to] gas giant planets just a few stellar radii away from their host stars are an active area of research. In the younger primordial disk with significant gas and dust density, the planet embryos will clear gaps in the disk. In this case, material can pile up at both the inner and outer edges of the gap. When the disk mass at the edges of one of these gaps is comparable to the mass of the planet embryo the disk will exert a torque that causes the planet [to either tighten or widen its orbit around the parent star, *i.e.*, causes the planet] to migrate. The outer edge of the disk causes inward migration while the inner edge of the disk can produce outward migration. When multiple planet embryos exist in the disk it is possible for the outer embryo to become locked into a resonant orbit with the inner planet, a process called convergent migration. As the disk clears, convergent migration can leave planets in resonant orbits that persist stably over the lifetime of the star. This effect is especially powerful for resonances where the ratio of the orbital periods ($P_{\text{outer}}/P_{\text{inner}}$) is close to an integer number, N . Planets with small N are said to be in mean-motion resonance (MMR) and the exchange of angular momentum between MMR planets is flagged by oscillations in eccentricity and orbital periods.”

7.4 Planetary atmospheric tides

Apart from magnetic torques and gravitational tides, there is also a class of tides associated with irradiation. “In general terms, tides are the periodic response to periodic astronomical forcing. In the [Earth’s] atmosphere, by far the dominant forcing agent is thermal excitation by solar radiation, although forcing by latent heat release [(*e.g.*, cloud formation)] can also be important. The dominant atmospheric tides are the diurnal tide and the semi-diurnal tide at double the frequency. In the lower and middle atmosphere, tides are excited primarily by the absorption of solar UV radiation by stratospheric ozone and solar near-IR radiation by tropospheric water vapor. The diurnal tide is forced about one-third by water vapor absorption and about two-thirds by ozone absorption. The semidiurnal tide is predominately forced by ozone absorption.

Although the diurnal component of the diurnal variation of solar heating is stronger than the semidiurnal component, there is a rough parity between the two because the semidiurnal tide responds more efficiently to ozone forcing than does the diurnal tide. This is because the region of ozone forcing is fairly deep and main semidiurnal modes with their comparatively long vertical wavelengths respond in phase over the forcing regions, while the diurnal tide with its fairly short wavelengths experience a degree of phase cancellation.”

In “[p]lanets with thick atmosphere [...], atmospheric tides can affect rotation. It is speculated that all planets [in the Solar System] formed with similar rotation rates and spun in the prograde sense (aligned with the total angular momentum of the Solar System). Gravitational torques can de-spin rotation toward synchronous rotation, but cannot produce retrograde rotation. The torques acting on the solar tidal bulge and coupling with the solid planet, however, can cause retrograde rotation and this is what may have produced the retrograde rotation of Venus. The present state of Venus is thought to be an equilibrium between gravitational and thermal atmospheric tidal torques. Clearly the resonances supported by planetary atmospheres can affect where equilibrium states might be found and thus the speed of retrograde rotation.”

More on tides and other large-scale wave phenomena in both oceans and atmospheres can be found in Ch. III:15.

Chapter 8

Particle orbits, transport, and acceleration

Chapter topics:

- Energy conversion from large-scale dynamics of magnetized plasma into the thermal reservoir, the energetic-particle reservoir, or both
- Single-particle motion in a magnetic field
- Particle scattering and transport: solar energetic particles, galactic cosmic rays, radiation belts
- Particle acceleration in shocks

Key concepts:

- Magnetic invariants
- Phase-space density and the collisionless Boltzmann equation
- Gradient and curvature drifts
- Diffusive scattering

8.1 Introduction

Deep inside stars and planets energy is exchanged between particles (including photons) so frequently that the distribution of velocities of the ions and electrons in stars, and of the atoms and molecules in planets, are essentially pure Gaussians (and thus the distributions of the magnitudes of the velocities pure Maxwellians) around the mean bulk velocity. With sufficient collisional interactions in a neutral medium, or in an ionized medium in the absence of magnetism, the mean bulk flows of different species in a mixture tend to be equal. The presence of a magnetic field, in contrast, is associated with a difference in bulk motions between negatively-charged electrons and positively-charged ions. This, in turn, leads to collisional interactions that convert the kinetic energy of bulk population motions into random kinetic energy, *i.e.*, the dissipation of electrical current equates to heating.

Where collisional time scales grow to time scales approaching those of physical processes, or even exceed these, velocity distributions can deviate from Maxwellians. The populations of non-thermal particles of most interest in the context of heliophysics are those of the highest energies. Among these are radiation-belt particles, but also those that originate from outside the Earth’s environment, and referred to as ‘cosmic rays’, which encompass solar energetic particles (SEPs), galactic cosmic rays (GCRs) and ‘anomalous cosmic rays’ (ACRs). ^[18] ^[19]

“To understand the ubiquitous presence of energetic particles it is important to realize that except for planetary ionospheres and the lowest layers of the Sun’s corona and below, most plasmas in the heliosphere are basically collisionless. That is, the mean free path of charged particles is larger than most scales of interest. For example, in the undisturbed solar wind, the mean free path for ions is of the order of 1 AU [(see also Table 3.4)]. The lack of such collisions means that there exists no primary mechanism that forces the particles to assume thermalized Maxwellian distributions. In fact, observed distributions, often on top of thermal (colder) approximate ‘core’ Maxwellians, almost universally contain energetic tails, which usually can be described by power laws. In real-world plasmas, there is a multitude of processes responsible for generating such supra-thermal and high-energy tails; usually, so-called wave-particle interactions are involved.”

This chapter touches on various aspects of how energy can be converted from large-scale dynamics of magnetized plasma into an increased energy content in the thermal reservoir, the energetic-particle reservoir, or both, as well as on the transport and loss of such energy once in these reservoirs. This chapter covers topics as diverse as GCR transport inward through the heliosphere to SEP transport outward from the corona; all of these topics have to do with conversion or transport of energy. The chapter starts with motions of individual particles and their transport within magnetic environments, then moves to mechanisms by which their energies can change to become so-called ‘energetic particles’. A description of how energy from non-thermal particles is deposited into the thermal energy reservoir with particular focus on the solar corona is partitioned off into Ch. 9.

Flares, CMEs as well as magnetospheric (sub-)storms extract their energy from what has been somehow stored in the magnetic field. This extraction is typically enabled by the phenomenon of reconnection, and both the total flux involved and the rate at which reconnection proceeds help set the magnitude of energetic-particle events. The chapter touches on reconnection and shocks, which are essential ingredients in both heating and impulsive phenomena, but only introduces the basics of these complicated processes, which remain far from understood.

¹⁸ Anomalous cosmic rays have a complex history: originally neutral particles in the interstellar medium, ionized by charge-exchange or photo-ionization in the solar wind, advected to the boundary regions of the heliosphere there to be accelerated. See Fig. 8.5 for where they appear in the energy spectrum.

¹⁹ For an introduction to how energetic particles are detected and their properties determined, see Ch. II:3.

8.2 Single particle motion

“The motion of every individual charged particle in the heliosphere can be described by the Lorentz force equation, Eq. (2.21). [...]” “For the simplest case of no electric field and a constant magnetic field in the z direction, the solution to Eq. (2.21) is straightforward. It is given by [20]:”

$$v_x = +v \sin \alpha \cos(\omega_g t - \phi) ; v_y = -v \sin \alpha \sin(\omega_g t - \phi) ; v_z = +v \cos \alpha, \quad (8.1)$$

where $\omega_g = qB/(mc)$ is the cyclotron (gyro-)frequency, α is called the pitch angle (note that our definition is such that $\alpha = 0$ implies the particle is moving directly along the magnetic field), ϕ is the phase angle, and v is the magnitude of the particle velocity.”

“A very important aspect of the Lorentz equation when discussing particle acceleration is that the electric field may change the energy of the particle but the magnetic field does not. This relation is shown by taking the dot product of the Lorentz equation with \mathbf{v} giving:

$$\mathbf{F} \cdot \mathbf{v} = q(\mathbf{v} \cdot \mathbf{E}) + \mathbf{v} \cdot (\mathbf{v} \times \mathbf{B}), \quad \text{or} \quad \frac{dW}{dt} = q(\mathbf{v} \cdot \mathbf{E}), \quad (8.2)$$

where W is the kinetic energy.

[In realistic situations magnetic and electric fields rarely occur in separate and uniform configurations. Even in the simple case of a dipole potential field,] the motion separates into three oscillatory types occurring at increasingly slower timescales, [visualized together in Fig. 8.1(right)]. On the fastest timescale, a particle gyrates around the field line as described above.

The second oscillatory type motion in the dipole relates to the particle’s velocity parallel to the magnetic field. As the particle follows the field line towards the poles, it moves through a gradient because the magnetic dipole field increases [when the particle approaches the planetary or solar] surface. The effect of this gradient is to convert the parallel motion of the particle into perpendicular motion as shown schematically in Fig. 8.1(left). As the particle moves toward the pole, the gradient effectively creates a Lorentz force opposite to the parallel motion. Eventually, the parallel velocity will go to zero and then reverse direction [ultimately] causing the particle to bounce between the southern and northern poles. The point at which the parallel velocity goes to zero is called the mirror point and the oscillation between the two poles is referred to as the bounce motion.

[In the case of a planetary magnetosphere dominated by a dipole, the particle will circle the planet] in an oscillatory manner known as drift motion. The azimuthal drift is caused by the radial gradient of the dipole field. Intuitively, this drift can be attributed to the changing gyroradius in different magnetic field strengths. In the stronger magnetic field the gyroradius will decrease and in the weaker field the

²⁰ Note that the gyrating charged particle emits gyro-synchrotron radiation, thereby losing energy, so that this orbital motion approximated by Eq. (8.1) – and thus also in Eqs. (8.4) and (8.5) – is not sustained indefinitely.



Figure 8.1: (left) Schematic diagram showing the Lorentz force as a particle moves into the magnetic field gradient at Earth's poles. [Fig. II:11.2] (right) Schematic diagram of particle motion in a dipole magnetic field. [Fig. II:11.4]

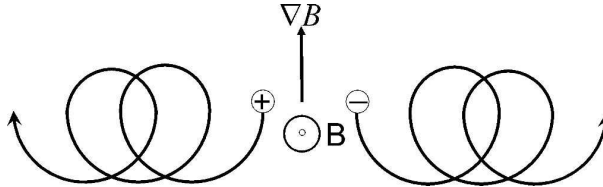


Figure 8.2: Schematic diagram for the gradient-B drift [(compare with a NASA/SVS animation at <https://svs.gsfc.nasa.gov/4263>)]. Fig. II:11.3]

gyroradius will increase creating the orbit shown in the schematic of Fig. 8.2. As protons and electrons gyrate in opposite directions, they also drift in opposite directions.”

More generally speaking, for particles moving through a magnetic field with a mixture of waves and turbulence, the latter two processes transition from drifts to scattering – to which we turn later in this chapter.

Guiding center motion

“Often, particle motion can be described by separating it into a drift velocity with gyromotion superimposed as in the examples provided here.

$\mathbf{E} \times \mathbf{B}$ drift: The $\mathbf{E} \times \mathbf{B}$ drift can be defined by including a uniform electric field in the Lorentz equation and separating the equation into components parallel and perpendicular to the magnetic field. [Let $\mathbf{B} = B\hat{\mathbf{z}}$.] In the parallel direction the Lorentz equation becomes

$$m\dot{v}_z = qE_z, \quad (8.3)$$

where E_z is the component of the electric field parallel to the magnetic field. This equation simply describes a particle accelerating along the magnetic field. In the perpendicular direction, assuming $\mathbf{E} = E_x\hat{\mathbf{x}} + E_z\hat{\mathbf{z}}$ [(so that $E_y = 0$)], the Lorentz equation becomes

$$\dot{v}_x = +\omega_g v_y + \frac{q}{m} E_x; \quad \dot{v}_y = -\omega_g v_x. \quad (8.4)$$

Taking the second derivative of the velocity gives

$$\ddot{v}_x = -\omega_g^2 v_x ; \ddot{v}_y = -\omega_g^2 (v_y + \frac{E_x}{B}). \quad (8.5)$$

These equations describe gyration superimposed on [a] drift in the $\mathbf{E} \times \mathbf{B}$ direction.

{@A100}

General force drift: [If for the electrical force $q\mathbf{E}$ we substituted another force \mathbf{F} (such as gravity)] into the $\mathbf{E} \times \mathbf{B}$ drift equation creates a general force equation, {A100}

$$\mathbf{v}_F = \frac{1}{\omega_g} \left(\frac{\mathbf{F}}{m} \times \frac{\mathbf{B}}{B} \right). \quad (8.6)$$

This equation can be used to define the drift velocity caused by any general force. Other types of drift include curvature drift caused by a centrifugal force related to the curvature of the dipole field lines, polarization drift that results from a slowly varying electric field, and a gravitational drift. [...]

Let us quantify the gradient and curvature drifts: [v_G and v_C] II:9.2.3 “For the special case in which $\nabla \times \mathbf{B} = 0$, these [are] given by:

$$\mathbf{v}_G = \frac{cW_\perp}{qB^3} \mathbf{B} \times \nabla |\mathbf{B}| \quad (8.7)$$

$$\mathbf{v}_C = \frac{2cW_\parallel}{qB^3} \mathbf{B} \times \nabla |\mathbf{B}| = \frac{2cW_\parallel}{qR_c^2 B^2} \mathbf{R}_c \times \mathbf{B} \quad (8.8)$$

where $W_\perp = (1/2)mv_\perp^2$ and $W_\parallel = (1/2)mv_\parallel^2$. Note that these expressions are for the case of non-relativistic particles. [The final expression in Eq. (8.8) is added to explicitly show the dependence on the curvature radius \mathbf{R}_c of the field; this latter expression holds also in a non-potential field.] {A101}

However, in most applications of interest $\nabla \times \mathbf{B} \neq 0$. A more general expression for the particle drift can be derived by expanding the magnetic field about the smallness parameter r_g/ℓ_t where r_g is the particle gyroradius and ℓ_t is the characteristic scale of the variation of the magnetic field. The resulting guiding center drift velocity, in the non-relativistic limit, is given by: {A102}

$$\mathbf{v}_{gc} = \left[v_\parallel + \frac{cW_\perp}{qB} \hat{\mathbf{e}}_B \cdot (\nabla \times \hat{\mathbf{e}}_B) \right] \hat{\mathbf{e}}_B + \frac{cW_\perp}{qB^2} \hat{\mathbf{e}}_B \times \nabla |\mathbf{B}| + \frac{2cW_\parallel}{qB} \hat{\mathbf{e}}_B \times (\hat{\mathbf{e}}_B \cdot \nabla) \hat{\mathbf{e}}_B \quad (8.9) \quad \{A102\}$$

where $\hat{\mathbf{e}}_B = \mathbf{B}/B$. ^[21] The gradient and curvature drifts are associated with the last two terms in this equation, which are in the direction normal to the magnetic field; however, it is important to note that there exists a component of the drift *along* the magnetic field in addition to these. {A103}

When Equation (8.9) is averaged over an isotropic distribution of particles, one obtains the drift velocity $\mathbf{v}_d = (cmv^2/q)\nabla \times (\mathbf{B}/B^2)$, which is commonly used in models of cosmic-ray transport.” {A103}

²¹ Note that Eq. (8.9) is a corrected version of Eq. (II:9.8).

The gradient-curvature drift in the terrestrial magnetosphere causes one of the primary mechanisms often discussed as an agent in space weather: the ring current. Seen from above the geographic north pole, positive particles drift clockwise and negative particles drift counter-clockwise. This differential motion leads to a westward ring current between about 2 and 9 Earth radii. This ring current is associated with a largely dipolar magnetic field with direction opposite to the Earth's field. The variability of this current is caused by the injection of particles into, and leakage from, the magnetosphere associated with solar-wind variability. The Dst (disturbance storm time) index [{A104}](#) used in space weather characterizations quantifies the strength of the ring current. The variation in the surface magnetic field at Earth owing to the ring current is of order 0.1 – 0.23 mG (see Table I:13.5). The phenomenon of a ring current is captured in an MHD description in principle, but because of the interest in how particles of different energies and anisotropic pitch-angle distributions behave, the inner-magnetospheric ring current is generally studied with a custom ring-current model that then is coupled to MHD magnetospheric and solar-wind models. [{A105}](#)

“The Lorentz equation and drift velocity derivations provide a feel for how single particles [behave ... but the analysis of] satellite measurements requires a more generalized view of particle motion because detectors do not measure the position and velocity of every particle in space to be propagated forward in time using the Lorentz equation. To this end, it is instructive to describe particle motion using aspects of the motion that are conserved when time variations of the magnetic field are slow. For charged particles in the magnetosphere, there are three such invariants associated with the gyro, bounce, and drift motion. Assuming that the invariants are conserved confines the particle location to within a shell [in a dipolar field such as that in the inner magnetosphere] about Earth.

First invariant: The first invariant is associated with the gyromotion of the particle about the field line and is given by:

$$\mu_m = \frac{p_{\perp}^2}{2mB}. \quad (8.10)$$

Here p_{\perp} is the relativistic momentum in the direction perpendicular to the magnetic field, m is the rest mass [...], and B is the field strength.

Second invariant: The second invariant corresponds to the bouncemotion of a particle along a field line and is given by:

$$J = \oint p_{\parallel} ds, \quad (8.11)$$

where p_{\parallel} is the particle momentum parallel to the magnetic field and ds is the distance a particle travels along the field line. It is convenient to rewrite the second invariant in terms of only the magnetic field geometry by the following manipulation. If no parallel forces act on a particle then momentum is conserved along a bounce path and $J = 2pI$

where p is momentum and

$$I = \int_{s_m}^{s'_m} \left(1 - \frac{B(s)}{B_m}\right)^{1/2} ds. \quad (8.12)$$

Here s_m is the distance of the particle mirror point, $B(s)$ is the field strength at point s , and B_m is the mirror point magnetic field strength. If the first invariant is conserved then K , as defined below, is also conserved.

$$K = \frac{J}{2\sqrt{2m\mu_m}} = I\sqrt{B_m} = \int_{s_m}^{s'_m} (B_m - B(s))^{1/2} ds \quad (8.13)$$

[...]

Third invariant: The third and final invariant corresponds to the drift motion of a particle [and is given by:

$$\Phi = \oint A_\Phi dl = \int \mathbf{B} dS. \quad (8.14)$$

In this equation A_Φ is the magnetic vector potential, dl is the curve along which lies the guiding center drift shell of the electron, \mathbf{B} is the magnetic field and dS is area.] Therefore, conservation of this invariant requires that an electron gyration always encloses the same amount of magnetic flux as it drifts [...]. In a dipole field this is equivalent to saying that the electron remains at fixed radial distance. The Roederer L parameter, commonly written as L^* , is another useful form of the third invariant [often used for the terrestrial magnetosphere]:

$$L^* = \frac{2\pi\mu_p}{\Phi R_E}, \quad (8.15)$$

where μ_p is the magnetic moment of the Earth's dipole field. The L^* parameter is the radial distance to the equatorial location where an electron would be found if all external magnetic fields were slowly turned off leaving only the internal dipole field."

8.3 Phase space density and Liouville's theorem

"Two more concepts are needed to finally interpret particle measurements from satellites: phase space density and Liouville's Theorem." "The number of particles per phase-space volume is known as the phase-space distribution function, f , which is a function of the 6-dimensions of phase space and time ($\mathbf{p}, \mathbf{r}, t$), where \mathbf{p} is the particle momentum vector ($\mathbf{p} = m\mathbf{v}$). The number density of particles at a given location at a given time, $n(\mathbf{r}, t)$ is related to the phase space distribution function by:

$$n(\mathbf{r}, t) = \int f(\mathbf{p}, \mathbf{r}, t) d^3\mathbf{p}, \quad (8.16)$$

where $d^3\mathbf{p}$ is the volume element of phase space. For example, for a Cartesian geometry $d^3\mathbf{p} = dp_x dp_y dp_z$ and for a spherical geometry it is $d^3\mathbf{p} = d\phi \sin \alpha d\alpha p^2 dp$ [...]. (α is the pitch angle).

The differential intensity [...] is related to the phase-space distribution function by

$$J = p^2 f. \quad (8.17)$$

Sometimes this is written as dJ/dE . This has units of particles per area, per time, per energy, per solid angle. If one integrates J over energy and solid angle (*i.e.*, a spacecraft detector with a given acceptance cone that sums over all energy channels), the result is the *flux density* of particles, or the number of particles crossing per area per time.”

“Our interest in working with phase space density is that it can be used to understand how collections of particles move rather than individual particles. More specifically, Liouville’s Theorem states that as the system evolves or moves along a trajectory in phase space the density must remain constant. The proof of this theorem is illustrated intuitively by considering a volume of phase space. As the particles in the volume are subjected to forces their position and momentum will change but the trajectories of particles in phase space can never cross. Trajectories crossing would imply the physical impossibility that two particles with the same position and momentum subjected to the same forces go in different directions. Thus, the particles act as an incompressible fluid [in phase space]. As they move, the volume can change shape but the density remains the same.

At first glance, Liouville’s Theorem seems to be an esoteric statement but in fact its application is quite powerful. The particle flux (number of particles per $\text{cm}^2 \text{sr keV}$) measured by a particle detector on a satellite, $J(E, \alpha, \varphi, \mathbf{x})$ where E is the energy, α is the pitch angle, φ is the gyro-phase, and \mathbf{x} is the position, can be directly related to the phase space density through the relation $J(E, \alpha, \varphi, \mathbf{x}) = f(\mathbf{x}, \mathbf{p})/p^2$. Liouville’s theorem states that the phase space density does not change as the particles move along a trajectory. We also know that if time variations of the magnetic field are slow, a particle’s trajectory must move along a contour of constant adiabatic invariants. Putting these two concepts together means that $f(\mu_m, J, L^*, \varphi_1, \varphi_2, \varphi_3)$ wherever it is measured must remain constant. (Here $\varphi_{1,2,3}$ are phase angles associated with each invariant. For simplicity, it is generally assumed that the phase space density does not vary with the phase angles.) Any change of phase space density implies that one of the invariants is broken. In fact, acceleration mechanisms always violate an invariant. Thus, an increase in phase space density expressed as a function of the adiabatic invariants is a sign that acceleration has occurred. Flux measurements, in contrast, can change simply because the magnetic field topology has changed making these data very difficult to interpret.”

8.4 The collisionless Boltzmann equation

Let us start with a general view of what we can do with the phase space density, looking specifically at what it takes to change it (or at what it takes to maintain it so that the adiabatic invariants can be applied to particle trajectories). You can review this section quickly on first pass, then revisit this when you reach the end of Sect. 8.5.2.

Throughout the heliosphere, we can generally ignore collisions between charged particles, particularly for the particles residing in supra-thermal tails of velocity distributions. Consequently, the distribution function for heliospheric charged particles generally satisfies the collisionless Boltzmann equation, which is a continuity equation in the 6D space of momentum and location coordinates $\mathbf{w} = [\mathbf{r}, \mathbf{p}]$ and time: $\partial f / \partial t + \nabla \cdot (f \dot{\mathbf{w}}) = 0$ (a 6D mathematical equivalent of Eq. 3.4, absent sources and sinks), or in another formulation ([using the index notation so that, for example, the vector for space coordinates is written $x_i = \mathbf{x} = x_x \hat{x} + x_y \hat{y} + x_z \hat{z}$, as for] momentum p_i (or velocity v_i); with acceleration a_i , and with implied summation over repeated indices):

$$\frac{\partial f}{\partial t} = -\frac{p_i}{m} \frac{\partial f}{\partial x_i} - F_i \frac{\partial f}{\partial p_i} + S - L, \quad (8.18)$$

where the components of the force F_i are given by

$$F_i \equiv ma_i = q \left(E_i + \frac{1}{mc} \epsilon_{ijk} p_j B_k \right) + \mathcal{S}_i. \quad (8.19)$$

Here, \mathcal{S}_i is a placeholder for any other force or sum of forces that may apply, including gravity; even radiative energy losses or gains could be incorporated (although we ignore these here). Sources S and losses L could represent couplings to other reservoirs, such as neutral atoms or dust, which could happen through charge exchange or photoionization. We ignore these terms further in this chapter.

Note that low-order velocity moments of the Boltzmann equation for combinations of interacting particle populations yield the equations of fluid dynamics. Take, for example, the case of a fully ionized hydrogen plasma with phase-space densities f_e and f_i for electrons and ions. The suitable combinations of the Boltzmann equations Eq. (8.18) for these phase space densities after multiplication by mv^α and integration over velocity space for $\alpha = 0, 1, 2$ yield, respectively, the continuity equation Eq. (3.4), the momentum equation Eq. (3.5), and the energy equation Eq. (3.6). A complete set of fluid dynamics equations would continue with ever higher moments until the entire phase space density has been described, but that is not practical. Instead, the series is commonly truncated by some approximation, known as 'closure'; see also Table 3.2.

A persistent electric field (such as in reconnection processes, see Sect. 6.4), for example, can change a particle's energy when that is accelerated along the field. Forces that can change the energy of particle populations need to be retained explicitly in whatever we do with Boltzmann's equation. Fluctuations in the magnetic fields in space and time (such as in Alfvén waves), in contrast, do not change a particle's energy (more on that in Sect. 8.5): they do scatter a particle in pitch angle. Repeated scattering in a perturbation field that is symmetric in the probability of scattering a particle in either direction can be described as diffusion. With that realization, Eq. (8.18) can be reformulated in a quasi-linear approximation by separating large-scale trends from small-scale fluctuations, denoting the large-scale average flow \mathbf{u} , and capturing the net effects of the small scale fluctuations in diffusion terms {A106} :

$$\frac{\textcircled{a}}{\partial t} = \frac{\partial}{\partial x_i} \left[\textcircled{b} \frac{\partial f}{\partial x_j} - \textcircled{c} f \right] + \frac{\partial}{\partial p_i} \left[\textcircled{d} \frac{\partial f}{\partial p_j} - \textcircled{e} f \right] + [\textcircled{f} - \text{L}], \quad (8.20)$$

$$\text{with } F_i = -\frac{1}{3} p_i \frac{\partial u_j}{\partial x_j} + \dots \quad (8.21)$$

Here, u is the mean velocity of the scatterers, which equals the flow speed of the bulk thermal plasma provided that comparable power resides in waves traveling in opposite directions. The explicitly listed term in F_i above represents the adiabatic momentum change.

The expressions \textcircled{b} & \textcircled{c} and \textcircled{d} & \textcircled{e} in Eq. (8.20) reflect fluxes in physical space and in momentum space, respectively. Terms \textcircled{b} and \textcircled{d} reflect diffusive processes; in geometric space with diffusion parameter κ_{ij} (with diagonal elements describing diffusion parallel and perpendicular to the magnetic field, and off-diagonal elements quantifying particle drifts) and in momentum or velocity space with diffusion parameter D_{ij} (which includes, among other things, pitch-angle scattering that does not affect the particles' energy); whereas we can more readily appreciate the symmetry between these two spaces, the physics of the scattering processes now lies hidden in the two diffusion tensors (see, for example, Sect. 8.5). Terms \textcircled{c} and \textcircled{e} reflect advection, in geometric space in \textcircled{c} and in momentum space (by the forces acting on the medium) in \textcircled{e} (but note the mixed partial derivatives in \textcircled{e} which means different groupings are possible).

Eq. (8.20) informs us on how particles move in the coupled 6-dimensional realm of geometric space and velocity space. When we talk about the transport of either solar energetic particles or galactic cosmic ray particles through the heliosphere, we look primarily at transport in geometric space which involves terms \textcircled{b} and \textcircled{c} : transport is affected by scattering and advection (in addition to, *e.g.*, geometric expansion in a spherical geometry, which involves term \textcircled{e}).

When we look into acceleration (and thus also heating) mechanisms, such as for shocks in Sect. 8.6, we need to figure out how particles move about in momentum space, *i.e.*, using expressions \textcircled{d} & \textcircled{e} , while crossing the shock in geometric space with expressions \textcircled{b} & \textcircled{c} . It often helps to focus on parts of the overall function f . For example, for the bulk of the plasma well within the thermal range of Maxwellian distributions, with relatively short mean-free paths compared to system scales and with frequent interactions with the collective, we have the MHD description (Ch. 3) and, for shocks, the Rankine-Hugoniot jump conditions (Sect. 5.3). In contrast, for a 'contaminant' population of solar energetic particles and galactic cosmic rays moving through, but to first order not interacting with, the background plasma flow of the solar wind, but being scattered by perturbations in its magnetic field, Eq. (8.20) provides a powerful tool, as we shall see next. Other descriptions below focus on narrow parts of the overall phase-space distribution, such as the supra-thermal particles that interact at shallow angles with a shock and scatter in the collective of particles around it, and for a sub-population of quite energetic particles with long mean-free paths that bounce

back and forth across a shock in a ping-pong fashion as they are scattered by waves. With this perspective, let us look at how this all describes the propagation of energetic particles through the heliosphere and the creation of energetic particles at shocks.

8.5 Particle scattering and transport

“To this point we have considered only smoothly varying electric and magnetic fields as compared to the radius of gyration of the particles, $r_g = v/\omega_g$. For such cases, the particle speed and pitch angle change very slowly compared to the cyclotron period. However, when the typical scale of the variation in the fields, L_t , is of the order of r_g , the speed, phase, and pitch angle can undergo more rapid changes. This leads to a form of scattering that is loosely analogous to classical scattering, although it differs in important ways. For instance, the particles do not collide off of one another, as in the lower portions of Earth’s atmosphere, nor do they collide off of large targets, like photons moving through a dense gas, but rather, they scatter off of irregularities in the magnetic field. Formally one can solve the equations of motion under the approximation that the amplitude of the magnetic fluctuations are small and show that there exists a resonance condition, $v_{\parallel} \sim L_t \omega_g$, for which the equations become undetermined. At such instances, the particle is said to ‘scatter’ and it reverses its pitch angle and its phase angle becomes randomized. [...]”

Because particle scattering is a stochastic process, it is most useful to perform a statistical analysis on a large number, or *ensemble*, of charged particles. The relationship between the average particle motion and the magnetic field can be determined from the quasi-linear theory. It is found that the dynamical behavior of the distribution function obeys the standard diffusion equation in classical statistical physics. [...]”

“It is important to keep in mind that this equation is strictly valid only for time scales that are long compared to the time in between scatterings (the scattering time) and spatial scales that are large to the distance traveled between scatterings (the mean-free path).” Because “the magnetic field in space exists in a highly electrically conductive plasma, the field moves with the flow of the plasma (it is said to be ‘frozen in’. In the limit of ideal magnetohydrodynamics (MHD), which is the limit we are concerned with for energetic-particle transport, there is no electric field in the frame moving with the plasma. Thus, as a charged particle scatters off of a magnetic irregularity, its energy in the frame of reference moving with the plasma remains unchanged. [Strictly speaking, this assumes that the magnetic field is stationary in this frame of reference which is factually incorrect because of the presence of waves with a variety of phase and group velocities, but a good approximation in the case of the transport of energetic particles that move much faster than the waves (*i.e.*, $v \gg v_A$, where v_A is the Alfvén speed).] From the perspective of such fast particles, the magnetic fluctuations, which provide the scattering centers, move with the bulk plasma. [...] In an inertial frame relative to which the plasma moves with a velocity u , the evolution of f satisfies the advection-diffusion] equation, which in one spatial dimension is given by”

$$\frac{\partial f}{\partial t} = \frac{\partial}{\partial x} \left(\kappa \frac{\partial f}{\partial x} \right) - u \frac{\partial f}{\partial x}, \quad (8.22)$$

“where κ is the diffusion coefficient. For the case of charged particles moving in an irregular magnetic field, κ is related to the statistical properties of the magnetic field, in particular, its power spectrum.” Here, we interpret f as integrated over all velocity space, so looking only at total numbers as a function of space. Thus, Eq. (8.22) is the 1D version of Eq. (8.20) for a case with constant u , in which the velocity integral for expression (d) disappears because scattering under these conditions does not change the overall energy of the population and (e) because there are no other forces assumed to act on the plasma.

“We note that for Eq. [8.22] we have assumed that the distribution function varies only in one spatial direction. This should not be confused with [...] the restriction on particle motion arising from fields that vary with only one spatial coordinate. By using Eq. (8.22), we have already assumed that the process is diffusive. If, for example, x is taken to be the direction normal to a mean magnetic field, then the use of this equation implies that the field must be fully three dimensional for cross-field diffusion to take place. The key is that the field is fully three dimensional but it is also statistically homogeneous in space.” “In two dimensions, there are two diffusion coefficients, one for each direction (plus cross terms which we can ignore for now). Consider the motion of particles in a turbulent magnetic field [22] whose average points along the z direction. Then, for example, in the x - z plane, the diffusion equation (neglecting the advection term discussed above and cross terms) is given by:

$$\frac{\partial f}{\partial t} = \frac{\partial}{\partial x} \left(\kappa_{\perp} \frac{\partial f}{\partial x} \right) + \frac{\partial}{\partial z} \left(\kappa_{\parallel} \frac{\partial f}{\partial z} \right), \quad (8.23)$$

where κ_{\perp} and κ_{\parallel} are the diffusion coefficients across the magnetic field and along it, respectively.

Because the time τ_s it takes for a charged particle in the heliosphere [or magnetosphere] to scatter is generally much longer than the time it takes to gyrate about a magnetic field (*i.e.*, $\omega_g \tau_s \gg 1$), particles tend to move much more closely along the magnetic field than across it. As such, κ_{\perp} is usually assumed to be much smaller than κ_{\parallel} . For this reason, many analyses simply neglect perpendicular transport. However, it is important to note that in many astrophysical plasmas of interest, perpendicular transport is the most important [...]

The motion of a particle across a magnetic field occurs in two ways: (1) the actual transfer of particles from one magnetic field line to the next resulting from scattering, or across the field arising from drifts, and (2) the motion of particles along magnetic lines of force that themselves meander in space in the direction(s) normal to the mean magnetic field. [...]

“In addition to scattering and advection with the flow, the particle speed itself can change. Principally, this can happen in two ways: (1) by scattering within a spatially varying flow [(*i.e.*, by term (c) of Eq. (8.20)], or (2) by diffusing in energy space because of collisions with randomly moving scattering centers. The latter of these

²² This volume does not go into the generation and properties of turbulence; for an introduction within the context of heliophysics, see I:7.

two [(related to D_{ij} in term (d) of Eq. 8.20, and related to dispersion in scatterer speeds)] is called second-order Fermi acceleration, or stochastic acceleration. This is an interesting topic, but is not considered in our discussion here. We examine further the first case.

Consider a particle moving in a given direction in an inertial frame which then scatters. Energy is conserved in the local plasma frame, but in the inertial frame the particle either gains or loses energy depending on whether it is moving initially against or with the flow \mathbf{u} . Suppose that at one scattering, it initially moves against the flow, and gains energy in the inertial frame (this is a head-on collision). When it next scatters, it will be moving initially with the flow and will lose energy. If the flow is everywhere uniform, then the particle loses the energy it gained in the previous scattering and there is no net energy gain. But, if the second scatter occurs at a different flow speed, there is a net change in the particle's energy. The term that accounts for this behavior is given by

$$\frac{p}{3} \nabla \cdot \mathbf{u} \frac{\partial f}{\partial p} \quad (8.24)$$

[(as in term (e) in Eq. 8.20 and the expression for F following it)]. Particles gain energy if this term is negative and lose energy if it is positive.

A particularly good example of this is particle acceleration at a shock. Consider the energy of a particle in a frame of reference moving with the shock. As a particle scatters in the flow behind the shock, it loses energy because the particle was initially moving with the flow. The particle then returns upstream where it scatters off of the incoming upstream flow leading to a gain in energy. The energy lost by the downstream scattering event is smaller than the energy gained by the upstream scattering event because the upstream flow speed is larger than that downstream. Thus, there is a net energy gain, which leads to an acceleration of particles [(more on that in Sect. 8.6)]. Note that at a shock, the flow goes from large to small (in the shock frame) so that the divergence is negative and Eq. (8.24) is negative, giving rise to acceleration.

It is also noteworthy that the energy change term is positive for the case of a constant radial solar wind speed. So, all charged particles *lose energy* in the adiabatically expanding solar wind!"

"The resulting superposition of the terms that we have discussed above, lead to the cosmic-ray transport equation. It is given by

$$\frac{\partial f}{\partial t} = \frac{\partial}{\partial x_i} \left[\kappa_{ij} \frac{\partial f}{\partial x_j} \right] - u_i \frac{\partial f}{\partial x_i} + \frac{p}{3} \frac{\partial u_i}{\partial x_i} \left[\frac{\partial f}{\partial p} \right] + S - L \quad (8.25)$$

[(which is very nearly the diffusion version of the collisionless Boltzmann equation of Eq. 8.20, but with $D_{ij} = 0$).] Note that we have written the diffusion coefficient κ_{ij} in its full tensor form [...]

The cosmic-ray equation is remarkably general. It has been used widely in most discussions of cosmic-ray transport and acceleration over more than three decades. It is a good approximation provided there is sufficient scattering to keep the pitch-angle

distribution nearly isotropic ^[23], and if the particles move substantially faster than the speed of both the background fluid and the characteristic speed of the MHD waves contained in the plasma.”

“All of the quantities in the transport equation, except for the diffusion tensor, are directly observed by spacecraft or can be accurately determined by using the hydromagnetic approximation. Consequently, determining transport coefficients poses a fundamental challenge in the modeling of cosmic rays.

In general, the diffusion tensor κ_{ij} is related to the magnetic field vector B_i , the diffusion coefficients parallel and perpendicular to the mean field, κ_{\perp} and κ_{\parallel} , and the antisymmetric diffusion coefficient, κ_A , as

$$\kappa_{ij} = \kappa_{\perp} \delta_{ij} - \frac{(\kappa_{\perp} - \kappa_{\parallel}) B_i B_j}{B^2} + \epsilon_{ijk} \kappa_A \frac{B_k}{B}, \quad (8.26)$$

where δ_{ij} is the Kronecker delta function ($\delta_{ij} = 1$ if $i = j$ and $\delta_{ij} = 0$ if $i \neq j$), and ϵ_{ijk} is the Levi-Civita symbol: $\epsilon_{ijk} = 1$, or -1 if (i, j, k) is an even or odd permutation of $(1, 2, 3)$, respectively, and $\epsilon_{ijk} = 0$ if any index is repeated. We have also introduced the antisymmetric diffusion coefficient κ_A . Note that the symmetric terms reflect the diffusion due to small-scale turbulent fluctuations; in contrast, the antisymmetric term contains the particle drifts caused by the spatial variations of the large-scale magnetic field.”

8.5.1 Solar energetic particles

“A particularly simple, yet illustrative example of the use of the cosmic-ray transport equation is the evolution of impulsively released particles from a point source. This is presumably a reasonable representation of the physics of solar-energetic particle transport after their release onto open magnetic field lines following their rapid acceleration in the vicinity of a solar flare. Of course, we must recognize that the earliest arriving particles suffer very little pitch-angle scattering, and therefore, the transport equation is not useful for describing these particles, but is adequate to describe the long-time behavior.

A proper treatment of the impulsive SEP problem should necessarily include, as a minimum, the effects of diffusion, advection with the solar wind, and adiabatic cooling. Spherical coordinates with the origin at the Sun would be a good choice. The resulting equation, even when simplified by making various assumptions about the choice of parameters can be impossible to solve analytically. For our purposes here, which is simply for illustration and by no means is meant to be directly comparable to SEP observations, it suffices to consider a Cartesian geometry, a constant diffusion coefficient, and to neglect both advection with the flow and energy change. The result is simply [Eq. (8.22) with $v = 0$], which is the 1D diffusion equation. The solution for an impulsive injection of particles at $x = 0$ at time, $t = 0$ is given by

$$f(x, t) = \frac{N_0}{\sqrt{4\pi\kappa t}} \exp\left(-\frac{x^2}{4\kappa t}\right), \quad (8.27)$$

²³ This should not to be confused with anisotropic diffusion resulting when $\kappa_{\perp} \neq \kappa_{\parallel}$.

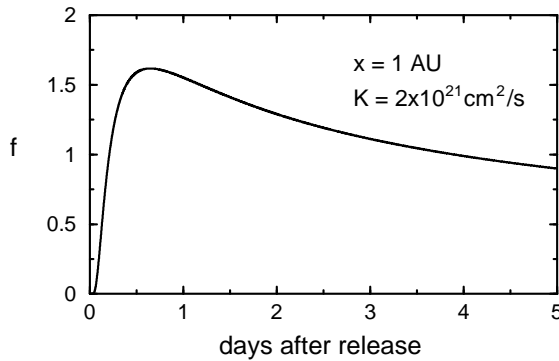


Figure 8.3: Solution to the one-dimensional diffusion equation for a point-source release at a position 1 AU away from an observer: $f(1, t)$ from Eq. (8.27). [Fig. II:9.10]

where N_0 is the number of particles released.

Figure 8.3 shows a plot of the distribution of particles, given by Eq. (8.27), at the location $x = 1$ AU, as a function of time (in days). The diffusion coefficient was taken to be $\kappa = 2 \times 10^{21} \text{ cm}^2/\text{s}$, and $N_0 = 10^{14}$. If, for example, these are 10-MeV protons, then the corresponding mean-free path would be about 0.1 AU. This profile has similarities to those seen at 1 AU following a flare or CME on the Sun [...]. An example of an impulsive-like solar-energetic particle event observed at 1 AU by the ACE spacecraft (ULEIS instrument) is shown in Fig. 8.4. Each dot represents a detection by the instrument of an individual particle. Plotted is the particle kinetic energy versus time. The earliest arriving particles are the ones with the highest energy since they move with the highest speed. The slower ones arrive later. This velocity dispersion leads to the characteristic profile shown in the figure.

It is clear from Fig. 8.4 that particles released at the Sun and observed near Earth undergo pitch-angle scattering in the inner heliosphere, because at any given time there is a range of particle energies detected. That is, high energy particles can arrive later because they have scattered in the medium between the source and the observer. Thus, the 'thickness' of the comma-shaped particle event seen in the middle of this figure is related to the scattering frequency of the particles. {A107} Aside from this, however, there are many features in this event that are difficult to explain with a diffusive-advection-energy change approach [...]

It is noteworthy to point out another feature of the event shown in Fig. 8.4. There are intermittent dropouts in intensity during each of the two distinct events shown. These dropouts have been interpreted as resulting from the passage of alternatively filled and empty 'tubes' of particle flux by the spacecraft. The connection to the source, *i.e.*, the flare site, determines which field lines are populated with particles and which are not. [... The dropouts suggest some braiding in the heliospheric magnetic field such that adjacent field lines can connect to different source regions on the Sun; see Fig. III:9.12.]

These observations indicate that solar-energetic particles associated with impulsive

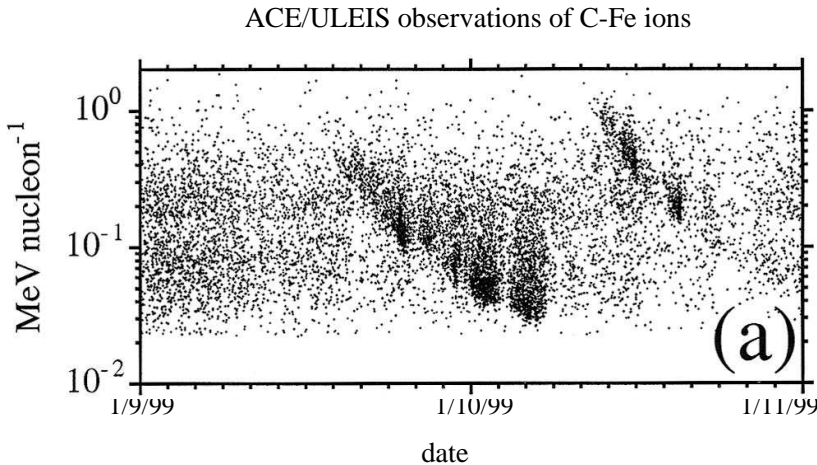


Figure 8.4: A solar energetic particle (SEP) event, associated with an impulsive solar flare, seen by ACE/ULEIS. Each dot represents the detection of a particle by the detector. Two distinct events are shown. [Fig. II:9.11; source: Mazur *et al.* (2000).]

solar flares undergo little cross-field transport, otherwise, these intermittent dropouts would not exist. This, of course, leads to the interesting puzzle of why galactic cosmic rays, or other types of energetic particles, do not exhibit such behavior. The answer is simply that the energetic particles in impulsive SEP events were relatively recently injected into the system and therefore have not had time to scatter sufficiently to become more spatially uniform. GCRs, however, have spent much more time in the Solar System (see Section 8.5.2). Thus, impulsive SEP events reveal the early time behavior of a collection of energetic charged particles moving in the heliospheric magnetic field.”

8.5.2 Galactic cosmic rays

“GCRs are cosmic rays that pervade interstellar space and enter the heliosphere from the outside. The vast majority of them are swept out of the heliosphere before ever reaching Earth’s orbit. [...] For] the purpose of a simple illustration of modulation, consider the steady-state Parker transport equation in one-dimensional spherical coordinates given by

$$\frac{\partial f}{\partial t} = \frac{1}{r^2} \frac{\partial}{\partial r} \left(r^2 \kappa \frac{\partial f}{\partial r} \right) - v \frac{\partial f}{\partial r} + \frac{2vp}{3r} \frac{\partial f}{\partial p} = 0, \quad (8.28)$$

[Note that this derives from Eq. (8.20) with \textcircled{a} set to zero and for $D_{ij} = 0$ and uses that in spherical symmetry with an assumed constant solar wind speed u (and neglecting gravity) one has $\partial v / \partial x_i = 2v/r$] (this simple illustration neglects the effect of the heliosheath and termination shock). Here we have taken the diffusion tensor to be symmetric and $\kappa_{rr} = \kappa$.

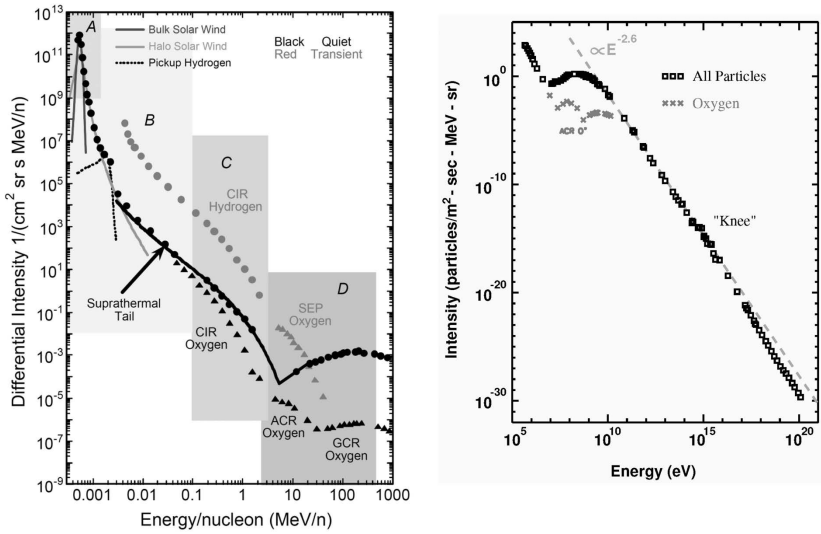


Figure 8.5: Energy spectra of energetic particles in the heliosphere (left) and for cosmic rays (right). The curves illustrate the energy spectra during quiet time and disturbed solar wind conditions. The dots and triangles represent the supra-thermal part of the spectrum and the particles accelerated at corotating interaction regions (CIRs), galactic cosmic rays (GCRs), and the anomalous cosmic rays (ACRs) together with Solar Energetic Particles (SEPs). The right figure shows the high-energy part of the galactic cosmic ray energy spectrum to TeV energies. Note the characteristic peak at about 10 MeV and the $E^{-2.6}$ power-law dependence for energies above the peak. [Fig. IV:12.2]

It is convenient to rewrite Eq. (8.28) in the following form:

$$\frac{1}{r^2} \frac{\partial}{\partial r} r^2 \left(\kappa \frac{\partial f}{\partial r} - v f \right) + \frac{2v}{3rp^2} \frac{\partial}{\partial p} (p^3 f) = 0. \quad (8.29)$$

Generally this equation is not easy to solve, but if we assume that the last term on the left (describing the energy change of diffusing particles) is negligible, the resulting equation is readily solved to yield

$$f(r, p) = f(R, p) \exp \left(- \int_r^R \frac{v}{\kappa(r', p)} dr' \right). \quad (8.30)$$

Equation (8.30) gives an exponential decay of particles from the source ($r = R$) inward, into the the Solar System (where $r < R$). Moreover, it is reasonable to expect the diffusion coefficient to increase with momentum p so that higher-energy particles have a larger diffusion coefficient than lower-energy particles. Thus, higher-energy particles have a longer exponential-decay length, or diffusive skin depth, than do lower energy ones. Thus, they more easily reach the inner heliosphere than lower-energy cosmic rays. This leads to a turnover in the spectrum that is due to modulation. This is in qualitative agreement with the observed cosmic-ray spectrum at Earth as shown in Fig. 8.5.”

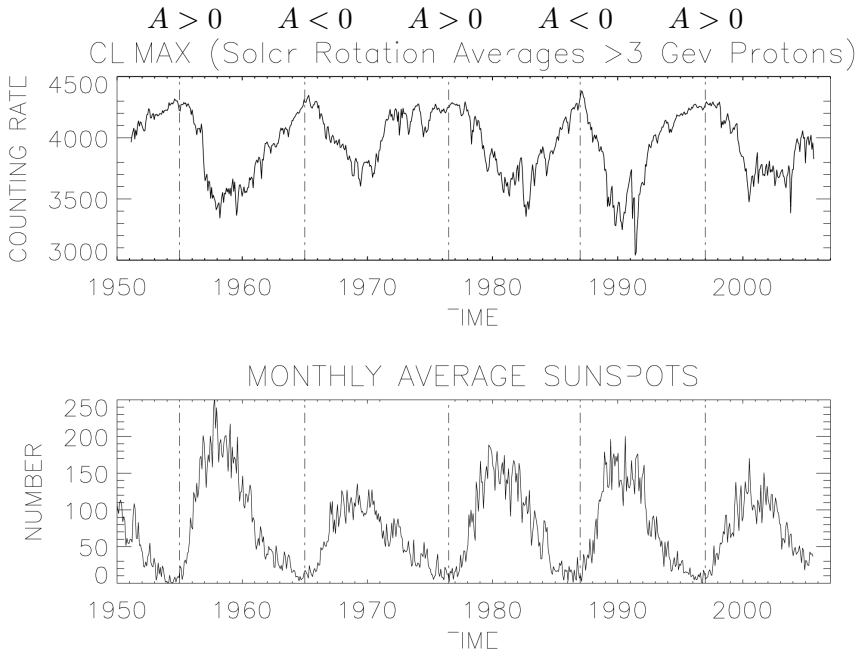


Figure 8.6: [top] Climax neutron monitor daily count rate of neutrons produced by the interaction of a primary cosmic ray with Earth’s atmosphere, which quantifies the modulation of galactic cosmic rays [near Earth orbit] during five sunspot cycles (shown in the bottom panel). Note the alternation in the cosmic-ray maxima between sharply peaked and more-rounded shapes. [The meaning of A is defined in Fig. 8.7. Fig. III:9.4]

The GCR intensity at a given orbital distance from the Sun is not a constant but varies with the solar cycle. “Shown in Fig. 8.6 is the daily count of neutrons produced by the impact of cosmic rays on the upper atmosphere, from ground-based neutron monitors. This is an indirect measure of the cosmic-ray flux in near-Earth orbit. The time-intensity profile shows a clear 11-year cycle that is coincident with the sunspot-number cycle. During periods of high solar activity, sunspot maximum, the cosmic-ray flux is low, and during periods of low solar activity, or solar minimum, the cosmic-ray flux is high. In addition to this, there is also 22-year cycle present (the alternating ‘leveled’ vs. ‘rounded’ cosmic-ray flux), which, as we discuss below, is related to the drift motions of cosmic rays.

The increased modulation during periods of solar maximum is related to a combination of effects related to the shedding of magnetic flux by the Sun at solar maximum. On the one hand, increased solar activity leads to more magnetic turbulence which decreases the diffusion coefficient in the outer heliosphere leading to more modulation. On the other hand, and in addition to this, the merging of more numerous transient shocks and coronal mass ejections in the distant heliosphere creates magnetic barriers (so-called global merged interaction regions, or GMIRs) which also reduce the transport of cosmic rays into the inner heliosphere. There is a lower level of magnetic turbulence and fewer magnetic barriers for cosmic rays to propagate through during solar minimum.

This is a qualitative explanation for the 11-year cosmic-ray cycle and its relation to the sunspot cycle.

The 22-year cosmic-ray cycle seen in Fig. 8.6 is related to the 22-year solar magnetic polarity cycle [because the] polarity of the Sun's magnetic field is important for the cosmic-ray drift that arises from the antisymmetric part of the diffusion tensor in Parker's transport equation. [...]

Including the drifts of cosmic rays has led to the widely accepted paradigm for cosmic ray transport shown in Fig. 8.7. Drift motions for protons during two different solar polarity cycles are shown. [...] During the period in which the solar magnetic field spirals outward in the north and inward in the south ($A > 0$) the GCR protons drift into the heliosphere from the polar regions of the heliosphere and outward along the heliospheric current sheet (which separates the two hemispheres and where the field reverses direction, hence the term 'current sheet'). During the opposite polarity, in which the solar field is inward in the north and outward in the south ($A < 0$), galactic cosmic-ray protons drift into the heliosphere along the current sheet. Note that in addition to the drift along the current sheet, there is also a gradient-B drift along the termination shock resulting from the jump in the magnetic field strength across the shock.

The explanation for the alternating leveled and rounded cosmic ray intensity involves both the drift motions of the cosmic rays shown in Fig. 8.7, and the 'waviness' of the heliospheric current sheet due to the offset of the solar magnetic axis and its rotation axis. When the 'tilt' is large, the current sheet is very warped, whereas, when it is small, the current sheet is much flatter (imagine the current sheet [forming above the rotating Sun with a tilted axial dipole, as in Fig. 5.7]). The current sheet is generally known to be relatively flat during the center of the solar cycle minimum. So, during the cycle in which the cosmic rays come into the heliosphere along the current sheet [when $A < 0$, so opposite to the depiction in Fig. 8.7], only when it is very flat will the full cosmic-ray flux be reached at Earth's orbit. Thus, during this phase, the cosmic-ray intensity will exhibit a rounded or 'peaked' time-intensity profile. When the cosmic rays come in along the poles of the heliosphere, the full intensity is reached much sooner and remains at a high level throughout solar minimum, and hence, during this phase, the time-intensity profile is more level, or flat."

8.6 Particle acceleration in shocks

Shocks provide an effective means to increase the kinetic energy of individual particles. For an ensemble of particles, this may shift their Maxwellian velocity distribution to a higher temperature, may distort that Maxwellian outside its core range, or lead to pronounced high-energy tails. Some form of shock heating and shock acceleration may play a role in processes as diverse as coronal heating (see Ch. 9) and the formation of solar energetic particles. "Some of the processes that heat particles at thermal energies will also elevate the energy at the upper part of the range. However, such enhancements are often only by a more or less constant, relatively minor factor. An example of this is the adiabatic heating of ions due to the magnetic field compression

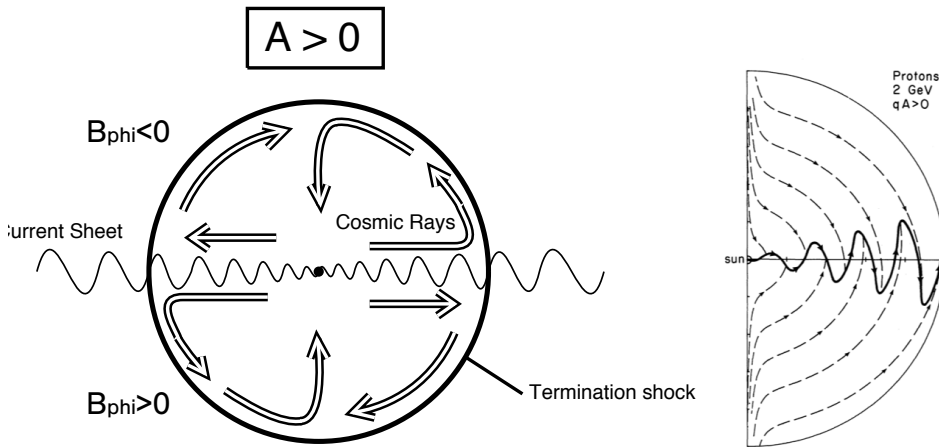


Figure 8.7: [(left) Simplified side view of the heliosphere, with the current sheet depicted by wavy lines, to illustrate the drift] motion of cosmic rays in the heliosphere for [one solar magnetic polarity. The two polarities of the heliospheric] field are separated by the heliospheric current sheet. The value of $A > 0$ is for the period during which the solar magnetic field is outward in the north and inward in the south. During the next sunspot cycle, $A < 0$, the heliospheric field polarities are reversed, along with the direction of cosmic-ray advection.] The termination of the solar wind is also shown. [This is a cropped version of Fig. II:9.14.] [(right)] Cosmic-ray drift motions in a Parker spiral magnetic field with a current sheet. The arrows shown correspond to the time when the northern-hemisphere heliospheric magnetic field is outward from the Sun ($[A > 0$, as in] 1975, 1996) for positively charged particles. The arrows [in both panels] reverse for the alternate sign of the magnetic field ($[A < 0$, as in] 1986, 2007) and for the opposite sign of the particle’s electric charge. [Fig. III:9.8; source right panel: (Jokipii and Thomas, 1981).]

at the relatively narrow oblique or nearly-perpendicular shocks associated with the compression of the plasma” (for a quantitative example for low- β conditions as they occur, for example, in the solar corona, see Fig. 5.3). “[T]he shocks of most interest to particle acceleration are MHD fast mode shocks, which compress both the density and the magnetic field. [Here, acceleration may span several orders of magnitude, and may significantly alter the shape of the energy distribution. However,] slow mode shocks may also play a role under certain circumstances.”

“All mechanisms that contribute to the acceleration of charged particles at shocks rely on the particle orbits in the spatial and temporal features of electric and magnetic field environment of the shock. Roughly speaking, such processes are called kinetic when they go beyond the fluid (MHD) properties of the shock, when they are related to the scales associated with the charged particle motion, and when they require some self-consistent back-reaction between the charged particles and the plasma, *e.g.*, in the form of wave generation. For the highest particle energies, gyro-radii are so large that the size of the shock transition and even that of many local waves no longer matter. Conversely, for the thermal and so-called supra-thermal particles (just above the thermal energy to several thermal energies), the intrinsic shock scales and locally-

generated waves do matter. As a consequence, the intrinsic shock scales and associated mechanisms play an important role not only for the general dissipation at the shock (the conversion to thermal energy), but also in providing a first, background level of energetic particles from 'seed particles' in the thermal and supra-thermal energy range. [...]

The two most important scales in collisionless shocks are the proton inertial length $\lambda_{\text{pi}} = c/\omega_{\text{pi}}$ (see Eq. 3.44; [ω_{pi} the ion plasma frequency]) and the proton gyro-radius $r_{\text{gp}} = m_{\text{p}}vc/eB$, which are related via the proton beta by $r_{\text{gp}}/\lambda_{\text{pi}} = \sqrt{\beta_{\text{p}}}$. [... The width of the transition for many shocks is the larger of λ_{pi} and the distance v_1/ω_{gp} which the upstream flow, moving at speed v_1 in the normal incidence frame (NIF, see Fig. 8.8), travels during the time $1/\omega_{\text{gp}}$ for a single gyration of a proton.] Exceptions are the almost perpendicular shock [see footnote 11 on terminology], which can be cyclically reforming and steepen to electron scales, and quasi-parallel shocks, which are not only reforming, but at sufficient Mach number have extended regions of steepening upstream waves, and highly non-linear turbulence downstream.”

“In most shocks in the heliosphere, the thermalization of the upstream flow is primarily achieved via the ion dynamics, whereas the electrons mostly 'just go along for the ride,' *i.e.*, they move almost adiabatically, with some subsequent scattering that fills otherwise inaccessible regions in the downstream velocity space. Any heating of the electrons (which can be quite small) is important in regulating the so-called cross-shock potential, because much of the electron phase space needs to be confined to the downstream by a potential, to prevent escape of the highly mobile electrons and to preserve overall charge neutrality. [...]

In typical shocks of the interplanetary medium, and in planetary bow shocks, it has been established that the reflection and gyration of the incoming ions plays a dominant role. At oblique shocks, part of the incoming ion phase space is reflected, but then convected back into the downstream. That is, after reflection, at sufficient Mach number, any upstream-directed parallel velocity of most thermal and even of many supra-thermal particles is not sufficient to overcome the general plasma drift into the shock. Much of the converted flow energy is initially stored in these gyrating ions, which during this process have attained elevated perpendicular temperatures from the magnetic field jump. Depending on parameters, it may take a while before these protons are thermalized downstream, typically in Alfvén wave turbulence driven by the temperature anisotropy $T_{\perp} > T_{\parallel}$. Generally speaking, the closer to perpendicular the shock, the more difficult it is for both particles and waves to escape upstream.

In contrast, in quasi-parallel shocks reflected (and partially gyrating) ions also play a role, but they can much more easily escape upstream against the flow, because the magnetic field direction is close to the shock normal. There, they generate both obliquely-propagating, compressional fast-mode waves, and parallel-propagating Alfvén waves. These waves can grow to large, non-linear amplitudes while convected back towards the shock, where the beam density and growth rate are largest. However, below Alfvén mach numbers of about $M_{\text{A}} < 2.8$, the majority of resonantly generated waves are no longer convected back and therefore do not steepen as easily and do

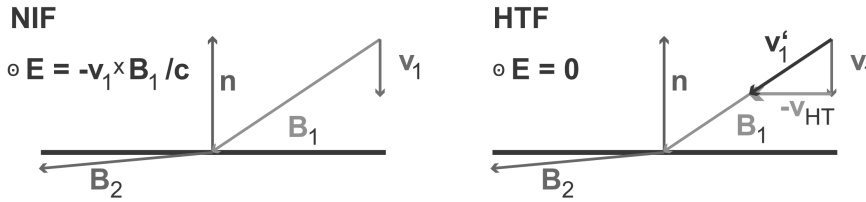


Figure 8.8: Comparison of the normal-incidence frame (NIF) and de Hoffman-Teller frame (HTF) at fast-mode shocks. The NIF is the shock frame in which the upstream flow is aligned with the shock normal. [...] Transformation to the HTF is along the plane shock surface until the upstream flow vector coincides with the magnetic field. [...] Fig. II:8.2]

not impact the shock any longer, thus resulting in fewer ions making it upstream to generate waves in the first place. [The] resulting lower level of turbulence also has a negative impact on ion acceleration to higher energies.”

“For most heliospheric shocks, proton acceleration is of prime interest. Protons can easily reach energies of tens, if not hundreds of MeV, and as such have a large range of societal consequences such as malfunction or destruction of equipment in space, and posing danger to astronauts or crew and passengers of high-flying aircraft. Electrons, on the other hand, are rarely accelerated to comparable fluxes at these energies, except perhaps at processes well inside the magnetosphere that periodically lead to huge enhancements of trapped populations (see Section 8.7).”

“For ions, and for the energy range typically observed in the heliosphere, it is well accepted that two distinct acceleration mechanisms are at play:” (a) shock-drift acceleration and (b) diffusive shock acceleration.

(a) Shock-drift acceleration

“[R]eflection of a portion of the incoming proton phase space [by the shock], and subsequent convection downstream, is the prime mechanism that eventually provides the [acceleration and heating] at quasi-perpendicular shocks. Even at highly oblique shocks, a small fraction of these ions will have sufficient parallel speed to make it upstream instead of being convected downstream, but the flux of such ions is strongly diminishing [with increasing angle between the shock normal and the upstream magnetic field,] making upstream wave generation increasingly difficult. Although the thermal proton gyroradius is typically comparable to the shock width, and that of supra-thermal ions clearly larger than the shock transition, surprisingly, many ions approximately behave adiabatically in simple shock transitions with sufficiently homogeneous upstream and downstream fields. A portion of the ion phase space then gains energy through their gyromotion under consideration of the shock electric fields. The family of such processes is called shock-drift acceleration (SDA).”

SDA “is a ‘kinematic’ process in the sense that the particles simply perform their usual, mostly adiabatic orbits in the given, static or average electric and magnetic fields of the shock transition, neglecting any scattering. [...]” “Consider a steady-state, one-dimensional shock. In this case, in the normal-incidence frame (NIF, see Fig. 8.8), there will be an out-of-plane electric field given by the cross-product of the upstream

flow and magnetic field [...] $\mathbf{E}_p = -\mathbf{v}_1 \times \mathbf{B}_1/c$. [The MHD Rankine-Hugoniot jump conditions are such that the strength of this electric field is the same upstream as downstream of the shock. {A108} This motional electric field is aligned with the direction of both the curvature and gradient drifts associated with the jump in \mathbf{B} across the shock (see Sect. 8.2, and around Eqs. (8.7) and (8.9)), in such a way that ions gain energy by the gradient drift and lose energy through curvature drift.] It turns out that at quasi-perpendicular shocks, gradient drift wins out for most ions, which then gain energy proportional to the distance they drift along \mathbf{E}_p .” {A108}

A perspective change to another inertial system provides an alternative interpretation: in the so-called de Hoffmann-Teller frame (HTF, see Fig. 8.8) a translational velocity of $v_{HT} = v_1 \tan \theta_{B_\perp}$ is introduced so that the upstream flow and magnetic field are aligned. As a result, there is no motional electric field in this reference frame, and only energy conservation and magnetic moment conservation come into play. In the HTF “energy is conserved in the absence of other processes, and the only allowed change absent scattering is between the perpendicular and parallel velocity components. For close to perpendicular shocks, the field-aligned velocity component becomes increasingly larger due to the transformation into the HTF. [...] Because the perpendicular energy gain under magnetic moment conservation is simply a factor based on B_2/B_1 , only ions with sufficient initial perpendicular energy may exchange large fractions of their velocity components, while slowing down significantly or reflecting in the magnetic field gradient and in the cross-shock potential. Subsequent back-transformation shows that they have gained energy proportional to the squared transformation velocity. While this energy gain can be huge close to $\theta_{B_\perp} \sim 90^\circ$, an increasingly smaller subset of phase space has sufficient perpendicular energy to effectively participate.” II:8.42

Other mechanisms have been proposed, for electrons and ions alike, some, like ‘shock surfing’ acceleration (SSA) rely on the differences in gyro-radii and on the cross-shock potential; see Sect. II:8.4 for some more information. The challenge with all is that without additional scattering mechanisms, all these processes are too limited in the portion of phase space that is affected, and in the amount of energy gain, to explain the large, highly-energized populations often observed. It has been argued, however, that mechanisms like SDA and SSA can add energy for particles already energized by another mechanism, or that they provide the seed particles for such other mechanism to continue the energization. Turbulence or particle-induced waves may provide the scattering required to access more of the phase space.

(b) Diffusive shock acceleration

Diffusive shock acceleration (also known as first-order Fermi acceleration) “is of ‘kinetic’ nature, in the sense that wave-particle interactions play the decisive role. As explained above, reflected or otherwise energized ions can easily escape into the upstream at quasi-parallel shocks, where they self-consistently” generate waves. Once grown sufficiently, these waves, and existing turbulence, diffusively scatter particles into a population that ranges from the far upstream to the far downstream. As the scattering centers converge owing to the compression associated with the shock, repeated scattering results in energization until they escape from the shock zone. II:8.41

“First-order Fermi acceleration produces a power-law distribution and intensities that depend on the shock strength (compression ratio ρ_2/ρ_1). Power-law distributions are as ubiquitous for SEPs as they are in cosmic plasmas, in general. [The] restricted temporal and spatial dimensions available lead to an upper cut-off of the spectra at high energies – typically between 10 MeV and 100 MeV for SEPs escaping interplanetary shocks. [...] For particles that are already significantly faster than the flow speed, the associated momentum gain of a returning particle is: $\delta p/p = (v_1 - v_2)/v(\cos \theta' - \cos \theta)$, where the prime denotes the new pitch angle. [Note that the particles involved are quite energetic and therefore have a mean free path length exceeding the shock width; thus they sense the shock as a delta function, with the value of $(v_1 - v_2)$ in the above expression reflecting the step associated with term \textcircled{e} in Eq. (8.20).]

If one now assumes an almost isotropic distribution of particles, one can average over all pitch angles, and the cos terms simply convert into a constant factor. One then proceeds to calculate the probability of escape downstream (which is simply given by the ratio of the downstream to upstream flux) versus the probability of an acceleration cycle. From the calculation it follows that the particle distribution assumes a power law with index q , which depends on the shock compression ratio: $q = 3r/(r - 1)$, where from mass continuity in the assumed one-dimensional shock: $r = v_1/v_2 = n_2/n_1$, *i.e.*, the compression ratio between the downstream and upstream densities. [...]

Because waves that make up efficient scattering centers should be generated self-consistently by the energetic ions, must exist for extended regions upstream and downstream of the shock, and should not be convected towards or away from the shock too quickly, diffusive shock acceleration is most efficient and easiest understood for fairly high Mach number, almost parallel shocks. Conversely, it is much less understood how this process can be so efficient at the low-to-medium Mach number, oblique shocks that make up most interplanetary shocks. In particular, at nearly perpendicular shocks, diffusive acceleration may require effective scattering across the magnetic field.”

There are multiple challenges to overcome in the study of diffusive shock acceleration, including the large number of particles that need to be tracked in numerical models, the relative roles of the various processes and their dependence on specific geometries, the generation of adequate turbulence to scatter particles, the complexities of the self-generated upstream wave field with multiple possible modes, the escape of the particles that have been energized from the upstream wave field as well as their further propagation through the turbulence in the solar-wind field, and the role of second-order Fermi acceleration in which particles scatter off counter-propagating waves, and, of course, the vast range of scales that needs to be treated. “It is also known that multiple shocks generate a much more efficient acceleration environment. Not only does the first shock leave a much more turbulent and seed-particle rich upstream for the following shock, but particles may scatter multiple times in both shocks. Of course, the upstream seed particle spectrum and background turbulence are highly variable in the solar wind in general, and will have an impact on achieved fluxes.”

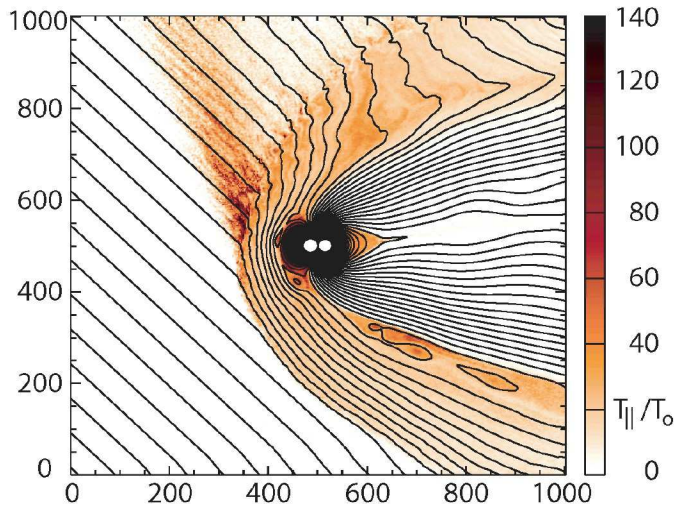


Figure 8.9: Example of a two-dimensional (2-D) hybrid simulation of the solar wind – magnetosphere interaction. Shown are magnetic field lines (upstream IMF angle $\theta = 45^\circ$) and, the normalized parallel ion temperature T_{\parallel} , as a proxy of ion acceleration. As well-documented in many observations of the Earth’s bow shock, the ion foreshock starts close to $\theta_{B_{\perp}} = 45^\circ$ with energized and back-streaming ions, and simultaneous excitation of waves (visible in the field line undulations). Conversely, at this scale, and with the number of pseudo-particles used in the simulation, there are virtually no upstream ions at larger shock-normal angles. [Fig. II.8.3; source: Krauss-Varban *et al.* (2008).] For a color version of this figure, see *arXiv:2001.01093*.

The Earth’s bow shock

II.5.1

“[P]lanetary bow shocks are of finite size, and as such, any production of energetic particles is both localized and highly non-local: some regions (*i.e.*, the quasi-parallel portion) are much more able to easily generate energetic ions, while any ions propagating upstream, or waves excited upstream of the oblique portion are quickly convected to a different portion of the finite-size bow shock, or around the obstacle, altogether. The general scale size of the Earth’s bow shock is of the order of $20R_E$ (Earth radii); the stand-off distance is [typically some $15R_E$. . .]here is an ion foreshock that starts somewhere below $\theta_{B_{\perp}} \sim 45^\circ$ and permeates the quasi-parallel domain, while the faster electrons form a foreshock boundary close to the perpendicular shock.

Figure 8.9 shows a snapshot of a 2-D bow shock simulation to further demonstrate this point. [. . .] The turbulence upstream and downstream of the quasi-parallel portion is clearly visible, as is the large enhancement of upstream-propagating, energetic protons. Conversely, there is virtually no upstream activity at or beyond 45° . [This approximate description conforms with the general state of the terrestrial environment and] also illustrates why there is so little activity upstream of the oblique portion beyond $\theta_{B_{\perp}} \sim 45^\circ$: any ions that manage to make it upstream of the oblique portion, and any waves generated there, are either convected into the quasi-parallel portion of the bow shock, or instead move past the finite-sized obstacle altogether.”

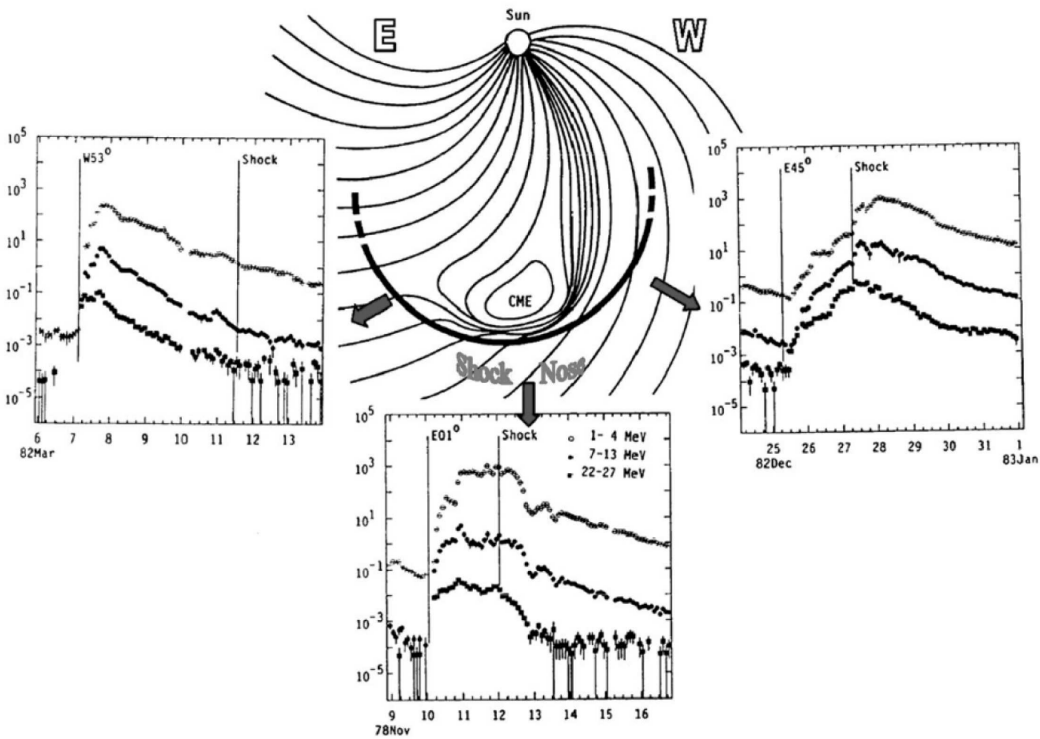


Figure 8.10: Intensity-time plots of particle fluxes ejected from three different solar longitudes with respect to the nose of the shock front. [IV:12.7; source: Reames (2013).]

Interplanetary shocks

“Both co-rotating interaction regions and CME-driven shocks are capable of accelerating charged particles; however, not surprisingly, the largest events are associated with the fastest CMEs and can reach Alfvén Mach numbers of 5 to 6, and occasionally even higher. These Mach numbers are comparable to the Earth’s bow shock; yet, energetic particle energies and fluxes observed at the bow shock are almost dismal compared to those at the largest CME-driven events. Yet, while the Earth’s bow shock virtually always generates upstream energetic ions, the same cannot be said for IP shocks. [...] Finally, the heliospheric termination shock is also generally viewed as capable of producing highly-energized ions.”

“Interplanetary (IP) shocks have a great variety of strength, and most of them are actually not particularly active when it comes to energetic particles. At the other extreme are IP shocks that are associated with strong solar energetic particle events (SEPs). Today, it is thought that SEPs are generated both by flare processes deep in the solar corona, and by shocks driven by coronal mass ejections (CMEs) [...] In fact, it is estimated that almost all of the magnetic energy released in flares goes

into energetic particles, with perhaps approximately equal share between the ions and electrons. These particles show up as 'prompt' events when observed at Earth: extremely energetic ions can traverse the distance from the Sun in minutes, with little delay compared to observed X-ray flare signatures at the Sun.

Conversely, so-called 'gradual' solar energetic particle events are generally accepted to be associated with coronal and interplanetary (IP) shock acceleration, driven by coronal mass ejections (CMEs). Even in this case, the most energetic particles are produced when the shock is in the corona, with resulting hard spectra that are observed at Earth within tens of minutes. However, production of energetic ions continues to 1 AU and beyond, and peak fluxes, with a softer spectrum [(meaning dropping faster with increasing particle energy)], often arrive at Earth with the shock itself – historically called energetic storm particle (ESP) events [(Fig. 8.10)]. {A109}

[F]orward propagating interplanetary (fast mode) shocks near 1 AU typically have an Alfvén Mach number $M_A < 3$, [only rarely reaching $M_A > 4$. D]espite their low Mach number, about one half of [the sample of] observed shocks had identifiable (albeit relatively low energy) upstream, energized ions and associated waves. [The] distribution of these ions [are] fairly isotropic, whereas in only a few cases, upstream beams were observed. This behavior also extends to higher energies and may be interpreted as a consequence of the large spatio-temporal scales of IP shocks, which rarely allows one to see the initial evolution of wave-particle interactions. While the large scales provide an important clue, and energetic seed particles may play an additional role, currently no scenario self-consistently accounts for the observed energetic ion environment of the weaker and oblique shocks.” {A109}

8.7 Relativistic particles in planetary radiation belts

8.7.1 Electron acceleration mechanisms

Earth's electron radiation belts are located at $L \approx 3 - 10$, typically peaking around $L \approx 4 - 5$ (where L is the radial distance in Earth radii where magnetic field lines of an unperturbed dipole would cross the magnetic equator). “Many acceleration mechanisms have been proposed to explain electron radiation belt flux increases at Earth but their exact contributions are still debated. Proposed acceleration mechanisms are often separated into two categories: internal (or local) source acceleration and external source acceleration. External source acceleration mechanisms are so named because they move electrons from outside geosynchronous orbit (at $6.6 R_E$) to the inner magnetosphere accelerating electrons through the transport process. They operate over large spatial and temporal scales that violate the particles' third adiabatic invariant. Internal source acceleration mechanisms, on the other hand, locally accelerate electrons in the inner magnetosphere inside of $6.6 R_E$. They operate on fast timescales and small spatial scales and violate all three adiabatic invariants. The most prominent of the proposed mechanisms in each category are listed below. [...]” IE:11.4.1

External acceleration mechanisms

“The manner in which external mechanisms accelerate particles can be illustrated starting with the assumption that the first adiabatic invariant [(Eq. (8.10))] is conserved.” IE:11.4.1.1

These mechanisms move electrons radially inward where the magnetic field is stronger. Because μ_m is conserved during the transport process, the increase in field strength requires that the particles' perpendicular energy also increase. The total energy gain is directly related to the amount of radial transport. The relationship between transport and acceleration is easy to describe using the conservation of the first adiabatic invariant but the explanation hides the complex physics of the acceleration. Ultimately, it is an electric field that transports and accelerates the electrons because the magnetic field cannot change the particle energy. What separates the acceleration mechanisms is the exact form and timescale of that electric field. The electric field in both shock-induced acceleration and substorm induced acceleration is a large-scale inductive electric field that sweeps through the magnetosphere as the global magnetic field changes.

The shock-induced electric field is caused by the compression of the magnetosphere as shocked solar wind passes Earth. [...] However, such large sudden events are rare [while] smaller more pervasive compressions do not contribute significantly to electron radiation belt flux increases. Thus, shock acceleration is usually only discussed for specific events and not the very common flux increases that occur with most geomagnetic storms.

The substorm electric field is produced when the stretched magnetotail is pinched off near $10 R_E$ and the remaining plasma is hurled Earthward resulting in a more dipolar magnetic field configuration. [With this mechanism, numerical models have difficulty in transporting electrons inside of $10 R_E$; it may be that substorms] contribute to a seed population of electrons at large radial distance but some other mechanism, such as radial diffusion, is necessary to bring the electrons into the inner magnetosphere. Hence, much of the acceleration debate focused on radial diffusion.

In the case of radial diffusion, the electric field is that of ultra-low frequency (ULF; 300 Hz to 3 kHz) waves that continuously agitate the magnetosphere. [...] The basic premise of the mechanism is that electric fluctuations induce small random perturbations of the electrons' position causing them to diffuse radially throughout the magnetosphere. The process is similar to diffusion in a gas only in this case the random walk motion of the particles is caused by electric fields instead of collisions. [...]

[Time] varying fields fluctuating specifically at the same frequency of an electron drifting about Earth [cause] rapid acceleration through a 'drift resonance'. Figure 8.11 gives a pictorial explanation of an electron drift resonance. [...] The electron drifting around Earth labeled e_1 [...] experiences an azimuthal electric field that continuously moves it inward causing the electron to gain energy. However, the electron, e_2 , that began at time $t = 0$ on the opposite side would have seen an electric field that pushed it radially outward in the same manner. Thus, the drift resonance causes electrons to diffuse radially inward and outward and decelerates as well as accelerates electrons.

[...] If electrons are acted on by [a randomly varying electric field, the net energy gain of the distribution of electrons] is determined by the phase-space density as a function of L . If electrons are uniformly distributed in L then the same number of electrons moves inward and gain energy as those that move outward and lose energy

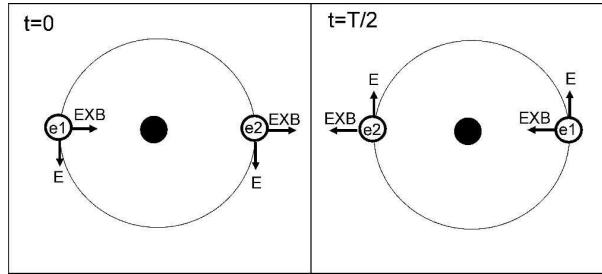


Figure 8.11: Schematic diagram of an electron in drift resonance with a ULF wave. The left panel shows two electrons labeled $e1$ and $e2$, the direction of the wave electric field, and the direction of the particle's $\mathbf{E} \times \mathbf{B}$ drift at time $t = 0$. The right panel shows the same properties half a wave period and electron drift period later. [Fig. II:11.7]

with no net energy gain. If the slope of f versus L is positive more particles move inward and gain energy than particles move outward and lose energy and the distribution of electrons gains energy. If the slope of f versus L is negative then the opposite occurs. [... The radial diffusion has been described by an approximation to the Fokker-Plank equation]

$$\frac{\partial f(L, \mu_m, K, t)}{\partial t} = L^2 \frac{\partial}{\partial L} \left(\frac{D}{L^2} \frac{\partial}{\partial L} [f(L, \mu_m, K, t)] \right). \quad (8.31)$$

Here $f(L, \mu_m, K, t)$ [(with K defined in Eq. 8.13)] is the phase-space density of electrons and D is the diffusion coefficient which is calculated separately for electric and magnetic field perturbations. [Later,] the theory was revisited and elaborated to include higher-order resonances caused by electron drift motion in more realistic non-dipolar fields that increase diffusion. However, doubt about the ability of radial diffusion to fully explain observations led to the development of new competing ideas regarding electron acceleration including the internal source acceleration mechanisms.”

Internal source acceleration mechanisms

“The internal source acceleration mechanisms discussed here accelerate electrons through interaction with the electric field of a VLF (3 kHz to 30 kHz) wave. The interaction is similar to the ULF wave resonance, but in this case the resonance occurs between the wave electric field and the gyration of the particle about the magnetic field instead of the drift about Earth. The EMIC-Chorus wave mechanism assumes the interaction with the wave can be described as a random walk diffusive process very similar to radial diffusion [(Fig. 8.12 illustrates characteristic domains of various waves in the terrestrial magnetosphere)]. This assumption is only valid when wave amplitudes are small. The non-linear whistler wave acceleration mechanisms describe how electrons interact with a monochromatic set of large amplitude waves when diffusion is no longer valid. {A110}

The resonance between an electron and a VLF wave can be illustrated by considering a VLF wave propagating at an angle θ from the direction of the magnetic field with magnetic and electric field perturbations perpendicular to the direction of propagation. The electron gyrating about the magnetic field will experience a constant electric {A110}

II:11.4.1.2

{A110}

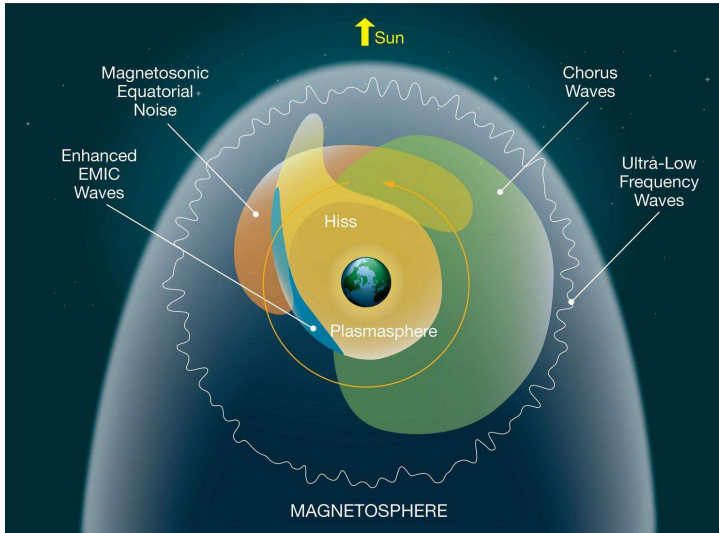


Figure 8.12: Characteristic wave types within a magnetosphere, here visualized for the terrestrial case, viewed from above the arctic. Credit: NASA’s Goddard Space Flight Center/Mary Pat Hrybyk-Keith. For a color version of this figure, see [arXiv:2001.01093](https://arxiv.org/abs/2001.01093).

field from the wave when the gyrofrequency of the electron equals the Doppler-shifted frequency of the wave [...]. In contrast to the ULF wave resonance, the VLF wave resonance will affect both the electron’s energy and pitch angle. [...]

The *Chorus-EMIC wave mechanism* proposes that electrons interact with both whistler Chorus and EMIC waves as the electron drifts about Earth in such a fortuitous way that the distribution is steadily pushed to higher energy. In this model, EMIC waves at dusk interact with electrons to produce an isotropic pitch angle distribution. The electrons continue their drift to the dawn side of the magnetosphere where Chorus waves are predominantly found. The diffusion curves for Chorus waves are such that an isotropic distribution will diffuse towards higher energy and larger pitch angles. The energized electrons now peaked near 90 degrees continue around to the dusk side of the magnetosphere where the EMIC waves are found. The EMIC waves interact with the electrons to again produce an isotropic pitch angle distribution but with no energy loss. This isotropic distribution is now primed to interact with the Chorus waves once again and gain energy. Because the electrons traverse the magnetosphere in less than 10 minutes, the mechanism can effectively increase the energy over periods of days.

The *non-linear whistler wave mechanisms* assume that electrons are energized through a resonant interaction with whistler waves. However, the previous diffusion model requires that wave amplitudes are small in order for diffusion to be an adequate approximation. If this is not the case, the interaction must be described in a more detailed manner. [... Under] the right conditions a 100 keV electron could be accelerated to MeV energies within minutes. These mechanisms have yet to be compared in detail with observations or included in any kind of global model of electron flux. However, new measurements of whistler waves suggest that the small amplitude assumption is

very often invalid making non-linear modeling an active area of interest.”

8.7.2 Proton acceleration in the radiation belt

“The structure and temporal variability of the proton radiation belt is strikingly different from its electron counterpart. Yet, some of the same mechanisms are proposed to explain the acceleration of these particles. The protons normally form only one belt [around $L = 1 - 3$] with fluxes that peak near $L = 1.5$ and they tend to be more stable. However, during highly geomagnetically active periods, such as brought about by the passage of a large shock and sometimes an accompanying solar energetic particle (SEP) event, fast and dramatic changes occur. Often these changes mean a complete reconfiguration where entirely new, sometimes transient proton belts are formed that may last days to years.

Simulations of proton motion in both analytical and MHD magnetic field models suggest that the new proton belts are formed when protons are transported radially inward by large induced electric fields that arise as a large shock passes the Earth. The mechanism is almost the same as proposed for some electron radiation belt acceleration events at Earth, except that forming a new proton belt requires an additional source of protons from the solar wind. Often large shocks are accompanied by very high fluxes of protons that are released from the Sun and further accelerated by the shock. Normally, Earth’s magnetic field acts as a protective bubble that only allows these solar protons to enter over the polar caps where they are absorbed into the atmosphere. However, as the shock passes Earth, the magnetic field is distorted such that the accompanying protons can gain access to the inner magnetosphere and become trapped in the field. Once trapped, they are swept up by the induced field and pushed to small radial distances and higher energies to form a new belt.”

8.7.3 Radiation belt losses at Earth

A “survey of electron radiation belt changes [...] found that only 53% of storms cause radiation belt flux levels to increase even though these storms signify increased energy input to the magnetosphere. In 19% of storms the flux actually decreased and in 28% the flux did not change [by more than a factor of two]. The variable response to energy input suggests that loss and acceleration rates are often comparable and ultimately compete to determine final flux levels. [...] The mechanisms that have been proposed to explain the loss of relativistic electrons are: drift out the magnetopause boundary, outward radial diffusion, and scattering into the atmosphere. Scattering can be caused by interactions with a thin current sheet, EMIC waves, or Chorus waves.

Loss of electrons through the magnetopause boundary occurs when the drift paths of electrons are altered as the magnetic field changes from a quiet time configuration to more disturbed conditions. During quiet times, the drift motion of an electron starting in the magnetotail is dominated by an electric potential field directed from dawn to dusk [(see Fig. 5.16)] that moves electrons Earthward. As the electrons get closer to Earth, the magnetic radial gradient causes a westward drift. Some of these drift trajectories will cross Earth’s magnetopause and the electron will be swept away by the solar wind. Closer to Earth, the trajectories of the electrons will be dominated by the gradient drift. Undisturbed, electrons in this near-Earth region will simply drift

about continuously on closed almost circular paths. [Model] results suggest that during geomagnetic storms, most of the outer electron radiation belts are emptied into the solar wind and replaced by an entirely new belt of accelerated electrons. [This plausible suggestion has not been observationally. It appears] that loss to the magnetopause was not an adequate explanation for electron flux depletions observed during more quiet conditions because the flux of energetic protons on similar drift paths did not decrease.

Radial diffusion [...] has also been proposed as a loss process. Radial diffusion acts to reduce gradients by pushing particles from high phase-space density to low phase-space density. The outermost closed drift orbit of the radiation belts represents a very steep gradient where the phase-space density goes to zero. If ULF waves are present, then radial diffusion will push particles outward to the magnetopause. [...]

Losses into the atmosphere occur when some mechanism scatters electrons to smaller pitch angles causing them to travel farther down the field line and collide with the neutral atmosphere. The current sheet, that forms in the magnetotail as the lobes are stretched and forced together by solar wind dynamics, is an effective scattering region. Scattering occurs when the magnetotail becomes stretched to the point that an electron bouncing along a field line can no longer make it around the kinked field without violating its first invariant. Traversing the kink changes the particle's pitch angle. Under certain conditions the pitch angle changes can be described as a diffusive process. [The] significance of this loss contribution has yet to be verified.

Chorus and EMIC waves [...] may also cause rapid loss into the atmosphere. Whether or not the waves produce net acceleration or loss depends on the initial gradients of the electron distribution as a function of pitch angle. [If] the appropriate distribution exists, EMIC waves are expected to cause losses on the timescales of several hours to a day. Whistler Chorus may cause losses on timescales of one day, but these estimates are sensitive to parameters such as the cold plasma density. Loss rates may increase to timescales less than a day during storm main phase when the plasma density is expected to vary [...]"

"The proton losses from the radiation belts have not been analyzed in the same details as the dramatic formation of new belts. New belts last from days to years. Mechanisms proposed to explain the disappearance of these belts include scattering caused by the kinked field, and interaction with EMIC waves. [There is no firm understanding of the proton loss mechanisms, and] it may be that more than one mechanism plays a role in each event."

Chapter 9

Convection, heating, conduction, and radiation

Chapter topics:

- Convective, radiative, and conductive energy transport
- Ubiquitous but structured magnetic field in the solar photosphere
- Coronal loop atmospheres
- Power laws for stellar atmospheric losses

Key concepts:

- Convective 'small-scale' dynamo action
- Magnetohydrostatic flux tubes: bright points to dark spots
- Optically thick/thin
- Wilson depression

9.1 Convective and radiative energy transport

One topic at the foundations of heliophysics remains to be introduced before we move on to comparative stellar and planetary astrophysics: which processes lead to a relatively steady background heating of the solar atmosphere in 'quiescence', *i.e.*, outside of obvious impulsiveness? These processes have their origin in the convection that occurs below the solar surface and in the diversity of waves that are generated by these convective motions.

The solar convection zone persists from a depth of about 200,000 km all the way to the surface. "Looking at the solar photosphere, we see the top of the convection zone in the form of granulation: Hot gas rising from the solar interior as part of the energy transport process reaches a position where the opacity is no longer sufficient to prevent the escape of radiation. The gas radiates and cools, and in doing so loses its buoyancy and descends. {A111} At the surface the gas density is of order 10^{-7} g/cm³ while the pressure is of order 10^5 dyne/cm², but decreasing exponentially with height with a scale height of some 100 km. (This small scale height is the reason that the solar {A111}

limb appears sharp as viewed with the naked eye.) Granular cells have dimensions of order 1 Mm, but numerical simulations indicate that convective length scales rapidly become larger as one proceeds below the solar surface. {ⓂA112} These motions, ultimately driven by the requirement that the energy generated by nuclear fusion in the Sun’s core be transported in the most efficient manner, represent a vast reservoir of ‘mechanical’ energy. {ⓂA112}

Looking closer, we see that granulation is not the only phenomenon visible at the solar surface. The quiet and semi-quiet photosphere is also threaded by magnetic fields that appear as bright points, as well as darker micro-pores and pores. These small-scale magnetic structures are, while able to modify photospheric emission, subject to granular flows and seem to be passively carried by the convective motions. Bright points are organized in a honeycomb-like pattern on the solar surface with a size scale larger than granulation, roughly 20 Mm; this pattern defines the so-called supergranular network and is suggestive of convective cells larger than granulation extending deeper into the solar interior.

Convective flows are also known to generate the perturbations that drive solar oscillations. Oscillations, sound waves, with frequencies mainly in the band centered roughly at 3 mHz or 5 minutes are omnipresent in the solar photosphere and are collectively known as p -modes (‘ p ’ for pressure). These p -modes are a subject in their own right and studies of their properties have given solar physicists a unique tool in gathering information on solar structure — the variation of the speed of sound c_s , the rotation rate, and other important quantities — at depths far below those accessible through direct observations. [...] {ⓂA113}

On average the photospheric gas pressure of $p_g = 10^5$ dyne/cm² is much greater than the pressure represented by an average unsigned magnetic field strength of 1 – 10 Gauss ($p_B = B^2/8\pi < 10$ dyne/cm²) that is observed. However, in the largely isothermal chromosphere, the gas pressure falls exponentially with a scale height of some 200 km, while the magnetic field strength falls off much less rapidly, even as the field expands [from the compact flux tubes that characterize it in the photosphere] and fills all space. Thus, depending on the actual magnetic field geometry, the magnetic pressure and energy density will surpass the gas pressure some 1500 km or so above the photosphere in the mid chromosphere. Another 1000 km, or 5 scale heights above the level where $\beta = 1$ (see Eq. 3.24), the plasma’s ability to radiate becomes progressively worse, while the dominance of the magnetic field becomes steadily greater. As we will explain below, any given heat input in this region cannot be radiated away, and will invariably raise the gas temperature to 1 MK or greater; a corona is formed. A corona that is bound to follow the evolution of magnetic field as the field in turn is bound to photospheric driving.” {ⓂA113}

“In Fig. 9.1 we show typical images of the quiet to semi-quiet photosphere as well as a plage region.^[24] These images are made in the so called G-band centered around

²⁴ ‘Plage’ is formally the bright chromospheric area over regions of enhanced magnetism in the photosphere, but is commonly also used to describe the interior of active regions, *i.e.*, regions of strongly enhanced mean magnetic field in the photosphere, outside of, but commonly in the immediate vicinity of,

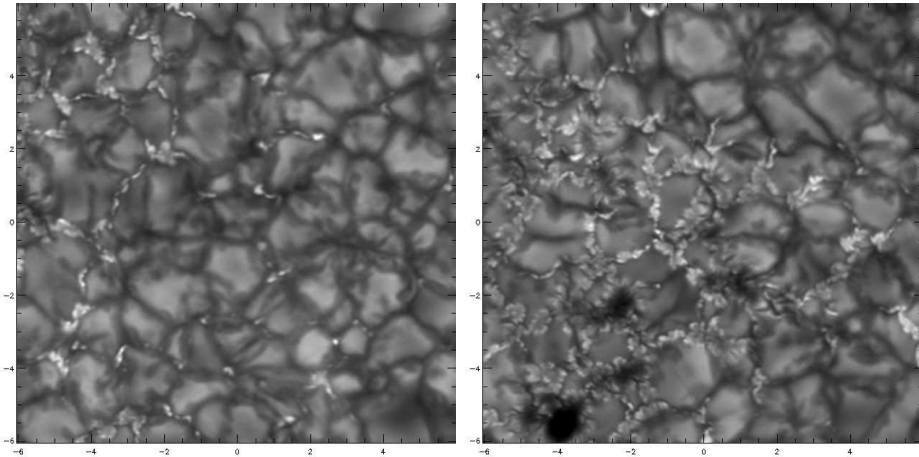


Figure 9.1: The image on the left shows a typical quiet photospheric region observed in the G-band with the Swedish 1-meter Solar Telescope. The image on the right shows a plage region where the total amount of magnetic flux penetrating the photosphere is larger. The axes of both panels are numbered in arcseconds measured on the Sun; 1 arcsec is approximately 725 km. The G-band near 4300 \AA contains several spectral lines, notably the lines of the CH-molecule, and is formed near the solar surface (the height where the optical depth $\tau_{5000\text{\AA}} = 1$); the granulation and intergranular lanes some 100 km above this height, bright points some 200 km below — as explained in the text. Bright points are regions of enhanced magnetic field embedded between the granular motions. Notice also that bright points are pulled into ribbons and may fill the entire intergranular lane. The image on the right shows a photospheric plage region. Notice the large number of phenomena showing complex structure; ribbons, 'flowers', micropores, as well as isolated and seemingly simple bright points. The magnetic field in this image is in places strong enough to perturb granulation dynamics and the granules appear 'abnormal' while displaying a slower evolution than in the quieter photosphere. [Fig. I:8.3]

4300 \AA which is formed some 100 km above the nominal photosphere. [...] {A114}

In [the left panel of] Fig. 9.1 we show examples of simple bright points in a fairly quiet region of the photosphere, *i.e.*, a region in which the magnetic field is too weak to significantly modify granular motions. Isolated bright points are seen to be constrained to intergranular lanes and do not seem to have any internal structure on the scales that are visible on this resolution. Isolated bright points appear to be passively advected towards the periphery of supergranular cells, where they gather and form the collection of bright points that define the supergranular network mentioned above. [...] {A114}

The right panel [of Fig. 9.1] shows a region of stronger average field strength, a *plage* region, than that found in the left-hand panel. Flux concentrations with larger spatial extent are embedded in (micro-)pores with distinctly dark centers. Such small dark micropores may be the smallest manifestation of the phenomena that produce pores and sunspots. The bright points in the plage region are not simple points but are seen to have structure and appear to modify the granular flow itself: The image

sunspots.

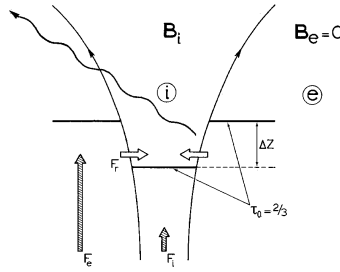


Figure 9.2: Concept of the magnetohydrostatic flux-tube model. One level of constant optical depth in the continuum, $\tau_0 = 2/3$, is shown, with the Wilson depression Δz . The hatched arrows F_i and F_e stand for the flux densities in the (non-radiative) energy flows inside and outside the flux tubes, respectively. The horizontal arrows indicate the influx of radiation into the transparent top part of the tube. The resulting bright walls are best seen in observations toward the solar limb (as seen along the oblique wavy arrow. [From Schrijver and Zwaan (2000)]

shows that granules near network bright points and in plage regions appear smaller, have lower contrast and in addition display slower temporal behavior than granules in weak field regions. Coalescing bright points in plage and network regions can form dark centers and thus become micropores if their density is large enough, or indeed brighten again if the granular flow breaks them apart into smaller flux elements. [...]

Substantial bundles of strong-field magnetic flux form dark pores and even larger ones form the dark sunspots. Relatively smaller bundles on the other hand are bright compared to the surrounding photosphere, particularly when seen somewhere between the center of the solar disk and the edge (or 'solar limb'). Qualitatively, this can be understood by the combination of radiative transport and MHD. Let us start with an essentially vertical flux bundle with an intrinsic field of ≈ 1 kG as commonly observed for such solar field structures. Such a tube has settled into pressure equilibrium between inside and outside, but as the field adds its own pressure, the gas pressure inside a tube at a given height is lower than outside. Radiative losses lead to cooling inside and outside the tube, but the field inside lowers the ability for convection to resupply heat relative to outside, so that the interior of the tube is cooler. Being cooler and less dense, the level at which the optical depth reaches unity inside the tube is lower than outside, leading to a 'depression' in the solar 'surface' (called the Wilson depression). The line of sight into the tube from a somewhat slanted perspective looks down on the flux-tube walls, which shows layers effectively under the surface, and thus brighter than the surrounding photosphere (appearing as what are known as 'faculae'; compare Fig. 9.2), [provided the tube is relatively narrow compared to the characteristic photon mean free path. For such a narrow tube, looking down into it shows a 'bright point' as we view the tube's photosphere that lies below, and is somewhat hotter, than the surrounding photosphere.] If the tube is wide, however, such as is the case for a pore or sunspot, the sideways heat transport cannot keep the atmosphere near the wall as hot as deep into the wall, causing a cooler and thus darker

wall around a dark interior, which is the manifestation of the penumbra and umbra of a sunspot. {A116} {A117} (A description of numerical models of radiative magneto-convection that reveals the quantitative details is given in Sect. I:8.2.1). Flux tubes typically rise into the photosphere with lower intrinsic field strengths, but the process of radiative cooling and hampered internal energy transport from below then lead to a 'convective collapse' by which a more or less isolated flux tube forms (from small faculae to large sunspots) with final field strengths of order 1 – 3 kG (larger at the center of larger structures). {A118}

{A116}
{A117}
{A118}

9.2 Heating and cooling of the solar outer atmosphere

The motions of the Sun's near-surface convection are a good fraction of the local sound speed, and thereby they generate a lot of acoustic power. Waves at frequencies below the acoustic cutoff frequency ω_a (defined in Activity 113) are trapped inside the Sun and can, in resonance patterns, set up one of millions of p -modes. But because the solar atmosphere above the surface has a temperature reversal into the chromosphere and corona, some degree of tunneling occurs, while higher-frequency waves can simply propagate upward through the atmosphere. All such waves steepen as they move into lower-density regions. The enhanced radiative losses during compression phases as well as dissipation through heating in the developing shocks together cause energy conversion from wave motion into thermal energy. Some of the heating of the solar chromosphere is due to such acoustic phenomena. However, the most pronounced non-radiative heating occurs at locations where magnetic field penetrates the solar surface.

Owing to the insulating atmosphere, the magnetic field of the Earth's dynamo couples to the terrestrial magnetosphere only through induction. The Sun's magnetic field, in contrast, is directly coupled from interior to atmosphere through the conduction of the plasma throughout. Consequently, the movements of the plasma in the convective envelope, from meridional circulation all the way down to sub-granular motions, drive processes in the solar atmosphere from the photosphere out to the distant heliosphere on time scales commensurate to the length scale involved, *i.e.*, from a decade down to minutes (Fig. 9.3).

The convective motions of the solar plasma, and the waves that these drive, couple into the magnetic field that threads the photosphere. The wave-like plasma motions transform into various magnetohydrodynamic wave types, while the convective motions 'braid' the higher field by the random walk of the footpoints 'line-tied' to the convective motions. In the higher atmosphere, these lead to wave interference and mode coupling, resonances, and field discontinuities (in a cascade of 'current sheets'). Add to that the insertion of new magnetic field emerging into the atmosphere as well as the removal from surface layers through reconnection between opposite polarities. All of these processes lead to high gradients in field and dynamics, and those to dissipation into heat (in the literature generally differentiated into low-frequency, braiding-dominated 'DC' mechanisms in contrast to higher-frequency, wave-dominated 'AC' mechanisms).

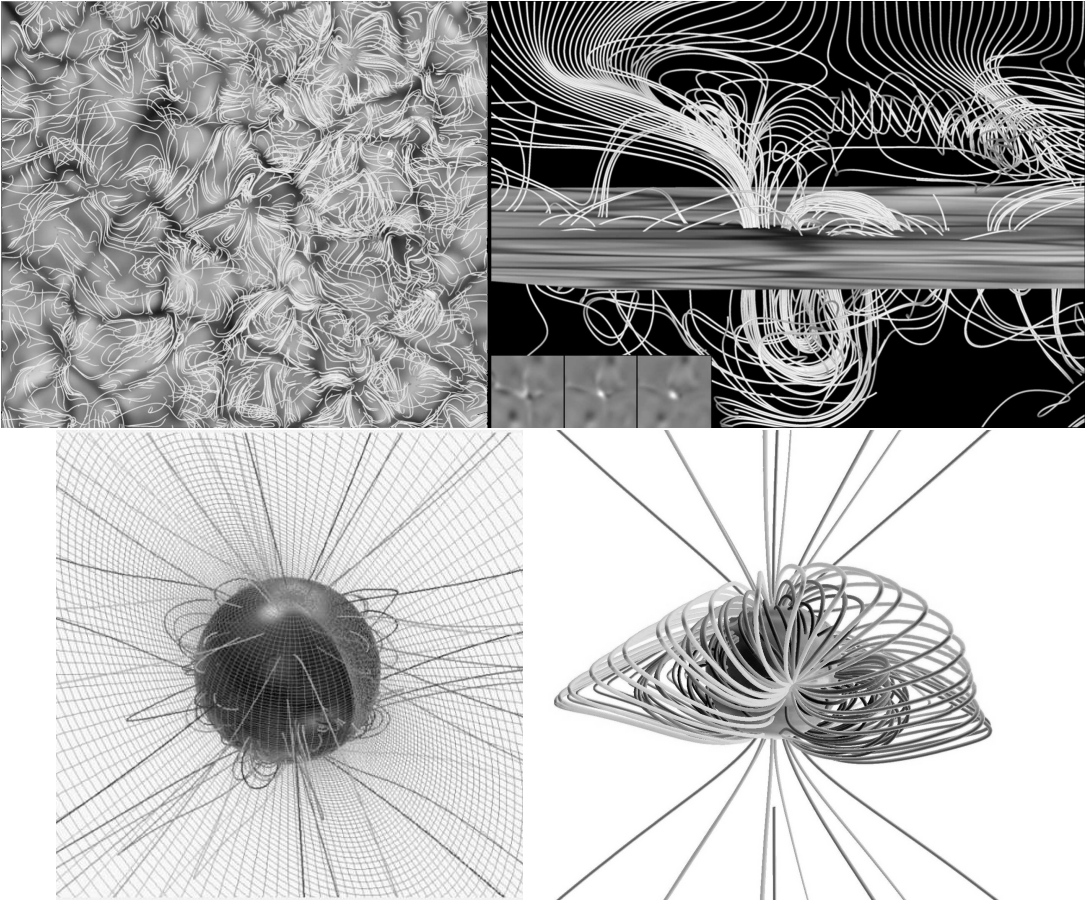


Figure 9.3: *Illustration of the multitude of scales in the solar magnetic field. The top panel shows a model computation of the magnetic field on the scale of the dominant convective motions at the solar surface, the 1000-km scale of the granulation (see also Fig. 9.1); the left panel is a top view of the solar surface with sample magnetic field lines overplotted, while the right panel shows a vertical cut through one of the convection cells to illustrate how the field in this model threads the surface sometimes multiple times, evolving on a time scale of a few minutes. The lower two panels show models of the global solar field, tracing field lines up to the cusps of the streamers that outline the topologically distinct regions of closed field and the field that is open to the heliosphere; this global scale field evolves on time scales of months to a decade. [Fig. I:1.2; sources for: [top](#) (from [Abbett, 2007](#)) and [bottom](#) panels.]*

It remains an open question as to which of the proposed heating mechanisms dominates (or more comprehensively the question of which mechanism dominates under what specific conditions), but observations make it clear that the magnetic field is both the conduit and the agent involved in heating the solar atmosphere.

These processes lead to the $\sim 20,000$ K chromosphere and at sufficient height to the multi-million degree corona. In order to understand why such high temperatures

arise, we need to “realize that the temperature of a plasma is set not only by the heat dissipated but also by the plasma’s ability to lose energy. {A119}

The coronal plasma has essentially three possible ways to shed energy: {A119}

1. Through optically thin radiation, mostly from carbon, oxygen, nitrogen, iron, and neon (and at lower temperatures from effectively thin hydrogen Lyman- α), given by

$$\Lambda(T_e) = n_e n_H f(T_e) \quad (9.1)$$

where n_e and n_H are the electron and total hydrogen densities and $f_{\text{rad}}(T_e)$ is a function of temperature dependent mainly on line emission and, at higher temperatures, on thermal bremsstrahlung. {A120}

2. Through thermal conduction along the magnetic field, with a (Spitzer) thermal conduction coefficient [25] {A120}

$$\kappa(T_e) = \kappa_0 T_e^{5/2} \quad (9.2)$$

3. The magnetically open corona can also lose energy through the acceleration of a solar wind. [...]

In short, when the plasma is dense, $n_e n_H$ is large and variations in the heat input can be dealt with by small changes in the plasma temperature which will remain on order 10^4 K or less (similar to the photospheric radiation temperature). Conduction on the other hand is very inefficient at these temperatures. However, the density drops exponentially with height, with a scale height of only some hundreds of kilometers for a 10^4 K plasma. The efficiency of radiative losses therefore drops very rapidly with height and *any* mechanical energy input will raise the temperature of the plasma. The temperature will continue to rise until thermal conduction can balance the energy input. Because thermal conduction varies with a high power of the temperature this does not happen until the plasma has reached 1 MK or so. Thus, we expect any and every heating mechanism to give coronal temperatures of this order [...]

The energy equation balances the thermal energy content of the plasma with energy input by heating (with a volumetric rate of ϵ_{heat}), loss by radiation, and transport through thermal conduction. Looking back at Eq. (3.6), most terms vanish in this approximation, while radiative losses, there not yet introduced, need to be added. Realizing that energy conduction occurs along the magnetic field, and with the cross section of a coronal loop is inversely proportional to the field strength ($A(s) \propto 1/B(s)$, with s the coordinate along the coronal field loop) we have:

$$\rho \frac{de}{dt} + p \nabla \cdot \mathbf{v} = \epsilon_{\text{heat}} - \frac{1}{A(s)} \frac{d}{ds} \left(A(s) \kappa \frac{dT}{ds} \right) - n_e n_H f_{\text{rad}}(T_e). \quad (9.3)$$

²⁵ Note the steep dependence on temperature of the thermal conductivity κ_{\parallel} in Eq. (9.2). In, say, a metal in terrestrial conditions κ is generally a constant, but in a low-density plasma in which Coulomb collisions dominate, this temperature dependence is a consequence of the increase in the characteristic mean-free path of the electron-ion collisions ($\lambda_{\text{mfp}} = v_{Te}/\nu_{ei} \propto T^2$, see Table 18.2) and the increase in the characteristic electron velocity ($\propto T^{1/2}$).

We can use the following rough approximations: $\kappa \approx 8 \times 10^{-7} T_e^{5/2}$ erg/cm/s/K and $f_{\text{rad}}(T_e) \approx 1.5 \times 10^{-18} T_e^{-2/3}$ erg/cm³/s for T_e in the range of 0.4 MK to 30 MK. The terms on the left of this equation are small in case the flows along the loop are sufficiently slow while any short-term variability in the heating should be relatively small compared to the internal energy content of the local plasma [for a loop in quasi-hydrostatic equilibrium]. Using that approximation along with Eq. (3.5) describes the general appearance of any slowly evolving coronal loop (but note that the radiative losses should not be approximated as above once looking into the 'transition region', *i.e.*, at the base of coronal loops where the temperature transitions from coronal to chromospheric values). Eq. (9.3) can be used to estimate, for example, the conductive time scale τ_{cond} (the ratio of thermal energy to the rate at which conduction over a thermal gradient transports energy) or the radiative time scale τ_{rad} (the ratio of internal energy to the time scale of radiative energy loss). The ratio of these two shows the conditions in which conduction is more important than radiation, or vice versa. This is most useful by combining these time scales with a relation that emerges from the modeling of quasi-static loops as a whole, made (by Rosner *et al.* (1978)) in the approximation of a constant cross section:

$$T_{a,6} \approx 2.8(n_{a,10}L_9)^{1/2} \quad ; \quad T_{a,6} \approx 7.3(\epsilon_{\text{heat}}L_9^2)^{2/7}, \quad (9.4)$$

for a loop apex temperature of $T_{a,6}$ MK, half length L_9 (in units of 10^9 cm) and apex density $n_{a,10}$ (in units of 10^{10} cm⁻³). Using the left-hand equation yields:

$$\frac{\tau_{\text{cond}}}{\tau_{\text{rad}}} = \frac{0.3}{T_{a,6}^{1/6}}. \quad (9.5)$$

This shows that for coronal loops as a whole, conduction tends to be somewhat more important than radiation in their response to energy input fluctuations, but that both need to be involved in modeling. {A121}

9.3 Magnetic activity and atmospheric radiation

“The magnetic field in the solar atmosphere is associated with the transport and dissipation of non-thermal energy; about one part in 10^4 of the Sun’s luminosity is radiated from the quiet chromosphere, and an order of magnitude less than that from the corona. For the most active stars [– or, largely equivalently, for the youngest stars (see Ch. 12) –] in contrast, a total of about 1% of the luminosity can be converted into outer-atmospheric heating. [...]

When measured for relatively large areas – *i.e.*, when averaging over an ensemble of similar atmospheric components – the radiative losses from the outer atmosphere increase with the [unsigned] magnetic flux density at the base. A variety of heating mechanisms has been proposed for the chromosphere, the corona, or – for many scenarios – both. Non-thermal energy is likely deposited into the corona in the form of electrical currents that are the result of the motion of the field’s photospheric footpoints that are moved about by convective flows. The cascade of such currents to smaller

scales, and the details of the eventual dissipation continue to be debated, as is the relative importance of wave dissipation. For the chromosphere, the situation is even less clear: waves of both predominantly magnetic and predominantly acoustic nature have been proposed to play a dominant role, but numerical simulations suggest that electrical currents and reconnection phenomena contribute if not dominate. [...] With the high degree of structure in the magnetic field within the chromosphere, different mechanisms may dominate in different environments. [...]

The chromospheric and coronal emissions [scale essentially] as power laws with each other and with the average magnetic flux density of the underlying field: $F_i \propto \langle |\mathbf{B}| \rangle^{b_i}$. The power-law index b_i between radiative and magnetic flux densities appears to be an essentially monotonic function of the formation temperature of the radiation observed, increasing from about 0.5 for chromospheric emission from $\sim 15,000$ K plasma to just over unity for X-ray emission from ~ 3 MK plasma; these power laws hold over a contrast in X-ray surface flux densities from $100\times$ below the quiet Sun to $100\times$ above the active Sun, spanning a total of nearly five orders of magnitude (much of which will be covered by the Sun over its lifetime [... (see Ch. 12)]).

The chromospheric and coronal heating of the Sun and of stars like the Sun are a function only of the magnetic flux density [...]. In other words, once the magnetic field is in the stellar atmosphere, the dissipation of that energy and the distribution of the energy over the outer-atmospheric domains are independent of stellar properties: stars with masses from about $0.09 M_\odot$ (equivalent to ≈ 90 Jupiter masses) to a few solar masses, with radii of $< 0.5 R_\odot$ to $> 50 R_\odot$, and with coronal X-ray flux densities ranging over a factor of 10^5 all adhere to the same scaling relationship within the measurement uncertainties and the intrinsic stellar variability.”

Chapter 10

Evolution of stars, activity, and astrospheres

Chapter topics:

- Stellar evolution from formation to end of life
- Scalings for stellar magnetic activity with age and rotation rate
- Activity cycles
- Stellar winds and astrospheres over time

Key concepts:

- Spectral type
- T Tauri, main-sequence, red giant
- White dwarf, supernova, neutron star
- Astrospheric hydrogen wall

10.1 Evolution of stars

This section summarizes stellar evolution in the context of heliophysics, *i.e.*, for stars like the Sun (defined below), stopping short of the final evolutionary phases (white dwarfs and neutron stars, as well as black holes and the supernovae on the path to their creation). “Here, we introduce only some principles, terminology, and properties needed within the present context:

In the strict definition, a star is a self-gravitating body in which gravity is countered by gas pressure that is maintained by nuclear fusion balancing the loss of thermal energy through the stellar surface. Before a star forms, a contracting cloud forms opaque but still nebulous Herbig-Haro objects associated with collapsing clouds, and then pre-main sequence T Tauri stars (the subject of Ch. 11). Once a balance between contraction and internal pressure has been found, stars are on the ‘main sequence’, where they spend by far the largest fraction of their lifetime. The term main sequence refers to the well-defined clustering of stars in any one of a variety of Hertzsprung-Russell diagrams, in which the stellar luminosity or a logarithmic equivalent (the

III:2.3.1

[absolute] 'magnitude') is plotted against the surface temperature or some filter ratio that measures the relative brightness in differently-colored filters (often the $B - V$ value is used, referring to the [absolute] Blue and Visible magnitudes, respectively). Examples of such brightness-color diagrams (often referred to as H–R diagrams) are shown in Figs. 4.2 and 10.1(left). Stars are generally characterized by their color, or an equivalent descriptor of their spectral properties called 'spectral type' (see the top of Fig. 4.2). [Stars on the high-temperature, left side of the HR diagram are called 'early' and those toward the right side 'late'; surface temperature and mass decrease monotonically along the main sequence through the spectral type series: O, B, A, F, G, K, M.]

When stars run out of hydrogen fuel in their cores, they evolve off the main sequence in the H-R diagram (see Fig. 10.1(left)) to become giant or supergiant stars. Their eventual fate depends on their mass: low-mass stars fade into ever-cooling white dwarfs, heavier stars eject some of their outer layers, while very heavy stars become supernovae and leave neutron stars or black holes behind. Objects that are too light to sustain hydrogen fusion during any stage of their evolution (although they may have phases with deuterium fusion) are called 'brown dwarfs', which have masses of [$\lesssim 0.07M_{\text{Sun}}$ or $\gtrsim 75M_{\text{Jupiter}}$]. These cool very slowly, taking billions of years to lose their thermal energy. Even cooler objects merge into the realm of the (heavy) jovian planets.

Before stars reach the main sequence, they migrate through the H-R diagram from the top right (as red giants), initially moving down (to become red subgiants), then curving towards the main sequence (increasing their temperature to become orange, yellow, white, or even blue stars) with a much weaker change in their luminosity than during their initial contraction phase [(see Figs. 10.5 and 11.6)]. All stars cooler than a surface temperature of about 10,000 K [(roughly from spectral type late-A)] have a 'convective envelope,' or mantle, immediately below their surfaces, and the coolest stars, be they young or old, are fully convective. All of these stars make up the ensemble of cool stars, [all of which display some degree of magnetic activity.] Beneath the convective mantles, if any, lie the 'radiative interiors' in which energy is transported diffusively by photons; fusion occurs within this interior in the deep 'core' of main-sequence stars (see Fig. 4.1 for a graphic comparison – not to scale – of internal structure along the main sequence). {A122}

{A122}

The evolutionary time scales are a sensitive function of mass. A star with a mass of, say, three solar masses evolves towards the main sequence in a few million years[, exhibiting magnetic activity except in the final birth phase near the main sequence.] On the main sequence, where they stay for 'only' ~ 0.4 Gyr, these stars have no magnetic activity, and they only resume magnetic activity after they evolve off the main sequence when they develop convective envelopes again for another 100 million years or so, until they rapidly evolve into what eventually [becomes a white dwarf after ejecting much of the outer layers; a star heavier than about nine solar masses ultimately] explodes as a supernova. A star of solar mass [(M_{\odot})] remains magnetically

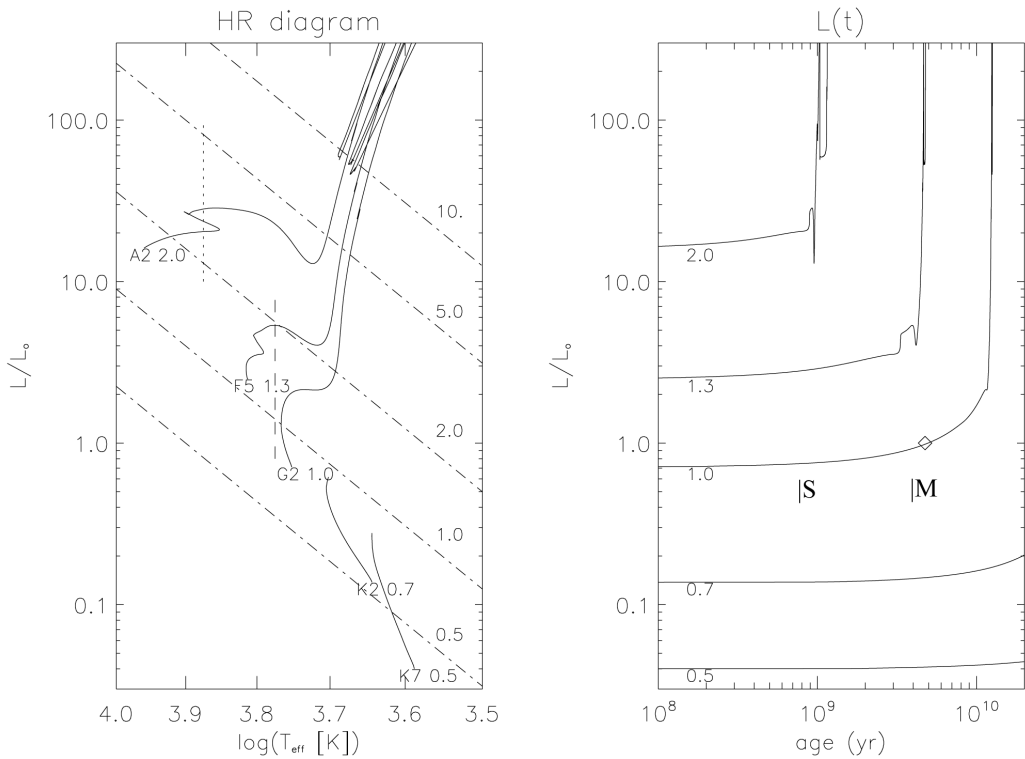


Figure 10.1: Evolutionary diagrams for luminosity, surface temperature, and age from the mature, main-sequence phase onward. The diagram on the left relates the stellar luminosity L (in present-day solar units) with the surface effective temperature (T_{eff} ; K) in a Hertzsprung-Russel diagram (for an initial helium abundance of $Y = 0.2734$ and 'metal' abundance (everything heavier than helium) of $Z = 0.0198$). Evolutionary tracks start on the 'zero-age main sequence' (ZAMS), and are labeled with the spectral type on the main sequence and the stellar mass (in solar units). The dashed line segment indicates where dynamo action reaches its full strength; for shallower convective envelopes (warmer stars), the activity level weakens until it has dropped by a factor of 100 at the dotted line segment relative to a Sun-like star at the same angular velocity. The slanted dashed-dotted lines indicate stellar radii, with labels in solar units. The diagram on the right shows the evolution of the stellar luminosity with stellar age (yr since ZAMS). The diamond shows the present-day Sun (see Fig. 10.2 for details on the Sun's red-giant phase). The approximate ages for which the oldest fossils of single-cell microbial life (S) and multi-cellular plants and animals (M) have been found on Earth are indicated (see Ch. III:4). [Fig. III:2.9]

active to some degree throughout the ~ 10 Gyr that it spends on the main sequence, and during the subsequent ~ 0.8 Gyr giant phase (its maximum radius may reach ~ 0.99 AU, and the maximum luminosity is likely to be around $5,200 L_{\odot}$) until it evolves into an ever-cooling white dwarf [after phases as giant star, ending in a series of pulses as the star gasps for fuel, during which time an appreciable fraction of its

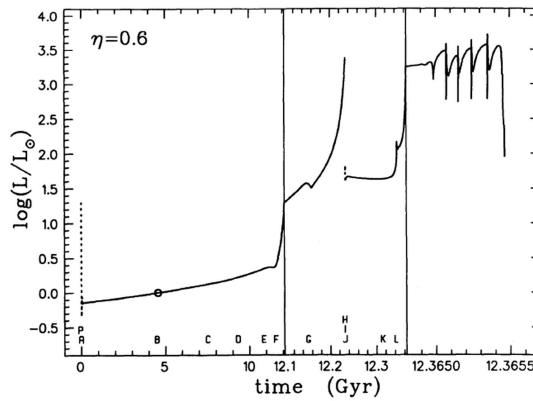


Figure 10.2: Evolution of the luminosity of the Sun over its full life span. The first 12 billion years show the gradual brightness as hydrogen is depleted in the core of the Sun’s main-sequence lifetime as a hydrogen-fusing star (cf. Fig 10.1). The large luminosity increases and pulses that follow this period include both the red-giant and asymptotic giant branch (AGB) phases when the Sun swells in size and loses appreciable mass to space. [Fig. III:4.5; source: Sackmann et al. (1993)].

outer layers is ejected (compare Fig. 10.2)]. An $0.2 M_{\odot}$ M9 brown dwarf takes ~ 1 Gyr merely to contract to the main sequence, changing little in effective temperature as it descends in the H-R diagram.

During this evolution, the stellar luminosity and its associated color ([characterized by the ‘effective temperature’, and with it the spectral irradiance]) continually change. Examples of evolutionary changes are given in Fig. 10.1 for stars from $0.5 M_{\odot}$ to $2.0 M_{\odot}$.

The young Sun should have been some 25% fainter at the start of the Archean Eon (at $\sim 3.8 \times 10^9$ yr ago, when life is presumed to have originated) than the current mature Sun according to stellar-evolution models. This should have resulted in a much cooler Earth, covered in ice. Yet, geological records show that there was liquid water on Earth even in the first billion years of its existence. How this could happen continues to be studied. The greenhouse effect as a result of the high concentration of carbon dioxide may have compensated the lower energy input from the young Sun. Alternatively, the Sun may have been significantly more massive, and therefore brighter, early in its life; if there has been substantial mass loss in a strong wind in the first billion years, this paradox would be resolved. [Analyses suggest that it is possible] that a more massive young Sun (brighter, and with somewhat tighter planetary orbits) is compatible with the present internal structure for a Sun with a mass up to about 1.07 present solar masses. [One such model starts] with a mass of 1.07 solar masses, has an initial irradiance at Earth that is 5% higher than at present (compared to 50% lower for the Standard Solar Model), would subsequently decrease to about 10% lower, and then increase again to the present value.” {A124}

10.2 Stellar activity and its evolution

10.2.1 Overall activity level

“The defining properties of stellar magnetic activity are the existence of variable coronal (X-ray) and chromospheric (UV-optical) emissions. These characteristics are observed for a wide variety of stars [(indicated in Fig. 4.2). ...] In single stars or in wide binaries, the activity level measured by emission from the chromospheres or coronae of these stars, or by the coverage by starspots, increases monotonically with increasing angular velocity to rotation periods as short as a few days. Rather than using the rotation period per se, however, studies of the rotation-activity relationships frequently use the Rossby number:

$$N_R = \frac{v_t}{2\Omega \sin(\theta)L_t} \sim \frac{P_{\text{rot}}}{\tau_{\text{conv}}}, \quad (10.1)$$

which is defined such that it measures the relative importance of the inertial to Coriolis forces ($\mathbf{v} \cdot \nabla \mathbf{v}$ and $\boldsymbol{\Omega} \times \mathbf{v}$, respectively) acting on a parcel of plasma of scale L_t moving with velocity \mathbf{v}_t in a rotating system with angular velocity Ω ; the Rossby number is an important metric in the theory of astrophysical dynamos, see around Eq. 4.2 and also Activity 52]. The central expression is a definition that includes the latitude, which is often neglected when estimating the global effect of rotation. When, moreover, the convective turnover time scale $\tau_{\text{conv}} = \pi L_t / v_t$ for characteristic length scales and velocities of the deepest (largest and slowest) convective motions in a stellar convective envelope is introduced, the commonly used final expression results. When using the Rossby number [estimated for the deepest layers of the convective envelope], the activity is seen to increase with rotation up to a value of $N_R \sim 0.1$ (see Fig. III:2.11). ^[26]

For even more rapidly rotating stars, the activity reaches a saturation level, and for stars with rotation periods of only a fraction of a day, supersaturation sets in, with

²⁶ A cautionary intermezzo: Sect. 9.3 gives power-law scalings between radiative losses from chromospheres and coronae over stellar surface areas with mean magnetic flux densities over these areas (which hold approximately without changes for areas up to entire hemispheres). The values of the power-law indices in these relationships depend on the formation temperatures of the spectral lines or bandpasses used (thus, for example, steepening towards higher-energy X-ray channels), while published values also depend on the correction for a reference level (there is a minimum or ‘basal’ level of chromospheric emission that needs to be subtracted first but different authors use different corrections). This dependence on the details of the diagnostics used are one cause behind the somewhat different power-law scaling between coronal and chromospheric radiative losses you find in the literature. There are other reasons why you may find other approximate parameterizations. For one thing, although the scaling in rotation-activity diagrams between a relative brightness in terms of luminosity or surface flux density ($L_i/L_{\text{bol}} \equiv F_i/F_{\text{bol}}$) versus Rossby number works fairly well, it does not work perfectly, and other authors, using other stellar samples, might prefer using F_i versus P_{rot} . As long as the stellar sample contains stars of rather comparable internal properties, the choice of metric does not matter, but for more diverse samples, scalings with these properties matter – no simple multiplicative scaling seems to lead to a single tight rotation-activity relationship for all cool stars. Other reasons for differing results from different studies include the fact that the relationships are not simple power laws and fits thus depend on the parameter range covered in stellar samples, and, of course, uncertainties in models for, *e.g.*, stellar ages, and intrinsic stellar variability combined with relatively small samples. You could review, for example, the study by Booth *et al.* (2017) for more discussion and for references.

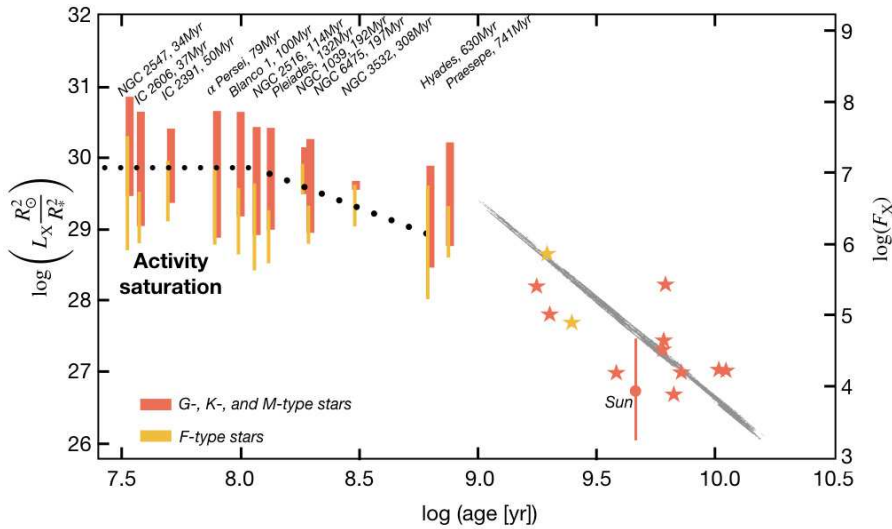


Figure 10.3: Relationship between stellar coronal X-ray brightness (in a passband from 6 \AA to 60 \AA , expressed as a luminosity scaled to the equivalent solar surface area on the left, and as a surface flux density on the right) versus age. Bars show data for open clusters: in orange for the range of G-, K-, and M-type stars observed, and in yellow for the generally less active F-type stars. Individual stars with ages above 1 Gyr are shown by stars, and the Sun as a filled circle (with its range over the solar cycle). The relationship shown by the gray line segment is a fit by Booth et al. (2017). The dotted line is a relationship for stars with $(B - V) \in [0.56, 0.79]$. [After Booth et al. (2017) and references therein.] For a color version of this figure, see arXiv:2001.01093.

activity decreasing with increasing angular velocity. It appears that when proceeding towards shorter rotation periods, the coronal activity saturates first, followed by chromospheric activity, and finally by starspot coverage. This has led to the suggestion that different processes set in at successively shorter rotation periods: centrifugal stripping (see Activity 14) of the high corona, saturation of the level to which non-thermal heating can be extracted from the near-surface convection or deposited into the chromosphere, and finally saturation of the dynamo process itself possibly by the coupling of the magnetic field and the plasma flows (see Section 4.5) or because the Coriolis force changes the large-scale circulation patterns that are involved in efficient dynamo action.

Main-sequence stars warmer than the Sun have shallower convective envelopes. Their magnetic activity is markedly suppressed compared to cooler stars with the same rotation period. This has been argued to be either because of the shallowness of their envelope or because of the short average turnover time of convection resulting in little influence of the Coriolis force that otherwise would introduce a preferential direction into the system. By spectral type F2 significant magnetic activity is observed, which rapidly increases in efficiency towards G0 as the convective envelope becomes deeper and the time scales of deep convective motions approach or exceed the [characteristic

mean] rotation period.

Magnetic fields are observed along the main sequence as far down the spectral scale as we have been able to identify and apply Zeeman sensitive spectral lines, *i.e.*, down to at least M9.5. At that point we have already reached the brown dwarfs, *i.e.*, astrophysical objects that are too small to have sustained hydrogen fusion in their cores.

For stars above the main sequence, activity is seen both in stars that have recently formed and are still contracting to the main sequence (pre-main-sequence stars, which include fully convective T Tauri stars) and stars that have exhausted their core hydrogen supply and are moving away from the main sequence, once again en route to a fully-convective giant phase, now sustained by nuclear fusion of helium and heavier elements in either their core or in shells surrounding a burned out core.

During their main-sequence phases, cool stars exhibit a variety of activity patterns. A clear activity cycle, as exhibited by the Sun ever since the Maunder minimum [(a period from about 1645 CE to 1715 CE during which sunspots were very infrequent and sometimes absent for multiple years)], is relatively rare, even for solar analogs: only roughly 60% of solar-like stars show a clear activity cycle, and the reasons for this and for those that set the cycle duration are still being researched (see Fig. 10.4).

A few Sun-like stars in the solar neighborhood are so-called flat-activity stars, showing no clear cycle at all, yet they rotate with a period similar to that of the Sun. Such stars have been argued to be in a state similar to the solar Maunder minimum [...]"

10.2.2 Flares

“Solar flares define power laws in spectra of frequency, N_f , versus peak brightness or overall energy, E_f . The spectrum of $N_f(E_f)$ can be approximated by a power law $N_f(E_f)dE_f \propto E_f^{\alpha_f}dE_f$ with $\alpha_f \approx -2$; the value of α_f reported in the literature depends on the instrument and wavelengths used, and on the sample used (active region flares, EUV quiet-Sun brightenings, etc.), and ranges from about -2.4 to -1.5 . The flare energies studied range from $\sim 10^{24}$ ergs to $\sim 10^{32}$ ergs [for the present-day Sun].”

The relatively small solar flares drown into a quasi-steady background emission if the Sun is observed as a star. It is not surprising, therefore, that stellar flare spectra are limited to large flares that stand out above the surface-integrated X-ray fluxes. [O]bservations of F through M type main-sequence stars [reveal] ubiquitous power laws with power-law indices near $\alpha_f = -2$ (with a possible mild steepening from cool to warm stars). Flare X-ray [energies for some cool stars] range up to 10^{35} ergs, *i.e.*, up to ~ 1000 times brighter than the largest solar flares, with no evidence for a cutoff energy. [For the more active stars in the population,] flare frequencies for energies exceeding 10^{32} ergs scale proportionally to the time-averaged X-ray emission, saturating as the X-ray activity saturates, and contribute some 10% of the total X-ray luminosity. [... A]dopting $\alpha_f \equiv -2$, and using a characteristic solar X-ray luminosity [around cycle maximum] of $L_{X,\odot} = 3 \cdot 10^{27} \text{ erg s}^{-1}$, supports a scaling for the frequency of large flares with energy E_f exceeding a threshold value of $E_{f,32}^*$ (in units of 10^{32} ergs, characteristic

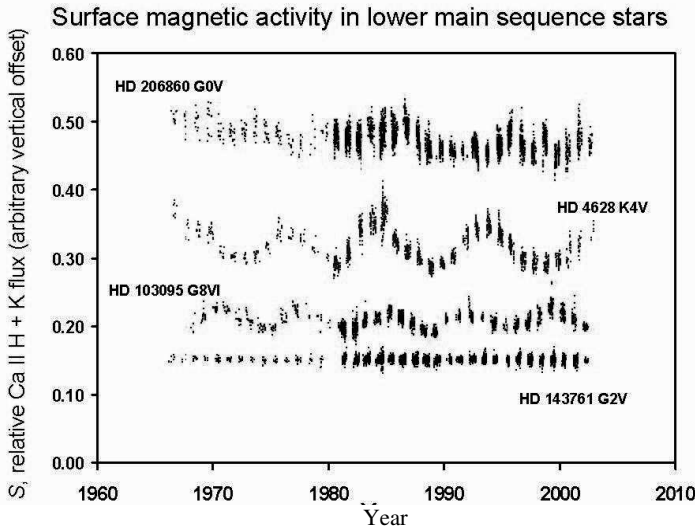


Figure 10.4: Examples of chromospheric activity cycles (as observed in the H and K resonance lines of singly ionized Ca, or Ca II H+K). Surface magnetic activity records of four stars on or near the lower main sequence from a survey begun by O.C. Wilson in 1966 at Mount Wilson Observatory. [The ratio of the flux in the emission cores of singly-ionized calcium lines in the violet (the Fraunhofer H and K lines at 393.3 and 396.8 nm) and photospheric flux in nearby regions of the spectrum, necessarily integrated over the unresolved stellar disks, is used as a proxy for stellar magnetic activity.] The strength of the H and K fluxes increases as the coverage by and intensity of magnetic surface features increases; on the Sun the H and K fluxes vary nearly in phase with the sunspot cycle. The four records show the counterpart of the Sun approximately 2 billion years ago (upper curve, HD 206860; $P_{\text{rot}} = 4.7$ d), and then three Sun-like stars, which show records similar to the present-day Sun, HD 4628 ($P_{\text{rot}} = 38$ d), HD 103095 ($P_{\text{rot}} = 31$ d, or $P_{\text{rot}} = 60$ d) and HD 143761 ($P_{\text{rot}} = 21$ d). Both HD 4628 and HD 103095 display decadal periodicities similar to the sunspot cycle. The star HD 143761 may be in a state like the Sun’s Maunder Minimum. The star HD 103095 is an extremely old (approximately 10 billion years) metal deficient subdwarf, and is shown as an example of the persistence of decadal magnetic activity cycles in a star of extreme age compared to the Sun. The spectral types are listed next to each record’s star name. Arbitrary vertical shifts in the average value of the H and K relative fluxes have been applied to show the records without overlap; the offsets are 0.0 (HD 143761), 0.02 (HD 103095), 0.09 (HD 4628) and 0.15 (HD 206860). [Fig. III:2.12]

of a large solar flare) of

$$N_f^*(E_f > E_{f,32}^*) \approx 0.26 \left(\frac{L_X}{L_{X,\odot}} \right)^{0.95 \pm 0.1} \left(\frac{1}{E_{f,32}^*} \right) / \text{day}. \quad (10.2)$$

[Note that this relationship derived from observations of very active stars lies some two orders of magnitude above the cycle-averaged frequency distribution observed for the time-average present-day Sun. This mismatch remains a mystery, as does the problem

of establishing whether flares of $> 10^{33}$ ergs can still occur on the current Sun, or whether that was only possible in the distant past. For young, active stars we can use the above expression to find that when] the Sun was only 0.1 Gyr old [...] flares with energies exceeding 10^{35} ergs would likely have occurred once per week, and those with energies exceeding 10^{38} ergs may have occurred about once per decade. {A125}

It appears that quiescent activity and flaring activity on stars scale with each other, as also seen in the rise and fall of quiescent and impulsive heating through the solar cycle. One result of this is that more active stars have a stronger high-temperature coronal component, so that the effective X-ray 'color temperature' or spectral hardness increases with activity. It also appears that larger flares are associated with higher characteristic temperatures, going from solar micro-flares to large flares on very active cool stars [...]" {A125}

10.2.3 Rotation rates

"The primary stellar property that determines the level of magnetic activity is the rate of rotation. The rate at which a star spins is influenced by the evolutionary changes in (1) the moment of inertia, (2) the angular momentum loss through a stellar wind, and (3) the angular momentum exchange in tidally interacting binaries. III:2.5

(1) The evolutionary changes in the global moment of inertia are readily computed from stellar evolutionary models (see the example in Fig. 10.5). These changes amount to several orders of magnitude during the first tens of millions of years of a star (when magnetic coupling with surrounding accretion disks are also important, see Ch. 11) and the final fraction of a Gyr, but during the main-sequence phase, they are generally negligibly small compared to the loss of angular momentum through the outflowing wind.

(2) The outflowing stellar wind is coupled to the stellar magnetic field, which introduces a relatively long arm over which the stellar wind can extract angular momentum, so that it eventually carries far more than its own specific angular momentum [(see Sect. 7.2.1)]. The torque on the star is applied by the magnetic field into the stellar interior, and the rapid convective motions cause the angular momentum to be extracted from the entire convective envelope. How much radial and differential rotation this sets up within the convective envelope remains under active study, but the argument is generally made that the convective envelope spins down as a whole. The coupling to the radiative interior underneath it occurs somehow by coupling to a primordial field, wave exchange, or slow flows. In rapidly evolving stars with shallow convective envelopes this may lead to a (temporary) strong differential rotation between envelope and interior. For the Sun, however, helioseismic measurements have shown that interior and envelope rotate at very nearly the same rate, with the interior matching the angular velocity of the differentially rotating envelope at a latitude of about 30° (see Fig. 4.7b).

The angular momentum loss leads to a spin down relative to the evolution in which only the total moment of inertia I is evolved as the star ages. During the main-sequence phase, I changes little (Fig. 10.5) so that most of the change of P_{rot} with age [is associated with magnetic braking. {A126} After the first Gyr when {A126}

{A125}

III:2.5

{A126}

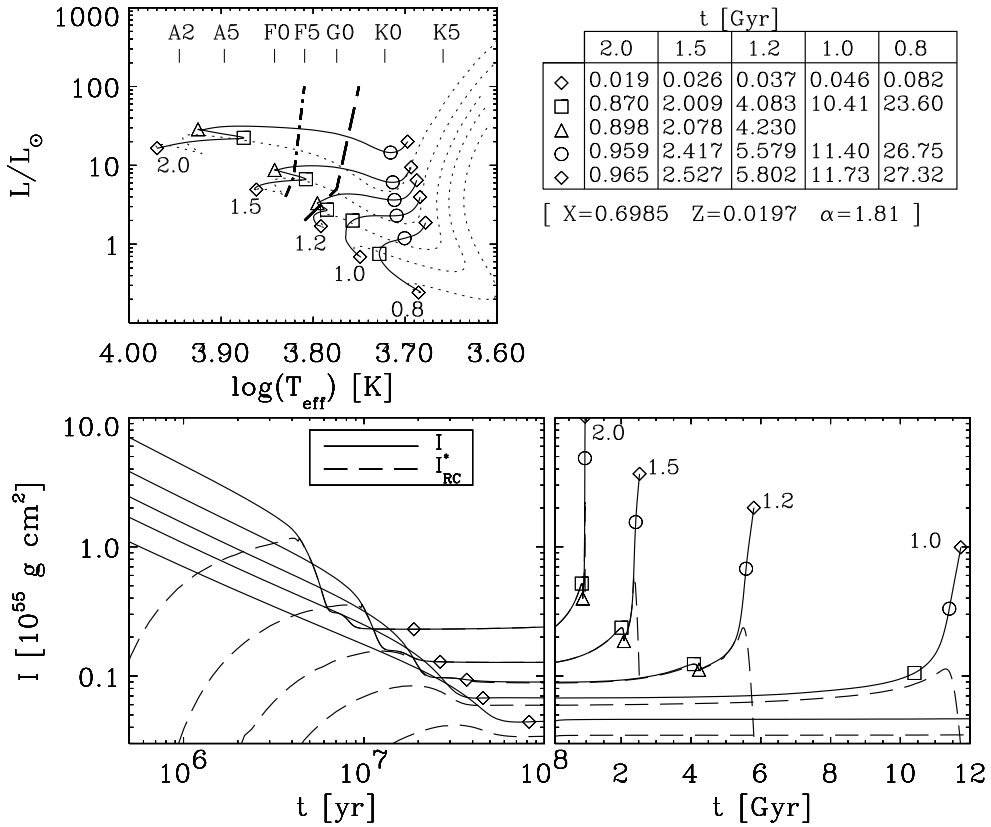


Figure 10.5: Evolutionary tracks (top panel) for late-type stars of various masses, from the pre-main sequence to main sequence (dotted curves in the top panel), and from there to the base of the giant branch (solid curves in the top panel). The diamonds indicate the zero-age main sequence (at the lower-left end of the solid curves) and the end of model computations. Stellar masses are given in units of the solar mass. The dashed-dotted curve marks the onset of envelope convection. Ages at selected points along the tracks are listed in the table in the top right of this figure for stellar masses indicated in the top row. The evolutionary variations of moments of inertia of the entire star (solid curves) and of the radiative interior below any convective envelope (dashed curves) are shown in the lower panels. [Fig. III:2.15]

dynamo saturation is important, the dependence of rotation rate on age t for Sun-like stars can be approximated by what is often referred to as the Skumanich law:]

$$\Omega_{\text{rot}} \propto t^{-1/2}. \quad (10.3)$$

For the present-day Sun, the time scale of angular momentum loss is ~ 1 Gyr. [...]

{A127}

{A127}

(3) [...] Even though the Sun is a single star, there are interesting lessons to be learned from close binaries. [...] It is the population of tidally-interacting binaries [...] that unambiguously showed us that activity is related causally to rotation, and only indirectly to stellar age [...] the combination of angular momentum loss by

magnetic activity of one or both of the binary components and their tidal interaction drains the system of angular momentum, which results in tightening of the orbits and that, in turn, to a spin-up of the stars' rotation rates and an increase of activity level with advancing age, contrary to what happens in single stars (see Ch. 7).

At present, there are no instruments capable of detecting stellar CMEs, leaving us only – for the time being, at least – with the Sun as the guiding star, and with assumptions for scalings of CME properties for other stars with different properties and ages.

10.2.4 Stellar infancy: birth to the zero-age main sequence

“Although the age range in this first age category is only a percent or so of the total main-sequence lifetime of the star, there are several important steps to the life of the star which occur during this time. [...] For this section we concentrate on ages ranging from stellar birth to the time it takes the star to reach the zero-age main sequence, at which point the star is in stable hydrostatic equilibrium, and there is negligible contribution to the stellar luminosity from any accretion-related processes. This time scale is a function of stellar mass, being approximately 50 Myr for a solar-mass star, and longer than 160 Myr for a star of $0.5 M_{\odot}$ or less. For the purposes of discussion, and because stellar ages can be uncertain by factors of two or more, we include stars of ages up to ~ 100 Myr. [...]

Magnetic activity in general is at a high level in these young stars because of their rapid rotation, but the interpretation can be confused by other processes occurring in the system which have similar observational characteristics to magnetic reconnection processes [as discussed in Ch. 11. ...] Flares some 100-1000 times more energetic than the biggest solar flares occur roughly once a week on these young, rapidly spinning stars. [...] Over slightly longer evolutionary time scales there is a decrease in flare rate.”

10.2.5 Stellar teenage years: ZAMS - 1 Gyr

“At this phase in a star's evolution, rapid rotation is still an important factor, although it has declined since the star's youth. According to [Eq. (10.3), a 'teenage'] solar mass star would have a rotation rate that is only a factor of 2–7 above the Sun's present-day rotation; activity that accompanies the faster rotation should be enhanced, but below the extremes represented by the youngest stars. [G- and K-type main-sequence stars spin down faster than their M-type counterparts (see Fig. 4.2 for their properties),] so by these ages, M dwarfs dominate the samples of active stars. The general decrease in activity levels compared to the extremes seen at young ages means that capturing flaring activity on stars of this age range (with the exception of M dwarfs) is more difficult to do systematically, and consequently there is a heavy bias towards the lower mass end in observations of flares on stars of this age range. The fact that M dwarfs are the most common type of star based on mass functions also contributes to this bias. There are open clusters (notably the Hyades at an age of ~ 800 Myr) which are nearby enough for sensitive studies of explosive events, although they are spatially dispersed compared to star forming regions and this makes it difficult to capture more than one or two objects in the field of view of typical astronomical

telescopes.

The possible dependence of stellar flare rate on evolutionary age can be explored by combining scaling relations between flare frequency and underlying coronal emission with those relating coronal and chromospheric emission, and others describing the decline of chromospheric emission with time. [The empirical scaling in Eq. (10.2)] between coronal flare rate and underlying stellar X-ray luminosity [appears to hold also for stars] with ages in this age range[. . . There are] scalings between coronal emission and different chromospheric emission indicators for cool main-sequence dwarfs, $L_X \propto L_{\text{chrom}}^y$ where $y \sim 1.5$ for C IV emission [from triply-ionized carbon typical of the transition region], $y \sim 2$ for Ca II HK emission and $y \sim 3$ for Mg II h emission[, the latter two being characteristic of singly-ionized Ca and Mg which are strong emitters from the chromosphere. . . Chromospheric emission declines with rotation rate, which can be transformed into a relationship with stellar age using Eq. (10.3) to be roughly

$$L_{\text{chrom}} \propto t^{-1/2}. \quad (10.4)$$

Simplifying] these relations to

$$N_f(> E_{f,c}) \propto L_X, \quad (10.5)$$

$$L_X \propto L_{\text{chrom}}^y, \quad (10.6)$$

where y takes on different values depending on the chromospheric emission being considered, and [with Eq. (10.4) ^[27]], suggests that the flare rate may decline with age anywhere from $N_f(> E_{f,c}) \propto t^{-0.75}$ to $N_f(> E_{f,c}) \propto t^{-1.5}$. [The] above scaling between flare rate and coronal luminosity cannot be used to 'correct' the flare rate of [young, active stars] to the solar flare rate via their coronal luminosity. This suggests a breakdown in the validity of a scaling relation approach [at ages, and commensurate rotation rates, between the 'teenage years' and the Sun's present age].

Single G stars in this age range exhibit flares at least as powerful as the largest solar flares, but occurring several times per day. [One example is κ Cet, a G5V star with an age of 300–400 Myr that exhibits 6.7 flares per day with energies of at least 10^{32} erg. The fraction of time that stars are clearly flaring in their coronal X-ray emission tends to decrease with age, from approximately 10% around 1 Myr to about 3% approaching 1 Gyr (see Fig. IV:2.8).]

10.2.6 Stellar adulthood: 1-5 Gyr

“The Solar System, and thus the Sun's, age measurement of 4568 Myr fits squarely within the 'stellar adulthood' phase of its life. Detections of flares on stars in this age

²⁷ Note that the power laws shown in this chapter relating stellar activity, wind, and rotation are not all consistent with each other. This is not all attributable to the sensitivity to the diagnostics used (see Activity 26), which tells us something is missing in how these various parameters really scale with each other, but observations and/or theory have yet to reveal what it is that is missing. Part of the discrepancy is likely the use of different stellar samples in different studies; compare, for example, the slopes of the power-law fits in Fig. 10.3: the slope for $L_X(t > 800 \text{ Myr})$ differs depending on the age range of the stars that is included in a study. Another reason may be a change in the dependence of the loss of mass and angular momentum somewhere around the age of 1 Gyr – come back to this after reading Sect. 10.3.2.

range are much fewer. The decline of flaring with age is generally assumed to follow the trends of other activity indicators, but whether this is in fact the case is an open question. Evidence that magnetic activity may not decline monotonically at Gyr ages comes from a few sources: [...] chromospheric activity in M dwarfs [may] not decline in the 1-10 Gyr range as fast as predicted based on extrapolating from objects with ages < 1 Gyr. [For stars older than a few Gyr, it appears that there is no evidence for further decay in quiescent chromospheric activity after the major decline in activity seen] in objects at ages of the Hyades and earlier (0.6 Gyr), [while] for clusters of about 2 Gyr and older (up to 4.5 Gyr) the same activity level was seen. [...]

Because the flare rate is expected to be low on older stars, a systematic search for flares in an older stellar population needs a large number of stars, and involves a relatively long stare coupled with fast cadence to detect and resolve the flaring emission from any other variability. The *Keplers* spacecraft's exquisite photometry can be re-purposed from finding evidence of transiting extrasolar planets around stars to looking for rare short-timescale flaring events on the stars themselves. [Energetic flares have been found in G-type main-sequence stars, even on apparently single solar-type stars] with rotation periods of 21.8 and 25.3 days, near the solar value, and thus approximately solar age. The energetics of these flares is large, with minimum flare energies in the range 10^{33} erg, and extending up to 10^{36} erg. [...]" {A128}

[A128]

10.3 Evolution of astrospheres

10.3.1 Effects of a variable ISM on heliospheric structure

"The solar wind does not expand indefinitely. Eventually it runs into the interstellar medium (ISM), the extremely low particle density environment that exists in between the stars [(cf. Fig. 10.6)]. Our Sun is moving relative to the ISM that surrounds the planetary system, so we see a flow of interstellar matter in the heliocentric rest frame, coming from the direction of the constellation Ophiuchus. The interaction between the solar wind and the ISM flow determines the large scale structure of our heliosphere, which basically defines the extent of the solar wind's reach into our Galactic environment. Other stars are naturally surrounded by their own 'astrospheres' (alternatively 'asterospheres') defined by the strength of their stellar winds, the nature of the ISM in their Galactic neighborhoods, and their relative motion."

[V.3.1]

"The Sun is now traveling through the ISM at a rate of 16–20 [parsecs (or pc, a unit of 3.26 light years)] per million years (Myr) compared to the average motion of nearby stars about the Galactic Center. {A129} The ISM has densities ranging from 10^4 cm⁻³ or higher in dense molecular clouds down to about 0.005 cm⁻³ in very low-density hot gas regions. Because the heliosphere will contract or expand by large factors when the Sun enters such high- or low-density regions, it is important to investigate when such environmentally driven changes could have occurred and will possibly occur by considering the Sun's historic and future path through the ISM."

[V.3.5]

[A129]

At present, the heliosphere resides inside of the partially ionized [local interstellar cloud (LIC)], with properties likely similar to other warm partially ionized clouds

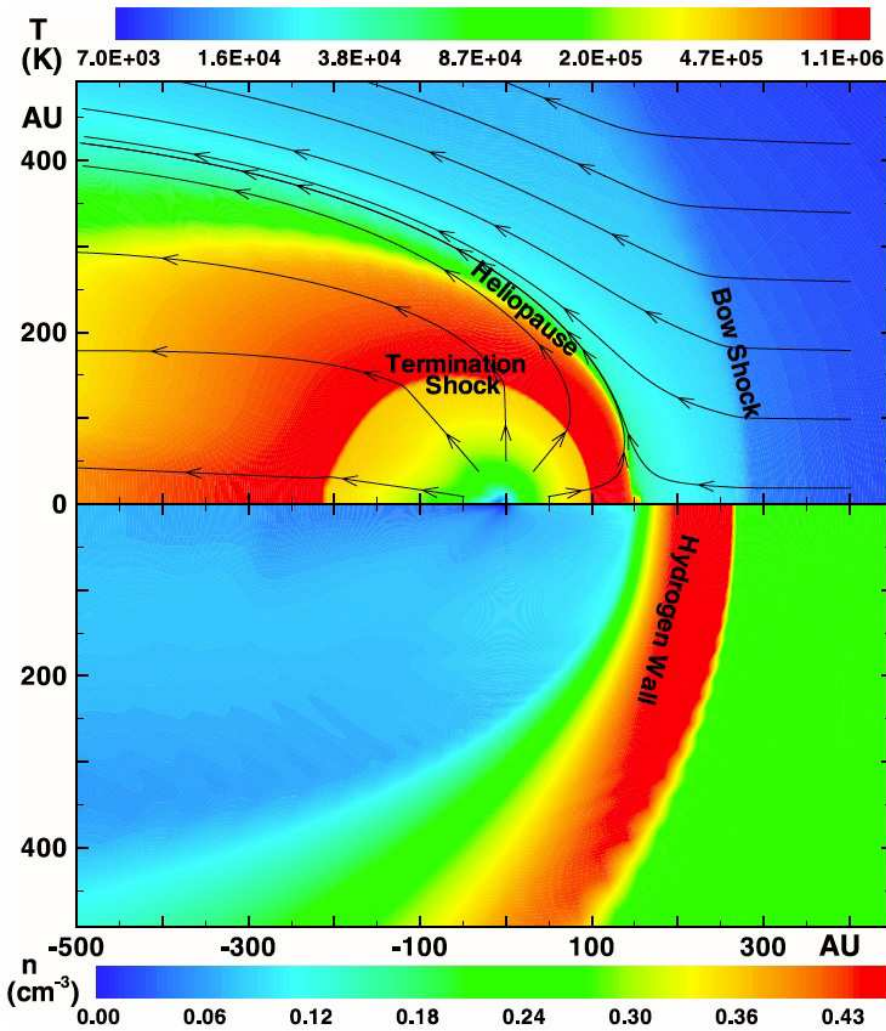


Figure 10.6: A 2.5D axisymmetric, hydrodynamic model of the heliosphere and the surrounding ISM. The upper panel shows plasma temperature and ISM streamlines, and the bottom panel shows neutral hydrogen density. [Note: the effective solar wind plasma temperature, increasing with heliocentric distance, is dominated by the energy density of pickup ions from several AU outward to the termination shock. Fig. IV:3.6; source: Müller and Zank (2004).] For a color version of this figure, see arXiv:2001.01093.

within 15 pc of the Sun. The Sun likely entered this cluster of local warm clouds about 1 Myr ago. However, on a larger scale, the Sun actually lies in a region called the Local Cavity, or Local Bubble, which is ~ 200 pc across and is filled mostly with fully ionized, low-density ISM. [No evidence has been found that the Sun has traveled through significantly denser regions over the last 30 Myr (500 pc) until about 7.5 Myr ago (120 pc) when the Sun was at the edge of the Local Cavity. It appears that the Sun will leave the LIC in less than 3000 yr. What will be the properties of this new

environment? [...]

Our ideas concerning the properties of the gas located between the warm local ISM clouds have undergone a radical change in the last 20 years. The gas between the clouds, extending out to roughly 100 pc from the Sun in what is now called the Local Cavity was originally assumed to be hot (roughly 10^6 K), fully ionized, and low density (roughly 0.005 cm^{-3}). This conclusion was based upon the predictions of the classical models and observations of diffuse soft X-ray emission consistent with the properties of the hot gas. This picture has since been complicated by the realization that X-ray emission from charge-exchange (CX) reactions between the solar wind ions and inflowing interstellar neutral hydrogen can explain much of the observed diffuse X-ray emission, except for the Galactic pole regions. [It has instead been] proposed that the Local Cavity is an old supernova remnant with photo-ionized gas at a temperature of about 20,000 K. The likely photo-ionizing sources are the hot stars ϵ CMa and β CMa and nearby hot white dwarfs like Sirius B. {A130} {A131}

How will the heliosphere change as the Sun passes through very different regions of the interstellar medium? [...] Figure 10.7 compares today's heliosphere properties with the Sun located inside of the partially ionized warm LIC to a model computed for the Sun surrounded by 10^6 K fully ionized interstellar plasma. The main difference between these models is that the hydrogen wall does not exist when the inflowing interstellar gas contains no neutral hydrogen atoms. The locations of the termination shock (TS), heliopause (HS), and bow shock (BS) are determined by pressure balance between the solar wind ram pressure and the thermal and ram pressure of the surrounding interstellar gas. In this comparison, the locations of the TS, HP, and BS are about the same in the two models because the high temperature and low density of the interstellar gas produce a pressure that is about the same as in the LIC. {A130} {A131}

When the Sun enters a region of much higher density or speed, and therefore higher ram pressure, the effect is to compress the heliosphere. For example, a model for $n_{\text{HI}} = 15 \text{ cm}^{-3}$, roughly 100 times that of the LIC, has a TS at 9.8 AU such that Uranus would move in and out of the TS and Neptune would be surrounded by hot, shocked plasma beyond the HP (upwind) or heliotail (downwind). Models of the heliosphere inside of a high-speed interstellar wind with corresponding high ram pressure would compress the heliosphere in a similar way. [A potential] cloud encounter that results in a stellar astrosphere being compressed to less than the size of the star's habitable zone [...] has been described as a 'de-screening event'. This] should happen when a star encounters an interstellar cloud with a number density of $600(M_{\odot}/M)^2 \text{ cm}^{-3}$, where M is the mass of the star. Only the densest ISM clouds are capable of this de-screening, with such clouds being relatively rare. The densest clouds are cold ($T \sim 100$ K) molecular clouds, with many of the refractory elements depleted onto dust grains. In addition to increased GCR exposure (see Ch. 14), a de-screening event caused by a molecular cloud encounter would also expose planetary atmospheres to high fluxes of interstellar dust, with potentially dramatic consequences [that include potential 'snowball Earth' states for climate. Given what we know about mass-loss

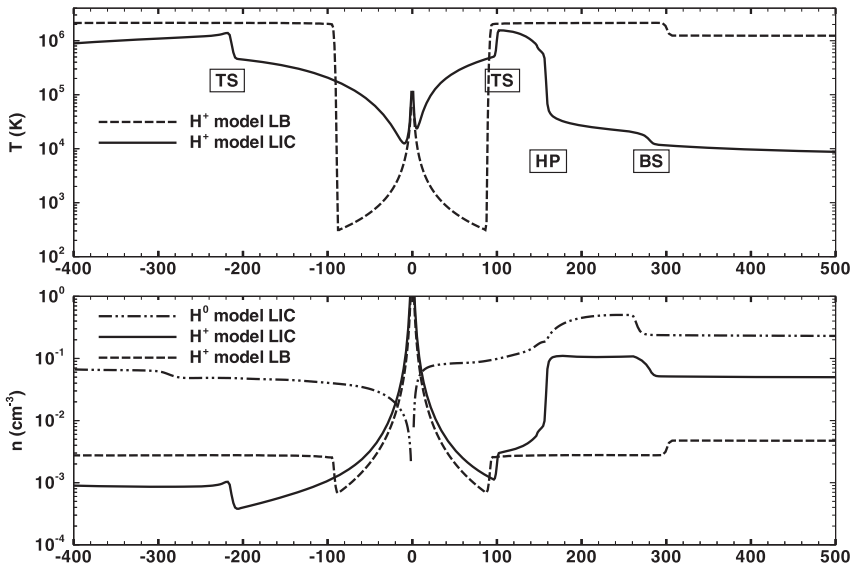


Figure 10.7: Top: Plots of the temperature vs. distance in Sun-Earth distances (astronomical units, or AU) relative to the Sun (interstellar flow upwind direction to the right and downwind to the left) for a heliosphere model with the Sun located inside of the local interstellar cloud (LIC; solid line) or inside a 10^6 K hot interstellar medium (dashed line, LB). The heliosphere in the LIC model has a termination shock (TS), heliopause (HP) and bow shock (BS) structure. Bottom: Density structures for the LIC neutral hydrogen (solid line), LIC protons (dot-dash line), and hot [Local Bubble (LB)] interstellar model protons (dashed line). Note that the hydrogen wall at 150–280 AU exists when the heliosphere is located inside partially neutral interstellar gas but not when it is inside fully ionized interstellar gas. [Fig. IV:3.8; source: Müller *et al.* (2009).]

and wind properties of stars (as discussed below), it appears] that habitable zone planets orbiting stars significantly less massive than the Sun (with spectral types of late K to M) are virtually never exposed to de-screening events, but de-screening may happen occasionally for stars with the Sun’s mass or larger. However, these calculations assumed that the relative velocity of these encounters is only 10 km s^{-1} . Assuming a faster encounter speed would increase the estimated frequency of de-screening events.”

10.3.2 Long-term evolution of stellar winds

In Sect. 5.5.8 we described how neutrals moving toward to the heliosphere leads to a ‘hydrogen wall’ outside of the heliopause through charge-exchange collisions in that region (see Figs. 5.1 and 10.6). {A132} “The importance of this hydrogen wall is that it is actually detectable in UV spectra from [the *Hubble Space Telescope (HST)*], not only around the Sun but around other stars as well.

The effect of heliospheric and astrospheric absorption on stellar HI Lyman- α spectra [(emitted in the stellar atmosphere by de-excitation from the first excited to the ground state in neutral hydrogen atoms and absorbed en route to Earth by the inverse process)] is described by Fig. 10.8, showing the journey of Lyman- α photons from the star to the observer. Most of the absorption is by interstellar gas in the line of sight from the star to the Sun, but the astrosphere and heliosphere provide additional absorption on the [red] and [blue] sides of the interstellar absorption, respectively. The effect of the hydrogen wall around the Sun is to provide additional red-shifted absorption on the right side of [relative to] the interstellar absorption feature because the neutral hydrogen gas in the solar hydrogen wall is slowed down and deflected relative to the inflowing interstellar gas. Conversely, the absorption by the hydrogen wall gas around the star is seen as blue-shifted relative to the interstellar flow from our perspective outside the astrosphere, and is therefore seen on the left side of the absorption line. [... By way of an example observation, the] bottom panel of Fig. 10.8 shows the HI (and [equivalent deuterium] DI) Lyman- α spectrum of the lower-brightness component of [the star] α Cen B. Most of the intervening HI and DI between us and the star is interstellar, but the ISM cannot account for all of the HI absorption. As mentioned above, the red-shifted excess on the right side is heliospheric and the blue-shifted excess on the left is astrospheric.” {A133}

“Currently, the only way coronal winds can be detected around other stars is through astrospheric Lyman- α absorption, but the number of astrospheric Lyman- α detections is still very limited. [... These measurements need to be interpreted in terms of models that] are extrapolated from a heliospheric model that successfully reproduces heliospheric absorption, specifically a multi-fluid model. These models assume the same ISM characteristics as the heliospheric model, with the exception of the ISM flow speed in the stellar rest frame, v_{ISM} , which can be computed using our knowledge of the local ISM flow vector and each star’s unique space motion vector. [...]

The astrospheric models are computed assuming different stellar wind densities, corresponding to different mass-loss rates, and the Lyman- α absorption predicted by these models is compared with the data to see which best matches the observed astrospheric absorption. [...] In order to look for some correlation between coronal activity and wind strength, Fig. 10.9 shows mass-loss rates (per unit surface area) plotted versus F_X [(the ratio of X-ray luminosity to surface [area])], focusing only on the main-sequence stars. For the low-activity stars, mass loss increases with activity in a manner consistent with the $\dot{M} \propto F_X^{1.34 \pm 0.18}$ power-law relation shown in the figure. For the ξ Boo binary, in which (like α Cen) the two members of the binary share the same astrosphere, Fig. 10.9 indicates how the binary’s combined wind strength of $\dot{M} = 5\dot{M}_\odot$ is most consistent with the other measurements if 90% of the wind is ascribed to ξ Boo B, and only 10% to ξ Boo A.

For $F_X < 10^6$ erg cm $^{-2}$ s $^{-1}$, mass loss appears to increase with activity. {A134}

However, above $F_X = 10^6$ erg cm $^{-2}$ s $^{-1}$ (*i.e.*, for more active, and thus generally younger stars) this relation seems to fail, a boundary identified as the ‘Wind Dividing

{A133} IV:3.7.2

{A134}

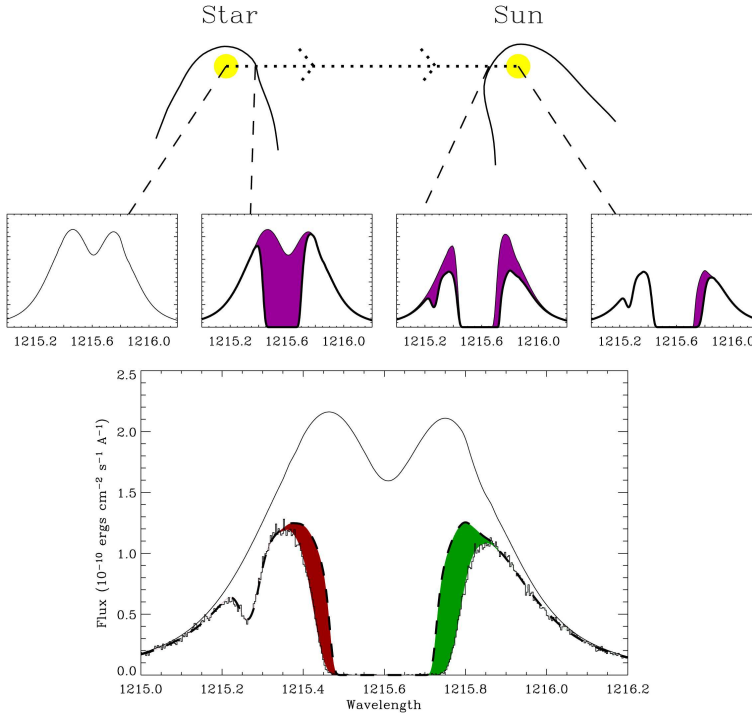


Figure 10.8: Top panel: The journey of a Lyman- α photon from a star through its astrosphere, the interstellar medium, and the heliosphere. Middle panels from left to right: The Lyman- α emission line emitted by the star, absorption due to the stellar astrosphere, additional absorption due to the interstellar medium, and additional absorption due to the heliosphere. Bottom panel: HST Lyman- α spectrum of α Cen B, showing broad HI absorption at 1215.6 \AA and DI absorption at 1215.25 \AA . The upper solid line is the assumed stellar emission profile and the dashed line is the ISM absorption alone. The excess absorption is due to heliospheric HI (green shading, vertical lines) and astrospheric HI (red shading, horizontal lines). [Fig. IV:3.7; source: Wood (2004).] For a color version of this figure, see arXiv:2001.01093.

Line’ in Fig. 10.9. Highly active stars above this limit appear to have surprisingly weak winds. This is suggested not only by the two solar-like G stars above the limit, ξ Boo A and π^1 UMa, but also by the two active M dwarfs above the limit, which have very modest mass-loss rates. (For Proxima Cen we only have an upper limit of $\dot{M} < 0.2\dot{M}_{\odot}$, while for EV Lac $\dot{M} = 1\dot{M}_{\odot}$.) The apparent failure of the wind/corona correlation to the right of the ‘Wind Dividing Line’ may indicate a fundamental change in magnetic field topology at that stellar activity level.

[...] Sophisticated spectroscopic and polarimetric techniques are also available for studying stellar [surface] magnetic fields. One interesting discovery is that very active stars usually have stable, long-lived polar starspots, in contrast to the solar example where sunspots are only observed at low latitudes. Perhaps the polar spots are indicative of a particularly strong dipolar magnetic field that envelopes the entire star and inhibits stellar wind flow, thereby explaining why very active stars have

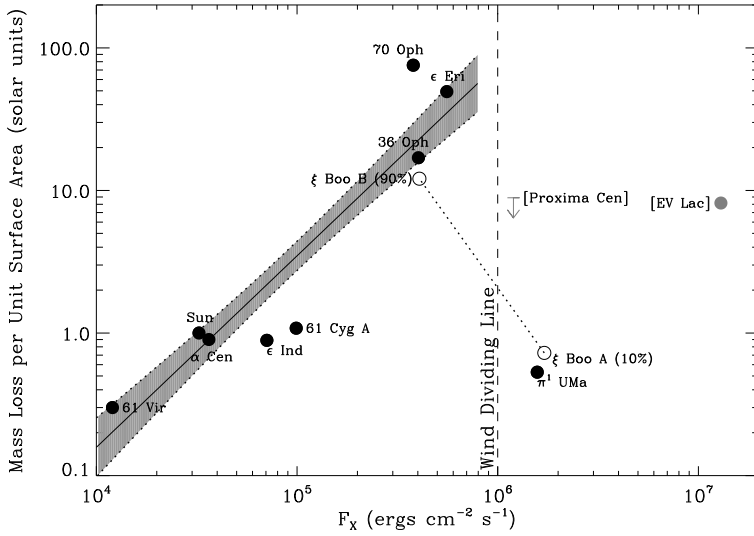


Figure 10.9: A plot of mass-loss rate (per unit surface area) versus X-ray surface flux density for all main-sequence stars with measured winds. Most of these have spectral types of G (like the Sun) or (cooler) K, but the two with square-bracketed labels are (much cooler) tiny M dwarf stars. Separate points are plotted for the two members of the ξ Boo binary, assuming ξ Boo B accounts for 90% of the binary’s wind, and ξ Boo A only accounts for 10%. A power law, $\dot{M} \propto F_X^{1.34 \pm 0.18}$, is fitted to the less active stars where a wind/corona relation seems to exist, but this relation seems to fail for stars to the right of the ‘Wind Dividing Line’ in the figure. [Fig. IV:3.12; source: Wood et al. (2014).]

surprisingly weak winds. Strong toroidal fields are also often observed for active stars. {A135}

Given that young stars are more active than old stars, the correlation between mass loss and activity indicated in Fig. 10.9 implies an anti-correlation of mass loss with age. [One parameterization of this is given by] $F_X \propto t^{-1.7 \pm 0.3} [\propto \Omega^{-3.4 \pm 0.6}]$. Combining this with the power-law relation from Fig. 10.9 yields the following relation between mass-loss rate and age:

$$\dot{M} \propto t^{-2.3 \pm 0.6} [\propto \Omega^{-4.6 \pm 1.2}] \tag{10.7}$$

[where the final expression above between brackets links to the intrinsic dependence on rotation rate via Eq. (10.3).] Fig. 10.10 shows what this relation suggests for the history of the solar wind, and for the history of winds from any solar-like star for that matter. The truncation of the power-law relation in Fig. 10.10 near $F_X = 10^6$ erg cm⁻² s⁻¹ leads to the mass-loss/age relation in Fig. 10.10 being truncated as well at about $t = 0.7$ Gyr. The plotted location of π^1 UMa in Fig. 10.10 indicates what the solar wind may have been like at times earlier than $t = 0.7$ Gyr.

[Fig. 10.10 indicates] that solar-like coronal winds can be up to two orders of magnitude stronger than the current solar wind at $t \approx 1$ Gyr. This makes it more likely that the erosive effects of stellar winds play an important role in planetary atmosphere

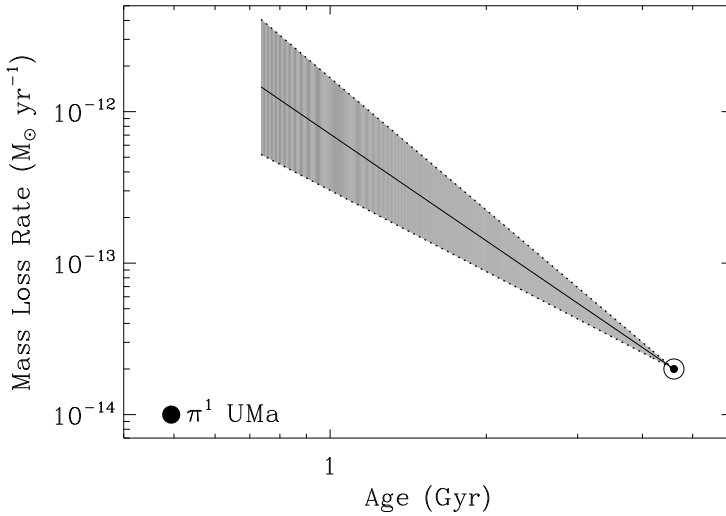


Figure 10.10: The mass-loss history of the Sun inferred from the power-law relation in Fig. 10.9. The truncation of the relation in Fig. 10.9 means that the mass-loss/age relation is truncated as well. The low mass-loss measurement for π^1 UMa suggests that the wind weakens at $t \approx 0.7$ Gyr as one goes back in time. [Fig. IV:3.13; source: Wood et al. (2005).]

evolution at these later ages” (see Ch. 12). {A136}

10.3.3 Astrospheric field patterns in time

“The extent and structure of astrospheres is determined by the radially-expanding super-Alfvénic stellar wind that drags the stellar magnetic field from the stellar corona through interplanetary space, until the wind is stopped by the Interstellar Medium (ISM). It is also determined by the rotation of the star. As a result, each astrospheric magnetic field (AMF) line has one end (or ‘footpoint’) attached to the stellar surface, while its location at each point in the astrosphere, $\mathbf{r}(r, \theta, \phi)$ (for co-latitude θ), is given by the following formula. It describes a spiral shape and is known as the ‘Parker Spiral’ [(Sect. 5.4, compare with Eq. 5.20)]:

$$\mathbf{B}(r) = B_0 \left(\frac{r_0}{r} \right)^2 \left[\hat{\mathbf{e}}_{\mathbf{r}} + \frac{(r - r_0)\Omega \sin \theta}{v_w} \hat{\mathbf{e}}_{\phi} \right]. \quad (10.8)$$

Here Ω is the stellar rotation rate (angular velocity), v_w is stellar wind speed (which is here assumed to be radial and fixed in time and space); r_0 is the actual base point of the AMF, and is at a reference distance from the stellar surface at which we assume the stellar wind is fully developed and has achieved its asymptotic speed and radial direction; B_0 is the magnetic field magnitude at that point. We can see that the radial component of the AMF has an r^{-2} dependence, while the azimuthal component has only a r^{-1} dependence. As a result, throughout most of the astrospheres, the AMF is dominated by the azimuthal field, which is a function of Ω , except for high latitudes (small θ) where the AMF lines are nearly radial.

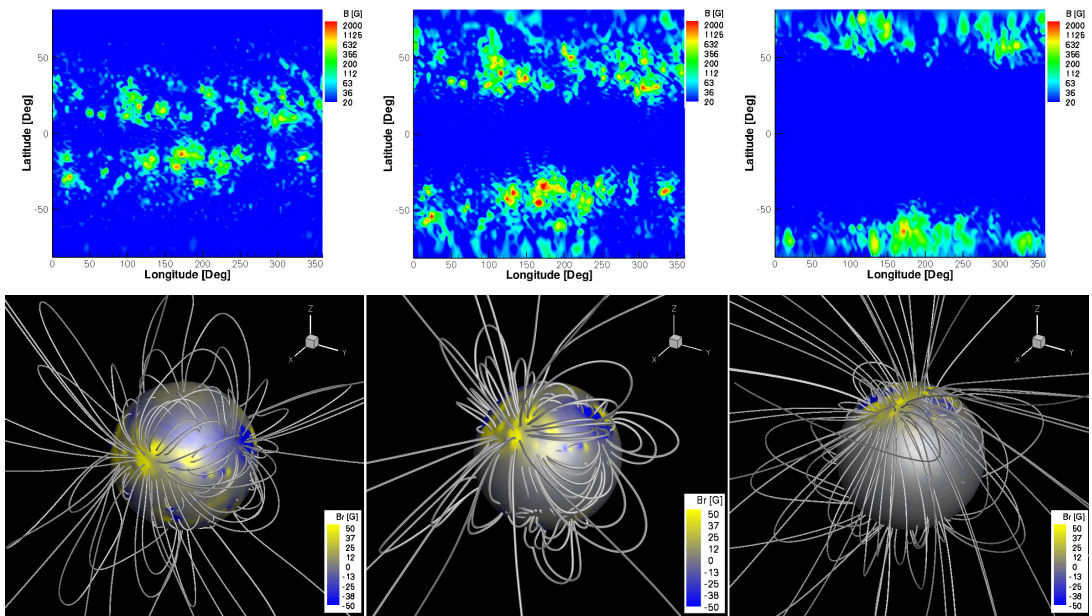


Figure 10.11: Top row: A map of the solar photospheric radial magnetic field (magnetogram) during Carrington Rotation 1958 (January 2000, solar maximum period) shown on the left. The middle and right panels show manipulation of the original map, where the active regions have been shifted by 30 and 60 degrees toward the poles, respectively. [Fig. IV:4.4; source: Cohen *et al.* (2012)] Bottom row: The three-dimensional magnetic field corresponding to the surface distribution of the photospheric radial magnetic field (shown on a sphere of $r = R_{\odot}$) during solar maximum (left), and for manipulated photospheric field with the active regions shifted by 30 (middle) and 60 (right) degrees toward the poles, as shown in the row above. [Fig. IV:4.5] For a color version of this figure, see *arXiv:2001.01093*.

Over time, stellar rotation periods evolve from less than one day for very active, young stars to about 20-100 days for older, main-sequence stars like the Sun. For very fast-rotating stars, the AMF spiral is completely dominated by the azimuthal component: the field is highly compressed, and its azimuthal component dominates even at relatively small distances from the star and inside the stellar corona, which typically extends to 10-20 stellar radii. In this case, even extended closed magnetic loops can be bent as a result of the fast rotation. This effect can have implications for the triggering of very strong stellar flares, and for the mass-loss rate of the star to the stellar wind. The right panel in Figure 5.5 shows how the compression of the AMF spiral changes for different stellar rotation periods. The other two panels show the AMF lines close to the star (up to 24 stellar radii). It can be clearly seen that the field lines are nearly radial for the slow, solar-like rotation period of 25 days, while the field lines are strongly bent in the azimuthal direction for a fast rotation period of half a day. {A137}

Equation (10.8) describes how a given magnetic field line changes with distance {A137}

for a given value of B_0 at its base (r_0), and a given asymptotic stellar wind speed v_w . However, the AMF is formed by a collection of field lines that are defined by some spherical distribution of B_0 at the base of the stellar corona. This distribution depends on the topology of the stellar magnetic field at a given time. In addition, the value of v also varies as it empirically depends on the expansion of the magnetic flux tubes and on the non-uniform distribution of B_0 . [...]

Over time, stellar activity appears at different latitudes, while changing in magnitude as the behavior of surface magnetic activity is highly tied to the rotation rate. Young active stars seem to have very strong large-scale magnetic fields with magnitude of several kilo-Gauss. For reference, the Sun's dipole field strength is of the order of 5-10 G, and while the magnetic flux density within active regions can be high (ranging up to well over a kiloGauss in sunspots), solar active regions are rather small in size. In addition, magnetic activity in active stars tends to appear at high-latitude, polar regions. This behavior is most likely related to the role of the fast stellar rotation in the stellar dynamo and meridional magnetic flux circulation. [...]

The appearance of stellar activity described above reflects a change in the distribution of B_0 . Therefore, it affects the shape of the AMF and the astrospheric volume. It is not clear how v_w changes for young stars as we cannot directly measure stellar winds of 'cool stars', *i.e.*, stars with a convective envelope beneath their surfaces such as in the case of the Sun. Some techniques to estimate mass-loss rates from cool stars are [outlined above]. However, these estimates do not separate the stellar wind speed from the density, so it cannot be obtained independently. Another cause for the lack of estimates for stellar wind speeds of cool stars is the incomplete theory about the solar wind acceleration. In order to demonstrate how the change in the photospheric field affects the three-dimensional structure, Figure 10.11 shows the distribution of the photospheric magnetic field and the shape of the three-dimensional magnetic field close to the Sun. The top-left panel is obtained using actual data of the photospheric field during a period of high solar activity. In the other two panels in the top row, the original data was manipulated, so that the active regions have been shifted by 30 and 60 degrees, respectively, towards higher latitudes to mimic the activity distribution of young active stars. It can be seen in the bottom panels that the large-scale field topology changes dramatically even if only the positions of the active regions are changed.”

We can presently observe CMEs only in the heliosphere [(but see Veronig *et al.*, 2021 on the use of coronal dimmings as proxies for stellar CMEs)]. For some discussion on CMEs in different astrospheres and their potential (but currently speculative) role in stellar angular momentum loss and stellar spin down, see Sect. IV:4.2.

Chapter 11

Formation of stars and planets

Chapter topics:

- Formation of stars and planetary systems
- Migration of young planets in accretion disks
- Angular-momentum transport in accretion disks
- Disk evaporation

Key concepts:

- Core-accretion model
- Protoplanetary disk
- Ice line
- Kelvin-Helmholtz time scale

11.1 Introduction

A star like the Sun begins its life within a relatively dense concentration of molecular gas, called a cloud 'core', somewhere in the interstellar medium. The density in such molecular clouds is of order $10^2 - 10^6 \text{ cm}^{-3}$, to be compared with, *e.g.*, the density of the local interstellar medium of roughly 10^{-1} cm^{-3} . "The mechanisms by which molecular clouds of many solar masses break up into stellar mass pieces are a matter of debate; probably turbulence generated in the process of forming the cloud produces the denser fragments which accrete to form stars [... G]iven the large sizes of protostellar clouds, they almost certainly contain enough angular momentum to form disks of substantial size and mass; thus, a major part of the story of star formation involves moving matter from a disk into a small, spherical protostar. {A138}

To make a star of a given mass M_{\odot} from a gas with temperature T_c , gravity must overcome the pressure support; this means that [the protostellar cloud must have a] radius $R_c \gtrsim 2 \times 10^4$ astronomical units (AU; [see the argumentation around Eq. 2.15]). {A139} We see pre-stellar dense concentrations of this size with properties such that they are likely to be on the verge of gravitational collapse. As these cloud cores have sizes $\sim 10^6$ times larger than the final radius of any resulting {A138} {A139}

star, it is clear that virtually all of the angular momentum of the initial cloud must be transferred somewhere else; in general, it must be to a circumstellar disk. In this way, the formation of stars necessarily leaves behind material which can in principle form planets.” {A140} The initial phase of star formation, and the clearing of the dust-rich environment of the protoplanetary disk happens on a time scale of just a few million years, as we shall see in Sect. 11.3.5, and this means that much of the growth phase of planets, or at least the sizable planetesimals that later coalesce to form fully-grown planets, must be completed by then.

“Confirmed and candidate exoplanets number in the thousands and search techniques include Doppler measurements, transit photometry, microlensing, direct [(and since 2019 also interferometric)] imaging and astrometry. Each detection technique has some type of observational incompleteness that imposes a biased view of the underlying population of exoplanets. In some cases, statistical corrections can be applied. For example, transiting planets can only be observed if the orbital inclination is smaller than a few degrees from an edge-on configuration. However, with the reasonable assumption of randomly oriented orbits, a geometrical correction can be applied to determine the occurrence rate for all orbital inclinations. In other cases, there is simply no information about the underlying population and it is not possible to apply a meaningful correction. For example, the number of planets with a similar mass (or radius) and a similar intensity of intercepted stellar flux as our Earth is not secure at this time because the number of confirmed detections for this type of planet [and orbit is too] small. {A141} {A142}

As a result of the sample biases and observational incompleteness for each discovery technique, our view of exoplanet architectures is fuzzy at best. There are no cases beyond the Solar System where the entire parameter space for orbiting planets has been observed. Instead, we piece together an understanding of exoplanet architectures by counting planets in the regimes where techniques are robust and then we estimate correction factors when possible. When drawing conclusions about the statistics of exoplanets, it is helpful to understand the incompleteness in this underlying patchwork of orbital parameter space.” Sections IV:5.2-5.6 provide brief descriptions of the methods and their limitations.

“Our view of exoplanets is still skewed by the observational sensitivities of the techniques that we use. However, the discoveries that have been made have helped us to revise our understanding of planet formation and the formation of the Solar System. We see that planet formation is a chaotic process and that disks are sculpted by gravitational interactions to a greater extent than we appreciated by considering our Solar System. We now know that almost every star has planets and that planet formation is far more robust than astronomers expected.”^[28] Although we do not touch on the process of forming binary star systems (or higher multiplerets), the outcome of the evolution of a molecular cloud to a planetary system often involves fragmentation

²⁸ Recent reviews on the making of planets in general and on giant planet formation and migration, see Space Science Reviews (2018) volume 214, pages 38 (by Paardekooper and Johansen) and 60 (by Lammer and Blanc, referred to as ^a below), as well as ‘One of ten billion Earths’ by Schrijver (2018).

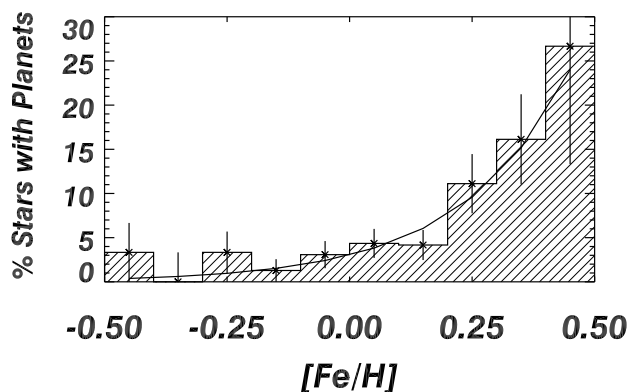


Figure 11.1: High metallicity stars are more likely to host gas-giant planets than sub-solar metallicity stars. $[Fe/H]$ denotes the ratio of the abundance of Fe relative to hydrogen, while the brackets mean that the logarithm has been taken of that ratio normalized to the solar value, so that the Sun would have a value of 0, and the scale reaches a factor of about three down and up on the left and right side, respectively; Fig. IV:5.12]

of the cloud into two or more stars: roughly one in every two 'stars' visible in the sky is, in fact, a double or higher-multiple star.

It may be counterintuitive, but our knowledge of the evolution of the formative phases of stars by accretion from spinning disks of gas and dust that contracted out of huge molecular clouds has been helped greatly by the hunt for exoplanets and their story of formation. It is for that reason that this chapter begins with a very concise summary of what has been learned about (exo-)planetary systems, thereafter to go 'back in time' to the gaseous phases of the protoplanetary disks and how the gases in these formed the central stars, and how some planets ended up being ejected from the forming planetary system. {A143}

11.2 (Exo-)Planets and (exo-)planetary systems

"The ultimate stage of disk evolution, in addition to accretion and photo-evaporation, involves the growth of planetary bodies. We now know [almost 4,000 (by late 2022) exoplanetary systems], with the number continually increasing. Of course, the first major surprise was the discovery of Jupiter-mass bodies at very small orbital radii. This emphasized the almost certain necessity of inward *migration*, as it appears unlikely that disks can be sufficiently massive at 0.02 – 0.1 [Sun-Earth distances (or astronomical units: AU)] to form such objects (unless disks are gravitationally unstable all the way to the central star). The other major surprise was how eccentric [many of the orbits of close-in, large exoplanets] are. These two features are probably related, especially if planet-planet scattering is responsible for much of the inward migration. Before discussing migration further, it is useful to consider how the planets would form in the first place.

The two major scenarios of planet formation are those of core accretion [(starting

with solids, and – once heavy enough, should that indeed occur – also accumulating gases)] and gaseous gravitational instability. [...] One strong piece of evidence for core accretion versus gaseous gravitational fragmentation” comes from one “of the first observed statistical correlations established[:] gas-giant planets form more frequently around metal-rich stars.^[29] This planet-metallicity correlation [(see Fig. 11.1)] was used as evidence for core accretion as the formation mechanism for gas-giant exoplanets that orbit closer than a few AU around their host main-sequence stars. [...] Interestingly, a similar correlation with host star metallicity has not been identified for smaller Neptune-like [...] planets. However, it remains unclear whether such correlation exists for rocky planets. [...]”

“In the core-accretion model for giant planet formation, solid bodies accumulate via collisions until the resulting core is sufficiently large that its gravity can pull in surrounding gas. There is some concern that core accretion might proceed too slowly to explain the observed disk clearing on timescales as short as 1 – 2 Myr in significant numbers of stars. There are two potential bottlenecks in the process. One is the formation of km-sized planetesimals from cm-sized objects. Such bodies are thought to be held together lightly – too large for effective sticking and too small for gravity to become important – and, as bodies of different sizes have different velocities due to gas drag, collisions between these objects might shatter them rather than build them up. In addition, [there is growing evidence that young planets in material-rich disks are subject to rapid inward migration, which would] require fast agglomeration, especially for Earth-sized objects, though studies suggest that this inference of rapid migration may not always be correct. Various schemes of dust concentration might help avoid shattering by reducing relative motions and increasing densities, perhaps through vortices or eddies or other turbulent structures.

Once km-sized planetesimals are made, collisions among them can lead to the building of terrestrial planets and giant-planet cores. The remaining bottleneck[, at least significant for giant planets,] is that of accumulating gas. The energy released by accretion of planetesimals and gravitational contraction of the envelope must be radiated by the outer envelope. If the opacity of the envelope is large, it must extend to large radii; in turn, this can limit the gas available for accretion, which must lie close enough that the tidal forces of the central star do not overcome the protoplanet’s gravity. [It appears] that, with sufficiently massive cores, giant planets can form within 1 Myr for an opacity $\sim 2\%$ of interstellar values, [because the opacity (dominated by dust) may be reduced due] to rainout of solid materials in the planetary envelope; as grain growth almost certainly precedes core formation, reduced dust opacity is an extremely plausible assumption. [...]

There is general agreement that terrestrial planets generally (fully) form later than the giant planets; gas drag is important in early stages but the final growth may well occur after gas removal from the disk. [O]nce growth to km-sized planetesimals has occurred, gravitational effects become important. At first the planetesimals grow by gravitational focusing; as they grow, eventually they excite or stir up other bodies,

²⁹ Note that astronomers have a habit of referring to all elements heavier than helium as ‘metals’.

making their relative velocities larger and limiting accretion. The result is thought to be a set of 'oligarchic' protoplanets with relatively similar masses (at least locally). After the oligarchs have swept up most of the available material, interactions between them dominate the subsequent evolution, with large impacts a major feature. This indicates that the final state of terrestrial planet systems is difficult to predict, as it is the result of chaotic growth.

Even after the terrestrial planets are essentially fully formed, significant system evolution can occur, simply because multi-body gravitating systems are generally not stable. A particularly interesting possibility is long-term evolution and migration due to interactions of an outer system of gas/ice giants with the planetesimals left in the outer disk, objects formed in regions with such low densities that growth to large bodies was not possible. [T]here probably has been outward migration of at least Neptune in our outer Solar System, based on the analysis of resonant structure in our own planetesimal system – the Kuiper Belt. One possible mechanism for explaining this migration is giant planet-planetesimal interactions. Such gravitational perturbations can result in the system becoming dynamically unstable, resulting in ejection and scattering of many planetesimals into high-eccentricity orbits; this has been suggested, in the so-called 'Nice' model, as an explanation for the late heavy bombardment seen in the impact history of the Moon (cf., [Sec. 12.1.1] ...)]. It has also been proposed as an explanation of the stunted growth of Mars, and moreover of the chemical gradient in the asteroid belt: silicate-rich and carbon/water-rich populations should have been differentiated by distance to the Sun (across the 'ice line' where the temperature would have been low enough to create water-rich asteroids only further out; see footnote 16), but actually show much overlap of the populations, albeit with a clear trend for the average chemical makeup as function of orbital radius. It is argued that this smoothed trend of what should have formed as a clear chemical segregation was introduced by gravitational interaction with migrating gas/ice giants (in what is referred to as the 'Grand Tack' model, in which the Jupiter-Saturn pair first migrated inward and subsequently outward). {A144} {A145}

11.2.1 Exoplanet formation

The solar nebula theory holds that the Sun and its attending planetary system formed out of a cloud of gas and dust (with dust making up, on average, about 1% of the total mass^a) that contracted into a spinning disk, with most matter migrating towards the center to form a star even as much of the angular momentum ended up in the orbiting planets that formed out of the cool disk material before the remainder of the gases were somehow cleared out (more on that below). "The solar nebula theory provides a theoretical description for the formation of the Solar System. Indeed, it has been said that this model is so elegant, that it is hard to imagine that it could be wrong. The solar nebula theory neatly explains most observations: the planets closest to the Sun form in a hot environment and as a consequence these planets are small and comprised of refractory elements (*i.e.*, elements [whose solids] withstand high temperatures); the more massive gas giants form beyond the ice line (a distance where it is cold enough for dust grains to be coated with icy mantles) where the feeding

{A144}

{A145}

IV.5.7.1

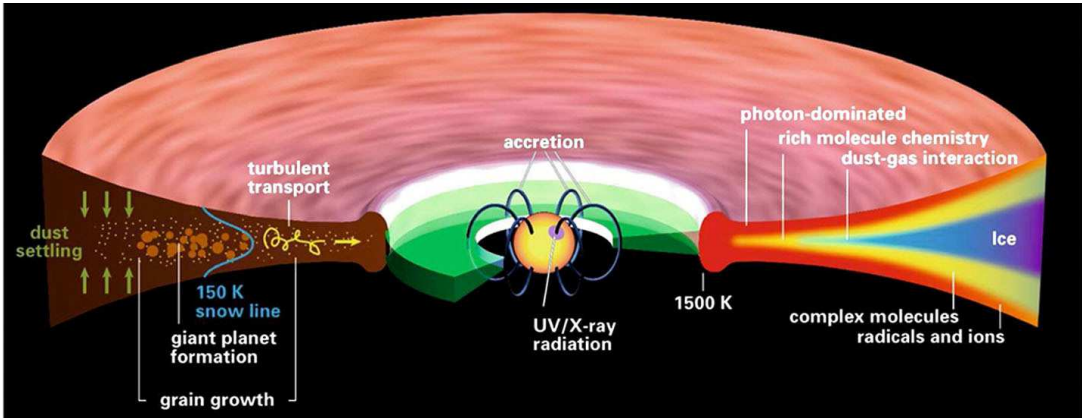


Figure 11.2: A sketch of the structure and processes of protoplanetary disks [with ages in the range of about 1–5 Myr. Fig. IV:5.9; source: Henning and Semenov (2013). For a color version of this figure, see arXiv:2001.01093.]

ground is more voluminous; jovian planets have moons that were either captured or that form as mini-solar-systems; the planets all orbit in the same direction in the disk because they inherit the same angular momentum vector; the Solar System is littered with leftover debris such as asteroids and comets. The theory supports the idea first suggested by Kant and Laplace that the proto-Sun was surrounded by a primordial spinning disk of dust and gas. All of the material that makes up the Sun drained through this disk. [...]

The mass of the protoplanetary disk is a fraction of the stellar mass and evolves with the central star. Our understanding of the physics and chemistry of protoplanetary disks is distilled in Fig. 11.2. The temperature is about 1500 K near the inner part of the disk and along the flared outer layers. These high temperatures are too hot for grain growth, but a few AU from the protostar, the disk mid-plane is cool enough for icy grains to stick and grow. The opacity of the disk is set by the dust, which gradually decouples from the gas and settles toward the mid-plane, increasing transparency of the disk over time. {A146}

{9FIV} Protoplanetary disks provide the initial conditions for planet formation. [...] In the first phase of planet formation, the planet grows by runaway accretion of solid material. The second phase of growth is very slow; both solid and gas accretion are nearly time-independent and this phase sets the planet formation timescale. Once the planet core reaches a mass of about $10M_{\oplus}$, [if indeed it succeeds in that,] the third phase of runaway gas accretion begins, growing the planet mass from 10 to a few hundred M_{\oplus} . [It has been] estimated that gas-giant planet formation should take roughly 10 Myr. However, observations of protoplanetary disks in the 1990s presented a conundrum: the primordial disks appear to be nearly ubiquitous around stars that are 1 Myr; at 2 Myr only about half of young stars have disks and by 10 Myr, the disks are essentially gone. Figure 11.9 shows the fraction of protoplanetary disks found in

young cluster stars.

One triumph that emerged from the discovery of exoplanets was a solution to the disagreement between theory and observations for the formation timescale of gas-giant planets. The first detected gas-giant planets orbited close to their host stars providing evidence that exoplanets could undergo orbital migration. Thus, planets were not restricted to a planetesimal feeding ground at a fixed orbital radius; instead, the planet embryos are pushed around in the disk by planet-planet interactions and tidal torques. The access to a wider part of the disk suggests a wider feeding zone for more rapid accretion of planetesimals that would shorten the second phase of gas-giant planet formation [...]"

11.2.2 Exoplanet migration

In Sect. 7.3.2 we already described the possibility that planets can change their orbits in the formation phase of a planetary system by tidal interaction with the surrounding disk. This is one scenario by which, for example, giant planets may ultimately find themselves orbiting their parent star at distances much closer than where they could readily form. "Another way to push exoplanets inward is through gravitational encounters. There are several proposed mechanisms that excite orbital eccentricity including secular migration, planet-planet scattering, and Kozai perturbation in which gravitational interactions result in coupled variations in orbital inclination and eccentricity. High eccentricity planets with a small enough periastron passage eventually experience tidal circularization and can end up in short-period orbits.

Different migration mechanisms predict distinct observables. A particularly interesting observable is stellar obliquity, the relative angle between the stellar rotation vector and the vector normal to the planet orbital plane. The stellar obliquity can be measured by observing the Rossiter-McLaughlin effect. This effect is caused by a transiting object blocking some of the light from a rotating star. [In the case of a prograde, low-obliquity planet, the transiting planet first] crosses the approaching limb of the rotating star, decreasing the contribution of blue-shifted light in the spectral line and a few hours later the planet crosses the receding limb of the rotating star, decreasing the contribution of red-shifted light. The systematic decrement of Doppler-shifted light in the composite spectral lines results in a distortion of line profile, which is (mis)interpreted as a change in the radial velocity of the star. The shape of the Rossiter-McLaughlin curve during transit is entirely dependent on the stellar obliquity. Consequently, the stellar obliquity is determined by modeling the anomalous radial velocity signals during a transiting event. {A147}

Disk-driven migration is expected to produce a small stellar obliquity whereas gravitational encounters that temporarily pump up the orbital eccentricity of gas-giant planets should result in a wide range of stellar obliquities including retrograde orbits. The latter has been observed for many transiting planets suggesting that high eccentricity mechanisms drive gas-giant planets inward. However, it has also been suggested that the observed stellar obliquity range may reflect a primordial stellar obliquity due to interactions between proto-planetary disk and a companion star. Interestingly, the small stellar obliquity of low-mass multi-planet systems suggests

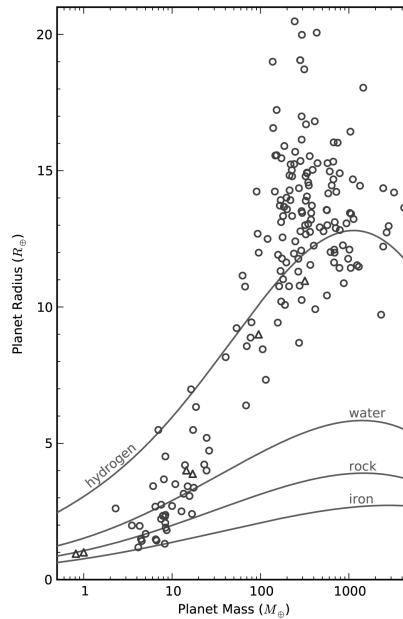


Figure 11.3: Masses and radii of well-characterized exoplanets (circles) and Solar-System planets (triangles). Curves show models for idealized planets consisting of pure hydrogen, water, rock (Mg_2SiO_4) or iron. [Fig. IV:5.11; source: Howard et al. (2013).]

well-aligned vectors for the stellar spin and planetary orbits. It is certainly possible that gas-giant and low-mass planets migrate by different mechanisms.

In summary, the most important revisions to the solar nebula model and our understanding of planet formation can be attributed to one source: the addition of dynamical interactions between planets and the primordial disk. These dynamical interactions speed up the accretion timescales, produce mean-motion resonances, scatter planets out of the disk into non-coplanar orbits that can be detected by the Rossiter-McLaughlin effect and even eject some planets.”

11.2.3 Exoplanet geology

Studies suggest that there may be “two characteristic planet radii ($1.7R_{\oplus}$ and $3.9R_{\oplus}$) that divide planets into three populations: terrestrial planets, gas-dwarf planets and gas-giant planets. [...] Both the mass-radius relationship and the transition radius from rocky to non-rocky planets help us to better understand the formation history of small planets. Planets that form *in situ* in the inner part of the disk would consist primarily of rocky materials and possibly a primordial H/He atmosphere. In comparison, planets that have undergone significant migration should contain more volatile materials such as astrophysical ice (H_2O , CO , and NH_3). The debate of whether close-in planets form *in situ* or migrate should eventually gain evidence from studies of exoplanet atmospheres that add constraints on their chemical composition.”

“Thousands of planet candidates were discovered by the *Kepler* mission, allowing

for precise measurements of exoplanet radii. The combination of the radius and mass measurements (either from the Doppler technique or from transit timing variations) provides a mean density for hundreds of exoplanets and allow us to begin considering the bulk composition of unseen planets that orbit stars hundreds of light years away from us. The varying bulk composition of exoplanets results in different curves that cut through the mass-radius parameter space shown in Fig. 11.3.

Planets with radii smaller than 4 times that of the Earth can exhibit a remarkable diversity of compositions. [...] Planets smaller than 1.5 Earth radii increase in density with increasing radius and seem to have a composition that is consistent with rock. Planets with radii between 1.5 and 4 times the radius of the Earth showed decreasing density with increasing radius, suggesting that the larger planet radius is a product of gaseous envelopes. [...] The significant amount of scatter in the mass-radius parameter space suggests a large diversity in planet composition at a given radius.”

With the growing number of exoplanet detections, one more thing has become abundantly clear: whereas the Solar System suggests a marked division between the four terrestrial planets (with masses of one Earth mass or less) and the four giant planets (with masses of 14.5 to 318 Earth masses), the exoplanet population overall has no such division, showing a continuum of masses from low to high^a.

11.2.4 Exoplanets and binary star systems

“Many stars in the solar neighborhood are components of multiple-star systems, [and exoplanets have been found orbiting one of the two components while others have distant circumbinary orbits. ...] The occurrence rate of circumbinary planets is estimated to be $\sim 10\%$ assuming the orbital plane of circumbinary planets roughly align with the binary orbital plane. The occurrence rate could be much higher if the orientation of planet orbits is more isotropic.

It is expected that planet formation may be impeded in systems where the binary stars have small separations (*e.g.*, $\sim 10\text{--}200$ AU). This is supported both by simulations and observations that find a smaller fraction of exoplanets in binary star systems. It is not surprising that the dynamics of binary star systems stir things up and challenges planet formation. What is surprising is that the planets exist there at all.”

11.3 Formation and early evolution of stars and disks

11.3.1 Observations of star-forming processes

Before the discovery that exoplanetary systems were about as common as stars (reached in the first decade of the 21st century) astronomers struggled to understand how angular momentum from the contracting pre-stellar cloud could be removed so that a star could form at all. There were studies on how Alfvén waves could carry angular momentum away, how fragmentation into multiple star systems could deal with the problem, or how winds from magnetized disks could extract angular momentum. Realizing that much of the angular momentum is left behind in the planetary system reduced the magnitude of the problem tremendously, and many of the earlier ideas

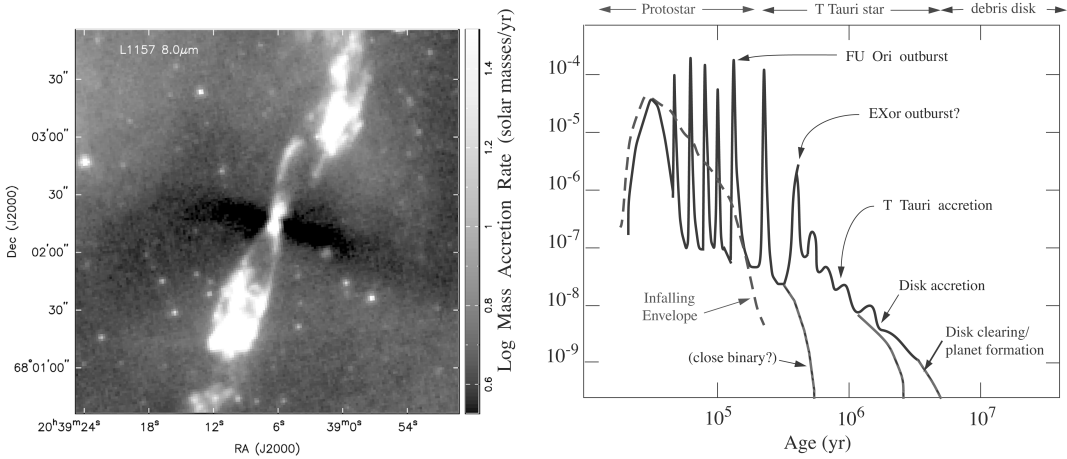


Figure 11.4: Left: An $8\ \mu\text{m}$ image of an accreting low-mass protostar. The darker, filamentary region running east-west (horizontally in the image) represents dust extinguishing the background radiation; this indicates that the densest, most massive region of the material falling in to make disk and star is far from spherically-symmetric. The bright regions running north-south (top to bottom) are due to protostellar continuum emission reflected from dust and molecular emission lines excited by a high-velocity, bipolar outflow thought to be driven from the innermost regions of the protostellar accretion disk. Right: Schematic diagram of a likely accretional history of a typical low-mass star. The dashed curve indicates the expected rate of infall of matter from the protostellar envelope (e.g., dense region indicated in the left-hand panel). The solid curve suggests a possible variation of accretion through the protostellar disk onto the central star, which may be steady at the earliest times but is subject to strong variations in accretion (so-called FU Ori outbursts). In this picture, material piles up in the disk due to the infall rate being higher than the disk can smoothly pass on to the central star; this leads to episodic bursts of accretion which drain the excess disk mass. Finally, after infall ceases, slower, more steady accretion occurs during the T Tauri phase, which may cease because either a binary companion or planets accrete the remaining mass. This results in ‘clearing’ the disk, i.e., removing most of the small dust and apparently most of the gas. Finally, secondary production of small amounts of dust can occur during the debris disk stage, when solid bodies collide and shatter. [Fig. III:3.2; source: Hartmann (2009).]

about where the angular momentum would end up have been left behind or now form a lesser challenge to the formation scenario of stars. “If we assumed that there were no planets and all the angular momentum resides in the Sun, this leads to an increase in the angular velocity by about a factor of 35. As a result the Sun would spin around its axis in about 18 hours instead of 27 days. Because the assumption of a homogeneous sphere underestimates the effective moment of inertia, the Sun would complete a rotation within about 12 hours which corresponds to a velocity of the photosphere in the order of $100\ \text{km s}^{-1}$ ” instead of the observed $2\ \text{km s}^{-1}$.

Nowadays, the view is that “[t]he accretion disk is basically an engine in which angular momentum is transferred outward to ever-decreasing amounts of material while the majority of the mass moves inward to the center. {A148} In the case of at

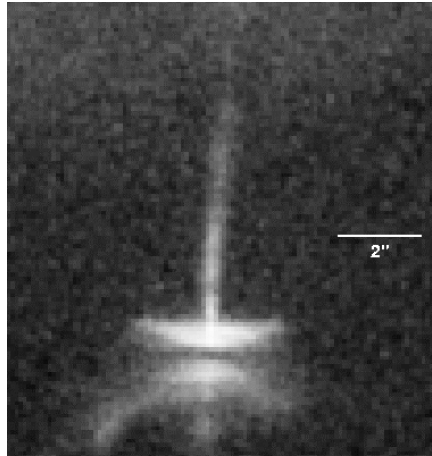


Figure 11.5: Optical image of the accreting young star *HH 30*, showing the upper surfaces of its dusty disk in scattered light (the dark lane is due to dust extinction of the central star by the disk), along with an optical, high-velocity, bipolar jet. For scale, 2 arcsec = 280 Astronomical Units. [Fig. III:3.3]

least moderately-ionized disks, it seems increasingly certain that magnetic turbulence provides the necessary angular momentum transport for accretion. The low ionization of protostellar disks is likely to render this mechanism ineffective over significant radial regions; gravitational torques can come to the rescue, moving most of the cloud mass into the central regions in any event. However, gravitational torques alone will leave a sizable amount of mass in the disk, of order 10%–30% of the central star mass. As this is much larger than estimated by many techniques, and substantially more than assumed in many models of planet formation, it may be necessary for additional angular momentum transport to occur via magnetic turbulence. On longer timescales, the remaining disk gas is probably removed by some mechanism of ejection due to stellar X-rays and extreme-ultraviolet (EUV) heating.

This picture of star formation has considerable observational support. Cold clouds of the mass and size indicated in Eq. (2.15) are seen in star-forming regions, some with already growing protostars (Figure 11.4, left). We also observe extended circumstellar disks around many young stars (Figure 11.5). The masses of these disks are at least $\sim 1\%$ that of the central star; with radii of hundreds of AU, they clearly must contain most of the system angular momentum. {A149}

The implication of this picture is that most of the mass of a star must pass through its disk; that is, stars are most directly formed by disk *accretion*. As shown schematically in the right side of Figure 11.4, disk accretion may not be steady if it cannot keep up with the infall to the disk; instead, early stellar evolution may be punctuated by outbursts of very rapid accretion followed by extended periods of slow mass addition. There is observational evidence for such accretional outbursts in the FU Orionis objects; their properties suggest that disks are likely to be quite massive, {A149}

at least in early stages.” {A150}

Magnetic fields are good candidates for the transport of angular momentum in a disk, as the differentially rotating disk (trying to have matter orbit the forming star in Keplerian orbits) would stretch embedded field, causing a back-reaction that works to reduce the differential rotation (see Sect. 7.2.3). That can work, provided that the disk material has a sufficient degree of ionization so that the field and the gases can effectively couple. Another process that can contribute to the transport of angular momentum is gravitational coupling; see Sect. 11.3.4 for a description of this process.

“The other major potential mechanism of disk angular momentum transport is that of winds. It is now thought that most of the angular momentum of disks results in expansion of the outer disk rather than simply being lost in a wind; however, because [Sun-like,] low-mass stars become slowly-rotating early in their existence (Sect. 11.3.3), it is quite possible that winds from the innermost disk regions play a central role in regulating the rotation of protostars.

Young stars with disks often eject powerful, collimated, bipolar winds or jets. These outflows are clearly the result of disk accretion. We can say this confidently because a) young stars without disks do not show this phenomenon, and b) mass ejection rates, as best we can determine, clearly scale with the accretion rate. Indeed, in the case of the most powerful low-mass outflows – those of the FU Ori objects – accretion is the only energy source large enough to account for the necessary driving.

The high degree of collimation seen in many jets (*e.g.*, Figure 11.5) favors magnetic fields, as well-developed theory shows that rotating fields can provide the necessary collimation. Moreover, the observed outflows or jets are relatively cold; that is, the sound speeds of the gas are well below escape velocity, making thermal acceleration unimportant; and thus magnetic acceleration is not only attractive but probably necessary. What is not clear is whether *outer* disk regions exhibit outflows, at least at a sufficiently significant level to affect disk evolution. [...]

Using the basic theory of magneto-centrifugal acceleration, spatially-resolved kinematics – expansion, rotation – of jets can be used to infer the origin of the outflow, below currently resolvable scales. Observations of jets using the *Hubble Space Telescope* have suggested that the source region for the observed optical jets is ~ 0.2 to 2 AU. These estimates must be regarded as uncertain, as it is very difficult to detect the jet rotation; the analysis must assume no asymmetries in the flow, which may be questionable, given the probable presence of complex internal shocks needed to heat the radiating jet gas.

While outflows clearly emerge from the inner disk, there is little evidence for significant mass loss from outer disks, which could take away significant amounts of angular momentum. In addition, there are difficulties with assuming that the disk wind dominates angular momentum transport even in the inner disk. Removing all the angular momentum by the wind involves removing all the accretion energy in the wind as well, leaving no remaining energy to radiate; but this is problematic, because some rapidly-accreting pre-main sequence disks are self-luminous. It seems more plausible that other mechanisms – the gravitational and magneto-rotational

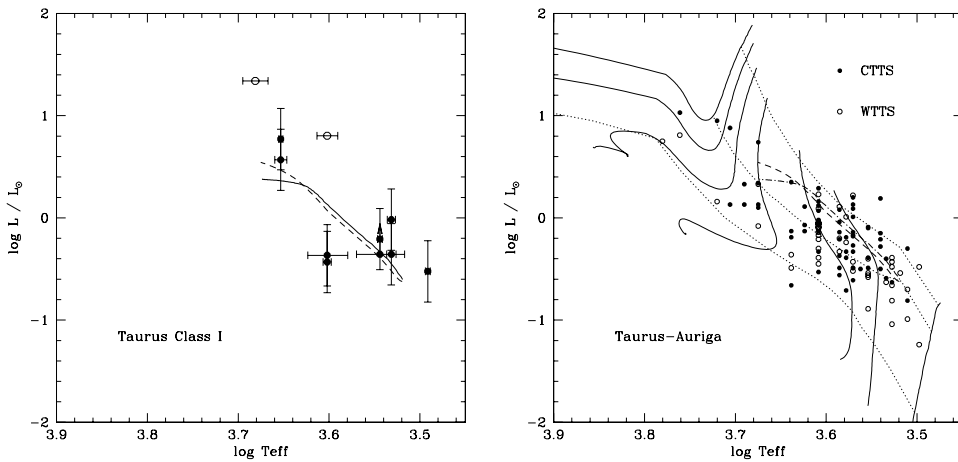


Figure 11.6: Hertzsprung-Russell diagram positions of Taurus protostars (left) and young ([pre-main sequence] T Tauri) stars (right). These plots of two observed quantities – the stellar luminosity L (in solar units) and the effective temperature T_{eff} – can be used directly to infer the stellar radius R via the equation $L = 4\pi R^2 \sigma T_{\text{eff}}^4$, and indirectly the stellar mass via evolutionary tracks. Left: Solid and dashed curves correspond to theoretical estimates of initial protostellar radii (‘birth lines’) as a function of effective temperature (which corresponds roughly to mass). The open circles denote objects in which most of the luminosity derives from accretion, not stellar photospheric radiation. The agreement between theory and observation is reasonably satisfactory given the uncertainties, showing that low-mass protostars do indeed begin their existence with radii only a few times larger than that of the Sun’s. Right: Standard stellar evolutionary tracks compared with observed HR diagram positions of T Tauri stars in the Taurus–Auriga star-forming region. The dashed lines show approximate isochrones for 1 Myr and 10 Myr, assuming contraction from very large radii, along with the birth lines of the left-hand panel. Ages of young solar-type stars are thus determined by the amount they have descended in the HR diagram from the birth line, due to gravitational contraction. [Fig. III:3.8; source: Hartmann (2009).]

instabilities – dominate the angular momentum transport of disks, with the winds being a byproduct of accretion. However, the slow rotation of low-mass protostars may require a powerful wind from the innermost regions to remove the final amount of angular momentum (Sect. 11.3.3).”

11.3.2 Properties of young stars

“Solar-type stars begin their lives with only modestly-larger radii than [in the state into which they settle as ‘mature’ stars (referred to as the ‘main sequence’ phase; [e.g., Fig. 4.2]). This is a consequence of (a) the need to have a significant gas opacity to trap thermal energy, and thus produce enough pressure to halt collapse, and (b) the fact that most of the energy of accretion is radiated outward rather than being trapped. Item (b) is ensured in general by the very high opacity of the protostar compared with the infalling material, and in particular by the angular momentum of the protostellar

core, which makes much (most) of the material land first on the disk rather than onto the central star.

In the absence of energy input, [so prior to the initiation of nuclear fusion, the star-to-be] contracts on the Kelvin–Helmholtz time scale

$$\tau_{\text{KH}} = \frac{3 GM_*^2}{7 R_* L_*} \quad (11.1)$$

where R_* is the protostellar radius and L_* its luminosity. This is basically the ratio of the internal energy divided by the rate at which energy is being lost, with the numerical coefficient set in this case by the assumption that the star is completely convective. {A151} More detailed calculations indicate that during protostellar accretion, the protostellar luminosity and radius have roughly those values which would yield a Kelvin-Helmholtz contraction time of the same order as the timescale for infall. In the case of the protostellar cloud described above, this timescale is $\sim R/c_s$, or a few times 10^5 yr.

For low-mass protostars, fusion of deuterium can play an important role in stopping protostellar contraction at early times. Deuterium fusion occurs at a significant rate when the central temperature reaches $\sim 10^6$ K; this results when $R_*/M_* \sim 5R_\odot/M_\odot$ for a completely convective star. However, as D has a very low abundance, its fusion represents a significant energy source for only a modest time at low masses and very short times for higher-mass, higher-luminosity objects. The result is that stars of masses $\lesssim 0.5M_\odot$ may be detected initially near the D main sequence in the Hertzsprung-Russell (HR) diagram (see Sect. 10.1 and Figs. 4.2 and 11.6), but the youngest higher-mass objects will be found below this 'birth line'. After D is exhausted, the solar-type star will then undergo Kelvin-Helmholtz contraction until it reaches the main sequence, as shown in Figure 11.6. {A152}

Stellar ages for very young stars are estimated from Kelvin-Helmholtz contraction timescales. The accuracy of these estimates depends mainly on uncertainties in two quantities: the stellar mass and the 'starting' radius for KH contraction (left-hand panel of Figure 11.6). Masses are mostly estimated from theoretical evolutionary tracks, though progress is being made in calibrating these from binary orbits and disk rotation; currently there are significant uncertainties for the lowest-mass stars. For higher masses, calibrations are better but the starting radius or birth-line position is uncertain, as it depends upon the precise thermal content of accreted matter rather than on the occurrence of D fusion (see Figure 11.6). For solar mass stars, the upshot is that ages are uncertain by a factor of two or more for Kelvin-Helmholtz estimates at ~ 1 Myr, and perhaps 30% at 10 Myr.

Stellar magnetic fields and activity are important for understanding the angular momentum 'problems' [...] In brief, large areas of the photospheres of very young stars are covered with strong magnetic fields, with $B \sim 2$ kG and covering (or filling) factors of tens of percent. Polar dark spots seem to be typical, though there are significant spots at other latitudes, and the spot areas/fields are not axisymmetric – explaining why there is often substantial rotational modulation of the optical/near-IR

stellar photospheric emission. [...] The variability of the rotationally-modulated starspot-produced light curves – on timescales of days, weeks, months, years – indicates that the fields are not fossil in origin but are produced by some sort of stellar dynamo. [...] The large-scale (dipolar) magnetic field strengths of these stars are important in understanding the interface between the accretion disk and the stellar photosphere. [...] While Zeeman *broadening* clearly demonstrates the existence of 2 kG photospheric fields over substantial areas of the star, the low measurements or upper limits of *polarization* suggest that there must be substantial [polarity] reversals to cancel out the net polarization; this would seem to indicate that the fields are of higher order than dipole, and thus that the large-scale (dipolar) component may be relatively weak, [although it appears that there are] non-negligible large scale fields nonetheless. {A:41}

An important consequence of the large magnetic fields of pre-main sequence stars is that the stellar magnetospheric pressure and torques truncate the disk accretion disks well above the stellar photosphere [(as sketched in Figs. 11.2 and 11.7)]. Magnetospheres are certainly present, given the strong fields found empirically. Moreover, it is clear from observations that [young, still fully convective, pre-main sequence] T Tauri stars accrete through their magnetospheres. The high H α emission and the strongly Doppler-broadened H α emission line profiles of accreting T Tauri stars are convincingly explained by some type of quasi-radial infall; this implies that the rapid rotation and slow radial drift of accreting material in the disk must be disrupted, most plausibly by the stellar magnetosphere (Figure 11.7). The magnitude of the observed velocity line widths can be explained only if the stellar magnetic field is strong enough to truncate the disk at least a few stellar radii above the photosphere, allowing the essentially freely-infalling gas to develop a large gravitationally-produced velocity.

In addition to broad emission lines, accreting T Tauri stars exhibit significant amounts of excess continuum emission at wavelengths running from the far-ultraviolet through the optical region. This ultraviolet-optical continuum emission is most plausibly explained as radiation produced in the accretion shock at the base of the magnetosphere, where the material in near-freefall comes to rest at the stellar photosphere. As described in the previous paragraph, it appears that the disk must be magnetospherically truncated at a few stellar radii above the photosphere; this implies that most of the energy generated by accretion will be radiated in this accretion shock. Estimates of mass accretion rates \dot{M} for T Tauri stars are thus generally based on setting the UV-optical emission excess luminosity $L_{\text{acc}} \sim GM_*\dot{M}/R_*$.

11.3.3 The rotation rate of very young stars

“One of the most striking problems of angular momentum transport is that very slowly-rotating low-mass stars are produced by accretion from rapidly-rotating disks. In general, T Tauri stars of masses $\lesssim 1M_\odot$ rotate at rates from a few tens of percent to less than ten percent of their breakup values. The problem of producing slowly rotating stars somewhat older is made much more difficult by the apparent requirement of spinning down the star at the same time it is accreting high-angular-momentum material. {A153} Of course, if magnetic stellar winds were intrinsically powerful enough to spin down stars rapidly, there is no problem; but spindown does not seem to

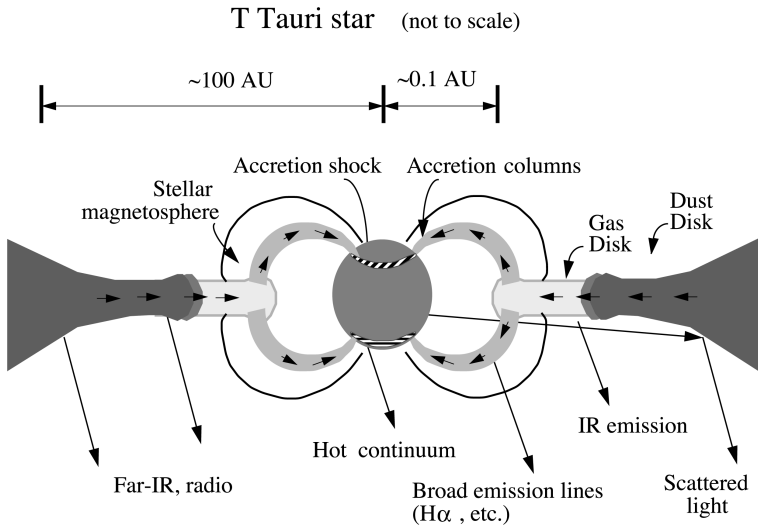


Figure 11.7: Schematic representation of magnetosphere-disk interaction in low-mass, pre-main sequence (T Tauri) stars, with diagnostics of specific regions labeled. [Compare this to the discussion of the 'open magnetosphere' of planets in Sect. 5.5.6 and the effects of corotation and its failure in Sect. 5.5.7. Fig. III:3.10; source: Hartmann (2009).]

be extremely rapid in non-accreting stars, at least not on timescales needed to explain the slow rotation in stars of ages ~ 1 Myr.

One possible option is that the magnetospheric coupling between the star and its disk transfers the angular momentum outwards at the necessary rate. However, there are difficulties with applying this model. In the first place *accretion*, which is observed in essentially all T Tauri stars with detectable inner disks, basically requires magnetic field lines tied to disk material inside of corotation; this spins down the gas so that it can accrete, spinning up the star. Spindown of the accreting star requires magnetic fields connected to the disk outside of corotation; thus, to explain T Tauri stars one would like one set of stellar magnetic field lines to be connected inside of corotation, and another outside of corotation, and somehow balance the angular momentum addition due to the accretion with coupling to the outer disk. Numerical simulations indicate that a quasi-steady state [with both types of connections] may be possible with a large enough turbulent diffusivity, but whether such diffusivities are realistic is unknown. [However, some] estimates of inner gas-disk radii are significantly inside of corotation, raising the question as to whether there is a strong enough large-scale magnetic field to effectively couple to the outer disk for spindown.

T Tauri magnetospheres are probably best thought of as a series of individual magnetic loops, not all of which are filled with accreting gas; this makes it easier to explain the very small covering factors of the hot (shocked) continuum regions on the stellar photosphere of order $\lesssim 1\%$. As at least some of the loops (if not most) must connect to the disk interior to corotation, it is almost certainly the case that magnetic field lines must tend to become twisted. Such twists rapidly lead to a 'ballooning out'

of closed field lines, with eventual opening up of field lines and possible ejection of mass, with reconnection following. [...]” Such processes would appear to make the angular momentum transfer from star to disk even less efficient, although processes related to winds and waves complicate the modeling and our understanding of how things work (as discussed in Ch. III:3.5). It is also possible that heating of part of gas coming into the stellar magnetosphere enables a hot stellar wind from within the star’s magnetosphere, which could lead to efficient magnetic braking. Clearly, for now, the loss of angular momentum from the material accreting onto the protostar remains an area of study.

11.3.4 Protoplanetary disks and gravity

“The mechanisms of angular momentum transport determine the mass distribution within the protoplanetary disk. It is important to understand whether gravitational instabilities dominate this transport, in which case accretion onto the central star is likely to decay away with time, leaving a relatively massive disk behind; or whether another mechanism not tied to gravity can reduce disk mass distributions leading to the epoch of planet formation.” III:3.6

The one non-gravitational mechanism of angular momentum transport that we currently understand (at some level) is the magneto-rotational instability (MRI; Sect. 7.2.3). It is possible that the upper layers of the otherwise cold disk can be non-thermally ionized by stellar X-rays [(as suggested in Fig. 11.2)] and cosmic rays [entering from outside the system], to the extent that a significant amount of mass and angular momentum transport can occur. If large amounts of the disk can be activated magnetically in this way, then the disk can behave essentially as a standard viscous disk, with most of the mass at large radii. However, X-ray and cosmic ray ionization are insufficient if small dust grains, which can absorb ions and electrons very efficiently, are not heavily depleted. [...] Whereas *Spitzer IRS (Infra-Red Spectrograph)* spectra suggest levels of depletion of 10^{-2} to 10^{-3} from interstellar medium values of small dust, it appears that] depletions of order 10^{-4} are needed for the MRI to operate robustly in upper disk layers.

As discussed earlier, it is plausible if not likely that protostellar disks are initially gravitationally unstable, given the need to accrete most of the mass of the central star through the disk and likely limited MRI transport in cold disks. If the MRI is inefficient, the disk could settle into a state of marginal gravitational instability, with the Toomre parameter

$$Q = \frac{c_s \Omega_e}{\pi G \Sigma} \sim 1.4 \quad (11.2)$$

where Ω is the Keplerian (presumed to be the epicyclic) angular frequency and Σ is the disk surface mass density [(the epicyclic frequency is the frequency at which a radially displaced parcel oscillates within the disk)]. The Q parameter basically results from satisfying two conditions: one, that gravity can overcome resisting gas pressure forces; and two, that gravity is stronger than the effects of angular momentum in opposing collapse. Larger values of Q mean that the disk is gravitationally-stable, while smaller values of Q indicate strong instability. In many instances disks tend to self-regulate;

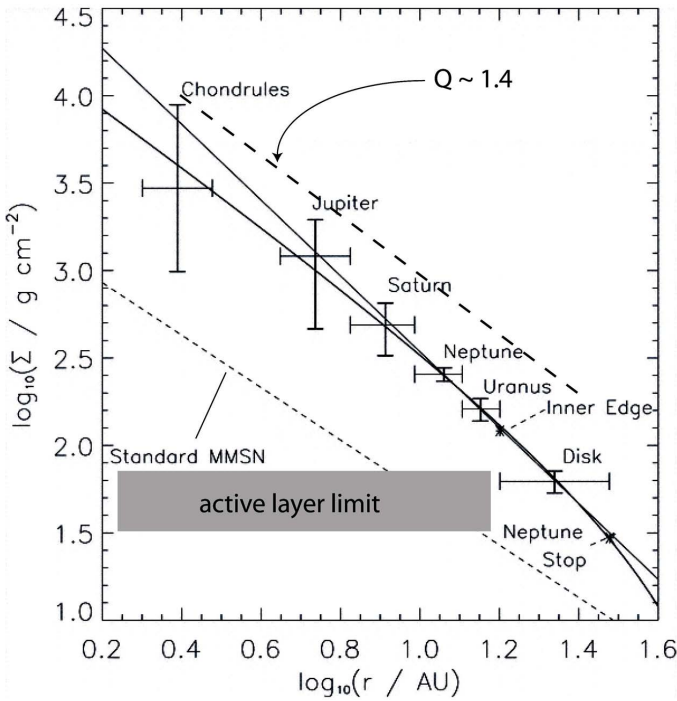


Figure 11.8: Two estimates of the minimum mass solar nebula. The lower, light-dashed curve indicates the usual estimate, derived from the current position of the giant planets and accounting for the missing light elements; the solid curves show a higher estimate based on the initial positions of the giant planets assumed in a model which has substantial outward migration of the giant planets. Limits on the expected MRI-active surface density due to non-thermal ionization and on the surface density expected for a marginally gravitationally-unstable disk (the dashed line showing the condition for the critical value of the 'Toomre Q ' parameter – see Eq. (11.2) – are also shown. [Fig. III:3.12; source: Desch (2007).]

strong instabilities tend to produce heating via shocks which raise c_s and thus increase Q , until the sound speed rises sufficiently that the instabilities heating the gas begin to decay.

Even if the MRI is reasonably well activated by non-thermal ionization, it may easily be insufficient over the 1 – 10 AU region to transport all the mass viscously; this could result in the general picture in which a 'magnetically dead' zone of the disk is sandwiched radially by MRI-active regions at small and large radii.

To develop this further, consider estimates of the mass distribution of the solar nebula. [Figure 11.8 compares two different estimates of the so-called 'minimum mass solar nebula' (MMSN), one using the so-called 'Nice' model (falling not far below the gravitational instability result with Eq. 11.2), which posits substantial inward migration of Jupiter and Saturn and outward migration of the Uranus and Neptune from their original positions, the other an older version based on the current positions of the giant planets. Both estimates lie] above the maximum $\Sigma \sim 100 \text{ g cm}^{-2}$ estimated

for non-thermal ionization by cosmic rays in the most optimistic scenario. While either version of the MMSN must be considered uncertain, the possibility that the solar nebula had a '[magnetically] dead zone' must clearly be considered. [...]

The consequence of a disk structure with a 'dead zone', as described in the previous paragraph, may be highly time-variable accretion during the protostellar phase. [The gravitational instability, GI] can be relatively efficient in transferring mass inward at large disk radii but tends to become inefficient at small radii; conversely, the MRI becomes increasingly important at small radii, especially at high mass accretion rates. If matter moving inward under GI dissipates enough energy locally in the inner disk, it can 'turn on' the MRI thermally, resulting in an onrush of mass onto the central star. This picture has been invoked to explain the FU Orionis outbursts [during which] of order $10^{-2}M_{\odot}$ gets dumped onto the central low-mass star over timescales $\sim 10^2$ yr. It is difficult to explain the FU Ori outbursts without having a large amount of disk mass at a few AU, well above that of the standard MMSN.

The possibility of gravitational instability [makes one reconsider] the possibility of forming giant planets directly through gravitational fragmentation [rather than by the core-accretion scenario described near the top of Sect. 11.2]. This suggestion runs into difficulty, however, because a low Q is not enough; the disk must be able to cool on something like an orbital period P_{orb} to continue fragmenting; otherwise perturbations shear out and transport angular momentum instead. This poses a problem for protostellar disks because they are so cold, and thus do not cool rapidly. The cooling timescale t_c for an optically-thick disk [...] is basically the energy content divided by the blackbody radiation loss. Numerically, for temperatures below 170 K, one finds

$$\frac{t_c}{P_{\text{orb}}} \sim 10^4 \left(\frac{M}{M_{\odot}} \right)^{3/2} R_{10}^{-9/4} \quad (11.3)$$

(with R_{10} is a characteristic scale in units of 10 AU), which poses an obvious difficulty for fragmentation in that the cooling time far exceeds the Keplerian period. (Things change on distance scales ~ 100 AU or larger, because the disk typically becomes optically thin, and thus cools much more rapidly than indicated by the above equation.)

Even if fragmentation could occur after infall ceases, one would still expect it to be more important early on, when the disk is more massive. It is not obvious how initial gravitational instability would explain the observed clearing of disks over millions of years."

11.3.5 Dust-disk evolution

"In the core accretion model for the formation of giant planets, and in all models of terrestrial planet formation, dust grains grow from sub-micron sizes to thousands of km. A starting point for thinking about how planets grow from disks is then considering observations of the evolution of disk dust, detected through its emission.

Figure 11.9 shows the estimated fractions of young stars in various groups with large dust-disk excesses as a function of age. [...] The overall result is that optically-thick dust disks (with the opacity probably dominated by particles of μm size or a bit less) disappear on timescales of a few Myr. While less is known about the presence of gas

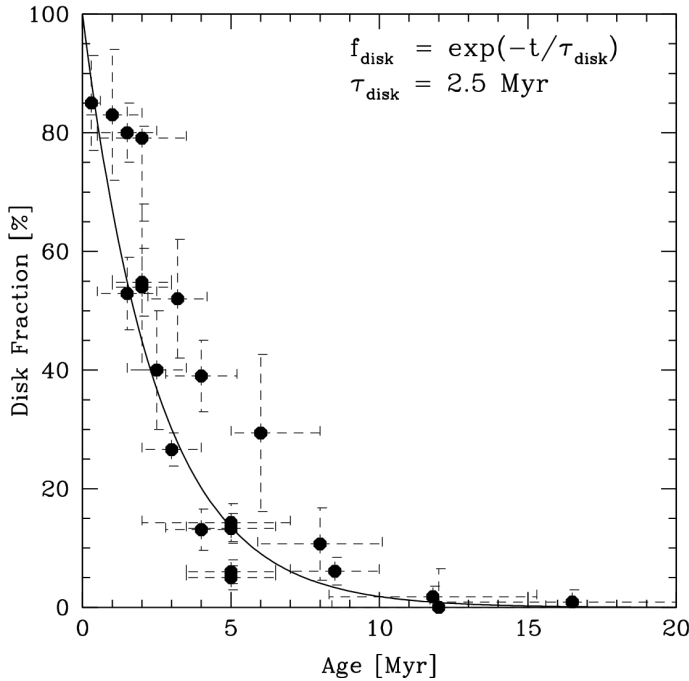


Figure 11.9: *Primordial disk fractions of stars in young clusters. These observations show that the dust disks only last for a few million years. [Fig. IV:5.10; source: Mamajek (2009). Note that since this figure was made the ages for very young stars systematically increased by $\sim 50\text{-}100\%$ for many of these young samples (see, e.g., work by Bell *et al.* (2013), by Bell *et al.* (2015); by Pecaut *et al.* (2012), and by Pecaut and Mamajek (2016).), so that the e-folding timescale for primordial disk loss is something like 4–5 Myr rather than the ~ 2 Myr shown in the figure (Eric Mamajek, private communication).]*

in the inner 10–20 AU, clearing of small dust particles seems generally accompanied by removal or disappearance of gas as well. It is important to emphasize that there is no single timescale for disk clearing. Some (inner) disks disappear immediately, perhaps because of disk disruption by a binary companion; others take a few Myr; a small percentage last for 10 Myr.

The disk can ‘disappear’ in one of three ways; mass can be accreted, ejected, or condensed into large bodies. It is difficult to accrete all the mass of the disk, as some must be left behind to take up the angular momentum; the outer disk is likely to expand over time and evolve on continually slower timescales. Evaporation of the disk may be important, though it is thought to take place over longer timescales than this (Sect. 11.3.6). Perhaps the strongest evidence for coagulation into larger bodies is the detection, either through spectral energy distribution fitting and/or imaging, of systems with substantive outer disks but inner disk holes or gaps. This is consistent with the idea that settling, grain growth, coagulation, and formation of large solid bodies occurs fastest in the inner disk, where the surface densities are largest.

Dust grains in the disk generally are thought to evolve to larger sizes, with a

decreasing population of small grains with increasing age. During this overall growth, dust is expected to settle vertically and drift radially. ^{A154} This evolution of dust in size and position in the disk can reduce and ultimately eliminate infrared excess emission, consistent with the observed disappearance of dusty disk emission over millions of years (Figure 11.9). In principle, dust growth can be extremely rapid: [the disk interior to about 10 AU may become] optically thin on timescales of 0.1 to 1 Myr, as dust particles settle and coalesce into larger bodies. The evolution of the mm fluxes is slower because of longer timescales of accumulation in the outer disk, with substantial reductions in mm-wave emission on timescales of 10 Myr. One might expect that turbulence would lengthen settling and growth timescales, but [it may actually stimulate] growth due to turbulent mixing. [...]

As particles grow in size, many effects converge to make evolution uncertain. For example, the difference in velocities between objects within an order of magnitude of meter size can result in their complete shattering or disruption. Turbulent eddies or whirlpools might help collect these objects at low velocities so that they can accrete, or alternatively disperse them more widely.

Can core accretion proceed fast enough to explain the observed disk clearing on timescales as short as [several] Myr? One problem is the formation of km-sized planetesimals from cm-sized objects. Such bodies are thought to be held together lightly – too large for effective sticking and too small for gravity to become important – and, as bodies of differing sizes have differing velocities due to gas drag, collisions between these objects might shatter them rather than build them up. Another problem is that the so-called Type I inward migration due to torques between the disk and the body is very rapid, making it important to grow quickly at ~ 1 Earth mass to avoid falling into the central star on a timescale < 1 Myr. These estimates have usually been made in the 'minimum' MMSN (Figure 11.8); the timescale for inward migration is inversely proportional to the surface density, so gravitationally-unstable disks may pose even bigger problems in this regard.

Once km-sized planetesimals are made, collisions among them can lead to the building of terrestrial planets and giant planet cores. The remaining bottleneck is that of accumulating gas which depends upon the opacity; larger opacities make it difficult for the growing planet to lose energy and allow additional material to be accreted. A reduction in opacity due to grain growth and depletion would help considerably in this regard.”

11.3.6 Disk evaporation

“As the planets are overabundant in heavy elements relative to the Sun, it is clear that most of the original gas in the solar nebula has been lost. Of course some of it accreted into the Sun, but it is unlikely that all of this material was removed in this way. For some time it was thought that a powerful solar-type wind was responsible for gas removal from the nebula. However, we now realize that the strong mass loss we see is not a solar wind but a disk wind; more importantly, the wind material is ejected perpendicular to, not into, the disk (Figure 11.5).

The high-energy radiation emitted by T Tauri stars provides a mechanism by which

the gas of the disk can be evaporated rather than accreted. In this case, rather than generating stellar mass loss from the star via a coronal wind, one can generate disk mass loss from a much lower temperature wind because the material is ejected from much farther out in the gravitational potential field, where the escape velocity is very much smaller than at the stellar surface. Using the usual Parker wind formula (*e.g.*, Eq. 7.11), and assuming photoionization and thus heating to a typical temperature of $\sim 10^4\text{K}$, the sonic point occurs for

$$R_s \sim \frac{GM_*}{2c_s^2} \sim 3.6 \frac{M_*}{M_\odot} \text{ AU}, \quad (11.4)$$

where the mean molecular weight is 0.67, appropriate for a gas of cosmic abundance with ionized hydrogen and neutral helium. Thus, ionizing photons have the potential for removing disk gas at radii of a few to ten AU from the central star.

To see the essential physics of the problem with a minimum of geometrical complication, assume that a volume of $4\pi R^3$ must be ionized, where R is a characteristic radius of escape. This estimate is justified because the gas must maintain its ionization over the disk to a distance comparable to its escape radius to flow out of the gravitational potential well. The balance between photoionization and recombination leads to

$$\Phi_i = 4\pi R^3 n_e n_p \alpha_B, \quad (11.5)$$

where Φ_i is the flux of ionizing photons from the central source, n_e and n_p are the electron and proton densities, respectively, and α_B is the Case B recombination rate for hydrogen. ^[30] Assuming complete ionization of hydrogen, the mass loss rate is

$$\dot{M} \sim 10^{-9} \Phi_{i,41}^{1/2} R_{10}^{1/2} M_\odot \text{ yr}^{-1}, \quad (11.6)$$

where $\Phi_{i,41}$ is the Lyman continuum photon flux in units of 10^{41}s^{-1} and R_{10} is a characteristic scale of the flow in units of 10 AU. This estimate illustrates the potential of photo-evaporation to remove disk gas over evolutionarily interesting timescales. Much more sophisticated treatments of the outflow have been considered, but this illustrates the basic result. [...]

Unfortunately, the true ionizing fluxes of young stars are not really known because interstellar absorption prevents direct detection [... , but there are observational results that suggest] evaporation of disks due to stellar magnetic activity occurs on timescales of order 10 Myr or more. Whether photo-evaporation plays a major role in the strong disk evolution from 1–10 Myr remains unclear.

Disks close to a hot luminous star can be photo-evaporated rapidly due not only to EUV (Lyman continuum) radiation but also by far-UV ($\sim 1000 \text{ \AA}$) radiation, which can heat the gas to temperatures $\sim 1000 \text{ K}$ as electrons are driven off grains. The

³⁰ 'Case B' recombination considers only recombinations in which the recombined electron transitions to the ground state via intermediate transitions; a direct transition to the ground state would emit a photon that could be absorbed and lead to ionization in which case no net recombination would have occurred.

FUV radiation thus can drive a wind off the outer disk, and may be more important in many systems if most of the disk mass resides at large distances. [...] Although the solar nebula appears to have been 'polluted' by ejection from a supernova, it is not clear that it was close enough to the massive star such that FUV radiation was important in evaporating Solar System gas." {A155}

}{A155}

Chapter 12

Irradiance, atmospheres, and habitability

Chapter topics:

- Terrestrial atmospheric composition and ocean coverage over time
- Comparison of the atmospheres of the terrestrial planets
- Solar irradiance, orbital changes, and the equilibrium temperature of planets
- The effects of stellar winds and geological activity on planetary atmospheres

Key concepts:

- Habitable zone
- Albedo
- Radiative forcing
- Atmospheric loss

12.1 Evolving planetary habitability

Historical records are too short for us to see first-hand accounts of Earth in a significantly different climatic state than the present one. There are, of course, reports on the relatively recent moderate (but nonetheless impactful) excursions from the mean climatic state, such as the Medieval Warm Period, the Little Ice Age, and the modern-day onset of global warming, but there have been much larger changes over the life of the planet. Substantial modifications of climate in the past have been attributed to the formative processes of Earth and asteroid impacts, to the evolving spectral output of the Sun and the stripping effects of the solar wind, to orbital changes in response to the gravitational pull by the giant planets, to the torque applied by the Moon, to geological and geochemical activity over eons (including the geodynamo), and – last but by no means least – to the emergence and evolution of life. This chapter provides brief introductions to each of these drivers of the terrestrial atmosphere and its climate system. This provides insight into the diversity of conditions on Earth over time, while also setting the stage for appreciating the challenge of establishing the ‘habitability’ of planets elsewhere in the universe.

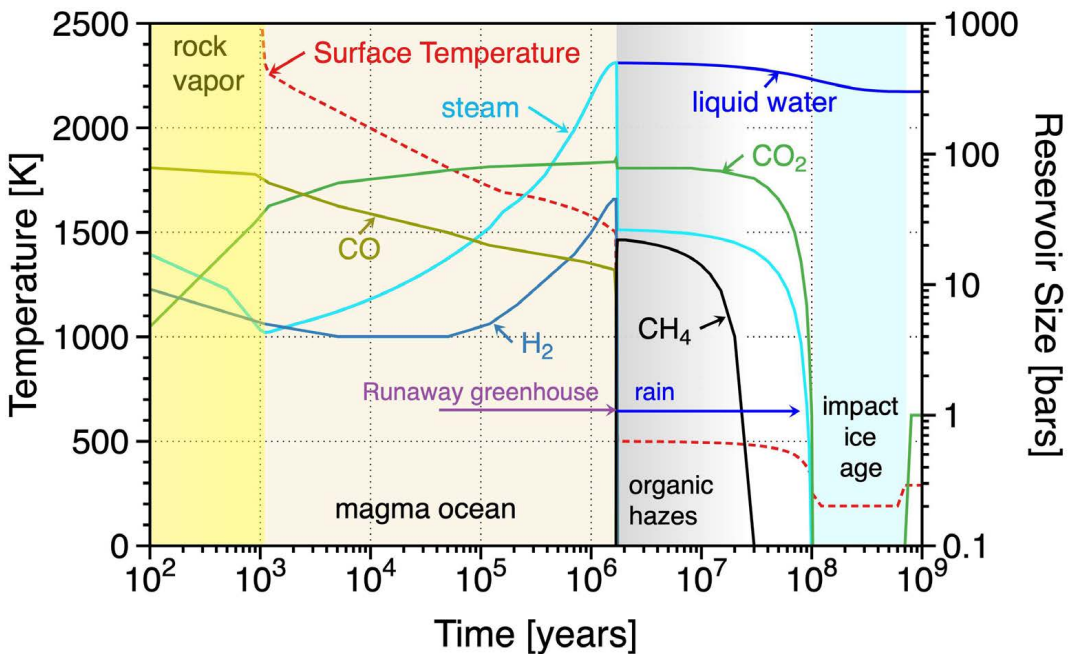


Figure 12.1: The Earth’s surface temperature and above-surface reservoirs of water and carbon dioxide after the Moon-forming collision. The surface temperature drops below 1000 K after a few million years when Earth’s steam atmosphere condenses, and it drops below 500 K to habitable conditions after about 100 million years when most of the atmospheric CO_2 is incorporated into the mantle. [This is an updated version, courtesy of Kevin Zahnle (July 2019), of the originally used Fig. III:4.3; the latter was from this [source](#): Zahnle et al. (2007).] For a color version of this figure, see [arXiv:2001.01093](#).

12.1.1 Earth’s formative phase

“Earth’s formation, like that of the other solid planets, occurred by accretion of solid materials. The processes began with particles of dust, but collision and sticking processes rapidly led to the formation of larger and larger bodies. An important aspect of the growth of rocky planets is the amount of a planet’s mass that is accreted in the form of large chunks. The accretional growth process yields a number of Moon to Mars-sized ‘embryos’ in a given radial region of the nebula. The final assembly of a rocky planet involves both the accretion of numerous large embryos as well as gravitational ejection of some of them to other locales [(including, as we now know through gravitational microlensing, out of a planetary system altogether and into interstellar space)].

This formation mode that includes impacts of very large bodies is indicated both by the numerical simulation of accretion processes and by evidence that our Moon formed as the result of the impact of a Mars-sized body with the growing Earth [...]

Following lunar formation, Earth’s post-impact atmosphere of vaporized silicates may have condensed in ~ 1000 yr (Fig. 12.1). The heat of the impact would have

melted and partly vaporized Earth’s mantle, but the resulting silicate magma ocean may have solidified in only a few million years. Once the magma ocean crystallized, cooling conditions would have allowed the large amount of water vapor injected into the atmosphere to condense and thus reduce the extreme greenhouse warming of the early Earth and allow surface temperatures to drop below 1000 K. {A157} Even with most of the water condensed, the atmosphere would still retain ~ 100 bars of CO_2 whose greenhouse warming would keep the Earth’s surface temperature at ~ 500 K, even though the early Sun was $\sim 30\%$ fainter than its present brightness. The final lowering of the Earth’s surface temperature to habitable conditions requires transfer of most of the atmospheric CO_2 to the mantle and crust, a process that can happen over a timescale of 10 – 100 Myr [... by the process of weathering (more on that below).] {A157}

[...] Earth’s oldest known rocks, whose properties could provide information about the early Earth, are just less than 3.9 billion years. This is a curious age: the Earth’s oldest surviving rocks formed just after a rock-destroying time period known as the Late Heavy Bombardment or LHB. [...] The origin of the LHB has long remained a mystery. Solar system formation models as well as the observed crater record suggests that the LHB was not just the tail end of the planetary accretion process. The presence of heavily cratered regions on other bodies, including Mars, suggest that the LHB may have been a Solar-System wide process. [...] The ‘Nice Hypothesis’ [(named after the city in France at whose university this hypothesis was first formulated)] suggests that a dramatic rearrangement of the outer planets gravitationally perturbed a large number of cometary bodies into orbits that penetrated the inner Solar System and cratered the surfaces of all Solar-System bodies [(see Sect. 11.2) ...]”

12.1.2 The habitable zone

“One of the most important requirements for life as we know it is water. The ability to retain surface water is the general basis of the concept of the Habitable Zone (HZ). As most commonly used, the habitable zone is an estimate of the range of distances from a star where an Earth-like planet can maintain surface water for extended periods of time. {A158} While a number of factors, including greenhouse gases, tilt of spin axis, planet composition, surface gravity and cloud properties can be important for habitability, the primary factor considered for the habitable zone is the most fundamental, just the distance from the star (see below around Eq. 12.3). For the present-day Sun, the habitable zone is generally considered to be the range from just inside Earth’s orbit to a region near or just beyond Mars’ orbit. The inner boundary is where surface water is lost to space by either a runaway greenhouse effect or the ‘moist greenhouse’ effect. In a full runaway, the surface temperature can exceed the critical point of water (374°C), *i.e.*, the temperature where liquid water and steam have the same density and are not distinguishable from each other. Due to the extreme greenhouse warming caused by an ocean mass of water vapor, the surface temperatures on an Earth-like planet can reach the melting points of rocks. In comparison, the moist greenhouse is gentle and occurs when the partial pressure of water vapor at high altitudes becomes sufficiently elevated so that a substantial flux of water can be transported into the stratosphere and beyond. At high altitudes, H_2O is decomposed {A158}

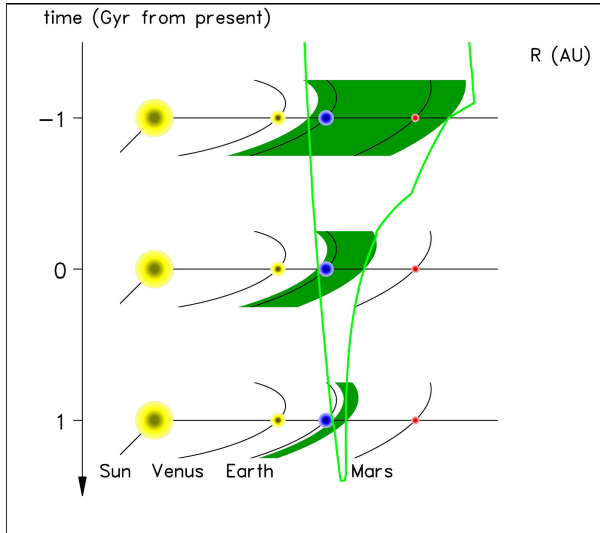


Figure 12.2: The photosynthetic habitable zone (pHZ) over time, from 1 Gyr in the past to 1 Gyr in the future. The inner edge of the pHZ moves outwards as the Sun becomes brighter with age and the outer edge moves inwards as surface warming leads to decline of CO_2 in the atmosphere to the point where photosynthesis is not possible. [Fig. III:4.1; modified from source: Franck *et al.* (2001); also [here on the web.](#)] For a color version of this figure, see [arXiv:2001.01093](#).

by UV photolysis and the liberated hydrogen ultimately escapes to space.

The outer edge of the habitable zone occurs when surface water freezes. A commonly quoted limit is 1.37 AU based on the onset of formation of CO_2 ice clouds. A more extended limit of 1.67 AU is based on the maximum greenhouse warming that could occur in a cloud-free CO_2 - H_2O atmosphere. The highest estimate and perhaps an upper limit is 2.4 AU based on a combination of cloud altitudes and particle sizes that could optimize radiative warming by CO_2 clouds [...]

For planets, the conventional habitable zone moves outward with time as their central stars brighten. Typical stars brighten by a factor of ~ 2.5 during their main-sequence lifetimes, the periods of their lives when they are stable stars fusing hydrogen to form helium. Main sequence stars of all mass brighten by a similar fraction as the ratio of He/H in their cores increases with time. At present, the Sun is nearing half its main-sequence lifetime and it is brightening at a rate of about 10% per billion years, and is currently about 30% more luminous than it was 4 billion years ago. More massive and less massive stars brighten at higher and lower rates proportionate to their total main-sequence lifetimes (cf., Fig. 10.1) [...]

The habitable zone concept becomes more complex when the ability to have photosynthesis is considered. A more restrictive consideration of surface habitability by organisms similar to plants and animals is the photosynthetic Habitable Zone or pHZ. Photosynthesis requires atmospheric levels of CO_2 above some critical limit, approximately 10 ppm for known plants. The pHZ of a given star (see Fig. 12.2 for

the case of the Sun) narrows over time as the star gets brighter. The inner edge moves outwards and the outer edge moves inwards. For a planet with land and surface water, weathering processes remove CO₂ from the atmosphere. The process involves sequestering CO₂ in carbonates and this becomes increasingly more effective as [brightening] stars produce warmer planetary surfaces. This process can cause the pHZ to shrink to zero. Estimates indicate that the Sun's pHZ will shrink to zero width when the Sun reaches an age of 6.5 billion years. The Earth, even now close to the inner edge of the habitable zone, will be left behind the moving pHZ, and lose most of its surface water, long before this time [...]" {A159}

12.1.3 Oxygen, methane, and carbon dioxide over time

"Prior to 2.4 billion years ago, the Earth's atmosphere was essentially devoid of free oxygen. Although it was being produced by photosynthetic organisms such as cyanobacteria as well as the photolysis of water vapor, it was efficiently removed from the atmosphere as it oxidized compounds on the surface and in the atmosphere. Before this time, the atmosphere was dominated by N₂ but it contained appreciable amounts of CO₂, water vapor and probably moderate amounts of CH₄, possibly up to the percent level. There is abundant evidence for low oxygen abundance on the early Earth including the oxidation state of various minerals, including iron oxide [...]" {A159} III:4.7

The crossover, *i.e.*, the appearance of oxygen and simultaneous loss of methane, occurred 2.4 billion years ago. At this time the Earth entered a severe ice age, also called a 'Snowball Earth' episode, during which the planet surface cooled to the point where ice formed at equatorial latitudes. It seems likely that this unusual cooling event was related to the rapid loss of significant greenhouse warming previously associated with the presence of methane." {A160}

"Photosynthesis is the primary means by which life on Earth derives energy from the Sun. The complex chemical processes involved with photosynthesis depend on the availability CO₂ in the atmosphere and CO₂ can be considered an essential 'food of life' on our planet. CO₂ on the present Earth is controlled by biogeochemical processes but in the future, as the Sun becomes brighter, the atmospheric CO₂ abundance will decline below the minimum (~10 ppm) amount needed to support plants. The end of CO₂ will mark the end of plants and animals that depend on direct contact with Earth's natural atmosphere [...]" {A160} III:4.9

We currently have major concerns with the CO₂ increase from burning fossil fuels and its global warming effects. However, this is a short-term problem. Ultimately, all of the atmospheric CO₂ will become locked up in carbonates and removed from the atmosphere. Even now, most of the CO₂ that has ever been in the atmosphere is already in carbonates. CO₂ is the dominant gas in the atmospheres of Venus and Mars and it must have been a major gas in the Earth's atmosphere before it declined due to carbonate formation. If Earth's total carbonate content were decomposed, it would yield over 20 atmospheres of CO₂, over 4×10^4 times the present CO₂ content of the atmosphere. As the Sun gets brighter, as all stars do as the hydrogen content of their cores is consumed, the Earth's surface temperature will increase and the CO₂ will decline as more and more is sequestered into carbonates. The removal process is related

to weathering of rocks, a process whose rate increases with increasing temperature. The presence of silicates, water and atmospheric CO₂, leads to the formation of carbonates. Presently, this process is dominated by biological processes such as the formation of shells, corals, and microscopic organisms such as foraminifera. {A161}

{191V} When atmospheric CO₂ is sufficiently depleted, Earth will have lost an important factor that has promoted the long-term stability of its surface temperature. Over Earth’s history, the abundance of carbon dioxide and its greenhouse warming effects have varied in ways that have counteracted changes in atmospheric temperature. When Earth cools over long time periods, the CO₂ abundance can rise and promote greenhouse warming. When Earth warms, the CO₂ abundance can decline and promote cooling. This effect is called the carbonate-silicate cycle and it is a case of negative feedback where change is resisted leading to stability. [...] Carbon is removed by weathering but is involved in a cycle because it is ultimately reintroduced back into the atmosphere. Carbonate deposits in the ocean floor are subducted beneath continents on ~100 Myr time scale where they are thermally decomposed and release CO₂ back into the atmosphere via volcanism. The CO₂ sink depends on weathering and carbonate deposition and the CO₂ source depends on subduction, an ongoing process associated with plate tectonics.”

12.1.4 Water over time

It appears that much of the water on the terrestrial planets may have been transported to the inner parts of the Solar System frozen within asteroids that were scattered from further out during phases of orbital changes of the giant planets, and then to Earth in collisions. Venus and Mars have lost their oceans a long time ago, as discussed in Sect. 12.4.1. Earth, too, will eventually lose the bulk of its water “when a critical threshold brightness is reached [in the Sun’s evolution]. Ocean loss is a drastic change for a planet, and for Earth it will mean a change to a seemingly ‘unearth-like’ state, a planet more like Mars than the blue planet of its past. [...] Even without oceans, Earth will probably always have regional ponds or lakes fed by water derived from the mantle. The mantle is a reservoir that may contain several ocean-masses of water.

The most likely fate of Earth’s oceans is loss by the ‘moist greenhouse’ effect, a process that occurs at present but at a very low rate. In this process, water is transported through the troposphere and stratosphere to heights where its hydrogen can be liberated by photolysis with solar UV photons [(Sect. 12.4.1)]. Near the exosphere the liberated hydrogen escapes to space, and forms Earth’s Ly α geocorona.

{A162} This process currently occurs at a rate of only a meter of ocean in a billion years due to the very low abundance of water vapor in the stratosphere. As the Sun warms, the partial pressure of water in the upper atmosphere rises and the timescale for water loss shortens. Modeling of this process indicates that the moist greenhouse effect will begin severely depleting the Earth’s oceans in about a billion years or less. If surface water is not largely depleted by the rather gentle moist greenhouse process in roughly 3 billion years, a much more severe process will take over when the Sun is about 35% brighter than it is at present (Fig. 10.2, also Fig. 10.1). In a runaway, increasing temperatures introduce more greenhouse gas thereby providing positive

feedback. This full runaway greenhouse advances to the critical point of water where density of water vapor equals the density of liquid water. In a runaway, the enormous amount of water vapor in the atmosphere produces greenhouse warming sufficient to melt surface rocks. Either the moist-greenhouse or the runaway-greenhouse process will result in the Earth's loss of its oceans to space and our planet will spend over half of its total life as an ocean-free planet, at least initially covered with salt and very oxidized rocks. [...]

The loss of oceans is likely to also lead to the end of plate tectonics. Hydrated minerals have lower melting points and in several ways the presence of water promotes the sinking of oceanic crust to subduct beneath continents. Without oceans it is expected that plate movement will stop and Earth – like all other planets in the Solar System – will cease to have subduction and the drift of continents. Without subduction, the Earth's major mechanism for cycling CO₂ back into the atmosphere will be lost.” When plate tectonics stops, this may also have major consequences for the planetary dynamo. {A163}

12.2 Atmospheres and climates of Venus, Earth, and Mars {A163}

In this volume, we focus on the terrestrial planets Venus, Earth, and Mars “because they are thought to have been habitable at their surfaces at some point during Solar System history. They formed under similar conditions, with early atmospheres that were more similar than they are today. The present day climates of Venus and Mars provide a useful contrast to that of Earth, and exploration of the root causes for differences in the present climates of all three planets allows us to better understand the processes that control climate on terrestrial exoplanets. Their current climates are summarized in Table 2.1 [...]. Despite their large differences in mass, the atmospheres of Venus and Mars have similar bulk compositions, with carbon dioxide (CO₂) comprising ~95% by volume, followed by molecular nitrogen (~3%) and argon (~1%). Earth's atmosphere, by contrast, is composed mainly of nitrogen and oxygen, followed by argon. {A164} Earth's atmospheric composition likely mirrored that of Venus and Mars early on, but much of Earth's atmospheric CO₂ now resides in carbonates on the ocean floors, leaving nitrogen as the most common constituent. Earth's abundant atmospheric oxygen is believed to have been contributed by photosynthetic bacteria. {A164}

The surface temperatures of the three planets also differ widely, in part due to the distance of each planet from the Sun and in part due to the quantity of greenhouse gases in each atmosphere. Earth is the only of the three planets with a surface temperature (and pressure) appropriate for liquid water to be stable for long periods of time, thanks to ~30 K of greenhouse warming. The Cytherean atmosphere is too hot for water to exist as liquid at the surface, while the Martian atmosphere has too low a surface pressure (liquid water would sublime, except at the lowest elevations). The atmosphere of Venus is very dry, indicating that any surface water driven into the atmosphere by the high temperatures no longer resides there. The atmospheric water content at Mars is an order of magnitude larger than at Venus and, given the low atmospheric pressure, is often nearly saturated. Despite the near 100% Martian relative humidity,

Earth still has roughly 50 times more water molecules (per number of particles of atmosphere) than Mars. The composition, temperature, and water content lead to different forms of precipitation on the three planets. Earth has a variety of forms of water precipitation, while Mars has carbon dioxide and water frost. Venus has no precipitation at the surface due to its high temperatures; any precipitation that forms higher in the atmosphere would turn to vapor before reaching the ground.

Circulation patterns on the three planets also differ. Earth possesses three circulation cells in each hemisphere, leading to prevailing winds organized by latitude. The circulation results, in a simplified sense, from an equator-to-pole temperature gradient that causes warm air to rise at the equator and fall at the poles. Earth’s rotation provides a Coriolis influence that breaks the circulation cells into three regions, keeping the warmest air relatively confined at low latitudes. Venus, by contrast, rotates very slowly. Thus, heat is transferred efficiently from the equator to polar regions, leading to uniform surface temperatures as a function of latitude and local time. Mars rotates at nearly the same rate as Earth but has only one circulation cell per hemisphere, though there are some arguments to suggest that while there is a net circulation, air tends to move in localized regional cells. Air at the surface of Mars moves sufficiently quickly to drive dust devil activity, while the surface of Venus is very still. At higher altitudes on Venus, however, the atmosphere super-rotates on timescales of days.

While Earth’s seasonal variations, caused by a 23.5° tilt relative to its orbital plane, will be well known to the reader, seasonal variations on Venus and Mars are substantially different. Venus has nearly no seasonal variation due to a very small ($\sim 3^\circ$) axis tilt. Mars has a tilt of 25° , similar to that of Earth, but the planet’s greater orbital eccentricity (a 21% difference between the perihelion and aphelion distances compared to 1.4% and 3.3% for Venus and Earth, respectively) leads to shorter and more intense summers in the southern hemisphere compared to the north. Strong heating during southern summer drives enhanced dust devil activity, which can couple across circulation cell boundaries and grow into planet-encompassing dust storms that last several weeks.”

“[A]bundant evidence points to changes in the climate of all three terrestrial planets on a variety of timescales. Here, we focus on evidence for climate change over tens of thousands of years or longer. [...] The most compelling evidence for climate change on Venus comes from measurements of the isotopes deuterium and hydrogen in the atmosphere today. Deuterium is far scarcer than hydrogen in the atmospheres of all planets. However, the ratio of deuterium to hydrogen (D/H) in the Venus atmosphere – about 2 deuterium atoms for every 100 hydrogen atoms – is more than 100 times the same ratio calculated for Earth and most other Solar System objects. There is little reason to expect that Venus formed with a D/H ratio significantly different from that of Earth, so we infer that the D/H ratio on Venus increased after the planet formed. Specifically, it is thought that hydrogen atoms (possibly from a primordial ocean ^[31])

³¹ Alternatives to a primordial ocean for Venus include a more recent reservoir, or perhaps one that continues to be replenished, from volcanic outgassing – possibly clustered in major events – or cometary supplies – see work cited in [this review by Marcq et al. \(2018\)](#)

preferentially escaped the planet's gravity compared to deuterium and were lost to space [...] – water was dissociated in the atmosphere and the hydrogen removed to space. [...]

[E]vidence for climate change on Earth is abundant and comes in many different forms. [...] The terrestrial climate record [derived from a diversity of sources (including growth rates of tree rings and corals, isotope ratios, gases trapped in air pockets in ice, geochemistry, fossils and sediments)] suggests that Earth's climate varies on many timescales, with departures in temperature of as much as 10–15°C over Earth's history. There are many inferred cold (glaciation) and warm periods that have been tied with changes in atmospheric conditions and diversity of life. Similarly, there are a few major changes in atmospheric composition, the most notable of which is the oxygenation of the terrestrial atmosphere more than two billion years ago, likely caused by the rise of oxygen-producing bacteria and the subsequent depletion of sinks for oxygen at Earth's surface. Analysis of the size and depth of fossilized raindrop imprints in sedimentary rock even suggests that Earth's surface pressure has varied by as much as a factor of two over 2.7 billion years. Taken together, the evidence provides a caution against interpreting the present day climates of other terrestrial planets too finely, and assuming only monotonic changes in planetary climates over billion year timescales. At the same time, one of the most notable aspects of the terrestrial record is the fact that water has existed as liquid at the surface for most of the planet's history, suggesting that despite short term deviations Earth's climate has been relatively stable over its history, in likely contrast to Venus and Mars.

Mars also provides several lines of evidence suggesting past climate that differs from today. [...] These include dry dendritic (branching) river valley networks, river delta deposits, possible regions of sedimentary rock, smoothed and rounded rocks imaged by Mars rovers, and possible ancient ocean shorelines. These features all suggest an ancient Mars where liquid water was abundant and active in shaping the surface of the planet. Further, highly eroded crater rims and a paucity of small craters relative to what might be expected from the abundance of large craters suggest that the ancient atmosphere was much more efficient at eroding surface features (*i.e.*, thicker) than today – perhaps as thick as 0.5-3 bars, or even more. [...] A number of Martian atmospheric isotope ratios (D/H, $^{38}\text{Ar}/^{36}\text{Ar}$, $^{13}\text{C}/^{12}\text{C}$, $^{15}\text{N}/^{14}\text{N}$, $^{18}\text{O}/^{16}\text{O}$) point to the stripping of atmospheric particles to space over billions of years, similar to the inference drawn from D/H measurements at Venus. [...] The isotope ratios suggest that 50-90% of the total atmospheric content has been removed to space from stripping processes alone.”

12.3 Irradiance, orbits, spin, and climate

12.3.1 Atmospheric effects and albedo

In this section we first look into equilibrium temperatures in the absence of a planetary atmosphere, and then proceed to see how an atmosphere modifies such an equilibrium. We will focus on planets orbiting our Sun, but the same arguments hold for exoplanets orbiting other stars, of course. “The fraction of the solar luminosity L_{\odot}

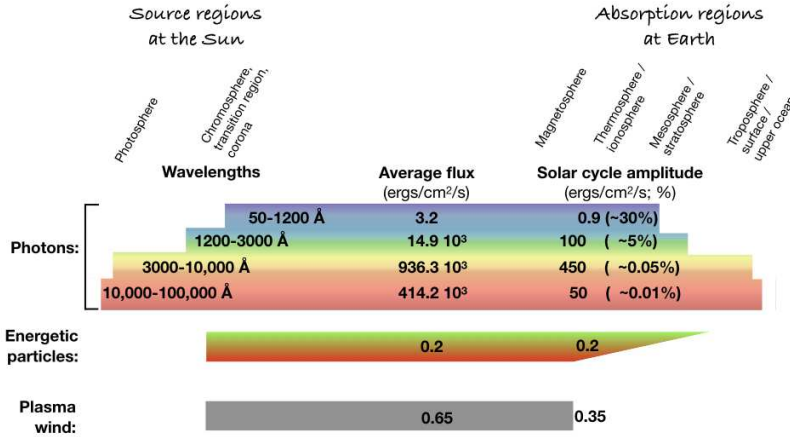


Figure 12.3: The flow of energy from the Sun to the Earth is compared for photons in four different wavelength bands, energetic particles, and the plasma wind. The numbers are approximate energies with their variations during an 11-yr solar activity cycle, in erg/cm²/s. Visible radiation connects the surfaces of the Sun and Earth while ultraviolet radiation connects their atmospheres. Particles and plasma connect the outer solar atmosphere primarily with Earth’s magnetosphere and high-latitude upper atmosphere. [After Fig. III:10.3] For a color version of this figure, see arXiv:2001.01093.

that is absorbed by a planet is given by the ratio of the planet’s cross section πR_p^2 to the area $4\pi d_p^2$ of a sphere containing the planet at distance d_p from the Sun, corrected for the albedo a ([the fraction of total incoming power that is reflected]):

$$\mathcal{P}_{p|a} = L_\odot \frac{\pi R_p^2}{4\pi d_p^2} (1 - a) \equiv \mathcal{P}_\odot (1 - a) \tag{12.1}$$

[where \mathcal{P}_\odot is defined as the total energy per unit time intercepted by the planetary disk. . .]” “The albedo is defined as the ratio of diffusely reflected to incident electromagnetic radiation and, therefore, lies in the interval 0 – 1. It is difficult to determine the total albedo of a planet because it is highly variable, ranging from less than 0.1 for water and forests to more than 0.8 for fresh snow. On Earth, the largest contribution comes from the clouds which cover about 50% of its surface. For the Earth an average albedo of 0.3 is usually assumed [.]”

“If we assume as a first approximation that a planet is an atmosphere-free black body and that the climate machine distributes the incoming solar radiation uniformly [(i.e., that effects of very low or very high spin rates can be ignored)], the emitted power is given by the law of Stefan-Boltzmann:

$$\mathcal{P}_{\text{emi}} = 4\pi R_p^2 \sigma T_{e|0}^4. \tag{12.2}$$

Under steady state conditions absorption and emission are equal and the temperature $T_{e|0}$ [(with index 0 to indicate absence of an atmosphere as we have here)] can be

III:12.3.4

III:12.3

Table 12.1: Comparison of the calculated temperatures of the planets for different combinations of planetary albedo a and stellar luminosity L in the absence of atmospheres, compared with the observed temperatures. [Table IV:11.3]

Planet	Effective temperature absent an atmosphere (°C)				Observed temperature (°C)
	Distance (AU)	$a = 0.5$ $L = 0.8$	$a = 0.3$ $L = L_{\odot}$	$a = 0.1$ $L = 1.3L_{\odot}$	
Mercury	0.38	77	130	175	180 to 420
Venus	0.72	-10	30	66	460
Earth	1	-50	-18	11	15
Mars	1.52	-95	-65	-40	-87 to 5
Jupiter	5.2	-175	-160	-150	-130
Saturn	9.54	-200	-190	-180	-180
Uranus	19.18	-220	-215	-210	-210
Neptune	30.06	-230	-225	-220	-210

calculated:

$$T_{e|0} = \left(\frac{L_{\odot}(1-a)}{16\pi\sigma d_p^2} \right)^{1/4}. \quad (12.3)$$

Note that the temperature of a planet does not depend on its size [...] {A165}

{A166}

In Table 12.1 the calculated equilibrium temperatures for the eight planets in the absence of atmospheres are compared to the measured ones. [...] Overall there is a reasonable agreement between the estimated and the observed temperatures. The largest discrepancy is observed for Venus. The reason is that Venus has a very dense atmosphere which consists for 96% of CO₂ [(see Table 2.1)] with clouds of SO₂ generating the strongest greenhouse effect in the Solar System. In the case of Earth, the difference between calculated (using the present values $a = 0.3$ and solar luminosity) and measured mean global temperature is 33 °C. This difference is also due to the natural greenhouse effect. It is important to note that the Earth needs the natural greenhouse effect to be habitable, but not necessarily an additional anthropogenic increase. The range of observed temperatures on Mars is very large because Mars has only a very thin atmosphere (0.3 millibar compared to 1 bar of Earth) and no liquid water to transport and distribute energy. Jupiter is considerably warmer than calculated (-110 °C instead of -160 °C). Most likely, this difference is due to gravitational contraction which provides an additional power at least as large as the solar insolation.”

The value of the planetary albedo is determined by the properties of the planetary surface and, if present, the planetary atmosphere. For the Earth, not surprisingly, the impact of the atmosphere in setting the overall albedo has been studied in great detail. “Perhaps, the best way to represent the exchanges of radiative energy in the atmosphere is to refer to Figure 12.4. This figure shows that [...] a large fraction of the

{A165} {A166}

III.16.2

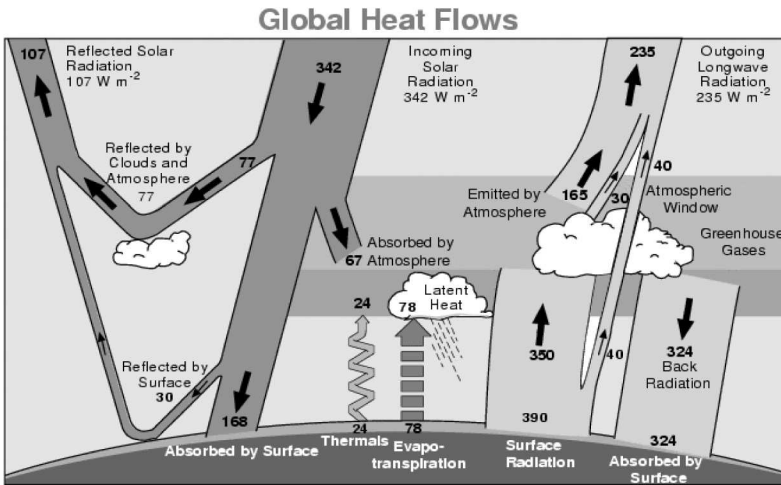


Figure 12.4: Exchanges of solar (shortwave) and terrestrial (longwave) energy in the Earth’s atmosphere. The flow of energy is expressed in Wm^{-2} ($kilerg/cm^2/s$), averaged over the entire Earth surface (i.e., over the day-night cycle). [Fig. III:16.2; source: Kiehl and Trenberth (1997).]

infrared radiation from the planetary surface] is absorbed by greenhouse gases in the atmosphere. These gases, whose temperature is lower than the surface temperature, re-emit radiation both towards space and towards the Earth’s surface [...]

For an illustrative first-order approximation of the sensitivity of the ground-level climate to the greenhouse effect of an atmosphere, we can look at a highly simplified version of the energy flow in which we disregard the mechanical and evapo-transpiration energies and assume that the atmosphere radiates equally in the upward and downward directions (which is a significant oversimplification as you can infer from Fig. 12.4), as sketched in Fig. 12.5. “[The e]ffective temperature $T_{e|A}$ can be related to surface temperature of a planet with an atmosphere under a few assumptions. Here, [one may approximate the planetary surface temperature in the presence of an atmosphere by]

$$T_{p|A} = (1 + \tau_A)^{1/4} T_{e|A}, \tag{12.4}$$

where $T_{p|A}$ is the [ground-level or] surface temperature and τ_A is the optical depth of the atmosphere.” Although proper radiative transfer is essential to quantify τ_A and thereby how atmospheric properties combine to set the ultimate planetary temperature, let us here look at a very “simple model of the radiative transfer processes described above [but allowing for a simple wavelength-dependent effect in radiative transport]; we represent the atmosphere by a single layer of radiatively active gases whose optical transmission is noted $\xi_{A\odot}$ and $\xi_{A,p}$ for shortwave (incoming solar) and longwave ([emitted planetary]) radiation, respectively. The radiative shortwave solar [power] and the longwave surface [luminosity] are noted by symbols $\mathcal{P}_{p|A}$ and L_p , respectively. L_A represents the radiative [power] emitted by the atmospheric layer and $T_{p|A}$, an indicator of the [planet’s] climate, represents the surface (ground) temperature. From

IV:7.3

III:16.2

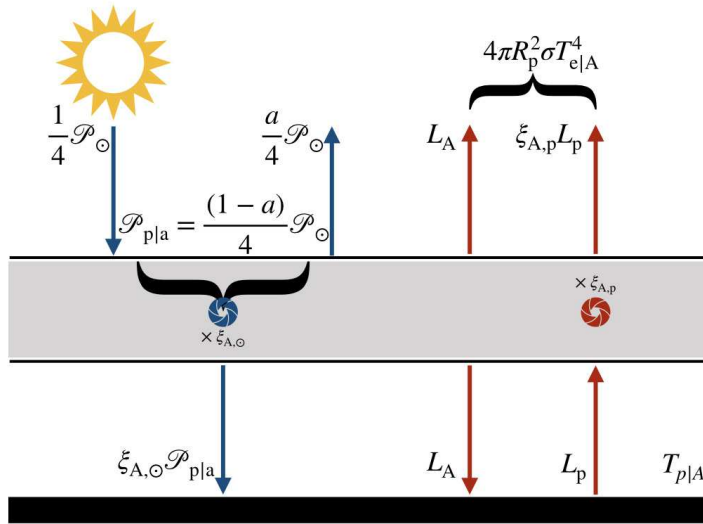


Figure 12.5: Simplified model of radiative exchange in the [atmosphere of a planet with a partially transparent atmosphere that balances incoming solar power \mathcal{P} and outgoing planetary luminosity L]. The optical transmission in the atmosphere is represented by $\xi_{A,\odot}$ in the shortwave ([solar, shown in blue]) spectral region and by $\xi_{A,p}$ in the longwave ([planetary, shown in red]) part of the spectrum. [This figure is a modified version of Fig. III:16.3 for consistency with symbols used in this text.] For a color version of this figure, see *arXiv:2001.01093*.

Figure 12.5, we derive the energy balance at the top of the atmosphere [and at the planet's surface, respectively]:

$$\mathcal{P}_{p|a} = (1 - a)\mathcal{P}_{\odot}/4 = \xi_{A,p}L_p + L_A ; \quad \xi_{A,\odot}\mathcal{P}_{p|a} = L_p - L_A. \quad (12.5)$$

We deduce that the surface temperature [in the presence of an atmosphere] is given by

$$T_{p|A} = T_{e|0} \left(\frac{1 + \xi_{A,\odot}}{1 + \xi_{A,p}} \right)^{1/4}, \quad (12.6)$$

where the planetary equilibrium temperature $T_{e|0}$ [is given by Eq. (12.3)]. For Earth, this] is equal to 255 K (-18°C) for $\mathcal{P}_{\odot}/4 = 342 \text{ Wm}^{-2}$ and for an albedo $a = 0.31$. Assuming that the atmosphere is approximately transparent to solar radiation, so that the shortwave transmission $\xi_{A,\odot}$ is close to 1.0, and adopting a longwave transmission $\xi_{A,p}$ of 0.2, the surface temperature [in the presence of its atmosphere] becomes

$$T_{p|A} = T_{e|0} \left(\frac{2.0}{1.2} \right)^{1/4} = 289 \text{ K [or } 16^{\circ}\text{C]}. \quad (12.7)$$

The value calculated by this simple model, tuned by approximating choices for $\xi_{A,\odot}$ and $\xi_{A,p}$ [(and suggesting an effective atmospheric optical depth in Eq. 12.4 for $\tau_A \approx 0.67$)], is in agreement with the observed temperature $T_{p|A,\text{obs}}$ (288 K). More

refined models account in greater detail for wavelength-dependent radiative transfer, vertical and horizontal heat transport in the atmosphere, energy and water exchanges at the Earth’s surface. Absorption coefficients for different molecules in different spectral regions are measured in the laboratory. [...] The simple conceptual model presented here can, however, be used to estimate to a first approximation the change in the surface temperature that would result, for example from a relative change in the solar input \mathcal{P}_\odot of 0.1%. We derive easily that, for constant $\xi_{A,\odot}$ and $\xi_{A,p}$,

$$\frac{\Delta T_{p|A}}{T_{p|A}} = \frac{\Delta \mathcal{P}_\odot}{4\mathcal{P}_\odot}. \quad (12.8)$$

For $T_{p|A} = 288$ K, we obtain a surface temperature change $\Delta T_{p|A}$ of 0.07 K for a solar-cycle TSI variation of $1500 \text{ erg/cm}^{-2}/\text{s}$. The amplitude of the solar variation is therefore a factor of 10 smaller than the surface temperature trend observed since the beginning of the industrial era. However, over a period of a decade or so, the solar signal should be significant compared to human-driven temperature trends, and should therefore be taken into consideration in the analysis of temperature records. [Studies] have shown that, even if the global temperature variation associated with solar forcing is small, changes in temperature patterns become significant at the regional scale.

A more accurate treatment requires that the transmission functions and the atmospheric emissivity change with the chemical composition of the atmosphere in response to Sun-induced climatic changes, that dynamical feedbacks be taken into account and that the influence of the ocean be considered. [...]” Many details go into establishing the ‘radiative forcing’ of an atmosphere, see, for example, the publications of the Intergovernmental Panel on Climate Change (IPCC) from which Figure 12.6 was taken to illustrate the often counteracting effects of atmospheric constituents on radiative forcing. {A167}

Equation (12.3) illustrates “four main ways in which planetary climate can be altered. First, the amount of radiation from the star (L_\odot) can change. The solar constant at Earth varies by only $\sim 0.1\%$ over the course of a solar cycle. [Evolutionary stellar-structure models] suggest that the Sun is $\sim 30\%$ brighter today than it was when the terrestrial planet[s formed (Fig. 10.1) ...]

Second, changes in the albedo (a) of a planet will change the amount of incident energy absorbed by the surface (and atmosphere). Variation in cloud cover, the extent of polar ices, vegetation, or wind blown dust, for example, can all change the albedos of the terrestrial planets, and will have an influence on the atmospheric energy budget. Venus has an albedo of ~ 0.9 , while the albedos of Earth (~ 0.3) and Mars (~ 0.25) are considerably lower. [...] {A168}

Third, characteristics of a planet’s orbit and rotation influence its energy budget. The amount of solar radiation encountering a planet varies with average orbital distance (d_p), with the result that Venus encounters roughly double the energy that Earth does, while Mars encounters $\sim 45\%$. Ellipticity of the orbit [(see Eq. 12.10) causes incident energy to vary] between 36% and 52% over a Martian year due to Mars’ relatively high orbital ellipticity. This explains why the southern summer at Mars (near perihelion) is

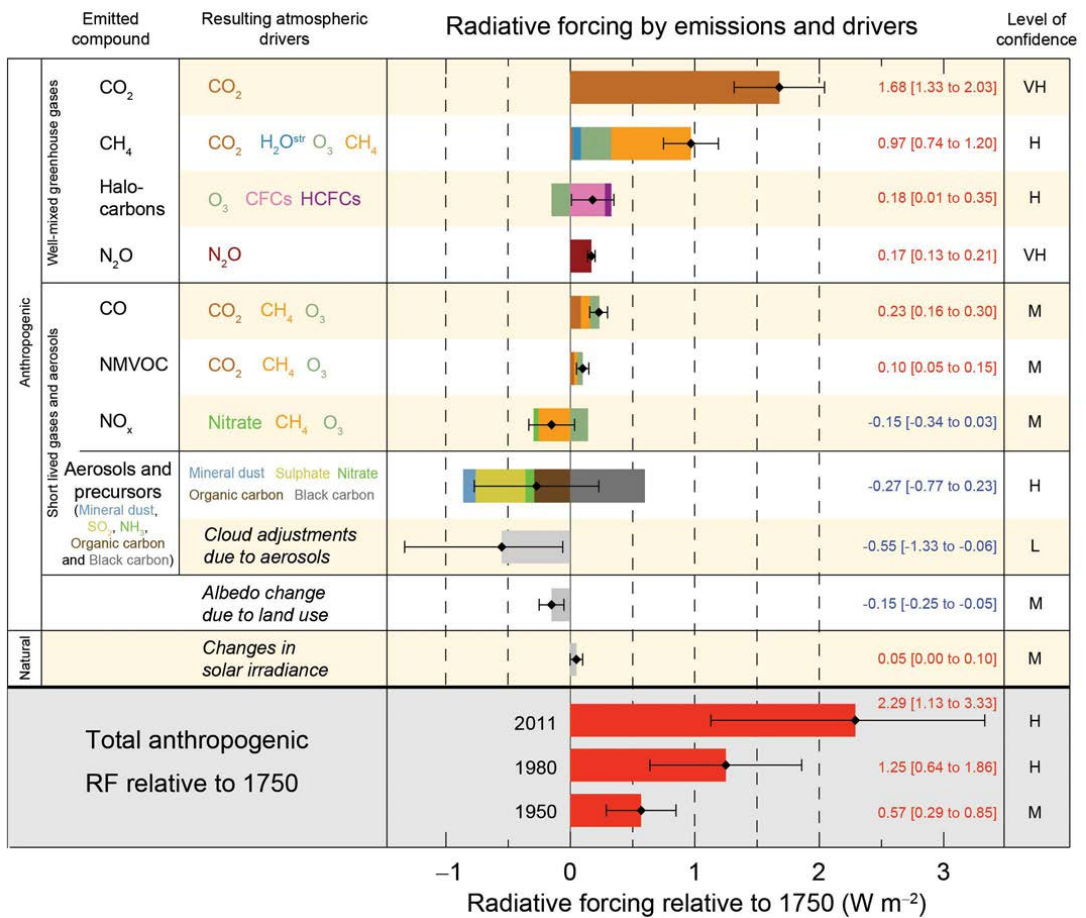


Figure 12.6: Radiative forcing estimates in 2011 relative to 1750 and aggregated uncertainties for the main drivers of climate change. Values are global average radiative forcing (RF), partitioned according to the emitted compounds or processes that result in a combination of drivers. The best estimates of the net RF are shown as black diamonds with corresponding uncertainty intervals; the numerical values are provided on the right, together with the confidence level in the net forcing (VH -- very high, H -- high, M -- medium, L -- low, VL -- very low). Albedo forcing due to black carbon on snow and ice is included in the black carbon aerosol bar. Small forcings due to contrails (0.05 W m^{-2} , including contrail induced cirrus), and HFCs, PFCs and SF₆ (total 0.03 W m^{-2}) are not shown. Concentration-based RFs for gases can be obtained by summing the like-colored bars. Volcanic forcing is not included. Total anthropogenic radiative forcing is provided for three different years relative to 1750. [From IPCC (2013).] For a color version of this figure, see arXiv:2001.01093.

more extreme than the northern summer. [Realizing that incident solar energy is not uniformly distributed by the thin atmospheres of the terrestrial planets, it will be clear that tilt also influences the amount of sunlight that reaches each part of a planet's surface, making some portions of the planet cold and other portions warm. This effect influences where ices form at the surface, removing some gases from the atmosphere

and changing albedo in some locations. Chaotic changes in the eccentricity, obliquity, and spin precession of Mars and Earth over periods of tens to hundreds of thousands of years are thought to contribute to climate variations (Sect. 12.3.2), though the range of variation in both orbital properties (especially tilt) and climate is estimated to be larger at Mars due to the lack of a large Moon.

Fourth, the amount of radiation-absorbing atmosphere (*i.e.*, greenhouse gases) influences surface temperatures. [...] The thick CO₂ atmosphere of Venus provides more than 500 K of greenhouse warming compared to the theoretical surface temperature in the absence of an atmosphere. Earth’s atmosphere provides approximately 30 K of greenhouse warming. This warming, while much smaller than at Venus, is crucial to keeping our average surface temperature above the freezing point of water, making life and many aspects of our climate possible. The atmosphere of Mars, while dominated by CO₂, is too thin to provide substantial greenhouse warming today. The temperature is warmed only ~5 K due to greenhouse gases [...].”

12.3.2 Orbital changes

The physical basis of orbital changes and of tidal effects on planetary rotation were discussed in Ch. 7. Here, we look in some detail at the orbital effects on climate. “[T]he distance d_p is a prime parameter for the temperature of a planet. [S]olar power decreases with the square of the distance or in other words that the relative change of the temperature is 1/2 of the relative change of the distance:

$$\frac{\Delta T_{e|0}}{T_{e|0}} = -\frac{1}{2} \frac{\Delta d_p}{d_p}. \quad (12.9)$$

[...] Because all the planets have elliptical orbits the distance is continuously changing. The eccentricity ranges from 0.0068 for Venus to 0.2056 for Mercury. The eccentricity of the Earth’s orbit is 0.017. That means the distance between Earth and Sun is 1.017 AU at the aphelion compared to 0.983 AU at the perihelion. This difference results in a change of insolation by about 10^5 erg/cm²/s” and would result in $\Delta T_{e|0} \approx 5$ K throughout the year, but that is strongly dampened by the thermal inertia of Earth’s oceans and land masses.

But not only does ellipticity of orbits lead to seasonal changes, the orbits actually evolve over time. “[A]ll the bodies in the Solar System are gravitationally coupled. This was known already since Newton’s time. [...] It was Milutin Milankovic who, for the first time, worked out the mathematical details of these disturbances [...] There are three orbital parameters of the Earth which are affected by the other planets, the Sun, and the Moon.

(1) Orbital eccentricity: [...] Integration over a full year] reveals the following relationship between the relative change in the annual amount of solar radiation S received by Earth and the relative change in the eccentricity e :

$$\frac{dS}{S} = \frac{e^2}{(1 - e^2)^{3/2}} \frac{de}{e}. \quad (12.10)$$

The largest change in e (0.06) which the Earth experienced over the past million years (Fig. 12.7) therefore leads to a very small change of 0.36 % in the annual mean

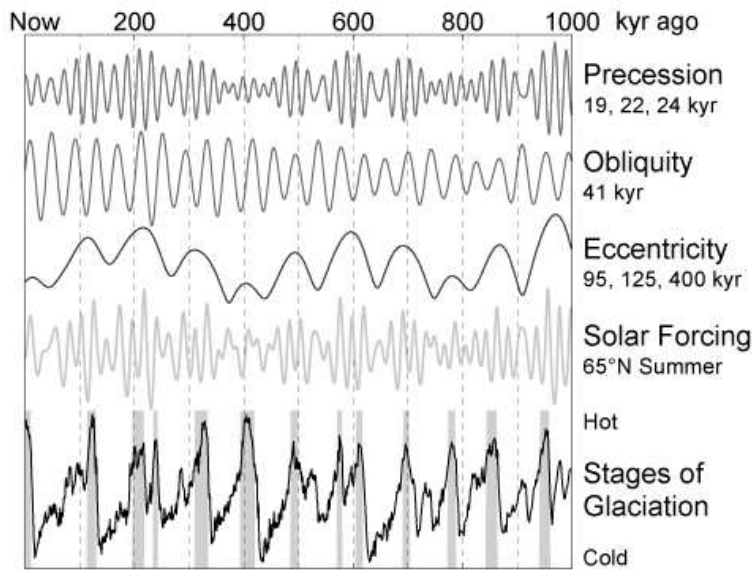


Figure 12.7: Earth's orbital parameters for the past million years. The first three panels show the three orbital parameters influenced by the other planets (mainly Jupiter and Saturn) and the moon (precession). The fourth panel exhibits the calculated solar forcing at 65° N. The lowermost panel shows sea level changes derived from stable isotope measurements on benthic foraminifera indicating glacial (cold) and interglacial (warm, grey bands) periods. [Fig. III:11.6]

insolation which corresponds to a mean global forcing of less than $10^3 \text{ erg/cm}^2/\text{s}$ [(compare Fig. 12.6 for present-day forcings)]. The changes in the eccentricity occur on time scales of 100,000 and 400,000 years. It is interesting to note that it is exactly this small change in the eccentricity which seems responsible for the 100,000-year cycle in the sequence of glacial and interglacial periods during the past 1,000,000 years (Fig. 12.7). This is a nice example that climate is a non-linear system and that even a small forcing can cause a large effect if feedback mechanisms are involved. Such a feedback mechanism could be that although a larger eccentricity does not change the mean annual insolation much, but with it the seasonality changes: colder summers on the northern hemisphere may result in a reduced melting of the winter snow enlarging the ice sheets and the albedo which further reduces the effective insolation.

(2) Obliquity: The tilt angle of the Earth's spin axis relative to the ecliptic plane varies between 22.1° and 24.5° with a periodicity of about 41,000 years. Contrary to the eccentricity changes the obliquity does not change the total amount of received solar radiation but only its latitudinal distribution. The larger the obliquity the stronger is the seasonality. A smaller obliquity reduces both the mean insolation and the summer insolation at high latitudes, thereby providing favorable conditions for ice ages.

(3) Precession: [...] Because the Earth is spinning, its shape deviates slightly from a sphere leading to an equatorial bulge. Tidal forces act on the bulge and force the [rotation] axis to precess. The periods of precession range from 19,000 to 24,000

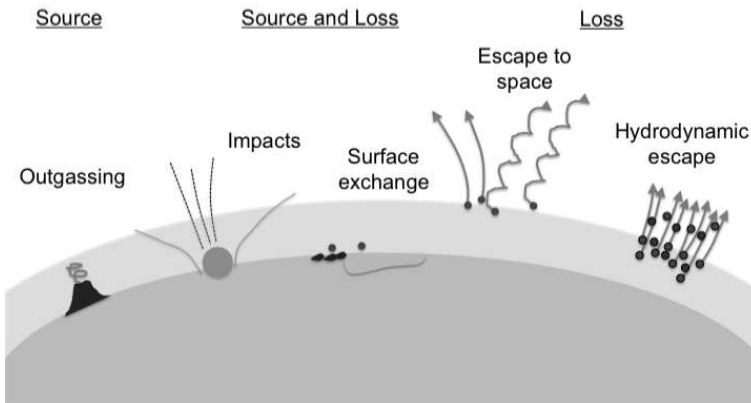


Figure 12.8: Source and loss mechanisms for planetary atmospheres. [Fig. IV:7.3]

years.

The calculated values of the three orbital parameters are plotted in Fig. 12.7, together with the corresponding summer insolation at 65°N , a latitude which is considered as critical for the formation of ice sheets as a result of cold summers. The bottom panel shows a compilation of $\delta^{18}\text{O}$ records from deep-sea sediments. Benthic foraminifera live in the deep sea and form CaCO_3 shells. After death, the shells are buried in the sediment layer by layer for millions of years. Measuring the $^{18}\text{O}/^{16}\text{O}$ isotope ratio with a mass spectrometer relative to a standard, expressed as $\delta^{18}\text{O}$, reflects the sea level. Water evaporating from the sea preferentially contains the lighter molecules H_2^{16}O . If the evaporated water stays on the continents forming glacial ice sheets the ocean becomes depleted in ^{16}O . Warm interglacial periods are indicated by grey bands. They normally last 10,000 to 20,000 years and occur with a typical periodicity of 100,000 years when the eccentricity is large.”

12.4 Planetary atmospheres, geological activity, and stellar winds

12.4.1 On time scales beyond millions of years

“[Planetary s]urface temperature and climate are strongly affected by the amount of greenhouse gases in an atmosphere, which can be viewed as a combination of the total number of particles in an atmosphere (surface pressure) and its composition. Several mechanisms are capable of changing atmospheric abundance and composition (Fig. 12.8) [...]

Volcanic outgassing from planetary interiors is thought to be the primary source for the terrestrial planet atmospheres we observe today. Water vapor is the most common gas released in terrestrial eruptions, followed by CO_2 . Other commonly released gases include sulfur dioxide, nitrogen, argon, methane, and hydrogen. Outgassing should be a declining source of atmospheric particles over Solar System history, as the interior

heat required to generate volcanic activity declines. [Earth is evidently volcanically active today, Venus likely is (although without signatures of active plate tectonics), while there is no direct evidence for ongoing activity for Mars.]

Atoms and molecules can be exchanged between a planet’s surface layers and its atmosphere via a variety of processes and over many timescales. For example, changes in temperature can increase condensation rates to the surface, forming surface liquids or ices (evident on Earth and Mars). Chemical reactions (weathering) can also remove particles from the atmosphere, and is typically most effective in warm or wet environments (evident on Venus, Earth, and Mars). Adsorption removes atmospheric particles that stick to surface materials. Most or all of these processes can be considered to be reversible. Release of particles back to the atmosphere can involve changes in temperature, chemical reactions (including reactions with sunlight), and geologic events that allow subsurface reservoirs access to the atmosphere.

All planetary atmospheres are subject to impact from asteroids, comets, dust, and even atoms and molecules. Impactors of all sizes can deliver volatile species to an atmosphere (*e.g.*, impact delivery is responsible for at least part of Earth’s water inventory as well as meteoritic layers observed in terrestrial planet ionospheres). Impacts can also remove atmospheric particles via collisions, and sufficiently large impactors can additionally accelerate atmospheric particles via impact vapor plumes and lofted surface material [...]. Monte Carlo simulations suggest impacts have resulted in a net gain of atmospheric gases for Earth and Mars over Solar System history, and a net loss for Venus. {A169}

Hydrodynamic escape occurs when a light species escapes (thermally) in sufficient abundance that it becomes equivalent to a net upward wind, and drags heavier species with it through collisions. This process is usually enabled by high solar EUV flux or another form of heating. It should have been significant for all of the terrestrial planets during the first few hundred million years after formation, stripping away most of their primordial atmospheres. [...]. {A169}

The removal of atmospheric particles to space from the upper layers of the atmosphere is commonly referred to as “escape to space”. This term typically excludes impacts by asteroids, meteoroids, and comets, and hydrodynamic escape is also often listed as a distinct process. Here, “escape to space” encompasses a set of approximately six processes, all of which provide escape energy to atmospheric particles. The energy is ultimately provided (sometimes directly, and sometimes indirectly) through interaction with the parent star and stellar wind. [...]. It is currently thought that atmospheric escape has played an important role in the evolution of the climates of both Venus and Mars by altering atmospheric pressure and trace gas abundance.”

“All particles escaping from a planetary atmosphere share three characteristics. The first is that they have sufficient energy to escape the gravity of the planet[, which means that their velocity should exceed the escape speed (Eq. 2.4 with r set to the radial distance from which the escape occurs, typically the exobase, discussed below). The values listed in Table 2.1 show that Mars has a much lower escape speed than Earth or Venus.] IV:7.5

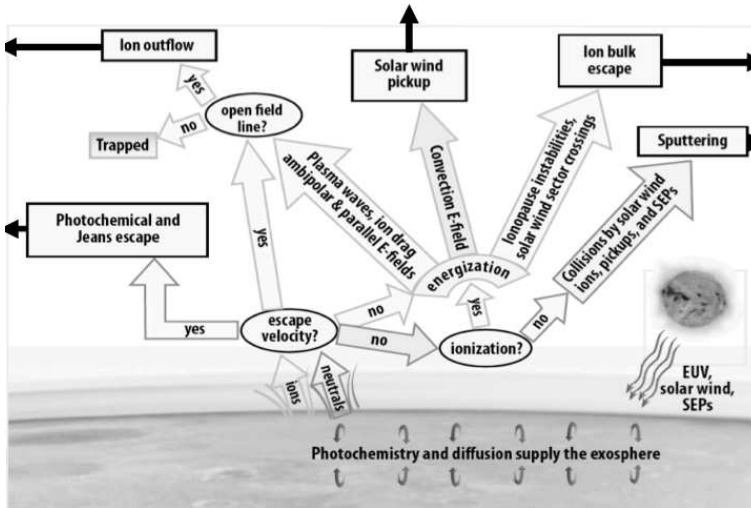


Figure 12.9: Flowchart showing pathways to energization and escape of particles from a planetary atmosphere. [... Fig. IV:7.4]

A second characteristic of an escaping particle is that it is unlikely to collide with other particles after acquiring sufficient escape energy. In planetary atmospheres, the region above which collisions are unlikely is termed the exobase, and is loosely defined as the location where the mean free path of a particle [(Eq. 2.17)] is equal to an atmospheric scale height [(Eq. 2.3) ...]

Finally, any escaping particles must not be confined to the planet by planetary magnetic fields. This requires either that an escaping particle be neutral, that the planet lack a magnetic field, or that any magnetic fields are weak enough that energized charged particles are able to easily traverse magnetic field lines. Venus lacks a measurable global magnetic field like that of Earth. Mars also lacks a global magnetic field but possesses localized regions of strongly magnetized crust that may locally trap energized atmospheric ions.

Due to the highly collisional nature of planetary lower atmospheres, escape is generally limited to three regions of the upper atmosphere: the thermosphere, the exosphere, and the ionosphere. The altitude and composition of these regions are summarized for each planet in Table 2.2 [...]"

IV:7.6

“A number of mechanisms are capable of giving atmospheric particles sufficient energy to escape from a planet [(see Fig.12.9.) Neutral particles can escape an atmosphere in one of three ways: (1) *Jeans escape*, (2) *photochemical escape*, and (3) *atmospheric sputtering*. [Ion loss processes can be grouped into three additional] categories: (4) *ion outflow*, (5) *ion pickup*, and (6) *bulk plasma escape*.]

(1) *Jeans (or thermal) escape* occurs because some fraction of neutral particles near the exobase will have sufficient energy to escape simply because the particles have a thermal distribution. Neutral temperatures near the exobase of all three planets are

sufficiently low ($\sim 250\text{--}1000\text{ K}$) that only species with small mass (H, D, and He) can escape via this mechanism in significant quantity. The process should be more efficient for Mars (due to its low gravity) and for Earth (due to its higher exobase temperature) than for Venus.

(2) *Photochemical escape* refers to the escape of fast neutral particles energized by sunlight-driven chemical reactions. These reactions typically involve dissociative recombination of an ionized molecule with a nearby electron, resulting in two fast neutral atoms. Photochemical escape fluxes depend upon ionospheric molecular densities near the exobase, as well as electron density and temperature. Photochemistry is thought to be the dominant loss process for neutral species more massive than hydrogen and helium at Mars. Fast atoms produced photochemically at Venus and Earth are typically not energetic enough to escape the larger gravity.

(3) *Atmospheric sputtering* occurs when atmospheric particles near the exobase receive sufficient energy from collisions to escape. Collisions occur when energetic incident particles (often ionospheric particles accelerated by electric fields near the planet) encounter the exobase. There are no unambiguous observations that sputtering is actively occurring at any of the terrestrial planets, [but] it may have been important earlier in Solar System history, especially for unmagnetized planets. [...]

(4) *Ion outflow* refers to the acceleration of low energy particles out of the ionosphere via plasma heating and outward directed charge separation (ambipolar) electric fields. In this case the ion acceleration can occur below the exobase, where collisions maintain a more fluid-like behavior. Ion outflow is the only significant ion loss process for the terrestrial atmosphere, and encompasses a number of processes referred to in the terrestrial literature, including wave heating, polar wind, and auroral outflow. [Analogues of these processes should be active for Venus and Mars.]

(5) *Ion pickup* refers to the situation where a neutral particle is ionized (via photons, electron impact, or charge exchange) and accelerated away from the planet by a motional electric field ($\mathbf{E} = -\frac{1}{c}\mathbf{v} \times \mathbf{B}$). Ion pickup occurs primarily for ionized exospheric neutrals (though some ionized thermospheric neutrals near the exobase region may escape via pickup as well). The motional electric field is usually supplied by the solar wind, so that the process is most relevant for compact magnetospheres unshielded by strong planetary magnetic fields (Venus and Mars) [...]

(6) *Bulk plasma escape* refers to any process which removes spatially localized regions of the ionosphere *en masse*. Bulk escape is relevant for unmagnetized planets, where the external plasma flow can create magnetic and/or velocity shear with the ionosphere. A popular example involves the Kelvin-Helmholtz instability, which may form at the ionopause of Venus or Mars and steepen into waves which eventually detach from the ionosphere. Other bulk escape processes are possible as well, such as transport via plasmoid-style flux ropes that may remove ionospheric plasma from Martian crustal magnetic field regions. {A170}

[Based on models and observations,] the present-day global escape rate for Venus is estimated to be $10^{24}\text{--}10^{26}\text{ s}^{-1}$. The escape rate for Earth is $10^{25}\text{--}10^{27}\text{ s}^{-1}$, and for Mars is $10^{24}\text{--}10^{26}\text{ s}^{-1}$. [Normalized per unit area, these rates] are on the order of

Table 12.2: *Properties of the solar wind and interplanetary magnetic field (IMF) at the terrestrial planets. [Table IV:7.4]*

	Venus	Earth	Mars
IMF strength	~0.10–0.12 mG	~0.06 mG	~0.03 mG
Solar wind speed	~400 km/s	~400 km/s	~400 km/s
Solar wind density	10–15 cm ⁻³	~6 cm ⁻³	~1–3 cm ⁻³
Alfvén speed	~70 km/s	~55 km/s	~45 km/s
Mach number	5–7	6–8	8–10
H ⁺ gyroradius	~1500 km	~2500 km	~5000 km
H ⁺ gyroradius / R_p	0.5	0.4	~3

10^6 – 10^9 cm⁻² s⁻¹. [These escape rates are a very small fraction of the column densities in the present-day atmospheres that range from 10^{23} – 10^{27} cm⁻², but they may be substantial when accumulated over ~4 billion years ($\sim 10^{17}$ s)]. For this latter point the two orders of magnitude uncertainty in escape rates are crucial; they are the difference between heliophysical drivers being the main loss mechanism for planetary atmospheres and merely an afterthought in determining present-day [atmospheres. . .]

Finally, it is important to keep in mind that escape to space not only influences atmospheric abundance but also atmospheric composition, which can be important in planetary evolution. One example is the aridity of the Cytherean atmosphere. The loss of atmospheric water is attributed to dissociation of the water in the atmosphere by sunlight, and the subsequent escape to space of oxygen. Water is only a trace gas in planetary atmospheres, but is an important greenhouse gas and is extremely important for habitability. So even if escape to space does not appreciably change atmospheric thickness, it may contribute in important ways to climate. Interestingly, the escape rates listed above, when converted to precipitable microns of water, amount to global layers of water only centimeters thick. More than this is assumed to have been lost from Venus, suggesting either that escape rates have changed over time (and are low today) or that other processes (such as impacts) have been important for removing water.”

“Observations, simulations, and common sense all tell us that atmospheric escape rates are not constant, and are influenced by a number of heliophysical drivers that vary on both short and long timescales. [. . .] The three main drivers are photons, charged particles, and electromagnetic fields. Photons deposit energy in atmospheres when they are absorbed by atmospheric particles. Extreme ultraviolet (EUV) and soft X-ray photons (generated in the solar corona and chromosphere, and not to be confused with solar luminosity) provide the dominant energy source in upper atmospheric regions. Charged particles in the solar wind also supply energy to planetary upper atmospheres and plasma environments. Table 12.2 summarizes some of the relevant quantities of the solar wind at each terrestrial planet. While density and velocity can each vary

independently, studies of solar wind influences on atmospheric escape (especially the induced magnetospheres of Venus and Mars) typically use solar wind pressure (ρv^2) as the organizing quantity. Finally, the solar wind carries a magnetic field, which creates a convection electric field (\mathbf{E}_{sw}) in the frame of the planet that depends upon solar wind velocity and interplanetary magnetic field (IMF) strength and orientation ([see around Eq. 3.11]). Magnetic and electric fields organize charged particle motion, and electric fields accelerate charged particles; both effects influence the ability of charged particles to escape a planet's atmosphere.

The external drivers of atmospheric escape vary on four main timescales. Billion-year timescales are associated with the age of the Sun, and both theoretical calculations and observations of Sun-type stars suggest that all three drivers should have declined in intensity with age (see Figs. 10.3, 10.10, and 13.5). EUV flux varies by factors of several over a solar cycle (from solar minimum to solar maximum), and solar wind pressure varies by factors of 2 – 10. The IMF, in particular, is a function of the solar rotation period, and all three drivers also vary on more rapid timescales of minutes to hours.

Variability in the heliophysical drivers should influence atmospheric escape rates. In general, an increase in solar EUV fluxes (*e.g.*, a transition from solar minimum to solar maximum) is expected to result in an increase in loss rates of neutral particles. Energy from solar photons heats the upper atmospheric neutrals, so that Jeans escape rates should increase with solar EUV. This is likely to be true at Mars, but not at Earth where hydrogen escape from the exobase is limited not by the available energy, but by the supply (via diffusion) of particles from lower altitudes. Jeans escape should be negligible at Venus today, but may have been significant in the past if either exobase temperatures or solar EUV fluxes were much higher. Energy from solar photons is also used to drive the chemical reactions necessary for photochemical escape, so that contemporary Martian photochemical escape should vary with EUV flux. Neutral escape rates should be largely insensitive to changes in both the solar wind and the IMF, except for sputtering rates from Venus and Mars, which are thought to be dominated by re-impacting atmospheric pickup ions and will therefore increase as the pickup ion population increases in response to changes in solar EUV.

Ion escape rates should also vary with the three drivers. An increase in solar wind pressure will cause a corresponding decrease in the size of the magnetospheric cavity at all terrestrial planets, effectively lowering the pressure balance altitude between the solar wind and planetary obstacle to the flow. For Mars, with an extended neutral corona, an increase in solar wind pressure exposes significant additional high-altitude neutrals to ionization and stripping by the solar wind (via electron impact and charge exchange). The IMF, by contrast, chiefly organizes the trajectories of escaping particles at Venus and Mars; large-gyroradius pickup ions are preferentially accelerated away from the planet in regions where \mathbf{E}_{sw} points away from the planet. At Earth, the orientation of the IMF affects the location and extent of cusp regions, from which outflowing ions escape. EUV fluxes have a more indirect effect. In total, one might expect the ion escape rate to increase at solar maximum due to the additional energy

input from EUV. At unmagnetized Venus and Mars, however, the increased ionospheric content deflects the solar wind around the planet at higher altitudes and can prevent the interplanetary magnetic field from entering the ionosphere. The escape of heavy ion species (which are concentrated at lower ionospheric altitudes) via pickup and bulk escape may therefore remain roughly constant, or even decrease during solar maximum periods, even as lighter ion species escape more efficiently.” {A171}

“A number of characteristics of a terrestrial planet itself influence the properties and energetics of upper atmospheric reservoirs for escape, including transient events such as dust storms (*e.g.*, for Mars), or longer-lived phenomena such as gravity waves that couple the lower and upper atmospheres. In the context of heliophysics, the nature of a planet’s intrinsic magnetic field is of the greatest relevance. [... Present-day Earth has an intrinsic magnetosphere] that deflects the solar wind at large distances from the planet ($\sim 10 R_{\oplus}$). There is an induced magnetosphere at Venus that deflects the solar wind at much closer distances ($\sim 1.3 R_{\oplus}$), and a similarly-sized (with respect to the planet) induced magnetosphere at Mars punctuated by ‘mini-magnetospheres’ tied to specific regions of the crust and that rotate with the planet. [...]

When considering the total atmospheric loss from a planet, it has often been assumed that the presence of a magnetic field results in lower escape rates. [However, we mentioned] that the measured atmospheric escape rates for Venus, Earth, and Mars are comparable within the current uncertainties. It has recently been proposed that magnetic fields, rather than shielding a planetary atmosphere from stripping by the solar wind, actually collect solar wind energy and transfer it to the ionosphere along field lines. Global magnetic field lines converge near the cusps, so that the energy is more spatially concentrated than for unmagnetized planets. The escape rate for a given planet may be comparable when it is magnetized, or even greater because planetary magnetic fields extend much further than the planet’s atmosphere, giving it a larger energy-collecting cross-section in the solar wind. One key difference with magnetized planets is that the concentrated energy in cusp regions is likely to lead to more efficient removal of heavy species.

There are a few caveats: [the estimated planetary atmospheric escape rates are quite uncertain, not all solar wind energy collected by a planet need go into removing atmospheric particles, and accelerated ions in Earth’s cusps may not escape the planet. Clearly multiple issues need to be understood] before we can determine whether magnetic fields protect an atmosphere from being lost.”

12.4.2 On time scales of up to several millennia

The Sun’s variability has affected Earth’s climate and atmospheric composition on astronomical time scales, but a multitude of studies looking for both causes and effects on shorter time scales suggest that the “conclusion at the time of this writing with respect to the importance of low-frequency solar variability in the most recent decades, and perhaps up to centuries, might be ‘Perhaps, but probably small’. The main reasons why uncertainties persist regarding this issue include these:

1. The ~ 150 -year instrumental record is too short to draw definitive statistical conclusions about the connection of any relation existing on the multi-decadal

time scale.

2. Forcing from anthropogenic greenhouse gases represent a significant overprint on trends since about 1850 CE. Because to first order the trends in proxies for solar activity indices and in greenhouse gas concentrations are similar, there is a statistical degeneracy which leads to ambiguous, and thus potentially misleading, conclusions unless great care is taken.
3. A similar problem of statistical degeneracy applies to the Little Ice Age interval of cool conditions during the last millennium (main phase about 1450 – 1850 CE), when mountain glaciers advanced in many regions and planetary temperatures were about 0.5°C lower. During the Little Ice Age, solar activity, as inferred from changes in radiogenic isotopes such as ^{14}C and ^{10}Be , appears to have varied similar to pulses in volcanism and slightly lower carbon dioxide levels. Ignoring this similarity in patterns of variability in internal and external (in planetary terms) climate drivers can lead to erroneous conclusions. {A172}

[...] “ There are, however, fingerprints of solar variability that locally stand out. For example, “[v]ariations in solar radiation over the 11-yr cycle as well as over the 27-d solar rotation period have substantial effects in the upper atmosphere where energetic photons penetrate and directly initiate photochemical effects. In the stratosphere and the troposphere, above which shortwave radiation is absorbed, the direct impact of solar variability becomes less pronounced. Solar signal in ozone and temperature, however, can be derived from observations above approximately 25 km altitude. Below this height, the situation becomes more complex because other dynamical signals such as those produced by climatic modes of variability (*e.g.*, El Niño) interfere with possible variations resulting from solar variability. III.16.7

Several mechanisms have been proposed to explain a plausible relation between solar variability and the observed 11-yr dynamical variability in the lower atmosphere. One of them is associated with disturbances produced in the upper atmosphere and resulting from ozone variations generated by changes in shortwave solar radiation. A second mechanism is linked to the ocean-surface response to 11-yr changes in the total solar irradiance. Observed weather patterns correlated with solar forcing could result from both downward-propagating disturbances produced in the stratosphere and upward-propagating perturbations generated at the surface of the ocean. To capture the amplifying mechanisms producing a dynamical response of the troposphere to solar variability, atmospheric models must therefore account for photochemical processes in the upper atmosphere and, at the same time, must be coupled to an ocean module. Despite many remaining uncertainties, much progress has been made in the last years to better understand how solar variability could potentially affect the climate system, particularly on decadal timescales.” {A173}

{A172}

III.16.7

{A173}

Chapter 13

Upper atmospheres and magnetospheres

Chapter topics:

- Spectral irradiance and the ionospheric chemistry of terrestrial planets
- Solar X-ray and UV emission and solar wind over time
- The ionosphere subject to evolving solar activity
- Impacts of the evolving geomagnetic field on the ionosphere

Key concepts:

- Photo-ionization and -dissociation
- Collisional recombination
- Gravitational stratification
- Gravitational differentiation

13.1 Upper-atmospheric chemistry and insolation

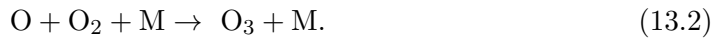
“As one moves up in altitude in a planetary atmosphere, several important changes in composition and structure are apparent. Most notably, as a consequence of hydrostatic equilibrium, the gas density decreases, *i.e.*, the air becomes ‘thinner’. [...] With decreasing density, the frequency of collisions between atmospheric molecules decreases to the point where bulk motions such as turbulence are no longer able to mix the atmosphere. Instead, molecular diffusion becomes the more rapid process and this also leads to a composition change whereby the lighter constituents, typically atomic species such as atomic oxygen, diffuse upward more rapidly than their heavier counterparts such as O₂, N₂ or CO₂. The region where the atmosphere is well mixed is known as the homosphere; the region where diffusive separation dominates is known as the heterosphere. [...]” Because “molecular diffusion coefficients (D) vary inversely as [the square root of the] molecular mass, the molecular diffusion velocities are greater for the lighter constituents and smaller for heavier constituents. Furthermore, they vary inversely as the total density (*i.e.*, diffusion of a gas is more rapid if collisions are less frequent), thus D increases with altitude.” {A174}

High in planetary atmospheres is also the region where the temperatures rise (Fig. 2.7) as a result of inefficient cooling while absorbing solar UV to X-rays. This absorption also acts to break chemical bonds and to liberate electrons from their orbits, thus creating the ionospheres. Earth’s upper neutral atmosphere is dominated by N_2 up to about 200 km (see Fig. 2.6), and the overlapping ionosphere is dominated by NO^+ and O_2^+ (see Fig. 13.2). Up to roughly 150 km and 200 km, respectively, Venus’ and Mars’ neutral atmospheres are dominated by CO_2 while O_2^+ dominates in the corresponding ionic components in the lower layers of their ionospheres. In the next 150 km above that, atomic oxygen is the dominant species in all three neutral atmospheres, while O^+ dominates for Earth, O_2^+ yields dominance to O^+ after the first 50 km or so for Venus, and O_2^+ dominates for Mars [(see Tables 2.1 and 2.2)]. High in this domain, ions are lifted higher than simple estimates of pressure scale heights might suggest because of the ambipolar effects associated with the free electrons. The compositional differences of the ionospheres are a consequence of the different pathways for photo-dissociation of molecules by solar radiation, which in turn feed a number of chemical reactions in the atmosphere.

An example of photo-dissociation is provided by the photo-dissociation of molecular oxygen (O_2)



which leads to the formation of two oxygen atoms. These atoms may react with molecular oxygen to produce ozone molecules (O_3)



Here, M represents a ‘third body’ (*e.g.*, N_2 , O_2 , Ar), which removes the thermal energy released by this exothermic reaction.” “This photo-chemical process constitutes the only significant ozone production mechanism above 20 km altitude” in Earth’s atmosphere. “In this example, the rate of ozone production [per unit volume] is directly proportional to the rate at which oxygen molecules are photo-dissociated:

$$\Pi(O_3) = 2J_{O_2}[O_2], \quad (13.3)$$

where J_{O_2} represents the photo-dissociation coefficient of O_2 and $[O_2]$ the number density of this molecule. The photo-dissociation frequency depends on the [local intensity of the solar radiation after having traversed the higher absorbing layers ($I(\lambda, z, \chi)$ for wavelength λ , height z , and slant or zenith angle χ)] and on the ability of the molecule to absorb solar photons at particular wavelengths. This last parameter is generally expressed as a wavelength-dependent absorption cross-section $\sigma_X(\lambda)$, which can also vary with temperature. In more general terms, the photo-dissociation frequency of a molecule X is expressed as an integral over all wavelengths that contribute to the decomposition of the molecule. The upper bound of this integral corresponds to the minimum energy required to break the molecular bond. The probability that the absorption of a photon leads to the dissociation of molecule X is expressed by

the quantum efficiency η_X , which also varies with wavelength and in some cases with temperature. Thus,

$$J_X = \int \sigma_X(\lambda, T(z)) I(\lambda, z, \chi) \eta_X(\lambda, T(z)) d\lambda. \quad (13.4)$$

^{A175} The solar actinic flux I must be calculated by a radiative transfer model that accounts for (1) absorption processes, (2) multiple scattering by air molecules and atmospheric particles, (3) cloud radiative transfer and (4) surface reflection. When considering upper and middle atmosphere processes, the most important contribution to photo-dissociation is the direct solar flux, so that the value of the actinic flux can be approximated by considering only absorption processes. In the lower atmosphere, multiple scattering and specifically cloud effects cannot be ignored. [...] The depth of penetration of solar radiation varies substantially with wavelength (Figure 2.4). [...]

The relative amplitude of the changes in the solar flux over the 11-yr solar cycle or the 27-d mean synodic solar rotation period decreases with increasing wavelengths (see Figures 2.3 and 12.3) and, as a result, the influence of solar variability is considerably more pronounced in the upper atmosphere [(where EUV and FUV are absorbed)] than in the lower layers [(where longer wavelength radiation is absorbed)]. Strong solar signals associated with the solar cycle are visible in the thermospheric temperature and air density, with impacts, for example, on satellite drag [(and, of course, on ionospheric densities)]. Substantial changes have also been reported in the concentration of nitric oxide (NO); these changes, however, are also related to the modulation of energetic particle precipitation associated with geomagnetic activity. Solar-related changes in the temperature, water vapor and polar mesospheric clouds have also been reported in the mesosphere. In the stratosphere, solar-driven changes in temperature and ozone concentrations have been observed. The influence of solar variability in the troposphere is [touched upon in Ch. 12]. A major forcing function for many of these changes is the variation of photo-dissociation rates. Together with the solar-induced changes in atmospheric heating resulting from the absorption of solar radiation by ozone and molecular oxygen, atmospheric models designed to simulate the response of the atmosphere account for the changes in the photo-dissociation coefficients of the different chemical compounds.”

Because ozone is an efficient absorber of solar UV radiation in the stratosphere it has received much attention. Having been generated by reaction (13.2), ozone is in principle “photo-dissociated



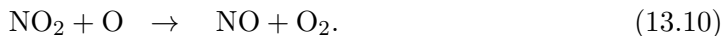
but, in most cases, this reaction does not constitute a net loss for stratospheric ozone because the oxygen atoms that result from this photo-decomposition usually recombine with molecular oxygen (reaction 13.2) to reproduce ozone. The net loss of ozone results from the reaction between oxygen atoms and ozone molecules that produce two oxygen molecules



The simple scheme presented here provides a first-order description of the ozone chemistry in the stratosphere and mesosphere. Photo-chemical models that account only for [the above] reactions tend to substantially overestimate the concentration of ozone in the middle atmosphere, as shown by numerous atmospheric observations. The discrepancy can be eliminated by considering several additional reactions that catalyze (*i.e.*, accelerate) the net loss mechanism represented by reaction (13.6). [T]he presence of the hydrogen atoms and hydroxyl radicals, produced in the upper atmosphere from the photo-dissociation of water vapor (H_2O), could generate an efficient catalytic cycle such as



[T]he most effective ozone destruction in the stratosphere results from a catalytic cycle involving nitrogen oxides



NO is produced in the stratosphere by the oxidation of nitrous oxide (N_2O), a long-lived compound released from soils by bacterial activity. It can also be produced in the upper layers of the atmosphere by the dissociation and ionization of molecular nitrogen (N_2) by energetic particles.

Additional destruction mechanisms must be considered including catalytic processes involving halogen compounds including chlorine (Cl) and bromine (Br). For example



Before the 1960s, the contribution of this cycle was relatively small. However, its importance has grown in the last decades as the atmospheric abundance of Cl has increased steadily due to the production of industrially manufactured chlorofluorocarbons (CFCs). The atmospheric lifetime of CFCs varies typically from 50 to 100 years, so that anthropogenic chlorine will remain for several decades in the stratosphere.

In the cold polar regions, and specifically in Antarctica, ozone can be efficiently destroyed in a layer between 12 km and 25 km where polar stratospheric clouds are formed. The solid or liquid tiny particles inside these thin and often invisible clouds that are present during winter provide surfaces for heterogeneous chemical reactions to operate. Chemical chlorine reservoirs such as HCl and ClONO₂, which are very slow to react in the gas phase, are rapidly converted on the surface of these cloud particles to form less stable molecules such as Cl₂ or HOCl. Large quantities of reactive chlorine atoms (Cl) are liberated via photo-dissociation as soon as the Sun returns in early spring. This chlorine activation leads to rapid ozone destruction with the formation of the springtime Antarctic ozone hole in September and October. These mechanisms are

less efficient in the Arctic, where the winter temperature is usually $10^\circ - 15^\circ\text{C}$ higher than at the opposite pole, and the presence of polar stratospheric clouds is therefore less frequent.

A full description of the ozone behavior requires that large-scale transport processes are taken into consideration, specifically in the lower stratosphere, where the photo-chemical lifetime of this molecule becomes much longer than the time constant associated with transport. Below approximately 25 km altitude, ozone can be regarded as a quasi-inert tracer that is more sensitive to advection and mixing processes than to photo-chemical transformations. This highlights why the global ozone distribution in the atmosphere is strongly affected by the meridional circulation, and specifically why the ozone column abundance reaches a maximum value at high latitudes at the end of the winter. The poleward meridional circulation transports ozone towards the Arctic where it accumulates from December to April before it is slowly destroyed by photo-chemical processes after the Sun returns in early spring. [...] The same dynamical process occurs in the southern hemisphere with a lag of 6 months. However, ozone does not easily penetrate poleward of 60°S due to the existence of a strong dynamical barrier provided by the intense southern polar vortex. The ozone maximum is therefore located in a latitude band located at about 60°S . Large-scale planetary waves that characterize the northern hemisphere winter dynamics do not allow the northern hemisphere polar region to be isolated from lower latitudes as is the case in the less dynamically disturbed Southern hemisphere stratosphere. The ozone maximum in the Northern hemisphere is thus located near the Pole.”

13.2 Maintaining ionospheres

13.2.1 Ionization

“The ionosphere is created by ionizing radiation, including extreme ultraviolet (EUV) and X-ray photons from the Sun, and [– in magnetized planets –] corpuscular radiation that is mostly energetic electrons, [which for Earth occurs mostly] at high magnetic latitude as auroral ‘precipitation.’ The solar photon output at these wavelengths, from $\sim 10 \text{ \AA}$ to the H I Lyman- α line^[32] at 1216 \AA , varies by factors ranging from ~ 2 to > 100 over the 11-yr solar activity cycle (*cf.*, Fig. 2.3), and is additionally variable on shorter time scales, including especially the 27-d solar rotation period. This causes dramatic variations in the temperature and density of the thermosphere and ionosphere. Changes in the solar wind and in the interplanetary magnetic field also affect the thermosphere/ionosphere through geomagnetic perturbations that result in transfer of energy from the magnetosphere, both in the form of auroral particle ionization and in the form of heat from the resulting currents imposed in the polar

III:13.2

³² Ions are denoted by their electrical charge, such as doubly-ionized C: C^{2+} . The line spectrum of such an ion is identified by a roman numeral that is one higher than the ionization charge, so the spectrum of C^{2+} is written in shorthand as C III; the numeral I is reserved for the spectrum of the neutral species, *e.g.*, CI for neutral carbon. Some spectral sequences have a proper name associated with them: for example, the H I Lyman sequence is a series of spectral lines absorbed or emitted when excited electrons transition from or to the ground state, respectively.

regions. An additional form of energy transfer is the generation of energetic electrons released in the ionization process. These electrons, referred to as photo-electrons in the case of photo-ionization and secondary electrons in the case of particle-impact ionization, have enough energy to excite, dissociate, and further ionize the neutral atmosphere as well as heat the ambient plasma. Solar ionization and its byproducts provide most of the ionization and heating of the thermosphere, and account for most of its 11-yr cyclic and 27-d rotational variation, but geomagnetic activity accounts for much of the shorter term variation on time scales from hours to days.

The details of ionospheric formation can be explained through examination of the photo-ionization and photo-absorption cross sections of thermospheric constituents. The ionization continua of N_2 , O, and O_2 all peak in the vicinity of 600 Å at tens of Megabarns ($1 \text{ Mb} = 10^{-18} \text{ cm}^2$). This causes their energy to be deposited largely in the F_1 region (compare [Figs. 2.4 and 2.9, and see Eq. 2.20 and the text preceding it.]) Short-ward of 600 Å, cross sections decrease and the radiation penetrates to lower altitude. At Earth, the intense solar He II emission at 304 Å deposits most of its energy near 150 km and 10 – 100 Å soft X-rays can penetrate to 100 km. Most of the E region is produced by longer wavelength radiation, particularly the C III line at 977 Å and the H I Lyman- β line at 1027 Å. These do not have enough energy to ionize N_2 and O but penetrate through gaps in the N_2 absorption spectrum to ionize O_2 to O_2^+ . Longward of 1030 Å, only the important minor species NO has a low enough ionization potential to be ionized by solar radiation. H I Lyman- α happens to fall at a low point in the O_2 absorption spectrum and so penetrates below 90 km, where ionization of NO to NO^+ and subsequent products create the D region. Thus, while the Chapman production function [(Eq. 2.20)] is approximately correct for any species at each wavelength, ionized regions are created by the superposition of many such functions [...]" {A176}

13.2.2 Recombination

“Positive ions have generally fast collision rates with electrons, so one would suppose that ionospheric production would be balanced by recombination and that the ions would be short-lived after sunset. However, atomic ions colliding with electrons have the problem common to all two-body reactions that a single atom is unlikely to result, because there is nothing to carry away surplus kinetic energy. Photon emission following collision of an atomic ion with an electron can stabilize the resulting atom; this radiative recombination is quite slow, with rate coefficients of the order of $10^{-12} \text{ cm}^3 \text{ s}^{-1}$. Although radiative recombination occurs and is important in the highest reaches of the ionosphere, it is insufficient as a loss mechanism for ions and electrons given their observed F region densities. Because the solar ionization frequency is $\sim 10^{-6} \text{ s}^{-1}$ at 1 AU, ion densities would be several orders of magnitude larger than observed if radiative recombination were the only loss mechanism. [What commonly happens is that atomic ions yield their charge to molecular ions in order to undergo rapid dissociative recombination, while in addition there is loss through diffusive transport.] *Dissociative recombination*, schematically $XY^+ + e^- \rightarrow X + Y$, has rate coefficients of the order of $10^{-7} \text{ cm}^3 \text{ s}^{-1}$ and is the fundamental loss mechanism for ions in dense

planetary ionospheres. In order for an atomic ion to become a molecular ion, *atom-ion interchange*, schematically $X^+ + YZ \rightarrow XY + Z^+$, or *charge exchange*, schematically $X^+ + YZ \rightarrow X + YZ^+$, must occur. Charge exchange reactions are typically fast if energetically possible, but atom-ion interchange rates depend on the nature of the reacting molecule, because a bond must be broken. {A177}

In regions of the atmosphere where molecules dominate, recombination chemistry is simplified because it is essentially a balance between ionization and dissociative recombination. [A] common approximation is the use of an effective recombination rate coefficient α_{eff} , the ion density-weighted average of the ion recombination rates. In photochemical equilibrium, the production rate [per unit volume] $\Pi(e^-) = \alpha_{\text{eff}}[M^+][e^-]$, where M^+ is the sum of the ions, and where square brackets denote number densities. Assuming charge neutrality, this yields

$$[e^-] = (\Pi(e^-)/\alpha_{\text{eff}})^{1/2}. \quad (13.13)$$

{A178} Applying the Chapman production function for solar radiation [(Eq. 2.20)] to obtain Π results in a Chapman 'layer', considering as above the caveats associated with use of that term. Thus, in molecular ionospheres, electron density varies approximately as the square root of the ionization rate profile. Eq. (13.13) is a particularly useful form for auroral ionization, where electrons (and sometimes protons or heavier ions) penetrate to ~ 100 km or deeper into Earth's atmosphere. {A179} {A180}

Although the F_2 region has some of the morphological appearance of this type of layer, it is at the wrong altitude, and in the atom-dominated region. It is not a Chapman layer at all, but a result of diffusive processes. O^+ has an increasingly long lifetime as altitude increases and the molecular fraction of the thermosphere decreases. Above 200 km it becomes subject to diffusion, but is still chemically controlled up to the peak of the F_2 layer near 300 km. Above this altitude, ambipolar diffusion takes over, where 'ambipolar' refers to the effect of electrical attraction between the ions and nearly massless electrons, resulting in a scale height for O^+ about twice that of O . {A181}

{A181} The F_2 region varies in response to thermospheric winds and electric fields, so the mid-latitude and equatorial ionosphere can be greatly influenced by auroral processes at high latitudes through their effect on thermospheric dynamics.

Figure 13.1(left) is provided as a guide to understanding the ion-neutral chemical processes described above. It is a greatly simplified schematic, but contains the essential species and reactions necessary to describe ionospheric photo-chemistry from 100 – 600 km. Ionization occurs primarily on the three major species N_2 , O , and O_2 by photon, photo-electron, and auroral particle impact. N_2^+ quickly loses its charge through dissociative recombination, atom-ion interchange with O to make NO^+ , and, at lower altitude, charge exchange with O_2 to make O_2^+ . Thus it is always low in density and negligible in the absence of production. O^+ loses its charge by molecule-ion interchange with N_2 and O_2 . Reaction with N_2 is slow, $\sim 10^{-12} \text{ cm}^3 \text{ s}^{-1}$, because of the high strength of the triple $N \equiv N$ bond. Reaction with O_2 is faster, $\sim 10^{-11} \text{ cm}^3 \text{ s}^{-1}$, but there is far less O_2 available. This is why O^+ is long-lived in the Earth's ionosphere, and why the F_2 region exists. O_2^+ loses its charge through dissociative recombination {A181}

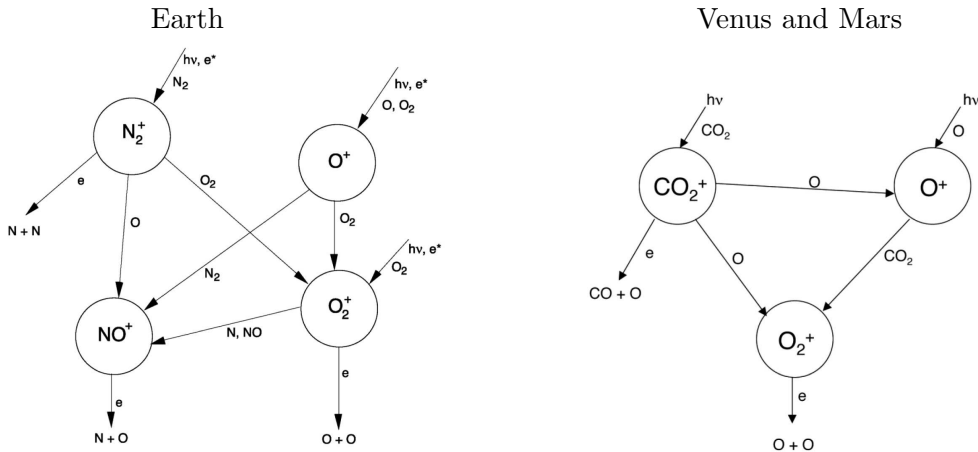


Figure 13.1: Simplified diagram of ionospheric chemistry in the upper atmosphere of Earth (left) and of Venus and Mars (right). [The relative ionization potential of these species is roughly indicated by the position in this diagram: higher position indicates higher ionization potential. Fig. III:13.4]

or through reaction with the odd-nitrogen species NO and N , which control the balance between O_2^+ and NO^+ in the E region. NO^+ , daughter of all the above and the 'terminal ion', is subject only to dissociative recombination. Figure 13.1(left) thus describes a mechanism for dissociating molecular gases. Ionization goes in the top [involving high energies], and dissociation comes out the bottom, because dissociative recombination is the only significant way out [of the cascade that is accessible given the energies involved].

Figure 13.1(left) [neglects the effects of hydrogen at high altitudes, where that] reacts by charge exchange with O^+ to make H^+ . N^+ is also a significant minor ion, created by photo-dissociative ionization of N_2 , that is neglected here. Doubly-ionized species are also ignored in this simplification. Although ground state $O^+(4s)$ does not have enough energy to make N_2^+ , metastable $O^+(2d)$ and $O^+(2p)$ are created by photon and electron impact ionization, and these can charge exchange with N_2 to form N_2^+ . It is possible that vibrational excitation of thermospheric N_2 can also accelerate the reaction of O^+ with N_2 .

In Earth's E region, there is a complex interplay between O_2^+ and NO^+ , due to the involvement of odd-nitrogen species with the ion chemistry, because O_2^+ is converted to NO^+ by reaction with NO and N . NO in particular is highly variable with solar activity, geomagnetic activity, and location, so this is a complicated problem. Older empirical and theoretical models which assumed that O_2^+ is the dominant E region ion, due to its production by solar H I Lyman- β radiation, have been superseded by evidence that NO^+ is generally observed to be the dominant E region ion, and considerable recent observational and modeling advances in understanding the high levels of NO and its importance to radiative cooling as well as ion chemistry have occurred.

In the D region, ion chemistry is entirely different due to the higher neutral density

which allows three-body attachment, particularly $2O_2 + e^- \rightarrow O_2 + O_2^-$. This sets in motion a complicated negative-ion chain involving carbon, nitrogen, and hydrogen compounds, including water, that finally results in mutual neutralization of negative and positive ions, schematically $M^+ + M^- \rightarrow M + M$. NO^+ created by H I Lyman- α ionization also initiates an involved positive-ion sequence, again involving hydration processes. [...]

13.2.3 Venus and Mars

“The terrestrial planets Venus, Earth, and Mars, are so named because of their fundamental similarity, and are presumed to have had common elemental origins. However, their subsequent evolution differed, due to their differing distance from the Sun, the smaller size of Mars, and the lack of rotation of Venus ([see Ch. 12]). Thus, their atmospheres are entirely different, and so are their upper atmospheres and ionospheres. Early exploration of Venus and Mars found that instead of persistent, high-altitude, F_2 -type ionospheres, these planets had less dense, lower-altitude ionospheres ([Fig. 2.6]) that more resembled Chapman ‘layers’, that were greatly attenuated at night, and consisted mostly of O_2^+ and other molecular ions. The presence of O_2^+ seems especially perplexing, because Earth is the planet we generally associate with the unusual and quite reactive oxygen molecule. At higher altitude, O^+ becomes an important species in the ionospheres of Venus and Mars, as on Earth, but at significantly lower density and without the same degree of persistence throughout the night. CO_2^+ is a minor ion on both planets. There is a basic similarity in their ionospheres, despite the vastly different density of their lower atmospheres. [...]

The reason that the ionospheres of Venus and Mars are different from that of Earth is that the molecular compositions of their atmospheres are different, and therefore the compositions of their thermospheres are different ([Fig. 2.6]). Table [2.1] gives a simple overview of the abundance of the primary atmospheric gases in the three terrestrial planets.

Aside from the large differences in surface pressure, the atmospheres of Venus and Mars are similar in composition, and N_2 is an important species on all three planets. N_2 requires more energy to dissociate than the oxygen compounds, however, so at thermospheric altitudes, atomic oxygen becomes important on all three planets. The Venus and Mars thermospheres are distinguished by high levels of CO_2 (and also CO) due to the underlying atmospheric composition, as shown in [Fig. 2.6].

On Earth, O^+ is a long-lived species in the high ionosphere because the $O^+ + N_2$ reaction is so slow and there are few other molecules to react with to make a short-lived molecular ion. On Venus and Mars, the reaction $O^+ + CO_2$ is quite fast, $\sim 10^{-9} \text{ cm}^3 \text{ s}^{-1}$, because CO_2 is much less strongly bound than N_2 . (The triple bond in $N \equiv N$ is [among the strongest known chemical bonds in nature, along with the triple bond in CO].) The reaction of $O^+ + CO_2$ produces O_2^+ , which is also produced by the reaction $CO_2^+ + O$. Ionization of the major thermospheric gases on Venus and Mars, O and CO_2 , is thus quickly converted into O_2^+ , which dissociatively recombines, resulting in the observed ionospheric morphology, lacking a significant F_2 region. A simplified schematic of these processes is shown in Figure 13.1(right). Thus, curiously, although

life-supporting Earth is the planet associated with O_2 , Venus and Mars are the planets with O_2^+ ionospheres.

The F_2 ionosphere is unique to Earth among the known planets. This is due to its peculiar atmosphere, lacking in CO_2 , dominated by N_2 , and carrying its oxygen in unusual and reactive states. Venus and Mars have nitrogen as well, but carbon and oxygen dominate their upper atmospheres, so it has little effect. Earth has a significant carbon budget, and once had much higher levels of CO_2 in its atmosphere, but most of its carbon is currently locked up in the crust in the form of carbonate rocks. Thus, the F_2 ionosphere may be a recent event in the history of Earth, an artifact of geology and biology.” {A182}

13.3 Setting geospace climate

13.3.1 Geospace climate response to solar photon irradiation

“The solar spectrum provides a [fairly] stable irradiance of $\sim 1360 \text{ W/m}^2$ ($\sim 1.36 \cdot 10^6 \text{ erg/s/cm}^2$) to the Earth’s upper atmosphere. Geospace [(the region of space near Earth down to, and including, the ionosphere-thermosphere)] responds to [roughly 2–6 ppm of that] this fraction of the solar spectrum lies between 30 and 3600 Å which extends from the X-ray through the ultraviolet part of the spectrum. The photons in this spectral range may ionize atoms and molecules or may deposit their energy directly into the thermal reservoir of the upper atmosphere. These processes are responsible for the ‘climate’ of the geospace-atmosphere interface whose regions are labeled the ionosphere and the thermosphere (IT). The IT in this sense is only weakly dependent on the Earth’s magnetic field or the solar wind. In this ‘climate’ scenario, the role of the terrestrial dipole field can be viewed as defining the boundary for the plasmasphere [(the inner magnetosphere filled with low-energy, cool plasma)] and then with the solar wind the magnetosphere. In the case of the Earth’s sister planets, Venus and Mars, the absence of a significant intrinsic magnetic field confirms that the IT development has been based on these three photo-chemical processes.

Now let us explore the question how geospace climate responds to extremes of the solar photon radiation. Figures 13.2 and 13.3 provide a comparison of the [1-D Global Averaged Ionosphere and Thermosphere (GAIT)] solar cycle climate of the thermosphere’s neutral densities, of the ionosphere’s plasma densities, and of the neutral and plasma temperatures respectively. Each panel is shown as a function of pressure level defined by $Z = \log p_0/p$, where p_0 is the reference pressure of $0.5 \cdot 10^{-3} \text{ dyn/cm}^2$, The corresponding altitude scale is also provided. For reference to observations, the dashed lines where present in Figure 13.2 and 13.3 correspond to profiles obtained from the MSIS-90 empirical model of the thermosphere.

A simple interpretation of this solar minimum to solar maximum climate change in the IT is that the effective IT energy deposition has almost quadrupled; hence, the neutral atmosphere, which at these heights is in hydrostatic equilibrium, leads to a hotter thermosphere; compare T_n in the two panels of Figure 13.3. In turn, the hotter thermosphere has redistributed neutrals now with relatively higher densities at higher altitudes; compare neutral densities in the two left-hand panels of Figure 13.2 using

{A182}

3:14:3

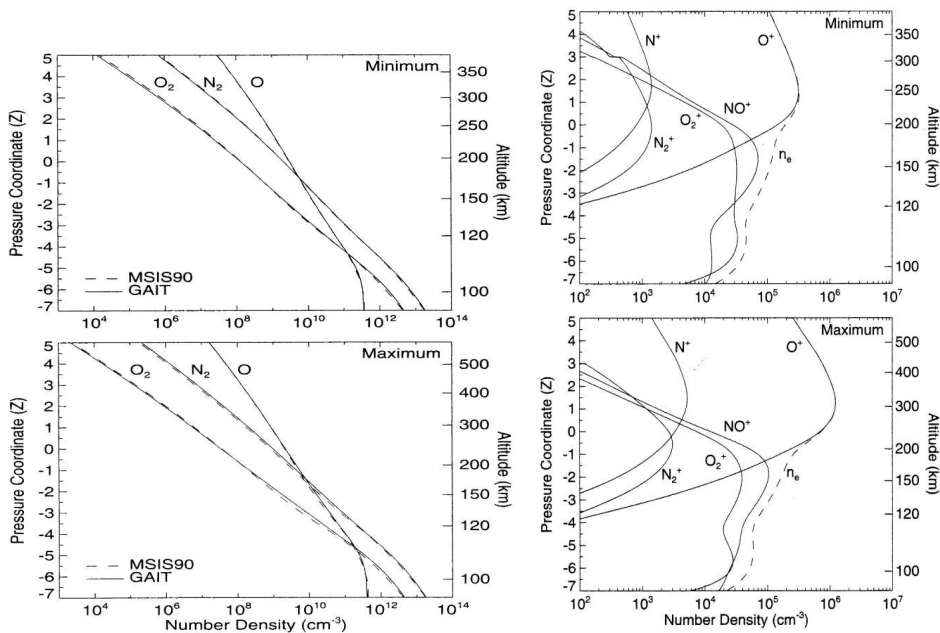


Figure 13.2: Left: Global mean number density profiles under the same conditions for the three major neutral species in Earth's upper atmosphere (N_2 , O_2 , and O) calculated using the GAIT model (solid lines) and the MSIS-90 empirical model (dashed lines). Right: Global mean number density profiles for five ion species in Earth's ionosphere (O^+ , NO^+ , O_2^+ , N^+ , and N_2^+) and the total electron density (n_e) calculated using the [1-dimensional Global Averaged Ionosphere and Thermosphere (GAIT)] model. Solar minimum (top) and solar maximum (bottom; assuming quiet geomagnetic conditions with $A_p = 4$). The discontinuity observed in the NO^+ and N_2^+ profiles at $Z = 3$ corresponds to where the photo-electron calculation stops. [Fig. III.14.1; source: Smithtro and Sojka (2005).]

the right side altitude scale. [...] A secondary but also important additional effect is that the composition is also being modified because of the different neutral masses. For the ionosphere, the consequences can readily be seen by comparing the two right-hand panels of Figure 13.2. [...] A comparison of the E and F layer peak density provides another useful scaling law, rule-of-thumb, in that the F -layer density scales linearly with the appropriate photon wavelength energy flux while that of the E layer is more like a square root dependence on energy flux [(compare with Eq. 13.13)].

That the different ionospheric layers respond differently to the solar spectrum creates the problem of deciding what the most suitable solar spectral representation is. In fact, even over the limited solar cycle energy flux range of a factor of about 4, the spectrum itself is variable and the E and F layers respond to different parts of the spectrum. {A183} The thermosphere is a somewhat better integrator as seen [from a] study in which four distinctly different representations of the solar spectrum were used as drivers for the GAIT model. As each spectral model was run over the solar cycle range of 2–8 erg/s/cm² [going into the ionospheric/thermospheric height {A183}]

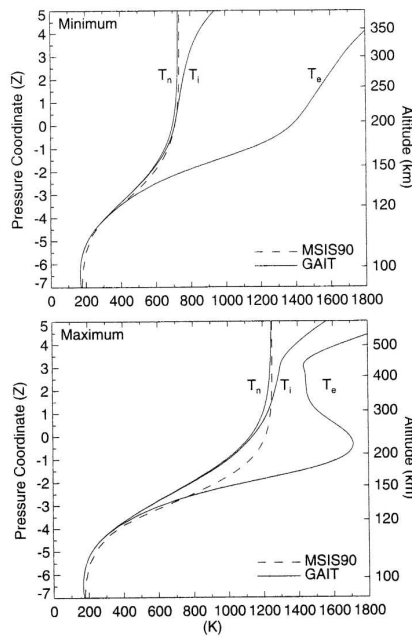


Figure 13.3: Global mean temperature profiles of Earth’s ionosphere/thermosphere calculated using the GAIT model [(solid lines). The three profiles correspond to neutral (T_n), ion (T_i), and electron (T_e) gases. The dashed lines show T_n for the MSIS-90 empirical model.] Solar minimum (top) and solar maximum (bottom) assuming quiet geomagnetic conditions ($A_p = 4$). [Fig. III:14.2; source: Smithtro and Sojka (2005).]

range,] the GAIT exospheric temperature was determined. The results are that the GAIT-model thermosphere responded linearly to each spectral model, and the same linear dependence is found for each. Note that the exospheric neutral temperature refers to the asymptotic, altitude-independent, temperature found at higher altitudes, see Figure 13.3 for specific solar minimum and maximum examples. The exosphere refers to the ionospheric plasma whose composition is light ions of hydrogen and helium that is located in altitude above the F layer.

[By combining various irradiance models computed for solar activity levels throughout the sunspot cycle] it is possible to extrapolate how the thermospheric exospheric temperature would trend for lower and higher levels of the solar EUV flux. [... The] procedure assumed that a linear dependence existed in the relevant EUV energy flux between solar minimum and solar maximum. An index S_{EUV} is defined to be 0 at solar minimum (energy flux of 3 erg/s/cm^2) and $S_{\text{EUV}} = 1$ at solar maximum (energy flux of 7 erg/s/cm^2). Then Maunder-Minimum type conditions correspond to $S_{\text{EUV}} < 0$ and grand maximum values correspond to $S_{\text{EUV}} > 1$. Note that the specific response to the solar cycle of each wavelength is different, hence S_{EUV} is applied to each wavelength separately to generate extreme solar spectra.” “[T]he Maunder Minimum S_{EUV} value would be between $S_{\text{EUV}} = -0.5$ and -1.0 . Figure 13.4 shows the GAIT ionospheric plasma composition for solar minimum ($S_{\text{EUV}} = 0$), $S_{\text{EUV}} = -0.5$, and $S_{\text{EUV}} = -1.0$.

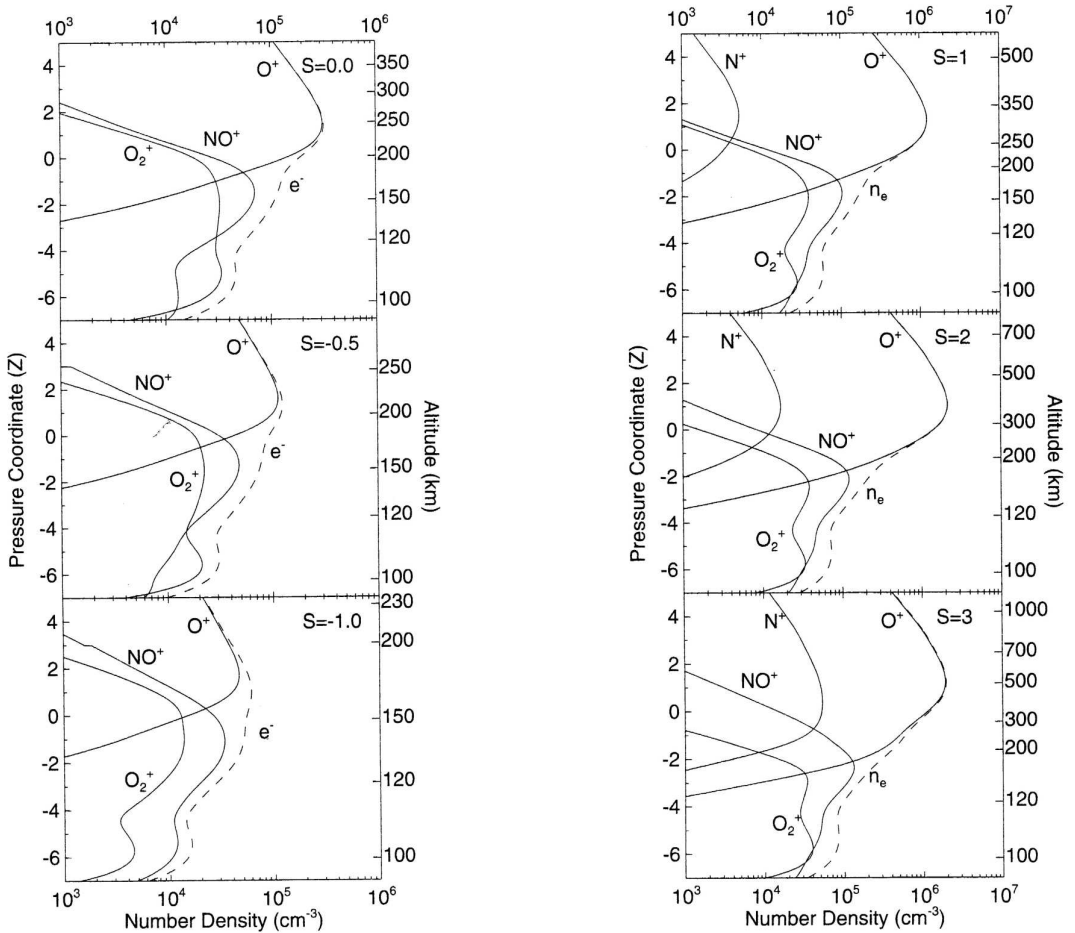


Figure 13.4: Global mean concentration of the ion and electron (dashed line) gases in Earth's upper atmosphere, calculated using the GAIT model for six different levels of the solar activity increasing from $S_{\text{EUV}} = -1.0$ to $S_{\text{EUV}} = 3$, clockwise from the bottom left. The profiles are plotted as a function of the pressure coordinate, $Z = \log p_0/p$, with the corresponding altitudes provided on the right-hand axis. [Fig. III:14.4; source: Smithgro and Sojka (2005).]

The earlier trends concerning the E and F layer are continued as the S_{EUV} value [is lowered. ...] The most significant ionospheric modification during the Maunder-Minimum period is that the molecular ion NO^+ peak below 200 km becomes significant; compare the top-left panel for $S_{\text{EUV}} = 0$ and the bottom-left panel $S_{\text{EUV}} = -1$ in Figure 13.4. This additional structure in the electron density profile is referred to as the F_1 layer. Indeed, in Figure 13.4 the $S_{\text{EUV}} = -1.0$ case almost has this F_1 electron density equal to that of the higher altitude F_2 peak. [...] These Maunder-Minimum scenarios provide significant problems for modern-day technology. For example: (1) using the ionosphere to propagate radio waves over the horizon is restricted to much lower frequencies because the maximum ionospheric density has decreased; and (2)

because the F_1 layer is located significantly lower than the F_2 layer propagation, paths for radio waves are also modified significantly. [On the other hand, (3)] with less ionospheric density in the path of GPS radio waves, the adverse role of the ionosphere in geolocation analysis is reduced.”

Now for a much more active Sun: “[a value of $S_{\text{EUV}} = 3$ can be used to characterize] the upper range of enhanced solar EUV flux to simulate grand-maximum type conditions. The grand maximum existed between 1100 and 1250 CE. An S_{EUV} value of 3 corresponds to doubling the solar maximum solar energy flux from 7 erg/s/cm^2 to just over 14 erg/s/cm^2 . The right-hand column in Figure 13.4 shows the GAIT-model ionospheric plasma distributions at solar maximum ($S_{\text{EUV}} = 1$), $S_{\text{EUV}} = 2$, and $S_{\text{EUV}} = 3$ from top panel to bottom panel. In all cases, the F_2 layer is the dominant layer with O^+ the dominant ion. As predicted from the normal solar cycle trend, this layer will rise, in this case from 300 km ($S_{\text{EUV}} = 1$) to about 500 km ($S_{\text{EUV}} = 3$). The F_2 peak density does not increase linearly with S_{EUV} ! Between $S_{\text{EUV}} = 2$ and $S_{\text{EUV}} = 3$ the F_2 peak density has remained at $2 \times 10^6 \text{ cm}^{-3}$. {A184}

This maximum in the F_2 peak density is by far the most significant change in the geospace climate in response to solar photon radiation. The processes responsible for this effect are: (i) the production of neutral O and, hence, its concentration has non-linearly decreased at altitudes at which the F_2 peak is created now as the thermosphere heats up as S_{EUV} increasing from 2 to 3; (ii) the O^+ production rate does increase linearly as S_{EUV} increases from 2 to 3; and (iii) the competition between these two processes leads to a maximum peak F_2 density at $S_{\text{EUV}} = 2$, and then as S_{EUV} increases further even a slight decrease in the peak density. The consequences for modern-day technologies under enhanced solar maximum, grand maximum conditions are: (1) the changing altitude of the F_2 layer leads to modified radio wave propagation paths; (2) that the peak F_2 density saturates only slightly above solar maximum values implies that the ‘radio’ reflection characteristics of the ionosphere are consistent with today’s ‘radio climate’; (3) the impact on trans-ionospheric radio applications such as GPS geolocation is somewhat adverse since the total electron content (the electron density integrated over a line of sight, *i.e.*, a column density) continues to increase even though the F_2 peak density becomes constant; and (4) because the ionosphere is significantly more dense, the absolute magnitude of plasma density irregularities would increase which would lead to greater scintillation problems with radio propagation.”

“In modeling the ionosphere and thermosphere as the solar EUV energy flux is changed, there are at least two impacts of significance for the outer reaches of geospace. First, assuming that the magnetosphere is somewhat similar to the state that we are familiar with, then the IT contributes plasma to the magnetosphere/plasmasphere and second, the IT electrical conductivity is a component of the magnetosphere-ionosphere (M-I) electrical coupling. Under the Maunder-Minimum type conditions, ionospheric outflow of plasma into the magnetosphere/plasmasphere will decrease because the ionospheric topside is colder and less dense. Under extreme conditions such as $S_{\text{EUV}} = -1$, the composition may also begin to change from atomic to molecular. In contrast, under $S_{\text{EUV}} = 2$ and upward, during grand-maximum conditions with

hotter topside, the outflow would increase and be very much O^+ dominated. Note that in these GAIT-type modeling studies the light ion, H^+ , has not been included, and therefore the remarks pertain to O^+ and heavier molecular ions. In contrast, the ionospheric conductivity changes are smaller because the major contribution comes from the E layer whose composition remains molecular. However, the decreasing dayside conductivity during Maunder-Minimum conditions would raise issues about how this impacts the M-I electric circuit response, *i.e.*, would this modify present-day concepts of voltage versus current generator descriptions of the M-I system? Under the grand maximum with enhanced conductivities and also the assumption of increased solar wind energy, would M-I coupling be characterized by significantly enhanced currents and electric field? Both scenarios would probably impact the morphology of auroral displays! This may lead to the most significant human experience of the geospace climate.”

13.3.2 Geospace climate at earlier terrestrial ages

Now let us look at the far larger range of solar activity as that evolved over the 4.6 Gyr history of Venus, Earth and Mars. “In earlier times, the solar EUV was more intense and, consequently, the thermosphere was much hotter, leading to the dominance of significantly different processes. [In particular, we look at] an early period when atomic hydrogen was in a blow-off phase as well as periods when high escape rates for the fastest particles in the energy distribution (‘Jeans escape’) of heavier species like H_2 , He, C, N, O existed [(compare Ch. 12). S]tudies also show that IR-radiating molecules like CO_2 , NO, OH, etc., control the exospheric temperature that, in turn, controls the Jeans escape rates for the neutral constituents. Hence, the results depend not only on a knowledge of solar EUV but also on the contribution of molecules such as CO_2 and H_2O in the earlier terrestrial atmosphere [that can be addressed, for example, with] a diffusive-gravitational equilibrium and thermal balance model to study heating of the earlier thermosphere.”

In an initial simulation, this model was used to evaluate the terrestrial exospheric temperature over the past 4.6 Gyr. Significant assumptions were made that the present-day composition as well as that of the lower atmosphere up to 90 km were the same then as they are today. The increased solar flux values at earlier ages [were estimated as] summarized in [Fig. 13.5].

Figure 13.6 shows [the simulated] history of the Earth’s exospheric temperature. Assuming that the blow-off temperature for atomic hydrogen is about 5000 K, the Earth’s first Gyr would exhibit a markedly different upper atmosphere where even the atomic atoms and molecular hydrogen would be approaching their thermal escape speeds. [T]his simple model becomes a rough estimate when in the life of the Sun (smoothing over time scales long compared to solar cycles) the exospheric temperatures exceed 10,000 K.

The major assumption that would be questioned for these earlier Earth ages would be the density of the IR radiating molecules such as CO_2 . In significantly earlier times,

Sun-like stars of different ages			
Name	Spectral type	P_{rot} (days)	Age (Gyr)
EK Dra	G1.5 V	2.7	0.1*
π^1 UMa	G1.5 V	4.9	0.3
χ^1 Ori	G1 V	5.2	0.3
κ^1 Cet	G5 V	9.2	0.7
β Com	G0 V	12.	1.6
Sun	G2 V	25.4	4.6
β Hyi	G2 IV	~ 28	6.7

* [Another study reports] an age of 0.03 – 0.05 Gyr.

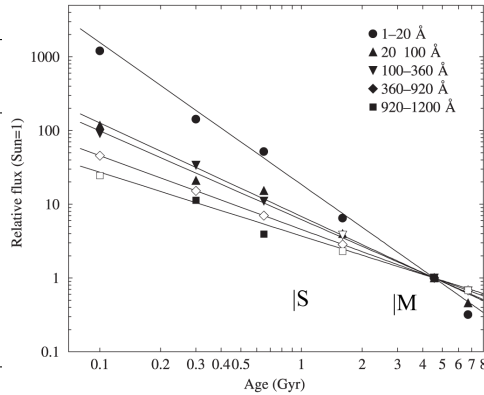


Figure 13.5: Spectral radiance versus age of solar-type stars (identified in the table on the left, with spectral type, rotation period, and estimated age), in solar units. Measurements are shown by filled symbols; missing data (open symbols) are derived from power-law fits (solid lines) for passbands from 1 to 1200Å. The approximate ages for which the oldest fossils of single-cell microbial life (S) and multi-cellular plants and animals (M) have been found on Earth are indicated. [Fig. III:2.14; source: Ribas et al. (2005).]

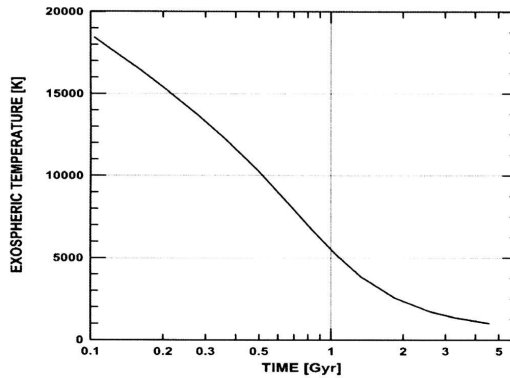


Figure 13.6: Evolution of the exospheric temperature, assuming Earth's present atmospheric composition, over the planet's history as a function of the solar XUV flux for a strongly limited hydrogen blow-off rate. [Fig. III:14.5; source: Kulikov et al. (2007).]

these would be expected to be larger. If this is the case, then their role in 'cooling' the thermosphere would increase. Defining the CO_2 mixing ratio relative to present atmospheric level (PAL) as 1, [...] Figure 13.7 shows how, indeed, significant increases in CO_2 will cool the upper atmosphere. In this figure, the 'XUV flux' is the scaling ratio of earlier age solar EUV compared to today. The current situation is shown at unit XUV flux. This shows that increasing CO_2 by a factor of 10 (10 PAL) leads to a drop of almost 600 K in the exospheric temperature from 1600 K to 1000 K. [...] Further work has shown that] by solar fluxes that are about 5 times the present average EUV energy flux of 5.1 erg/s/cm^2 , the composition of the upper thermosphere will be dramatically

Historical values of the solar EUV fluxes relative to the present-day value. [Table III:14.1]

Time	Solar flux multiplier
3.5 Gyr ago	factor ~6
3.8 Gyr ago	factor ~10
4.33 Gyr ago	factor ~ 50
4.5 Gyr ago	factor ~100

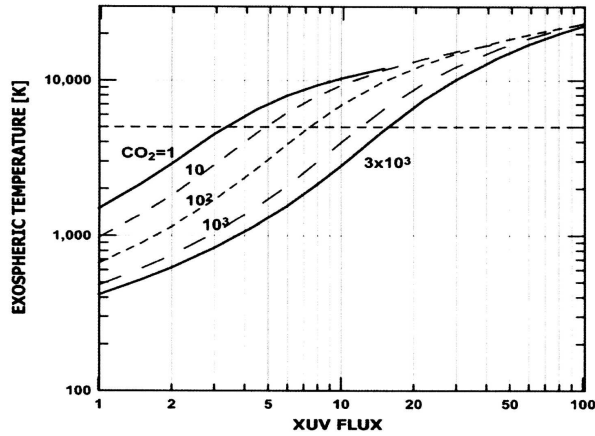


Figure 13.7: Earth’s exospheric temperatures for different levels of CO₂ abundance in units of PAL (Present Atmospheric Level: 1 PAL for CO₂ = 330 ppm) in the thermosphere as a function of solar XUV flux. The numbers by the curves correspond to CO₂ volume mixing ratios expressed in PAL. The horizontal dashed line shows the blow-off temperature of atomic hydrogen. [The Table lists estimated XUV flux levels relative to the present day. Fig. III:14.6; source: Kulikov et al. (2007).]

different from today as the Jeans escape mechanism becomes effective for hydrogen as well as other atomic species. [Model studies (see III:12.3.3 for some details and references)] indicate that at earlier ages of the Earth’s upper atmosphere-ionosphere, the response to increased solar EUV flux was a heating of this part of geospace with the following impacts on the geospace climate: (1) for exospheric temperatures of 5000 K and above, the upper atmospheric composition would be dramatically different due to Jeans escape fluxes of hydrogen and other atomic species; (2) the altitude of the F₂ layer would increase to heights above 2000 km; (3) the F₂ layer peak density would become constant; (4) the total electron content of the ionosphere would increase linearly with increasing solar EUV flux.

The geospace climate would change from an ionospheric standpoint when the solar energy flux slightly exceeds levels of the present-day solar maximum. From the thermospheric point of view, the geospace climate would change when the solar flux EUV reaches about 20 erg/s/cm² (three times the present-day solar maximum values). [...]” {A185}

13.3.3 Geospace climate and Earth’s magnetic field

“[T]he outer boundary of geospace is defined to be the magnetosphere, and specifically, the magnetopause. It is created by the solar wind that interacts with an intrinsic property of the Earth, the magnetic field. Consequently, in this section questions concerning how long-term trends of the solar wind and Earth’s magnetic field are considered in discussing the long-term geospace climate. Of specific interest are the conditions under which the geospace would be dramatically changed. [...]”

“Perhaps the geospace response to flips in the Earth’s dominant dipolar field is the

{A185} III:14.5
 III:14.5.1

most frequently discussed geospace 'what if' scenario. Geological evidence obtained in the last century has clearly proven that the Earth's magnetic field, especially its dominant dipole component, has reversed many times during geological times. The most recent reversal occurred 0.78 Myr ago. Prior to this reversal the 6 most recent occurred at 0.99, 1.07, 1.19, 1.2, 1.77, and 1.95 Myr ago. [Reversals] occur at quite irregular intervals with the shortest time between reversals being at the Cobb Mountain reversal pair separated by only about 10,000 years. [... R]eversals occur when the dipole field strength is relatively weak.

[...] The specific 'N-S' or 'S-N' dipole orientation itself would not introduce significant geospace climate changes. Perhaps, the most obvious would be that the solar wind northward versus southward reconnection morphology would be reversed. What is significantly more important would be the magnitude of the Earth's field and the orientation of its dipole component."

"Over the past 100 years, the Earth's dipole moment has decreased by about 5% from 8.3×10^{25} to 7.8×10^{25} erg/G, while three-thousand years ago, it was at almost 12×10^{25} erg/G, at its highest value during the Holocene era. From [Ch. 5 it is clear that] it is the balance between the Earth's magnetic field and the solar wind pressure that determines the outer boundaries of the magnetosphere/geospace. Hence, a larger (or smaller) dipole moment with otherwise the same solar wind conditions would increase (or reduce) the size of geospace. In turn, this would reduce (or increase) the size of the polar cap, and auroral regions would move poleward (or equatorward). However, a 5% change in the [virtual axial dipole moment (VADM)] would probably not have a dominant impact on geospace because the solar wind pressure varies by more than this over its normal solar cycle. Considering earlier times when the VADM did decrease to values as low as, if not lower than, [a quarter of the present-day value,] the geospace climate may well have been dramatically different, especially during solar maximum type conditions. The magnetosphere would have been severely reduced, and in volume regions such as the plasmasphere it would have almost been reduced to ionospheric altitudes and in the 'open' polar regions would extend to mid-latitudes. The effectiveness of plasma sheet energization processes would also have been changed, causing impacts on ring currents, electrojets, as well as the visible aurora. Perhaps, the energy transfer to geospace would simply decrease as the magnetosphere's cross section to the solar wind decreases, and consequently, all internal energy processes would be similarly scaled down.

The extreme scenario of the dipole reversal is the idea that the VADM for a time period is extremely small, approximately zero. If the higher-order multipole terms are also negligible, then the Earth's atmosphere is unprotected. But this is the Venus and Mars type scenario and extensive analysis has been done on these planetary atmospheres. At present, the scientific techniques that provide information on the reversals are unable to be specific on this question, but a near-zero magnetic field appears to last no longer than a few thousand years, if that."

"The scenarios for the geospace climate dependence on tilt angle between the Earth's rotational axis and dipole axis provide vivid geometries of geospace regions

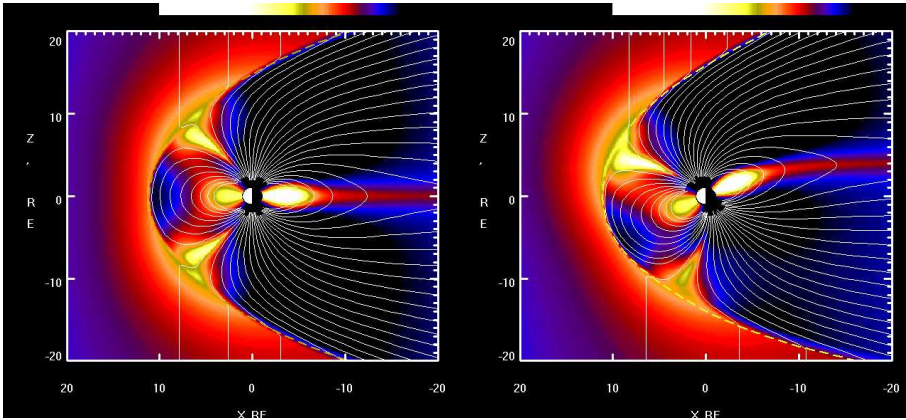


Figure 13.8: Field lines plotted in the noon-midnight meridian plane for an untitled planetary dipole embedded in the solar wind (left) and a dipole tilted in the noon-midnight meridian by 30° (right). The colors show the difference in the magnitudes of the field in the $x - z$ plane of a model field including the effects of a solar wind compared to that of a dipole field; positive differences are shown in blue to black, negative differences in red through yellow to white. [source NASA's CCMC; see also Fig. III:14.13] For a color version of this figure, see [arXiv:2001.01093](https://arxiv.org/abs/2001.01093).

such as the plasmasphere, plasma sheet, cusps, auroral zones, and open/closed field line regions. For extreme tilt angles, a significant question would be how rapidly these region can evolve and replenish themselves. [...] Figure 13.8 provides a pair of noon-midnight cross sections through the Earth's magnetosphere for a 0° and 30° tilt. In the left panel, all the conventional magnetosphere regions can be identified and their evolution over a day would be shown at each time, as seen in this panel for a constant solar wind. Our present-day tilt scenario is somewhat different; in the northern hemisphere it is approximately 10° while in the southern hemisphere it is almost 15° .

However, even with this tilt, the fundamental magnetospheric regions found in Figure 13.8(left) are present all day with relatively small wobbles in the geocentric-solar-ecliptic coordinate system (GSE; x , Earth-Sun line; z , ecliptic north pole) of this figure. Both cusps are dayside and wobble in latitude. The plasmaspheric equatorial plane is that of the 'average' dipole and would wobble in 24 hours about the GSE- x axis. Even today, the concept of the plasmasphere's 'average' dipole orientation is not fully explored since it is well known that the Earth's equatorial fields are not well represented by a pure dipole component.

Over time scales of decades and more, the tilt angle as well as its geographic longitude wander. Indeed, this has been identified as a major factor in complicating the historic auroral observation data base. For example, when an aurora was observed at lower mid-latitudes as described in Sect. 13.3, was this due to an especially strong or geo-effective solar storm (CME) or did the Earth's dipole tilt have a particularly large value at that time, making this terrestrial location a much higher geomagnetic

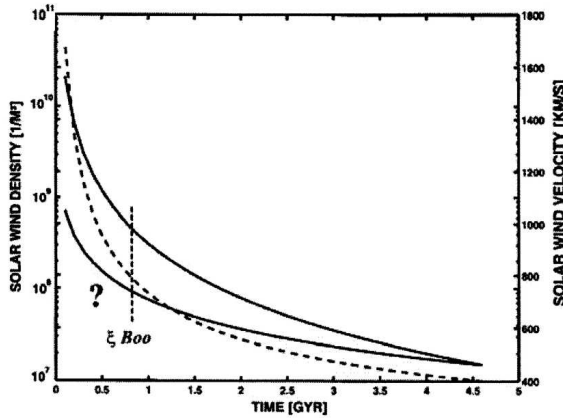


Figure 13.9: Evolution of the observation-based minimum and maximum stellar wind densities (in units of m^{-3}) scaled to 1 AU (left scale; solid lines) obtained from several nearby solar-like stars. On the right scale is the solar wind speed for the stellar wind evolution (dashed line). [The star ξ Boo sits on the ‘wind dividing line’; mass loss appears strongly reduced for stars younger than that, contrary to the simple extrapolation shown here, see Fig. 10.9. Fig. III:14.14; source: Lundin et al. (2007).]

latitude?

The right-hand panel in Figure 13.8 shows the magnetospheric geometry for a specific ‘UT’ during northern-hemisphere summer solstice when the tilt can reach some 30° . At other times of the day, as the Earth rotates, this geometry changes significantly. Six hours earlier or later, the $x - z$ GSE cross section might look similar to the symmetric geometry in the left panel. However, the cusps would be displaced in the y GSE direction and the plasma sheet would have a large tilt in $y - z$ GSE cross section. As the tilt angle increases beyond 35° , would the normal diurnal independences of the magnetospheric morphologies remain? For example, would auroral zones still be referred to as a north and a south auroral oval? In the extreme case of a tilt approaching 90° , does the plasma sheet in the $x - z$ GSE cross section have two plasma sheets at certain UTs? Under these conditions with the same VADM and solar wind, dramatically different geospace climate would be observed in the form of auroral sightings as well as terrestrial magnetic field records of the electrojets and ring currents.”

13.3.4 Geospace climate dependence on the solar wind

What are the effects of the long-term evolution of the solar wind on the geospace climate? “Most of today’s knowledge of the early Sun’s history, normally referred to times that the Sun reached its zero-age main sequence (ZAMS) has been obtained from studies of Sun-like stars, *i.e.*, main-sequence G and K stars. [The] time dependences for the solar wind velocity (v_{sw}) and density (n_{sw}) at 1 AU [have been coarsely approximated by]:

$$v_{sw} = v_* \left[1 + \frac{t}{\tau_{sw}} \right]^{-0.4} ; \quad n_{sw} = n_* \left[1 + \frac{t}{\tau_{sw}} \right]^{-1.5}, \quad (13.14)$$

where $v_* = 3200$ km/s, $n_* = 2.4 \times 10^4$ cm $^{-3}$ and $\tau_{\text{sw}} = 2.56 \times 10^7$ yr. [...]” {ⓂA186}

Figure 13.9 shows the large spread in the range of the n_{sw} dependence since the Sun reached ZAMS about 4.6 Gyr ago. Note that the [above approximations and the curves] shown in Figure 13.9 have as a reference a present-day n_{sw} of 20 cm $^{-3}$ (2×10^7 m $^{-3}$) and a $v_{\text{sw}} = 400$ km/s. Today’s solar cycle and solar storms have periods when the density can almost be a factor of 10 higher and the velocity reaches 1000 km/s. These enhanced conditions are associated with storms and superstorms in geospace that can persist for days while the solar wind remains perturbed. If the Earth’s intrinsic magnetic field were then as it is today, would geospace at 2 to 3 Gyr ago be in a continuous superstorm state? Figure 13.9 shows that at these times the solar wind’s pressure would permanently be at, or exceed, superstorm solar wind conditions. Would the auroral phenomena be permanent displays and exist to very low latitudes, or would perhaps M-I coupling require an unsustainable flow of ionospheric plasma into the magnetosphere? The past geospace climate over the Holocene, *i.e.*, the human time period, was not significantly affected by long-term changes in the solar wind while at very early ages it could well have been a very illuminating dynamic M-I coupling environment.” {ⓂA186}

Chapter 14

Cosmic rays and magnetic fields over time

Chapter topics:

- Evolution of terrestrial energetic-particle exposure
- Radionuclides as proxies of long-term magnetic variability
- Transport and deposition of radionuclides
- Exposure to supernovae

Key concepts:

- Cosmogenic radionuclides
- Tree rings, ice sheets, and rocks as records
- Cut-off rigidity
- Force-field approximation

14.1 Introduction

Energetic particles can affect electronics components and presents a health hazard for astronauts, particularly when outside the magnetosphere, such as en route to the Moon or to Mars (as described in Chs. II:13 and II:14). The energetic particles discussed in this chapter originate at the Sun, in the solar wind, and in the Galaxy beyond the heliosphere. Observation of their variability tells us about their sources and about conditions en route to Earth.

Collisions of the most energetic among these particles with bodies in the Solar System lead to the formation of radionuclides that subsequently decay with half-lives of various durations. If such radionuclides are stored in suitably 'stratified' natural archives – such as in long-lived snow deposits or growth rings of trees – their concentrations measured through such archives shine a light on intensities and variability in times from before instrumental records. Even unstratified 'archives', such as lunar and meteoric rocks, serve as dosimeters in which depth profiles of cosmogenic radionuclides contain

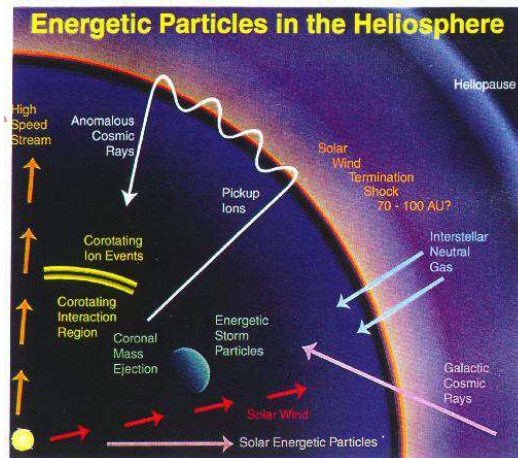


Figure 14.1: Sources of energetic particles in the heliosphere. [IV:12.1; source CalTech.] For a color version of this figure, see arXiv:2001.01093.

information on particle energies and fluxes, and the different decay time scales some information on the exposure history.

In the present chapter, we focus on changes in exposure over time scales up to billions of years, and on what these changes tell us about solar activity, galactic cosmic rays, the state of the heliosphere, and the terrestrial magnetic field.

“Energetic particles in the energy range between 1 eV to 10^{20} eV can be found everywhere in our Solar System as sketched in Fig. 14.1. Their sources can be either outside our Solar System from galactic [and extra-galactic interstellar space or inside our Solar System, including the Sun, interplanetary space, and planetary magnetospheres]. The types of energetic particles range from electrons to charged atoms and molecules to neutral atoms and molecules as well as dust particles. Fig. 8.5 shows the particle intensity versus energy of various types of energetic particles (left) and for cosmic rays (right).”

14.2 Long-term energetic-particle exposure of Earth

The exposure of Earth to energetic particles over many millions of years can be derived from the study of various cosmogenic radionuclides found in rocks (including those brought back from the Moon by the Apollo astronauts) and ice deposits (in Greenland and Antarctica). On time scales up to thousands of years we find signals in the biosphere (primarily in tree rings).

14.2.1 Generation of cosmogenic radionuclides

“Cosmogenic radionuclides are produced by nuclear interactions of the galactic cosmic rays (GCR) with atoms (N, O, Ar) in the atmosphere; the contribution of solar cosmic rays is negligible because of their low energies.” “Galactic cosmic radiation originates outside our Solar System but generally within our Milky Way galaxy and

is treated as [isotropic. This radiation consists of atoms that] have been ionized and accelerated to very high energies, probably by [shock fronts of] supernova remnants. The GCR population consists of about 87% protons and 12% α particles, with the remaining 1-2% heavier nuclei with charges ranging from 3 (lithium) to about 28 (nickel). Ions heavier than nickel are also present, but they are rare. Electrons and positrons constitute about 1% of the overall GCR.”

“To reach the atmosphere, the GCR have to propagate through the heliosphere which forms a bubble with a radius of about 100 AU around the Sun that is filled with solar plasma carrying magnetic field [as discussed in Ch. 8. It is appropriate] to use the transport equation [Eq. (8.25)] to parameterize the intensity of the GCR, however the so-called force-field approximation has proven to be a [reasonable simplification] near Earth. This approximation describes the modulation effect of the Sun on the energy spectrum of the GCR in terms of a parameter Φ called the solar modulation function” and comes about as follows:

“If one assumes spherical symmetry, and then considers only high energy cosmic rays, for which the dimensionless modulation quantity rv/κ , which measures the strength of the modulation, is small, a very simple analytic solution can be obtained. The form of this solution corresponds exactly to that obtained for charged particles influenced by [an electric] field with a potential given as a function of heliocentric radius r by

$$\Phi(r) \propto \int_r^D [v_{sw}/\kappa] dr \tag{14.1}$$

[with the solar wind velocity v_{sw} assumed constant and κ an equivalent radial diffusion coefficient, also assumed to be a simple constant, for the full expression in Eq. (8.20).]

{A187} Note that this is not a real electrostatic potential because it affects positively and negatively charged particles in the same way. [Moreover, observations show a strong dependence of the cosmic-ray intensity on heliographic latitude which cannot develop in the force-field approximation.] Attempts to fit the data yield values of $\Phi \approx 300$ MeV near 1 AU. Because of the use of an effective potential energy, this approximation is called the ‘force-field’ solution. [...] “The solar modulation function Φ basically corresponds to the average energy lost by a cosmic ray proton on its way to the Earth.

Figure 14.2 shows the differential energy spectrum of the GCR proton flux for different levels of solar activity. A value of $\Phi = 0$ MeV corresponds to the local interstellar spectrum outside the heliosphere. [The spectrum shown here is an estimate (dependent on the model approximation and on the properties of the interstellar medium and the solar wind) made before Voyagers 1 and 2 had reached the interstellar medium, which appears to have happened in late 2018.] Figure 14.2 shows that the shielding effects of the open solar magnetic field and the advecting solar wind are most pronounced at the low energy end of the spectrum. As a consequence, GCR particles above about 20 GeV are hardly affected by the varying heliospheric magnetic field.

Before reaching [the terrestrial atmosphere], the cosmic ray particles have to overcome a second barrier, the geomagnetic field. This field prevents particles with too

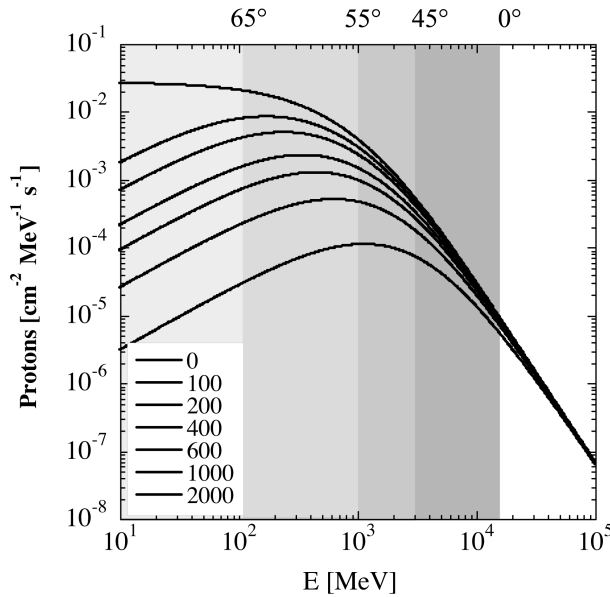


Figure 14.2: Differential galactic cosmic ray proton fluxes for different levels of solar activity ranging from a value of the solar modulation function $\Phi = 0$ MeV (Eq. 14.1), corresponding to the local interstellar spectrum arriving at Earth without any solar influence, to $\Phi = 2000$ MeV which corresponds to a very active Sun. There are similar curves for cosmic ray alpha particles and heavier nuclides. The vertical bands illustrate the effect of the geomagnetic field which cuts off all protons approaching vertically with an energy below about 100 MeV for a geomagnetic latitude of 65° ; below 1 GeV for 55° , and below 3 GeV for 45° . At 0° the cut-off energy is 13.9 GeV for the present geomagnetic field. [Fig. III:11.11]

low rigidity (momentum per unit charge) from reaching the top of the atmosphere. In a first approximation, the geomagnetic field is considered as a dipole and in this case the cut-off rigidity depends only on the angle of incidence and the geomagnetic latitude. At low latitudes the cut-off rigidity for vertical incidence is presently ~ 14.9 GV. This means that a cosmic ray proton needs a kinetic energy of at least 14 GeV ($14.9\text{-}m_p c^2$) to reach the top of the atmosphere (see shaded bands in Fig. 14.2) [...]

If a primary cosmic ray particle makes its way through the heliosphere and the geomagnetic field and enters the atmosphere it will interact quickly with an atomic nucleus of oxygen, nitrogen, or argon. Because the energies of incoming particles are generally very high, only part of their kinetic energy is transferred to the first atom they hit. They continue their travel and hit a few more atoms until their energy is dissipated. Each collision results in the generation of secondary particles covering the full spectrum of hadrons and leptons, which either decay or interact with other atoms of the atmosphere. In this way a cascade of secondary particles develops which can be simulated using Monte Carlo techniques. Table 14.1 shows the different production reactions for the radionuclides ^{14}C , ^{10}Be , and ^{36}Cl , and the resulting mean global production rates for the present geomagnetic field intensity and a solar modulation function equal to $\Phi = 550$ MeV. {A188}

Table 14.1: *Properties for some cosmogenic radionuclides including nuclear production reactions and globally-averaged production rates for the present geomagnetic field and a solar modulation of $\Phi = 550$ MeV. (EC: electron capture). All nuclear reactions are induced by high-energy secondary particles generated by the primary cosmic-ray particles (so-called spallation reactions). The only exception is ^{14}C which is almost totally produced by thermal neutrons interacting with nitrogen. [Table III:11.4]*

Isotope	half life (yr)	decay	target	nuclear reaction	production rate ($\text{cm}^{-2}\text{s}^{-1}$)
^{14}C	5730	β^-	N,O	$^{14}\text{N}(\text{n,p})^{14}\text{C}$ $^{16}\text{O}(\text{p,3p})^{14}\text{C}$ $^{16}\text{O}(\text{n,2p1n})^{14}\text{C}$	2.02
^{10}Be	1.5×10^6	β^-	N,O	$^{14}\text{N}(\text{n,3p2n})^{10}\text{Be}$ $^{14}\text{N}(\text{p,4p1n})^{10}\text{Be}$ $^{18}\text{O}(\text{n,4p3n})^{10}\text{Be}$ $^{18}\text{O}(\text{p,5p2n})^{10}\text{Be}$	0.018
^{36}Cl	0.30×10^6	β^- , EC	Ar	$^{40}\text{Ar}(\text{n,1p4n})^{36}\text{Cl}$ $^{40}\text{Ar}(\text{p,2p3n})^{36}\text{Cl}$ $^{36}\text{Ar}(\text{n,p})^{36}\text{Cl}$	0.0019

The simulations show that the majority of the secondaries are neutrons followed by protons. Both, in turn, collide with atmospheric atoms initiating spallation reactions that generate the cosmogenic nuclides that are archived for us in ice (^{10}Be , ^{36}Cl) or tree rings (^{14}C). In addition, the cosmic-ray produced neutrons have been monitored continuously since 1951 by so-called neutron monitors. [These measurements show that whenever] the magnetic activity is high (at high sunspot count) the shielding is strong and the neutron flux is low. [...] Many studies have shown that the 11-yr and longer-term variations are faithfully reproduced in the cosmogenic data, and they and the neutron monitor data have been inter-calibrated to yield a continuous cosmic-ray record for the past 10,000 years.

As an example, the combined effect of solar activity and geomagnetic field on the relative production rate of cosmogenic nuclides is shown for ^{10}Be in Fig. 14.3. The relative dipole component of the geomagnetic field μ_r varies between 0 and 2, 1 being the present field. For $\mu_r = 1$ and $\Phi = 550$ MeV (long-term average), the ^{10}Be production rate is normalized to 1. It should be noted that the dependence of the production rate on μ_r and Φ is nonlinear.” {A189}

14.2.2 Transport and deposition of cosmogenic radionuclides

“The fate indeitcosmogenic radionuclides!transport and depositionof a cosmogenic nuclide after its production in the atmosphere depends strongly on its geochemical properties. Within a short time, ^{10}Be becomes attached to aerosols and follows their pathways. ^{14}C on the other hand oxidizes to $^{14}\text{CO}_2$ and is exchanged between

{A189} III:11.42

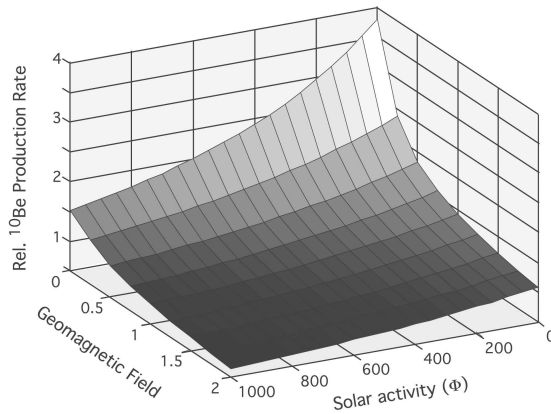


Figure 14.3: Dependence of the ^{10}Be production rate on the geomagnetic field intensity (in units relative to today’s field) and the solar activity (expressed by the solar modulation function Φ , Eq. 14.1). The production rate is normalized to the present strength of the geomagnetic field and solar activity corresponding to a solar modulation function of 550 MeV (matching the long-term average). [Fig. III:11.12]

atmosphere, biosphere and ocean. After a mean residence time of 1 to 2 years, ^{10}Be is removed from the atmosphere mainly by wet precipitation. The flux F of cosmogenic nuclides from the atmosphere into, for example, a polar ice sheet is proportional to the atmospheric production rate Π : $F = \psi \Pi$. Locally and temporally, ψ can vary due to changes in the atmospheric transport and deposition processes. The degree of variability depends very much on how well the atmosphere is mixed. In the case of ^{14}C , the large atmospheric $^{14}\text{CO}_2$ reservoir leads to an atmospheric residence time of 6 to 7 years and therefore to a complete mixing. In the case of the aerosol-bound nuclides the residence times are shorter, roughly 1 – 2 years; mixing in the troposphere is not complete. After deposition, some of the nuclides become incorporated into natural archives such as ice sheets, glaciers, sediments, and tree rings.

For our purpose, a useful archive stores the complete flux of nuclides from the atmosphere in a stratigraphically undisturbed way and records the time accurately. Excellent archives in this respect are ice sheets which directly collect the atmospheric precipitation containing ^{10}Be . Typically, they cover the last several 10^5 years with a time resolution per sample ranging from 1 year at the top to decades or centuries near the bottom. However, due to the flow characteristics of ice, dating is difficult, especially in the deeper part of ice cores.

Tree rings represent an ideal archive for the atmospheric $^{14}\text{C}/^{12}\text{C}$ ratio. So far, by chronologically matching trees of different ages, the atmospheric $^{14}\text{C}/^{12}\text{C}$ ratio has been reconstructed back to approximately [14 kyr BP (before present, relative to 1950 CE)]. Potentially, the full range covered with today’s measuring techniques (40 to 50 kyr) will be traceable in tree rings in the future.” {A190}

14.3 Radionuclides as proxies of magnetic variability

“What can be learned by measuring cosmogenic nuclides in ice? [...] In an archive, changes in the concentration can result from changes either in the production rate Π or in the Earth-system processes ψ (transport and deposition). Changes due to radioactive decay can be corrected for, if a reliable time scale is available. Changes in the production rate can be caused by heliomagnetic and geomagnetic modulation of the cosmic-ray flux. Episodic solar proton events can cause short but intense cosmic radiation, but do not contribute much to the total production rate due to the relatively low proton energies. Changes in the system on the other hand are related to the atmospheric transport and mixing processes as well as to the local precipitation rate.

The question arises how the different causes of concentration changes can be separated. A straightforward answer to this question is to combine several nuclide records from different sites. Comparing ^{10}Be with ^{14}C permits separating production from system effects. Changes in the production rate due to helio- and geomagnetic modulation of the cosmic-ray flux are reflected both in ^{10}Be and in ^{14}C in a very similar way. Changes within the Earth system, however, are expected to affect ^{10}Be and ^{14}C in a completely different way because the geochemical behavior of these nuclides is fundamentally different. [...] Of course, this argument is useful only over the range of the radiocarbon dating (last 50 kyr) and requires a high precision [record of $\Delta^{14}\text{C}$ that] is not yet available for the period 13 – 50 kyr BP. The next step is to separate heliomagnetic and geomagnetic signals. In principle, these two signals could be separated by looking at two radionuclide records, one from the equator and one from the regions of the magnetic poles. Without latitudinal atmospheric mixing, the record from the magnetic pole would only reflect solar modulation because geomagnetic shielding disappears at high latitudes, whereas the signal in the equatorial record would be dominated by geomagnetic modulation. However, as a result of atmospheric mixing, this is not the case.

Solar modulation effects have been found in cores from Greenland and Antarctica. The same is true for geomagnetic modulation effects like for the Laschamp event at about 40 kyr BP, when the magnetic dipole field was close to zero. This event is present in the high latitude ice-cores from the Arctic and from Antarctica (GRIP, Vostok, Byrd, Dome C, Taylor Dome). Radionuclide records from low-latitude ice cores are still rare [and have a smaller potential due to dating and other problems.]

Another approach is to assume that solar modulation effects generally occur on shorter time scales than geomagnetically induced production changes. Applying low-pass filters with cut-off frequencies in the range of $1/2000$ and $1/3000 \text{ yr}^{-1}$ on cosmogenic nuclide fluxes provides production signals in good agreement with paleomagnetic intensity records based on remanence measurements. {A191}

The task of separating the different causes of variability observed in radionuclide records is complicated by the fact that some of the causes are coupled. For example, changes in solar activity affect atmospheric processes and possibly also induce, to a smaller extent, climatic changes. Therefore, additional information from other measured parameters should be included to obtain a complete and consistent picture {A191}

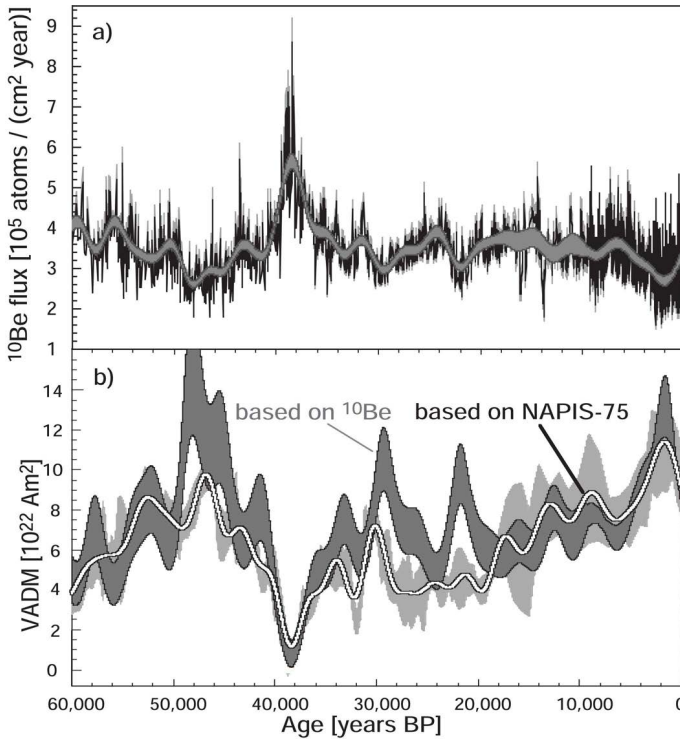


Figure 14.4: Comparison of (a) ^{10}Be data with (b) the geomagnetic dipole field for the past 60,000 years. Panel (a) shows a compilation of ^{10}Be data from the GRIP and GISP ice cores in Greenland. Panel (b) compares the dipole field derived from ^{10}Be (panel a) to that from remanence data (NAPIS-75) measured in ocean sediment cores. [Fig. III:11.14]

of what happened during the period of investigation. In the following, we discuss how the intensity of the geomagnetic dipole field and the solar variability can be derived from cosmogenic nuclides.”

14.3.1 Geomagnetic field

Fig. 14.4a shows “a compilation of ^{10}Be data from the GRIP and the GISP ice cores drilled in central Greenland [...] covering the past 60,000 years. To correct for the lower precipitation rate during glacial times (10 – 60 kyr BP) the ^{10}Be flux has been calculated and smoothed (gray band). The plot shows a significant peak at about 40 kyr BP. To check whether the smoothed curve does reflect the geomagnetic dipole field as expected from Fig. 14.4 the corresponding changes in the dipole field intensity have been calculated based on its relationship with the ^{10}Be production shown in Fig. 14.3. The result is compared in Fig. 14.4b with the completely independent reconstruction NAPIS-75 which was derived from remanence measurements in Atlantic sediment cores. Overall the agreement is good and confirms that the ^{10}Be peak at 40 kyr BP corresponds to the Laschamp event when the dipole field intensity was almost zero but did not reverse.”

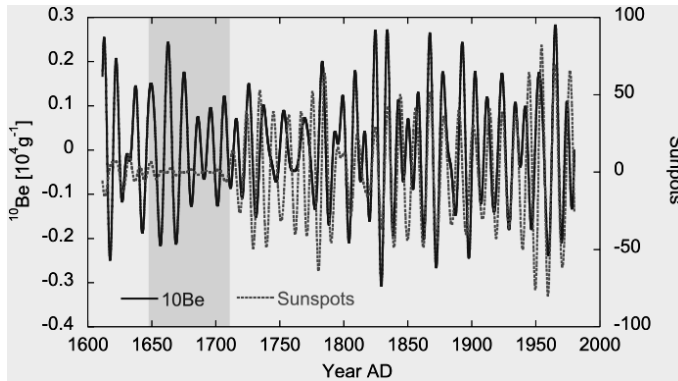


Figure 14.5: Comparison of the ^{10}Be concentration measured in the Dye 3 ice core from Greenland with the sunspot number after applying a band-pass filter (8 – 16 years). Note that during the Maunder Minimum 1645 – 1715 (shaded area) when almost no sunspots were observed ^{10}Be shows a clear 11-yr sunspot cycle. [Fig. III:11.15; source: Beer et al. (1994).]

14.3.2 Solar variability

“We return now to the discussion of solar variability and discuss to what extent cosmogenic radionuclides can expand our knowledge about long-term solar variability. In a first step, we compare annual ^{10}Be data with the sunspot record which represents the longest observational data of solar variability. A resolution of one year is about the limit because it corresponds to the mean travel time for a ^{10}Be atom produced in the atmosphere to reach the Earth surface where it is stored in, for example, an ice sheet. Fig. 14.5 shows a comparison of the ^{10}Be concentration from Dye 3, Greenland, with the sunspot number. Both records have been band-pass filtered (8 – 16 yr). While during the Maunder Minimum (shaded area between 1645 and 1715) hardly any sunspots were observed, the solar dynamo clearly continued to produce open magnetic field modulating the cosmic rays and the ^{10}Be production.

The overall good agreement between ^{10}Be and sunspot numbers gives us confidence to extend the time interval over the Holocene, *i.e.*, about the last 10,000 years. During this period the climate was relatively stable compared to glacial times and therefore we can assume that transport and deposition effects did not disturb the production signal in the ^{10}Be record. This assumption is confirmed by global circulation model (GCM) runs which show that the transport effects were relatively stable during the climatic conditions prevailing during the Holocene. So, indeed, to a first approximation they can be neglected. This is not the case for the geomagnetic field which exhibits significant long-term changes.

Using Monte Carlo simulations, the effect of the geomagnetic dipole field has been removed and we are left with the solar modulation function Φ [...] The data of Fig. 14.6 have been low-pass filtered with a 150 yr cutoff. The most striking features of the Φ record are the many distinct minima which correspond to grand solar minima such as the Maunder (M), Spörer (S), Wolf (W), and Oort (O) minima. The fact that Φ never reaches zero means that there is always some residual open magnetic flux;

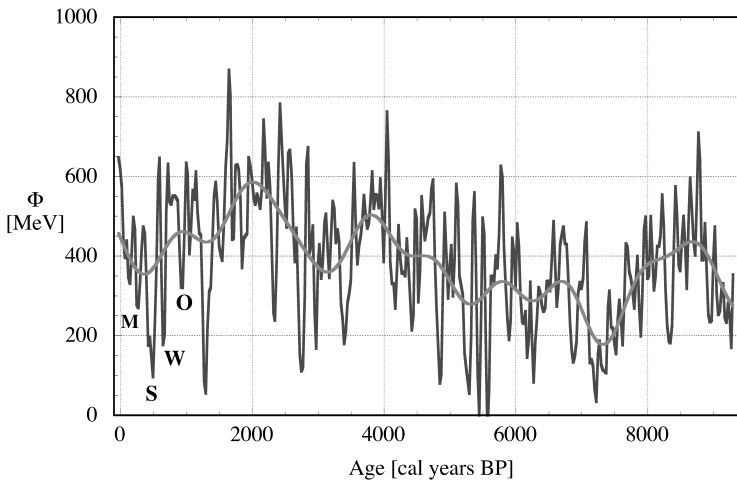


Figure 14.6: Solar modulation function Φ from the present (0 BP corresponds to 1950) back to 9350 BP. The black curve shows data that have been low-pass filtered with a cut-off of 150 years; the smooth grey curve with 1000 years. The most recent solar minima are indicated: M: Maunder; S: Spörer; W: Wolf, and O: Oort. [Fig. III:11.16]

in other words the solar dynamo seems to weaken from time to time, but, as a close inspection of the unfiltered data shows, it never stops. The two exceptions in Fig. 14.6 are due to uncertainties in the data.

The maxima are less pronounced. It is interesting to note that the present level of solar activity is comparatively high, although there were earlier periods with similar or possibly even higher activity around 2000, 4000, and 9000 BP. There is also a clear long-term trend indicated by the thick line that is low-pass filtered with a cut-off of 1000 years.”

For periods covering 10^5 yr to over 10^6 yr the obvious radionuclide archives are ocean sediments that go back many millions of years, such as ^{10}Be and ^{26}Al . The price one pays for the long records is the reduced temporal resolution owing to the very small sedimentation rates and additional processes related to the transport of the radionuclide into the sediment. As is the case for tree ring records, these radionuclides are sequentially stored as they are taken from the atmosphere, in contrast to radionuclides measured in rocks, which we discuss next, that are continually produced and that therefore provide only an integral measure of the production rate. The only time information available comes from the different half-lives. It is therefore important to measure as many distinct radionuclides as feasible.

14.3.3 Very-long time scale variability in cosmic-ray exposure

“The record of the galactic cosmic-ray flux on a million-year time scale can be inferred from induced nuclear reactions in extraterrestrial matter of known exposure geometry, such as lunar rocks or meteorites. Nuclear reactions produce a variety of radioactive and stable nuclei that can be measured and related to the incident cosmic ray flux. The radionuclides ^{81}Kr (2.1×10^2 yr half-life), ^{36}Cl (3.0×10^5 yr), ^{26}Al ($7.2 \times$

10^5 yr), ^{10}Be (1.6×10^6 yr) and ^{53}Mn (3.7×10^6 yr) represent a good set of monitors for cosmic ray flux variations on this time scale. Among the chondritic meteorites which were studied extensively, the production rates of the above radionuclides can vary because of differences in size and shielding conditions. These, when analyzed, reflect a constant ($\pm 10 - 15\%$) galactic flux over the $10^5 - 10^7$ yr time scale, which matches the average present-day flux.”

“There are few radioisotopes with appropriate half-lives that can be used for [times scale of $10^7 - 10^9$ yr] and only ^{129}I (1.6×10^7 yr) and ^{40}K (1.3×10^9 yr) have been studied so far.

Chondritic meteorites cannot be used to study variations in the cosmic ray flux on longer time scales, because their exposure ages (time between being formed and striking the Earth) are typically less than a few tens of million years. Fortunately, there are numerous recovered iron meteorites which were exposed in space as small bodies for up to two billion years since being formed, and which are well suited for this purpose. The measurement of all three isotopes of potassium permits the detection of the cosmic-ray-produced component which is superimposed to potassium initially present in the meteorite. For the period of $0.2 - 1.0$ Gyr ago, essentially constant ^{38}Ar production rates are observed, and agreement between ages determined from ^{38}Ar and from ^{40}K and ^{41}K .” It appears (Wieler *et al.*, 2013) that not much has changed in terms of long-term variability in solar activity or long-term trends in GCR fluxes coming into the heliosphere over the past billion years, to within a factor of ~ 1.5 , based on a variety of radionuclides in meteoritic samples and terrestrial sediments combined . . . but realize that variability below time scales of hundreds of thousands to millions of years cannot be detected within these records. {A192}

14.4 Exposure to supernovae

There is evidence of at least one nearby supernova in the very early formation phases of the Solar System when the terrestrial planets had yet to fully take shape. Then, the Sun was still embedded within its birth cluster, and it appears that one of its heavy siblings exploded prior to the cluster falling apart. {A193} There are some stars relatively nearby that are candidates to go supernova in the distant future, but none so close that the explosion would directly affect the solar system. Indirect effects, however, are possible: in the case of a blast wave from a nearby supernova, for present-day conditions of the solar wind, pressure “balance between the supernova shock wave and the solar wind produces extreme heliosphere models that have the same physical structures as the models with the heliopause at 1.4 times the distance of the termination shock in the upwind direction but with both located very close to the Sun. [A] supernova located at ≈ 9 pc from the Sun would create a heliopause that penetrates to within 1 AU, subjecting the Earth to an infusion of supernova debris including iron and other heavy atoms. {A194} The discovery of the radioisotope ^{60}Fe with a half-life of 1.5 Myr in a deep-sea ferromanganese crust and dated to 2.8 ± 0.4 Myr ago indicates that a nearby supernova explosion likely occurred [around that time (and perhaps another (Wallner *et al.*, 2016) some 6 – 9 Myr ago).]

The effect on the Earth of a nearby supernova and the effect on more distant planets from supernovae at distances up to 30 pc will include an increase in the amount of neutral hydrogen atoms, dust, supernova metals, and Galactic cosmic rays reaching the planet's atmosphere. The latter would influence the planet's magnetosphere and change the planet's atmospheric chemistry, including the important molecule ozone.”

Chapter 15

Applied heliophysics, *mutatis mutandis*

Our advancing understanding of the processes that are part of the network of Sun-planet connections in heliophysics is being applied and tested in innovative studies of star-exoplanet couplings. A small sampling from the already extensive and rapidly growing literature illustrates the fertile and diverse fields that heliophysics finds in astrophysics at large:

- For ultracool stars near the boundary of the stellar and substellar regimes, where coronal heating fails as the photosphere decouples from the magnetic field because of weak ionization, an analogy has been identified with Jupiter's magnetosphere in which failure of co-rotation introduces stresses in the field that ultimately lead to an auroral radio signature that can have a counterpart in ultracool stars (e.g., [a paper by Schrijver \(2009\)](#), and [work by Pineda and Hallinan \(2017\)](#)).
- For cool stars in general, signatures of stellar winds are evasive other than indirectly through magnetic braking over many millions of years, but where such a wind collides with the interstellar medium a neutral-hydrogen wall forms whose optical depth for, e.g., Lyman α radiation provides a field-independent measurement of mass-loss rates ([see Wood *et al.* \(2005\)](#)).
- Another signature of stellar winds may be found in observations of the bow shock around the magnetosphere/exosphere of a transiting exoplanet during pre-transit phases ([see Cauley *et al.* \(2015\)](#)).
- The stellar winds and their coupling with exoplanetary atmospheres can be modeled using codes developed for our Solar System, providing insight into star-planet couplings and exoplanetary magnetospheric activity for systems well outside the parameter domain of our own home in the local cosmos (such as for TRAPPIST-1 – see [Fig. 15.1](#) – [see Garraffo *et al.* \(2017\)](#)).
- The exposure of exoplanets to the stellar equivalent of solar energetic particles is being estimated by applying astrospheric models that include turbulence by which energetic particles are scattered, which enables, for example, quantitative estimates of particle radiation for exoplanets in stellar habitable zones ([see](#)

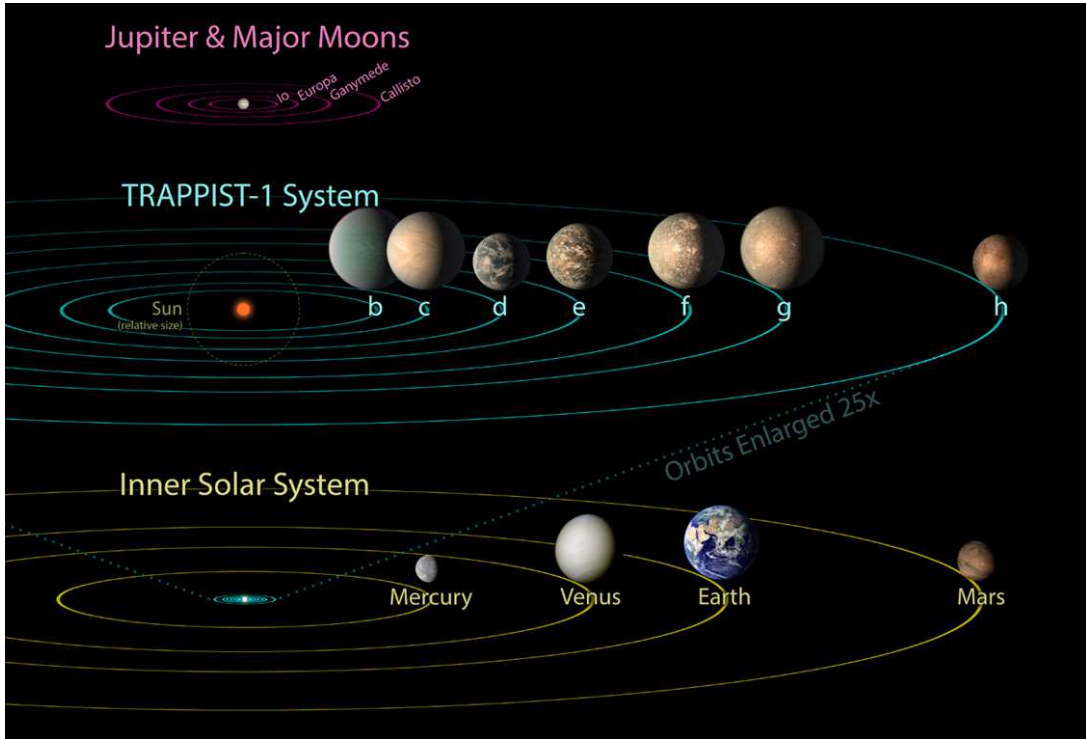


Figure 15.1: Comparison of the orbits of the major moons of Jupiter, of the known TRAPPIST-1 planets, and the inner Solar System. The planets and moons are shown on the same scale, but vastly enlarged relative to the orbital scales. Courtesy: NASA/JPL-Caltech. For a color version of this figure, see [arXiv:2001.01093](https://arxiv.org/abs/2001.01093).

[Fraschetti et al. \(2019\)](#)).

- The galactic cosmic ray exposure for exoplanets can be quantified based on modified heliospheric models, such as for the TRAPPIST-1 planets that orbit deep inside a strong-field astrosphere (see [Struminsky et al. \(2018\)](#)).
- The effects of stellar radiation and of stellar and galactic cosmic rays on the chemistry of exoplanetary atmospheres is being analyzed guided by, and calibrated against, solar-terrestrial spectral models and terrestrial tropospheric and ionospheric models (see [Scheucher et al. \(2018\)](#)).
- Evolution of the chemical makeup of planetary atmospheres subject to differences in insolation, rotation, atmospheric and oceanic circulations, and chemical weathering provide insight of the impacts of each of these on planetary habitability (see [Jansen et al. \(2019\)](#)) and help guide target selection for the search for biosignatures. The same is true on evolutionary timescales for the role of plate tectonics and volcanism (see [Foley and Smye \(2018\)](#)).

It should be no surprise that stellar and exoplanetary-system sciences conversely continue to provide crucial information for heliophysics:

- The very formation of stars and their planetary systems is being observed, models

- being refined, and results compared to empirical evidence from within the Solar System (e.g., see [Lammer and Blanc \(2018\)](#), and other papers in that volume).
- Over the past few decades, observations of stars of various spectral types and evolutionary phases have revealed the fundamental ingredients for stellar dynamos – rotation and convection – and quantitative information on how these set stellar atmospheric activity (e.g., see [Schrijver and Zwaan \(2000\)](#)) and how the Sun’s activity and wind have changed over its lifetime (see [Güdel \(2007\)](#), and see [Ó Fionnagáin et al. \(2019\)](#)), and from that how the Earth’s magnetopause distance would have changed over time (see [Pognan et al. \(2018\)](#)).
 - The multitude of exoplanetary systems continues to clarify the formative processes of planetary systems in general, and of the Solar System in particular, with strong evidence for migration of planetary orbits, the impact of that on the formation of Mars, and the possible cause of the Late Heavy Bombardment and the transport of water to the terrestrial planets by gravitational scattering (e.g., see [O’Brien et al. \(2014\)](#)).

The exchange of concepts, knowledge, and models between the domains of heliophysics, stellar astrophysics, and exoplanetary sciences is only in its beginning phases: expanding observational and computational capabilities will propel these fields forward, catalyzed by a joint approach. One such area that requires a joint approach is already developing under the name of ‘transit light source effect’ (see [Rackham et al. \(2018\)](#), and [Rackham et al. \(2019b\)](#), and [Rackham et al. \(2019a\)](#)): exoplanetary transit spectroscopy (e.g., see [Deming and Louie \(2019\)](#)) to study the chemical makeup and dynamics of an exoplanetary atmosphere is unavoidably linked with the analysis of the non-magnetic atmosphere (see [Dravins et al. \(2017a\)](#), and [Dravins et al. \(2017b\)](#)) and of the magnetic structures on the stellar atmosphere (e.g., see [Pinhas et al. \(2018\)](#); and [Zhang et al. \(2018\)](#)). Thus as we learn about exoplanetary atmospheres we will at the same time learn about starspots and stellar active regions at a resolution that has so far been unobtainable. That will provide information on how stellar dynamos structure their magnetic field from the scale of starspots upward that may prove critical to the development and validation of a predictive model for solar and stellar magnetic activity. That, in turn, will diminish the uncertainties on properties of stellar winds and their impacts over time on planetary atmospheres.

15.1 Activities to take you beyond the present-day solar system

The purpose this book is to give you fundamental insights into the couplings between the Sun, its planets, and the interstellar medium, with particular focus on Venus, Earth, and Mars. The text could only give you an introduction to the multitude of aspects of the field of heliophysics and the links to other disciplines, although many of the related fields – such as nuclear physics, geophysics, biochemistry, meteorology, and radiative transfer – were only mentioned or implied in passing. With this book, you have the basic tools in hand to explore the Solar System over time, from its formation

to its ultimate demise (although it stops short of the very end when the Sun transforms into a white dwarf, while the Earth may end up either evaporated and blown into interstellar space or pulled apart and spiraling into the white dwarf’s atmosphere, or a combination of these). This book also gives you the tools to look outward and into the future: you have the basic concepts available now to explore the multitude of new worlds that are being discovered, analyzed, and inspected for potential signs of life (such as the TRAPPIST-1 system sketched in Fig. 15.1). It is an exciting time for all of that. Why not start exploring with the final set of activities?

{A195} {A196} {A197} {A198} {A199} {A200}

{A195} {A196} {A197} {A198} {A199} {A200}

{A195} {A196} {A197} {A198} {A199} {A200}

{A195} {A196} {A197} {A198} {A199} {A200}

{A195} {A196} {A197} {A198} {A199} {A200}

{A195} {A196} {A197} {A198} {A199} {A200}

{A195} {A196} {A197} {A198} {A199} {A200}

Chapter 16

Activities

Chapter 1. Stars, planetary systems, and the local cosmos

{A1} *Look up* what type of astrophysical body is a true 'star'. Contrast that to 'white dwarf star', 'brown dwarf star', and 'neutron star': none of these are true stars in their present state and only two of which have ever been. 'Brown dwarfs' take up the mass interval between true stars and (exo)planets. /p. 3/

{A2} *Look up* the definition of 'planet'. Note that, formally, the term 'planet' has only been defined by the International Astronomical Union for bodies within the Solar System; the term 'exoplanet' is reserved for bodies like planets in other planetary systems, although for these, and certainly for the joint collective, the term 'planets' is often used. What differentiates a planet (in the broader sense of the definition) from a star (hint: it is not that a planet orbits a star, see for example 'rogue planets.') /p. 3/

{A3} *Look up:* Many 'stars' we see in the night sky are binaries, including, for example, the brightest star in the night sky, Sirius (α CMa). More complex multiple-star systems may be less frequent, but are nonetheless common. (a) Look up the example of Castor (α Gem) for an example of a sextenary, and then explore some more on [star systems](#) in general. (b) Create a table of a few of the more famous of these (such as Sirius, Proxima Centauri, and Polaris) and list the properties of the stars that they contain. We get to the meaning of 'spectral type' in Ch. 4. (c) You will see that stars go by many names: compare these and look up their roots, for example [at the IAU](#) or on [Wikipedia](#). /p. 3/

{A4} *Look up:* Review the vocabulary in Tables 1.1 and 1.2. Choose a term (or, if you want, more than one) that you are not familiar with and look up more information on it. In your own words, write an expanded definition for that term in a few sentences. /p. 3/

{A5} *Look up:* Remind yourself of Maxwell's equations that are mathematical renditions of these properties: (1) electric monopoles are linked with an electric field; (2) there are no magnetic monopoles; (3) variations in the magnetic field are associated with

a circulating electric field; and (4) a circulating magnetic field implies either steady currents or time-dependent electric fields, or both. Good news: once we have reached magnetohydrodynamics in Ch. 3, Maxwell's equations are in principle superfluous as they are contained within the MHD equations; if you are interested in how that works, see [Spruit \(2016\)](#) (Sections 1.1.1–1.1.9). By the way, a really useful resource for all things related to plasma physics (and how to convert between different unit systems) is the online [NRL Plasma Formulary](#). Make a table that matches each equation (and add often-used names for them); use the NRL Plasma Formulary to compare and contrast the Gaussian and SI unit formulations. Which formulation do you like better? /p. 8/

Chapter 2. Neutrals, ions, and photons

{A6} *Consider:* Planetary lower atmospheres are dominated by molecular substances, transitioning to atomic elements with a relatively low admixture of ions and electrons as one moves up through the ionospheres and thermospheres, while magnetospheres and the solar outer atmosphere and wind are comprised predominantly of charged particles. (a) Compare thermal kinetic energies in different settings with molecular binding energies of, say, water and carbon dioxide. (b) Also compare the energy of X-ray and EUV photons with ionization energies of atomic hydrogen and oxygen. See Tables 2.1, 2.3, and 2.4 for conditions in different settings. /p. 13/

{A7} *Look up* and compare images of the Sun's magnetic field and atmosphere in different phases of the solar cycle, such as [those](#) obtained with the *HMI* and *AIA* instruments on *SDO* (NASA's *Solar Dynamics Observatory*). Note that such images are typically in false color, and with non-linear intensity scales to accommodate brightness contrasts. You could go to the [AIA and HMI summary site](#) of the Solar Dynamics observatory (<http://sdowwww.lmsal.com/>), use the [Helioviewer](#) interface (<https://helioviewer.org>) to combine with other instruments and have a longer time base, or explore [cygnet tools](#) at the *iSWA* (Integrated Space Weather Analysis System at the CCMC: <https://iswa.gsfc.nasa.gov>), for example. For the largest contrast, compare inactive phases in 2008-2009 and 2018-2019 to active phases in 2001-2003 and 2013-2014 and also for the rising and falling phases in between. Make a table of the different properties that you notice from magnetic maps and from coronal images for each phase, including at least sunspot prevalence at different latitudes and coronal brightness. /p. 18/

{A8} *Consider* why for a fully-ionized, hydrogen-dominated plasma we see $p = 2nkT$. For the answer, see below Eq. (2.7). /p. 20/

{A9} *Consider:* At the solar surface we see a mean 'molecular mass' of $m \approx 1.3m_p$ while in the fully-ionized corona $m \approx 0.6m_p$ (for proton mass m_p). Explain why. (A hint: see Fig. 2.12.) /p. 20/

{A10} (a) *Show:* Compute scale heights H_p in the Earth's atmosphere for molecular nitrogen (the dominant component) at a range of temperatures, and compare these with the value $H_{p\odot}$ for the atomic hydrogen-dominated gas in the solar photosphere, and for the CO₂-rich atmospheres of Venus and Mars. Use the data in Tables 2.1

and 2.3. (b) Consider how the value of $H_{p\odot}/R_\odot$ contributes to the appearance of the Sun as having a well-defined surface. (c) Also, consider why neutral, atomic hydrogen dominates in the solar photosphere (see Fig. 2.12 for the answer). /p. 20/

{A11} *Show:* One way to quantify the 'strength' of storms in different planetary atmospheres is to compare the dynamic pressure ρv^2 for the maximum surface winds listed in Table 2.1 (which also lists base pressure, temperature, and dominant molecule, from which ρ can be derived). Compare those values with the dynamic pressure in the solar wind using Table 2.4. Note: 1 bar = 10^6 dyne/cm². /p. 20/

{A12} *Show:* The fastest flows (in any direction, not only in the vertical, gravitationally stratified direction) that can be accommodated in a quasi-hydrostatic situation can be estimated from the fact that the gas pressure $p = \zeta nkT$ (with $\zeta = 1$ for a neutral gas and $\zeta = 2$ for a fully ionized hydrogen gas) should well exceed the flow's dynamic pressure ρv^2 . Look at Fig. 2.1 and add the horizontal lines where the two pressure terms are equal for a variety of flow velocities and corresponding temperatures; compare with the conditions discussed later in this chapter for the solar wind. /p. 20/

{A13} Ⓢ *Show:* (a) With the values in Table 2.4, how long do the slow and fast solar-wind streams take to reach Earth? (b) How many degrees does the Sun rotate between the moment these wind streams leave the Sun and the moment they arrive at Earth? (c) How long for Neptune? (d) Given that the wind flows out essentially radially, what is the apparent direction of the wind relative to the direction of the Sun as observed from the orbiting Earth (with an orbital velocity of about 30 km/s)? [Solution in Sect. 17.1] /p. 22/

{A14} *Show:* The momentum balance in Eq. (2.7) describes a radially-flowing wind over a non-rotating Sun. In reality, the Sun is rotating, and the magnetic field reaching into the heliosphere enforces the wind to co-rotate with the Sun, out to a distance where it becomes too weak to enforce such co-rotation (somewhere between 10 to 20 solar radii, or 0.05 to 0.1 AU). (a) Show that for a sufficiently slowly rotating Sun, ignoring the centrifugal force is warranted. (b) At what rotation period of a star like the Sun does the centrifugal force at, say, $2R_\odot$ counteract gravity by more than 10%? The centrifugal force in the wind would have been important for the very young Sun, see Sec. 10.2.1. Moreover, in the early phases of star-disk systems, centrifugal forces may be important in driving a cold wind; see Sect. 7.2.4. /p. 23/

{A15} Ⓢ *Show:* What powers the solar wind in the basic model discussed here? To see the answer, rewrite Eq. (2.7) or Eq. (2.10) to an energy equation (a version of Bernoulli's law) with the terms for the kinetic and potential energy in the Sun's gravitational field, plus a term that reflects the work done by the expanding gas both geometrically and by acceleration; the energy for that expansion in the isothermal approximation is provided by the efficient thermal conduction by the electron population (see Eq. (9.2) and footnote 25.). The real-world solar wind is not isothermal, certainly not far from the Sun (compare the coronal temperatures in Table 2.3 with near-Earth wind properties in Table 2.4), and moreover is provided some additional power (in the form of heating and pressure) by waves and turbulence. [Solution in Sect. 17.2] /p. 23/

{A16} Ⓢ (a) *Show*: Estimate the mean-free path for collisions between electrons in the fast and slow solar wind near Earth based on Tables 2.4 and 18.2. (b) Despite these large numbers, the use of pressure and temperature as defined from Maxwellian velocity distributions is useful in the heliosphere. Discuss how this may come about. [Solution in Sect. 17.3] /p. 24/

{A17} *Background*: Note that there is another class of solutions allowed in principle by Eq. (2.10), namely a 'solar breeze,' although that is incompatible with the outer boundary condition of negligible pressure: starting at low speed and never becoming transonic. Where does a 'solar breeze' reach its maximum velocity? By the way: in principle, Eq. (2.10) allows for an inflow: where v is negative, dv/dr needs to be of opposite sign also. This inflow, accelerating from infinity towards the star, is known as Bondi accretion. However, such inflow is unlikely to occur as an isothermal flow from infinity because the interstellar medium is typically cold, with low ionization and thus low heat conductivity by electrons. Consequently, compression would raise the temperature of the inflow. Moreover, be aware that the quasi-hydrostatic approximation fails for the inner regions of such an infall, starting already well outside the critical point! So, the equation may allow it, but reality does not. /p. 24/

{A18} *Consider*: The fact that concentrations of atomic nitrogen are not shown in Fig. 2.6 should make you wonder given that molecular nitrogen is the most common species in the troposphere. (a) Why is atomic nitrogen rare in the upper atmosphere? Hint: compare the molecular binding energies of nitrogen, oxygen, and water. For example, see the Wikipedia article on [bond-dissociation energy](#). (b) Also calculate the wavelength of a photon needed to dissociate oxygen and nitrogen. (c) What region of the spectrum is that in? /p. 29/

{A19} *Consider*: The concept of optical depth applies to any gas, be it an interstellar medium, a planetary atmosphere, or the solar atmosphere. Optical depth is an integral of absorption along a line of sight, and thus as useful for incoming as for outgoing radiation. (a) Explain why the layers contributing most to the light from the solar photosphere (remind yourself of its definition!) are geometrically higher as you look away from disk center. (b) What can you infer about the stratification of the solar atmosphere from the fact that the Sun (emitting close to black-body radiation over much of the optical spectrum) is brightest near disk center, darkening towards the limb? (c) The solar corona seen in X-rays or extreme ultraviolet (EUV) has essentially double the intensity just outside the solar limb compared to that just inside the limb when there are no active regions along these lines of sight? Why does that imply that the corona is optically thin, *i.e.*, small compared to the typical photon mean free path through it? /p. 30/

{A20} *Show*: You can think of the optical depth as the mean number of absorbers within the cross-section along a photon's path from infinity to height h . The probability of suffering zero absorptions, and thus making it to h , is $\exp(-\tau)$. The intensity at h is then an integral from infinity over the expected number of absorptions along the way. Combine that with Eq. (2.18) to derive Eqs. (2.19) and (2.20). /p. 31/

{A21} Ⓢ *Show:* A similar expression to Eq. (2.20) derived for photons holds for energetic particles (from, say, 1 keV/nucleon to 1 GeV/nucleon) losing their energy when propagating into a relatively dense medium (from the Earth's magnetosphere into its atmosphere, from the solar corona into its chromosphere or photosphere, or from interplanetary space into a spacecraft hull). Typical solar energetic particles in the range of 10–100 MeV can penetrate a medium up to a column density of a few grams per cm^2 (see, *e.g.*, Carron, 2007 on energetic particles passing through matter; it shows that the collisional energy loss rate per unit column density (expressed, for example, as $\text{MeV}/(\text{g}/\text{cm}^2)$) – mainly caused by transfer to bound electrons of the target – for non-relativistic energies scales as $\sim (Z/A)z^2/E$ for a charge z of the energetic particle with kinetic energy E and for an atomic number Z of the target with atomic weight A ; the book can be found online at <https://library.oapen.org/handle/20.500.12657/50879>). Very roughly, estimate how far down that is into Earth's atmosphere, into the Martian atmosphere, into the solar lower atmosphere, and into an aluminum shell of a spacecraft. List all of the values you used and all the assumptions you make (you may have to look some things up on outside sources). Start by making the simplest assumptions: an isothermal stratified atmosphere for Earth, Mars, and the solar photosphere given a characteristic temperature and gravity, and a uniform density for an aluminium shell. Comment on the reasonableness of your answers. (For context, see, *e.g.*, Sects. II:1.6, II:13.4, and II:14.4.) [Solution in Sect. 17.4] /p. 31/

{A22} Ⓢ *Show:* (a) Work through Eqs. (2.22–2.25) to confirm that the effect of the collisions of charged particles in the ionosphere with the neutral thermospheric component is to rotate the net current from the direction of \mathbf{E} at high altitudes towards the negative $\mathbf{E} \times \mathbf{B}$ direction at low altitudes. As the expressions assume \mathbf{B} to be in the z direction, you could chose \mathbf{v} in the x direction to describe a horizontal velocity near the geomagnetic pole. (b) In that same coordinate system, what is the direction of the current at about 125 km in the daytime terrestrial ionosphere where $\sigma_P \approx \sigma_H$ (see, *e.g.*, Fig. I:12.5. Remember: figures from the printed books are accessible at <https://heliophysics.ucar.edu/resources>). [Solution in Sect. 17.5] /p. 34/

{A23} (a) *Look up* what defines a 'sunspot' and what an 'active region'. Are all sunspots associated with active regions? Are all active regions associated with sunspots? (b) A record of sunspot counts over many decades is shown in Fig. 4.5: what is the typical latitudinal range over which sunspots and sunspot groups occur? In Sect. 10.3.2 you will read about high-latitude and even polar starspots on rapidly-rotating, active stars, as the Sun would have been in its first few hundred million years. /p. 36/

{A24} *Show:* (a) Use Table 18.2 to show that Eq. 2.26 yields ion gyroradii r_{gi} for thermal motions if v_{ion} is set to the mean thermal velocity. (b) Then estimate energies of (1) non-thermal particles so that their r_{gi} are comparable to the length-scale of the geomagnetic field for which you can use the Earth's radius (this value is important for the terrestrial ring-current, which is a manifestation of particles drifting across the magnetic field because the heavy, energetic ones sense the gradient in the field strength; see Sect. 3.4) and (2) for perturbations in the heliospheric field for which you could take, say, 0.1 AU (these variations are important for the propagation of solar energetic

particles, see Ch. 8, and for incoming cosmic rays, see Ch. 14). (c) Compare with values in Table 3.4, compare these to mean-free path lengths there, and bear these results in mind going into Ch. 3. /p. 37/

{A25} *Show and Look up:* An intriguing property of dust is that, if the particles are small enough, radiation pressure is important in their momentum equation. Assuming neutral dust particles, estimate at what (density-dependent) size photon pressure from solar illumination exceeds solar gravity (note that this is independent of distance to the Sun for a completely transparent solar wind). There is a surprise here for dust of any size: the orbital motion of the dust causes photon absorption (and assumed isotropic re-radiation of that energy) to lead to a 'brake' on the orbital velocity, causing larger dust particles to spiral inward; look up the '[Poynting-Robertson drag](#)' to see how that works. From this, realize that dust needs to be continually replenished somehow in the Solar System, generally by impact collisions and by disintegrating comets. /p. 37/

Chapter 3. MHD, field lines, and reconnection

{A26} *Look up* magnetic maps of the solar surface (such as made with the HMI instrument on NASA's Solar Dynamics Observatory) and make a movie at an image cadence of a few hours and a duration of one week; you could use [HelioViewer](#) or an [ISWA cygnet](#). Compare one for 2013–2014 (near cycle maximum, with multiple sunspot groups dispersing into the surrounding network of small-scale flux patterns) to 2017–2018 (around cycle minimum, with only the small scales on the disk). Note the changes that you see in the movie and time and length scales of these changes. /p. 39/

{A27} *Background:* Throughout this volume we use 'field line' only for lines of force of the magnetic field. The concept can be applied to any field, however, including a flow field (such as in Fig. 4.10(C), then often referred to as streamlines) and the gravitational field. Field lines of \mathbf{B} and \mathbf{g} are fundamentally different in one key respect: a magnetic field line never ends (because there are no magnetic monopoles) while gravitational field lines start from a point of mass. As to magnetic field lines, note that there are drawings in this book, as in many other resources, where field lines are shown to start from one polarity and end on another. As magnetic field has no monopoles, such drawings should not be misread to mean that field lines end, but only that their rendering in the diagram is incomplete, *i.e.*, merely terminated for simplicity, for lack of information, or to restrict the discussion to a particular region of interest. /p. 40/

{A28} Ⓢ *Show:* This text uses cgs-Gaussian units. In other texts (including many of the chapters of the Heliophysics book series) you will find SI units. Look into conversions from one system to another and transform the momentum and induction equations, Eqs. (3.5) and (3.3), from cgs to SI. [Solution in Sect. 17.6] /p. 44/

{A29} *Show:* Note that $\nabla \cdot \mathbf{B} = 0$ is not needed to complement the MHD equations in Table 3.3 as long as the initial condition satisfies that equation. Take the divergence of Eq. (3.3) to prove that. Use the same operation on $\nabla \times \mathbf{B} = \frac{4\pi}{c} \mathbf{j}$ to show that currents in MHD have no sources or sinks. /p. 44/

{A30} *show:* Use a vector calculus identity and Gauss' law to show that term (1) in

Eq. (3.3) comprises compression, shear, and advection. /p. 47/

{A31} *Background:* The so-called 'Boussinesq approximation' is intermediate to fully compressible and incompressible, and in principle internally inconsistent: it assumes a fluid for which (and in numerical codes replaces Eq. (3.4) by) $\nabla \cdot \mathbf{v} = \mathbf{0}$ but allows density variations in the term in the force balance that includes gravity (and thus allows for buoyancy). This approximation works well if the flow can be characterized as 'nearly incompressible'. For settings where the scale of the density stratification is large compared to processes of interest the incompressible approximation can be valid; in such settings, compressibility becomes only important in structures like shock waves, but is ignorable if the flows are much slower than the sound and Alfvén speeds. Advanced, for the curious: In planetary atmospheric envelopes and stellar interiors alike, zones of relatively low temperature under relatively strong gravity are highly stratified compared to the scales of flows within them. In such settings, numerical codes have been developed under the 'anelastic' approximation. This approximation provides a better description of the density in stratified settings than the pure Boussinesq one while filtering out sound waves that would require much higher spatio-temporal resolution of the code. [This article by Durran and Arakawa \(2007\)](#) introduces and compares several 'anelastic' approximations. /p. 47/

{A32} *Show:* Formulate the ion equivalent of Eq. (3.9) (remember Newton's third law, and with $m_e/m_i \rightarrow 0$) and derive Eq. (3.11) (using $m_e \mathbf{v}_i + m_i \mathbf{v}_e = m_i \mathbf{v}_i + m_e \mathbf{v}_e + m_i[\mathbf{v}_e - \mathbf{v}_i] + m_e[\mathbf{v}_i - \mathbf{v}_e]$) and also the corresponding momentum equation (absent gravity): $\rho d\mathbf{v}/dt = \mathbf{j} \times \mathbf{B} - \nabla p$. Then add gravity and compare to Eq. (3.5). /p. 49/

{A33} *Show,* for a fully-ionized single-species plasma, the equivalence of Eq. (3.11) and $\mathbf{j} = \Sigma_e \cdot (\mathbf{E} + \frac{1}{c} \mathbf{v} \times \mathbf{B})$ with Eqs. (2.22)-(2.25). /p. 49/

{A34} *Show:* (a) Look back at Fig. 2.1 and review the ranges shown of the value of the plasma β from Eq. (3.24) to get a feel for where plasma pressure gradients might dominate magnetic pressure gradients or vice versa. (b) Add lines (on a printed version, using a pdf editor, or a hand-drawn version) for unit plasma β for field strengths of 1 μG (as found in the outer heliosphere and interstellar medium; see Chs. 5 and 10) and for 0.1 MG (considered characteristic of the field strength of flux bundles at the bottom of the solar convective envelope where the principal processes in the solar dynamo are considered to operate; see Ch. 4). /p. 51/

{A35} \textcircled{S} *Show:* (a) Take the momentum equation of Eq. 3.5 – for a stationary state of the solar wind, ignoring viscosity, sources, and sinks – to assess the usefulness of the plasma β (Eq. 3.24, and Table 18.2). (b) Estimate β for the solar wind (1) near Earth for the slow and fast solar wind as in Table 2.4 (use the electron temperatures) and (2) around $10R_\odot$ (roughly the closest approach of the Solar Orbiter; use a temperature of 1 MK there). For (2), assume a radial field and a radial flow (which is not too bad within Earth's orbit for these rough estimates, see Section 5.4). (c) Use the same momentum equation as above to show that the ratio of dynamic (or ram) pressure to magnetic pressure also arises naturally (to which we return for the magnetopause standoff distance). (d) The simplest Parker solar wind model as discussed in Section 2.2

ignores the magnetic field; where is that appropriate in the Parker model? [Solution in Sect. 17.7] /p. 51/

{A36} *Show:* Compare values for c_s and v_A for the environments listed in Table 3.4. You may approximate $\gamma \approx 1$ and so use Eq. (2.5); also use Eq. (3.30); assume a hydrogen-dominated, fully-ionized plasma for all settings in the table. Use km/s. Note that magnetic perturbations are faster in all settings except in the solar interior; equivalently, magnetic forces are more likely to dominate in all settings except in the solar interior where hydrodynamic forces dominate because (show this:) $\beta \sim c_s^2/v_A^2$. /p. 53/

{A37} Ⓢ *Show:* In solar physics, the simple concept of flux tubes are commonly used as an approximation of the state of the magnetic field in near-photospheric layers: embedded in a field-free atmosphere is a bundle of field separated from its surroundings by a thin current envelope. (a) Assuming an ideal plasma without flows, show that the atmosphere within a thin flux tube (*i.e.*, one that is small compared to the scale of variations of condition along the tube) is in hydrostatic equilibrium regardless of the path of the flux tube through the atmosphere. (b) Show how pressure balance (incorporating both gas and magnetic components) determines the cross section of the tube. [Solution in Sect. 17.8] /p. 56/

{A38} *Show:* (a) Make comparisons of energy densities for the solar wind as in Sec. 3.5.2 at other bodies in the Solar System (using Table 5.2). Why comparisons of energy densities in planetary magnetic fields (Table 5.2) and in the surrounding solar wind are informative is discussed in Ch. 5. (b) Why would you expect the flow energy density and the magnetic field energy density to be comparable at only a few solar radii from the Sun? /p. 62/

Chapter 4. Dynamos of Sun-like stars and Earth-like planets

{A39} *Advanced/Group:* The transition from radiative diffusion to convective enthalpy transport in the deep convective envelope is gradual: the fraction of total energy carried as a diffusive radiative flux gradually drops while that of the enthalpy flux (total heat content: internal energy plus work term) smoothly increases, making convection the dominant transport about 35,000 km above the bottom of the convective envelope, or roughly after a single pressure scale height (see Sect. 4.3). (a) Can you think of other terms that would be involved in the energy transport equation in a stellar convective envelope? A fair idea of the answer, along with a quantitative comparison of the relative importance of the processes involved in carrying energy through the convective envelope, can be found, for example, in [this analysis by Brun *et al.* \(2004\)](#), in particular their Fig. 3 (note that they show transport by convection that is resolved by their model and by (parameterized) unresolved – ‘subgrid-scale’ – convection). (b) Argue why the dominant energy transport shifts from radiative, via large-scale enthalpy, to ‘unresolved eddy flux’ going outward. /p. 64/

{A40} *Show:* Figure 4.2 is a brightness-color diagram (known as a Hertzsprung-Russell, or

HR, diagram) using typical astronomical units: absolute visual magnitude M_V , which is a logarithmic measure of stellar brightness, and spectral color $B - V$, which is the logarithm of the ratio of two brightnesses measured in different color bands (often using logarithmic brightness B and V , or less commonly R for blue, visual, and red). The table in that figure maps spectral type (see footnote 8), $B - V$, effective temperature T_{eff} and a correction factor BC that relates visual and bolometric brightnesses (see equations below that table). Using this information, estimate stellar radii R_* for Sirius A, ϵ Eri, 61 Cyg A, and AD Leo, realizing that $L_* = (\sigma T_{\text{eff}}^4)(4\pi R_*^2)$, with the Stefan-Boltzmann constant $\sigma = 5.7 \times 10^{-5} \text{ erg/cm}^2/\text{sec/deg}^4$. Sketch a double-logarithmic L - T_{eff} version of the HR diagram and draw lines of constant radius in it. Then compare that to Fig. 10.1. /p. 64/

{A41} *Look up:* (a) How is the Sun's magnetic field observed? Look up the effects on photons propagating through a plasma threaded by a magnetic field. This results in the 'Zeeman effect' of line splitting and of circular and linear polarization. For relatively weak field or relatively low wavelengths, the Zeeman splitting of 'magnetically sensitive' spectral lines is generally less than the thermal line width (and less than the Doppler width for rapidly rotating stars), so that what is in principle line splitting for individual atoms becomes line broadening when averaging over populations of atoms and over entire stellar disks. (b) Estimate at what field strength B_Δ (G) the Zeeman splitting $\Delta\lambda_B$ (\AA) equals the thermal line broadening; use $\Delta\lambda_B = 4.7 \times 10^{-13} g\lambda^2 B$, assuming a Landé factor $g = 2$, $\lambda = 5000 \text{ \AA}$, and using a thermal line broadening associated with the thermal velocity for iron atoms. Note that B_Δ is inversely proportional to λ . /p. 69/

{A42} *Look up:* Compare a series of solar magnetograms over the past ~ 22 years (using, e.g., *SOHO/MDI* and – since mid-2010 – *SDO/HMI* observations, which can be accessed with, e.g., helioviewer.org, the JHelioviewer app, or at iswa.gsfc.nasa.gov; a sampling of once per Carrington rotation suffices). How do the magnetic patterns change over time in terms of overall activity, latitudinal distribution, polarity patterns on the northern versus southern hemisphere, ...? /p. 69/

{A43} *Show:* Work through how Eq. (4.1) is obtained by taking the dot product of Eq. (3.3) with \mathbf{B} , integrating over the total volume of the system, and assuming no Poynting flux or currents (or at most only a force-free field) leave the volume. Use vector identities ($\mathbf{a} \cdot (\nabla \times \mathbf{b}) = (\nabla \times \mathbf{a}) \cdot \mathbf{b} - \nabla \cdot (\mathbf{a} \times \mathbf{b})$, $\mathbf{a} \cdot (\mathbf{b} \times \mathbf{c}) = \mathbf{b} \cdot (\mathbf{c} \times \mathbf{a})$), Eq. (3.2), and Gauss's theorem. Note that there is a summary of vector calculus identities in Table 18.3 and more on [vector calculus identities](#) on Wikipedia. /p. 72/

{A44} *Look up* sample images of solar granulation, the most easily detectable pattern of convection reaching into the solar surface layers. What are the characteristic length and time scales of granulation? Also look up the larger-scale flow patterns of mesogranulation and supergranulation, and compare these in a table. /p. 73/

{A45} *Show:* Estimate the time it takes for the solar equator to execute one more full rotation than the poles in the same time. Use the data shown in Fig. 4.7b. /p. 74/

{A46} *Background:* Helioseismology uses resonant waves that run through the solar

interior. These pressure-mode (or p mode) waves (generated by the turbulent convective motions) probe a range of depths depending on the wavelength and resonance conditions. At depth, downward traveling waves refract upward as the sound speed increases with temperature. If their frequency is below the 'acoustic cutoff period' around the photosphere upward traveling waves are reflected back into the interior, even as they are detectable around their upper turning point both in brightness (by compression and dilation) and velocity (through the Doppler effect on spectral lines). The combination of refraction and reflection leads to a cavity in which resonances occur. Intuitively, the cutoff frequency comes about because if the wavelength of a pressure wave exceeds a few pressure scale heights, there is essentially no restoring pressure force as the bulk of the atmospheric mass is simply lifted and lowered in response to the wave so that the solar surface acts as an open boundary condition and reflects the wave. Based on that argument, make a rough estimate of the acoustic cutoff period for the solar photosphere at around 5800 K (a later Activity will let you develop the relevant equations for an isothermal atmosphere). Waves with shorter periods continue to travel upward, while those with longer periods mostly reflect but partly tunnel through into the hotter chromosphere. /p. 74/

{A47} *Background:* To hear how helioseismology can measure rotation rates of stars (and, with enough different modes, of layers within stars) you can do the following experiment: Hold up a bell dangling from a string, strike it, and listen. Then twist up the string, let the bell spin freely, hit it and listen once more. The modulation in intensity that you hear for the spinning bell results from the beat of the Doppler effect working differentially on waves running with and against the spin direction. This is the essence of how helioseismology measures the Sun's internal rotation. /p. 74/

{A48} *Show:* Compare the Rossby number for deep solar convection to that of the Earth's core for a flow velocity of order 1 mm/s and for a scale equal to the core radius or shell thickness. /p. 75/

{A49} *Show:* If we take the Sun's polar field – averaging at cycle minimum to be about 5 Gauss – how long would it take to wind that field into a strength of some 10^5 G – which is the estimated minimum field strength for flux bundles to coherently survive their rise through the convective motions in the Sun's envelope to emerge as active regions – if the rotational shear were maximally used and if no back-reaction on that flow occurred? Hint: remember the field line stretch-and-fold from Fig. 4.6, look at the illustration in Fig. 4.9, remember that field line density is equivalent to characteristic field strength, use the result from Act. 45, and consider 'compound interest.' /p. 75/

{A50} *Background:* Consider that the assumption of a separation of scales as for the 'mean field dynamo theory' is also made in hydrodynamics when 'internal energy' (which includes the kinetic energy of the random motions of the gas particles) is 'separated from' the 'kinetic energy' of bulk motion. This assumption is commonly made with little consideration of why it works: there must be a scale that is small compared to flows of interest but large enough that low-order moments of the velocity distribution (like temperature and pressure) are defined by so many particles that there is negligible

random noise when determined for a 'small' volume. Consider that in the context of the words in Table 3.2. /p. 77/

{A51} Ⓢ *Show:* (a) Take the mean-field induction equation Eq. (4.12) and the expression for Eq. (4.13) as approximated in Eq. (4.15) to find a mean-field form of the general induction equation Eq. (3.3). Group the 'diffusive' (η , β) terms together. (b) Using the values for the solar meridional flow and random-walk diffusive dispersal below, estimate the order of magnitude of the advection, α , and diffusive terms. For these order of magnitude comparisons, approximate for the mean field $\nabla \approx 1/R_{\odot}$; in solar near-surface layers 'small-scale' supergranular random walk with \mathbf{v}' or order 0.1 km/s leads to $\beta \approx 300 \text{ km}^2/\text{s}$; the large-scale advective term of the surface meridional flow has an average value of order $\bar{v} = 5 \text{ m/s}$ (reaching a mid-latitude maximum of about 15 m/s); estimate τ_{corr} from this value of β with Eq. (4.16), which corresponds to the characteristic evolutionary time scale of the dispersing supergranular convection; with that, estimate α using the characteristic supergranulation length scale of 30,000 km; then compare the order-of-magnitude values of the three terms expressed as time scales for the magnetic field. Note that the 'turbulent diffusivity' β far exceeds the 'resistive diffusivity' η in stellar dynamos (and see Activity 53 how the above helps in understanding how surface flux dispersal can be described quite well by a random-walk diffusive description). [Solution in Sect. 17.9] /p. 79/

{A52} *Show:* Relate the Rossby number in Eq. (4.2) to the dynamo number C_{Ω} and the magnetic Reynolds number \mathcal{R}_m in Eq. 4.20: $N_R = \mathcal{R}_m/C_{\Omega}$. /p. 79/

{A53} Ⓢ *Show:* One of the basic concepts behind Babcock's idea is that magnetic field at the solar surface is largely advected like a scalar quantity. Consequently, the field disperses in the random motions of the surface convection (with an equivalent diffusion coefficient of $D \approx 250 \text{ km}^2/\text{s}$) subject to the large-scale advection of the differential rotation and meridional flow. (a) To see how this can be, use the 'ideal' version of Eq. (3.3) (which ignores resistivity) and assume that the field is always vertical to the surface (a good approximation to the observed photospheric field, except during emergence and cancellation; a result of the buoyancy of flux bundles – see Activity (37) – and show that it has the same properties as Eq. (3.4) for the advection of a scalar (without the source and loss terms in that version). Note that this formulation is linear, so that you can think about N and S polarities as diffusing separately, and can sum these results to obtain the net result; this helps visualize why the active-region tilt angle is important in reversing the polar fields from cycle to cycle. (b) Question: with this value of D , what is the characteristic time scale for flux to disperse over the solar surface (hint: Eq. 3.20)? (c) With that in mind, how important is the meridional advection from equator to pole (with a characteristic velocity of 10 m/s) in transporting the field within the duration of a solar cycle? Remember that Activity 51 shows how the diffusion coefficient β associated with (super-)granular random walk adds to the molecular/resistive diffusion coefficient η . [Solution in Sect. 17.10] /p. 86/

{A54} *Show:* Joy's rule, that the leading polarities (in the direction of rotation) of active regions emerge statistically closer to the equator than the trailing polarities (see Fig. 4.4,

for example), is the reason why eventually flux of the trailing polarity builds up a polar cap that reaches its maximum strength at cycle minimum. For some interval around that time, the bulk of the heliospheric field originates from the polar caps. Estimate the total flux in the solar wind (assuming an isotropic flux density at Earth orbit; use Table 2.4); what is the corresponding magnetic flux density averaged over the solar surface? This total flux is the equivalent of only a few large active regions (Fig. 4.4) although it is in fact composed of a fraction of the flux from the ensemble of all bipolar regions emerging over a cycle. /p. 86/

{A55} *Consider:* (a) Why are solar photospheric flux tubes buoyant (hint: look back at Activity (37)? What is the maximum density contrast between interior and exterior for a 1 kG flux tube? (b) For an essentially zero-density flux tube at the solar surface, show that the buoyancy force per unit length (causing the tube to buoy towards vertical) dominates the dynamic pressure force exerted by a convective flow (which could bend the tube away from vertical) of $v = 1$ km/s for any tube with diameter $2a$ exceeding just a few km. Indeed, observations show flux tubes to be essentially vertical to the photosphere (except around emergence and collisional cancellation when magnetic curvature forces of the field arching from one polarity to the opposite one are strong). /p. 86/

{A56} *Advanced/Group:* Further study: [The work by Lemerle and Charbonneau \(2017\)](#) describes an interesting dynamo experiment in which the Babcock-Leighton concept is combined with surface flux transport modeling (see Activity 53) to create a quasi-regular dynamo in which convection-induced fluctuations on the tilt angle of emerging active regions (perturbations on Joy's rule, see Activity 54) provide the stochastic noise that can lead to cycle-to-cycle differences and even extended periods of weak cycling (as in the Maunder Minimum period for the Sun), something also reported on in [a paper by Karak and Miesch \(2017\)](#). /p. 87/

{A57} *Look up:* Make a summary of the essential distinctions between the dynamo concepts discussed up to this point: $\alpha\Omega$ (with or without α quenching, which itself can be strong/catastrophic or not); interface; flux-transport; and Babcock-Leighton. /p. 87/

{A58} *Background:* The dynamo model in Fig. 4.13 is characterized by five dimensionless numbers. Two, the magnetic Reynolds number and the Rossby number, are defined in Eqs. (3.18) and (4.2), respectively. Look up the meaning of the other three: Ekman, magnetic Prandtl, and Rayleigh. These three are important numbers when computing the flows and their coupling, but not encountered until this Figure in this text because the solar dynamo models that were discussed and shown in the figures are kinematic, relying on a given, not consistently computed, flow pattern. The dynamo model behind Fig. 4.13, in contrast, computes flow, field, and their interaction, and thus also needs these remaining three dimensionless numbers specified. /p. 92/

{A59} *Look up:* Summarize the contrast between the dynamo of a terrestrial planet with that of stars as discussed in this Ch. 4: consider, among others, flow speed, rotation period, stratification, differential rotation, meridional advection, and Rossby

and magnetic Reynolds numbers. /p. 93/

Chapter 5. Flows, shocks, obstacles, and currents

{A60} *Advanced/Group:* To build a comparison of the different conditions, keep pen(cil) and paper at hand to sketch the various configurations as you read about how flows interact with bodies in the planetary system. Working in a reference frame in which the body is at rest, assume a spherical object, and let a flow move past it from left to right. Then prepare to make drawings in two orthogonal planes: the first plane is defined by the flow vector and the magnetic field carried in the flow (you may assume the field to be normal to the flow), while the second plane is normal to the first. Draw streamlines of the flow and subsequently add magnetic field lines. If you are good at 3-D renderings, also try a visualization such as in Fig. 5.11. /p. 97/

{A61} *Show:* Write the Eqs. (5.2) and (5.8)–(5.12) for the hydrodynamic limit, and derive the temperature ratio between the post- and pre-shock media. You should find that the density contrast $r_\rho = ((\gamma + 1)M_s^2)/(2 + (\gamma - 1)M_s^2)$ and the pressure ratio $r_p = (2\gamma M_s^2 - (\gamma - 1))/(\gamma + 1)$ where $M_s = v_1/c_{s1}$ for sound speed c_s . Note there is a maximum value for r_ρ but not for r_p as function of M_s . What are the values for r_ρ and r_p for $\gamma = 5/3$ for M_s near unity and for $M_s \gg 1$? /p. 102/

{A62} *Show:* At what distance from the Sun does the solar-wind model discussed in Sect. 5.4 have $|B_r| = |B_\phi|$ for typical values of the slow and fast solar wind? What are typical values for B_ϕ/B_r at 1 AU, 5 AU (*cf.* Fig. 5.9), and at the ice giants? /p. 106/

{A63} *Show:* Compare the relative radial dependence of the magnetic fields in the solar wind model of Sect. 5.4 with the values listed in Table 5.2. Also: use these scalings to demonstrate that the plasma β tends to a constant value far from the Sun. You may assume the temperature of the solar wind to be essentially constant compared to the changes in distance and density. /p. 106/

{A64} Ⓢ *Show:* The solar wind stretches the high-coronal magnetic field into the heliosphere into a roughly radial field below the Alfvén radius. This enables an analogy with electrostatics: the field of electric charges placed above a flat perfect conductor can be computed by placing mirror charges opposite to the conducting surface, which then naturally has the electric field perfectly normal to the conducting surface. Analogously, in a magneto-static consideration above the spherical Sun (of unit radius) called the potential-field source-surface (or PFSS) model, the magnetic field can be approximated by placing mirror 'charges' on a sphere at distance d_{SS}^2 which then has the field perfectly radial at d_{SS} . Empirically, $d_{SS} \approx 2.5$ (where that 'source surface' is taken as the foundation of the heliospheric field; the virtual surface with mirror charges used to compute the potential field below d_{SS} is then at d_{SS}^2). This model (introduced by Schatten *et al.* (1969)) works remarkably well below d_{SS} on large scales. The heliospheric field is approximated by a continuation from that source surface, subject to the Parker spiral.

(a) For illustration, simplify the source-surface model by a 2-d sketch of a potential field involving charges (of alternating polarity: N-S-N-S-N-S) placed on a straight line

and another line parallel to it involving mirror charges of opposite polarity. Sketch the equivalent of the foundation of the heliospheric current sheet and examples of 'closed' field lines (the equivalent of coronal loops closing back onto the solar surface) and 'open' field lines (the equivalent of field stretched out into the heliosphere), at the base of which we find dark 'coronal holes' in X-ray images of the Sun. Consider how the X-points that form on the midpoints between these lines are like the 'helmet streamers' seen in coronagraphs and during eclipses.

(b) For a sphere, show that the mirror charges on the surface at d_{SS}^2 are $-d_{\text{SS}}$ times the strength of those on the solar surface. [Solution in Sect. 17.11] /p. 107/

{A65} *Show:* In case you wonder how much solar-wind material actually hits, say, the lunar surface, estimate the mass flux density per unit area over a time interval Δt , with ion density $n_{\text{sw}} \approx 10 \text{ cm}^{-3}$ and $v_{\text{sw}} \approx 500 \text{ km/s}$ at Earth (and Moon), ignoring long-term change. Express that in units of $\text{mg/cm}^2/\text{Myr}$. /p. 112/

{A66} Ⓢ *Show:* For the solar wind flowing onto a non-conducting, non-magnetized sphere, use estimates of wave speeds to sketch the density wake, the slow-mode refilling, and the fast-mode rarefaction front in a plane defined by the flow vector and the field vector, and in a plane defined by the flow vector and perpendicular to the field; assume the field vector to be perpendicular to the flow vector. You may compare the result with measurements for the case of the Moon (in Fig. IV:10.7). [Solution in Sect. 17.12] /p. 112/

{A67} *Background:* On the largest scales, there may be a long magnetotail to the entire heliosphere, that may even be oblate because of the tension force of the interstellar magnetic field. Although alternative views propose a much shorter tail, making the heliosphere more like a bubble, it is illustrative to see how such a moderate flattening by the interstellar magnetic field might work. Have a look at, *e.g.*, [McComas et al. \(2013\)](#), in particular their Figure 9. /p. 114/

{A68} *Show:* Use Eqs. (5.2) and (5.8-5.12) to calculate that in the case of a strong shock (in which the thermal energy of the solar wind upstream of the bow shock can be ignored) the temperature just downwind of the bow shock is given by $(3m_{\text{p}}/32k)v_{\text{sw}}^2$ for a wind speed of v_{sw} , and that the density contrast across the shock is a factor of 4 (show that is true anywhere along the shock). Use this to estimate the angle from the upwind direction out to which the flow remains supersonic just inside the shock front (remembering that the transverse component of the velocity is unaffected by the shock). /p. 117/

{A69} Ⓢ *Show:* What is the expression for the temperature of the gas at the stagnation point on the magnetopause assuming that the flow continues adiabatically after the shock (*i.e.*, that it conserves the sum of bulk kinetic and thermal energies)? Calculate that temperature for $v_{\text{sw}} = 800 \text{ km/s}$. [Solution in Sect. 17.13] /p. 118/

{A70} Ⓢ *Show:* (a) Use Eq. (5.22) to calculate the scaling of R_{CF} with orbital radius (in AU), planetary magnetic field at the surface, and planetary radius. For Earth and the giant planets, estimate for each of the planets the model-based magnetopause distance R_{CF} setting $\xi = 2$. Assume the following: that the solar wind speed averages to roughly

the same value at all the planets (say $v_{\text{sw}} = 400 \text{ km/s}$). Use info in Tables 5.2 and 5.3. (b) For Earth and Saturn, compare R_{CF} to the orbital radii of Moon, Enceladus and Titan. [Solution in Sect. 17.14] /p. 118/

{A71} *Show:* With the fastest recorded solar-wind gusts at $v_{\text{sw}} \approx 2500 \text{ km/s}$, calculate the required plasma density to push the magnetopause to within geosynchronous orbit according to Eq. (5.22)? /p. 118/

{A72} *Background:* Illustrative diagrams like Fig. 5.14 typically show the interplanetary magnetic field (IMF) as lying within the $x - z$ plane of such diagrams. In reality, the three IMF components $B_{x,y,z}$ are typically of comparable magnitude. Because of the relative tilt of the rotation and magnetic dipole axes relative to the Earth's orbital plane, the orientation of the Earth's magnetic axis relative to the incoming wind changes in the course of the year. Consider how the diagrams should look when drawn in three dimensions for a few different combinations of $B_{x,y,z}$. Look up the 'Russell-McPherron effect' which attributes the semi-annual variations in geomagnetic activity largely to the relative orientation of the Earth's dipole axis: maximum geomagnetic activity around the equinoxes, minimum around solstices. *Advanced/Group:* Try sketching a version of Fig. 5.14 under these other circumstances. Consider where the reconnection points are and the shape of the separatrix. Keep in mind that the $x - z$ cut may not be the best plane to use. /p. 119/

{A73} *Show:* Use the equation for a dipole field to show that the ratio of maximum to minimum field strength on a sphere equals 2. Look up the oblateness of Jupiter and Saturn and see if it accounts for the ratio of minimum to maximum surface field in Table 5.3. Interpret your finding. /p. 119/

{A74} *Advanced/group:* Make a list of the similarities and differences between 'corotation' in a planetary magnetosphere and in the solar wind, and consider the four conditions for corotation and how they compare to conditions in the solar wind. Include (a) the absence of a sufficiently neutral atmosphere in the Sun to decouple the motions between internal and heliospheric fields (associated with a concept called 'line tying', which we touch upon in Sec. 6.3.1), and (b) the very term 'corotation' which to a heliospheric physicist does *not* include the component of $\mathbf{v} \parallel \mathbf{B}$ but is limited to the pattern of the field, not the plasma itself. /p. 125/

{A75} *Advanced/Group:* Consider the possible equivalent of a Dungey cycle for the heliospheric field subject to reconnection with an interstellar magnetic field. Think about the effect of the super-Alfvénic stellar wind. What would things look like in case there were no coronal heating? Consider the Sun's global dipole and how that would then interact with the incoming interstellar medium. /p. 127/

{A76} *Advanced/Group: What if? A discussion activity:* Many so-called 'hot Jupiters' have been found among the exoplanet population: giant planets that orbit very close to their parent stars. What would the estimated magnetopause distance $R_{\text{CF,hJ}}$ be if Jupiter were orbiting the present-day Sun at 0.05 AU? For a younger Sun (see Ch. 12) the solar wind would have been stronger, pushing $R_{\text{CF,hJ}}$ to below the orbital radius of Ganymede; describe what that would mean for this 'hot-Ganymede' moon? /p. 127/

{A77} *Background:* Advanced, for the curious: Things get more complicated when objects are smaller than the gyration radii of particles in the flow, or when ionization processes occur when neutral particles from an 'atmosphere' move into an approaching flow, or both. If you are interested in seeing how these complications play out, have a look at this study of comet 67P by Behar *et al.* (2017) using observations by the Rosetta spacecraft. /p. 127/

Chapter 6. Magnetic (in-)stability and energy pathways

{A78} *Consider* how a non-potential state can arise or be strengthened in the solar atmosphere and in a magnetosphere, including the roles of plasma motions and induction. Eq. (3.3) and 3.5 provide the mathematical basis; Eq. (4.1) is illustrative for the overall energy budget. /p. 130/

{A79} *Look up:* The processes of electromagnetic radiation from a plasma involve three fundamentally distinct processes: bound-bound (i.e., electron transitions from an excited state to a lower-energy state), free-bound (radiative recombination), and free-free (Bremsstrahlung) emission. Aurorae and flare ribbons are caused by collisions of downward-propagating, energetic charged particles with the atmosphere below. Aurorae observed from the ground include both free-bound and bound-bound emission from ions and molecules, respectively (there is X-ray emission, too, but that does not penetrate to ground level). Look up which ions and molecules dominate (and at which color(s)) in the terrestrial aurora, and which emission processes are involved with these. See also Activity 119 for the contrast with solar coronal emission. /p. 130/

{A80} *Show:* The average speed of a CME between Sun and Earth is close to 500 km/s while the fastest have speeds exceeding 3000 km/s. (a) How long are the transit times from Sun to Earth? Compare the average and peak CME speeds to typical wind speeds (Table 2.4). (b) Describe qualitatively what happens in the interaction with slow and fast wind streams for average CMEs and for the fastest CMEs. (c) Draw a sketch or cartoon to accompany your description. /p. 130/

{A81} *Background:* The phenomena discussed in Ch. 6 are all part of what is referred to as space weather. To explore how aspects of space weather are quantified review the NOAA webpage <https://www.swpc.noaa.gov/noaa-scales-explanation> that lists the types of 'storms,' their potential effects, and their approximate frequency within a solar cycle. Make a table of the types of measurements you would need to have awareness of these different storms; include in that table the different spacecraft and instruments that could be used. N.B. For current space weather conditions, forecasts, and more see [the website](https://www.swpc.noaa.gov) of the Space Weather Prediction Center: <https://www.swpc.noaa.gov>. /p. 130/

{A82} (a) *Look up* locations and properties of the Earth's (1) electron and proton radiation belts, (2) ring current, and (3) plasma sheet. Create a table containing their locations, characteristic particle energies, and their densities. (b) What is the typical energy density for each population? /p. 136/

{A83} *Show:* The energy processed by the magnetosphere during a magnetic storm is of

order $E_{\text{storm}} = 5 \times 10^{23} - 5 \times 10^{24}$ erg from moderate storm to superstorm. Compare that to an order of magnitude estimate of the energy $E_{\text{mag},\oplus}$ contained in the geomagnetic field (by, say, using a scale of $3R_{\oplus}$ and a characteristic field strength of 0.1 G) and with the incoming total energy E_{sw} of the solar wind during the storm period (with typical conditions for the fast solar wind and an active cross section of πR_{CF}^2 , and a storm duration of 1-10 h). What are the values of $E_{\text{storm}}/E_{\text{mag},\oplus}$ and $E_{\text{storm}}/E_{\text{sw}}$? Compare these values to solar equivalents when you reach Activity 87. /p. 141/

{A84} *Show:* 'Chromospheric evaporation' is a misnomer because there is no phase transition involved: the heating of chromospheric material from $\approx 10^4$ K to of order $\approx 5 \times 10^6$ K causes the pressure and the associated pressure scale height to increase. What are the pre-heating and post-expansion scale heights for the above temperatures? (Look back at Sect. 2.2.) What assumptions did you make when doing the calculation? How do these compare to the solar radius? /p. 151/

{A85} Ⓢ *Show:* (a) For a given temperature, why does the coronal soft X-ray brightness scale essentially with the square of the particle density? (b) Let a given coronal loop have an initial loop-top density n_0 at temperature T_0 and let an impulsive heating event change these to n_1 and T_1 . With $T_{0,1}$ within the range of about 0.4–30 MK the radiative losses scale as $P(T) \propto T^{-2/3}$. If the temperature changes from 1 MK to 5 MK and the density increases by a factor of 25, show that the ratio of radiative cooling time scales is not too different from unity. Time scales for conductive losses exhibit a somewhat larger ratio; why? [Solution in Sect. 17.15] /p. 151/

{A86} (a) *Consider:* Describe what is seen in Fig. 6.14: how can a CME be imaged, and why is that best done from space, or from a very high mountain top? (b) Argue why the CME in this image is not likely to envelop Earth. (c) What would an Earth-bound CME look like? (d) Can you differentiate that from one moving in the opposite direction? /p. 154/

{A87} *Show:* The energy processed during a strong to intense solar flare and CME is of order $E_{\text{flare}} = 10^{30} - 10^{33}$ erg. (a) Compare that to an order of magnitude estimate of the energy $E_{\text{AR},\odot}$ contained in the field of an active-region core (by, say, using a scale of 30,000 km and a characteristic average magnetic flux density of 300 G).)b) What is the value of $E_{\text{flare}}/E_{\text{AR},\odot}$? (c) How does this compare to $E_{\text{storm}}/E_{\text{mag},\oplus}$ and $E_{\text{storm}}/E_{\text{sw}}$ in Activity 83? /p. 154/

{A88} *Show:* One phenomenon associated with many CMEs is a so-called 'coronal dimming', in which a large fraction of the quiet-Sun solar corona fades for some time. Think about the potential causes: temperature change (so the signal moves from one bandpass to another), quasi-adiabatic expansion of the coronal field, and entrainment of coronal plasma in the erupting CME. Estimate the fraction of the volume of entire quiet-Sun corona (at a density of some 10^7 cm^{-3}) that would need to be involved if it were to move out with an erupting field configuration if that made up, say, 25% of the erupting mass of, for example, 10^{15} g. /p. 154/

{A89} *Look up:* For a sense of scale: how many nuclear bombs are needed to match the energy released in a large solar flare of 10^{32} erg? /p. 154/

{A90} *Advanced/Group*: Advances in numerical capabilities are making a big difference in understanding magnetic instabilities, how and where associated plasma heating occurs, and how combinations of plasma flows and a variety of temperatures in plasmas along a line of sight through the optically thin corona lead to observables. Such work shows how apparently non-thermal signatures in spectra can emerge from line-of-sight integration through thermal plasmas. If you would like to learn more about how observables based on numerical work help guide the interpretation of real-world observables, a paper (with illuminating graphics) by Cheung *et al.* (2019) provides a good example. /p. 154/

Chapter 7. Torques and tides

{A91} *Look up* what T Tauri stars are, and what differentiates the 'classical' T Tauri star from the 'weak-line' variant. List a few primary properties of T Tauri stars. /p. 160/

{A92} Ⓢ *Show*: Verify the numbers in the conclusions about stellar magnetic braking for the present-day Sun at the end of Sect. 7.2.1. [Solution in Sect. 17.16] /p. 162/

{A93} *Show*: For comparison: what is the approximate ratio of forces exerted on the Earth of the total solar irradiance onto the Earth's surface to the solar-wind pressure on the magnetopause? In your estimate, ignore reflection by and radiation from Earth's atmosphere, use an approximate Chapman-Ferraro radius for the cross section of the magnetosphere interacting with the solar wind, and maximize the solar wind pressure by ignoring the term involving v_2 in Eq. (7.3). This exercise shows why solar sails are designed for photon pressure rather than solar-wind dynamic pressure (note that some are designed to couple to induced electromagnetic effects, not dynamic pressure). /p. 162/

{A94} Ⓢ *Show*: (a) Looking only at gravitational forces, how close to a solar-mass object would the Earth need to be to be pulled apart by tides? Whereas this is impossible with the Sun, an Earth-sized planet could be pulled apart if it approached a white dwarf or neutron star (and something like that is involved in 'contaminating' some white-dwarf atmospheres with heavy elements). (b) An object of lesser density can be pulled apart, however, during a sufficiently close approach to the Sun: estimate at what distance comet 67P (with a mass of about 10^{16} g and characteristic dimension of 3 km) would have to come to the Sun to be broken up (ignore tensile strengths, spin, and orbital forces, thus accounting only for gravitational forces to hold the object together). Some Sun-grazing comets (such as the Kreutz family) have been observed to go through this breakup process. [Solution in Sect. 17.17] /p. 168/

{A95} *Consider* what it means for solar eclipses that the Moon is moving away from the Earth: at some future time, the Moon will be so far away that no more total solar eclipses can occur anywhere on Earth. (a) Assuming the Moon continues to move away at 4 cm/yr, roughly when will the last total solar eclipse occur? Confirm that the answer is somewhat more than 600 million years. (b) Describe the effect on lunar eclipses. /p. 169/

{A96} *Show*: One of the ways in which exoplanets are detected is to look spectroscopically at the displacements of the star about the barycenter of the exoplanetary system. How

large is the velocity amplitude, and how large the associated Doppler shift at visible wavelengths, for the Sun-Jupiter system? /p. 169/

{A97} *Show*: What is the upper limit to the Sun's rotation rate in its red-giant phase? Formulate your arguments. You may ignore solar mass loss in this estimate. Use Fig. 10.5. This upper limit shows that the Sun's outer layers are rotating (much?) more slowly than the Earth is orbiting it, so that the tidal bulge on the Sun will be traveling through, and dissipating energy within, the solar outer envelope. /p. 169/

{A98} *Look up*: Between the phases of tidally-locked binaries and merged binaries are (semi-)contact binaries in which mass transfer can occur as one of the binary components becomes larger than its 'Roche lobe', either because the star swells up in late evolutionary phases (see Ch. 10) or because the orbit shrinks by 'magnetic braking'. (a) Now or after reading Ch. 10, look up the definition of 'Roche lobe' and the properties of RS CVn, Algol, W UMa, and FK Com objects as characteristic phases in the evolution of different types of close binary stars toward single stars. (b) Make a list of these classes to summarize the masses of the two components involved in each class, their orbital separation, and their magnetic activity. /p. 171/

{A99} *Look up*: The Earth's equatorial bulge is nowadays used to keep satellites in a Sun-synchronous orbit, which is useful for satellites that need to scan the entire surface of the Earth, and also to enable Earth-orbiting satellites to have an uninterrupted view of the Sun throughout the year. (a) Look up and summarize how this works. (b) Why is this important for solar and heliospheric observations? /p. 171/

Chapter 8. Particle orbits, transport, and acceleration

{A100} Ⓢ *Show*: Use Eq. (8.5) to formulate (in a general vector expression) the magnitude of the $\mathbf{E} \times \mathbf{B}$ drift (in case you need a hint: assume the velocity can be described by an oscillatory component plus a constant drift). /p. 179/

{A101} Ⓢ *Show*: Rewrite Eqs. (8.7) and (8.8) to show that the drift velocity scales as the product of the particle's velocity and the gyroradius relative to the typical length scale in the gradient of the field, *i.e.*, as $v(r_g/\ell_t)$. /p. 179/

{A102} *Consider*: Why do you think that bounce and drift motions are commonly ignored for the solar corona but are of dominant importance in the terrestrial magnetosphere? Hint: look at Table 3.4, specifically λ_{mfp} and r_{gi} compared to L_s . /p. 179/

{A103} *Show*: Use a vector identity to show that the final term in Eq. (8.9) transforms into the central expression in Eq. (8.8) for a potential field. /p. 179/

{A104} *Look up* the magnetometer observatories that contribute to the Dst Index. What do you notice about the latitude of their location? /p. 179/

{A105} Ⓢ *Show*: (a) Estimate the orbital period associated with the drift velocity as in Eq. (8.7) for a purely equatorial motion for a proton with kinetic energy of 50 keV orbiting, respectively, at 2 and 10 planetary radii r_p for, for example, Mercury, Earth (where the ring current is contained roughly within these distances), and Jupiter. Use the equatorial field strengths B_e as in Table 5.3 and $B(r) = B_e(r_p/r)^3$ for the equatorial

dipole field. (b) Is the non-relativistic approximation warranted for this proton? (c) And for an electron of the same energy? [Solution in Sect. 17.18] /p. 179/

{A106} *Advanced/group*: If you are interested in the origin of the terms in Eq. (8.20) you could review classic papers with fairly 'intuitive' introductions to the equation by, *e.g.*, Harm Moraal (1976) or Luke Drury (1983), the latter also including how term \textcircled{d} arises. Or you could look at the paper by John Quenby (1984) which also describes the so-called 'force-field solution' that you will find in Sec. 14.2.1 on cosmogenic radionuclides. For each term, identify conditions or a circumstance (solar corona, solar wind, inner magnetosphere, etc.) where it provides an important contribution. /p. 183/

{A107} \textcircled{S} *Show*: (1) Some SEP events suggest that the particles arrive to the observer with little or no scattering in the inner heliosphere. This most often holds for the earliest arriving particles. Assuming this to be the case, answer the following: (1a) For the moment ignoring diffusive dispersal, use a ballistic model to estimate the time at which the particles in the first event shown in Fig. 8.4 were released at the Sun. Consider whether you need to account for a relativistic correction. Note that the display in Fig. 8.4 implicitly uses the approximation that the energy of SEPs scales (roughly) with their mass. (1b) With that timing information, estimate the path length for the mean of the particle population from the Sun to the Earth; why is that larger (by some 10%-20%) than the Sun-Earth distance? Remember Sect. 5.4. (2) Now assume that the bulk of the particles following the early arrivers propagates subject to scattering. Use Eq. (8.27) together with the time of the peak in the particle flux, with the initial event time and path length derived in (1), to show that the diffusion coefficient κ at ≈ 0.04 MeV/nucleon is very roughly 10^{21} cm²/s. Note the dropouts in Fig. 8.4; these are discussed in the next-to-last paragraph of Sect. 8.5.1. [Solution in Sect. 17.19] /p. 189/

{A108} *Show*: Review the Rankine-Hugoniot jump conditions (Eqs. 5.2 and 5.8–5.12) and show that the motional electric field $\mathbf{E}_p = -\mathbf{v}_1 \times \mathbf{B}_1/c$ is constant across a steady-state, one-dimensional shock. /p. 196/

{A109} *Consider*: Interpret the flux profiles as a function of time shown in Fig. 8.10 for the three different perspectives (with Earth in the direction of the arrows for three different events). Argue for the differences in timing of the solar event (first vertical line in each panel) and the passage of the shock (second line) relative to the timing of the peak fluxes. /p. 201/

{A110} *Look up* the properties of (whistler) chorus waves, (ELF/VLF) hiss, and EMIC waves. Make a list or table of these properties. How do they differ? What do they have in common? /p. 203/

Chapter 9. Convection, heating, conduction, and radiation

{A111} *Look up*: (a) What drives tropospheric convection? (b) Why is there no significant convection in the stratosphere (consider the role of ozone)? (c) Is there an equivalent of a stratosphere on Venus? On Mars? (d) Is there lower atmospheric convection? Formulate your arguments. The Web can help. The answers are 'yes' (with a role for

ozone only on Earth). /p. 207/

{A112} Ⓢ *Show:* The scale of the granulation in the photosphere of the Sun (and analogously of other cool stars) follows from a comparison of energy loss by radiation (effective once the plasma can radiate into space, with a time scale of order 20 s) and supply by upflows. Work through this estimate: just below the photosphere, the largest contribution to energy being carried upward resides in latent heat of recombination of ionized hydrogen (with an ionization fraction of order 0.1); balance that with photospheric black-body radiation; use this to derive a minimum upward flow v_z needed to balance radiative losses. Then match timescales, and use that $v_h \leq c_s = (kT/m_p)^{1/2}$: for overturning convective flows, the horizontal time scale of ℓ_h/v_h should equal the vertical one ℓ_z/v_z , for a typical horizontal granular scale ℓ_h and overturning depth $\ell_z \approx H_p \approx 400$ km somewhat below the photosphere. (This argument is developed in III:5.2.1) [Solution in Sect. 17.20] /p. 207/

{A113} Ⓢ *Show:* Sound waves in an isothermal, hydrostatically-stratified atmosphere are 'evanescent', *i.e.*, non-propagating, at frequencies below the acoustic cutoff frequency $\omega_a = c_s/2H_p$ (for sound speed c_s and pressure scale height H_p , see Eqs. 3.31 and 2.3). (a) Can you argue intuitively why (think of the need for a restoring force roughly within a wavelength)? (b) Estimate the value of ω_a for the solar atmosphere. Why are p -modes only observed at frequencies below about ω_a ? (c) Now derive an approximate dispersion relation in simplified geometry for *isothermal non-dissipating* perturbations: Start from Eqs. (3.4), (3.5) and (2.3) for a hydrostatic 1-d (*i.e.*, plane-parallel with only vertically-propagating waves), non-magnetized plasma (mind the sign of g) and combine them retaining terms to first order for perturbations $\rho = \rho_0 + \rho_1$ and $v = v_0 + v_1$, where ρ_0 and $v_0 \equiv 0$ describe the background stratified atmosphere at rest. Then factor out the exponential growth of the amplitude with height by substituting $v = u \exp(z/2H_p)$ and use $u \propto \exp(i[kz - \omega t])$ to obtain a dispersion relation that has propagating waves (real values of k) only for frequencies above ω_a (a somewhat different approach can be found in I:8.3 in which the approximation of isothermal perturbations is dropped). Lower frequency waves reflect and can form standing p -modes if they meet the criteria for global resonance, while higher frequency waves can propagate, but will steepen (readily into shock waves) as they propagate into the lower-density atmosphere. [Solution in Sect. 17.21] /p. 208/

{A114} *Look up:* The 'G band' is a narrow spectral interval centered on electronic transitions of the CH molecule, mixed in with spectral lines from multiple metals. For the interested: look up the 'Fraunhofer lines' and their designations. This old nomenclature from the days in which the solar spectrum was first studied is still used for some of these 'lines'. Which elements and ions are responsible for these lines and bands: C, D, H, K, and G? /p. 208/

{A115} Ⓢ *Show:* Stars have a range of surface gravities, typically increasing monotonically along the main sequence toward lower effective temperatures and lower mass (see the table associated with Fig. 4.2), and substantially lower in evolved ('giant' and 'supergiant') stars than in main-sequence (or 'dwarf') stars. Qualitative insight is

provided by the following exercise: using the concepts of optical depth (and the fact that the stellar photosphere is around unit optical depth for continuum emission) and hydrostatic equilibrium (Ch. 2), show that the photospheric pressure would scale proportional with gravity in the idealized case of an isothermal atmosphere; focus explicitly on the optical depth relationship in Eq. 2.19. In reality, radiative transport and convective motions modify that scaling for a real non-isothermal atmosphere, but the trend is in the correct direction. With this insight, argue for the trend of intrinsic field strength of photospheric magnetic concentrations with gravity: from ~ 1.4 kG in mid F-type dwarf stars to ~ 3.2 kG in late K-type dwarf stars, and well below 1 kG for cool giants. [Solution in Sect. 17.22] /p. 210/

{A116} *Consider:* The transition from bright to dark magnetic structures occurs at a scale of roughly 200 – 300 km. What does that say about the typical photon-mean free path ℓ_{ph} in the photosphere? Compare that value to the corresponding pressure scale height, and argue why $\ell_{\text{ph}} \gtrsim H_p$ just at the photosphere. /p. 210/

{A117} *Consider:* Explain why observed field strengths inside flux tubes exceed the equipartition field strength (the field strength in an imaginary completely evacuated tube in pressure equilibrium with the surrounding field-free gas) at the level of the photosphere outside the tube. Hint: where is the photosphere inside a partially-evacuated tube relative to that in the surrounding gas? /p. 210/

{A118} *Consider:* When the total solar irradiance (TSI) is smoothed over time scales of, say, a week, the Sun is brighter at sunspot maximum than at sunspot minimum, but when looking at TSI curves with a resolution of a day or so, the presence of large sunspots leads to dips when these are near the central meridian. Explain this qualitatively by the mix of faculae, pores, and spots in and around active regions. Once you formulate a hypothesis, verify this by looking at, for example, Fig. III:10.7 and figures such as Fig. 3 in [the study](#) by ? (?) compared to sunspot records that can be found at <https://www.sidc.be/silso/monthlyssnplot>. /p. 210/

{A119} *Consider:* The processes of electromagnetic radiation from a plasma involve three fundamentally distinct processes: bound-bound, free-bound (radiative recombination), and free-free (Bremsstrahlung) emission. (a) The Sun’s coronal emission, caused by excitation collisions of partially ionized with thermal electrons, is dominated by the first, except for flares when the last is also important; why? (b) Which ions are typically strong contributors to the coronal X-ray and EUV emission from an active region at ~ 3 MK? Hint: combine elemental abundances with ionization energies (such as given on the [Wikipedia page](#) on “ionization energies of the elements”). For the solar corona under most conditions, the dominant radiative losses are from C, N, O (below about 0.5 MK), and Fe (above about 0.5 MK). /p. 212/

{A120} *Consider:* Eq. (9.1) contains a product of electron and hydrogen densities, but hydrogen is fully ionized at coronal temperatures and thus has no spectral lines that can be excited through collisions with electrons. Why is it acceptable to express it this way? Hint: consider elemental the mix of ions. /p. 213/

{A121} (S) *Show:* (a) Use Eq. (9.4) to estimate typical volumetric heating rates ϵ_{heat}

for a coronal region over 'quiet Sun' (*i.e.*, outside of active regions; with coronal field strengths of order 5 G, loop-top temperatures of ≈ 1 MK, and loop half lengths $L \sim 4 \cdot 10^9$ cm) and for an active (sunspot-bearing) region (with coronal field strengths of order 100 G, loop-top temperatures of ≈ 3 MK, and loop half lengths $L \sim 15 \cdot 10^9$ cm). (b) Compare these to the thermal energy densities of the gas based on densities estimated from Eq. (9.4) with the above loop properties. (c) Also compute the ion gyro-radius, the ion sound speed, the loop crossing time, and the ratio of the plasma pressure to the magnetic field pressure (*i.e.*, compute values of plasma- β (Eq. 3.24)). (d) Are these numbers consistent with the concept of an isolated, field-dominated loop with an atmosphere is (near-)hydrostatic equilibrium? [Solution in Sect. 17.23] /p. 214/

Chapter 10. Evolution of stars, activity, and asterospheres

{A122} *Look up:* For an interactive visualization of stellar evolution and their tracks in an HR diagram see <https://starinabox.lco.global/>. Use the data tables to create a diagram of main-sequence life time vs. stellar mass, and formulate a power-law approximation $\tau_{\text{MS}} \approx \epsilon (M_*/M_\odot)^\psi$ (save that for comparison with Activity 193). Note how the heaviest stars outlive this power law approximation, in part because they lose a lot of mass while on the main-sequence. /p. 218/

{A123} *Show:* What fraction of the Sun's hydrogen would need to be converted to helium to keep it at (roughly) its current brightness throughout the time it spends on the main sequence? Once core hydrogen is consumed, the stellar internal structure changes considerably, enough to ignite fusion in higher layers as the star moves into its giant phase. Use $E = mc^2$. Start by making some simplifying assumptions. Be sure to state your assumptions and explain your approach. Which assumptions could you refine? Could you use a different approach? /p. 218/

{A124} *Show:* (a) What is the current mass loss rate due to the solar wind? Compare that to the mass loss due to fusion. Assuming these rates to be constant over the Sun's life time (although neither is: discuss the causes of these changes), what would be the mass of the early Sun (in units of the current solar mass). (b) How much greater would the mass loss have to be, averaged over time, to increase the early Sun's mass to $1.07M_\odot$? /p. 220/

{A125} *Consider:* Note that integration over the power in flares as parameterized in Eq. (10.2) diverges when the lower and upper limits extend to $[0, \infty]$. Compile a list of processes that could be at play in introducing cutoffs to the integral on either side and of your reasons to include them. The answer remains under study: it is not clear over what range Eq. (10.2) holds its slope, or what determines the energy of the 'largest flare', or how and how much relatively tiny 'nano-flares' contribute to coronal heating. But considering the possibilities should prove educational. /p. 224/

{A126} © *Show:* Review Fig. 10.5 to estimate the mass of the least-massive post-main-sequence star (say, past the phase marked by a turn towards cooler surfaces marked by the squares, and only considering single stars) that could exist in the present-day Universe. Identify the symbols with the various evolutionary phases of a star of less

then 2 solar masses, including: main sequence, red giant, and white dwarf. Note: this activity is a warm up for activity 127. [Solution in Sect. 17.24] /p. 225/

{A127} *Show:* Fig. 10.5 can be used to illustrate how astronomers determine the ages of 'open clusters' of stars (other than by the modern means of asteroseismology): assuming that all stars in a cluster are formed at about the same time, the shape of the HR diagram for stars in a cluster reveals the age when compared to theoretical evolutionary tracks as in the panel on the upper left. Try this: assume the stars are all close to 1 Gyr old, as in the open cluster called NGC 2355, then mark the approximate positions of the stars at that age in the upper-left panel (the HR diagram with evolutionary tracks) of Fig. 10.5 estimating also where stars of intermediate masses might show up, and realize how the turnoff from the main sequence in such a cluster HR diagram reveals the age of the cluster (see the discussion of Activity 126 in Sect. 17.24. Open clusters all have the low-mass end of this HR diagram in common, so even if the distance to a cluster is not known, the distance can be determined by shifting that low-mass tail to overlap with that of a cluster of known distance. Also: look up the definition of 'open cluster' in contrast to a 'globular cluster'. /p. 226/

{A128} *Consider:* The minimum flare energy given here is instrumental, not intrinsic. Argue why the empirical lower limit of flares detectable by an instrument like *Kepler* is limited to of order 10^{33} ergs. Note that this lower limit exceeds the energies observed (to date, at least) for solar flares. /p. 229/

{A129} *Show:* Just to get an impression of relative velocities: what is the ratio of the characteristic speed of the Solar System relative to the local ISM to the speed of at which the Solar System orbits the Galactic center, 8 kpc away, once every 230 Myr? /p. 229/

{A130} *Show:* With average values for solar wind density and velocity (assuming a radial outflow at constant velocity and with a density as specified in Table 2.4), at what distance from the Sun does the total pressure of the solar wind equal the total pressure of the local interstellar medium (LISM) for estimated values of $B_{\text{LISM}} \approx 3 \mu\text{G}$, $T_{\text{LISM}} \approx 8000 \text{ K}$, $n_{\text{p,LISM}} \approx 0.06 \text{ cm}^{-3}$, $n_{\text{H,LISM}} \approx 0.18 \text{ cm}^{-3}$, and a movement of 25 km/s of the heliosphere relative to the LISM? These values of densities and temperatures assume the Sun to still be inside the Local Interstellar Cloud rather than in the surrounding Local Cavity or Local Bubble (see, *e.g.*, Sect. IV:3.2). Use $B_{\phi} \approx B_r$ near Earth. How do the contributions from the thermal pressure, magnetic pressure, and dynamic (or ram) pressure of the solar wind and the LISM compare at the heliopause (computed in the rest frame of the heliopause)? Look at Sect. 5.5.8 for the physics involved. /p. 231/

{A131} *Show:* Repeat Activity 130 for the range of ISM densities of 0.005 to 10^4 cm^{-3} (as described in the beginning of Sect. 10.3.1), assuming a present-day spherically-symmetric, constant-velocity solar wind, and the same temperature and field strength for the ISM as in the LISM used in Activity 130? Which pressure components dominate in the solar wind and ISM for the highest and lowest densities. Compare your result with Fig. 10.7. /p. 231/

{A132} *Show:* For charge exchange only, and assuming (very approximately, as done initially (Holzer, 1972) decades ago) a velocity-independent cross section for resonant-charge exchange of solar wind protons with ISM neutral hydrogen of $\sigma_{\text{CX}} \approx 2 \cdot 10^{-15} \text{ cm}^2$, what fraction of H^0 , looking at the population after passing through the 'hydrogen wall' and moving in a straight line towards the Sun, would reach Earth orbit for present-day slow wind conditions? In reality, other processes are major players: radiation pressure (for neutral hydrogen primarily by repeated Lyman α absorption followed by isotropic re-emission) pushes outward on the atoms, and photo-ionization in the Sun's EUV and X-rays presents a significant loss term. It appears that Lyman α radiation pressure on ISM H^0 just balances solar gravity, see Schwadron *et al.* (2013) /p. 232/

{A133} *Consider:* The Lyman α line (1215.67 Å), as the brightest UV emission line of late-type stars, is an important diagnostic in the study the energy budget of stellar chromospheres. But, as discussed in the text, much of the strongest emission is taken away by absorption of the line core by circumstellar and interstellar hydrogen. What is the common property of late-type stars that enable us to observe the Lyman α line mostly as emitted by these stars? Quantify a threshold value for that property to be useful. Once you formulate the answer, you can look at Youngblood *et al.* (2022) for a study of suitable target stars. /p. 232/

{A134} *Show* that the power lost in X-rays from the present-day solar corona (estimated from Fig. 10.3 or 10.9) is roughly twice the power lost in the solar wind (using the expressions in Sec. 3.5.2), and that these numbers would have been comparable for the young Sun at the 'wind dividing line' if the characteristic wind speed would have been the same. /p. 233/

{A135} *Consider:* Place the coronal activity level corresponding to the 'wind dividing line' in the rotation-age diagram in Fig. 10.3. How old would the Sun have been when it reached the 'wind dividing line'? What does this imply about the activity for the Sun? What about the solar wind? Other consequences? /p. 234/

{A136} *Show:* Estimate the size of the heliosphere and the terrestrial magnetopause distance for a young Sun at an age of 700 Myr, assuming unchanged LISM conditions and geomagnetic properties. /p. 235/

{A137} *Consider:* Section 10.3.3 mentions a solar rotation period of 25 d while the caption to Fig. 5.6 mentions 27 d. What is the reason for using these two different values in the different contexts? /p. 236/

Chapter 11. Formation of stars and planets

{A138} Ⓢ *Show:* (a) How many Earth masses of elements carbon or heavier are contained in a solar mass cloud of solar composition? Most of that material in the original cloud ended up inside the Sun, of course. (b) What fraction, roughly, of the original cloud would need to remain in the disk to ultimately form the planets? (c) Why are the answers to these two questions largely independent of each other (think about what mostly makes Jupiter and Saturn). [Solution in Sect. 17.25] /p. 239/

{A139} *Show:* Compare the critical protostellar cloud radius $R_c(M_\odot) \gtrsim 2 \times 10^4$ astronom-

ical units to distances between stars in star-forming regions such as the Orion Nebula. Express that distance in light years and in parsecs, and compare those to the distances to the nearest stars for the present-day Sun. /p. 239/

{A140} Ⓢ *Show:* Another way of formulating Eq. (2.15) is to say that the mass of the cloud must exceed a certain value. (a) Reformulate Eq. (2.15) as function of cloud temperature T_c , cloud density n_c , and stellar mass M_* (Note: this is similar to what is known as the Jeans Mass, which is commonly derived from energy imbalance or by a comparison of sound and free-fall time scales in a perturbation analysis). This shows that $M_* \sim f M_\odot T_c^{3/2} / n_c^{1/2}$. (b) Derive the value of the constant $f \approx 2$ assuming, for simplicity, that the gas consists predominantly of molecular hydrogen. For n_c of order 100 cm^{-3} estimate M_* for $T_c \approx 10 \text{ K}$, characteristic of present-day molecular clouds (realizing this is a rough order-of-magnitude estimate). Early in the life of the Universe, with only H and He in the mix, the interstellar gas lacked many of the strong emission lines of heavier elements, could therefore not cool as efficiently, leaving interstellar clouds significantly warmer, roughly of order 100 K. (c) Use the derived expression to show that this favors the formation of much heavier stars, even when starting from a higher density of order 10^4 cm^{-3} . How this contributed to the evolution of elements heavier than H and He (known as 'metals' to astronomers) over the history of the Universe is discussed in a review by Johnson (2019) [Solution in Sect. 17.26] /p. 239/

{A141} *Show:* (a) Estimate the orbital Doppler swings and the fractional dimming during solar transits observed from afar of Mercury, Earth, and Jupiter. (b) Also estimate how close a Jupiter-like exoplanet (with an albedo of 0.5) should orbit for the fractional bolometric dimming during a secondary eclipse (when the planet moves behind the star) to be about 1 millimagnitude (which is the noise level for the telescope of the *Kepler* spacecraft for a 13th magnitude star at 1-minute exposure times). (c) Consider at what wavelength range the contrast is optimal. Use, e.g., the fact sheet at <https://nssdc.gsfc.nasa.gov/planetary/factsheet/>. (d) Compare the Doppler signals with the thermal widths of spectral lines, and consider what to use as reference wavelengths. (e) How large is the Doppler swing added to the stellar signals owing to Earth's orbit around the Sun? /p. 240/

{A142} *Look up* and summarize the principles of the five detection methods of exoplanets, and consider what the strengths, weaknesses, and technological challenges are for each method and how these depend on planetary mass, size, and orbital radius. Note: activities 96 and 141 ask about Doppler signals and transit photometry. /p. 240/

{A143} *Look up:* Star-forming regions and disks around young stars are best observed in the near-infrared region of the spectrum. Look into what wavelengths are often used for such observations, and consider why ('Why is the sky blue?'), given that dust sizes in the interstellar medium peak around a few tenths of a micron. /p. 241/

{A144} *Consider:* Figure 11.2 shows a curved 'snow line' (or 'ice line'). What is the reason behind that? /p. 243/

{A145} *Look up* the 'Grand Tack' hypothesis and describe the likely consequences for the growing Mars, for the asteroid belt, and for water distribution by scattered asteroids

into the inner solar system. /p. 243/

{A146} *Consider:* Figure 11.2 shows a clearing near the central star. This is associated with the magnetic field of the rotating star. Consider what processes are at play there and the role of the following: accretion rate, ionization fraction, diffusion of field into the ionized gaseous disk, orbital and angular velocities, the corotation radius, winding up of magnetic field that connects the star to the disk, centrifugal force, etc. There is no easy concept for this: you can look at the literature of MHD models of T Tauri accretion disks to see how complex the coupling is. Store your thoughts: the star-disk interaction leading to the clearing is discussed in Sect. 11.3.2. /p. 244/

{A147} *Show:* (a) Sketch and describe the observable signatures in high-resolution spectra of transiting planets for orbits of different obliquity (including effectively retrograde planets). (b) Also: estimate transit times for planets around of solar-mass star at distances such as Mercury, Earth, Jupiter, and Neptune. Use, e.g., [this fact sheet](https://nssdc.gsfc.nasa.gov/planetary/factsheet/): <https://nssdc.gsfc.nasa.gov/planetary/factsheet/>. /p. 245/

{A148} *Show:* Estimate the total values and ratios of mass and angular momentum in the planetary system and in the Sun (use Fig. 10.5). /p. 248/

{A149} *Show:* Iron, oxygen, and silicon make up three quarters of the Earth's mass. Iron is some 30% of the total. In the interstellar medium, iron makes up about 1 part in 1,000 of total mass. How many Earth-equivalents of iron does a circumstellar disk with a mass of 1% of the Sun contain? /p. 249/

{A150} *Consider:* List similarities and differences with Solar-System magnetic instabilities as discussed in Ch. 6 when reading about things like FU-Orionis outbursts and 'ballooning out' of magnetic field in ejections of mass from corona and disk, likely driven by necessarily failing attempts of the forces at play to impose corotation. /p. 249/

{A151} *Show:* The internal energy of the star in Eq. (11.1) is derived from the so-called 'virial theorem' which states that the total gravitational energy E_{grav} is related to the total thermal energy E_{thermal} as $E_{\text{grav}} = -2E_{\text{thermal}}$ if $\gamma = 5/3$ as for a monoatomic ideal gas. Derive this from Eq. (3.5) assuming a field-free stationary state for a spherically symmetric ball of gas: $dp/dr = -GM(r)\rho/r^2$. (a) One way to do so is to multiply both sides by $4\pi r^3$, integrate (in part 'by parts') from center to surface (where $p(R)$ essentially vanishes, and realizing that the internal energy per unit volume of the gas is given by $u = p/(\gamma - 1)$ for an adiabatic exponent γ . The result is equivalent to the virial theorem. Eq. (11.1) can be used for the present-day Sun to show that continued gravitational contraction cannot support the solar energy budget over the age estimated for the Earth based on radio-nuclide dating (note a factor of two difference between thermal and gravitational time scales). (b) What is the present-day value of τ_{KH} in Eq. (11.1) for the Sun? /p. 252/

{A152} *Show:* Draw lines of equal radius (as multiples of the solar value) in Fig. 11.6, using $\log(T_{\text{eff},\odot}) = 3.762$. /p. 252/

{A153} *Show:* (a) Derive the expression for the breakup rotation rate of stars as function of mass and radius. (b) What is the value for the Sun? Ignore distortion from spherical symmetry for this estimate. /p. 253/

{A154} *Consider:* The key mechanism by which dust is expected to settle into the center of an accretion disk is hydrodynamic drag. Explain how this works. Consider orbital inclination and effects of gas pressure, gravity, and stratification. /p. 258/

{A155} *Look up:* For further study/reading: Most stars are born in groups of substantial numbers (often in what are called 'open clusters'). In such clusters, stars of a range of masses are formed (statistically yielding the 'initial mass function'). The heaviest among these evolve fastest, and if heavy enough can end their lives in a 'supernova'. The open cluster is eventually pulled apart by the 'galactic tides', which limits the exposure of planetary systems to nearby supernovae and to gravitational perturbation of the orbits of the planets. Look up the terms between quotation marks. The occurrence of a nearby supernova appears consistent with several properties of the solar system, including one of several possible means for the early melting of small bodies (as reflected in what are known as 'chondrules'). Look at [the study](#) by [Portegies Zwart et al. \(2018\)](#) for more on this. /p. 260/

Chapter 12. Irradiance, atmospheres, and habitability

{A156} *Show:* For an impression of order-of-magnitude numbers, estimate the energy involved in a collision between an Earth-mass body and an Mars-mass body at an impact velocity of, say, 14 km/s. Ignoring the energy going into the formation of the Moon in such a process, but rather assuming all mass and energy remain within the newly formed body, estimate the average temperature increase if all energy were distributed throughout half of the volume of the mantle, and that that material has a specific heat of approximately 10^7 erg/g/K. /p. 264/

{A157} *Show:* Make an order of magnitude estimate of the cooling time of Earth's atmosphere after impact of a Mars-mass body: assume an impact velocity of 14 km/s, that all kinetic energy remains within the near-surface layers and atmosphere; an optically thick atmosphere of vaporized silicate; and a characteristic temperature of the radiating vapor of, say, 2000 K. /p. 264/

{A158} *Consider:* Although the definition of 'habitability' commonly involves the requirement of liquid surface water, some definitions are more relaxed. Perhaps other surface liquids can serve as agents in support of life (such as ethane and methane lakes and seas on that cover 1.6 million square kilometers, or 2% of the surface, of Saturn's moon Titan) or perhaps subsurface water (as encapsulated seas or even globe-spanning layers) can support life. With that in mind, explore the moons of the giant planets that are thought to meet at least the condition of large reservoirs of some liquid somewhere, in particular: Europa, Callisto, Ganymede, and Io at Jupiter, Enceladus and Titan at Saturn, and Triton at Neptune. Which three power sources are thought to be most important in maintaining liquid states on giant-planet moons? /p. 265/

{A159} *Background, for the curious:* Photosynthesis depends on the chemicals involved and as such is sensitive to the spectral energy distribution of the star. You could search the literature on developments in this area, but for stars substantially different from our Sun that work remains hypothetical. [Here](#) is a possible entry point. (a) Look up

where the main absorption bands of chlorophyll and β -carotene lie relative to the solar spectrum at sea level. (b) How does the solar spectrum change under water for, for example, flora in the oceans? /p. 266/

{A160} Consider: Sect. 10.3.1 describes the possibility of the Solar System moving through dense, cold interstellar clouds, which could greatly enhance the dust environment of Earth. Review the study by Pavlov *et al.* (2005) for the potential effects on terrestrial climate, including periods of strong glaciation and potentially the triggering of a 'Snowball Earth' state. /p. 267/

{A161} Consider the evolving CO₂ content of the atmosphere of a lifeless terrestrial planet. Which of the following parameters would influence the atmospheric CO₂ content over time: (1) atmospheric mass and composition, (2) chemical composition of seas and oceans, (3) continent sizes and placement, (4) fractional coverage by liquids in seas and oceans, (5) motion through, and density of, local interstellar medium, (6) orbital obliquity, (7) orbital period (length of the planetary 'year'), (8) planetary mass, (9) planetary radius, (10) planetary spin obliquity, (11) planetary spin rate (length of the planetary 'day'), (12) planets elsewhere in the planetary system, (13) plate tectonics, (14) properties of moons, (15) spectral type of the central star, (16) stellar spin rate. Formulate your arguments for each. You may want to read on in Ch. 12 and return here later to complete the activity. /p. 267/

{A162} Look up what constitutes the geocorona. /p. 268/

{A163} Consider: What role does plate tectonics likely play in dynamos in terrestrial planets? Reminder: Sect. 4.1.1. /p. 269/

{A164} Consider: The Earth's argon is predominantly Argon-40, whereas that in the universe at large, as in the Sun, is Argon-36. What is the source of Argon-40 in Earth's atmosphere? /p. 269/

{A165} Show: At what distance would an Earth-equivalent exoplanet need to orbit an $0.6 M_{\odot}$ M0 V star to reach the same global 'equilibrium temperature', all other things being equal? You may disregard effects associated with the difference in the stellar spectral energy distribution on the exoplanet, but you should not ignore the bolometric correction in estimating the total stellar irradiance. How long would a year last on such a planet compared to Earth's? Use Fig. 4.2. Note: such close-in planets are subject to very strong tidal forces that will synchronize spin and orbital periods, causing these exoplanets to lose their day-night cycles. That, in turn, invalidates your estimate – why? /p. 273/

{A166} Show: Beyond the furthest planet: The New Horizons spacecraft flew by Kuiper Belt Object 2014 MU₆₉ on 2019/01/01, the most distant body visited by a spacecraft to date, at an orbital distance of ~ 44 AU. Estimate the surface temperature of 2014 MU₆₉, which has an albedo of ~ 0.1 . Compare your estimate to the observed temperature in the paper by Stern *et al.* (2019). /p. 273/

{A167} Show that the simple model in Fig. 12.5 yields an estimate consistent with Earth's global temperature rise of about one degree (observed between 1850 and 2010) based on the increase in anthropogenic radiative forcing as shown in Figure 12.6 within the

uncertainty indicated in that figure. /p. 276/

{A168} *Show*: Compare the values of \mathcal{P}_{abs} from Eq. (12.1) for Venus and Earth. Explain qualitatively why Venus' surface temperature exceeds Earth's; Section 12.3.1 provides the answer. /p. 276/

{A169} *Show*: To get an idea of scales: estimate the size of a comet that would double the CO_2 content of Earth's atmosphere. How does that compare to, e.g. comet 1P, the target of the *Giotto* mission, and 67C, the target of the *Rosetta* mission? /p. 281/

{A170} *Consider*: (a) What is the basis of the Kelvin-Helmholtz instability? This instability also occurs between the terrestrial magnetosphere and magnetopause flow because the magnetic tension is not strong enough to stabilize the developing waves. (b) Why is this geospace phenomenon not listed as a process for 'bulk outflow'? /p. 283/

{A171} *Consider*: Make a table summarizing which atmospheric loss processes work on each of the terrestrial planets. Which two processes are most effective for the present-day Earth based on the description in Sect. 12.4.1? /p. 285/

{A172} *Background*: Human impacts on climate appear not to be limited to the Industrial Revolution! Have a look at a [study by Koch *et al.* \(2019\)](#): they argue that the large population reduction in the Americas following the arrival of European conquerors and settlers, and the resulting reforestation of abandoned agricultural lands, was a significant part of the change in atmospheric CO_2 in the late 16th Century and in the 17th Century. /p. 287/

{A173} *Consider*: Compile a list of all the processes involved in setting a planetary climate system that reflects at least all those mentioned in Chs. 11 and 12. You can assimilate relevant processes from Activity 161 here as a start. /p. 287/

Chapter 13. Upper atmospheres and magnetospheres

{A174} Ⓢ *Show*: The approximate scaling of the molecular diffusion coefficient D (measuring the mean square displacement per unit time) with molecular mass m and particle density n follows from energy equilibrium of the constituent particles. Formulate D as function of the collisional cross section σ and of temperature and density in the case of self-diffusion, *i.e.*, for molecules diffusing among themselves. For a mixture of components, mutual diffusion needs to be considered. [Solution in Sect. 17.27] /p. 289/

{A175} *Show*: Work through the units of Eqs. (13.3) and (13.4) to show that η_X is an efficiency per unit energy per unit wavelength. /p. 291/

{A176} *Show*: Indicate the various wavelengths mentioned in Sect. 13.2.1 on Figure 2.4, add the equivalent wavelengths for the first ionization energies of H, C, N, O, N_2 , O_2 and CO_2 , and indicate height ranges of the three main layers of the Earth atmosphere as shown in Figure 2.2. /p. 294/

{A177} *Consider* the similarities and differences between the charge-exchange reactions described here and two- and three-body gravitational interactions, specifically what is needed for the capture of interplanetary spacecraft into closed orbits, or the capture of planetary bodies as moons of planets. For the latter, look up the concepts proposed for

the capture of Triton, the largest moon of Neptune, orbiting that planet in a retrograde orbit (which implies it has to involve a capture well after the formation of the planet). /p. 294/

{A178} *Consider:* Note the equivalence between Eq. (13.13) and Eq. (11.5) for a volumetric ionization rate of $\Pi(e^-) \propto \Phi_i / (4\pi R^3)$. This means that α_{eff} is, in effect, for a 'case B' recombination, *i.e.*, excluding the possibility that emitted photons in recombination are absorbed to lead to another ionization event. Consider what could happen to avoid that. Also see a parallel with the formulation of what can be viewed as the inverse in Eq. (9.3): for a stationary, isothermal case, the 'incoming' volumetric heating ϵ_{heat} balances the outgoing radiation $n_e n_H f_{\text{rad}}$ in which the product of ion and electron densities is a measure for the number of collisions leading to excitation, to compare with the ionizing radiation in the ionosphere which balances the recombination in which the product of ion and electron densities is a measure for the number of collisions leading to recombination. /p. 295/

{A179} *Show:* (a) Use Figs. 2.3 and 2.4 to argue why the solar-cycle variability in the ionospheric electron density seen in Fig. 2.9 is much higher at high altitudes than near the base of the terrestrial ionosphere. (b) Also: argue, roughly, why the contrast in electron densities between day and night in Fig. 2.9 is larger at lower altitudes. /p. 295/

{A180} *Background:* One might think that collisions between particles that can 'bond' and thereby be taken out of a population under study, such as electrons and positively-charged ions that combine into a neutral particle, might have a good analogy in how flux concentrations in the solar photosphere behave: the concentrations perform a random walk and in collisions opposite magnetic polarities 'cancel', *i.e.*, disappear from the population of magnetic charges. Yet the scaling behavior between the strength of the source (the total of emerging bipoles per unit time) and sinks (the total of canceling flux per unit time) is different: the square root dependence reflected in Eq. (13.13) does not show up, but instead a near-linear dependence appears (as shown in a study by Schrijver (2001)). Consider the reasons: when the Sun's activity increases, flux concentrations grow larger by collision thereby countering the increase in collision frequency expected; larger concentrations are less mobile within the evolving convective motions; fragmentation and coagulation are seeking a balance; while in general the large-scale meridional flow aids in separating polarities (a process that is countered in an ionosphere by the tendency towards charge neutrality). /p. 295/

{A181} (a) *Show* for the simplified case of a fully-ionized stationary gas that the scale height for ions is twice that for the corresponding atoms in a neutral atmosphere by combining the momentum equations for ions and electrons (see Eq. 3.9 and Activity 32) in comparison to that equation for a neutral species. (b) And remind yourself how this is consistently incorporated in the MHD equations. /p. 295/

{A182} *Consider:* Review Figs. 2.6, 13.1, and 13.2 and think through the dominant reactions described in Sects. 13.2.2 and 13.2.3. (a) Convert the ionization energies to equivalent wavelengths and then use Fig. 2.4 to estimate approximate depths of

maximum penetration. (b) Considering photo-ionization and the reaction pathways in Fig. 13.1 argue why the O_2^+ height profile in Fig. 13.2 might have a double peak. Ionization energies: O 13.6 eV, O_2 12.1 eV, N_2 15.6 eV, CO_2 13.8 eV. /p. 298/

{A183} *Consider:* Trace which part of the solar spectrum provides the predominant power to the *E* and *F* layers of the terrestrial ionosphere and overlapping thermospheric regions, and note that the power going into the *F* layer exhibits a larger variation over the solar cycle than that going into the *E* region. See Sect. 13.2.1 and Figs. 2.3, 2.4 and 2.9. /p. 299/

{A184} *Show:* Upward traveling radio waves with frequencies below the plasma frequency are evanescent within the ionosphere and are reflected downward, thus enabling 'over the horizon' or 'skywave' communication. Look up the plasma frequency (Eq. 3.41), typical ionospheric electron densities within the ionosphere, and resulting values for the radio frequencies useful for such communication. See, *e.g.*, Fig. 6.1 for an overview of the EM spectrum with an indication of various radio bands (including what differentiates propagation of AM and FM bands). Similarly, radio waves from outside Earth cannot penetrate the ionosphere at frequencies below that corresponding to the layer of the largest electron density. Estimate the lowest frequency of, say, solar radio emission that can be observed by a ground-based observatory. Mind the factor of 2π . /p. 302/

{A185} *Show:* Using information from this chapter and Ch. 10, (a) estimate when the solar EUV flux dropped to a level that the thermospheric climate became comparable to the present-day state; and (b) summarize the ionospheric changes over geological time scales as far as the models discussed here are concerned. /p. 305/

{A186} (S) *Show:* (a) Assuming a similar geomagnetic field, use the expressions in Eq. (13.14) to derive an estimate of the magnetopause distance over time. (b) Show that for a young Sun this comes down to $\sim 1.25R_\oplus$ (with Eq. 5.22). [Solution in Sect. 17.28] /p. 308/

Chapter 14. Cosmic rays and magnetic fields over time

{A187} *Advanced/Background:* If you are interested in how Eq. (8.20) can be approximated by something like Eq. (14.1) you can find the origin of this transformation in a [study by Gleeson and Axford \(1968\)](#). /p. 313/

{A188} *Show:* To appreciate how little radionuclide material there is to work with, compute the global annual production in kg for ^{14}C and ^{10}Be . That production rate puts roughly one ^{14}C atom per 10^{12} atoms of ^{12}C in living tissue through uptake of atmospheric CO_2 by plants and their subsequent consumption by animals. /p. 314/

{A189} (S) *Show:* The ^{10}Be production rate for Mars would be about 2.5 times the terrestrial rate if it had a terrestrial atmosphere. Show why based on data in this text. [Solution in Sect. 17.29] /p. 315/

{A190} *Consider:* Over the past century the concentration of ^{14}C in the biosphere has dropped because of fossil-fuel burning. (a) Why? (b) Argue why this leads to an ambiguity in ^{14}C dating if no other information on the age of an object is known.

/p. 316/

{A191} *Look up* 'paleomagnetic dating' in relation to the 'remanence measurements' mentioned in Sect. 14.3. /p. 317/

{A192} *Consider/Show:* How are the decrease of stellar rotation speed, magnetic activity, and mass-loss rate on long time scales compatible with the 'essentially constant' GCR exposure over the past ≈ 1 Gyr? The answer has to do with the fact that the Sun is already an aged star, and can be traced to its relatively weak magnetic braking over the past 1 Gyr, and thus relatively little decrease in coronal activity and mass-loss rate. The limited impact on GCRs at Earth orbit over time also suggests that the heliospheric variability (leading to diffusive GCR scattering) has not changed too much. Estimate the changes over time using Eqs. (10.3) and (10.7), and Fig. 10.3. /p. 321/

{A193} © *Look up/Show:* Heavy stars evolve much faster than low-mass stars, and can, if heavy enough, explode in a supernova even as lower-mass stars and their planetary system within the same molecular cloud are still in their formative phases. Stars spend most of their lives (typically some 85–90% of its full life time prior to the supernova or white-dwarf phases) fusing hydrogen on the 'main sequence' which runs diagonally through a Hertzsprung-Russell (luminosity-temperature) diagram (*e.g.*, Figs. 4.2 and 10.1). The heaviest stars are of order $100 M_{\odot}$ at which mass their outer layers are almost blown off by radiation pressure. The least massive stars are about $0.08 M_{\odot}$ below which sustained hydrogen fusion is impossible. Stars heavier than about $8 M_{\odot}$ end their lives in supernovae (close binaries with mass transfer muddy that simple threshold). (a) Estimate the life times τ_* of stars on the main sequence at 100, 8, 0.5 and $0.08 M_{\odot}$ based on a simple scaling assuming that luminosity L_* is maintained by using a fixed fraction of stellar mass M_* so that $\tau_* \propto M_*/L_*$ and that along the main sequence – very roughly – $L_* \propto M_*^{7/2}$ while $\tau_{\odot} \approx 10^{10}$ yr. (b) Assuming there were only single stars in the Sun's birth cluster, what is the highest age $\tau_{\odot\text{SN}}$ of the Sun when a supernova could have happened within that cluster? (c) For stars heavier than about $0.5 M_{\odot}$ the initial mass function (IMF, the number of stars formed as a function of their mass) can be approximated by $\xi(M)dM \approx \xi_0 M^{-7/3} dM$. For there to have been at least one supernova within $\tau_{\odot\text{SN}}$ yr, what is the minimum number of stars with masses between, say, $0.5 M_{\odot}$ and $2 M_{\odot}$ (Sun-like stars) that should have been in the Sun's birth cluster. That number lies comfortably below the content of many young clusters, such as the Orion Nebula, Hyades, and Pleiades clusters with roughly 100 to 1,000 member stars. But there is radionuclide evidence that the young Sun was in fact exposed to a supernova when it was a mere 1.8 Myr old. (d) Repeat the above for the lowest-mass star to go supernova within that time, and estimate the corresponding minimum number of stars with masses between 0.5 and 2 solar masses (which is almost an order of magnitude larger than the number under (3) above, but compatible with the estimated solar birth cluster mass of 500 to 3000 M_{\odot}). These are, of course, rather rough approximations and stellar structure and evolution models can do a much better job, but it gives an impression of what it takes to make such estimates and yields approximations that are good for an initial exploration; if you want, you can do somewhat better with piece-wise approximations that you can find

on the web. For more on this, and on where the Sun’s siblings have gone, see [Portegies Zwart \(2009\)](#). [Solution in Sect. 17.30] /p. 321/

{A194} *Show:* Estimate how much stronger the dynamic pressure of the incoming supernova wave front needs to be than the present-day IMF, assuming comparable solar-wind properties, to push the heliospheric boundary to within 1 AU. See Activity 130. /p. 321/

Chapter 15. Applied heliophysics, *mutatis mutandis*

{A195} *Background/Advanced/Group:* ‘**What if**’ scenarios: If you would like to think well ‘outside the box’ of things explicitly discussed in this book and in the Heliophysics volumes then consider this: what are things like when settings change? You could think of exoplanets with different host stars, orbits, and atmospheres, but there will be limited guidance by what we actually know from the literature. (1) For an example not too far from home, you could consider [Titan](#), the only moon (natural satellite) in the solar system with a substantial atmosphere that is mostly N_2 (some 97%) and CH_4 (much of the remainder). *Activity 1:* Find Titan’s equivalent values for the quantities listed in Table 2.1; use, example, [Wikipedia](#) and its references for a start. *Further reading on Titan:* You can find publications on the (photo-)chemistry of its atmosphere leading to an ionosphere rich in HCNH^+ and C_2H_5^+ . The chemical network in the high atmosphere leads to heavy organic molecules and aerosols that are deposited onto Titan’s frozen surface and into its hydrocarbon lakes. Titan orbits within Saturn’s magnetosphere, generally shielded from the direct impacts of the solar wind. However, the solar wind causes Saturn’s magnetosphere to be highly asymmetric, and thus the environment through which Titan orbits is highly [dependent on its orbital phase](#). Cosmic rays and energetic particles from Saturn’s magnetosphere penetrate deep into Titan’s atmosphere causing ionization and influencing chemical pathways. Titan has no intrinsic magnetic field (*i.e.*, no functioning magnetic dynamo) but an induced magnetosphere that changes as the moon orbits the rotating giant planet Saturn. There may be subsurface areas of liquid water, a water-ammonia mixture, or different mixtures in different locations and at different depths. Life might exist under these circumstances, and the traditional definition of ‘habitability’ as involving liquid surface water may need rethinking as we learn more. (2) For something far from home, consider the compact 7(?)–planet system of TRAPPIST-1 (see Fig. 15.1) on which much is being written: execute an [ADS search](#) (at <https://ui.adsabs.harvard.edu>) for refereed papers with ‘TRAPPIST-1’ in the title. *Activity 2:* For at least one of the TRAPPIST-1 exoplanets, complete the first six lines of Table 2.1 – the rest remains unknown. *Activity 3:* Consider how those environmental conditions would affect the overall space environment. /p. 326/

{A196} *Show:* **Observing exoplanetary atmospheres:** (1) Approximate the contrast $C_{*,\text{p}}(\lambda)$ between exoplanetary atmospheric radiation and stellar surface radiation, assuming both star and planet radiate as black bodies (using Planck’s law $B(\lambda, T)$; ignoring center-to-limb effects), as function of wavelength, of the temperatures of star (T_*) and planet (T_{p}), and of the effective radii of star ($R_*(\lambda)$) and planet ($R_{\text{p}}(\lambda)$).

Show that $C_{*,p}(\lambda = 10 \mu\text{m}) \approx (20 * R_*(\lambda)/R_{p(\lambda)})^2$ for $T_* = T_\odot$ and $T_p = T_\oplus$. (2) What is $C_{\odot,\oplus}(\lambda = 10 \mu\text{m})$? This value shows how hard it is to separate stellar and planetary signals (it is easier for closer-in, warmer, planets and for larger planets, such as hot Jupiters). (3) Why does the IR domain of the wavelength spectrum provide optimal access to the exoplanetary spectrum using a secondary eclipse (when the planet moves behind the star)? (4) At what wavelength does $B(\lambda, T)d\lambda$ peak for a planet at $T_p = T_\oplus$ (use Wien's displacement law)? (5) For transit spectroscopy, in contrast, optical wavelengths are most suitable for G- and K-type stars; why? See [the tutorial by Deming and Louie \(2019\)](#) on exoplanet transit spectroscopy for answers and for more on this topic. /p. 326/

{A197} **Exoplanetary atmospheric spectroscopy:** How does wavelength-dependent transparency of an exoplanetary atmosphere lead to wavelength-dependent transit depths $\mathcal{T}(\lambda)$, and thereby yield spectral signatures of atmospheric chemicals? Basically, the apparent radius of exoplanet-plus-atmosphere depends on wavelength because the atmospheric opacity does. But the transit depth also depends on whether there are features on the stellar disk within the transit path. This provides information on, *e.g.*, starspot properties. (a) Sketch how these two signals combine into the observed transit depth signal $\mathcal{T}(\lambda, t)$ over a transit. (b) Consider how one might go about disentangling these two signals. See the reference in Activity 196 for more information. /p. 326/

{A198} *Consider: Comparative heliophysics:* Look up the properties of the stars α CMa A, the Sun, and TRAPPIST-1. Consider how the following properties differ for a planet (unconfirmed to exist in the case of α CMa A) orbiting each of these stars within the continuously habitable zone: (a) the size and color of the star, (b) the maximum possible age of the planet, (c) the duration of the orbital year and constraints on the length of the planetary day, (d) possible constraints on the planetary dynamo (subject to what we know about these at present), (e) the Alfvén Mach number of the stellar wind, (f) the magnetopause distance (assuming comparable planetary dynamos), (g) constraints on loss of planetary water, (h) the potential of measuring interstellar neutral hydrogen from an orbit near that planet, (i) the spectrum of the stellar and galactic cosmic rays (assuming the same spectrum external to the planetary system). /p. 326/

{A199} *Consider: Energetic particles in TRAPPIST-1:* TRAPPIST-1 is a very different world from our Solar System. The central star — itself only first observed in 1999 — is merely 1/8th the size of the Sun, only slightly larger than Jupiter. Its brightness is almost 2,000 times less than that of the Sun. The star is orbited by seven known exoplanets (first published on in 2016), much like Earth in size and mass, but all very close to their star. At least three of these seven planets are estimated to orbit within the liquid-water habitable zone. You can start reading up on TRAPPIST-1 using an ADS search, but for this Activity review [the study by Garraffo *et al.* \(2017\)](#) on the astrosphere, and [the study by Frascchetti *et al.* \(2019\)](#) of the possibly very intense radiation environment of the planets. The role of heliophysics in this is evident throughout these studies: (1) identify the processes you have read about in this book that are elements of these studies. (2) Use what you learned in this text to explain why

the wind is mostly sub-sonic around the seven planets. (3) With dynamic pressures 3 to 6 orders of magnitude higher than for Earth, what does that do for the planetary magnetopause distances? (4) Although this system is diminutive, its astrosphere is potentially huge: estimate the distance to the astropause assuming the system is subject to ISM conditions similar to those for the Solar System. /p. 326/

{A200} © Consider/Advanced/Group: **Arriving at Earth's climate from scratch:** In Activity 173 you compiled a list of all the processes involved in setting a planetary climate system that reflected at least all those mentioned in Chs. 11 and 12. Now, complement that list with the additional topics discussed in Ch. 14. Do not forget to add relevant thoughts from your notes for Activity 195! Then review that list and flag those processes that are beneficial to life as we know it on Earth and those that are detrimental to it. The duality of many, perhaps most, of the entries on your list should make you think about how our Earth, as it is in its present state, is a consequence of a remarkable interplay of often simultaneously beneficial and detrimental processes, including, perhaps, a series of fortuitous developments. Consider the extraordinary challenge of thinking about 'habitability' of any of the other thousands of exoplanets found to date, including what the phrase 'habitability' itself adds to that challenge given how little we know about life itself. Better yet, write an essay on this to share with fellow students, with teachers, and perhaps a much larger readership. [Solution in Sect. 17.31] /p. 326/

Chapter 17

Solutions and supplemental text for selected activities

17.1 Activity 13: Solar wind travel time

(a,b) The solar wind speed is $v_{\text{sw}} = (4.3 \text{ to } 9) 10^7 \text{ cm/s}$, and the Sun-Earth distance is $d_{\oplus} = 1.5 10^{13} \text{ cm}$, so the time for the solar wind to reach Earth is $\Delta t_{\oplus} = d_{\oplus}/v_{\text{sw}} = 1.9 \text{ to } 4.0 \text{ days}$ (during which the Sun has rotated 25° to 53°).

(c) $d_{\text{Neptune}} = 30 \text{ AU}$, so $\Delta t_{\text{Neptune}} = 30t_{\oplus} = 57 \text{ to } 120 \text{ days}$ (or $\approx 2 \text{ to } 5$ solar rotations).

(d) The angle of the incoming wind at Earth relative to the Sun-Earth line is given by $\arctan(v_{\text{orb}}/v_{\text{sw}})$ for an orbital velocity of v_{orb} : 1.9° to 4.0° .

Note: Because the Sun has rotated 25° to 53° in the 2 to 4 d that it takes for the solar wind to reach Earth, the field lines that connect the Sun to the Earth typically start from around that longitude west of the Sun's central meridian (using the common geocentric reference for directions on the Sun as seen in the sky). This is important to understand the typical source region on the Sun for solar energetic particles reaching Earth: as they follow the Parker spiral (Sect. 5.4), they preponderantly originate from the western side of the Sun; this is discussed in Ch. 8.

17.2 Activity 15: Parker solar wind; basics

Start with Eq. (2.10):

$$\frac{1}{v} \frac{dv}{dr} \left\{ v^2 - \frac{2kT}{m_p} \right\} = \left\{ \frac{4kT}{m_p r} - \frac{GM_{\odot}}{r^2} \right\}. \quad (\text{i})$$

With $e_{\text{kin}} = \frac{1}{2}\rho v^2$, $e_{\text{grav}} = -GM_{\odot}\rho/r$, and $p_{\text{gas}} = 2\rho kT/m_p$ for a fully-ionized hydrogen-dominated gas, this can be rephrased as a balance of specific energies and work by isothermal expansion:

$$\frac{d}{dr} \left\{ \frac{e_{\text{kin}}}{\rho} + \frac{e_{\text{grav}}}{\rho} \right\} = \frac{p_{\text{gas}}}{\rho} \left\{ \frac{1}{v} \frac{dv}{dr} + \frac{2}{r} \right\} = -\frac{p_{\text{gas}}}{\rho} \left\{ \frac{1}{\rho} \frac{d\rho}{dr} \right\}, \quad (\text{ii})$$

where the rightmost term follows from the central expression using the time-independent continuity equation Eq. (3.4) absent sources and sinks in a spherical geometry:

$$\rho \nabla \cdot \mathbf{v} = -(\mathbf{v} \cdot \nabla) \rho \rightarrow \frac{1}{r^2} \frac{d}{dr} r^2 v = -v \frac{d}{dr} \rho. \quad (\text{iii})$$

In words: the changes in kinetic and potential energy are compensated by the work done by the change in volume of the isothermal gas (expressed in the central expression of Eq. (ii) in terms of radial expansion by the velocity gradient and lateral expansion because of the geometry). And that work/energy is supplied by what keeps the plasma (near-)isothermal: electron heat conduction from the coronal heat source.

Problem: for an isothermal wind, the terminal velocity is essentially unbounded, and thus the required energy to power it is also formally unbounded. That issue goes away if we would allow the temperature to decrease with distance so that actual heat conduction can do its job properly (and satisfy the energy equation) at the expense of somewhat more complicated math. If you did that, then the energy available to power the solar wind would be set by $\kappa(T)dT/dr$ at the coronal base (with $\kappa(T)$ the Spitzer thermal conductivity as in Eq. 9.2).

Analogy to the Laval nozzle

Some people draw a comparison between the solar wind subject to gravity and a *de Laval* nozzle absent gravity. For a stationary, one-dimensional, isothermal flow through a geometry with cross section $A(r)$, and without magnetic field, gravity, viscosity, or sources or sinks for particles, the continuity and momentum equations (Eqs. 3.4 and 3.5) simplify to:

$$\frac{d}{dr}(\rho v A) = 0 ; \quad \rho v \frac{dv}{dr} = -\frac{2kT}{m_p} \frac{d\rho}{dr}, \quad (\text{iv})$$

which can be combined to read

$$\frac{1}{v} \frac{dv}{dr} \left\{ v^2 - \frac{2kT}{m_p} \right\} = \frac{2kT}{m_p} \frac{1}{A} \frac{dA}{dr}. \quad (\text{v})$$

Comparison with Eq. (i) suggests:

$$\frac{2kT}{m_p} \frac{1}{A} \frac{dA}{dr} = \left\{ \frac{4kT}{m_p r} - \frac{GM_\odot}{r^2} \right\}. \quad (\text{vi})$$

This has a solution

$$A(r) \propto r^2 \exp\left(-\frac{e_{\text{grav}}}{e_{\text{gas}}}\right), \quad (\text{vii})$$

with a minimum where $-2e_{\text{grav}} = e_{\text{gas}}$ below which gravitational potential energy acts like a constricting nozzle and beyond which the 'nozzle' eventually 'expands' as r^2 .

Insights: (1) The solar wind is enabled by the high coronal temperature (electron conduction and high conductive flux - see Eq. (9.2) and Note 25: high mean-free path in Coulomb collisions), which supplies energy to beyond the point where the thermal

energy equals the (unsigned) gravitational potential energy (= kinetic energy of the escape velocity); (2) there is a hidden energy transport in the assumption made in the model under discussion that the gas is isothermal, which violates the equation for internal energy (Eq. 3.6) because you cannot have conductive energy transport without a thermal gradient; (3) a different formulation of the same equation(s) provides different insights.

17.3 Activity 16: Mean free paths and MHD

(a) The 'mean' or 'characteristic' mean-free path length (in cm) for heliospheric electron-electron interactions (because we are talking about electron thermal conduction) as derived from quantities in Table 18.2:

$$\bar{\lambda}_{\text{mfp},e} \approx \frac{v_{Te}}{\nu_{ee}} \sim 1.1 \cdot 10^4 \frac{T_e^2}{n_e}. \quad (\text{viii})$$

Near Earth, with Table 2.3, for slow and fast wind:

$$\bar{\lambda}_{\text{mfp},e} \approx 2 \cdot 10^{13} - 4 \cdot 10^{13} \text{ cm or } 1.3 - 2.6 \text{ AU.}$$

Note: the relevant velocity here is the random velocity v_{Te} of the electrons superposed on the much lower bulk flow v_{sw} . What is the characteristic ratio v_{Te}/v_{sw} at 1 MK?

(b) Closer to the Sun, $\bar{\lambda}_{\text{mfp},e}$ is much smaller (because of the higher density) and Maxwellian distributions are a fair approximation. The electron mean-free path equals the density scale height roughly around the critical point in the isothermal Parker solution, which at 10^6 K lies at $\approx 6R_{\odot}$ (which defines the base of the largely collisionless exosphere). Why does MHD still provide a fair approximation for the solar wind beyond that point? We can look at one of Gene Parker's lessons: "... it is widely believed that the large-scale bulk motion within a body of collisionless gas or plasma is not described by the Newtonian equations of hydrodynamics ... But whether interparticle collisions happen or not, the bulk flow conserves particles, momentum, and energy, and when those three conservation conditions are written down, they provide the equations of hydrodynamics, with the familiar gradient of [pressure], compressibility, etc. Most textbooks derive these hydrodynamic equations by computing the zero, first, and second velocity moments of the collisionless Boltzmann equation, but the simple idea of flux conservation of particles, momentum, and energy can be used directly (Parker, 2007)."

Moreover, in the collisionless domain of the heliosphere, you need to realize that there are collective electromagnetic interactions and magnetic perturbations (gradients, including waves: turbulence) that scatter particles and help maintain fair validity of the concepts of temperature and pressure as in thermodynamics. See Sect. 3.1 and Table 3.2 for more on the assumptions behind MHD and its general applicability to bulk properties even in collisionless settings.

There is also the following argument that has been explored:

Push or pull? Push and pull?

An (extreme) alternative to the (equally extreme) hydrodynamic (or fluid) approximation is the *collisionless approximation*. In the latter, an ambipolar electrostatic potential builds up between the low-mass electron population and the high-mass ion population. One way to think about the resulting wind is this: The fastest electrons (which, by the way, are least affected by collisions) can overcome the gravitational potential barrier, but they cannot flow out in bulk without taking the ions (and lower-energy electrons) lest they increase the electric potential as they would leave a charged Sun behind. So any sustained bulk electron flux must be balanced by an ion flux (which has to deal with its much higher gravitational potential that is only partially countered by the electric potential), which happens when the electrostatic field that builds up sufficiently counters the gravity on the ions to pull them along.

A very rough approximation and the assumption of Maxwellian tails (maintained by the hot electron reservoir in the corona below the 'exosphere') shows that the electric potential energy at the exobase would be roughly double the enthalpy of a Maxwellian electron-proton plasma: $\sim 5kT$ vs. $\sim 5kT/2$ (see Meyer-Vernet (1999) who provides a very readable introduction of the collisionless 'exospheric' model of the solar wind)

You can expect that the resulting solar wind (mass flux and speed) is determined by the high-energy tail of the velocity distribution . . . which is not likely to be that of a true Maxwellian precisely because the fastest particles have an even lower cross section for Coulomb collisions and thus interact even less: plasmas are notorious for having non-thermal high-energy tails.

The reality of the solar wind is neither fully hydrodynamic nor fully collisionless, that of course also includes a magnetic field and its perturbations. But, as it turns out, the net behavior of the fluid and exospheric approximations is much the same because it is governed by unavoidable conservation laws:

N.B. A historical note: Parker (1960) took the wind density at Earth to be 100 cm^{-3} (interestingly much lower than in his 1958 paper where he says that "Biermann infers densities at the orbit of earth ranging from 500 hydrogen atoms/ cm^3 on magnetically quiet days [to much higher during storms]"). In his 1960 paper, he simply noted that "the mean-free path for interparticle collisions is small compared with the dimensions of the flow" and used standard hydrodynamic equations, assuming collective behavior and Maxwellian statistics. Also, at the time, he could assume "that the extension of solar gas into interplanetary space comes from the entire corona. Hence the observations altogether suggest that the whole corona flows hydrodynamically outward into space".

Interestingly, Parker (2014) says: "Hardly anyone believed the trans-sonic expansion of the solar corona. So I had the field to myself for about four years, elaborating the analytic theory of the expanding corona, producing two hydrodynamic models of the heliosphere depending on the existence or absence of an interstellar wind."

17.4 Activity 21: Penetration depth of energetic particles

Assuming an isothermal atmosphere dominated by particles of mass m_a at temperature T_a , the density $n(h)$ as a function of height h above a reference level with density n_o and the column density $N(h)$ from infinity to altitude h are given by

$$n(h) = n_o e^{-\frac{h}{H_p}} ; N(h) = \int_h^{\infty} n(x) dx = n_o H_p e^{-\frac{h}{H_p}}, \quad (\text{ix})$$

for a density scale height H_p given by Eq. (2.3). The altitude at which a vertically-moving incoming energetic particle has penetrated a column mass of μ_{col} is thus given by:

$$h = H_p \ln(m_a n_o H_p / \mu_{\text{col}}). \quad (\text{x})$$

For energetic particles that penetrate to a column depth of $\mu_{\text{col}} = 10 \text{ g/cm}^2$:

	Species	m_a (g)	n_0 (cm^{-3})	T_a (K)	g (cm/s^2)	H_p (km)	a_p (km)
Earth	N_2	$4.7 \cdot 10^{-23}$	$3 \cdot 10^{19}$	288	980	8.6	47
Mars	CO_2	$7.3 \cdot 10^{-23}$	$3 \cdot 10^{17}$	210	370	11.	17
Sun	H	$1.7 \cdot 10^{-24}$	10^{17}	5780	$2.7 \cdot 10^4$	175.	-90

You can combine typical densities and scale heights for the solar corona and chromosphere to show that these domains cannot efficiently stop particles of these energies.

Note that for Earth and Mars, these penetration altitudes are well above where the isothermal approximation is valid, while the negative value for the Sun shows that such particles can just penetrate the photosphere (in the process leading to γ -ray emission and nuclear reactions resulting in, among others, neutron-capture line emission and positron-annihilation line emission; see *e.g.*, Schrijver *et al.*, 2006 for a multi-mission study of a bright solar flare). For Al, with a mass density of 2.7 g/cm^3 , the penetration depth required to reach $\mu_{\text{col}} = 10 \text{ g/cm}^2$ is 3.7 cm.

17.5 Activity 22: Collisions and conductivities

(a) High in the atmosphere, collision frequencies are low, and thus magnetization high, while deeper in the atmosphere the magnetization is small. As the Pedersen conductivity σ_P is, as stated in the text, dominated by the ion term, a first-order Taylor expansion yields, for singly-ionized ions high and low altitudes, respectively:

$$\begin{array}{ll} \text{high collision frequency :} & \text{low collision frequency :} \\ \sigma_P \approx \frac{n_e e c}{B} \frac{1}{M_i} & \sigma_P \approx \frac{n_e e c}{B} M_i \\ \sigma_H \approx \frac{n_e e c}{B} \left(-\frac{1}{M_e^2} + \frac{1}{M_i^2} \right) & \sigma_H \approx \frac{n_e e c}{B} (M_e^2 - M_i^2) \end{array}$$

For \mathbf{E} as specified in the Activity:

$$\mathbf{E} \equiv \begin{pmatrix} 0 \\ E \\ 0 \end{pmatrix} \quad (\text{xi})$$

so that,:

$$\begin{array}{ll} \text{high (to first order) :} & \text{low :} \\ \mathbf{j} \approx \begin{pmatrix} 0 \\ \frac{1}{M_i} \\ 0 \end{pmatrix} \parallel \mathbf{E} & \mathbf{j} \approx \begin{pmatrix} +M_e^2 - M_i^2 \\ M_i \\ 0 \end{pmatrix} \end{array}$$

where the righthand result shows \mathbf{j} rotated in the direction of $-\mathbf{E} \times \mathbf{B}$ assuming that $M_i > M_e$.

(b) When $\sigma_H = \sigma_P$, the current direction is horizontal at 45° from the electric field direction in the geometry specified in the Activity.

17.6 Activity 28: cgs to SI

The momentum equation in the two unit systems read:

$$\begin{array}{l} \text{cgs: } \rho \frac{\partial \mathbf{v}}{\partial t} + \rho(\mathbf{v} \cdot \nabla) \mathbf{v} = +\rho \mathbf{g} - \nabla p + \frac{1}{4\pi} (\nabla \times \mathbf{B}) \times \mathbf{B} \\ \text{SI: } \rho \frac{\partial \mathbf{v}}{\partial t} + \rho(\mathbf{v} \cdot \nabla) \mathbf{v} = +\rho \mathbf{g} - \nabla p + \frac{1}{\mu_0} (\nabla \times \mathbf{B}) \times \mathbf{B} \end{array}$$

The induction equation is the same in cgs as in SI units, as are the other equations in Table 3.3 because they either have \mathbf{B} in all terms so that the conversion factors cancel, or they have no term with \mathbf{B} and no conversion is needed.

The online NRL Plasma Formulary not only has a conversion table from cgs to SI and *vice versa*, it is full of other information on plasmas.

17.7 Activity 35: Plasma β in the Parker solar wind

(a) For a stationary state and ignoring viscosity and plasma sources/sinks (modified Eq. 3.5):

$$\rho(\mathbf{v} \cdot \nabla) \mathbf{v} = +\rho \mathbf{g} - \nabla p + \frac{1}{4\pi} (\nabla \times \mathbf{B}) \times \mathbf{B} + \dots \quad (\text{xii})$$

which for orders of magnitude reads like:

$$\mathcal{O}\left(\frac{1}{2} \rho v^2 / \ell\right) = \dots - \mathcal{O}(p/\ell) + \mathcal{O}(B^2/8\pi\ell) + \dots \quad (\text{xiii})$$

Here, the plasma- β_{gas} naturally arises from a comparison of the final two terms on the right (*cf.*, Eq. 3.24):

$$\beta_{\text{gas}} = \frac{p/\ell}{B^2/8\pi\ell} = 3.5 \cdot 10^{-15} \frac{nT}{B^2}, \quad (\text{xiv})$$

(where n is the total number density of particles, *i.e.*, ions plus electrons).

(b) Approximating the solar wind as a fully-ionized hydrogen plasma, $\beta_{\text{gas}} \approx 2.5 - 0.6$ near Earth and (with $n \approx (4600 - 1400) \text{ cm}^{-3}$ and $B \approx 0.03 \text{ G}$), $\beta_{\text{gas}} \approx 0.04 - 0.01$ at $10R_{\odot}$. That might suggest that the magnetic field is not important near Earth orbit but not quite ignorable close to the Sun. However, see (d) below.

(c) Alternatively, a plasma β_{ram} can be based on the dynamic (or ram) pressure of the flow, *i.e.* in a comparison of the term on the left with the final term on the right in Eq. (xiii):

$$\beta_{\text{ram}} = 1.1 \cdot 10^{-23} \frac{nv^2}{B^2}, \quad (\text{xv})$$

Using the same velocities (ignoring the wind's acceleration with solar distance), this yields $\beta_{\text{ram}} \approx 6 - 20$ near Earth and $\beta_{\text{ram}} \approx 0.1$ at $10R_{\odot}$, leading to the same conclusion as above. However:

(d) In Parker's initial approximation (Parker (1958)), the flow is strictly radial, and he ignores rotation. Thus $\nabla \times \mathbf{B} \equiv 0$, so there is no effect of the magnetic field: the approximation is internally consistent. In reality, the field is not ignorable, hence models such as that discussed in Section 5.4 (in which a wind can act as a magnetic brake).

The plasma β_{ram} based on the ram pressure is commonly used to assess the balance between, for example, the solar wind and a planetary magnetic field (see Sect. 5.5.5).

N.B: dimensionless numbers provide insight into the relative importance of terms, but note: you have to assess them *at a given scale* (although in this particular case, the scale length cancels out when comparing terms but that is not generally so; see, for example, Activity 51), so be careful with them in, *e.g.* turbulent spectra, such as in solar convection where a term may seem ignorable at one scale but is important nonetheless through scale couplings, and also where small scales enable large-scale evolution, as in reconnection.

17.8 Activity 37: Thin flux tube and hydrostatic equilibrium

(a) The MHD momentum equation Eq. (3.5) for a static situation reads:

$$+\rho\mathbf{g} - \nabla p + \frac{1}{4\pi}(\nabla \times \mathbf{B}) \times \mathbf{B} = 0 \quad (\text{xvi})$$

Take the dot product of that equation with $\hat{\ell}$, a unit vector anywhere along the field \mathbf{B} , and realize that the Lorentz force is strictly perpendicular to \mathbf{B} , to find;

$$\rho\mathbf{g} \cdot \hat{\ell} = \nabla p \cdot \hat{\ell}, \quad (\text{xvii})$$

which describes the hydrostatic equilibrium inside the tube.

(b) In a direction \hat{n} normal to gravity we have

$$-\nabla p \cdot \hat{n} - \frac{1}{8\pi}(\nabla B^2 \cdot \hat{n}) + \frac{1}{4\pi}((\mathbf{B} \cdot \nabla)\mathbf{B} \cdot \hat{n}) = 0. \quad (\text{xviii})$$

Because we assume a thin flux tube small compared to variations in the surrounding magnetic field, we can compare the conditions inside the magnetized tube to the unmagnetized outside (with a thin current sheet forming the transition). The final term in the above equation is approximately the same inside and outside the tube and thus cancels in the following when comparing interior i and exterior e of the tube:

$$\nabla p_i + \frac{1}{8\pi} \nabla B^2 \approx \nabla p_e, \quad (\text{xix})$$

which shows that the total pressure within the tube follows the stratification of the atmosphere around it, with the internal field strength (and thus flux tube diameter) adjusting by expansion of the tube as set by the gas pressures inside and outside the tube.

17.9 Activity 51: Mean-field induction equation

(a) Substituting and rearranging as specified in the Activity yields:

$$\begin{aligned} \frac{\partial \bar{\mathbf{B}}}{\partial t} &= \nabla \times (\bar{\mathbf{v}} \times \bar{\mathbf{B}}) - \nabla \times ((\beta + \eta) \nabla \times \bar{\mathbf{B}}) + \nabla \times (\alpha \bar{\mathbf{B}}) \\ \mathcal{O}\left(\frac{B}{\tau}\right) &= \mathcal{O}\left(\frac{vB}{\hat{\ell}}\right) - \mathcal{O}\left(\frac{(\beta + \eta)B}{\hat{\ell}^2}\right) + \mathcal{O}\left(\frac{\alpha B}{\hat{\ell}}\right) \end{aligned}$$

(b) Using the provided numbers gives: $\tau_{\text{corr}} \sim 1$ d, $\alpha \sim -0.01$ cm/s. The time scales for the three terms on the righthand side (for a characteristic length scale $\hat{\ell} = R_{\odot}$) are: $\hat{\ell}/\bar{v} \approx 4$ yr for the advection term, $\hat{\ell}^2/\beta \approx 50$ yr for the diffusive term (as $\beta \gg \eta$), and $\hat{\ell}/|\alpha| \approx 2$ yr for the growth/decay term.

17.10 Activity 53: Babcock-Leighton surface flux dispersal

(a) Start with the induction equation Eq. (3.3) assuming that the diffusion coefficient is (1) a constant and (2) describing the dispersal by random convective motions, so here represented by β from Eq. (4.16):

$$\frac{\partial \mathbf{B}}{\partial t} = \nabla \times (\mathbf{v} \times \mathbf{B}) - \beta \nabla \times (\nabla \times \mathbf{B}). \quad (\text{xx})$$

Using vector identities and the divergence-free nature of the magnetic field we can use

$$\nabla \times (\mathbf{v} \times \mathbf{B}) = -\mathbf{B}(\nabla \cdot \mathbf{v}) + (\mathbf{B} \cdot \nabla) \mathbf{v} - (\mathbf{v} \cdot \nabla) \mathbf{B}, \quad (\text{xxi})$$

and

$$\nabla \times (\nabla \times \mathbf{B}) = -\nabla^2 \mathbf{B}. \quad (\text{xxii})$$

Substituting these final two into Eq. (xx) and regrouping yields:

$$\frac{\partial \mathbf{B}}{\partial t} + (\mathbf{v} \cdot \nabla) \mathbf{B} = -\mathbf{B}(\nabla \cdot \mathbf{v}) + \beta \nabla^2 \mathbf{B} + (\mathbf{B} \cdot \nabla) \mathbf{v}. \quad (\text{xxiii})$$

Reading from the very left side, the first three terms are analogous to the continuity equation for the scalar density in Eq. (3.4), and the next term reflects the diffusive nature of the (super-)granular motions. For a purely radial field moving in strictly horizontal flows, the final term disappears, and then Eq. (xxiii) becomes a diffusion equation for the scalar quantity B reflecting the purely radial field.

(b) The characteristic time scale for flux to diffuse over the solar surface is $R_{\odot}^2/\beta \approx 60$ yr. That is significantly longer than the solar cycle, which puzzled the early researchers of this mechanism because, at the time, the slow meridional advection had not yet been discovered. But its time scale of $R_{\odot}/v_{\theta} \approx 20$ yr for a flow that peaks around 10 m/s. Together, the large-scale advection and the diffusive dispersal can result in a 22-year cycle period (see Sheeley, 2005 for a historical review of the flux-transport mechanism).

17.11 Activity 64: Solar surface to heliosphere: PFSS

On part (a): What does the streamer belt look like in source-surface models for the Sun?

A figure like that which you were asked to draw is shown in Fig. 17.1. The top panel (with equal charges apart from their sign or polarity) gives the impression that each bipolar area (such as active regions on the Sun) is associated with a helmet touching on the plane of symmetry but that is not true in general; the bottom panel has some larger monopoles on either side (like the polar caps on the Sun around solar cycle minimum) which results in an overarching field because of the large dipole moment involved (larger charge and longer base). That field 'caps' some of the potential 'helmets' underneath.

Additional question: from *Wikipedia* (2022/08/01): "Helmet streamers are bright loop-like structures which develop over active regions on the Sun." Is the Wikipedia entry correct? NO! "... the most prominent white-light features (i.e., the bright streamer stalks) occur at those longitudes where the latitude of the plasma sheet reaches a local maximum or minimum $d\lambda/d\phi \approx 0$; when these "stationary points" are located close to the sky plane, the sheet is viewed edge-on, and the number of scatterers in the line of sight is greatest." (From Wang *et al.* (2000)).

Look at Fig. 5.7 for a 3D representation of model PFSS extrapolations and compare that to what you have learned from your drawing and Fig. 5.7.

On part (b): Simplifications: (1) only one pair of mirror charges needs to be considered: if the field is radial on some sphere for that pair, than any other similar pair added will conserve that property; (2) we can look at this in the (x, y) plane and can rotate the charges to lie on the x axis; (3) we can think of this as a problem in electrostatics (which allows monopoles but the magnetic Sun does not). And we can simplify it to a 2d analysis here because of points (1) and (2) above.

The field of a point charge of charge q at \mathbf{r}_i is given by:

$$\mathbf{E}_i = q_i \frac{\mathbf{r} - \mathbf{r}_i}{|\mathbf{r} - \mathbf{r}_i|^3}. \quad (\text{xxiv})$$

Let charges 1 and 2 be located at $(1, 0)$ and $(\alpha, 0)$, respectively.

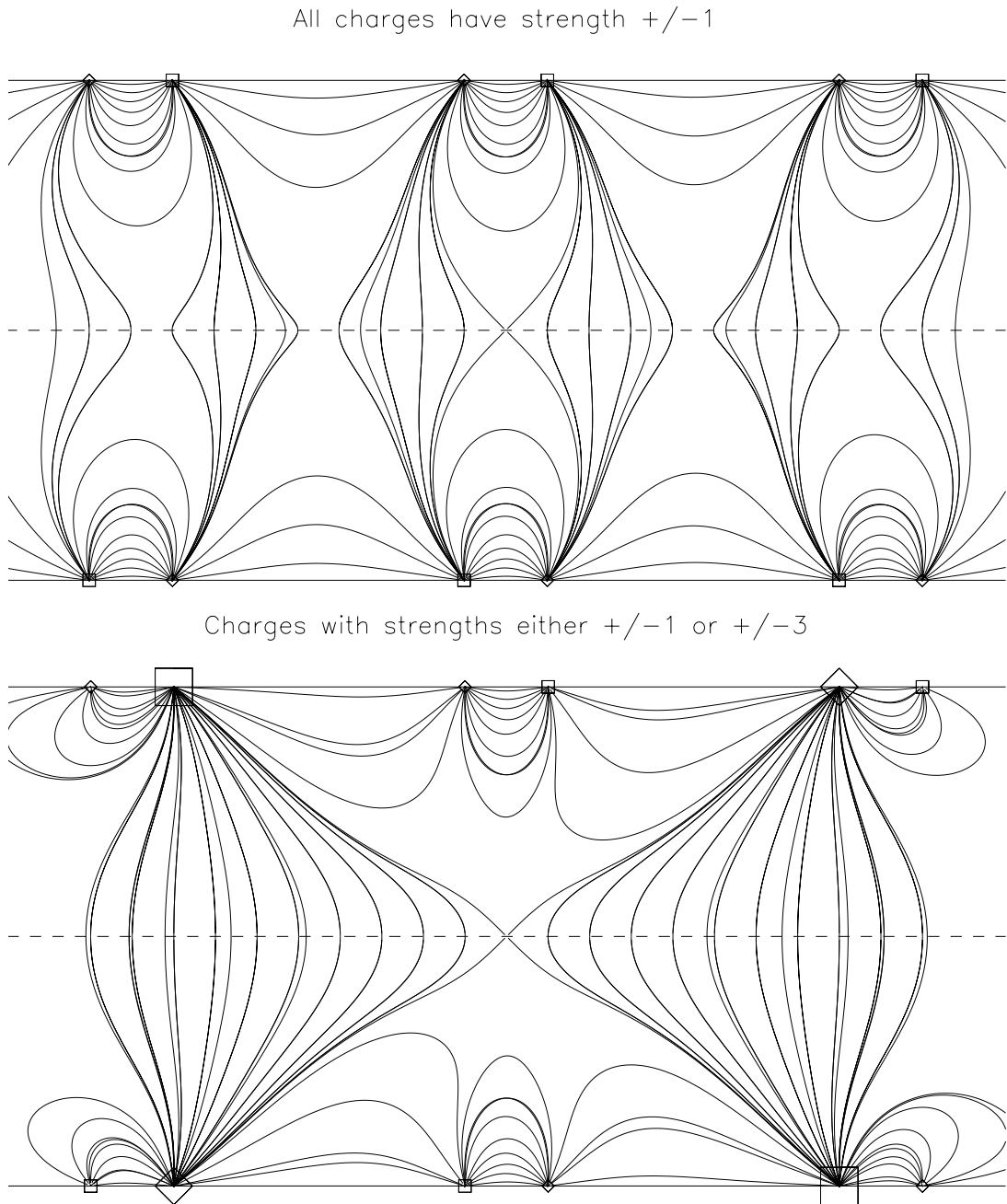


Figure 17.1: Concept of mirror charges in a potential field of mixed-polarity monopoles leading to nulls and 'helmets.' The size of the charge symbols reflects their strength: equal in the top panel and with a few larger ones in the bottom panel. The dashed line, centered between the charges and their mirror charges, is where the field is strictly vertical everywhere or null as in the X points. In the analogy with the spherical PFSS model for the coronal base of the heliospheric field (in which, by definition for a potential field, there are no currents), the portion below the dashed line is equivalent to the coronal domain while above it the field is assumed to be fully radial (while spiraling outward further away for a rotating star).

The requirement that the field becomes radial at a distance r_{SS} from the origin can be expressed as the requirement that the vector field anywhere on that circle is normal to the tangent to that circle. For a vector and its unit-length normal

$$\mathbf{r} = \begin{pmatrix} r \cos \theta \\ r \sin \theta \end{pmatrix}; \hat{\mathbf{r}}_{\perp} = \begin{pmatrix} \sin \theta \\ -\cos \theta \end{pmatrix} \quad (\text{xxv})$$

this translates to the requirement that

$$(\mathbf{E}_1(\mathbf{r}) + \mathbf{E}_2(\mathbf{r})) \cdot \hat{\mathbf{r}}_{\perp} = 0. \quad (\text{xxvi})$$

Use a unit radius for the Sun and a TBD radius α for the mirror surface and put the charges at $(1, 0)$ and $(\alpha, 0)$. Then, working through the math, you end up with:

$$(\alpha^2 + 2\alpha r \cos \theta + r^2)^{3/2} q_1 + (r^2 + 2r \cos \theta + 1)^{3/2} \alpha q_2 = 0, \quad (\text{xxvii})$$

which holds true at any θ for $r_{\text{SS}} = \sqrt{\alpha}$ and $q_2 = -\sqrt{\alpha} q_1$. So, for a source surface radius (where the field becomes radial – sorry for the confusing term here!) at $r_{\text{SS}} = 2.5R_{\odot}$, the mirror charges need to be placed at $6.25R_{\odot}$ and be of strength -2.5 times the surface charges.

N.B. An alternative (equivalent) approach is to quantify the fact that a surface that is normal to a field anywhere on it is an equipotential surface.

Insights: (1) the model naturally explains the formation of streamer cusps (see Fig. 5.7); (2) below the source surface, the expansion of the magnetic field can be sub-radial or super-radial (which is an important factor in determining wind speed). But: the PFSS model does not describe field dynamics, and by definition there are no currents within the PFSS field.

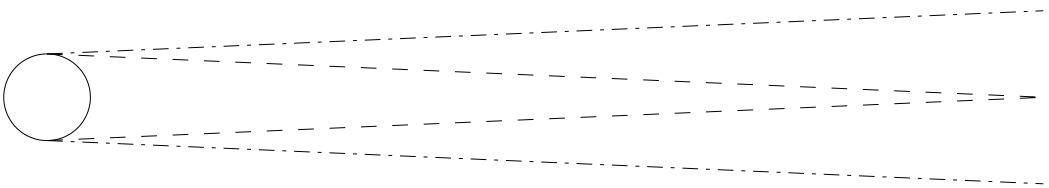


Figure 17.2: Sketch of a solar-wind wake behind the non-conducting Moon. The refilling of the wake is outlined by the dashed lines, the expansion of the rarefaction front by the dashed-dotted lines.

17.12 Activity 66: Solar wind behind a non-conducting body

The wake behind the Moon (see Fig. 17.2) is filled at the slow mode speed $\min(v_A, c_s)$ while the rarefaction front moving outward from the object moves at a speed dependent on the direction relative to the magnetic field: perturbations along the field move at

$\max(v_A, c_s)$ while those perpendicular to the field move at $(v_A^2 + c_s^2)^{1/2}$ (see Sect. 3.3). For typical slow solar wind conditions around the Moon taken from Table 2.4 (using the ion temperature), using expressions from Table 18.2, we have $v_A = 30$ km/s and $c_s = 18$ km/s (ignoring γ here), giving us parallel and perpendicular fast-mode and slow-mode velocities of $v_{\text{fm},\parallel} = 30$ km/s, $v_{\text{fm},\perp} = 35$ km/s and $v_{\text{sm}} = 18$ km/s, respectively.

With these numbers, the wake behind the Moon should disappear at a distance of $v_{\text{sw}}/v_{\text{sm}} \approx 20$ lunar radii (with an opening angle at the top of $2 * \text{atan}(v_{\text{sm}}/v_{\text{sw}}) \sim 4.8$ degrees (dashed lines in Fig. 17.2), while the rarefaction front should move away from the edge of the Moon at angles of $\text{atan}(v_{\text{fm},\parallel}/v_{\text{sw}}) \sim 4.0$ degrees and $\text{atan}(v_{\text{fm},\perp}/v_{\text{sw}}) \sim 4.7$ degrees, respectively (dashed-dotted lines in Fig. 17.2).

See, *e.g.*, Zhang *et al.* (2014) for observations and MHD simulations of the lunar wake.

17.13 Activity 69: Temperature at the wind stagnation point

If we approximate the solar wind as a fully-ionized hydrogen gas and ignore the relatively small amount of kinetic energy in the electrons, then from energy conservation it follows that once the solar wind has come to a standstill at the stagnation point just outside the terrestrial magnetopause, and after sufficient collisional interactions in the dense setting there, its temperature is approximately given by the energy comparison per hydrogen ion:

$$T_{\text{sp}} = \frac{1}{4} \frac{m_{\text{H}}}{k} v_{\text{sw}}^2 + T_{\text{sw}}. \quad (\text{xxviii})$$

With $T_{\text{sw}} \approx 2.4 \cdot 10^5$ K for the characteristic ion temperature of the fast solar wind (Table 2.4) at $v_{\text{sw}} = 800$ km/s, we find $T_{\text{sp}} \sim 20$ MK.

This approximation ignores the fact that the electron and ion temperatures are not the same in the solar wind and also that the parallel and perpendicular temperatures are the same. We can make the point, however, that this should not matter much in estimating T_{sp} because it is clear from the magnitude of the terms on the righthand side of Eq (xxviii) that the wind's thermal energy is small compared to its bulk kinetic energy. What matters more is that we are not dealing with a pure hydrogen plasma: helium adds extra mass and extra electrons. We could make the approximation for T_{sp} a little better by taking that into account.

With the fractional hydrogen abundance $X = 0.73$, helium abundance $Y = 0.26$, and ignoring heavier elements, again assuming a fully-ionized plasma, and ignoring the thermal energy in the wind, Eq (xxviii) transforms to:

$$T_{\text{sp}} = \frac{1}{2} \frac{m_{\text{H}}}{k} v_{\text{sw}}^2 \left(\frac{1 + Y/X}{2 + 3Y/X} \right), \quad (\text{xxix})$$

from which, again for the fast solar wind as above, $T_{\text{sp}} \sim 15$ MK.

This looks perhaps unexpected: T_{sp} is substantially larger than the temperature of the corona from which the energy is drawn, but there is a conversion step that occurs

in the solar wind – thermal energy to work by expansion and additional conducted thermal energy to thermal energy – that makes this possible.

17.14 Activity 70: Magnetopause distances

(a) The magnetopause distance is determined (see Sect. 5.5.5) primarily by the requirement that the total pressure (plasma plus magnetic) must have the same value on both sides of the discontinuity. At the Chapman-Ferraro distance of Eq. (5.22), the linear momentum flux density (or dynamic pressure) in the undisturbed solar wind, $\rho_{\text{sw}} v_{\text{sw}}^2$, at the sub-solar region equals the interior magnetic pressure of the dipole field, $B(r) = (1/8\pi)(\mu_{\text{p}}/r^3)^2$ with $\mu_{\text{p}} = B_{\text{p}} R_{\text{p}}^3$ the magnetic dipole moment of the planet with equatorial field B_{p} and radius R_{p} , with an extra factor $\xi \simeq 2$ to roughly correct for the added field from magnetopause currents:

$$R_{\text{CF}} \approx R_{\text{p}} \left(\frac{B_{\text{p}}^2}{2\pi \rho_{\text{sw}} v_{\text{sw}}^2} \right)^{1/6} = 1.7 \cdot 10^{10} \frac{R_{\text{p}}}{R_{\oplus}} \left(\frac{B_{\text{p}}^2}{n_{\text{sw}}} \right)^{1/6}, \quad (\text{xxx})$$

where the solar wind speed has been set to 400 km/s in the righthand expression.

Note the weak dependence on n_{sw} : $1000^{1/6} \approx 3$.

With data from Tables 5.2 and 5.3:

Planet	B_{p} (G)	n_{sw} (cm^{-3})	R_{p}/R_{\oplus}	$R_{\text{CF}}/R_{\text{p}}$	R_{CF} (cm)
Earth	0.3	7.	1	9	$6.3 \cdot 10^9$
Jupiter	4.3	0.2	11.2	43	$3.1 \cdot 10^{11}$
Saturn	0.21	0.07	9.4	19	$1.1 \cdot 10^{11}$
Uranus	0.23	0.02	4.0	24	$6.1 \cdot 10^{10}$
Neptune	0.14	0.006	3.9	24	$6.2 \cdot 10^{10}$

N.B This does it not work well for Jupiter (and also Saturn): $R_{\text{CF},\text{Jup}}$ is some 43 planetary radii but the observed magnetosphere is 50 – 100 planetary radii, and it also varies substantially with changing solar wind parameters. For the size difference, see Fig. 5.13 and its discussion. On the size variability, Fran Bagenal in [HI:13.2.2] writes: “This greater compressibility of the jovian magnetosphere is due to a significant contribution of the plasma pressure in the equatorial plasma sheet as well as a substantial system of azimuthal currents that weaken the radial gradient of the magnetic field compared to a dipole.”

(b) For orbital radii d_{orb} around their planet, we have $r \equiv R_{\text{CF}}/d_{\text{orb}} \approx 0.16$ for Earth’s Moon, $r = 4.6$ for Enceladus, and $r = 0.9$ for Titan. Consequently, Earth’s Moon is always outside the magnetosphere except when it crosses Earth’s geotail, Enceladus is always well inside the magnetosphere, and Titan can be in or out depending on the solar wind conditions.

17.15 Activity 85: Coronal loop cooling time scales

(a) The EUV and X-ray emissions from the solar corona are dominated by de-excitation from electron-ion collisions (line emission) with a weak contribution from

free-free emission, both of which scale with $n_e n_i$ (for a given spectral line, you have to bear in mind that n_i refers to the density of the corresponding ion so that the ionization balance comes into the line strength; here, however, we look at the total energy loss from the plasma for which $n_r \propto n_e$).

(b) The radiative cooling time scales as the ratio of the thermal energy content of the plasma to the rate of energy loss, so:

$$\tau_{\text{rad}} \propto \frac{nT}{n^2 P(T)} \propto \frac{T^{5/3}}{n} \propto \frac{L}{T^{1/3}}, \quad (\text{xxxix})$$

where the final expression results by introducing the scaling law Eq. (9.4), which you will encounter in Ch. 9, to eliminate n .

The conductive time scale for a loop with a length scale L and with constant cross section scales as the ratio on the thermal energy content of the plasma to the order-of-magnitude estimate of the rate of heat conduction (based on the central term on the righthand side of Eq. 9.3):

$$\tau_{\text{cond}} \propto \frac{nT}{\frac{T^{7/2}}{L^2}} = \frac{nL^2}{T^{5/2}} \propto \frac{L}{T^{1/2}}, \quad (\text{xxxixii})$$

again using Eq. (9.4) for the final expression.

For plasma at 1 MK and 5 MK, respectively, $\tau_{\text{rad}}(1 \text{ MK})/\tau_{\text{rad}}(5 \text{ MK}) \approx 1.7$ and $\tau_{\text{cond}}(1 \text{ MK})/\tau_{\text{cond}}(5 \text{ MK}) \approx 2.2$. The latter shows a somewhat larger contrast because of the steep dependence of electron conduction on the thermal gradient.

17.16 Activity 92: Magnetic braking of the Sun

The typical slow solar wind carries a kinetic energy flux density from the Sun given by

$$F_{\text{kin,sw}} = \frac{1}{2} n_{\text{sw},\oplus} m_{\text{H}} v_{\text{sw},\oplus}^3 \frac{d_{\oplus}^2}{R_{\odot}^2} = 3 \cdot 10^4 \text{ erg/cm}^2/\text{s} \approx \frac{1}{3} F_{\text{corona}}, \quad (\text{xxxixiii})$$

with \oplus denoting values at Earth.

Approximating the field as radial (so that it scales as $1/r^2$, as does the solar wind density), and the solar wind speed as constant within the distance d_{\oplus} to the Earth, the Alfvén radius is found by equating the solar wind speed to the Alfvén speed, yielding for the slow solar wind, using values for wind density and speed at Earth:

$$r_{\text{A}} \approx \frac{B_{\oplus} d_{\oplus}}{(4\pi n_{\oplus} m_{\text{H}})^{1/2} v_{\text{sw}}} \approx 20 R_{\odot}. \quad (\text{xxxixiv})$$

The time scale for angular momentum loss for the present-day Sun through the solar wind (using numbers for the slow wind in the quantitative estimates) is, with Eq. (7.1), given by:

$$\tau_{\text{J}} = \frac{J}{|\dot{J}|} = \frac{3I}{8\pi r_{\text{A}}^2 n_{\oplus} m_{\text{H}} v_{\text{sw}}^3} = \frac{24\pi I v_{\text{sw}}}{\Phi_{\text{open}}^2} \approx 3 \cdot 10^{17} \text{ s} \approx 10^{10} \text{ yr}, \quad (\text{xxxixv})$$

where the final expression with symbols shows the dependence on solar wind speed and the level of solar activity expressed as function of the open flux Φ_{open} in the heliosphere.

17.17 Activity 94: Tidal breakup

(a) In order for an object to be pulled apart by tidal forces, the gradient of the gravitational pull of the central object (with mass M at a distance d) across the object (with mass m and radius R) has to exceed that object's own gravitational pull, *i.e.*,

$$\frac{GM}{(d-R)^2} - \frac{GM}{d^2} > \frac{Gm}{R^2}. \quad (\text{xxxvi})$$

With first-order Taylor expansion for $d \gg R$ and resorting of terms:

$$d_{\text{breakup}} = \left(\frac{2M}{m}\right)^{1/3} R. \quad (\text{xxxvii})$$

For the Earth, with $m = 6 \cdot 10^{27}$ g, $R = 6.4 \cdot 10^8$ cm, and $M = M_{\odot} = 2 \cdot 10^{33}$ g: $d_{\text{breakup}} = 6 \cdot 10^{10}$ cm or 0.0035 AU.

(b) For an object like comet 67P: $d_{\text{breakup}} = 0.015$ AU or $3R_{\odot}$.

Note: With this simplest of descriptions, for a 1.5 km diameter comet with a density of some 0.4 g/cm^3 , the breakup distance for an approach to Jupiter is estimated as $d_{\text{breakup}} = 1.3 \cdot 10^{10}$ cm or 1.8 Jupiter radii. For a detailed study of the 1992 breakup of comet Shoemaker-Levy 9 on its approach of Jupiter to 1.33 planetary radii, see [Movshovitz *et al.* \(2012\)](#).

17.18 Activity 105: Drift velocity

(a) Given the specifications in the Activity, the magnitude of the gradient drift can be expressed as

$$|v_{G,\perp}(r)| = \frac{cW_{\perp}}{qB} \frac{3}{r} = \frac{3cW_{\perp}}{qB_e r_p} \left(\frac{r}{r_p}\right)^2. \quad (\text{xxxviii})$$

For Earth, $|v_{G,\oplus}(2R_{\oplus})| \approx 3 \text{ km/s}$ and $|v_{G,\oplus}(10R_{\oplus})| \approx 80 \text{ km/s}$ (with an orbital period of $P_{G,\oplus}(10R_{\oplus}) = 5 \text{ ks}$). For Mercury, $|v_{G,\text{Merc}}(2R_{\text{Merc}})| \approx 8 \text{ km/s}$ and $|v_{G,\text{Merc}}(10R_{\text{Merc}})| \approx 200 \text{ km/s}$ (with an orbital period of $P_{G,\text{Merc}}(10R_{\text{Merc}}) \approx 0.7 \text{ ks}$).

For Jupiter, $|v_{G,\text{Jup}}(2R_{\text{Merc}})| \approx 0.02 \text{ km/s}$ and $|v_{G,\text{Jup}}(10R_{\text{Merc}})| \approx 0.5 \text{ km/s}$ (with an orbital period of $P_{G,\text{Jup}}(10R_{\text{Jup}}) \approx 100 \text{ d}$).

(b) Relativistic energies for ions and electrons are in the range of 100 MeV and 100 keV, so the non-relativistic approximation is warranted at 50 keV.

(c) Except for the direction of the drift, the results are the same for electrons because there is no mass dependence in $v_G(r)$.

17.19 Activity 107: SEP paths and scattering

(1a,b) The earliest-arriving solar energetic particles have undergone little if any scattering. The particles' energy yields a velocity, and with the known Sun-Earth distance, that might be seen to suffice to derive an estimated time for the explosive event. BUT: particles follow the Parker spiral, the tightness of which depends on the history of the solar wind speed. So instead of working with a single timing, we can use

the difference Δt of two arrival times $t_{1,2}$ and energies $E_{1,2}$ to determine both event time t_0 and path length ℓ (which is the same for these particles), from which:

$$\ell = \Delta t / (v_2^{-1} - v_1^{-1}) ; t_0 = t_1 - (\ell / v_1). \quad (\text{xxxix})$$

Looking at the first arrivals at 0.3 MeV/n ($v_1 \approx 7500$ km/s for protons) in Fig. 8.4 we see $t_1 \approx 15$ UT, while at 0.04 MeV (with $v_2 \approx 2800$ km/s for protons) we estimate $t_2 \approx 01$ UT on the next day. With $\Delta t \approx 3.6 \cdot 10^4$ s, $\ell \approx 160 \cdot 10^6$ km, as expected somewhat longer than the distance from the solar surface to the Earth: $149.6 - 0.7$ km. From this: t_0 should be about 6 h prior to t_1 so 1999/01/09 9 UT.

(2) Differentiating Eq. (8.27) for t yields:

$$\frac{\partial f(x, t)}{\partial t} = \frac{1}{2t} f(x, t) \left(\frac{x^2}{2\kappa t} - 1 \right), \quad (\text{xli})$$

which has an extremum at $\kappa = x^2 / (2t)$. The estimated peak time in particle density at 0.04 MeV/n is 1999/01/10 4 UT, some 19 h after the estimated event time, so that $\kappa \sim 1.9 \cdot 10^{21}$ cm²/s.

17.20 Activity 112: Setting the scale of granulation

Based on the text in [III:5.2.1]: Consider a single convection cell, or granule, with an upflow region surrounded by narrow downflow lanes. The vertical velocity at its center v_z must be large enough to balance the radiative losses at the surface. The convective enthalpy flux just under the photosphere is dominated by the latent heat flux associated with hydrogen ionization so to get an idea for what v_z is needed we can set

$$\rho N_A v_z y \chi_H = \sigma T^4, \quad (\text{xlii})$$

where y is the ionization fraction, N_A is Avogadro's number, χ_H is the ionization energy for hydrogen, σ is the Stefan-Boltzmann constant, and ρ and T are the density and temperature. For photospheric conditions ($y \sim 0.1$, $T \sim 5800$ K, $\rho \sim 2 \times 10^{-7}$ g/cm³), this gives a minimum vertical velocity v_z of about 2 km s⁻¹.

With this we can estimate the maximum horizontal size L of granules from mass conservation. If a granule simply overturns without altering the local density appreciably, then the continuity equation implies

$$L \sim D v_h / v_z, \quad (\text{xliii})$$

where D is the vertical scale and v_h is the horizontal velocity (assuming a cylindrical geometry with upflow in the center and downflow around the periphery adds a factor of 1/2). The pressure-driven horizontal flows are unlikely to exceed the sound speed $c_s \sim 10$ km s⁻¹, so with v_z from Eq.(xliii) and $D \sim H_p \sim 400$ km, we find that the horizontal scale of granules should not exceed about 1-2 Mm.

17.21 Activity 113: Acoustic cutoff

(a) In an isothermal, gravitationally stratified atmosphere, a wave at the acoustic cutoff frequency propagates over a distance of $c_s/\omega_a = 2H_p$ within one period, which means that it is moving almost the entire mass in the atmosphere above. Consequently, there is no substantial force to counter the expansion of the wave, so no restoring pressure force, only the gravitational force of the lifted atmosphere above, so the wave cannot propagate (but is evanescent) and is reflected. In the Sun, with $H_p(z)$ a function of z as the temperature drops outward (up to a near-photospheric temperature minimum below the chromosphere) waves with frequencies below ω_a for around (roughly) the temperature minimum are reflected and can form resonant standing (p -mode) waves within the Sun, while waves at higher frequencies can propagate out of the solar interior.

(b) For the solar photosphere and an ideal mono-atomic gas with $\gamma = 5/3$:

$$\omega_{a,\odot} = \frac{c_s}{2H_p} = \frac{\gamma g_\odot}{2c_s} = 0.02 \text{ s}^{-1}, \quad (\text{xliii})$$

with an acoustic cutoff period of $P_a = 2\pi/\omega_a \approx 5 \text{ min}$. Oscillations at lower frequencies are trapped, while higher-frequency ones can reach into the chromosphere. For comparison, the acoustic cutoff period for the actual non-isothermal solar photosphere is about 200 s (Jiménez *et al.*, 2011).

(c) Now, let us look at the idealized situation from the Activity. Using that the background is stationary ($v_0 = 0$) and hydrostatically stratified:

$$\rho_0 g = -\frac{\partial p_0}{\partial z} \rightarrow \rho_0(z) = \rho_b e^{-\frac{z}{H_p}} \quad (\text{xliv})$$

the linearized continuity and momentum equations are:

$$\frac{\partial \rho_1}{\partial t} = -\rho_0 \frac{\partial v_1}{\partial z} - v_1 \frac{\partial \rho_0}{\partial z} = -\rho_0 \frac{\partial v_1}{\partial z} + \frac{\rho_0 v_1}{H_p}, \quad (\text{xlv})$$

$$\rho_0 \frac{\partial v_1}{\partial t} = -g \rho_1 - c_s^2 \frac{\partial \rho_1}{\partial z}, \quad (\text{xlvi})$$

because with $\gamma = 1$ (for isothermal perturbations) $\rho_1 = c_s^2 p_1$.

Taking the time derivative of the linearized momentum equation and substituting the linearized continuity equation leads to:

$$\frac{\partial^2 v_1}{\partial t^2} - c_s^2 \frac{\partial^2 v_1}{\partial z^2} = -g \frac{\partial v_1}{\partial z}. \quad (\text{xlvii})$$

Because in this non-dissipative scenario the kinetic energy in the wave is a conserved quantity, we can anticipate a solution that scales like

$$v_1 = u e^{z/2H_p} \quad (\text{xlviii})$$

so that $\rho_0 \langle v_1^2 \rangle$ is independent of z . Combining these last two equations leads to:

$$\frac{\partial^2 u}{\partial t^2} - c_s^2 \frac{\partial^2 u}{\partial z^2} = -\frac{c_s^2}{4H_p^2} u. \quad (\text{xlix})$$

With $u = u_0 \exp(-i(kz - \omega t))$ this yields the dispersion relationship

$$c_s^2 k^2 = \omega^2 - \omega_a^2, \quad (\text{i})$$

which has propagating solutions only for $\omega > \omega_a$.

17.22 Activity 115: Optical depth and field strength

Eq. (2.19) discussed the optical depth, τ , in terms of incoming radiation, but it is equally valid of course for outgoing radiation and it can help establish the column depth of a stellar photosphere. Looking at it for light propagating vertically through an isothermal atmosphere, we thus have:

$$\tau = \sigma_a n(h) H_p, \quad (\text{li})$$

where the product of the number density $n(h)$ at height h with the scale height $H_p = kT/mg$ at that level represents the integrated content of an isothermal stratified column of gas above that point. If we focus on the lower main sequence, then (approximating data in Eker *et al.* (2018) in their Fig. 6 (top) below 1.2 solar masses):

$$\frac{R_*}{R_\odot} \approx \frac{M_*}{M_\odot}. \quad (\text{lii})$$

Consequently, at $\tau \approx 1$ and with $p \propto nT$ we have

$$p \propto \frac{1}{M_*}. \quad (\text{liii})$$

For a maximally evacuated flux tube the external gas pressure balances the internal magnetic pressure so that $p \approx B^2/8\pi$ and therefore

$$B \propto \frac{1}{M_*^{1/2}}. \quad (\text{liv})$$

For stellar masses of $1.7 M_\odot$ at F0 and $0.6 M_\odot$ at late-K, and with a field strength of some 2 kG for the Sun, we can estimate 1.5 kG for F0 V stars and 2.6 kG for late-K MS stars. That is not quite the contrast supported by observations (from about 1.4 kG to 3.2 kG), but then opacities depend on density and temperature (increasing with both for near-photospheric conditions), and atmospheres are neither isothermal nor plane parallel.

17.23 Activity 121: Properties of coronal loops

(a,b,c) Quiet-Sun, mixed-polarity area: $B = 5 \text{ G}$, $T = 1 \text{ MK}$, $L = 4 \cdot 10^9 \text{ cm}$:
 $\epsilon_{\text{heat}} \approx 6 \cdot 10^{-5} \text{ erg/cm}^2/\text{s}$, $n_e \approx 3 \cdot 10^8 \text{ cm}^{-2}$, $e \approx 0.1 \text{ erg/cm}^3$,
 $r_{\text{gi}} = 200 \text{ cm}$, $c_s = 30 \text{ km/s}$, $\beta \approx 0.1$, and loop crossing time $L/c_s \approx 1300 \text{ s}$.

Active region: $B = 100 \text{ G}$, $T = 3 \text{ MK}$, $L = 15 \cdot 10^9 \text{ cm}$:
 $\epsilon_{\text{heat}} \approx 2 \cdot 10^{-4} \text{ erg/cm}^2/\text{s}$, $n_e \approx 8 \cdot 10^8 \text{ cm}^{-2}$, $e \approx 1. \text{ erg/cm}^3$,
 $r_{\text{gi}} = 16 \text{ cm}$, $c_s = 160 \text{ km/s}$, $\beta \approx 0.002$, and loop crossing time $L/c_s \approx 500 \text{ s}$.

(d) The values of the ion gyroradii are very small compared to the loop length, the plasma β substantially below unity, and the loop crossing times of pressure perturbations shorter (although marginally for the quiet Sun) than the cooling and heating time scales of the loops (which should equal, on average, e/ϵ_{heat} for a quasi-equilibrium state). So the concept of an isolated quasi-stationary loop is warranted for the corona, provided that heating occurs fairly steadily (or in sufficiently small and frequent events).

17.24 Activity 126: Least-massive post-main-sequence star

For a star of $1M_{\odot}$ it takes 10.4 Gyr to turn substantially off the main sequence (marked by the squares in Fig. 10.1). For the next less-massive star in the table in that figure at $0.8M_{\odot}$ it takes already 24 Gyr, so given the age of the Universe of some 13.8 Gyr, the least-massive post-main-sequence star cannot be substantially lighter than some $0.95M_{\odot}$.

When star formation started after the Big Bang is an active field of study. The analysis by Xiang and Rix (2022) suggests that in our own Galaxy it started some 13 Gyr ago, only 800 Myr after the Big Bang. These authors searched for stars in the subgiant phase, just beyond the main-sequence turnoff: these are good markers to study stellar ages because that phase is relatively brief thus narrowing the uncertainty interval. But because they are short-lived, a large sampling of stars with known distances is required to build up a sufficiently-large sample. Fortunately, the Gaia astrometry mission combined with the LAMOST spectroscopy survey provided such a view of the Galaxy, which was then combined with model isochrones. Spectroscopy showed that that first phase of Galactic thick-disk and halo star formation continued for some 5 to 6 Gyr during which the interstellar medium (ISM) out of which these stars formed was enriched with heavier elements (by well over an order of magnitude for Fe, for example).

17.25 Activity 138: Earth masses in the Sun-forming cloud

(a) One source of solar-system elemental abundances is Lodders (2019) who lists these in her Table 8. A mass-weighted sum of the abundances for all elements truncating at no. 92) compared to that for elements heavier than B yields the requested mass fraction for elements N and heavier (for elements i with abundance A_i and atomic mass m_i):

$$f_N = \frac{\sum_6^{92} A_i m_i}{\sum_1^{92} A_i m_i} \approx 0.007. \quad (\text{lv})$$

With these abundances, the number of Earth masses of elements heavier than C contained in a solar-mass cloud is given by:

$$n_{\odot} = \frac{f_N * M_{\odot}}{M_{\oplus}} \sim 2000. \quad (\text{lvi})$$

(b) The fraction f_{pl} of the original cloud that would need to remain in the disk to

ultimately form the planets is given by the sum of the masses of all planets relative to that of the Sun: $f_{\text{pl}} = 0.0013$.

(c) These two numbers, f_N and f_{pl} , are largely independent of each other because the giant planets are predominantly made up of H and He.

17.26 Activity 140: The Jeans Mass

(a) With

$$M_* = \frac{4}{3}\pi R_c^3 \mu m_p n_c, \quad (\text{lvii})$$

the radius can be eliminated from Eq. (2.15) so that the limiting mass can be expressed as

$$M_* \approx \left(\frac{3}{4\pi}\right)^{1/2} \left(\frac{k}{G}\right)^{3/2} \left(\frac{1}{\mu m_p}\right)^2 \frac{T_c^{3/2}}{n_c^{1/2}} = 8.2 M_\odot \frac{T_c^{3/2}}{\mu^2 n_c^{1/2}}. \quad (\text{lviii})$$

(b) For molecular hydrogen, with $\mu = 2$, that means that $f \approx 2$.

(c) At 10 K and with $n = 10^2 \text{ cm}^{-3}$ we have $M_* \approx 7M_\odot$. At 100 K and with $n = 10^4$ we have $M_* \approx 20M_\odot$.

17.27 Activity 174: Molecular diffusion coefficients

A diffusion coefficient, measuring the rms displacement per unit time, scales as the product of the mean free path length $\hat{\ell}$ and the characteristic velocity \hat{v} :

$$D \sim \frac{\hat{\ell}^2}{\hat{\tau}} = \hat{\ell}\hat{v}, \quad (\text{lix})$$

with \hat{v} the characteristic time between collisions. With

$$\hat{\ell} = \frac{1}{\sigma n} \quad \text{and} \quad kT = \frac{1}{2}mv_{\text{th}}^2, \quad (\text{lx})$$

we have

$$D \sim \left(\frac{2kT}{\mu}\right)^{1/2} \frac{1}{\sigma n} \propto \frac{\sqrt{T}}{\sqrt{mn}} \quad (\text{lxi})$$

17.28 Activity 186: Earth's magnetopause distance over time

(a) Combining the various approximation leads to

$$\frac{R_{\text{mp}}(t)}{R_p} \approx \frac{(\xi B_p)^{1/3}}{(8\pi m_H n_* v_*^2)^{1/6}} \left(1 + \frac{t}{\tau_{\text{sw}}}\right)^{0.38}. \quad (\text{lxii})$$

(b) With $\xi = 2$ and $B_p = 0.31 \text{ G}$ as for the present-day Earth:

$$\frac{R_{\text{mp}}(t)}{R_\oplus} \approx 1.25 \quad t < \tau_{\text{sw}} \quad \frac{R_{\text{mp}}(t)}{R_\oplus} \approx 5t_{\text{Gyr}}^{0.38} \quad t \gg \tau_{\text{sw}}$$

17.29 Activity 189: ^{10}Be production on a hypothetical Mars

Read Fig. 14.3 down to a zero geomagnetic field and compare the result with that for the present-day Earth.

17.30 Activity 193: Exposure to supernovae

(a,b) Combination of the scalings provided in the Activity yields an approximate main-sequence life time τ_* for stars of mass M_*

$$\tau_*(M_*/M_\odot) \sim 10^{10}(M_*/M_\odot)^{-5/2} \text{ yr}, \quad (\text{lxiii})$$

(which is only some 10% below the full life time) which gives

$$\tau_*(100) \sim 10^5 \text{ yr}, \tau_*(8) = \tau_{\odot\text{SN}} \sim 6 \cdot 10^7 \text{ yr}, \tau_*(0.5) \sim 6 \cdot 10^{10} \text{ yr}, \tau_*(0.08) \sim 6 \cdot 10^{12} \text{ yr}.$$

Note that the lowest-mass stars can in principle live longer than the universe with its age of $1.4 \cdot 10^{10}$ yr. Beware: stars heavier than about $20 M_\odot$ live appreciably longer than estimated from the above scaling law (compare Activity 122), but that has no impact on the next sub-Activity:

(c) Integrating the initial mass function $\xi(M)$ from $8M_\odot$ to $100M_\odot$ shows that $\xi_0 \gtrsim 21$ in order for there to be at least one supernova within $\tau_{\odot\text{SN}}$. Combining that with the integral of $\xi(M)$ from $0.5M_\odot$ to $2M_\odot$ shows that there should be $N(0.5 - 2) \gtrsim 40$ stars in the neighborhood for the Sun (and its solar system) to be exposed to a supernova within its birth cluster.

(d) For a star to go supernova within 1.8 Myr, its mass should exceed about $32M_\odot$. Doing as above then yields $\xi_0 \gtrsim 133$ and $N(0.5 - 2) \gtrsim 250$ stars.

17.31 Activity 200: Reaching Earth's climate from scratch

Table 17.1 is a non-exhaustive list of properties that influence the habitability of planets.

Table 17.1: *Some of the properties that influence the habitability of planets*

<i>Property</i>	<i>Beneficial</i>	<i>Detrimental</i>
Dense stellar neighborhood	Supernova at suitable distance can trigger star formation in a <u>molecular cloud</u>	Supernovae. Tidal disruption of planetary orbits or system
Metallicity of initial cloud	Higher metallicity correlates with higher likelihood of planetary system	
Multiple star system		Orbital instability
Stellar mass	Lower mass: longer life time	Very low mass: dim stars have habitable zones so close that spin-orbit synchronization occurs, and stellar activity decays much more slowly. Low-energy photons may hamper photosynthesis. High <u>mass: short life time</u>
Evolution of stellar <u>brightness</u>		Migration of habitable zone
Stellar magnetic activity: photons, wind, CMEs	Energetic radiation may benefit the early evolution of life. Wind shields from galactic cosmic rays. Sustained drop in activity by <u>magnetic braking</u>	Irradiation of life with energetic photons and particles. Stripping of planetary atmosphere
Star-planet distance	Habitable if at the correct distance	Tidal spin-orbit synchronization <u>when too close in</u>
Giant neighbor planets in the system	Shield against comet/asteroid impacts well after system formation	Orbital migration could lead to planetary destruction. Effective shielding from impacts may supply too little water to terrestrial planets
Asteroid belt	May be important for creation of <u>settings suitable for life</u> ¹	Frequent asteroid impacts can <u>destroy life</u>
Orbital eccentricity	Circular orbits provide stable <u>irradiance</u>	Strong seasonal effects for <u>eccentric orbit</u>
Planetary mass	Intermediate mass retains chemically diverse atmosphere	Low mass: loss of atmosphere. High mass could mean predominant H/He atmosphere
Satellite companion	Stability of spin axis	
For a satellite of a giant planet	Tidal effects may keep water liquid and dynamo functioning for a long time, even far from the star, and for 'rogue planet'	Potential for strong radiation environment
Planetary dynamo	Protects against energetic particles	
Planetary water content	Water essential to known life	Absence of near-surface water may cause shutdown of planetary dynamo, with consequences for atmosphere
Plate tectonics	Important for dynamo action and atmospheric composition (<i>e.g.</i> , CO ₂ weathering can be balanced by volcanic activity)	Too much activity can lead to an inhospitable climate

¹ See, *e.g.*, [Osinski *et al.* \(2020\)](#), [Childs *et al.* \(2022\)](#)

Version history

1.1 2019/10/24: Original version.

1.2 2019/10/30: Deleted cover figure and compressed large-volume figures to fit into arXiv's 15MB limit. Added explicit references and associated bibliography, corrected a few URLs to figure sources, and made the Astrophysics Data System (ADS) the primary path to the literature in URLs throughout. Added version history. Added explanation of Heliophysics volume numbers to Preface.

1.3 2022/01/15: **Note: the numbering of some activities has changed because several new ones have been added in this version while others have been omitted or moved from the chapter they were originally in! For most Activities, this leaves their numbers unaffected or changes their number by 1 or 2 up or down.**

Modified caption to Fig. 2.1. Final paragraph of Sect. 6.1.2: removed '[a Dst index of]'. Added reference to list of space weather texts by [Knipp and Cade \(2020\)](#) in the Preface. Modified caption to Table 2.2. Added geomagnetic (sub-)storm to the glossary in Tables. 1.1 (split up from the original single page, continuing in Table 1.2), and differentiated magnetic and the (traditional) chromospheric plage in the definition of active region. Clarified captions to Fig. 5.1 and Fig. 5.3. Clarified text following Eq. (6.1). Corrected several minor typographical errors and descriptions of omitted or modified figures. Modified the table in Fig. 4.2 to contain stellar masses. Modified the text immediately following Activity 7. Modified Activity 11. Included Parker reference in the text leading up to Eq. (2.4). Corrected sign for β term in Eq. (4.15). Corrected 'interplanetary' to read 'interstellar' in the second line of Sect. 5.5.8.

Added a classification for all activities: "Look up," "Consider," "Show," "Background," or "Advanced/Group."

Added 9 new Activities: 4, 30, 48, 73, 104, 124, 133, 176, 179.

Added or modified tasks within 78 Activities: 2, 3, 5, 7, 13, 15, 17, 18, 19, 21, 23, 24, 26, 27, 28, 34, 36, 39, 41, 42, 44, 45, 46, 49, 51, 52, 54, 55, 64, 66, 72, 74, 75, 78, 79, 80, 81, 82, 84, 88, 91, 93, 94, 95, 98, 99, 106, 107, 110, 114, 115, 117, 118, 119, 120, 121, 123, 124, 125, 126, 127, 129, 130, 131, 132, 135, 138, 139, 142, 174, 181, 182, 184, 185, 193, 195, 199.

Omitted 7 Activities from V1.2 in V1.3: Nos. 30, 36, 94, 99, 110, 116, 125 (made into a footnote), 129, 130, and 134.

Moved within the chapter: 28. Moved to another chapter: 195.

2.0 2022/09/21: **Note: the numbering of activities has changed once more because several new ones have been added in this version while others have been omitted or moved from the chapter they were originally in!**

Activities are no longer shown as footnotes while their compilation in Ch. 16 is now shown at regular font size. New are solutions and supplemental text to selected activities; these are marked with Ⓢ in the Activity identifier in-line and in margin. New also are itemized key topics and concepts at the start of each chapter, and appendices with useful numbers and vector identities. A subject index was added. References to the original text were moved into the margin.

Ⓢ

Added new Activities: 16, 35, and 122, and removed Activities 28, 73, 105, and 134 (as numbered in V1.3). Corrected minor typographical errors. Added the official name to the provisional designation of 2014 MU₆₉ in Ch. 1, increased the number of exoplanets 'now' known to over 5,000, and modified how the JWT is described. Added 'circulating' to items (3) and (4) in Activity 5. Corrected expression for magnetic energy density in Eq. (3.57). Clarified that ion densities are given in Tables 2.4 and 5.2. Added note ^d in Table 18.2 for clarity. Corrected Eq. (9.2).

Rephrased tasks (1) and (2) in Activity 64. Added option to rewrite Eq. (2.7) to Activity 15. Corrected expression for specific internal energy in the caption of Table 3.3. Corrected mirror charge strength in Activity 64, clarified that distances are expressed in solar units, and separated the activity more clearly into two parts. Added a quantitative question to Activity 70. And modified Activity 37, Activity 85 (to point ahead to the RTV scaling law), Activity 113 (to apply to isothermal perturbations), and Activity 121 (to clarify what the numbers imply, and for lowered field strengths).

Added Figs. 2.5 and 2.8.

2.1 2024/03/26: Made Activity labels active links to the respective Activity and added page numbers to the Activity. Added navigation hint for Mac OS Preview in Preface. Corrected R_{\odot} in the list of constants and a few minor typographical errors.

List of Figures

2.1	Temperature-density diagram for heliophysics.	14
2.2	Average vertical temperature profile through Earth's atmosphere.	16
2.3	Solar <i>vs.</i> 5770 K black body spectrum, and solar-cycle variability.	19
2.4	Altitude of penetration of the solar radiation with wavelength.	19
2.5	Solar corona over the solar limb.	21
2.6	Profiles of major species in upper atmospheres of Venus, Earth, Mars.	28
2.7	Temperature profiles for solar min. and max. for Venus, Earth, Mars.	28
2.8	Regions of the ionosphere.	29
2.9	Ionosphere for night/day, high/low solar activity.	30
2.10	Classical Chapman profile.	31
2.11	Interactions of plasma with neutrals.	33
2.12	Typical density and ionization in iono- and chromosphere.	35
4.1	Radiative and convective internal structure of main-sequence stars.	65
4.2	Activity across the Hertzsprung-Russell diagram.	66
4.3	Polarity of the geomagnetic field for the past 120 million years.	67
4.4	Solar magnetogram, and frequency of emerging magnetic bipoles.	70
4.5	Butterfly diagram: sunspot latitudes versus time.	71
4.6	Two possible flux-rope dynamos.	72
4.7	Photospheric convection spectrum and solar internal rotation.	73
4.8	Columnar convection in a rotating spherical shell.	74
4.9	Effects of large-scale flows, and a young-Sun magnetogram.	77
4.10	Ingredients of dynamo models.	81
4.11	A minimal linear $\alpha\Omega$ dynamo solution.	82
4.12	A Babcock-Leighton dynamo solution.	85
4.13	Velocity and magnetic field for a planetary dynamo model.	92
5.1	Shocks around CMEs, the heliosphere, and Earth's magnetosphere.	100
5.2	Diagram: upstream and downstream of a shock.	101
5.3	Iso-contours of shock heating as a function of $\theta_{B\perp}$ and M_A	103
5.4	Magnetospheric field subject to a Carrington-level storm.	104
5.5	Spiraling asterospheric magnetic field for different rotation periods.	106
5.6	Sketch of the heliospheric current sheet.	107

5.7	The Sun's magnetic field and its extension into the heliosphere.	108
5.8	Solar wind v and p (1D model) for a high-speed stream.	109
5.9	A corotating interaction region in the solar equatorial plane.	111
5.10	Plasma flow (non-)conducting body.	113
5.11	Draping solar magnetic flux tubes around a conducting ionosphere. . .	115
5.12	A magnetically closed magnetosphere.	117
5.13	Total pressure (magnetic plus plasma) with distance from a planet. . .	119
5.14	A magnetically open magnetosphere.	120
5.15	Numerical model of the magnetosphere of Ganymede.	122
5.16	Magnetospheric convection on the Earth's surface.	126
6.1	Overview of the electromagnetic spectrum.	132
6.2	Evolution of flare emissions, and concepts of particle acceleration. . . .	133
6.3	Sketch of the flow of energy during a flare.	134
6.4	Geomagnetic field variation for two characteristic magnetic storms. . .	135
6.5	Topology of the magnetotail in a wind-dominated magnetosphere. . . .	139
6.6	Ribbon motion in solar flare reconnection.	139
6.7	Three different ways to use magnetic energy to power a flare or CME. .	142
6.8	Ideal-MHD evolution of a 2D arcade with a flux rope.	145
6.9	An isolated toroidal flux rope.	147
6.10	A stable toroidal equilibrium.	147
6.11	The three-dimensional flux-rope model).	148
6.12	Current density surfaces for an unstable Titov-Démoulin equilibrium. .	149
6.13	Numerical simulation of a storage model.	150
6.14	Observation of a CME, and CME kinetic energy <i>vs.</i> flare class.	154
6.15	The Sweet-Parker and Petschek field configurations.	155
6.16	Syrovatskii's field configuration.	157
7.1	Angular momentum transfer in a shearing disk.	165
7.2	Connected accretion disk, stellar wind, and stellar magnetosphere. . .	166
7.3	Two bodies orbiting their barycenter, and their tidal acceleration. . . .	168
7.4	Distant-future diameter of the Sun and the size of Earth's orbit. . . .	170
8.1	Particle motions in magnetic field.	178
8.2	Schematic diagram for the gradient-B drift.	178
8.3	1-dimensional particle diffusion from a point-source.	189
8.4	SEP event associated with an impulsive solar flare.	190
8.5	Energy spectra of energetic particles in the heliosphere and for GCRs. .	191
8.6	Modulation of galactic cosmic rays during five sunspot cycles.	192
8.7	Drift motion of cosmic rays in a Parker-spiral heliospheric field.	194
8.8	Normal-incidence frame (NIF) <i>vs.</i> de Hoffman-Teller frame (HTF). . .	196
8.9	2-D hybrid simulation of the solar wind – magnetosphere interaction. .	199
8.10	Particle flux profiles from three different solar longitudes.	200
8.11	An electron in drift resonance with a ULF wave.	203

8.12	Characteristic wave types within a magnetosphere.	204
9.1	Granulation in quiet-Sun and plage observed in the G-band.	209
9.2	Solar flux-tube model.	210
9.3	The multitude of scales in the solar magnetic field.	212
10.1	Luminosity, surface temperature, and age of evolving Sun-like stars. . .	219
10.2	Evolution of the luminosity of the Sun over its full life span.	220
10.3	Age-activity relationship for main-sequence stars.	222
10.4	Examples of cycles in stellar chromospheric activity.	224
10.5	Moments of inertia of evolving stars.	226
10.6	A 2.5D axisymmetric, hydrodynamic model of the heliosphere.	230
10.7	Heliosphere-ISM models for different ISM parameters.	232
10.8	Lyman- α : the journey of photons; the emission line; and α Cen B . . .	234
10.9	Mass-loss rate vs. X-ray flux density for MS stars.	235
10.10	The inferred mass-loss history of the Sun.	236
10.11	Surface field maps and associated heliospheric fields.	237
11.1	Planet-metallicity correlation for gas-giant planets.	241
11.2	Structure and processes of protoplanetary disks.	244
11.3	Masses and radii of selected exoplanets and Solar-System planets. . . .	246
11.4	Accreting protostar and likely accretional history of a low-mass star. . .	248
11.5	Optical image of the accreting young star HH 30.	249
11.6	HR diagram: Taurus protostars and young (T Tauri) stars.	251
11.7	Magnetosphere-disk interaction in low-mass, pre-main sequence stars. . .	254
11.8	Estimates of the minimum mass solar nebula.	256
11.9	Primordial disk fractions of stars in young clusters.	258
12.1	Earth's T and H ₂ O and CO ₂ after Moon-forming collision.	264
12.2	The photosynthetic habitable zone (pHZ) over time.	266
12.3	Sun-Earth energy flow: photons, energetic particles, solar wind.	272
12.4	Exchanges of solar and terrestrial energy in the Earth's atmosphere. . .	274
12.5	Simplified model of radiative exchange in the Earth's atmosphere. . . .	275
12.6	Radiative forcing (RF) bar chart for Earth's climate.	277
12.7	Earth's orbital parameters for the past million years.	279
12.8	Source and loss mechanisms for planetary atmospheres.	280
12.9	Flowchart for energization and escape of atmospheric particles.	282
13.1	Ionospheric chemistry for Earth, Venus, Mars.	296
13.2	Model of the Earth's ionospheric density profiles.	299
13.3	Model for the mean Earth-iono-/thermospheric temp. profiles.	300
13.4	Global mean ion and electron profiles for Earth <i>vs.</i> solar activity. . . .	301
13.5	Spectral radiance versus age of solar-type stars.	304
13.6	Evolution of the exospheric temperature.	304
13.7	Earth's exospheric temp. with CO ₂ and solar XUV flux.	305

13.8	Field lines for untilted and tilted planetary dipoles in the solar wind. .	307
13.9	Evolution of the min. & max. stellar wind densities at 1 AU.	308
14.1	Sources of energetic particles in the heliosphere.	312
14.2	Differential GCR proton fluxes for different levels of solar activity. . .	314
14.3	^{10}Be production rate <i>vs.</i> geomagnetic field strength and solar activity.	316
14.4	^{10}Be data and geomagnetic dipole field for the past 60,000 years. . . .	318
14.5	Bandpass-filtered ^{10}Be concentration and sunspot number.	319
14.6	Solar modulation function Φ from the present to 9350 BP	320
15.1	Systems to scale: Jupiter, TRAPPIST-1, and the inner Solar System.	324
17.1	Concept of mirror charges in a potential field	372
17.2	Sketch of the lunar solar-wind wake	373

List of Tables

1	Heliophysics: definition.	vii
2	Chapters in the Heliophysics book series sorted by theme (1).	viii
2	Chapters in the Heliophysics book series sorted by theme (2).	ix
3	Heliophysics and space weather	xi
1.1	Basic glossary (A–F).	4
1.2	Basic glossary (G–Z).	5
2.1	Climates of terrestrial planets.	15
2.2	Chemical species in the upper atmosph. of Venus, Earth, and Mars.	17
2.3	Domains in the solar atmosphere, with fundamental properties.	18
2.4	Fast and slow solar wind; basic parameters.	22
3.1	Structures in the magnetic field.	41
3.2	MHD approximation and the concept of 'closure'.	43
3.3	MHD equations.	45
3.4	Plasma parameters in different environments.	59
5.1	Plasma properties upstream of solar-system bodies.	99
5.2	Properties of the solar wind near the planets.	121
5.3	Intrinsic magnetic fields of Solar System bodies.	121
6.1	Solar flare classifications.	131
12.1	Temperatures of the planets for different albedo and stellar luminosity.	273
12.2	Solar wind and interplanetary magnetic field at the terrestrial planets.	284
14.1	Production reactions and rates for cosmogenic radionuclides.	315
17.1	Properties that influence the habitability of planets	384
18.1	Selected physical constants.	411
18.2	Selected plasma quantities; summary.	412
18.3	Vector identities.	413

Bibliography

Abbett, W. P.: 2007, ApJ 665(2), 1469, doi:10.1086/519788

Asai, A., Yokoyama, T., Shimojo, M., Masuda, S., Kurokawa, H., & Shibata, K.: 2004, ApJ 611(1), 557, doi:10.1086/422159

Beer, J., Baumgartner, S. T., Dittrich-Hannen, B., Hauenstein, J., Kubik, P., Lukasczyk, C., Mende, W., Stellmacher, B., & Suter, M.: 1994, in J. M. Pap, C. Frohlich, H. S. Hudson, and S. K. Solanki (Eds.), *Invited Papers from IAU Colloquium 143: The Sun as a Variable Star: Solar and Stellar Irradiance Variations*, 291

Behar, E., Nilsson, H., Alho, M., Goetz, C., & Tsurutani, B.: 2017, Mon. Not. R. Astron. Soc. 469, S396, doi:10.1093/mnras/stx1871

Bell, C. P. M., Mamajek, E. E., & Naylor, T.: 2015, Mon. Not. R. Astron. Soc. 454(1), 593, doi:10.1093/mnras/stv1981

Bell, C. P. M., Naylor, T., Mayne, N. J., Jeffries, R. D., & Littlefair, S. P.: 2013, Mon. Not. R. Astron. Soc. 434(1), 806, doi:10.1093/mnras/stt1075

Benz, A: 2002, *Plasma Astrophysics, second edition*, Kluwer, Springer, Astrophysics and Space Science Library, Vol. 279

Booth, R. S., Poppenhaeger, K., Watson, C. A., Silva Aguirre, V., & Wolk, S. J.: 2017, Mon. Not. R. Astron. Soc. 471(1), 1012, doi:10.1093/mnras/stx1630

Bougher, S. W. & Roble, R. G.: 1991, J. Geophys. Research 96(A7), 11045, doi:10.1029/91JA01162

Brun, A. S., Miesch, M. S., & Toomre, J.: 2004, ApJ 614(2), 1073, doi:10.1086/423835

Burkepile, J. T., Hundhausen, A. J., Stanger, A. L., St. Cyr, O. C., & Seiden, J. A.: 2004, Journal of Geophysical Research (Space Physics) 109(A3), A03103, doi:10.1029/2003JA010149

Carron, N. J.: 2007, *An Introduction to the Passage of Energetic Particles through Matter*

- Cauley, P. W., Redfield, S., Jensen, A. G., Barman, T., Endl, M., & Cochran, W. D.: 2015, *ApJ* 810(1), 13, doi:10.1088/0004-637X/810/1/13
- Charbonneau, P.: 2010, *Living Reviews in Solar Physics* 7(1), 3, doi:10.12942/lrsp-2010-3
- Charbonneau, P.: 2014, *Ann. Rev. Astron. Astrophys.* 52, 251, doi:10.1146/annurev-astro-081913-040012
- Cheung, M. C. M., Rempel, M., Chintzoglou, G., Chen, F., Testa, P., Martínez-Sykora, J., Sainz Dalda, A., DeRosa, M. L., Malanushenko, A., Hansteen, V., De Pontieu, B., Carlsson, M., Gudiksen, B., & McIntosh, S. W.: 2019, *Nature Astronomy* 3, 160, doi:10.1038/s41550-018-0629-3
- Childs, Anna C., Martin, Rebecca G., & Livio, Mario: 2022, arXiv e-prints arXiv:2209.02860
- Cohen, O. & Drake, J. J.: 2014, *ApJ* 783(1), 55, doi:10.1088/0004-637X/783/1/55
- Cohen, O., Drake, J. J., & Kóta, J.: 2012, *ApJ* 760(1), 85, doi:10.1088/0004-637X/760/1/85
- Crooker, N. U., Gosling, J. T., Bothmer, V., Forsyth, R. J., Gazis, P. R., Hewish, A., Horbury, T. S., Intriligator, D. S., Jokipii, J. R., Kóta, J., Lazarus, A. J., Lee, M. A., Lucek, E., Marsch, E., Posner, A., Richardson, I. G., Roelof, E. C., Schmidt, J. M., Siscoe, G. L., Tsurutani, B. T., & Wimmer-Schweingruber, R. F.: 1999, *Space Sci. Rev.* 89, 179, doi:10.1023/A:1005253526438
- Deming, D. & Louie, D. and Sheets, H.: 2019, *PASPs* 131(995), 013001, doi:10.1088/1538-3873/aae5c5
- Desch, S. J.: 2007, *ApJ* 671(1), 878, doi:10.1086/522825
- Dravins, D., Ludwig, H.-G., Dahlén, E., & Pazira, H.: 2017a, *A&A* 605, A90, doi:10.1051/0004-6361/201730900
- Dravins, D., Ludwig, H.-G., Dahlén, E., & Pazira, H.: 2017b, *A&A* 605, A91, doi:10.1051/0004-6361/201730901
- Drury, L. Oc.: 1983, *Reports on Progress in Physics* 46(8), 973, doi:10.1088/0034-4885/46/8/002
- Durrant, D. R. & Arakawa, A.: 2007, *Comptes Rendus Mecanique* 335(9), 655, doi:10.1016/j.crme.2007.08.010
- Eker, Z., Bakış, V., Bilir, S., Soyduğan, F., Steer, I., Soyduğan, E., Bakış, H., Açıgavuş, F., Aslan, G., & Alpsyoy, M.: 2018, *Mon. Not. R. Astron. Soc.* 479(4), 5491, doi:10.1093/mnras/sty1834

- Foley, B. J. & Smye, A. J.: 2018, *Astrobiology* 18(7), 873, doi:10.1089/ast.2017.1695
- Forbes, T. G. & Priest, E. R.: 1995, *ApJ* 446, 377, doi:10.1086/175797
- Franck, S., Block, A., Bloh, W., Bounama, C., Garrido, I., & Schellnhuber, H. J.: 2001, *Naturwissenschaften* 88(10), 416, doi:10.1007/s001140100257
- Fraschetti, F., Drake, J. J., Alvarado-Gómez, J. D., Moschou, S. P., Garraffo, C., & Cohen, O.: 2019, *ApJ* 874(1), 21, doi:10.3847/1538-4357/ab05e4
- Garraffo, C., Drake, J. y J., Cohen, O., Alvarado-Gómez, J. D., & Moschou, S. P.: 2017, *ApJL* 843(2), L33, doi:10.3847/2041-8213/aa79ed
- Gleeson, L. J. & Axford, W. I.: 1968, *ApJ* 154, 1011, doi:10.1086/149822
- Güdel, M.: 2007, *Living Reviews in Solar Physics* 4(1), 3, doi:10.12942/lrsp-2007-3
- Hartmann, L.: 2009, *Accretion Processes in Star Formation: Second Edition*, Cambridge University Press, Cambridge, UK
- Hathaway, D. H., Beck, J. G., Bogart, R. S., Bachmann, K. T., Khatri, G., Petitto, J. M., Han, S., & Raymond, J.: 2000, *Solar Phys.* 193, 299, doi:10.1023/A:1005200809766
- Henning, T. & Semenov, D.: 2013, *Chemical Reviews* 113(12), 9016, doi:10.1021/cr400128p
- Holzer, T. E.: 1972, *J. Geophys. Research* 77(28), 5407, doi:10.1029/JA077i028p05407
- Howard, A. W., Sanchis-Ojeda, R., Marcy, G. W., Johnson, J. A., Winn, J. N., Isaacson, H., Fischer, D. A., Fulton, B. J., Sinukoff, E., & Fortney, J. J.: 2013, *Nature* 503(7476), 381, doi:10.1038/nature12767
- IPCC: 2013, in T.F. Stocker, D. Qin, G.-K. Plattner, M. Tignor, S.K. Allen, J. Boschung, A. Nauels, Y. Xia, V. Bex, and P.M. Midgley (Eds.), *Summary for Policymakers*, Cambridge University Press, Cambridge, United Kingdom and New York, NY, USA
- Jansen, T., Scharf, C., Way, M., & Del Genio, A.: 2019, *ApJ* 875(2), 79, doi:10.3847/1538-4357/ab113d
- Jia, X., Walker, R. J., Kivelson, M. G., Khurana, K. K., & Linker, J. A.: 2008, *Journal of Geophysical Research (Space Physics)* 113(A6), A06212, doi:10.1029/2007JA012748
- Jiménez, A., García, R. A., & Pallé, P. L.: 2011, *ApJ* 743(2), 99, doi:10.1088/0004-637X/743/2/99
- Johnson, J. A.: 2019, *Science* 363(6426), 474, doi:10.1126/science.aau9540
- Jokipii, J. R. & Thomas, B.: 1981, *ApJ* 243, 1115, doi:10.1086/158675

- Kallenrode, M.-B.: 2003, *Journal of Physics G Nuclear Physics* 29(5), 965
- Karak, B. B. & Miesch, M.: 2017, *ApJ* 847(1), 69, doi:10.3847/1538-4357/aa8636
- Kiehl, J. T. & Trenberth, K. E.: 1997, *Bulletin of the American Meteorological Society* 78(2), 197, doi:10.1175/1520-0477(1997)078<0197:EAGMEB>2.0.CO;2
- Knipp, D. J. & Cade, W. T.: 2020, doi:10.5281/zenodo.3843629
- Koch, A., Brierley, C., Maslin, M. M., & Lewis, S. L.: 2019, *Quaternary Science Reviews* 207, 13, doi:10.1016/j.quascirev.2018.12.004
- Krauss-Varban, D., Li, Y., & Luhmann, J. G.: 2008, in Gang Li, Qiang Hu, Olga Verkhoglyadova, Gary P. Zank, R. P. Lin, and J. Luhmann (Eds.), *American Institute of Physics Conference Series*, Vol. 1039, p. 307
- Kulikov, Y. N., Lammer, H., Lichtenegger, H. I. M., Penz, T., Breuer, D., Spohn, T., Lundin, R., & Biernat, H. K.: 2007, *Space Sci. Rev.* 129(1-3), 207, doi:10.1007/s11214-007-9192-4
- Lammer, H. & Blanc, M.: 2018, *Space Sci. Rev.* 214(2), 60, doi:10.1007/s11214-017-0433-x
- Lemerle, A. & Charbonneau, P.: 2017, *ApJ* 834(2), 133, doi:10.3847/1538-4357/834/2/133
- Linsky, J. L.: 1985, *Solar Phys.* 100, 333, doi:10.1007/BF00158435
- Lodders, Katharina: 2019, arXiv e-prints arXiv:1912.00844
- Lundin, R., Lammer, H., & Ribas, I.: 2007, *Space Sci. Rev.* 129(1-3), 245, doi:10.1007/s11214-007-9176-4
- MacNeice, P., Antiochos, S. K., Phillips, A., Spicer, D. S., DeVore, C. R., & Olson, K.: 2004, *ApJ* 614(2), 1028, doi:10.1086/423887
- Mamajek, E. E.: 2009, in Tomonori Usuda, Motohide Tamura, and Miki Ishii (Eds.), *American Institute of Physics Conference Series*, Vol. 1158 of *American Institute of Physics Conference Series*, p. 3
- Marcq, E., Mills, F. P., Parkinson, C. D., & Vanae, A. C.: 2018, *Space Sci. Rev.* 214(1), 10, doi:10.1007/s11214-017-0438-5
- Mazur, J. E., Mason, G. M., Dwyer, J. R., Giacalone, J., Jokipii, J. R., & Stone, E. C.: 2000, *ApJL* 532(1), L79, doi:10.1086/312561
- McComas, D. J., Dayeh, M. A., Funsten, H. O., Livadiotis, G., & Schwadron, N. A.: 2013, *ApJ* 771(2), 77, doi:10.1088/0004-637X/771/2/77

- Meyer-Vernet, N.: 1999, *European Journal of Physics* 20(3), 167, doi:10.1088/0143-0807/20/3/006
- Moraal, H.: 1976, *Space Sci. Rev.* 19(6), 845, doi:10.1007/BF00173707
- Movshovitz, Naor, Asphaug, Erik, & Korycansky, Donald: 2012, *ApJ* 759(2), 93, doi:10.1088/0004-637X/759/2/93
- Müller, H.-R., Frisch, P. C., Fields, B. D., & Zank, G. P.: 2009, *Space Sci. Rev.* 143(1-4), 415, doi:10.1007/s11214-008-9448-7
- Müller, H. R. & Zank, G. P.: 2004, *Journal of Geophysical Research (Space Physics)* 109(A7), A07104, doi:10.1029/2003JA010269
- Ngwira, C. M., Pulkkinen, A., Kuznetsova, M. M., & Glocer, A.: 2014, *Journal of Geophysical Research (Space Physics)* 119(6), 4456, doi:10.1002/2013JA019661
- Ó Fionnagáin, D., Vidotto, A. A., Petit, P., Folsom, C. P., Jeffers, S. V., Marsden, S. C., Morin, J., do Nascimento, J. D., & BCool Collaboration: 2019, *Mon. Not. R. Astron. Soc.* 483(1), 873, doi:10.1093/mnras/sty3132
- O'Brien, D. P., Walsh, K. J., Morbidelli, A., Raymond, S. N., & Mandell, A. M.: 2014, *Icarus* 239, 74, doi:10.1016/j.icarus.2014.05.009
- Osinski, G. R., Cockell, C. S., Pontefract, A., & Sapers, H. M.: 2020, *Astrobiology* 20(9), 1121, doi:10.1089/ast.2019.2203
- Parker, E. N.: 1958, *ApJ* 128, 664, doi:10.1086/146579
- Parker, E. N.: 1960, *ApJ* 132, 175, doi:10.1086/146910
- Parker, Eugene N.: 2007, *Conversations on Electric and Magnetic Fields in the Cosmos*
- Parker, E. N.: 2014, *Research in Astronomy and Astrophysics* 14(1), 1, doi:10.1088/1674-4527/14/1/001
- Pavlov, A. A., Toon, O. B., Pavlov, A. K., Bally, J., & Pollard, D.: 2005, *Geophys. Res. Lett.* 32(3), L03705, doi:10.1029/2004GL021890
- Pecaut, M. J. & Mamajek, E. E.: 2016, *Mon. Not. R. Astron. Soc.* 461(1), 794, doi:10.1093/mnras/stw1300
- Pecaut, M. J., Mamajek, E. E., & Bubar, E. J.: 2012, *ApJ* 746(2), 154, doi:10.1088/0004-637X/746/2/154
- Pineda, J. S. & Hallinan, G. and Kao, M. M.: 2017, *ApJ* 846(1), 75, doi:10.3847/1538-4357/aa8596

- Pinhas, A., Rackham, B. V., Madhusudhan, N., & Apai, D.: 2018, *Mon. Not. R. Astron. Soc.* 480(4), 5314, doi:10.1093/mnras/sty2209
- Pognan, Q., Garraffo, C., Cohen, O., & Drake, J. J.: 2018, *ApJ* 856(1), 53, doi:10.3847/1538-4357/aaaebb
- Portegies Zwart, S., Pelupessy, I., van Elteren, A., Wijnen, T. P. G., & Lugaro, M.: 2018, *A&A* 616, A85, doi:10.1051/0004-6361/201732060
- Portegies Zwart, S. F.: 2009, *ApJL* 696(1), L13, doi:10.1088/0004-637X/696/1/L13
- Quenby, J. J.: 1984, *Space Sci. Rev.* 37(3-4), 201, doi:10.1007/BF00226364
- Rackham, B., Pinhas, A., Apai, D., Haywood, R., Cegla, H., Espinoza, N., Teske, J., Gully-Santiago, M., Rau, G., Morris, B. M., Angerhausen, D., Barclay, T., Carone, L., Cauley, P. W., de Wit, J., Domagal-Goldman, S., Dong, C., Dragomir, D., Giampapa, M. S., Hasegawa, Y., Hinkel, N. R., Hu, R., Jordán, An., Kitiashvili, I., Kreidberg, L., Lisse, C., Llama, J., López-Morales, M., Mennesson, B., Molaverdikhani, K., Osip, D. J., & Quintana, E. V.: 2019a, *Bull. Am. Astron. Soc.* 51(3), 328
- Rackham, B. V., Apai, D., & Giampapa, M. S.: 2018, *ApJ* 853(2), 122, doi:10.3847/1538-4357/aaa08c
- Rackham, B. V., Apai, D., & Giampapa, M. S.: 2019b, *Astron. J.* 157(3), 96, doi:10.3847/1538-3881/aaf892
- Reames, D. V.: 2013, *Space Sci. Rev.* 175(1-4), 53, doi:10.1007/s11214-013-9958-9
- Ribas, I., Guinan, E. F., Güdel, M., & Audard, M.: 2005, *ApJ* 622(1), 680, doi:10.1086/427977
- Rosner, R., Tucker, W. H., & Vaiana, G. S.: 1978, *ApJ* 220, 643, doi:10.1086/155949
- Sackmann, I.-J., Boothroyd, A. I., & Kraemer, K. E.: 1993, *ApJ* 418, 457, doi:10.1086/173407
- Schatten, K. H., Wilcox, J. M., & Ness, N. F.: 1969, *Solar Phys.* 6(3), 442, doi:10.1007/BF00146478
- Scheucher, M., Grenfell, J. L., Wunderlich, F., Godolt, M., Schreier, F., & Rauer, H.: 2018, *ApJ* 863(1), 6, doi:10.3847/1538-4357/aacf03
- Schrijver, C. J.: 2001, *ApJ* 547(1), 475, doi:10.1086/318333
- Schrijver, C. J.: 2009, *ApJL* 699(2), L148, doi:10.1088/0004-637X/699/2/L148
- Schrijver, C. J., Bagenal, F., & Sojka, J. J. (Eds.): 2016, *Heliophysics: Active Stars, their Astrospheres, and Impacts on Planetary Environments*, Cambridge University Press, Cambridge, UK, (Volume IV)

- Schrijver, C. J., Hudson, H. S., Murphy, R. J., Share, G. H., & Tarbell, T. D.: 2006, *ApJ* 650(2), 1184, doi:10.1086/506583
- Schrijver, C. J., Kauristie, K., Aylward, A. D., Denardini, C. M., Gibson, S. E., Glover, A., Gopalswamy, N., Grande, M., Hapgood, M., Heynderickx, D., Jakowski, N., Kalegaev, V. V., Lapenta, G., Linker, J. A., Liu, S., Mandrini, C. H., Mann, I. R., Nagatsuma, T., Nandy, D., Obara, T., O'Brien, P. T., Onsager, T., Opgenoorth, H. J., Terkildsen, M., Valladares, C. E., & Vilmer, N.: 2015, *Advances in Space Research* 55(12), 2745, doi:10.1016/j.asr.2015.03.023
- Schrijver, C. J. & Siscoe, G. L. (Eds.): 2011, *Heliophysics: Plasma Physics of the Local Cosmos*, Cambridge University Press, Cambridge, UK, (Volume I)
- Schrijver, C. J. & Siscoe, G. L. (Eds.): 2012a, *Heliophysics: Evolving Solar Activity and the Climates of Space and Earth*, Cambridge University Press, Cambridge, UK, (Volume III)
- Schrijver, C. J. & Siscoe, G. L. (Eds.): 2012b, *Heliophysics: Space Storms and Radiation: Causes and Effects*, Cambridge University Press, Cambridge, UK, (Volume II)
- Schrijver, C. J. & Siscoe, G. L. (Eds.): 2015, *Heliophysics: Space Weather and Society*, published online at NASA's Heliophysics Summer School site, <https://cpaess.ucar.edu/sites/default/files/heliophysics/documents/HSS5.pdf> (Volume V)
- Schrijver, C. J. & Zwaan, C.: 2000, *Solar and Stellar Magnetic Activity*, Cambridge University Press, Cambridge, UK
- Schrijver, K.: 2018, *One of ten billion Earths: How we Learn about our Planet's Past and Future from Distant Exoplanets*, Oxford University Press, Oxford, UK
- Schröder, K. P. & Connon Smith, Robert: 2008, *Mon. Not. R. Astron. Soc.* 386(1), 155, doi:10.1111/j.1365-2966.2008.13022.x
- Schwadron, N. A., Moebius, E., Kucharek, H., Lee, M. A., French, J., Saul, L., Wurz, P., Bzowski, M., Fuselier, S. A., Livadiotis, G., McComas, D. J., Frisch, P., Gruntman, M., & Mueller, H. R.: 2013, *ApJ* 775(2), 86, doi:10.1088/0004-637X/775/2/86
- Sheeley, Neil R., Jr.: 2005, *Living Reviews in Solar Physics* 2(1), 5, doi:10.12942/lrsp-2005-5
- Smithtro, C. G. & Sojka, J. J.: 2005, *Journal of Geophysical Research (Space Physics)* 110(A8), A08305, doi:10.1029/2004JA010781
- Spruit, H. C.: 2013, arXiv e-prints arXiv:1301.5572
- Stern, S. A., Weaver, H. A., Spencer, J. R., & *et al.*, : 2019, *Science* 364(6441), aaw9771, doi:10.1126/science.aaw9771

- Struminsky, A. B., Sadovskii, A. M., & Zharikova, M. S.: 2018, *Geomagnetism and Aeronomy* 58(8), 1108, doi:10.1134/S0016793218080169
- Thompson, M. J., Christensen-Dalsgaard, J., Miesch, M. S., & Toomre, J.: 2003, *Ann. Rev. Astron. Astrophys.*41, 599, doi:10.1146/annurev.astro.41.011802.094848
- Titov, V. S. & Démoulin, P.: 1999, *A&A* 351, 707
- Török, T., Kliem, B., & Titov, V. S.: 2004, *A&A* 413, L27, doi:10.1051/0004-6361:20031691
- Tsurutani, B. T., Gonzalez, W. D., Gonzalez, A. L. C., Guarnieri, F. L., Gopalswamy, N., Grande, M., Kamide, Y., Kasahara, Y., Lu, G., Mann, I., McPherron, R., Soraas, F., & Vasyliunas, V.: 2006, *Journal of Geophysical Research (Space Physics)* 111(A7), A07S01, doi:10.1029/2005JA011273
- Vasyliunas, V. M.: 1976, in *Magnetospheric Particles and Fields*, p. 99
- Veronig, Astrid M., Odert, Petra, Leitzinger, Martin, Dissauer, Karin, Fleck, Nikolaus C., & Hudson, Hugh S.: 2021, *Nature Astronomy* 5, 697, doi:10.1038/s41550-021-01345-9
- Wallner, A., Feige, J., Kinoshita, N., Paul, M., Fifield, L. K., Golser, R., Honda, M., Linnemann, U., Matsuzaki, H., Merchel, S., Rugel, G., Tims, S. G., Steier, P., Yamagata, T., & Winkler, S. R.: 2016, *Nature* 532(7597), 69, doi:10.1038/nature17196
- Wang, Y.-M., Sheeley, N. R., Socker, D. G., Howard, R. A., & Rich, N. B.: 2000, *J. Geophys. Research* 105(A11), 25133, doi:10.1029/2000JA000149
- Wieler, R., Beer, J., & Leya, I.: 2013, *Space Sci. Rev.* 176(1-4), 351, doi:10.1007/s11214-011-9769-9
- Wood, B. E.: 2004, *Living Reviews in Solar Physics* 1, 2, doi:10.12942/lrsp-2004-2
- Wood, B. E., Müller, H.-R., Redfield, S., & Edelman, E.: 2014, *ApJL* 781(2), L33, doi:10.1088/2041-8205/781/2/L33
- Wood, B. E., Müller, H. R., Zank, G. P., Linsky, J. L., & Redfield, S.: 2005, *ApJL* 628(2), L143, doi:10.1086/432716
- Xiang, Maosheng & Rix, Hans-Walter: 2022, *Nature* 603(7902), 599, doi:10.1038/s41586-022-04496-5
- Youngblood, A., Pineda, J. S., Ayres, T., France, K., Linsky, J. L., Wood, B. E., Redfield, S., & Schlieder, J. E.: 2022, arXiv e-prints arXiv:2201.01315
- Zahnle, K., Arndt, N., Cockell, Ch., Halliday, A., Nisbet, E., Selsis, F., & Sleep, N. H.: 2007, *Space Sci. Rev.* 129(1-3), 35, doi:10.1007/s11214-007-9225-z

Zhang, H., Khurana, K. K., Kivelson, M. G., Angelopoulos, V., Wan, W. X., Liu, L. B., Zong, Q. G., Pu, Z. Y., Shi, Q. Q., & Liu, W. L.: 2014, *Journal of Geophysical Research (Space Physics)* 119(7), 5220, doi:10.1002/2014JA020111

Zhang, Z., Zhou, Y., Rackham, B. V., & Apai, D.: 2018, *Astron. J.*156(4), 178, doi:10.3847/1538-3881/aade4f

Subject index

- A** _____
- accretion disk 243
 - angular momentum
 - transfer 166, 240
 - acoustic cutoff frequency 211
 - ACR *see* cosmic
 - active region *see also* definition, 4, 209
 - activity
 - belt 71
 - cycle 69
 - stars 224
 - activity cycle *see* sunspot
 - activity-age relationship 225
 - adiabatic heat flow 68
 - albedo *see also* definition, 272
 - climate 271
 - Alfvén
 - speed 52
 - wave 53
 - ambipolar
 - diffusion 57, 295
 - effect 290, 366
 - Ampère's law 50, 54
 - angular momentum
 - loss 225
 - transport 160
 - anomalous resistivity 61
 - arcsecond, equivalent length 209
 - astrosphere 4, 229
 - absorption 233
 - field pattern 236
 - Lyman α signal 233, 323
 - atmosphere
 - blow-off 303
 - composition
 - terrestrial planets 17, 297
 - escape
 - Jeans loss 303
 - mechanisms 282
 - rate 283
 - escape rate
 - magnetic field 286
 - variability 285
 - exoplanets 324
 - hydrodynamic escape 281
 - insulating 122, 124
 - losses
 - scaling 215, 222, 228, 304
 - molecular diffusion 289
 - ozone 290
 - stellar influence 323
 - tide 160, 172
 - upper atmosphere 289
 - variable F/E/UV flux 291
 - atmospheric
 - separation and mixing 25
 - atom-ion interchange 294
 - aurora 4, 122, 134, 136, 141, 293, 295, 303, 306, 307, 342
 - auroral substorm 134
- B** _____
- Birkeland current 126, 136
 - Boltzmann equation 182
 - Boussinesq approximation 90
 - bow shock 117, 127, 232
 - stellar wind 323
 - breakout model 149
 - bright point 4, 208, 209
 - brown dwarf 218
 - butterfly diagram *see also* definition, 71, 86
- C** _____
- carbon dioxide
 - evolution 267
 - inevitable decline of 267
 - centrifugal stripping 222
 - centripetal acceleration 125
 - Chapman
 - layer 295
 - profile 31
 - Chapman-Ferraro distance 118
 - charge exchange 36, 128, 232, 294
 - chromosphere 4, 18
 - conductivity 36
 - ionization fraction 35
 - chromospheric evaporation 151
 - climate
 - asteroid impact 281
 - change
 - ice core data 280
 - Milankovic forcing 278
 - obliquity 279
 - Earth 263
 - energy balance 273
 - equinox precession 280
 - factors for change 276
 - feedback mechanisms 279
 - forcing 287
 - ionosphere
 - magnetic field 305
 - response to solar
 - variation 298
 - irradiation 298
 - orbital change 278
 - radiative forcing 277
 - role of oceans 276
 - solar variability 6
 - solar wind 308
 - terrestrial planets 15
 - Venus, Earth, Mars 269
 - volcanic outgassing 280
 - young Earth 303
 - cloud core *see also* definition, 239

- CME *see* flare
- collision frequency 26
- collisionless skin depth 123
- collisions
 Earth atmosphere 26
 plasma/neutral atmosphere 123, 124
- comparative studies
 conductive anisotropy 36
 ionization fraction
 chromosphere, ionosphere 36
- compositional convection 69
- conductivity 34, 50
 collisions 367
 Hall 34
 parallel, perpendicular 33
 Pedersen 34
 tensor 34
- contraction time scale
 Kelvin-Helmholtz 252
- convection 73
 (Busse) columns 91
 composition 69
 compositional 68
 Ledoux criterion 73
 mixing length theory 73
 Schwarzschild criterion 73
- convective envelope 64, 218
- cool star *see also* definition, 218
- Coriolis effect
 influence on climate 270
- Coriolis force 63, 75, 79, 81, 86, 90–93
- corona 4, 18
 conductive loss 213
 heating mechanism 211
 loop 213
 quasi-static 214
 radiative loss 213
- coronal
 dimming 154
 hole 4
 loop 4, 21
 cooling time scale 375
 properties 380
 mass ejection 4, 154
 flare association 130
 without major flare 152
- corotating interaction region (CIR) 111
- cosmic ray 190
 11-year cycle 192
- 22-year cycle 192
- cut-off rigidity 314
- energy change 186
- exoplanets 324
- force field solution 313
- rigidity *see also* definition, 314
- solar modulation function 313
- transport equation 187
 variability 320
- cosmogenic radionuclides 315
 formation 312
- ice cores and tree rings 316
- proxies of magnetic activity 317
- transport and deposition 316
- current sheet 40, 41
- current-driven instability 138
- curvature drift *see* particle
- cutoff frequency 211, 379
- D**
- de-screening event 231
- Debye length 60
- decay time scale 51
- definition *see also* glossary
 active region 4
 active region belt 4
 advection-dominated regime 51
 albedo 272
 astrosphere 4
 aurora 4
 bright point 4
 chromosphere 4
 cloud core 239
 cool star 218
 corona 4
 coronal hole 4
 coronal loop 4
 coronal mass ejection 4
 cosmic ray rigidity 314
 Dst index 133
 exobase 282
 exosphere 4, 26
 facula 4
 filament, prominence 4
 flare 4, 131
 flux tube 4
 geomagnetic (sub-)storm 5
 geomagnetic storm 133
- granulation 5
- habitability 2
- habitable zone 265
- heliophysics vii
- heliosphere 5
- heterosphere 289
- homosphere 289
- ionosphere 5
- magneto-rotational
 instability 165
- magnetosphere 5
- main sequence 217
- mesosphere 5
- obliquity 159
- photosphere 5
- plasma 13
- pressure scale height 20
- reconnection 56
- solar cycle 5
- solar irradiance 5
- star 217
 giant 66
 main-sequence or dwarf 66
 supergiant 66
- stratosphere 5
- sunspot 5
- supergranulation 5
- thermosphere 5
- Toomre parameter 255
- transition region 5
- troposphere 5
- Wilson depression 210
- Dessler-Parker-Sckopke theorem 141
- deuterium fusion 252
- differential intensity 182
- differential rotation *see also* solar, 80
 geostrophic cylinders 91
 internal 225
 near-surface shear layer 74
 stars 89
 tachocline 74
- diffusion
 cross field 186
 dominated regime *see also* definition, 51
 equation
 phase space 185
 molecular
 diffusion coefficient 382
 tensor 188

time scale	51	number	79, 81	Europa	114
diffusive shock acceleration	197	planetary	65	exoplanet	240, 241
dimming	154, 343	power source	71	51 Pegasi b	11
dipolarization	140, 153	principles	69	formation	243
dipole moment	<i>see also</i>	saturation	221	gas-dwarf	246
definition, 116		settings	63	gas-giant	246
planetary	120	stars	88	geology	246
discontinuity: contact,		strength	64	in binary-star systems	247
rotational, tangential		stretch-twist-fold	72	migration	245
41, 103		illustration	72	search techniques	240
disk		terrestrial planets	90	terrestrial	246
dust disk evolution	257	waves	83–85	TRAPPIST 1 b–h	326
evaporation	259	E		exosphere	4, 26, 27
evolution	241	Earth		cooling by CO ₂	304
photo-evaporation	260	atmosphere and climate	269	F	
protoplanetary	255	bow shock	199	facula	4, 210
disk wind	166, 250	climate	263	fast-mode wave	53
magneto-centrifugal		core	67, 68	field equations	
acceleration	250	tangent cylinder	91, 93	gravity	40
dissociative recombination	294	formative phase	264	magnetic field	40
drag		geospace climate	298	field line	40, 54
collisional	123, 124	magnetic field	305	applicability of concept	54
plasma-neutral	124	solar wind	308	equation	54
tangential	125	younger Earth	303	filament <i>see also</i> definition,	154
Dreicer electric field	61	heat flow	67	cavity	154
Dst index <i>see also</i> definition,	141	interior	66	eruption	150
relation to magnetosphere		magnetic field	67	first-order Fermi acceleration	
energy	141	plate tectonics	67, 69	197, <i>see</i> particle	
Dungey cycle	125	pre-biotic	264	FK Comae stars	171
dust	257	ring current	32	flare	4, <i>see also</i> definition
disk	257, 258	water over time	268	injection model	143
grain evolution	258	electrojet	134	bolometric detection	152
dusty plasma	37	electromagnetic skin depth	83	breakout model	149
dynamo		electromagnetic spectrum	132	bulk energy	152
Ω effect	93	electromotive force	78	classification	131, 132
α effect	79, 80, 86, 90, 93	electron plasma frequency	58,	current sheet model	143
α quenching	83, 84	123		force free field model	143
$\alpha\Omega$ model	80, 84	electron skin depth	57	frequency	131, 225
α^2 model	91	electron-inertial length	57, 123	in the EM spectrum	132
advection dominated	85	energetic		Neupert effect	151
amplitude saturation	83	particle		phases	150
approximating models	75	acceleration	193	gradual	153
Babcock-Leighton	86	exposure	312	impulsive	153
Cowling's theorem	76	particles	175	power-law spectra	223
cycle period	82, 83, 85, 87	diffusion	377	pre-eruption field	148
eigenfunction	82	other stars	323	ribbon	130
flux transport	85, 86	penetration depth	367	motion	153
homogeneous fluid	64	shock acceleration	193	spectral evolution	133
instability-driven	87	sources	312	stellar	223
interface	84	energy		storage model	142
kinematic approximation	76	from planetary rotation	163	substorm resemblance	153
mean-field	77	equilibrium temperature	355	UV continuum	152
nonlinearity	83				

- white light 152
 flat-activity star 223
 flow
 accretion disk 97
 around a magnetized body 116
 around astrosphere 97
 around planetary bodies 96
 closed magnetosphere 116
 conducting body 114
 Ganymede 116
 in ideal MHD 97
 Mars 115
 modified by waves 96
 non-conducting body 112
 shock 100
 Venus 115
 wake 112
 wind onto interstellar medium 127
 with reconnection 97
 flux
 dispersal
 Babcock-Leighton 370
 rope 144
 tube 4, *see also* definition, 54, 90
 concept 210
 field strength and optical depth 380
 hydrostatic equilibrium 369
 force-free field 48
 models 143
 3d 146
 fossil magnetic fields 89
 frozen-in field theorem 55
 FU Orionis outburst 247, 249
G _____
 G-band 208
 Ganymede 116, 122
 GCR *see* cosmic
 geomagnetic (sub-)storm 5
 dipole geospace effect of tilt 306
 field dipole strength variation 306
 reversals 306
 geomagnetic field long-term variations 318
 geospace climate dependence on dipole strength 306
 dependence on photon irradiation 298
 during grand maximum 302
 effect of dipole tilt 306
 impact of sustained EUV increase 305
 variation over geological time scales 303
 geostrophic balance 91
 cylinders 91
 global merged interaction region 110, 192
 glossary *see also* definition, 4, 5
 granulation 5, 207
 scale 378
 gravitational collapse condition for 25, 239
 instability 255, 257
 potential energy 23
 tide *see* tide
 torque 173, 249
 guiding center motion *see* particle
 gyrofrequency 49, 177
 gyromotion 177
 gyroradius 37, 185
H _____
 habitability *see also* definition, 2
 evolving 263
 habitable zone *see also* definition, 265
 photosynthetic 266
 ultimate fate of 169
 Hall conductivity 34, 125
 current 49
 effect 57
 height-integrated current 124
 helicity flow 90
 heliopause 127, 232
 Heliophysics book chapters viii, ix
 book series viii
 heliophysics *see also* definition, 7
 and space weather xi
 online resources xii
 heliosphere characteristic energies 62
 mean free path 365
 Herbig-Haro object 217
 Hertzsprung-Russell diagram 66, 217, 219, 226, 252, 334
 homosphere 27
 HR diagram *see* Hertzsprung-Russell diagram
 hydrodynamic escape *see* atmosphere
 hydrogen wall 232
 hydrostatic balance 20
I _____
 ice ages 280
 insolation variation with orbital eccentricity 278
 instability ballooning 140
 current-driven 138
 gravitational 255
 interchange 140
 magneto-rotational 255
 tearing mode 138
 interglacials 280
 interplanetary magnetic field 116, 118
 shock 200
 particle acceleration 200
 interstellar medium 127, 229
 Io 114
 ion plasma frequency 58
 ion skin depth 58
 ion-inertial length 58
 ion-neutral coupling 31
 ionizing radiation galactic cosmic rays 312
 ionosphere *see also* definition, 5, 122, 123
 D region 294
 D region chemistry 296
 E region 294, 296
 *F*₁ region 294
 *F*₂ region 295
 *F*₂ region unique to Earth 298
 particle precipitation 136
 collisional heating 136
 domains, layers 28

- ion-neutral coupling 31
ionization 'chemistry' 295
ionization degree 29
ionization fraction 29, 35
ionization rate 30
Joule heating 136
Mars 297
molecules and ionization
 balance 295
photo-ionization 293, 294
planetary 123
recombination 294
solar variability 298
terminology 28
Venus 297
- ionosphere-magnetosphere
 coupling 125
- ionosphere-thermosphere
 conditions for young Earth
 305
- ionospheric Ohm's law 34, 123
- ISM *see* interstellar medium
- J** _____
- Jeans escape process 303
Jeans mass 382
Joy's rule 86
- K** _____
- Kelvin-Helmholtz contraction
 time scale 252
- kinetic helicity 79
kinetic process
 description 194
- L** _____
- Larmor frequency 49
Laschamp event 317
late heavy bombardment 265
line of force: definition 54
line tying 142, 144, 211
Liouville's theorem 181
little ice age
 and Maunder Minimum 287
local interstellar cloud 229
Lorentz force 91
lunar 18.6-year cycle 169
Lundquist number 60
- M** _____
- magnetic
 activity
 angular momentum loss
 225
 binary stars 226
 evolution 325
braking 161, 225, 376
cell *see also* definition, 41
diffusion equation 51
diffusion time 79
diffusivity 50, 80
dipole
 planetary 116
energy storage 130
field
 axisymmetric 76
 Earth 68
 induced 96
 non-axisymmetric 77
 of Solar-System bodies
 121
 planets 67
 small-scale 77
 Sun *see* solar
field line 54
flux rope 86
instabilities 129
plage 209
reconnection 119
Reynolds number 71, 79, 90
storm *see also* definition,
133
 Earth 141
structures 41
torque 161
magnetization 34
magneto-rotational
 coupling 165
 instability *see also*
 definition
magnetogram *see* solar
magnetopause *see also* definition,
117, 119
 Chapman-Ferraro distance
 118
 distance 375
 evolution 382
 reconnection 120
 reconnection line 127
 shape of 118
 sub-solar distance 118
- magnetosheath *see also*
 definition, 117
magnetosonic wave 53
magnetosphere 5, *see also*
 definition
 characteristic scale size 118
 closed 116, 117
 convection 125, 126
 corotation 124
 EM radiation 136
 energy from planetary
 rotation 135
 explosive energy release 137
 interaction with ionosphere
 122
magnetic topology change
138
magnetopause force 163
magnetotail force 163
neutral particle escape 137
open 117–119
reconnection rate 126
solar wind 308
stellar 253
stellar, T Tauri 254
torque 162
ultra cool stars 323
- magnetosphere-ionosphere
 interaction 122
- magnetotail 163
 current sheet 163
 plasma sheet 163
 Venus, Mars 114
- main sequence 66, 88, *see also*
 definition, 217, 218,
220, 251
magnetic activity 223
stellar wind 308
- mantle convection
 Earth 67
- Mars
 atmosphere and climate 269
 atmospheric composition
 297
 ionosphere 297
 magnetic field draping 114
 remanent magnetism -
 solar wind 115
mass loss 235
 angular momentum loss 225
Maunder Minimum 69, 223, 300
 and little ice age 287
mean free path 26

- electron-ion 58
 heliosphere 365
 methane
 evolution 267
 meridional circulation 84, 86
 mesosphere 5
 MHD
 approximation 122
 closure 43
 closure prescription 9
 collisionless conditions 365
 continuum assumption 44
 coupling 125
 description 8
 equations 45
 terms 46
 fluid approximation 44
 ideal 51
 induction equation 49, 50
 dynamo 70
 ideal 51
 introduction 42
 philosophy 43
 validity 44
 micropore 209
 Milankovic climate forcing 278
 minimum mass solar nebula 256
 mixing length theory 73
 moist greenhouse effect 268
 moment of inertia 161
 stars 225
 momentum equation
 ionospheric 124
 MRI *see* instability
N_____
 Neupert effect *see* flare
 Nice model
 hypothesis 265
 planet formation 243, 256
O_____
 obliquity 279
 oceans
 and plate tectonics 269
 inevitable loss 268
 Ohm's law 49
 generalized 34, 56, 60
 Ohmic current 123
 open magnetic flux 120
 optical depth *see also* definition,
 30
 orbital
 eccentricity 278
 interaction 171, 245
 orbital synchronization *see* tide
 oxygen
 evolution 267
 ozone
 hole 292
 photo-chemistry 290
 role of bromine, chlorine
 292
P_____
 p modes 208
 parallel conductivity 34
 Parker
 spiral 105
 transport equation 187
 Parker spiral 236
 Parker-Yoshimura sign rule 83
 particle
 acceleration 187
 first-order Fermi 198
 interplanetary shocks 200
 curvature drift 179
 drift
 general force 179
 E×B drift 178
 energization
 equation 177
 general force drift 179
 gradient drift 32, 179
 invariants 180
 motion
 gyration 177
 bounce motion 177
 guiding center 178
 invariant 180, 181
 invariants 180
 L parameter 181
 mirror point 177
 single 177
 precipitation 136
 scattering 185
 resonance condition 185
 particle-wave interaction 203
 Pedersen
 conductivity 34, 125
 current 126
 perfect gas law 20
 PFSS model
 approximation 107
 surface to heliosphere 371
 phase space density 181
 photo-chemistry 290
 photo-dissociation 291
 photo-ionization 293
 photosphere 5, 18
 photosynthetic habitable zone
 266
 pHZ *see* photosynthetic
 habitable zone
 pickup 37
 pitch angle 177
 planet
 formation 172
 'Nice' model 243, 256
 core accretion 242
 disk evaporation 259
 dust-disk evolution 257
 scenarios 241
 habitability 2
 migration 172
 planet-atmosphere coupling 124
 planetary
 insolation
 annual variation at
 Earth 278
 distance, eccentricity 278
 radiation balance 272
 system
 formation 325
 orbit migration 325
 planet migration 243
 planetesimal 242, 259
 plasma *see also* definition
 β *see also* definition, 53, 55
 characteristic scale-lengths
 60
 dusty 37
 oscillations
 time and length scales
 123
 properties in different
 settings 14, 59
 sources 38
 waves 52
 plate tectonics 69
 likely end of 269
 polar cap
 potential 126
 polytropic approximation 9
 pore 209
 potential field 48
 source surface model *see*
 also PFSS

- Poynting flux 72
 precession *see* tide, 171, 279
 of equinoxes and climate 280
 pressure balance 117
 pressure scale height 20
 protoplanetary disk 243, 244
 protostar
 deuterium fusion 252
 disk 166
 rotation 251
 protostellar
 cloud 25, 239
 disk
 ionization 249
- Q** _____
- quasi-hydrostatic balance 20
- R** _____
- radiation balance for planets 272
 radiation belt
 acceleration 201
 proton acceleration 205
 proton losses at Earth 206
 radiative
 equilibrium temperature 275
 forcing *see* climate
 heat flow 68
 recombination 294
 Rankine-Hugoniot jump
 conditions 102
 reconnection 154
 failure of frozen-in field
 condition 56
 important length scales 59
 Petschek 155
 Sweet-Parker 155
 Syrovatskii-Green 156
 terms in generalized Ohm's
 law 57
 topology in magnetosphere 138
 X-line 127
 relativistic electron acceleration
 mechanism 201
 external 201
 internal 203
 remanent magnetism 115
 resistivity and dissipation 57
 Reynolds number, magnetic *see*
 also definition, 51
 Reynolds rules 78
 Rossby number 75, 221
 Rossiter-McLaughlin effect 245
 rotation-activity relationship 222
 rotational discontinuity 41
 runaway acceleration 61
- S** _____
- scale height
 change with altitude 27
 density 90
 dependence on mass 27
 SEP *see* solar
 shielding current 40
 shock
 heating versus acceleration 193
 illustration in different
 settings 100
 jump conditions 102
 particle acceleration 193
 slow mode 194
 wave 100, 101
 shock-drift acceleration 196
 shock-induced acceleration 202
 Skumanich law 226
 slow-mode wave 53
 solar *see also* flare
 activity
 long-term variations 319
 radiative losses 214
 atmosphere
 domains 18
 heating 211
 radiation 214
 atmospheric heating 214
 differential rotation 74, 76,
 80, 86
 illustration 77
 energetic particles
 impulsive-event problem 188
 point-source evolution 188
 evolution 170
 irradiance
 climate driving 274
 penetration depth 20, 294
 photo-dissociation 20
 solar cycle 18
 magnetic field 69, 212
 magnetogram 70
 oscillations 208
 variability and climate 6
 wind 22
 critical point 24
 de Laval nozzle 364
 dynamic pressure 118
 energy source 363
 global merged
 interaction regions
 (GMIRs) 110
 interaction region 110
 interaction with
 planetary magnetic
 field 116
 magnetic braking 161
 near-Earth conditions 22
 non-conducting body 373
 Parker spiral 105
 pressure balance 118
 shock waves 110
 stream interactions 107
 stream structure in inner
 vs. outer heliosphere 110
 travel time 363
 variation on geological
 time scale 308
 wake 373
 sound speed 52
 space weather xi
 impact of grand maximum 302
 spectral type 218
 spin-orbit coupling 168
 star
 activity
 adulthood 228
 birth to ZAMS 227
 age estimate 252
 convection 88
 convective envelope 222
 dynamo 88
 early-type, core convection 88
 evolution
 time scale 226
 flare 223
 formation 239, 325
 angular-momentum
 problem 253
 birth line 251, 252
 observations 247

- intermediate mass 88
 internal structure 65
 magnetic activity 221, 223
 magnetic field 252
 mass loss 235
 properties 66
 solar-type 89
 Vega (α Lyrae) 152
 young star properties 251
 young-star activity 227
 star-disk coupling 160
 stellar
 activity 221
 cycle 223
 flat-activity 223
 saturation 221
 convection 64
 evolution
 brightening with age 266
 time scales 218
 magnetosphere 253
 T Tauri 254
 moment of inertia 225
 outer atmospheres
 heating 215
 rotation rate 225
 wind evolution 232
 stratification 16, 20, 22, 24, 63, 64, 74, 87–89
 stratosphere 5
 streamer belt 107, 108, 212, 371
 substorm
 Earth 140
 auroral breakup 134
 electric field 202
 expansion phase 134, 140
 growth phase 140
 recovery phase 134
 resemblance to flare 153
 Sun *see also* star
 active regions 86
 differential rotation 80
 formation in star cluster 383
 large-scale field 65
 mass loss 220
 polar magnetic field 86
 tachocline 80
 sunspot 5
 cycle 5, 69
 stars 223
 supergranulation 5, 208, 209
 supernova 218, 231, 261, 313, 321
 exposure 321, 383
T _____
 T Tauri star 160, 217
 accretion rate 253
 excess continuum 253
 tachocline 74, 91
 tangential drag 125
 Taylor-Proudman theorem 91
 tearing mode instability 138
 temperature scale height 68
 termination shock 127, 232
 thermal conduction 17, 23, 213
 coronal loop 55, 213
 thermal wind 93
 thermosphere 5
 composition
 seasons 27
 interhemispheric
 circulation 27
 temperature profile over
 geological time scales 304
 winds 34
 thermosphere-ionosphere
 coupling 124
 tidal
 acceleration 168
 bulge 169
 friction and rotational
 retardation 169
 tide 172
 binary stars 171
 breakup 377
 gravity 168
 irradiation 172
 orbital synchronization 170
 ozone, water-vapor
 absorption 173
 precession 171
 Toomre parameter *see also*
 definition, 255
 torque *see* gravitational,
 magnetic, 162
 total electron content (TEC) *see*
 also definition, 302
 transit light source effect 325
 transition region 5, 18
 transport equation
 Parker's 187
 troposphere 5
 turbulent
 diffusion 79
 electromotive force 78
 mixing 27
V _____
 Venus 115
 atmosphere and climate 269
 atmospheric composition
 297
 ionosphere 297
 magnetic field draping 114
 vertical winds 21
 viscous force 91
W _____
 water
 evolution 268
 wave
 Alfvén wave 52
 fast and slow mode 52
 steepening 101
 travel time 123
 wave-particle interaction
 Chorus-EMIC 204
 Wilson depression 210
 wind *see* disk, solar, stellar
 dividing line 235, 351
Z _____
 zero-age main sequence (ZAMS)
 219, 227

Physical constants, plasma quantities, and vector identities

Physical constants and other numbers

Table 18.1: Selected physical constants (cgs).

Quantity	Symbol	Value	Units
1 eV equivalent wavelength	-	$1.2 \cdot 10^{-4}$	cm
1 eV equivalent energy	-	$1.6 \cdot 10^{-12}$	erg
1 eV equivalent temperature	-	$1.2 \cdot 10^4$	K
arcsecond on the Sun	-	≈ 725	km
Astronomical Unit	AU	$1.5 \cdot 10^{13}$	cm
Avogadro's number	N_A	$6.0 \cdot 10^{23}$	mol ⁻¹
Boltzmann constant	k	$1.4 \cdot 10^{-16}$	erg/K
Earth mass	M_{\oplus}	$6.0 \cdot 10^{27}$	g
Earth radius	R_{\oplus}	$6.4 \cdot 10^8$	cm
Elementary charge	e	$4.8 \cdot 10^{-10}$	esu
Electron mass	m_e	$9.1 \cdot 10^{-28}$	g
Gravitational constant	G	$6.7 \cdot 10^{-8}$	dyne cm ² /g ²
Planck constant	h	$6.6 \cdot 10^{-27}$	erg s
Proton mass	m_p	$1.7 \cdot 10^{-24}$	g
Solar Luminosity	L_{\odot}	$3.8 \cdot 10^{33}$	erg/s
Solar mass	M_{\odot}	$2.0 \cdot 10^{33}$	g
Solar radius	R_{\odot}	$7.0 \cdot 10^{10}$	cm
Speed of light (vacuum)	c	$3.0 \cdot 10^{10}$	cm/s
Stephan-Boltzmann constant	σ	$5.7 \cdot 10^{-5}$	erg/cm ² /s/K ⁴

Plasma quantities

Table 18.2: Plasma quantities, mostly for thermal motions in fully-ionized plasmas.^a

Name/Symbol	Value ^b	Description
Frequencies and rates		
f_{ge} (Hz)	$2.8 \cdot 10^6 B$	electron gyrofrequency
f_{gi} (Hz)	$1.5 \cdot 10^3 B \frac{Z}{\mu}$	ion gyrofrequency
Thermal collision frequencies for fully ionized plasmas:		
ν_{ee} (s ⁻¹)	$3.6 \frac{n_e}{T_e^{3/2}} \ln(\Lambda)$	electron-electron collision rate
ν_{ii} (s ⁻¹)	$0.06 \frac{n_i}{T_i^{3/2}} \frac{Z^4}{\mu^{1/2}} \ln(\Lambda)$	ion-ion collision rate
ν_{ei} (s ⁻¹)	$\approx 0.5 \nu_{ee}$	electron-ion collision rate
Thermal length scales		
r_{ge} (cm)	$0.022 \frac{T_e^{1/2}}{B}$	electron gyroradius
r_{gi} (cm)	$0.95 \frac{T_i^{1/2}}{B} \frac{\mu^{1/2}}{Z}$	ion gyroradius
λ_D (cm)	$6.9 \frac{T^{1/2}}{n^{1/2}}$	Debye length
Velocities		
v_{Te} (km/s)	$3.9 T_e^{1/2}$	electron thermal velocity
v_{Ti} (km/s)	$0.091 T_i^{1/2} \frac{1}{\mu^{1/2}}$	ion thermal velocity
c_s (km/s)	$0.091 T_e^{1/2} \frac{\gamma^{1/2} Z^{1/2}}{\mu^{1/2}}$	ion sound velocity
v_A (km/s)	$2.2 \cdot 10^6 B \frac{1}{\mu^{1/2} n_i^{1/2}}$	Alfvén velocity
Dimensionless numbers		
electron Hall coeff.	$\frac{f_e}{\nu_{ee}} \approx 8 \cdot 10^5 \frac{B T_e^{3/2}}{n_e}$	electron gyro- to collision freq. ^c
ion Hall coefficient	$\frac{f_i}{\nu_{ii}} \approx 2.2 \cdot 10^4 \frac{B T_i^{3/2}}{n_i Z^3 \mu^{1/2}}$	ion gyro- to collision frequency ^c
plasma β	$3.5 \cdot 10^{-15} \frac{n_t T}{B^2}$	thermal to magnetic energy ^d

^a See <https://www.nrl.navy.mil/ppd/content/nrl-plasma-formulary>; ^b in cgs-Gaussian units. Symbols: B magnetic field strength (G); T temperature in K, n density in cm⁻³; γ the adiabatic index; $\ln(\Lambda)$ the Coulomb logarithm (typically 10 to 20, cf. Table 3.4); μ ion mass in units of the proton mass; $n_{e,i}$ electron or ion density; Z ion charge state; ^c for $\ln(\Lambda) \approx 10$; ^d where n_t the total particle density (ions plus electrons).

Vector identities

Table 18.3: Vector identities.

$$\begin{aligned} \mathbf{A} \cdot (\mathbf{B} \times \mathbf{C}) &= \mathbf{C} \cdot (\mathbf{A} \times \mathbf{B}) = \mathbf{B} \cdot (\mathbf{C} \times \mathbf{A}) \\ \mathbf{A} \times (\mathbf{B} \times \mathbf{C}) &= (\mathbf{A} \cdot \mathbf{C})\mathbf{B} - (\mathbf{A} \cdot \mathbf{B})\mathbf{C} \\ \nabla \times (\nabla \times \mathbf{A}) &= \nabla(\nabla \cdot \mathbf{A}) - \nabla^2 \mathbf{A} \\ \nabla \cdot (f\mathbf{A}) &= f\nabla \cdot \mathbf{A} + \mathbf{A} \cdot \nabla f \\ \nabla \times (f\mathbf{A}) &= \nabla f \times \mathbf{A} + f\nabla \times \mathbf{A} \\ \nabla \cdot (\mathbf{A} \times \mathbf{B}) &= \mathbf{B} \cdot (\nabla \times \mathbf{A}) - \mathbf{A} \cdot (\nabla \times \mathbf{B}) \\ \nabla \times (\mathbf{A} \times \mathbf{B}) &= \mathbf{A}(\nabla \cdot \mathbf{B}) - \mathbf{B}(\nabla \cdot \mathbf{A}) + (\mathbf{B} \cdot \nabla)\mathbf{A} - (\mathbf{A} \cdot \nabla)\mathbf{B} \\ \nabla \times \nabla f &= 0 \\ \nabla \cdot (\nabla \times \mathbf{A}) &= 0 \end{aligned}$$
